

# **Raman Spectroscopy and its Application in Nanostructures**

## Description of the cover

The transmission electron microscope (TEM) image on the cover shows the laser ablation synthesized silicon nano-wires (Si NWs) with average diameter of  $13 \pm 3 \text{ nm}^1$ . In the upper part of TEM image, the first observed Raman spectrum of Si NWs is shown together with the Raman spectrum of bulk silicon (Bulk Si) for comparing<sup>2</sup>.

<sup>1</sup>D.P. Yu, C.S. Lee, I. Bello, G.W. Zhou, and Z.G. Bai, *Synthesis of nano-scale silicon wires by excimer laser ablation at high temperature*, Solid State Commun., **105**, 403(1998).

<sup>2</sup>Bibo Li, Dapeng Yu, and Shu-Lin Zhang, *Raman spectral study of silicon nanowires*, Phys Rev B, **59**, 1645(1999).

# Raman Spectroscopy and its Application in Nanostructures

SHU-LIN ZHANG

*Peking University, Beijing*



A John Wiley & Sons, Ltd., Publication

This edition first published 2012  
© 2012 John Wiley & Sons Ltd.

*Registered office*

John Wiley & Sons Ltd, The Atrium, Southern Gate, Chichester, West Sussex, PO19 8SQ, United Kingdom

For details of our global editorial offices, for customer services and for information about how to apply for permission to reuse the copyright material in this book please see our website at [www.wiley.com](http://www.wiley.com).

The right of the author to be identified as the author of this work has been asserted in accordance with the Copyright, Designs and Patents Act 1988.

All rights reserved. No part of this publication may be reproduced, stored in a retrieval system, or transmitted, in any form or by any means, electronic, mechanical, photocopying, recording or otherwise, except as permitted by the UK Copyright, Designs and Patents Act 1988, without the prior permission of the publisher.

Wiley also publishes its books in a variety of electronic formats. Some content that appears in print may not be available in electronic books.

Designations used by companies to distinguish their products are often claimed as trademarks. All brand names and product names used in this book are trade names, service marks, trademarks or registered trademarks of their respective owners. The publisher is not associated with any product or vendor mentioned in this book. This publication is designed to provide accurate and authoritative information in regard to the subject matter covered. It is sold on the understanding that the publisher is not engaged in rendering professional services. If professional advice or other expert assistance is required, the services of a competent professional should be sought.

The publisher and the author make no representations or warranties with respect to the accuracy or completeness of the contents of this work and specifically disclaim all warranties, including without limitation any implied warranties of fitness for a particular purpose. This work is sold with the understanding that the publisher is not engaged in rendering professional services. The advice and strategies contained herein may not be suitable for every situation. In view of ongoing research, equipment modifications, changes in governmental regulations, and the constant flow of information relating to the use of experimental reagents, equipment, and devices, the reader is urged to review and evaluate the information provided in the package insert or instructions for each chemical, piece of equipment, reagent, or device for, among other things, any changes in the instructions or indication of usage and for added warnings and precautions. The fact that an organization or Website is referred to in this work as a citation and/or a potential source of further information does not mean that the author or the publisher endorses the information the organization or Website may provide or recommendations it may make. Further, readers should be aware that Internet Websites listed in this work may have changed or disappeared between when this work was written and when it is read. No warranty may be created or extended by any promotional statements for this work. Neither the publisher nor the author shall be liable for any damages arising herefrom.

*Library of Congress Cataloging-in-Publication Data*

Zhang, Shu-Lin.

Raman spectroscopy and its application in nanostructures / Shu-Lin Zhang.

p. cm.

Summary: "This book will be a useful contribution to an active area of physics research, and will describe the basic knowledge on three-dimensional (traditional) Raman spectroscopy and then discuss the main features of low-dimensional Raman spectroscopy"— Provided by publisher.

Includes bibliographical references and index.

ISBN 978-0-470-68610-2 (hardback)

1. Raman spectroscopy. 2. Nanostructured materials—Spectra. I. Title.  
QC454.R36Z43 2012  
543'.57—dc23

2011037455

A catalogue record for this book is available from the British Library.

HB ISBN: 978-0-470-68610-2

Set in 10/12pt Times Roman by Thomson Digital, Noida, India

# Contents

<i>Preface</i>	ix
<i>Acknowledgements</i>	xiii
<b>Part I Fundamentals of Raman Spectroscopy</b>	<b>1</b>
<b>1 Basic Knowledge of Raman Spectroscopy</b>	<b>3</b>
1.1 Spectrum and Spectroscopy	3
1.2 Scattering and Raman Scattering	5
1.3 Fundamental Features of Raman Scattering Spectra	9
1.4 Discovery of the Raman Scattering Effects and Observation of the First Raman Spectrum	10
1.5 Historical Development of Raman Spectroscopy	13
References	16
<b>2 Fundamental Theory of Light Scattering</b>	<b>19</b>
2.1 Description of Scattering	20
2.2 Macroscopic Theory of Light Scattering	26
2.3 Microscopic Theory of Light Scattering	39
References	45
<b>3 Experimental Foundation of Raman Spectroscopy</b>	<b>47</b>
3.1 Generality of Raman Spectral Measurements	47
3.2 Experimental Apparatus	56
3.3 Main Performance Parameters of Raman Spectrometers	79
3.4 Experimental Measurements	83
3.5 Data Processing of Recorded Raman Spectra	88
3.6 A Typical Example of Vibration Raman Spectra – Raman Spectrum of CCl <sub>4</sub>	94
3.7 Interference Spectrometer and Fourier Transform Optics	97
References	104
<b>4 Introduction to Modern Raman Spectroscopy I-New Raman Spectroscopic Branch Classified Based on Spectral Features</b>	<b>105</b>
4.1 Non-visible Excited Raman Spectroscopy	106
4.2 Resonant Raman Spectroscopy (RRS)	106
4.3 High-Order/Multiple-Phonon Raman Spectroscopy (MPRS)	110

4.4	Raman Spectroscopy under Extreme Conditions	114
4.5	Polarized Raman Spectroscopy (PRS)	115
4.6	Time-Resolved (Transient) Raman Spectroscopy (TRRS)	116
4.7	Space-Resolved Micro-Raman Spectroscopy and Raman Microscopy	118
4.8	Surface-enhanced Raman Spectroscopy (SERS)	119
4.9	Near-Field Raman Spectroscopy (NFRS)	121
4.10	Tip-enhanced Raman Spectroscopy (TERS)	130
4.11	Non-linear and Coherent Raman Spectroscopy (NLRS)	136
4.12	Coherent Anti-Stokes Raman Scattering (CARS)	138
4.13	Stimulated Raman Scattering (SRS)	145
	References	150
<b>5</b>	<b>Introduction to Modern Raman Spectroscopy II-New Raman Spectroscopic Branch Classified Based on Applied Objects</b>	<b>153</b>
5.1	Common Spectroscopic Basis Related to the Study and Application of Raman Spectroscopy	153
5.2	Chemistry Raman Spectroscopy	158
5.3	Condensed Matter Raman Spectroscopy	160
5.4	Biological and Medical Raman Spectroscopy	166
5.5	Geology and Mineralogy Raman Spectroscopy	175
5.6	Art and Archeology Raman Spectroscopy	177
5.7	Industry Raman Spectroscopy	178
5.8	Raman Spectroscopy in National Security and Judicature	181
	References	182
	<b>Part II Study of Nanostructures by Raman Spectroscopy</b>	<b>185</b>
<b>6</b>	<b>General Knowledge of Nanostructures</b>	<b>187</b>
6.1	Nanostructure, Characteristic Length, and Dimension	187
6.2	Nanomaterials	188
6.3	Properties of Nanostructures	190
6.4	Finite Size and Specific Surface	192
6.5	The Study of Nanostructure	196
	References	197
<b>7</b>	<b>Theoretical Fundamentals of Raman Scattering in Solids</b>	<b>199</b>
7.1	General Knowledge of Lattice Dynamics	200
7.2	Microscopic Model of Lattice Dynamics	213
7.3	Macroscopic Model of Lattice Dynamics	222
7.4	Lattice Dynamics of Amorphous Matter	229
7.5	Raman Scattering Theories in Solids	230
	References	246

<b>8 Theoretical Fundamentals of Raman Scattering in Nanostructures</b>	<b>249</b>
8.1 Superlattices	250
8.2 Nanostructure Materials	264
8.3 Micro-Crystal Models	283
8.4 Amorphous Feature and PDOS Expression of Nanostructure Raman Spectra	296
8.5 First-Principles/ <i>ab initio</i> Calculation of Nanostructure Raman Spectra	298
References	306
<b>9 Routine Raman Spectra of Nanostructures</b>	<b>309</b>
9.1 Characteristic Raman Spectra of Semiconductor Superlattices	310
9.2 Characteristic Raman Spectra of Nanosilicon	318
9.3 Characteristic Raman Spectra of Nanocarbons	325
9.4 Characteristic Raman Spectra of Polar Nano-Semiconductors	337
9.5 Multiple-Phonon Raman Spectra	343
9.6 Anti-Stokes Raman Spectra	352
References	357
<b>10 Raman Spectroscopy of Nanostructures with Exciting Laser Features</b>	<b>361</b>
10.1 Raman Spectra with Changing of Exciting Light Wavelengths – Resonant Raman Spectra	361
10.2 Raman Spectra with Exciting Laser Polarization	373
10.3 Raman Spectra with Exciting Laser Intensity	378
References	392
<b>11 Raman Spectra with Samples of Nanostructures</b>	<b>395</b>
11.1 Effects of Sample Sizes on Raman Spectra of Nanostructures	395
11.2 Effects of Sample Shapes on Raman Spectra in Nanostructures	409
11.3 Effects of Sample Component and Micro-structure on Raman Spectra in Nanostructures	413
References	417
<b>12 Electron-Phonon Interactions in Raman Spectroscopy of Nanostructures</b>	<b>419</b>
12.1 Abnormal Raman Spectral Features in Nanostructures	419
12.2 Origin of No FSE on Phonons	420
12.3 Fröhlich Interaction in Nanostructures	423
12.4 Theoretical Raman Spectra of Non-polar and Polar Nano-Semiconductors	424
12.5 Amorphous Feature of Nanocrystal Raman Spectra of No FSE on Phonons and the Breaking of Translation Symmetry in Nano-Semiconductors	426
References	428

<b>Appendices</b>	<b>429</b>
<b>Appendix I Electromagnetic Waves and Lasers</b>	<b>429</b>
I.1 Electromagnetic Wavelength	429
I.2 Laser Types	430
I.3 Laser Lines and Ionic/Atomic Lines of Gas Lasers used Commonly in Raman Spectroscopy	432
<b>Appendix II Standard Spectral Lines</b>	<b>438</b>
II.1 Spectral Lines of Mercury Lamp in Visible Range	438
II.2 Standard Lines of Neon Spectral Lamp	439
<b>Appendix III Raman Tensors</b>	<b>442</b>
III.1 Raman Tensors and Symmetric Attributes	442
III.2 Applications of Raman Tensors	447
<b>Appendix IV Constitution, Polarity, and Symmetry Structure of Crystals</b>	<b>452</b>
IV.1 Constitution, Polarity, and Crystal Structure of Crystals	452
IV.2 Syngony and its Basic Vector, Bravais Lattice, and Point Group Symmetry	455
<b>Appendix V Brillouin Zones, Vibration Modes, and Raman Spectra of Typical Ordinary and Semiconducting Crystals</b>	<b>458</b>
V.1 Brillouin Zones and Symmetrical Points of Cubic System	458
V.2 Vibrational Modes and their Symmetries of Several Crystals	460
V.3 Structures, Symmetries, and Raman Spectra of Several Semiconducting Crystals	461
<b>Appendix VI Physical Parameters, Constants, and Units</b>	<b>466</b>
VI.1 Periodic Table of the Elements	466
VI.2 Electronic Structure of Atoms	467
VI.3 Common Physical Constant and the Performance Parameters of Optical Glass	470
References	472
<b>Index</b>	<b>473</b>

# Preface

## 1 Background

In the last 20 years, after the generation of new nanostructures, study of the corresponding Raman spectra also began. First, the size of samples measured by common Raman spectral experiments is up to 1000 nm, however, Raman scattered light originates from objects related to atoms and molecules in matter, for example, the chemical bonds in molecules and the elementary excitations in solids, such as phonons, electrons, magnons, polaritons and so on. Therefore, the studying objects are at atomic and molecular levels, which means that Raman spectroscopic study of nanostructures is not affected by specimens being at the nanoscale and information on microstructure and inner movement of nanostructures is easily obtained directly, which is an advantage for any new nanostructure. Second, due to ever-advancing technology, Raman spectral detective sensitivity has been enhanced more than a million times and spatial resolution can reach a few nanometers, resulting in the “historical” Raman instrument becoming the “popular” and conventional one in use today.

The above two reasons bring an increasing number of people from non-Raman spectroscopic fields to join the Raman spectroscopic research ranks, especially in the nanostructure materials field. Meanwhile, due to intense interest in nanostructures today, many scholars in the Raman spectroscopic field have also joined research in Raman spectroscopy in nanostructures. These two groups tend to lack the knowledge of Raman spectroscopy and nanostructures, respectively. In addition, both groups also want to know the basic features, development, and up-to-date state of Raman spectroscopy in nanostructures, so that they can reach the peak of science and technology from the “predecessors’ shoulders”. Clearly, these needs call for a book that can provide both basic and current knowledge related to Raman spectroscopy, nanostructures, and Raman spectroscopy in nanostructures, which is written in the hope that it does indeed meet these needs.

From the late 1970s, I started my research in Raman spectroscopy. With the limited research funding at that time, I had to start my research alone, developing a laser Raman instrument based on an outdated prism spectrometer. The successful development of that instrument marks the first Raman spectrometer in a laboratory in China and also, first-hand, I gained the experimental techniques. Thus, I was later able to reconstruct the commercial large-type Raman spectrometer through replacement of the original optical components, in sample optics and original data acquisition and processing systems, with home-made components. This greatly improved the performance of the commercial Raman spectrometer over the original, for example, the Raman spectra in low frequencies with wide spectral range ( $3\text{--}120\text{ cm}^{-1}$ ) could be measured, which created a good foundation for the high level of Raman spectroscopy in nanostructures to come later. In 1985, as a visiting scholar in the Klein research group and then a part-time associate professor at the University of Illinois at Urbana-Champaign, I transferred my research work to Raman spectroscopic studies of

superlattices, meaning my Raman spectroscopic work in nanostructures began. In the last quarter of the twentieth century, I did not leave this field and thus I saw the birth of many landmark nanostructures, such as porous silicon, carbon nanotubes, diamond nanoparticles, polar semiconductor SiC nanorods, ZnO nanoparticles and so on, and left my footprint on Raman spectroscopy in nanostructures. Since the Raman instrument gradually became popular, an increasing number of new people joining the Raman spectroscopic ranks wanted to learn and understand the fundamentals of this discipline. Thus, from the beginning of the 1990s, I was frequently invited to lecture at various academic units. For example, I was invited to teach a graduate course with one semester “Fundamentals of Raman spectroscopy” at the Graduate School of Chinese Academy of Science. After 1998, I was invited to give plenary or invited talks in the field of Raman spectroscopy in nano-semiconductors in six of the International Conferences on Raman spectroscopy and had to write the review works. In 2008, based on the above work, I published a book, written in Chinese, which is related to Raman spectroscopy and nano-semiconductors. All of the above make me realize why I may have received an invitation from Wiley, which was decided based on the recommendation of other scientists, to write a book entitled “Raman Spectroscopy and its Application in Nanostructures” and contribute it to my old and new colleagues in the field.

## 2 Highlight

Historically, Raman spectroscopy is first an experimental science; the discovery of Raman scattering by C.V. Raman is not based on theoretical expectations but solely on experimental work. This book will emphasize experimental work that has become increasingly dependent on experience. The experimental observations reflect that observations and theory of the phenomena can capture the essence of that phenomena. Scientific research should finish the task to reveal the nature of the phenomena. Therefore, the principles of Raman scattering and analysis of experimental phenomena will be introduced theoretically. In addition, the successful development of instruments and the improvement of experimental techniques depend largely on understanding the principles of Raman scattering and Raman instruments in depth, which necessarily involves the relevant theoretical issues. Therefore, in this book, we will take into account both experimental and theoretical approaches. Considering that some readers will not be theoretical scientists, the theoretical explanation focuses on revealing the essence of the problem rather than complex theoretical analysis and calculations.

This book has two parts: fundamentals of Raman spectroscopy and Study of Nano-structures by Raman Spectroscopy.

### 2.1 Part I Fundamentals of Raman Spectroscopy

In the first chapter, after describing the general concept of spectra, the focus is on the scattering produced by the irradiation of matter and the fundamental features of Raman scattering spectra. There follows a short description of the discovery of Raman scattering and the historical development of Raman spectroscopy.

In the second chapter, first the illustration of scattering experiments by a schematic diagram is given. Then, the basic physical quantities of scattering, that is, the scattering cross sections,

differential cross sections, and transition probabilities are described. In the last two sections of the chapter, the macro- and micro-theories of light scattering are introduced, by which the origin and nature of the fundamental features of Raman spectra are described.

A large part of the third chapter involves the technical aspects of experiments and is mostly written on the basis of experimental work in my laboratory. This book is aimed at readers new to the Raman spectroscopic field, who may not yet have acquired professional Raman experimental basics. The description relating to experimental techniques will be specific and given generous space. First, the generality of Raman spectral measurements will be mentioned, which includes the relationship between observed Raman spectral features and the differential scattering cross section, as well as the techniques key to measurements. Then the experimental apparatus will be described by using a constructive scheme layout. With the grating spectrometer used mostly as an example, the function and the technical requirements of various constituent parts in spectrometers are introduced. The introduction of measurement techniques will be mentioned after the description of main performance parameters of Raman spectrometers. In measurement techniques in particular, the intensity and polarization dispersions of the light wavelength excited in optical elements and the corresponding correction technology are described, which often tend to be overlooked. The measurement techniques focus on the choice and regulation of instrument parameters. The data processing of recorded Raman spectra is introduced with the help of some practical examples, which is a necessary step to obtain the correct results from the original spectra and perform correct spectral analysis and research, particularly in the case of weak spectral signals. In Section 5 of the chapter, a typical example of vibration Raman spectra, specifically the Raman spectra of  $\text{CCl}_4$ , is introduced. In the last section, a brief introduction of the non-grating spectrometer and the Fourier transforms optics are described.

As with all scientific and technological development, the technology and application of Raman spectroscopy are also growing, resulting in many new branches and greatly expanding Raman spectral applications. The fourth chapter introduces these new branches from the view of spectroscopy. The fifth chapter focuses on the introduction of new branches of Raman spectroscopy from the view of application.

## 2.2 Part II Study of Nanostructures by Raman Spectroscopy

Obviously, to apply Raman spectral research to nanostructures, we first need an understanding of nanostructures. Therefore, the first chapter of Part II is dedicated to describing nanostructures. First, we note that from a strictly scientific point of view, nanostructures should be defined by using the so-called “characteristic length”. Then some important properties of nanostructures are introduced, including two basic characteristics having essential effects on Raman spectra: the limited scale and huge specific surface are highlighted. Then the history of generation and study of nanostructures are mentioned briefly. From an historical perspective of development and structural characteristics, we classify the two-dimensional layered structures (superlattices and multiple quantum wells) and one- and zero-dimensional structures (nanowires, nanotubes, and nanodots, etc.) into two categories. In addition, the Raman spectra of polar and non-polar nano-semiconductors are very different. Correspondingly, the research and application of Raman spectroscopy will be discussed, distinguished by the above classifications.

It is not enough to merely describe the basics of Raman spectroscopy, as its content is deduced based on an infinite system and does not fit nanostructures with limited scale, which means that Raman spectral features and scattering theory in nanostructures will clearly be different from those in bulk solids. The nanostructures discussed in this book are solids with nanoscales, therefore, in Chapter 7, the theoretical fundamentals of Raman scattering in solids will be explained first, of which the introduction is very short as there are a large number of textbooks the reader can refer to. In Chapter 8, based on the theory of Raman scattering in solids, the finite size effects on Raman spectroscopy of nanostructures are explored and the relevant representative macro- and micro- theoretical models of Raman spectra of nanostructures are described. Because the number of atoms inside nanostructures is greatly reduced, the rigorous quantum mechanical calculation, a major development in theoretical physics and theoretical chemistry in recent years, is introduced briefly in the section entitled “First-principles/*ab initio* Calculations of Nanostructure Raman Spectra”.

Chapters 9–11 describe the Raman spectra in nanostructures under different experimental conditions. Chapter 9 is devoted to the first-order (single phonon), high-order (multi phonon) Stokes and anti-Stokes Raman spectra of different samples under fixed excitation wavelength, polarization, and weak power irradiation, all of which are the so-called “Routine Raman spectra of nanostructures”. The first category is the so-called intrinsic Raman spectra or fingerprint spectra, which are the basic spectra in scientific research and analytical applications. In Chapter 10, the Raman spectroscopic features are described where the sample conditions remain unchanged while the excitation wavelength, polarization characteristics, and power do change. The change of excitation wavelengths often induces a so-called resonance Raman spectrum, and change of laser power is often used to obtain variable-temperature Raman spectra. Chapter 11 describes the Raman spectra of nanosample characteristics such as sample sizes, shape, components, and microstructures due to the preparing and outside conditions of samples.

In Chapters 9–11, we describe some specific Raman spectroscopic results in nanostructures observed in recent years, of which an abnormalities observed in the optical phonons of polar nano-semiconductors are very interest: the Raman frequencies do not change with sample sizes. In the final chapter, Chapter 12, we explore the source and nature of this abnormal phenomenon based on the properties of optical phonons and the electron-phonon interaction in polar semiconductors differing from other phonons. This is verified, by experimental observations and theoretical calculations corroborating each other, that the source of the abnormal phenomenon is the Fröhlich long-range Coulomb electron-phonon interaction possessed uniquely in the optical phonons in polar nano-semiconductors. The nature of this abnormal phenomenon is the breaking of translational symmetry, which was confirmed by the optical phonon Raman spectra of polar nano-crystalline semiconductors displaying the amorphous characteristics. The above results also suggest that the scale criterion of translational symmetry is different in bulk matter and nanomatter: it is the same for all objects in bulk matter, while it varies for different objects in nanostructures.

# Acknowledgements

In the Preface, I mentioned that this book is partly based on my past decades of research work. This research received ongoing support from the Natural Science Foundation of China, the National Basic Research Program of China and Research Grants Council (RGC) of Hong Kong. Many colleagues and students attended the various periods of study supported by the above funds. To this end, first I wish to thank them for their support and hard work. In the process of writing this book, many colleagues, such as Dr. K.T. Yue, Dr. Peter Dunten, Dr. Hui Zhang, Dr. Li Zhang, Dr. Pengwei Wang, Dr. Lei Xia, Dr. Chunxiao Wang, Bo Shuang, Dongyao Li, Tianyi Sun, Bing Xu, Yanchao Xin, and Dong Zhao participated in the individual chapters of transitional writings, respectively, in which Mr. Bo Shuang, Dr. Lei Xia, and Dr. Chunxiao Wang participated in some technical work in Part II. For their contributions, I would like to express my sincere thanks. Finally, I would like to thank my wife Sujuan Li for the consistent support of my work.



**Plate 1 (Figure 1.1)** Examples of spectra: (a) a rainbow; (b) a scheme of spectra by a dispersive element prism

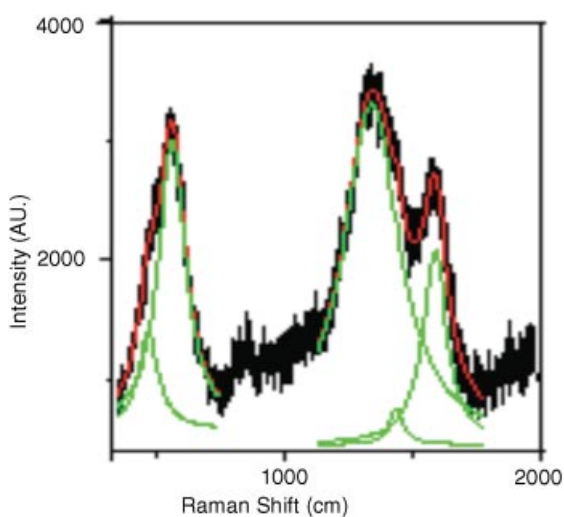


**Plate 2 (Figure 3.40)** A sample of smoothing and fitting: original (black), smoothed (red), and fitting (green) spectra

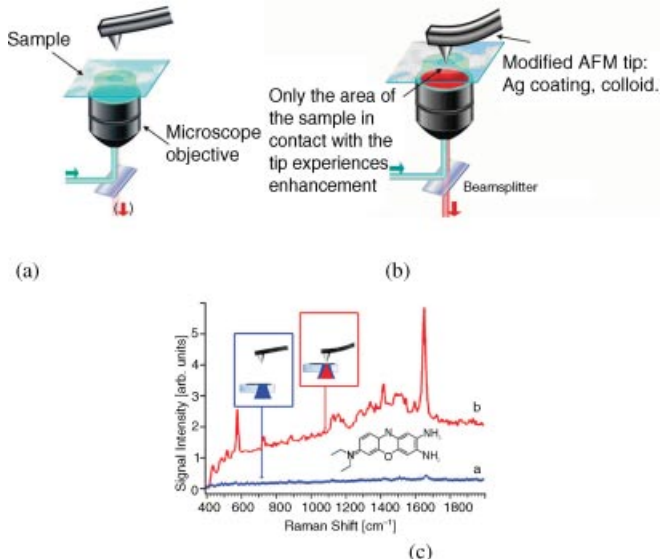


**Plate 3 (Figure 4.27)** Tip configurations of Normal (a), tip enhanced (b) silver coated tip probes with 10–15 nm thickness, and observed Raman spectra (c) correspondingly [62]

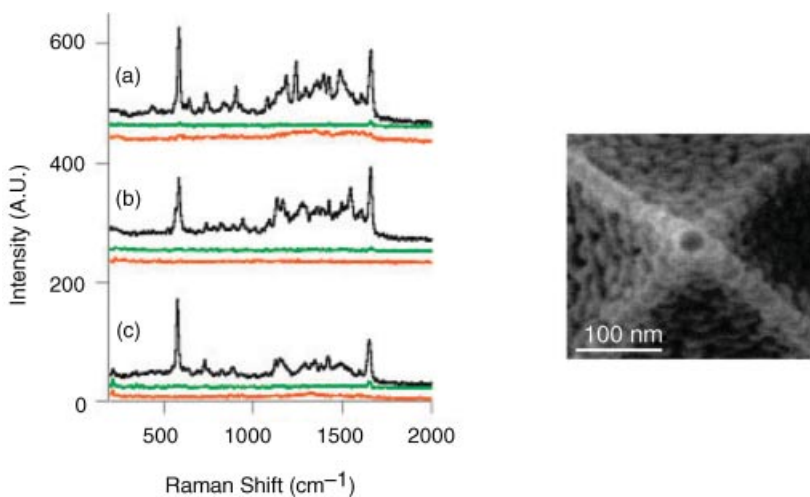


**Plate 4 (Figure 4.28)** Left: The Raman spectra of brilliant cresyl blue thin film acquired with tip in contact (black) and retracted (green traces) are shown for Ag coated (a) SiO<sub>2</sub>, (b) SiO<sub>x</sub>/SiN, and (c) AlF<sub>3</sub>/SiN tips. The orange traces are the tips' spectra collected after the experiments. Right: High-quality SEM image of an Ag-coated tip used in the experiments [65]

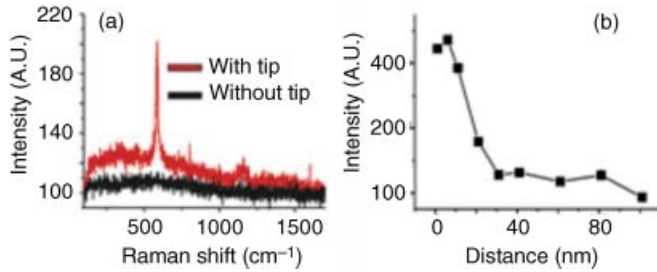


**Plate 5 (Figure 4.30)** (a) TER spectra from a few ( $< 10$ ) BCB molecules and (b) dependence of Raman intensity on tip-sample distance [66]

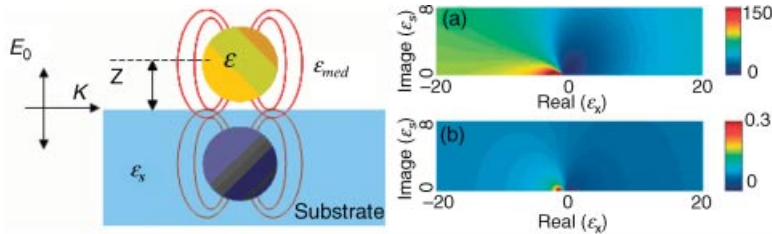


**Plate 6 (Figure 4.31)** Image dipole (left) and calculated influence of the substrate on the electric field enhancement (right): (a) Enhancement map at the tip apex as a function of the substrate permittivity. Tip radius  $r = 20 \text{ nm}$ , tip length  $l = 1000 \text{ nm}$ , tip angle  $\alpha = 15^\circ$ , and tip-substrate distance  $1 \text{ nm}$ . (b) Effective polarizability map of a dipole  $1 \text{ nm}$  above an infinitely large substrate as a function of the permittivity of the substrate [78]

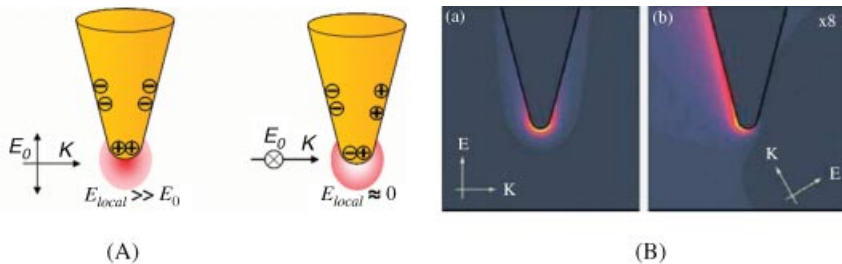


**Plate 7 (Figure 4.32)** Lightning rod effect showing the polarization direction of the incident radiation. (A) Physical picture and (B) calculated field distribution at a sharp Au tip with a diameter of  $5 \text{ nm}$ . (a) Field distribution for an incident electric field vector parallel to the tip shaft showing localization of the electric field at the tip apex. (b) Field distribution for an incident electric field oriented non-parallel to the tip shaft. The field is no longer confined to the tip apex [80]

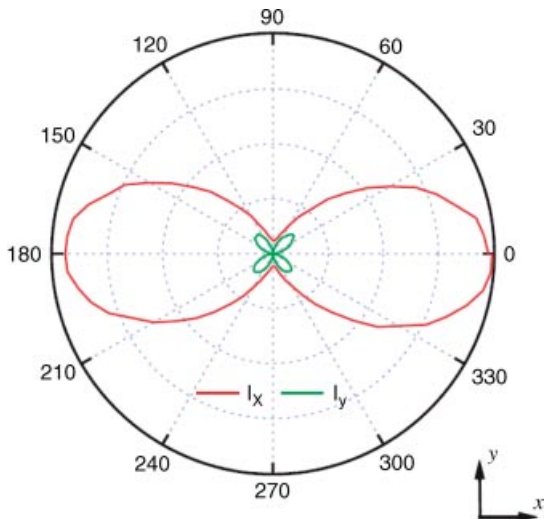


**Plate 8 (Figure 4.37)** CARS polarization responses  $I_x$  and  $I_y$  (represented as polar plots) for pure water when the Stokes linear polarization is set parallel to the  $x$ -axis and the pump linear polarization rotates from  $0^\circ$  to  $360^\circ$  [94]. Reprinted from F. Munhoz, et al., Raman depolarization ratio of liquids probed by linear polarization coherent anti-Stokes Raman spectroscopy, *J. Raman Spectrosc.*, 40, 775 (2009) with permission of John Wiley and Sons

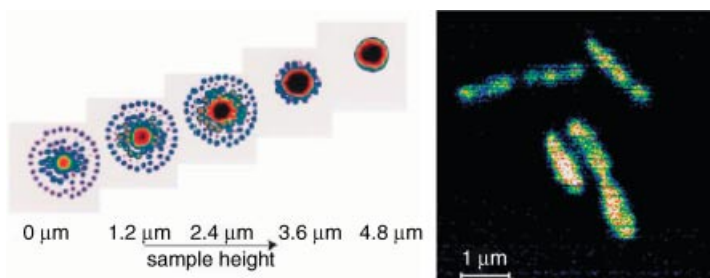


**Plate 9 (Figure 4.40)** The first image of single biological cell by s CARS microscope [97]

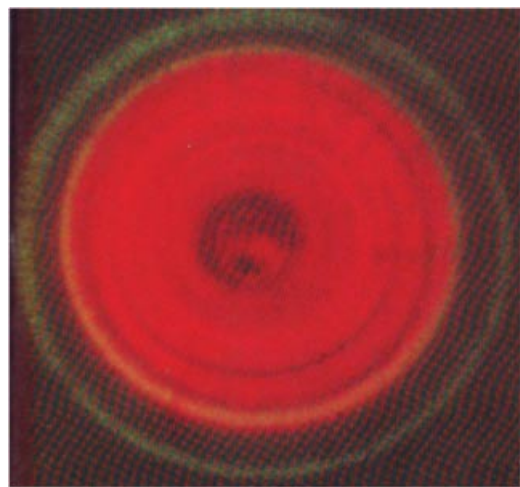


**Plate 10 (Figure 4.43)** An angle-dependent Raman spectrum of SRS [103]

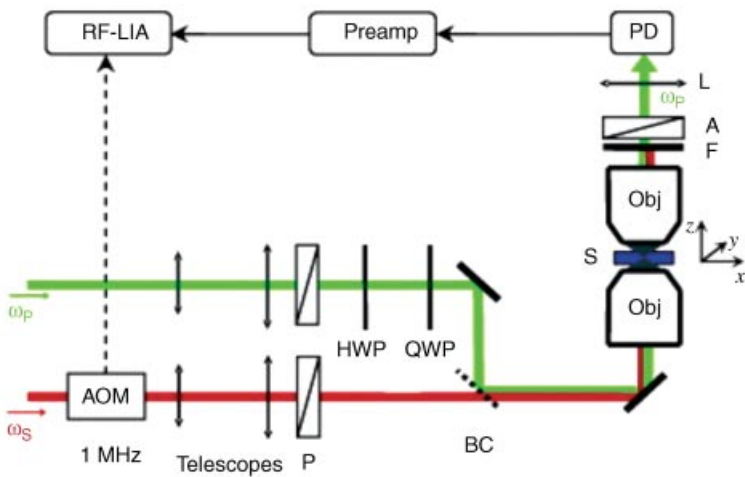


**Plate 11 (Figure 4.44)** Schematic of the SRS microscope configured for SRL detection. (P, polarizer; HWP/QWP, half/quarter-wave plate; BC, dichroic beam combiner; Obj, objective lens; F, filter; A, analyzer; L, lens; S, sample; AOM, acoustooptical modulator; PD, photodiode detector; Preamp, pre-amplifier; RF-LIA, radio-frequency lock-in amplifier [105])

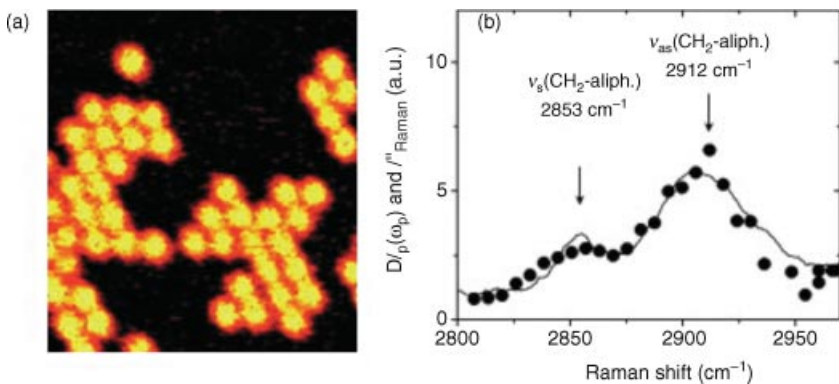


**Plate 12 (Figure 4.45)** SRS microscopy of a polystyrene bead. (a) SRL image of self-assembled 2.4  $\mu\text{m}$  polystyrene beads in water recorded with pump and Stokes beams at 716 nm and 904 nm, corresponding to a Raman shift of 2904  $\text{cm}^{-1}$ . The average power of each beam was 5 mW. The image size measures 23.1  $\mu\text{m} \times$  25.6  $\mu\text{m}$  (140  $\times$  155 pixels) with a pixel dwell time of 4 ms. (b) Measured SRL spectrum (filled circles) of a single 2.4  $\mu\text{m}$  polystyrene bead recorded with the Stokes wavelength at 901 nm and the pump wavelength tuned from 711 to 719 nm. The average power of each beam was 10 mW. Both the aliphatic symmetric  $\nu_s(\text{CH}_2)$  and anti-symmetric  $\nu_{as}(\text{CH}_2)$  Raman modes of polystyrene at 2853 and 2912  $\text{cm}^{-1}$ , respectively, are clearly resolved. Shown for comparison as a solid line is the parallel-polarized spontaneous Raman spectrum  $I_{\text{Raman}}^{\parallel}$  of bulk polystyrene [105].

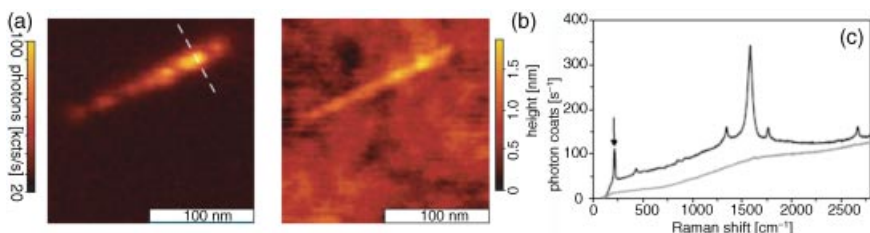


**Plate 13 (Figure 5.13)** (a) NF Raman image from G band of carbon, (b) topographic image, (c) near-field Raman spectrum detected on top of the SWNT at the position marked in (a) (NF (black line) and far-field (blue line)) [12]

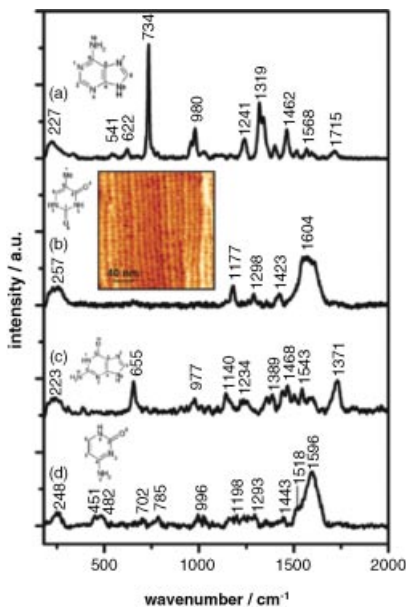


**Plate 14 (Figure 5.19)** TERS spectra (background-corrected) of DNA bases adsorbed at Au(111): (a) adenine; (b) thymine; (c) guanine; (d) cytosine; normalized to 1 s integration time at 2 mW incident power. Inset shows an example of an STM image of a thymine self-assembled monolayer of Au(111) recorded after 12 h adsorption with an Au probe [24]

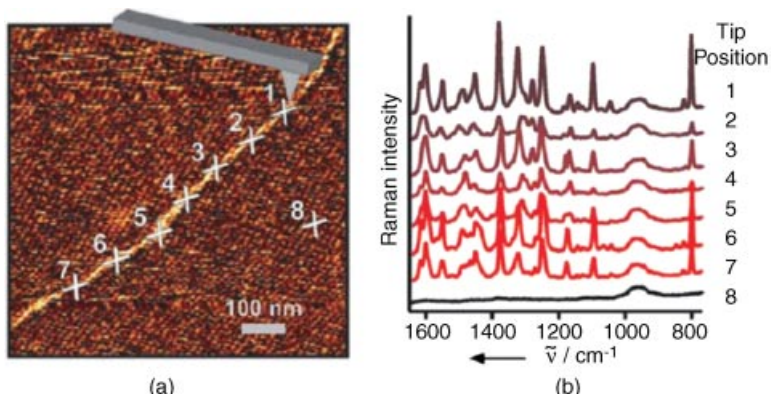


**Plate 15 (Figure 5.20)** AFM topography image (a) and TERS spectra (b) of a polycytosine homopolymer. Eight spots are shown corresponding to the positions where TERS measurements were taken. (b) The TERS spectra taken at the eight positions [27]

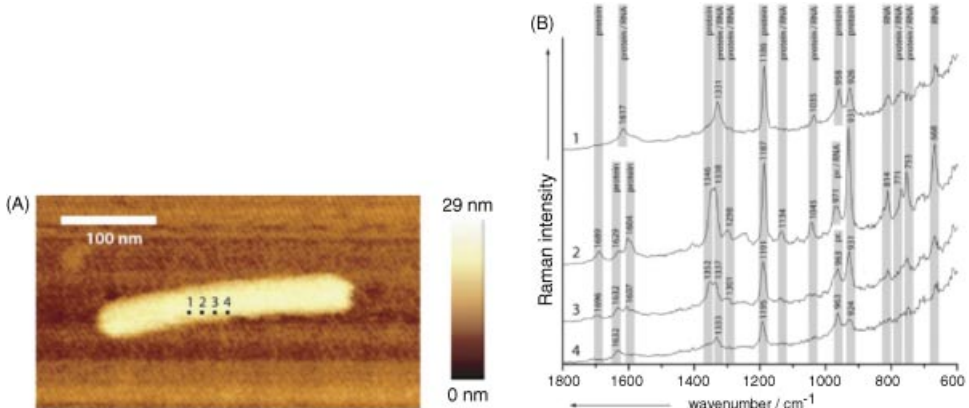


**Plate 16 (Figure 5.21)** TERS investigations of a single tobacco mosaic virus particle. (a) AFM image of the investigated virus particle. The positions of the TERS tip in respect to the virus particle are marked. (b) The TERS spectra of the virus particle recorded at various positions [28]

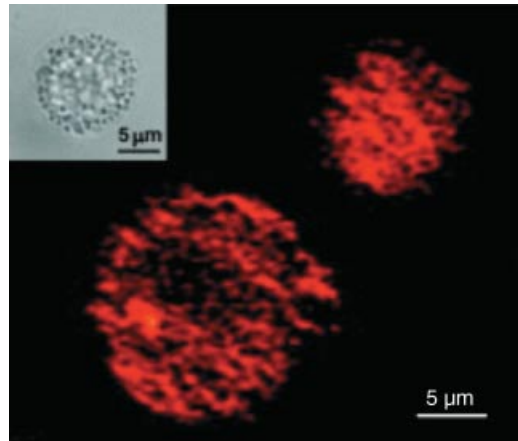


**Plate 17 (Figure 5.23)** SRL images of unstained human HL60 cells in an aqueous environment. The size of the image is  $38.3 \mu\text{m} \times 33.6 \mu\text{m}$  ( $200 \times 170$  pixels). The pump and Stokes beams were at  $746.5$  and  $852$  nm with powers of  $7.5$  and  $30$  mW, respectively. The corresponding Raman shift was  $1659\text{ cm}^{-1}$  on resonance with the C=C stretching vibrations. The image pixel dwell time was  $10$  ms [31]

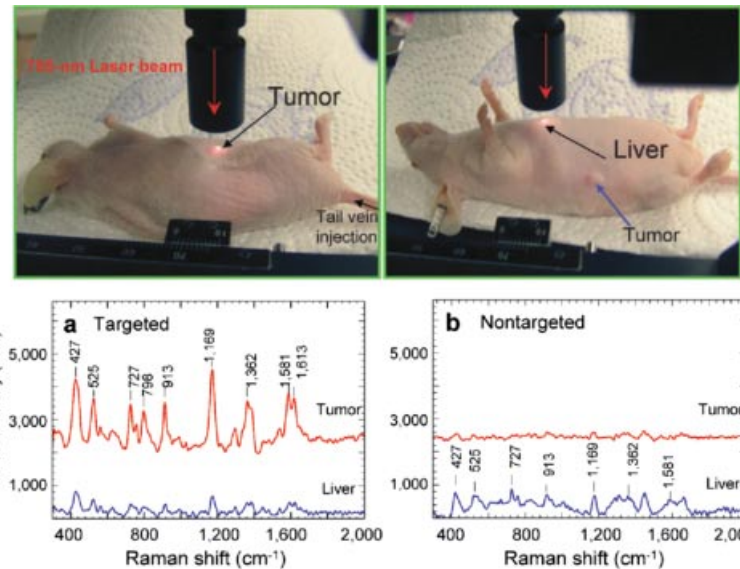


**Plate 18 (Figure 5.25)** *In vivo* cancer targeting and surface-enhanced Raman spectra. Top: Photographs of a laser beam focused to the tumor site or to the anatomical location of liver. Lower: Raman spectra obtained from the tumor and the liver locations by using (a) targeted and (b) non-targeted nanoparticles [29]

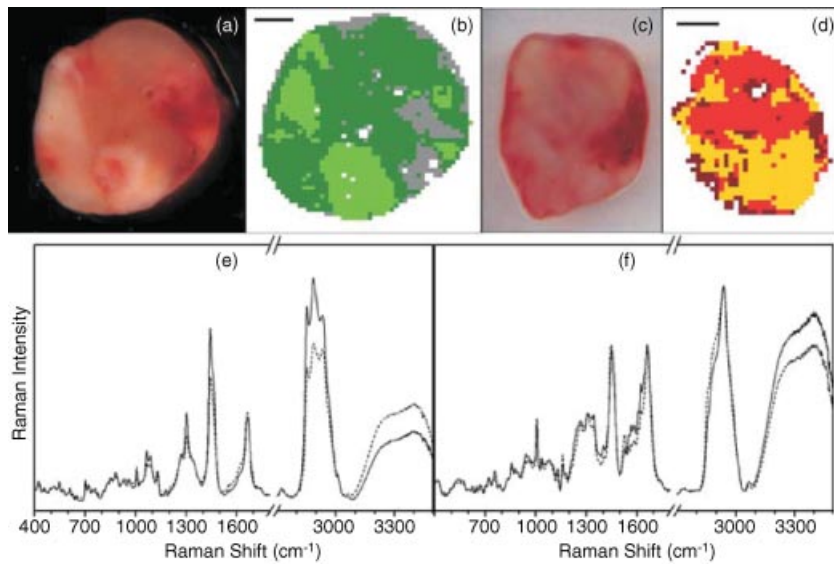


**Plate 19 (Figure 5.27)** Photographs of Raman imaging of non-dried normal brain tissue (a, b) and a brain metastasis of lung cancer (c, d). Raman images were segmented into three clusters by k-means cluster analyzes. Raman spectra of the light green (solid in (e)), dark green (dashed in (e)), red (solid in (f)), and orange clusters (dashed in (f)), are due to proteins, lipids, hemoglobin, carotene, and water differing throughout the spectra [34]

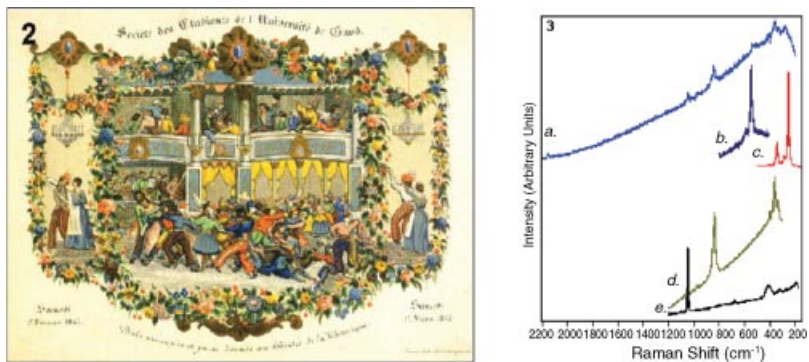


**Plate 20 (Figure 5.32)** Raman spectra (3) of colored regions of porcelain card (2) [49]

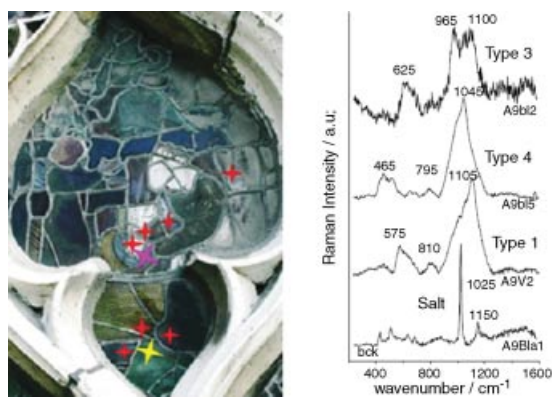


**Plate 21 (Figure. 5.33)** Rose window panes and its Raman spectra [50]

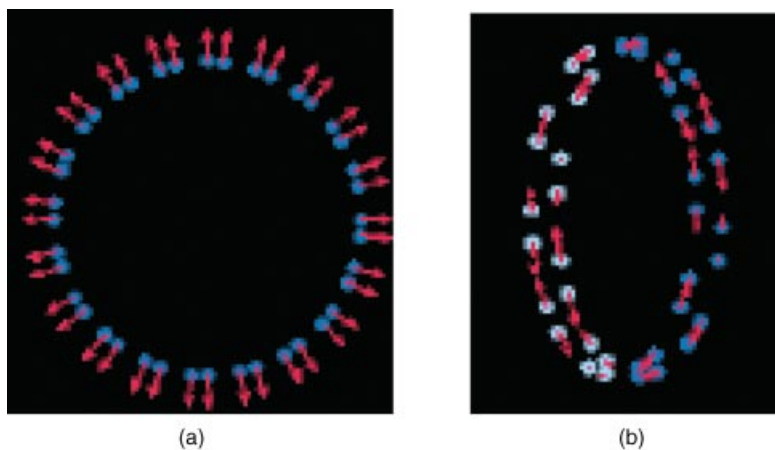


**Plate 22 (Figure 9.27)** Specific vibration manners of RBM (a) and G mode (b) [53]

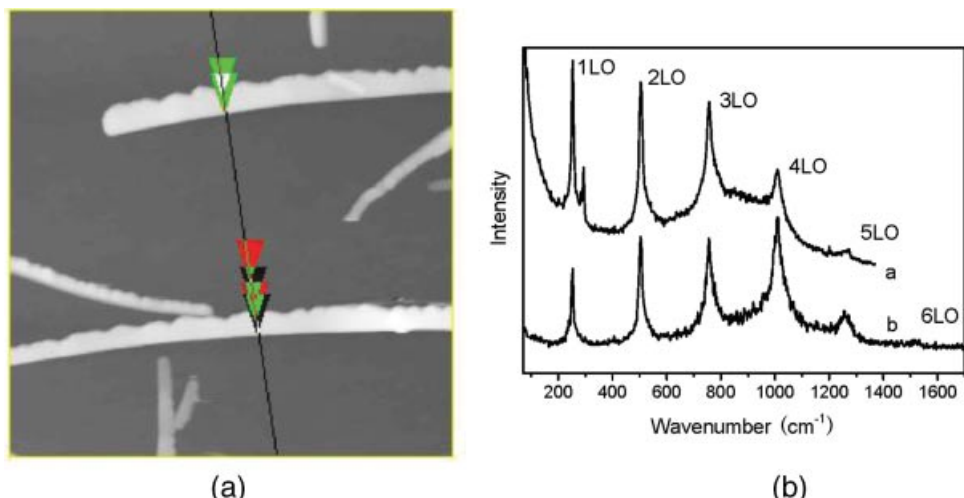


**Plate 23 (Figure 10.2)** Atomic force microscopy (range is  $2 \times 2 \mu\text{m}$ ) (a) and MP Raman spectra excited by the laser of  $442 \text{ nm}$  with  $0.04 \text{ mW}$  power (b) of mono- root ZnSe nanowire. In (a), the white horizontal sawtooth-like bar is the ZnSe sample, while the fine slash is the scanning path in the Raman measurement

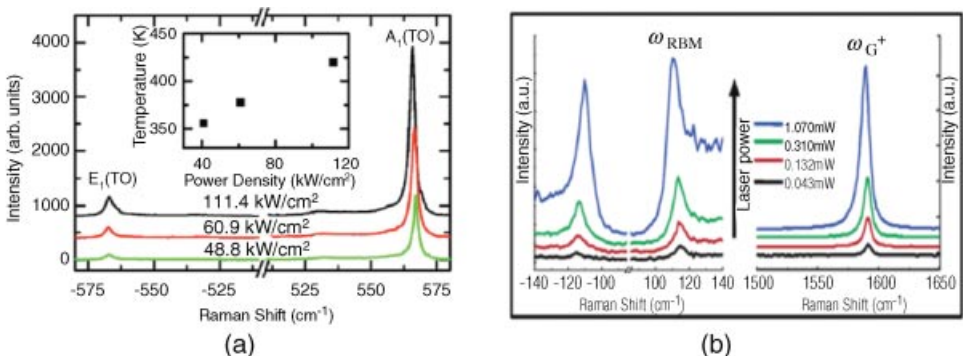


**Plate 24 (Figure 10.26)** Stokes and anti-Stokes Raman spectra of freestanding single GaN nanorod (a) and suspending isolated single-layer CNTs (b) with lasers with different power densities [33,34]

# **Part I**

## **Fundamentals of Raman Spectroscopy**

# 1

## Basic Knowledge of Raman Spectroscopy

The term “Raman spectroscopy” is an abbreviation of “Raman scattering spectroscopy”. Basic knowledge of Raman spectroscopy can be gained by understanding the meaning of three words: “spectroscopy”, “scattering”, and “Raman”.

### 1.1 Spectrum and Spectroscopy

Spectroscopy can be considered in three parts: theory, experiment, and application. These will be described in more detail later. In this section, only spectrum are discussed.

#### 1.1.1 Optical Spectrum

A band of colors is called a “spectrum”. The rainbow, as shown in Figure 1.1a (see color Plate 1 for the original Figure 1.1), is one example of a spectrum. A spectrum is usually one recorded by an artificial dispersive element called a spectrograph, as shown in Figure 1.1b.

#### 1.1.2 Classification of Spectra

##### 1.1.2.1 Classification Based on Optical Effects

When a medium is illuminated by light, the interaction between the light and the medium produces many kinds of optical effects and phenomena. Figure 1.2 shows some examples of major optical effects.

The spectrum is a record of all the optical effects. As such, the spectra can be divided into many types, based on the different optical effects such as reflection, transmission, absorption, emission (fluorescence, luminescence), and scattering spectra. All of these spectra help us to understand the kind of interactions and the inner structure and motion of the medium.

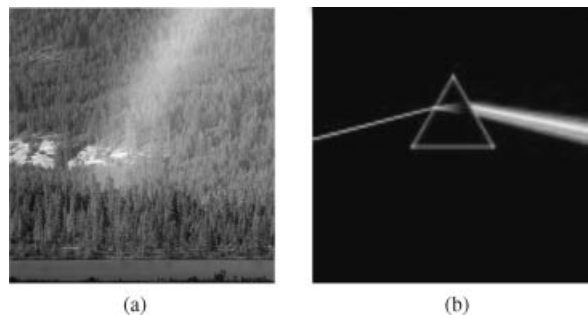


**Figure 1.1** Examples of spectra: (a) a rainbow; (b) a scheme of spectra by a dispersive element prism

For example, the measurement and understanding of atomic spectra led to the elucidation of the atom's inner structure and played a key role in the establishment and development of quantum theory.

This book concentrates on discussion of scattering spectra. Light scattering based on fundamental and broad ideas is introduced in detail in the next section.

### 1.1.2.2 Classification Based on Spectral Parameters

The spectrum, as a record of optical effects mentioned above, reflects the dependence of electromagnetic radiation intensity on its relevant parameters.

The radiation intensity,  $I$ , can be expressed as

$$I = |E|^2 \quad (1.1)$$

where  $E$  is the electric field given by

$$E(\mathbf{r}, t) = E_0(\mathbf{r}, t) e^{i(\mathbf{k} \cdot \mathbf{r} - \omega t)} \quad (1.2)$$

where  $\omega$ ,  $\mathbf{k}$ ,  $\mathbf{r}$ ,  $t$ , and  $E_0$  are the measured frequency (the reciprocal of wavelength  $\lambda$ ), wave vector (representing the propagating direction), position vector, time, and the amplitude of the electric field, respectively. These are the only relevant parameters in the measurement of spectra.

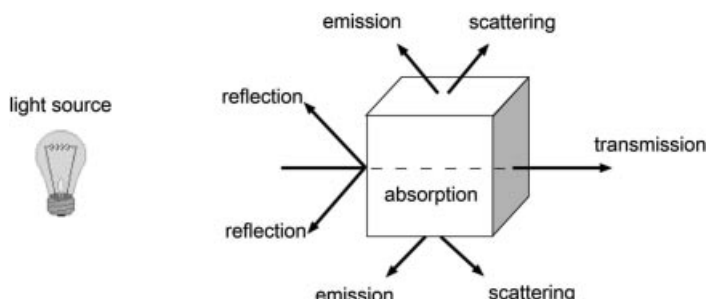


**Figure 1.2** Different optical effects caused by interaction between light and a medium. Reprinted from S.-L. Zhang, Raman Spectroscopy and Low-dimensional nanoscale Semiconductors, Science Press, (2008)

Depending on the spectral parameter of interest, the measured spectra can be classified into different categories. With respect to different excited light wavelengths  $\lambda_0$ , spectra with spectral intensity  $\mathbf{I}$  on the rest of the parameters  $\omega$ ,  $\mathbf{k}$ ,  $\mathbf{r}$ ,  $t$ , and  $\mathbf{E}_0$  have been classified as:

- *Visible and non-visible excited spectra*: these spectra are excited by visible and non-visible light, respectively. The non-visible excited spectra are further divided into ultraviolet (UV), infrared (IR), and Terahertz (THz,  $\lambda = 0.1 \sim 1$  mm) excited spectra, and so on.
- *Visible and non-visible spectra*: the recorded spectral wavelength  $\lambda$  is localized in the visible and non-visible range. The non-visible spectra are further divided into the UV, IR, and THz spectra, and so on.
- *Spontaneous and stimulated spectra*: these spectra are due to spontaneous and stimulated radiation, respectively.
- *Linear and non-linear spectra*: the spectral intensity  $\mathbf{I}$  depends on the first- and high-order of parameters  $\mathbf{E}_0$ , respectively.
- *Single- and multi-order spectra*: these are the spectra at the single- and multiple-folded frequency  $\omega$  of the Raman mode, respectively.
- *Angle distributed spectrum*: this is the dependence of spectral intensity  $\mathbf{I}$  with respect to the direction of the parameter  $\mathbf{r}$  of the measured position, that is, the propagating direction of spectral light, or the direction of parameter  $\mathbf{k}$ .
- *Polarized and non-polarized spectrum*: this spectrum is measured under excitation by polarized light and detection in a fixed polar direction, that is, in the direction that excited and recorded  $\mathbf{E}$  are both fixed.
- *Steady state and transient (time resolved) spectra*: this is the spectral intensity  $\mathbf{I}$  with respect to the parameter  $t$  at a long and very short duration, respectively (Figure 1.3a,b).
- *Far- and near-field spectra*: this is the measured spectral intensity  $\mathbf{I}$  in the region of magnitude of the position parameter  $\mathbf{r} \gg \lambda$  (light wavelength) and  $\ll \lambda$ , respectively.
- *Frequency and image spectra*: the former records the spectral intensity  $\mathbf{I}$  variation with spectral parameters,  $\omega$ , and the latter is the spectral intensity  $\mathbf{I}$  distribution at a single wavelength at various sample positions,  $r_0$  (Figure 1.3c).

Early traditional spectroscopy was measured with excitation by a mercury vapor lamp and the spectra were basically records of the spectral intensity with frequencies in the visible; they were spontaneous, linear, non-polarized, steady-state, and far-field spectra. In contrast, the spectra of non-visible, stimulated, non-linear, polarized, transient, near-field, and image at a spectral line are a more recent development. Since occurrence of the new-style Raman spectroscopy is mainly due to the introduction of the laser into the Raman spectrometer, it is now called laser Raman spectroscopy.

## 1.2 Scattering and Raman Scattering

### 1.2.1 General Scattering

Scattering is a common phenomenon in nature. When an incident particle hits the target along a certain direction (Figure 1.4), the direction and even the energy of the incident particle may be changed due to the interaction between the particle and the target, thus causing the scattering.

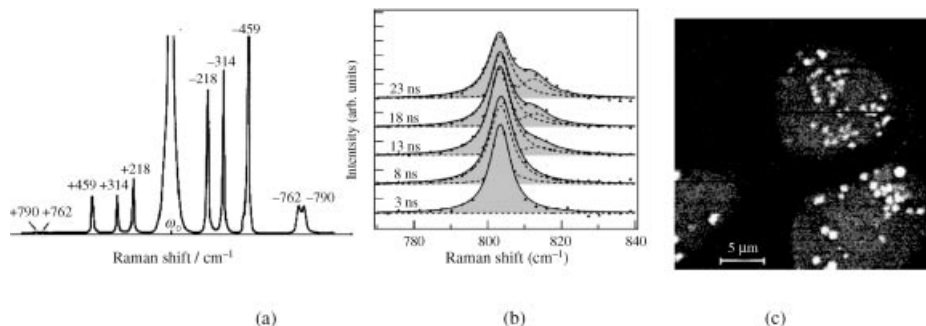


**Figure 1.3** Examples of various kinds of spectra: (a) Steady Raman spectrum of  $\text{CCl}_4$ . Reprinted from S.-L. Zhang, *Raman Spectroscopy and Low-dimensional nanoscale Semiconductors*, Science Press, (2008). (b) Transient spectra of ring-breathing mode of cyclohexane under shock compression. The solid and dashed lines show the fitted Lorentzian function and the separated peaks, respectively [2]. Reprinted from in A. Matsuda, G. Kazutaka and K. Kondo, *Time-resolved Raman spectroscopy of benzene and cyclohexane under laser-driven shock compression*, *Phys Rev B*, 65, 174116 (2002) with permission of the American Physical Society. (c) Image of spectral line of unstained and live HeLa cells [3]. Reprinted from A. Zumbusch, G. P. Holtom, and S. X. Xie, *Three-Dimensional Vibrational Imaging by Coherent Anti-Stokes Raman Scattering*, *Phys Rev Lett*, 82, 4142 (1999) with permission of the American Physical Society

Scattering experiments have been an important method used to observe the interactions as well as the inner structure and motion of matter, on both macroscopic and microscopic scales. For example, E. Rutherford's experiment in 1911 verified that the atom has a nucleus with a small positive charge. A.H. Compton's experiment in 1920 proved that light possesses particle-like property. The scattering experiments in these classical examples used charged particles and alpha particles as the incident particles, respectively. Nowadays, most experiments of elementary particles still use scattering experiments of various incident particles and targets.

Based on the different kinds of incident particles, scattering can be categorized as neutron scattering, electron scattering, and photon (electromagnetic wave) scattering.

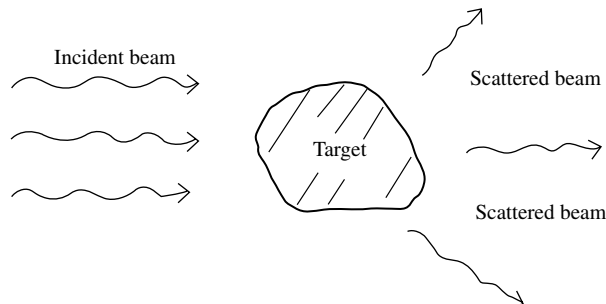


**Figure 1.4** Diagram of scattering phenomena. Reprinted from S.-L. Zhang, *Raman Spectroscopy and Low-dimensional nanoscale Semiconductors*, Science Press, (2008)

**Table 1.1** Estimated values of energies and wavelengths of incident particles used in the scattering experiments of solid matter. Reprinted from S.-L. Zhang, *Raman Spectroscopy and Low-dimensional nanoscale Semiconductors*, Science Press, (2008)

Category of Incident Particles	Energy		Wavelength nm	Uncertainty of Energy $\Delta E/E$
	eV	Hz		
Photon (Electromagnetic wave)	Visible laser	$10^{-2}$	$10^{14}$	$10^{-1}$
		$10^0$	$10^{16}$	$5 \times 10^2$
	X-ray	$10^3$	$10^{19}$	$10^{-1}$

Photon scattering can be sub-divided into gamma ray scattering, X-ray scattering, and (visible) light scattering, which uses light with different energies. Table 1.1 lists the common incident particles in the study of condensed matter, their energies, and their wavelengths.

Various kinds of scattering yield different information, which makes them particularly suitable for the study of various objects. For example, X-rays with a typical energy of 1 keV are suitable for detecting the location of atoms or ions in condensed matter, that is, its microstructure and geometric symmetry. Visible light, with energy of about 1 eV, is suitable for studying the molecular vibration and elementary excitation in condensed matter.

## 1.2.2 Visible Light Scattering

Visible light scattering is a phenomenon commonly observed in our daily life. When visible light travels through a uniform media such as purified glass or water, light cannot be observed in the media when viewed from the side. However, most media are not perfectly uniform and small particles (impurities) may exist (e.g., liquid with suspended particles or colloids). These impurities enable us to see the light ray in the media from the side. This is due to light scattering off the irregularities or particles in the media.

Based on different scattered objects, visible light scattering can be classified into many kinds, as described below.

### 1.2.2.1 Molecular Scattering

Molecular scattering is due to scattering caused by density fluctuations of molecules in pure gases or liquids from thermal motion, and for which the size of fluctuation is smaller than the wavelength of incident light. This can lead to critical opalescence, which is due to a huge amount of light scattering caused by large fluctuations at the critical point.

Lord Rayleigh, a British physicist, proposed his Law in 1897 when he was studying the intensity of molecular scattering [4]. Rayleigh's Law says that the intensity of scattered light is inversely proportional to the fourth power of the wavelength of the incident light.

### 1.2.2.2 Tyndall Scattering

In 1868, Tyndall found that when white light is scattered by suspended particles in liquids, the scattered light is blue with partial (linear) polarization [5]. Tyndall scattering is induced by particles in the media with a size comparable to or a little larger than the wavelength of the incident light, such as colloids, latex, smoggy air, and so on. When C. Mie studied Tyndall

## 8 Raman Spectroscopy and its Application in Nanostructures

scattering in 1908, he found that, in contrast to molecular scattering, the fourth power relation was not followed [6]. In some literature, Tyndall scattering is also called Mie scattering.

### 1.2.2.3 Electron Light Scattering

Electron light scattering includes different modes of scattering by free electrons, such as Compton scattering and Thomson scattering. These types of scattering are discussed later in this book.

Electron light scattering also includes scattering by other charged particles, for example, light scattered by the electrons/holes, impurity charges and spins in condensed matter. The latter scattering is also called spin scattering. These types of scattering will also be discussed later in this book.

### 1.2.2.4 Atomic Light Scattering

Since the nucleus is too heavy to induce visible light scattering, atomic light scattering of visible light is actually scattered by orbital electrons.

### 1.2.2.5 Molecular Light Scattering

Molecular light scattering refers mainly to scattering by vibration and rotation of chemical bonds in chemical or biological molecules.

### 1.2.2.6 Solid Light Scattering

Solid light scattering is, in fact, due to scattering by “quasi-particles” in solids. “Quasi-particles” are also called “elementary excitations”, and the important quasi-particles in light scattering are phonons (the quanta of lattice vibration waves), excitons, magnetons, and plasmons, and so on.

## 1.2.3 Inelastic and Raman Scattering

As mentioned in Section 1.2.1, the energy of the incident particle, for example, light, can be changed in the scattering process. In the twentieth century, people began to pay attention to the change of energy, that is, the change in wavelength, of the scattered light relative to that of the incident light. In light scattering experiments, the unit of the wavelength change is usually expressed as the reciprocal of wavelength ( $\text{cm}^{-1}$ ). Table 1.2 lists light scattering classified into three categories, depending on the change in energy. Scattering with a change of light energy of less than  $10^{-5} \text{ cm}^{-1}$  is called Rayleigh scattering. Changes of about  $0.1 \text{ cm}^{-1}$  were first observed by Brillouin in 1922 and are thus called Brillouin scattering [7]. Changes larger than  $1 \text{ cm}^{-1}$  are called Raman scattering, as was first observed by C.V. Raman in 1928 [8]. When the wavelength (energy) of scattered light is the same as the incident light, it is known as elastic scattering. When the wavelength of the scattered light is

**Table 1.2** Energy change and corresponding classification of visible light scattering. Reprinted from S.-L. Zhang, *Raman Spectroscopy and Low-dimensional nanoscale Semiconductors*, Science Press, (2008)

Change Range of Energy	Name of Category	Property of Scattering
$< 10^{-5} \text{ cm}^{-1} \sim 0$	Rayleigh	Elastic
$10^{-5} \sim 1 \text{ cm}^{-1}$	Brillouin	Inelastic
$> 1 \text{ cm}^{-1}$	Raman	Inelastic

different, it is known as inelastic scattering. As the energy change in Rayleigh scattering is caused by the recoil of the target, it can still be regarded as elastic scattering. So Brillouin and Raman are inelastic scattering.

The above shows that Raman scattering is an inelastic light scattering, with energy change larger than  $1\text{ cm}^{-1}$ .

### 1.3 Fundamental Features of Raman Scattering Spectra

Different spectra embody different properties and features, due to the difference in the mechanism generating the spectra. Raman scattering spectra is abbreviated as Raman spectra usually and have their own characteristics also, distinguishing them from other spectra.

Figure 1.5 shows the Raman spectra of  $\text{ClC}_4$ , in which  $\omega_0$  is the frequency of the incident light. The energy is usually represented by wavenumber ( $\text{cm}^{-1}$ ), while the wavenumber of the incident light,  $\omega_0$ , is set as zero on the wavenumber axis. The frequency of scattered light,  $\omega_S$ , relative to that of incident light, is called the Raman frequency or Raman shift. The basic features of Raman spectra will be discussed using the example in Figure 1.5.

#### 1.3.1 Frequency

There are two basic features of Raman frequency.

- The frequency difference of Raman scattered light relative to that of incident light  $\omega_0$  can be negative and positive, of which the frequency of the former and the latter are known as the Stokes frequency  $\omega_S$  and anti-Stokes frequency  $\omega_{AS}$ , respectively. The absolute values of  $\omega_S$  and  $\omega_{AS}$  are equal; namely:

$$|\omega_S| = |\omega_{AS}| \quad (1.3)$$

Besides, the frequency of Raman scattering is independent of that of the incident light  $\omega_0$ .

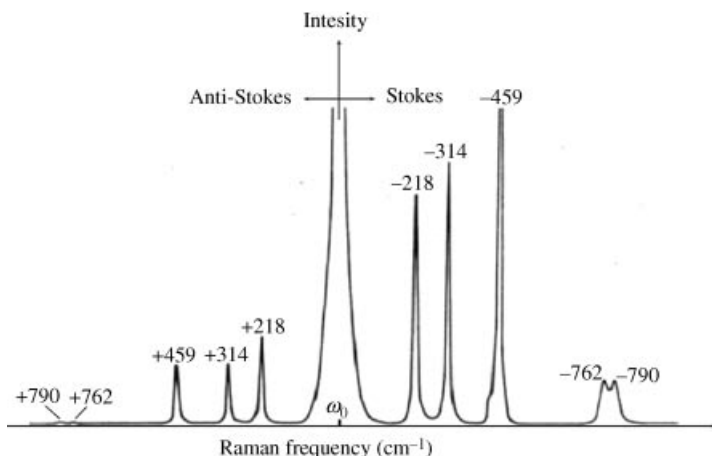


**Figure 1.5** Raman spectrum of  $\text{ClC}_4$ . Reprinted from S.-L. Zhang, *Raman Spectroscopy and Low-dimensional nanoscale Semiconductors*, Science Press, (2008)

## 10 Raman Spectroscopy and its Application in Nanostructures

- As mentioned above, the scattering originates from the interaction between the incident particles and scattered system. According to the energy conservation law, all scattering processes, including Raman scattering, must obey this relationship:

$$E_S - E_0 = E_K \quad (1.4a)$$

where  $E_0$ ,  $E_S$ , and  $E_K$  represent the energy of incident light, the scattered light, and the scattered system,  $K$ , respectively.

As the energy,  $E$ , is given by  $E = \hbar\omega$ , where  $\hbar$  is the reduced Planck constant, the Equation (1.4a) can be rewritten as:

$$\hbar(\omega_S - \omega_0) = \hbar\omega_k \quad (1.4b)$$

which can be reduced to

$$\omega_S - \omega_0 = \omega_k \quad (1.4c)$$

In most cases,  $E_k$  is an innate property of the system and is independent of the frequency of the incident light,  $\omega_0$ . Thus, the Raman frequency ( $\omega_S - \omega_0$ ) must also be independent of the frequency of the incident light according to Equation (1.4c). Furthermore, it becomes evident that the absolute value of the Stokes frequency  $\omega_S$  equals that of the anti-Stokes frequency  $\omega_{AS}$ .

The above mentioned two basic features of Raman frequency originate from energy conservation laws, so they are universal.

### 1.3.2 Intensity

The intensity of Raman scattering is very weak and usually amounts to just  $10^{-6} \sim 10^{-12}$  of that of the incident light. It has been a major constraint to the application and development of Raman scattering in the past.

The intensity of a Stokes line,  $I_S$ , is much stronger than that of the anti-Stokes line,  $I_{AS}$ , and the ratio of their intensities can be expressed as

$$I_S/I_{AS} \sim \exp(\hbar\omega/k_B T) \gg 1 \quad (1.5)$$

where  $k_B$  and  $T$  stand for the Boltzmann's constant and the absolute temperature, respectively.

### 1.3.3 Polarization

When the orientation of molecules and crystals is fixed in space and the incident light is polarized, the polarization of scattered light is determined by the symmetry of molecular structure and crystals. This produces a selection rule in polarized Raman spectra, which is also known as the polarization selection rule and can be used to analyze the ascription of Raman peaks and the symmetry of crystals.

## 1.4 Discovery of the Raman Scattering Effects and Observation of the First Raman Spectrum

### 1.4.1 Discovery of Raman Scattering Effects [9]

In 1921, C.V. Raman was returning to India from England. When his ship was traveling in the Mediterranean Sea, he was deeply impressed by the beautiful blue color of the seawater.



**A New Type of Secondary Radiation.**

If we assume that the X-ray scattering of the 'unmodified' type observed by Prof. Compton corresponds to the normal or average state of the atoms and molecules, while the 'modified' scattering of altered wave-length corresponds to their fluctuations from that state, it would follow that we should expect also in the case of ordinary light two types of scattering, one determined by the normal optical properties of the atoms or molecules, and another representing the effect of their fluctuations from their normal state. In accordance with this view, we have now examined whether this is actually the case. The experiments we have made have confirmed this anticipation, and shown that in every case in which light is scattered by the molecules in dust-free liquids or gases, the different radiation of the ordinary kind, having the same wave-length as the incident beam, is accompanied by a modified scattered radiation of degraded frequency.

The new type of light scattering discovered by us naturally requires very powerful illumination for its observation. In our experiments, a beam of sun-light was converged successively by a telescope objective of 18 cm. aperture and 390 cm. focal length, and by a second lens of 5 cm. focal length. At the focus of the second lens was placed the scattering material, which is either a liquid (carefully purified by repeated distillation *in vacuo*) or its dust-free vapour. To detect the presence of modified scattered radiation the method of complementary light-filters was used. A blue-violet filter, followed by a yellow-green filter and placed in the incident light, completely extinguished the track of the light through the liquid or vapour. The reappearance of the track when the yellow filter is transferred to a place between it and the observer's eye is proof of the existence of a modified scattered radiation. Spectroscopic confirmation is also available.

Some sixty different common liquids have been examined in this way, and every one of them showed the effect in greater or less degree. That the effect is a true scattering, and not a fluorescence is indicated in the first place by its position in comparison with the ordinary scattering, and secondly by its polarization, which is in many cases quite strong and comparable with the polarization of the ordinary scattering. The investigation is naturally much more difficult in the case of gases and vapours, owing to the excessive feebleness of the effect. Nevertheless, when the vapour is of sufficient density, for example with ether or amylene, the modified scattering is readily demonstrable.

C. V. RAMAN,  
K. S. KRISHNAN.

210 Bowbazar Street,  
Calcutta, India,  
Feb. 16.

121, 501-502; 1928

**Figure 1.6** Photo of Raman and copy of his note published in Nature [8]. Courtesy of Avril Rhys.

He thought of Rayleigh's proposal that the blue color of seawater was due to the reflection of light from the blue sky. But Raman did not accept this explanation and carried out a simple experiment while still on the ship. He set a Nicol prism at the Brewster angle in order to eliminate the reflected light from the seawater surface; nevertheless, the light from the deep

seawater still exhibited the blue color. This led Raman to conclude that the blue color of seawater came from the scattering of seawater itself.

After Raman returned to India, he immediately started to research the scattering of water. In 1923, K.R. Ramanathan, a scholar in his research team, focused sunlight into water and other liquids held in slender-necked bottles and put light filters in the path of the incident and the scattering direction. Since the two filters chosen were complementary, allowing no light to pass through when both were placed together, the incident light ray should not have been seen from the other side. However, he observed light in the scattered direction. Ramanathan thought that the light originated from the weak fluorescence caused by impurities in the liquid; but even after repeated purification of the liquid, the weak “fluorescence” still remained.

Raman did not agree with his colleague’s explanation of “the residual fluorescence”. He thought that “the weak fluorescence” was similar to the newly found Compton effect of X-rays. In the winter of 1927, Raman deduced the Compton scattering formula using the classical approach, and apparently confirmed that the weak fluorescence was indeed similar to the Compton effect, that is, a certain kind of non-coherent scattering resulted in a wavelength change. Then Raman immediately instructed his students to improve the experiment, purifying and observing liquid time after time. In January 1928, they found that the scattered light from pure glycerin appeared green instead of the conventional blue color. This greatly encouraged them to do further research. On February 7<sup>th</sup>, 1928, K.S. Krishnan proved that “the weak fluorescence” observed by Ramanathan was pervasive in many kinds of organic liquids and their vapors. Eventually, after all the experimental results had been validated by Raman himself, he submitted a “note” titled *A New Type of Secondary Radiation* to the magazine *Nature* on February 16<sup>th</sup>, 1928. The note was rejected by the reviewer of the magazine. However, the publisher decided to publish anyway and it came out in *Nature* on March 31<sup>st</sup> [8]. Two years later, in 1930, the note of less than half a page led Raman to the Nobel Prize. Soon after, the research and application of Raman scattering became an active research field, which has continued to this day.

In the same year that Raman and Krishnan published their work, Russian scientists G. Landsberg and L. Mandelstam independently published their discovery of the same kind of scattering, but observed in crystalline quartz [10]. This scattering is also referred to as “combination scattering” in the Russian literature, although most scientists call it “Raman scattering”. Later experiments showed that the scattering observed by Raman and Landsberg were the two satellite lines of the Rayleigh line predicted by A. Smekel in 1923 [11].

In *A New Type of Secondary Radiation* [8], Raman described their experimental equipment in detail (Figure 1.7). Sunlight was focused by two lenses: the first was an 18 cm diameter objective lens for a telescope with a focal length of 230 cm and the second was a lens with a 5 cm focal length. The scattering material was placed at the focal point of the second lens. The material was a liquid purified through distillation many times in a vacuum or its dustless vapor. The two optical filters in the setup were complementary blue-purple and yellow-green filters. The blue-purple filter was set in the path of the incident optics, so that no yellow-green light could pass through the liquid and vapor. When the yellow-green filter was placed between the sample and observer’s eye, the re-appearance of yellow-green light served as evidence of Raman scattering.

The history mentioned above illustrates several interesting and meaningful developments of great experiments. First, the discovery by Raman originated from his observation of

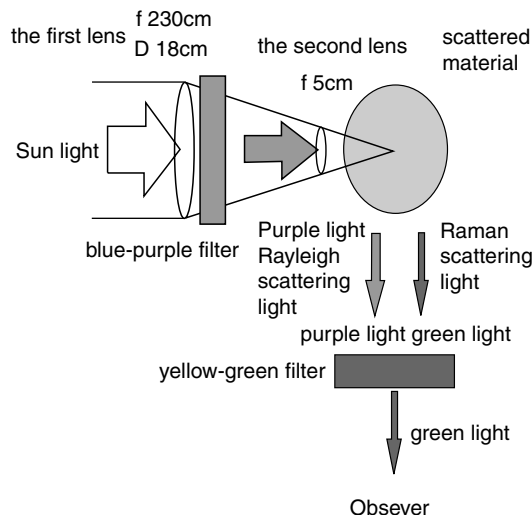


**Figure 1.7** The experimental setup of Raman scattering as observed by Raman. Reprinted from S.-L. Zhang, *Raman Spectroscopy and Low-dimensional nanoscale Semiconductors*, Science Press, (2008)

the blue color of seawater, a common phenomenon that had apparently been explained by a great scientist. Second, the published note by Raman was a conclusion drawn from the accumulation of many meticulous and careful experiments carried out over seven years, and done with no awareness of a theoretical prediction for this effect. Only the theoretical understanding developed by Raman himself convinced him that the experimental results were not invalid and encouraged him to continue with more experiments. Finally, his experimental results were obtained by using very simple equipment. It was said that the entire setup cost only 500 rupees at the time.

#### 1.4.2 The First Raman Spectrum

When Raman submitted his note to *Nature* in 1928, he was not content with the present experimental results. On 7<sup>th</sup> and 28<sup>th</sup>, using benzene, he observed sharp spectral lines in the blue-green region of the spectroscope with excitation by sunlight and the 435.9 nm spectral line of a mercury vapor lamp, respectively. Furthermore, based on the experimental setup of Raman, Krishnan took the first Raman scattering spectrum that included both Stokes lines and anti-Stokes lines using a Higer Baby's quartz spectrograph. Figure 1.8 shows the earliest published Raman scattering spectrum of CCl<sub>4</sub>.

### 1.5 Historical Development of Raman Spectroscopy

#### 1.5.1 The Rapid Growth and Early Development of Raman Spectroscopy

After the publication of the first two important papers by Raman [8], a huge surge of research and application of Raman spectra came out almost instantly around the world. In 1928, when

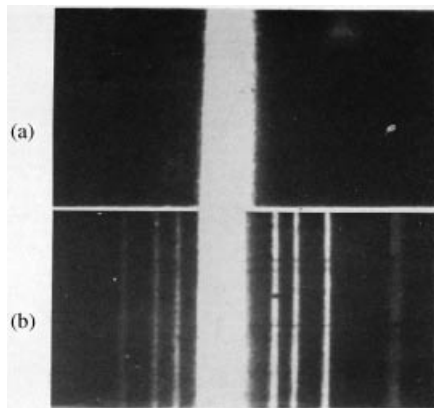


**Figure 1.8** The earliest published Raman scattering spectrum of  $\text{CCl}_4$  by Raman [1]. Reprinted from S.-L. Zhang, *Raman Spectroscopy and Low-dimensional nanoscale Semiconductors*, Science Press, (2008)

Raman published his note in *Nature*, more than 60 papers pertinent to the Raman effect were published. And over 1757 papers on Raman spectroscopy had been published internationally by 1939 [12]. The decade after 1928 was the period when Raman spectroscopy grew rapidly and progressed prosperously. At the end of this period, in 1939, a review book on Raman spectroscopy *Vibrational Spectra & Structure of Polyatomic Molecules* [13] was published by Ta-You Wu, a professor at Peking University, during the difficult time when China was at a war (Figure 1.9). The book is the first overall review of Raman

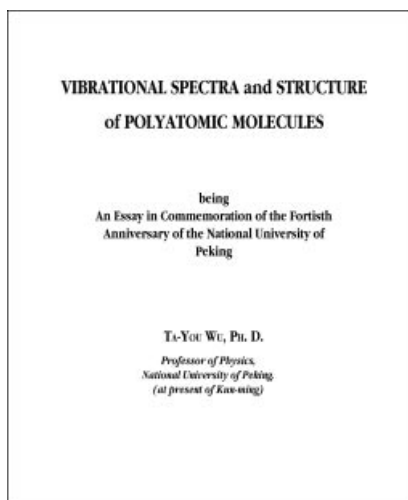


**Figure 1.9** The cover of *Vibrational Spectra & Structure of Polyatomic Molecules* by Wu [13]. Reprinted from S.-L. Zhang, *Raman Spectroscopy and Low-dimensional nanoscale Semiconductors*, Science Press, (2008)

spectroscopy experiments and became an instant reference book in this field. It is still cited worldwide today, after 60 years.

### 1.5.2 The Quiet Period of Raman Spectroscopy

As mentioned earlier, Raman scattering is very weak, while the intensity of Rayleigh scattering and other spurious light are always much stronger. With the use of spectral lines of a mercury vapor lamp as the excitation light source in the early Raman spectral experiments, Raman spectra could only be applied to studies on chemical molecular vibration. At the same time, due to the rapid development of IR devices and techniques during World War II, IR spectroscopy was making huge progress. Therefore, after the war, spectral research of chemical molecular vibrations was dominated almost entirely by IR spectroscopy, leaving Raman spectroscopy relatively quiet.

In this “silent period,” theoretical research in understanding vibration spectra was not stagnant. The book, *Dynamical Theory of Crystal Lattices* [14], published in 1954, was an outstanding representative of work in this area (Figure 1.10). This book was written by the

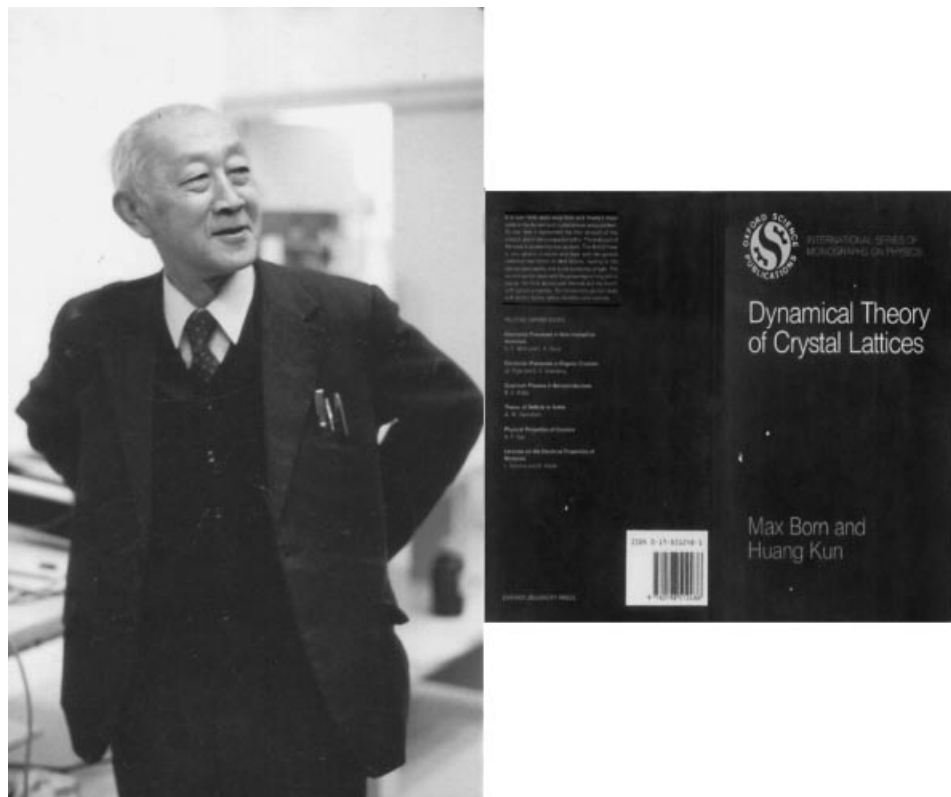


**Figure 1.10** The cover of *Dynamical theory of Crystal Lattices* by Max Born and Kun Huang [16]. Reprinted from S.-L. Zhang, *Raman Spectroscopy and Low-dimensional nanoscale Semiconductors*, Science Press, (2008)

Nobel laureates Max Born and Kun Huang. The last chapter of the book “The Optical Effects” is practically dedicated to Raman scattering. In this last chapter, based on discussion of universal and profound problems in published literature in the past [15], the authors developed a theory of light scattering. The book has gone through three editions and been re-printed many times. In the third edition [16], published in 1985, the publisher offered an evaluation of the impact of the book: “It is over 30 years since Born and Huang’s major works on the dynamics of crystal lattices was published. At that time it represented the final account of this subject and in many respects it still is.” In fact, the book is held widely as the classic on solid state physics (especially on phonon physics) and lays the theoretical foundation for solid state Raman spectroscopy developed ten years later due to the invention of the laser.

### **1.5.3 The Renaissance and Flowering of Raman Spectroscopy**

With the invention and availability of the laser in 1960 [17], the mercury vapor lamp as an excitation source of Raman spectrometer was soon replaced. In 1962, less than two years after the laser was invented, the first laser Raman spectra with excitation by a ruby pulse laser at 694.3 nm was published [18], marking the re-birth of Raman spectroscopy and the end of the traditional spectroscopy by excitation with the mercury vapor lamp.

In this new period of Raman spectroscopy, the studied objects are no longer restricted to chemical molecules. Nearly any object that is able to interact with light has been studied by Raman spectroscopy. The scientific and technological areas studied and applied by Raman spectroscopy have included single molecule, solid state matter (minerals, crystals, glasses, ceramics, disordered materials, nanostructure materials, . . .), liquid, organism, medicines, and so on.

In addition, some Raman spectral phenomena, which could not be studied by excitation light intesity in traditional Raman spectroscopy, are now possible because of the laser.

With further development of lasers (in terms of wavelength, with shorter and shorter duration) and significant improvement of other components of Raman spectrometers, the observable Raman spectra are different from the old ones spectroscopically. These developments will be discussed in greater depth in Chapters 3 and 4.

## **References**

- [1] Zhang, Shu-Lin (2008) *Raman Spectroscopy and Low-imensional Nano-semiconductors*, Science Press, Beijing
- [2] Matsuda, A., Kazutaka, G., and Kondo, K. (2002) *Phys. Rev. B.*, **65**, 174116.
- [3] Zumbusch, A., Holtom, G.P., and Xie, S.X. (1999) *Phys. Rev. Lett.*, **82**, 4142.
- [4] Rayleigh, L. (1871) *Phil. Mag.*, **XLI**, 274, 447.
- [5] Tyndall, J. (1868–1869) *Proc. Roy. Soc.*, **19**, 223.
- [6] Mie, G. (1908) *Ann. Physik*, **25**, 377.
- [7] Brillouin, L. (1922) *Ann. Phys. (Paris)*, **17**, 88.
- [8] Raman, C.V. and Krishnan, K.S. (1928) *Nature*, **121**, 501.
- [9] Jayaraman, A. (1989) C.V. Raman, the man and scientist, in *Raman Spectroscopy Sixty Years On* (eds H.D. Bist, J.R. Durig, and J.F. Sullivan), Elsevier Science Pub. Co. Inc., New York, p. xix.
- [10] Landsberg, G. and Mandelstam, L. (1928) *Naturwiss*, **16**, 557, 772.

- [11] Smekal, A. (1923) *Naturwiss.*, **11**, 873.
- [12] Hibbenm, J.H. (1939) *The Raman Effect and its Chemical Applications*, Reinhold Publishing Co., New York.
- [13] Wu, T.Y. (1939) *Vibrational Spectra & Structure of Polyatomic Molecules*, The China Science Co., Shanghai.
- [14] Born, M. and Huang, K. (1954) *Dynamical Theory of Crystal Lattices*, Oxford University Press, Oxford.
- [15] Themer, O. (1952) *Proc. Phys. Soc.*, **65**, 38.
- [16] Born, M. and Huang, K. (1985) *Dynamical Theory of Crystal Lattices*, Oxford University Press, Oxford.
- [17] Maiman, T.H. (1960) *Nature*, **187**, 493.
- [18] Porto, S.P.S. and Wood, D.L. (1962) *J. Opt. Soc.*, **52**, 251.

# 2

## Fundamental Theory of Light Scattering

The theory of light scattering should explore and describe clearly the mechanisms as well as predict and explain the features of light scattering. The theory also provides the foundation and methods of theoretical arithmetic, by which we can work out the theoretical results of scattering from light scattering experimental conditions. This will help to explain the experimental phenomena and explore the nature of these phenomena.

The theory of light scattering can be categorized into two types: macroscopic (classic) theory and microscopic (quantum) theory. The earliest studies of classic theory were related to measurements of the intensity of light scattering by the English physical scientist Lord Rayleigh in 1871. Rayleigh proved that the intensity of scattered light is inversely proportional to the fourth power of the wavelength of incident light [1]. In 1922, L. Brillouin published the earliest quantum theory study of light scattering [2], predicting the existence of long-wave acoustic waves in light scattering. In 1923, A. Smekal studied the quantum theory of light scattering using a model with two energy levels, and predicted the existence of satellite lines on both sides of the Rayleigh scattering line [3]. These two predictions were confirmed by experiments later and were named Brillouin scattering and Raman scattering, respectively.

The theory of light scattering based on quantum mechanics has made a great contribution to understanding the nature and features of light scattering; however, the workload of the quantum theory calculation is too huge for precise calculations. In recent years, the precise calculation by quantum theory, that is, the *ab initio* calculation, has started gradually, aided by the rapid growth of hardware and software techniques of computers. Even so, the precise calculation is still limited to systems with only hundreds or, at most, several thousand atoms. Therefore, the *ab initio* or first-principles calculation of light scattering still has to rely on phenomenological or semi-phenomenological theories.

The theories introduced in this chapter are only used to present the principle of light scattering and the origin of its basic features. The concrete models and methods of theory calculation will be introduced in Part II of this book.

## 2.1 Description of Scattering

### 2.1.1 Scattering Experiments

The scattering experiment described in Figure 2.1 involves four main parts: incoming beam, scattered beam, target, and detector. The incoming beam could be a particle beam or electromagnetic radiation beam, of which the incident and scattered directions are fixed and unfixed, respectively. The target could be elementary particles, atoms, molecules, gas, or condensed state matter, and so on. The direction of scattered beams in the experiment is often decided by the azimuth of the detector, so it can only probe a part of the scattering beam from the target matter, the region of overlap of the incoming beam, and the solid angle subtended by the detector.

If the incident and scattered beams used in experiments are electromagnetic waves, such as laser or X-ray beams, the incident wave and scattered wave are expressed by the plane wave Equation (2.1) and spherical wave Equation (2.2), respectively.

$$E_0 e^{i(k_0 \cdot r - \omega_0 t)} \quad (2.1)$$

$$\frac{E_s}{r} e^{i(k_s \cdot r - \omega_s t)} \quad (2.2)$$

In the above equations,  $r$  and  $t$  represent the positional vector of target and time, respectively, and  $E_0$ ,  $k_0$ , and  $E_s$ ,  $k_s$  are the amplitude and wave vector of incident and scattered electromagnetic waves, respectively.

The incoming beam and scattered beam in Figure 2.1 can also be a particle beam such as the neutron and electron. In this case, the process of scattering could also be described by using the model of particle collision, as shown in Figure 2.2. In the model of particle

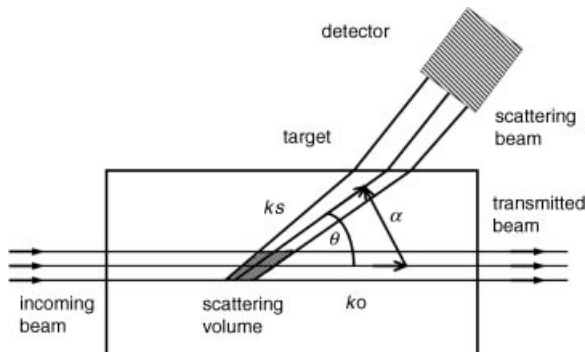


**Figure 2.1** Schematic diagram of scattering experiments. Reprinted from S.-L. Zhang, Raman Spectroscopy and Low-dimensional nanoscale Semiconductors, Science Press, (2008)

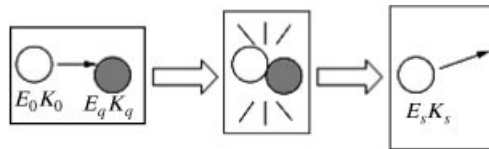


**Figure 2.2** Model of particle collision for the scattering process. Reprinted from S.-L. Zhang, Raman Spectroscopy and Low-dimensional nanoscale Semiconductors, Science Press, (2008)

collision, first the particle beam with energy  $E_0$  and momentum  $\hbar\mathbf{k}_0$  hits the target particles with energy  $E$  and momentum  $\hbar\mathbf{q}$ ; thus, the collision between incident particle and target particle occurs, resulting in the scattered particles with energy  $E_s$  and momentum  $\hbar\mathbf{k}_s$ .

Based on the conservation laws of energy and momentum, the energy and momentum of the collision system have the relation

$$E_0 - E_s = E \quad (2.3)$$

$$\hbar(\mathbf{k}_0 - \mathbf{k}_s) = \hbar\mathbf{q} \quad (2.4)$$

If the electromagnetic wave is considered as a particle-photon, the scattering process could also be described as similar physically to the particle collision. The relations between the physical parameters of the electromagnetic wave and the photon particle are listed in Table 2.1.

The discussion above shows that the process of wave scattering can also be described as a process of particle collision. Therefore, we often refer to the scattering process as a collision process. In the process of collision, if the energy of the scattered particle changes compared with the energy of the incident particle, the collision is called an inelastic collision, otherwise it is called an elastic collision. Accordingly, if the energy of the scattered wave is different from that of the incident wave, the scattering is called inelastic scattering, otherwise it is called elastic scattering.

### 2.1.2 Scattering Probability and Differential Scattering Probability

The scattering probability is defined as the ratio of the number of scattered particles to the number of total incident particles in a unit time. If only taking into account the scattered particles in the unit solid angle, or in the unit solid angle within a certain energy range, the corresponding scattering probabilities are both named the differential scattering probability.

**Table 2.1** The physical parameter relation between an electromagnetic wave and photon. Reprinted from S.-L. Zhang, Raman Spectroscopy and Low-dimensional nanoscale Semiconductors, Science Press, (2008)

Photon	Electromagnetic Wave
Energy $E = \hbar\omega$	Frequency $\omega = kc = 2\pi c/\lambda$
Momentum $\mathbf{P} = \hbar\mathbf{k}$	Wavevector $ \mathbf{k}  = 2\pi/\lambda$ $\lambda$ : Wavelength; $c$ is velocity of light.

In a scattering experiment, the scattering probability and the differential scattering probability both are basic physical quantities, and so can be measured. For example, the scattered spectrum is one of the measurements of scattering probability. The scattering probability can also be obtained by theoretical calculation. The nature of experimental phenomena can be understood by comparing experimental and theoretical scattering probabilities.

### 2.1.3 Scattering Cross Section and Differential Scattering Cross Section

The hard-sphere model shown in Figure 2.3 introduces the scattering probability, in which the incident and target particles are modeled by the hard sphere and the target consists of a single layer of particles. In such a model, there is no deformation or multiple scattering of particles. In Figure 2.3, the incident and target particles are marked A and B, respectively. The area and particle number of the target are  $F$  and  $N$ , respectively.

#### 2.1.3.1 Scattering Cross Section

Obviously the collision happens only when the center of incident particles A enters the circular area  $\sigma$  with a radius of  $a + b$ , where  $a$  and  $b$  are the radii of particles A and B, respectively. Therefore, the size of  $\sigma$  only reflects the magnitude of the collision probability and is called the scattering cross section, which is determined by the nature of the scattering system itself. As a result, the scattering probability  $\rho$  depends on the scattering area of all scattered particles  $N\sigma$  divided by the area of the target  $F$ , that is

$$\rho \equiv \text{Total scattering area/target area} = N \times \sigma/F \quad (2.5)$$

However, if it is assumed that the number of incident particles A entering area  $F$  in 1 second is  $N_0$ , and the number of scattered particles is  $N_{0,S}$ , the scattering probability should be

$$\rho \equiv N_{0,S}/N_0 \quad (2.6)$$

The number of the incident particles A passing a unit area in 1 second is only the current density and marked as  $j_0$ , while the particle current density traveling along the direction of the incident beam z is marked as  $j_{0,z}$ , and Equation (2.6) can be re-written as

$$\rho \equiv N_{0,S}/(j_{0,z} \times F) \quad (2.7)$$

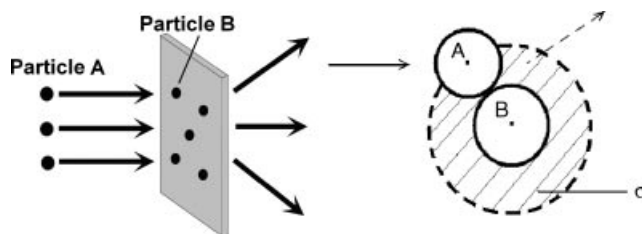


**Figure 2.3** Hard-sphere collision model describing the scattering process. Reprinted from S.-L. Zhang, *Raman Spectroscopy and Low-dimensional nanoscale Semiconductors*, Science Press, (2008)

Comparing Equation (2.5) and Equation (2.7), the scattering cross section can be expressed as

$$\sigma \equiv (1/N) N_{0,S}/j_{0,Z} \quad (2.8)$$

### 2.1.3.2 Differential Scattering Cross Section

The scattering cross section is seldom measured in experiments, so the differential scattering cross section is usually measured. One of the definitions of the differential scattering cross section is the ratio of the number of particles scattered into the solid angle  $d\Omega$  with energy range  $E_1$  to  $E_1 + dE_1$  to the number of incident particles.

We use the polar coordinates shown in Figure 2.4 to describe the expression of the differential scattering cross section. If we let the current density of scattered particles at position  $r$  with energy  $E_1$  be  $j_1(r)$  and  $r^2 d\Omega$  is the area opened up by solid angle  $d\Omega$  at  $r$ , then the number of particles with energy range  $E_1$  to  $E_1 + dE_1$  scattered into solid angle  $d\Omega = \sin\theta d\theta d\varphi$  is

$$\mathbf{n} \cdot \mathbf{j}_1(\mathbf{r}) r^2 d\Omega dE_1 \quad (2.9)$$

where  $\mathbf{n}$  represents the direction of  $\mathbf{r}$  and also stands for the direction of the scattered beam.

With particles incident along the direction  $z$  and current density  $j_{0,Z}$ , the differential scattering cross section of incident particles with current density  $j_{0,Z}$  and scattered particles of energy range  $E_1$  to  $E_1 + dE_1$  scattered into the solid angle  $d\Omega$  is

$$\frac{d^2\sigma}{d\Omega dE_1} = \frac{r^2}{N \times j_{0,Z}} \mathbf{n} \cdot \mathbf{j}_1(\mathbf{r}) \quad (2.10)$$

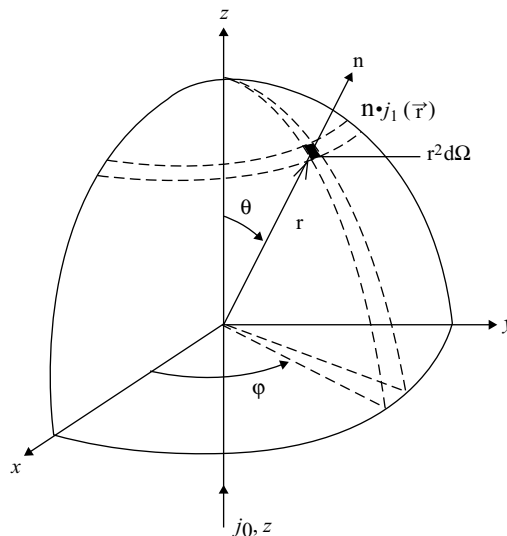


**Figure 2.4** Schematic diagram of the differential scattering cross section discussed in polar coordinates. Reprinted from S.-L. Zhang, Raman Spectroscopy and Low-dimensional nanoscale Semiconductors, Science Press, (2008)

In the above derivation, any properties of the incident and target particles are not involved, therefore the expression of the differential scattering cross section should be universally applicable to all kinds of scattering, with only the practical expression of the current density  $j$  varying for different kinds of scattering.

### 2.1.4 Classical and Quantum Physical Expressions of Scattering Cross Sections

#### 2.1.4.1 Classical Electromagnetic Wave Formulation of Scattering Cross Sections [4]

In classical electromagnetic wave theory, the light scattering process is described as the target particle being affected by the incident wave and then inducing a scattered wave. In light scattering, the effect of the magnetic component  $\mathbf{B}$  can be neglected and thus light can be expressed only by using the electric field  $\mathbf{E}$ , as

$$\mathbf{E}(\mathbf{r}, t) = E e^{i(\mathbf{k} \cdot \mathbf{r} - \omega t)} \quad (2.11)$$

where  $E$  is the amplitude of  $\mathbf{E}$ ;  $\mathbf{k}$  is wave vector, which also stands for the propagated direction of the light wave; and  $\omega$  is the frequency of the light wave. In electromagnetic radiation, the energy of the electromagnetic field passing through a unit area in a unit time is defined as the energy-flux density, that is, the Poynting vector  $\mathbf{S}$  expressed as

$$\mathbf{S} = \frac{c}{8\pi} \mathbf{E} \times \mathbf{B} \quad (2.12)$$

where  $c$  is velocity of light. If  $\mathbf{n}$  represents the propagated direction of electromagnetic wave energy, when neglecting magnetic field effects, the time average of energy-flux density in direction  $n$  is

$$\frac{c}{8\pi} \mathbf{n} < |\mathbf{E}|^2 > \quad (2.13)$$

Since the Poynting vector  $\mathbf{S}$  is equal to the current density  $j$ , based on the Equations (2.10) and (2.11), the classical electromagnetic expression of the differential scattering cross section of light scattering-at position  $\mathbf{r}$  is

$$\frac{d^2\sigma}{d\Omega dE_1} = \frac{r^2}{NS_{0,Z}} \mathbf{n} \cdot \mathbf{S}_1(\mathbf{r}) = \frac{r^2}{N < E_{0,Z}^2 >} \mathbf{n} < |E_1(\mathbf{r})|^2 > \quad (2.14)$$

where  $S_{0,Z}$  and  $E_{0,Z}$  are the energy-flux density and electric field strength of the incident wave along the incident direction  $z$ ;  $S_1(\mathbf{r})$  and  $E_1(\mathbf{r})$  are the energy-flux density and electric field amplitude of the scattered wave at position  $\mathbf{r}$ .

#### 2.1.4.2 Quantized Particle Description of Scattering Cross Section

In quantum physics, the particle collision model in Figure 2.2 can be seen as the transition between quantized energy levels of incident and target particles due to the interaction between them, as illustrated in Figure 2.5.

As shown in Figure 2.5, before the interaction between incident and target particles, a number  $n_0$  of incident particles stay in the plane wave state  $|k_0\rangle$  of energy  $E_0$  with the probability  $P_{n0}$ , while a number  $n_1$  of target particles stay in the eigenstate  $|n_0\rangle$  of energy  $E_{n0}$ . Due to the interaction between particles, the incident particle is scattered into the

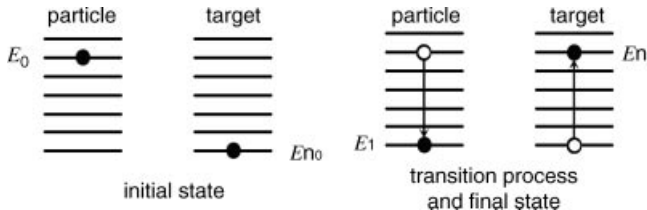


**Figure 2.5** Schematic diagram of the transition between quantized energy levels of incident and target particles in the particle collision model. Reprinted from S.-L. Zhang, Raman Spectroscopy and Low-dimensional nanoscale Semiconductors, Science Press, (2008)

quantum state ( $k_1, d^3k_1$ ) of energy  $E_1$  and momentum  $\hbar\mathbf{k}_1$ . The quantum states of incident and scattered particles can be expressed respectively as

$$|n_0, \mathbf{k}_0\rangle = |n_0\rangle |\mathbf{k}_0\rangle \quad (2.15)$$

and

$$|n_1, \mathbf{k}_1\rangle = |n_1\rangle |\mathbf{k}_1\rangle \quad (2.16)$$

If we express the particle transition probability in time period  $t$  from quantum state  $|n_0, k_0\rangle$  to  $|n_0, k_1\rangle$  as  $P(n_0, \mathbf{k}_0; n_1, \mathbf{k}_1; t)$ , the transition probability in the unit time is

$$R(n_0, \mathbf{k}_0; n_1, \mathbf{k}_1; t) \equiv \frac{d}{dt} P(n_0, \mathbf{k}_0; n_1, \mathbf{k}_1; t) \quad (2.17)$$

Considering that the interaction between the incident and target particles mainly occurs at equal energy and assuming that the probability of target particles equate to the energy  $E_0$  of incident particles before the collision is  $P_{n0}$ , the scattered probability of incident particles will be proportional to probability  $P_{n0}$ . Therefore, the total number of incident particles scattered into the state ( $k_1, d^3k_1$ ) around  $k_1$  is

$$N_0 \sum_{n_0, n_1} P_{n0} R(n_0, \mathbf{k}_0; n_1, \mathbf{k}_1; t) N(\mathbf{k}_1) dk_1 \quad (2.18)$$

where  $N_0$  stands for the total number of the incident particles in the plane wave state  $|k_0\rangle$ ;  $N(k_1)dk_1$  is the number of incident particles in the states range ( $k_1, d^3k_1$ ). Using the polar coordinates shown in Figure 2.4 to describe momentum space and by noting that the mass

and energy of particles are  $m$  and  $E_1 = \frac{\hbar^2 k_1^2}{2m}$ , respectively, then

$$dk_1 = \frac{m}{\hbar^2 k_1} dE_1$$

and the volume element in momentum space is

$$d^3k_1 = \sin \theta d\theta d\varphi k_1^2 dk_1 = \frac{mk_1}{\hbar^2} dE_1 d\Omega \quad (2.19)$$

Therefore, we obtain the number of particles scattered into solid angle  $d\Omega$  in unit time with energy range  $E_1$  to  $E_1 + dE_1$  as

$$\mathbf{j}_1(\mathbf{r}) \cdot \mathbf{n} r^2 dE_1 d\Omega = N_0 \frac{mk_1}{\hbar^2} N(\mathbf{k}_1) \sum_{n_0, n_1} P_{n0} R(n_0, \mathbf{k}_0; n_1, \mathbf{k}_1; t) dE_1 d\Omega \quad (2.20)$$

where  $j_1(r)$  and  $n$  stand for the particle current density and scattering direction, respectively. Thus, the differential cross section expressed by Equation (2.10) can be expressed as

$$\frac{d^2\sigma}{dE_1 d\Omega} = \frac{mk_1}{\hbar^2 j_{0Z}} N(\mathbf{k}_1) \sum_{n_0, n_1} P_{n_0} R(n_0, \mathbf{k}_0; n_1, \mathbf{k}_1; t) \quad (2.21)$$

where  $j_{0Z}$  is the current density of incident particles in the incident direction  $z$ .

The current density  $j$  in light and particle scattering corresponds to the Poynting vector  $S$  and transition probability  $R$ , respectively. The Poynting vector  $S$  and transition probability  $R$  can be deduced by solving the electrodynamics equation in classical mechanics and the time dependent Schrodinger equation of quantum mechanics, respectively. For the scattering cross section of condensed state matter,  $S$  and  $R$  can also be expressed by the space-time correlation function, and the differential cross section will provide the microstructure of the scattered target and information describing the elementary excitation spectrum. This content will be discussed in the following sections.

## 2.2 Macroscopic Theory of Light Scattering

In the macroscopic theory of light scattering, the theory of electrical dipole radiation in classical electrodynamics is mostly used as the theoretical foundation. In this theory, the scatter in targets, such as electrons, atoms, molecules, and elementary excitations in solid including phonons, spinons . . . , are modeled as the dipoles.

### 2.2.1 Electrical Dipole Radiation and Induced Electrical Dipole Moment

#### 2.2.1.1 Electric Dipole Radiation

Based on classical electrodynamics [4], as shown in Figure 2.6, there is an oscillating electric dipole moment  $\mathbf{P}$  with frequency  $\omega$  located at the origin of the coordinate and  $r$  is the position vector of the measured point, of which the distance away from the origin is much larger than the wavelength of radiated light. The electric field  $E$  of radiation produced by  $\mathbf{P}$  can be expressed as

$$E = -\frac{\omega^2 p \sin \theta}{c^2 r} \cos(\omega t - kr) \mathbf{e}_E \quad (2.22)$$

where  $p$  is the amplitude of dipole moment  $\mathbf{P}$ ;  $c$  is the velocity of light;  $k = \omega/c$  stands for the amplitude of wave vector  $\mathbf{k}$ ;  $\mathbf{e}_E$  represents the unit vector of the direction normal both to  $\mathbf{r}$  and in the plane determined by  $\mathbf{r}$  and  $\mathbf{P}$ ; and  $\theta$  is the angle between  $\mathbf{r}$  and  $\mathbf{P}$ .

Based on Equations (2.22) and (2.12), the energy flux density  $S$  radiated by  $\mathbf{P}$  at  $\mathbf{r}$  is

$$S = \frac{\omega^4 p^2 \sin^2 \theta}{4\pi^2 c^3 r^2} \cos^2(\omega t - \mathbf{k} \cdot \mathbf{r}) \mathbf{e}_r \quad (2.23)$$

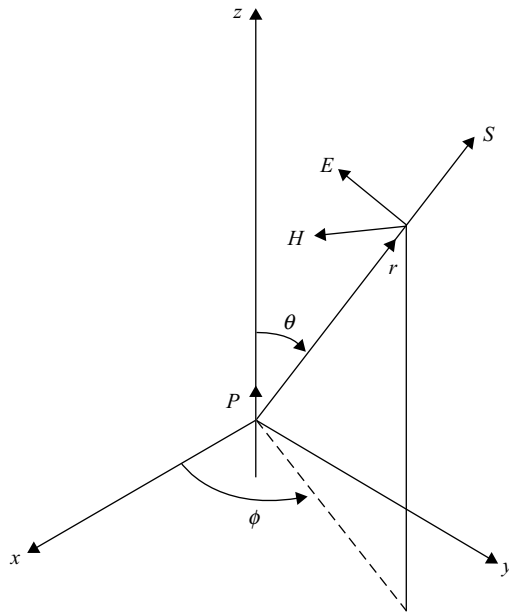


**Figure 2.6** Schematic diagram of the radiation from the oscillating electric dipole moment  $\mathbf{P}$  expressed in polar coordinate system. Reprinted from S.-L. Zhang, Raman Spectroscopy and Low-dimensional nanoscale Semiconductors, Science Press, (2008)

where  $\mathbf{e}_r$  is the unit vector of the direction of  $\mathbf{r}$  and also the direction of  $\mathbf{S}$ . Based on Equation (2.13), the average energy-flux density caused by  $\mathbf{P}$  in a cycle is

$$\langle S \rangle = \frac{\omega^4 P^2}{8\pi c^3 r^2} \sin^2 \theta \mathbf{e}_r \quad (2.24)$$

Therefore, according to the formula of differential scattering cross section in Equation (2.10), the differential scattering cross section of light scattering is

$$\frac{d^2\sigma}{d\Omega dE} = \frac{1}{Nj_{0Z}} \frac{\omega^4}{8\pi c^3} P^2 \sin^2 \theta \quad (2.25)$$

where  $N$  is the number of the induced electricity dipole, and  $j_{0Z}$  is the incident energy-flux density along the incident direction Z.

Therefore, to obtain the differential scattering cross section of light scattering, it is necessary to know the electricity dipole  $\mathbf{P}(t)$  induced by incident light and the scattering light produced by the induced electricity dipole  $\mathbf{P}(t)$ . Therefore, in the classical theory of light scattering, to obtain the differential scattering cross section we need to find induced oscillating electricity dipole moment  $\mathbf{P}(t)$ .

### 2.2.1.2 Induced Electric Dipole Moment and Polarizability Tensor

When a beam of light enters a system containing charged particles and due to the interaction between incident light and these particles, the particles will be forced to move and induce the electric dipole moment. If the incident light is weak, the induced electric dipole moment  $\mathbf{P}$

will be the linear function with the incident electric field  $\mathbf{E}$  and can be expressed as

$$\mathbf{P} = \alpha \cdot \mathbf{E} \quad (2.26)$$

where  $\alpha$  is the ratio of induced dipole moment to the field  $\mathbf{E}$ , described as polarizability, which reflects the property of the medium itself.

In general, the directions of  $\mathbf{P}$  and  $\mathbf{E}$  are not the same, so  $\alpha$  is a second-order tensor written as

$$\alpha \equiv \begin{pmatrix} \alpha_{xx} & \alpha_{xy} & \alpha_{xz} \\ \alpha_{yx} & \alpha_{yy} & \alpha_{yz} \\ \alpha_{zx} & \alpha_{zy} & \alpha_{zz} \end{pmatrix} \quad (2.27)$$

Correspondingly, the tensor form of Equation (2.26) could be written as

$$\begin{pmatrix} P_x \\ P_y \\ P_z \end{pmatrix} = \begin{pmatrix} \alpha_{xx} & \alpha_{xy} & \alpha_{xz} \\ \alpha_{yx} & \alpha_{yy} & \alpha_{yz} \\ \alpha_{zx} & \alpha_{zy} & \alpha_{zz} \end{pmatrix} \begin{pmatrix} E_x \\ E_y \\ E_z \end{pmatrix} \quad (2.28)$$

where  $E_x, E_y, E_z$  and  $P_x, P_z$  are the Cartesian components of  $\mathbf{E}$  and  $\mathbf{P}$ , respectively.

Now we need to solve the practical form of the differential scattering cross section of the light scattering listed in Equation (2.25) based on the classical theory of electricity dipole radiation. We will begin with some simple scatters, for example, of atoms and molecules, from which we can gain an understanding of the mechanism of light scattering and basic features of light scattering spectra.

## 2.2.2 Light Scattering of Isolated Atoms

An atom is constructed of an atomic nucleus and an electron of charge  $e$  and mass  $m$ , in which the electron is captured by the atomic nucleus around which it orbits. The movement of electrons can be described as simple harmonic oscillations with a frequency  $\omega = (K/m)^{1/2}$ , where  $K$  is the force constant of the simple harmonic oscillator.

According to the theory of classical electrodynamics, the displacement of an electron (or an ion) will induce an electrical dipole moment  $\mathbf{P}$ . This electrical dipole moment induced by a simple harmonic oscillation of electrons can be expressed as

$$\mathbf{P}(t) = -er(t) \quad (2.29)$$

If the atom is affected by the external electric field of incident light expressed as

$$\mathbf{E}_0 = \mathbf{n}_0 E_0 e^{-i\omega_0 t} \quad (2.30)$$

where  $n_0$  and  $\omega_0$  are the oscillated direction and frequency, respectively, the displacement  $\mathbf{r}$  of electrons captured by the atomic nucleus can be solved by the classical motion equation:

$$m\ddot{\mathbf{r}} = -K\mathbf{r} - m\gamma\dot{\mathbf{r}} + e\mathbf{n}_0 E_0 e^{-i\omega_0 t} \quad (2.31)$$

Where the first item is the bound force of the atomic nucleus to the electron with a force constant of the simple harmonic oscillation  $K$ ; the second item is the damping force of the

damping coefficient  $\gamma$ ; the third item is the force produced by the external electric field. The solution of this differential equation is

$$\mathbf{r}(t) = \left(\frac{e}{m}\right) \frac{1}{\omega_0^2 - \omega^2 + i\omega_0\gamma} \mathbf{n}_0 E_0 e^{-i\omega_0 t} \quad (2.32)$$

Substituting Equation (2.32) into Equation (2.29) and comparing the result with Equation (2.26), we obtain the expression of the atomic polarizability  $\alpha(\omega_0)$  as

$$\alpha(\omega_0) = \left(\frac{e^2}{m}\right) \frac{1}{\omega^2 - \omega_0^2 - i\omega_0\gamma} \quad (2.33)$$

Using the equations of electric dipole radiation in Section 2.2.1, we can obtain the intensity and energy-flux density of the induced electrical dipole moment radiation field of the atom. Substituting them into Equation (2.14) of the differential scattering cross section, we have the differential scattering cross section of the light scattering of an isolated atom:

$$\frac{d^2\sigma}{d\Omega dE} = \frac{1}{Nj_{0Z}} \frac{e^4 E_0^2}{8\pi m^2 c^3} \frac{\omega^4}{(\omega_0^2 - \omega^2)^2 + \omega_0^2 \gamma^2} \sin^2 \theta \mathbf{e}_r \quad (2.34)$$

### 2.2.3 The Light Scattering of Molecule [5]

A molecule consists of atoms associated with various kinds of chemical bonds and various configurations in space. A solid usually consists of atoms or ions arranged in space with various interactions. Therefore the molecule and solid have a common feature in spatial arrangement so we only need to concentrate on molecule scattering in our discussion on the general principle relatives to vibration light scattering.

#### 2.2.3.1 Polarization of Medium

As mentioned above, the matter including molecules consists of many atoms or ions, thus its electrical dipole moment including either intrinsic ones and induced ones cannot be described by the electrical dipole moment of one atom alone. Thus we define the polarization and polarizability of matter to describe the electrical dipole moment of matter.

We assume in light scattering that the matter is non-conductive, non-magnetic, non-absorbed, and the average distance between atoms of scattered matter,  $a$ , is considerably less than the light wavelength (i.e.,  $\lambda \approx 10^3$  nm). Now we introduce micro-polarization of the medium at position  $\mathbf{r}$ ,  $\mathbf{P}_{\text{micro}}(\mathbf{r}, t)$ , which is seen as the sum of the electric dipole moment of the atoms localized in the microscopic region of matter. If  $\mathbf{r}_i(t)$  and  $\mathbf{P}_i(t)$  stand for the position and the electric dipole moment of the  $i$ -th atom, respectively, then  $\mathbf{P}_{\text{micro}}(\mathbf{r}, t)$  can be expressed as

$$\mathbf{P}_{\text{micro}}(\mathbf{r}, t) \equiv \sum_i \mathbf{p}_i(t) \delta(\mathbf{r} - \mathbf{r}_i(t)) \quad (2.35)$$

while the macroscopic polarization  $\mathbf{P}(\mathbf{r}, t)$  is the average of  $\mathbf{P}_{\text{micro}}(\mathbf{r}, t)$ , as shown in Figure 2.7. If the size of volume element  $\Delta V$  is  $d$ ,  $a$  the average distance between atoms of

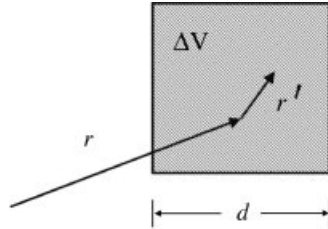


**Figure 2.7** Schematic diagram of the macroscopic polarization  $\mathbf{P}(\mathbf{r}, t)$  as the average of microscopic polarization  $\mathbf{P}_{\text{micro}}(\mathbf{r}, t)$ . Reprinted from S.-L. Zhang, *Raman Spectroscopy and Low-dimensional nanoscale Semiconductors*, Science Press, (2008)

scattered matters,  $\lambda$  the wavelength of incident light, and  $a \ll d \ll \lambda$ , we have

$$\mathbf{P}(\mathbf{r}, t) \equiv \frac{1}{\Delta V} \int_{\Delta V} d\mathbf{r}'^3 \mathbf{P}_{\text{micro}}(\mathbf{r} + \mathbf{r}', t) \quad (2.36)$$

### 2.2.3.2 The Induced Dipole Moment and Polarizability

Due to thermal motion or other sources, the atoms or ions in molecules vibrate around their equilibrium position, and the molecule polarizability  $\alpha$  would be different from that of a molecule in equilibrium; and would be relative to the position charge of atoms in the molecule. Therefore,  $\alpha$  is the function of the coordinate  $\mathbf{r}$  of the atom nucleus, and can be expressed as the Taylor expansion in normal coordinate  $Q$  and corresponding component  $\alpha_{ij}$  of  $\alpha$  a

$$\alpha_{ij} = (\alpha_{ij})_0 + \sum_k \left( \frac{\partial \alpha_{ij}}{\partial Q_k} \right)_0 Q_k + \frac{1}{2} \sum_{k,l} \left( \frac{\partial^2 \alpha_{ij}}{\partial Q_k \partial Q_l} \right)_0 Q_k Q_l + \left( \frac{\partial^3 \alpha_{ij}}{\partial Q_k \partial Q_l \partial Q_m} \right)_0 Q_k Q_l Q_m + \dots \quad (2.37)$$

$Q_k$ ,  $Q_l$ , and  $Q_m$  are normal coordinates of vibration modes with frequency  $\omega_k$ ,  $\omega_l$ , and  $\omega_m$ , respectively, and the sum extends to all the normal coordinates; the symbol  $(\cdot)_0$  indicates the value at the equilibrium position, so  $(\alpha_{ij})_0$  is the polarizability of the atoms at equilibrium.

To avoid complex mathematical derivations and explore the physical nature of problems clearly, we will make some simplifications. First, we keep Equation (2.37) to the first-order term only, which is a good approximation of the small vibrations around equilibrium. Second, we only discuss the vibration related with the normal coordinate  $Q_k$  and the relative polarizability  $\alpha_k$ 's with  $k$  component, of which the components are

$$(\alpha_{ij})_k = (\alpha_{ij})_0 + (\alpha'_{ij})_k Q_k \quad (2.38)$$

where

$$(\alpha'_{ij})_k = \left( \frac{\partial \alpha_{ij}}{\partial Q_k} \right)_0 \quad (2.39)$$

Thus the polarizability tensor corresponding to the component expression in Equation (2.38) can be expressed as

$$\alpha_k = \alpha_0 + \alpha'_k Q_k \quad (2.40)$$

Then the induced electrical dipole moment of the vibration  $k$  related with the normal coordinate  $Q_k$  is

$$\mathbf{P}_k = \mathbf{a}_k \cdot \mathbf{E} \quad (2.41)$$

Substituting Equation (2.41) into Equation(2.25), we obtain the differential scattering cross section of vibration  $k$ :

$$\left( \frac{d^2\sigma}{d\Omega dE} \right)_k = \frac{1}{Nj_{0Z}} \frac{\omega^4}{8\pi c^3} (\mathbf{a}_k \cdot \mathbf{E})^2 \sin^2 \theta \quad (2.42)$$

## 2.2.4 Description of the Mechanism and the Basic Features of Light Scattering Based on Classical Theory of Light Scattering

Based on the discussion of classical theory, we now understand some aspects of the mechanism and basic features of light scattering.

### 2.2.4.1 The Mechanism of Light Scattering

Based on classical theory, we see there are similarities and differences between atom- and molecule-light scattering, both in mechanisms and in features.

The scattering originating from atoms and molecules is different: the former is caused by vibration of the captured electrons in the atom and the latter is due to the atoms or ions vibrating in the molecules, although both vibrations are around their equilibrium point. As a result, the energy of electrons in the atoms and molecules do not change and do change in the scattering process, respectively, resulting in the energy of the atom being changed or not in the scattering process for atom and molecule scattering, respectively. The action of the electrons in molecules in the scattering process will be discussed later.

Comparing the expressions of differential scattering cross sections of atoms and molecules in Equation (2.34) and Equation (2.51), respectively, we see that the intensity feature of light scattering for isolated atoms and molecules is different. The scattering intensity of molecules is proportional to the fourth order of scattered light frequency  $\omega$ . This also indicates that the Rayleigh law that the scattering intensity is proportional to the fourth order of *incident* light frequency  $\omega_0$  is an approximate result. Unlike molecules, the dependence of atom scattering intensity on the incident light frequency  $\omega_0$  is more complex. Based on Equation (2.34) and noting that  $\omega_0$  and  $\omega$  stand for the frequency of incident light and electron vibration, respectively, we obtain the dependence of the differential scattering cross section on the incident light frequency  $\omega_0$  for an isolated atom, as shown in Figure 2.8.

- $\omega_0 \ll \omega$

As the frequency of incident light,  $\omega_0$  is much lower than that of electron vibration  $\omega$ ,  $\mathbf{a}(\omega_0)$  becomes a constant and the frequency of scattered light caused by the induced dipole moment is the same as the frequency of incident light, implying it is only Rayleigh scattering. And from formula (2.34), it can be obtained expressed as

$$d\sigma/d\Omega \propto \omega_0^4 \quad (2.43)$$

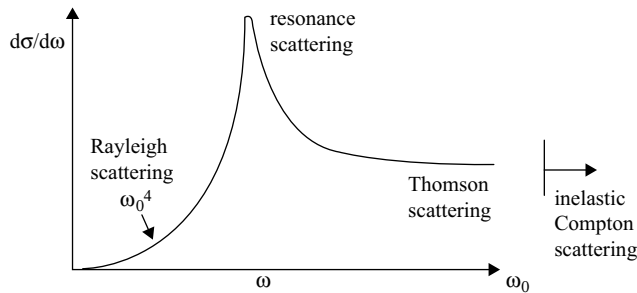


**Figure 2.8** Dependence of differential scattering cross section on incident light frequency  $\omega_0$  for an isolated atom. Reprinted from S.-L. Zhang, *Raman Spectroscopy and Low-dimensional nanoscale Semiconductors*, Science Press, (2008)

- $\omega_0 \approx \omega$

This is where the frequency of incident light  $\omega_0$  is close to that of electron vibration  $\omega$ . Here there is a strong resonant scattering and the differential scattering cross section is very large.

- $\omega_0 \ll \omega < mc^2/\hbar$

This means that the frequency of incident light is very high and thus the electrons can be considered as not bonded by the atomic nucleus. As a result, the differential scattering cross section is expressed as

$$\frac{d\sigma}{d\Omega} = \frac{1}{2} (1 + \cos^2 \theta) \left( \frac{e}{mc^2} \right)^2 \quad (2.44)$$

Equation (2.44) corresponds to Thomson's scatter of free electrons. From Equation (2.44), we see that the intensity of Thomson's scatter is independent of the frequency of incident light.

- $\omega_0 \geq mc^2/\hbar$

This indicates that the incident light has a much higher frequency or the energy of incident photons  $\hbar\omega_0$  is much higher than the zero rest mass of electron  $mc^2$ . In this case, the classical theory does not apply and inelastic Compton scattering occurs.

#### 2.2.4.2 Raman Activity

If a certain scattering source such as a vibration mode  $K$  of molecules can cause Raman scattering under light excitation, then this scattering source, that is, the vibration mode, is considered as Raman activity. From Equation (2.50) we see that the condition of Raman activity is the derivative of polarizability respective to the coordinate  $Q$  of vibration mode  $K$ ,  $\alpha'_k \neq 0$ .

It is well-known that the matrix form of polarizability tensor  $\alpha$  is determined by the space symmetry of scattering sources and then the non-zero matrix element  $(\alpha_{ij})_k$  in  $\alpha_k$  will be

correlated to the symmetry of the source. So long as the matrix form of  $\alpha_k$  is the same, the number and symmetry of scattering spectral peaks are the same, even though the practical scattering sources are different. Of course, the practical content of the non-zero matrix elements of different  $ij$  could be different, implying that the frequency and the intensity of scattering spectral peaks could be different.

Raman activity also means that there is a Raman scattering selection rule in relation to the space symmetry of the sources. This rule demands a specific geometry in the observation of a polarized Raman spectrum, while it also provides the criterion in the assignment of Raman peaks of polarization scattering spectra.

If a system processes the unchanging property under a certain symmetry transformation, it is believed to have the symmetry corresponding to the transformation. Table 2.2 shows an example of a three atom molecule. This molecule has the symmetry transformation of immobility, the rotation of 180° around axis  $z$ , and the inversions against the  $x-z$  and  $y-z$  plane, which are marked as  $E$ ,  $C_2(z)$ ,  $\sigma_{xz}$ , and  $\sigma_{yz}$  in that order. After going through all the above transformations, the change situations represented by “1” and “−1” do and do not coincide, respectively. Corresponding to this symmetry, the form of polarizability  $\alpha_k$  induced by dipole moment  $P_k$ , and differential polarizability  $\alpha'_k$  ( $k = Q_1$ ,  $Q_2$ , and  $Q_3$ ) can be seen in Table 2.2.

From Table 2.2, we find:

- The vibration modes with the same symmetry (e.g.,  $Q_1$  and  $Q_2$ ) have the same form of polarizability  $\alpha_k$  and electric dipole moment  $P_k$ . In contrast, the modes with different symmetry (e.g.,  $Q_1$ ,  $Q_2$  relative to  $Q_3$ ) have different forms of polarizability  $\alpha_k$  and electric dipole moment  $P_k$ . Therefore, under the excitation of the same polarized light, the characters of scattering light, such as the number of spectral lines and the polarization characters, are the same for  $Q_1$  and  $Q_2$  but different for  $Q_1$ ,  $Q_2$  relative to  $Q_3$ .
- The vibration modes  $Q_1$ ,  $Q_2$ , and  $Q_3$  are all Raman active, while their tensor forms of polarizability  $\alpha_k$  and electric dipole moment  $P_k$ 's are different, thus resulting in the detecting conditions of their Raman spectra being different, that is, the polarized directions, propagated directions, and the mutual relation of incident light and observed scattering light are different. The above requirement forms the so-called Raman experimental selection rule. For instance, in the case where the polarized directions of incident light and observed scattered light are parallel, the Raman spectra of vibration modes  $Q_1$  and  $Q_2$  can be observed, but it is impossible for  $Q_3$  mode. However, if the polarized directions of incident light and observed scattered light is crossed, the observed results would be opposite for the modes  $Q_1$ ,  $Q_2$  relative to  $Q_3$ .

Except for the symmetry in above discussion, we have not involved any other properties of molecules, such as their mass, their force constant and so on, therefore the above conclusions are universal as long as the symmetry remains the same. Even though the chemical components of materials are different, as long as their symmetries remain the same, their Raman spectra have the same number and polarization characteristics. Of course, since different chemical components imply different masses and force constants, the other characters such as frequency and intensity of Raman peaks are different. As an example, some Raman spectra of several crystalline semiconductors are shown in Figure 2.9. All of these semiconductors belong to the cubic group of zincblende structure but the components are different, which can be clearly seen from the figure.

**Table 2.2** Various vibration modes  $K$  and the corresponding symmetry property, polarizability  $\alpha_k$ , induced dipole moment  $\mathbf{P}_k$ , differential polarizability  $\alpha'_k$  ( $k=Q_1$ ,  $Q_2$ , and  $Q_3$ ), and Raman activity for a three atomic molecule. Reprinted from S.-L. Zhang, *Raman Spectroscopy and Low-dimensional nanoscale Semiconductors*, Science Press, (2008)

Molecular Structure			
Vibration Mode	  		
Transformation	$E$	1	1
	$C_2(z)$	1	-1
	$\sigma_{xz}$	1	1
	$\sigma_{yz}$	1	-1
Symmetry	Holohedral Symmetry	Holohedral Symmetry	$C_2(z), \sigma_{yz}$ Symmetry
$\alpha_K$	$\begin{pmatrix} \alpha_{1,xx} & 0 & 0 \\ 0 & \alpha_{1,yy} & 0 \\ 0 & 0 & \alpha_{1,zz} \end{pmatrix}$	$\begin{pmatrix} \alpha_{2,xx} & 0 & 0 \\ 0 & \alpha_{2,yy} & 0 \\ 0 & 0 & \alpha_{2,zz} \end{pmatrix}$	$\begin{pmatrix} 0 & 0 & \alpha_{3,xz} \\ 0 & 0 & 0 \\ \alpha_{3,zx} & 0 & 0 \end{pmatrix}$
$\mathbf{P}_K$	$\begin{pmatrix} \alpha_{1,xx} & E_x \\ \alpha_{1,yy} & E_y \\ \alpha_{1,zz} & E_z \end{pmatrix}$	$\begin{pmatrix} \alpha_{2,xx} & E_x \\ \alpha_{2,yy} & E_y \\ \alpha_{2,zz} & E_z \end{pmatrix}$	$\begin{pmatrix} \alpha_{3,xz} & E_z \\ 0 & 0 \\ \alpha_{3,zx} & E_x \end{pmatrix}$
$\alpha'_K$	$\neq 0$	$\neq 0$	$\neq 0$
Activity	YES	YES	YES

The Raman spectrum is a powerful tool in the study of symmetry of matter, especially for crystalline materials. Also, the information of the structure and symmetry of crystals is an important foundation to the study of crystal Raman spectroscopy.

#### 2.2.4.3 Basic Features of Scattered Light

In general, the features of a beam of light can be described by its frequency, polarization, intensity, and phase. Below, will be discussed the classical light scattering theory, by using the light scattering of molecule as the practical specimen.

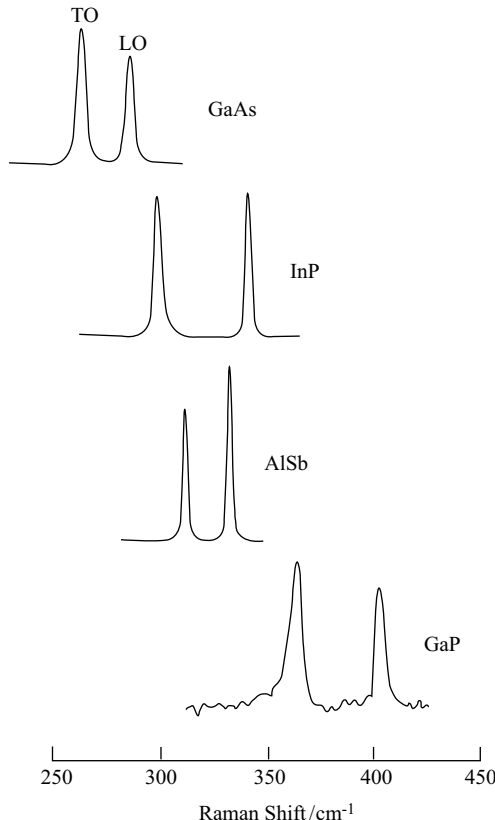


**Figure 2.9** Raman spectra of several crystalline semiconductors belonging to the same cubic group of zincblende structure but with different chemical components. Reprinted from S.-L. Zhang, *Raman Spectroscopy and Low-dimensional nanoscale Semiconductors*, Science Press, (2008)

- Frequency characteristics

If the amplitude of atom vibrations in a molecule is not too large and can be described by a simple harmonic vibration, and the relation between vibration coordinate  $Q_k$  and time  $t$  can be expressed as

$$Q_k = Q_{k0} \cos(\omega_k t + \varphi_k) \quad (2.45)$$

where  $Q_{k0}$  is the vibration amplitude, and  $\omega_k$  and  $\varphi_k$  are the frequency and initial phase of the vibration, respectively. Substituting Equation (2.41) into Equation (2.38) and Equation (2.40), respectively, we obtain

$$(\alpha_{ij})_k = (\alpha_{ij})_0 + (\alpha'_{ij})_k Q_{k0} \cos(\omega_k t + \varphi_k) \quad (2.46a)$$

$$\alpha_k = \alpha_0 + \alpha'_k Q_{k0} \cos(\omega_k t + \varphi_k) \quad (2.46b)$$

The electric field  $\mathbf{E}$  of light with frequency  $\omega_0$  can be expressed as

$$\mathbf{E} = \mathbf{E}_0 \cos \omega_0 t \quad (2.47)$$

where  $\mathbf{E}_0$  is the amplitude of  $\mathbf{E}$ .

Based on the above discussion, we know that an induced dipole moment  $\mathbf{P}$  will be induced when a molecule is irradiated by the electric field  $\mathbf{E}$  of a light wave. For a typical vibration  $Q_k$ , substituting Equation (2.40) and Equation(2.47) into Equation(2.26), we obtain the induced dipole moment  $\mathbf{P}_k$  of vibrating mode  $k$

$$\begin{aligned} \mathbf{P}_k &= \alpha_k \cdot \mathbf{E} = \alpha_0 \cdot \mathbf{E}_0 \cos \omega_0 t + \frac{1}{2} Q_{k0} \alpha'_k \cdot \mathbf{E}_0 \cos[(\omega_0 - \omega_k)t + \varphi_k] \\ &\quad + \frac{1}{2} Q_{k0} \alpha'_k \cdot \mathbf{E}_0 \cos[(\omega_0 + \omega_k)t + \varphi_k] \end{aligned} \quad (2.48)$$

Introducing

$$\mathbf{P}_0 = \alpha_0 \cdot \mathbf{E}_0 \quad (2.49)$$

$$\mathbf{P}_{k0} = \frac{1}{2} Q_{k0} \alpha'_k \cdot \mathbf{E}_0 \quad (2.50)$$

Equation (2.48) can be written as

$$\mathbf{P}_k = \mathbf{P}_0 \cos(\omega_0 t) + \mathbf{P}_{k0} \cos[(\omega_0 - \omega_k)t + \varphi_k] + \mathbf{P}_{k0} \cos[(\omega_0 + \omega_k)t + \varphi_k] \quad (2.51)$$

Then introducing

$$\mathbf{P}_0(\omega_0) = \mathbf{P}_0 \cos(\omega t) \quad (2.52)$$

$$\mathbf{P}_0(\omega_0 \pm \omega_k) = \mathbf{P}_{k0} \cos[(\omega_0 \pm \omega_k)t + \varphi_k] \quad (2.53)$$

Now Equation (2.51) can be expressed further as

$$\mathbf{P}_k = \mathbf{P}_0(\omega_0) + \mathbf{P}_k(\omega_0 - \omega_k) + \mathbf{P}_k(\omega_0 + \omega_k) \quad (2.54)$$

Substituting Equation (2.48) into Equation(2.25), we obtain the differential scattering cross section of vibration  $Q_k$ :

$$\left( \frac{d^2\sigma}{d\Omega dE} \right)_k = \frac{1}{Nj_{0Z}} \frac{\omega^4}{8\pi c^3} (\mathbf{a}_k \cdot \mathbf{E})^2 \sin^2 \theta \quad (2.55)$$

Equation (2.54) shows that the induced dipole moment has three components  $\mathbf{P}_0(\omega_0)$ ,  $\mathbf{P}_0(\omega_0 + \omega_k)$ , and  $\mathbf{P}_0(\omega_0 - \omega_k)$ , therefore, as soon as light scattering occurs, they must produce three kinds of radiation with frequencies of  $\omega_0$ ,  $\omega_0 + \omega_k$ , and  $\omega_0 - \omega_k$ , which are Rayleigh, Stokes, and anti-Stokes scatterings, respectively.

Moreover, we can also see that the process of light scattering is similar to that of frequency (not amplitude) modulation of electromagnetic waves or of frequency mixing

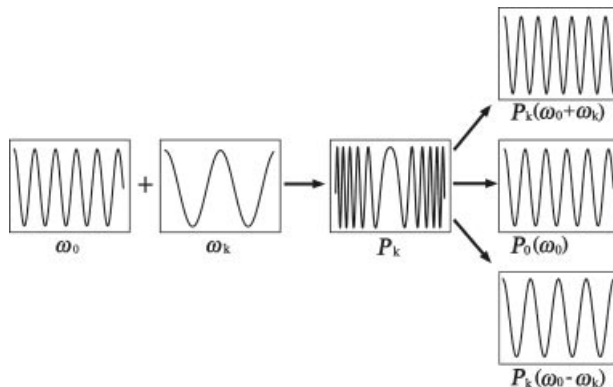


**Figure 2.10** Simulation of the electromagnetic wave frequency modulation process of light scattering. Reprinted from S.-L. Zhang, Raman Spectroscopy and Low-dimensional nanoscale Semiconductors, Science Press, (2008)

in nonlinear optics [6]. Figure 2.10 simulates the frequency modulation process of electromagnetic waves. In the modulation of electromagnetic waves, the incident light equals the carrier wave with frequency  $\omega_0$ , and the oscillating wave of scatters equals a signal wave with frequency  $\omega_k$ . After the carrier wave with  $\omega_0$  is modulated by a signal wave with  $\omega_k$ , according to the modulation theory, the outgoing wave must include the radiation of sum frequency ( $\omega_0 + \omega_k$ ) and slip frequency ( $\omega_0 - \omega_k$ ), except for the carrier wave frequency  $\omega_0$ . Obviously, they are Rayleigh, Stokes, and anti-Stokes scattering, respectively.

- Intensity characteristics

Note that the observed Raman scattering intensity  $I$  is relative to differential scattering cross section directly:

$$I = \frac{d^2\sigma}{d\Omega dE} \quad (2.56)$$

Substituting the expanded Equation (2.48) of dipole moment into Equation (2.25), we obtain the light scattering intensity of the mode  $Qk$ :

$$I_k = \left[ \frac{\langle Q_{k0} \rangle (\omega_0 \mp \omega_k)^4}{32\pi c^3} \sin^2\theta \right] |\alpha'_k \cdot \mathbf{E}_0|^2 \quad (2.57)$$

Equation (2.57) shows that Raman scattering intensity is proportional to the intensity of incident light  $|\mathbf{E}_0|^2$  and the quadruplicate of scattered light frequency ( $\omega_0 \pm \omega_k$ ). Also Equation (2.57) indicates that the scattered light intensity is the quadruplicate of incident light frequency  $\omega_0$ , indicating that the famous Raleigh law is only an approximate one.

- Polarization characteristics

Section 2.2.1 mentioned that the polarization of incident light and scattered light is linked by the polarizability tensor. Based on Equation (2.28) of the induced dipole moment  $\mathbf{P}$ , we learn:

First, by the reaction between the external electric field with fixed polarization direction and the scatters with a fixed orientation in space, the scattered light is also polarized but its polarization direction is not necessarily the same as that of incident light.

Second, if the special orientation of scatters, such as molecules, crystals, and so on, is not fixed, even if the incident light is plane polarized, the polarization direction of scattered light is not only different from that of the incident light, but also the scattered light is perhaps not plane polarized.

From Equation (2.28), when  $E_x$ ,  $E_y$ , and  $E_z$  are definite, namely the incident light has fixed polarized directions, the  $P_x$ ,  $P_y$ , and  $P_z$  of scatters are totally determined by polarization tensor  $\alpha$ . Since the form of  $\alpha$  is determined by the symmetry of the system, that is, scatters, the polarized Raman spectrum will provide information on the symmetry of the system.

Moreover, from the expression of differential scattering cross section in Equation (2.25), the induced dipole moment  $\mathbf{P}$  influences the differential scattering cross section and the differential scattering cross is the reflection of the intensity of scattered light. Therefore, the information of the change for the polarized state in scattering spectra is extracted by using the comparing measurement of the intensity change of spectral line.

- Phase characteristics

In Equation (2.23),  $\mathbf{k} \cdot \mathbf{r}$  is the expression of phase  $\varphi$ . In the experiment of light scattering, the frequency, polarization, and intensity will be reflected directly in spectra and so can be directly measured, while the phase has no direct reflection in spectra and is usually hidden by the spectral intensity and spatial distribution. It is well-known that if the phases of two beams of lights are interrelated, they will cause interference and thus the light propagated will be enhanced in one direction and weakened in the other direction. Therefore, if the phases between the incident light and the scattered light, as well as between the light from different scatters are interrelated, the scattered light intensity would not be the simple sum of intensities of the light beams originated from different scattering sources.

First, concerning the phase problem of scattered and incident light, from Equation (2.51), the phase of scattered and incident light in Rayleigh and Raman scatterings are the same and different, respectively. Therefore, Rayleigh scattered light and its incident light are coherent and thus Rayleigh scattering has directivity in space. However, Raman scattered light and its incident light are incoherent and Raman scattered light does not have any specific direction in the spatial distribution of intensity.

Second, a practical scattering experiment is usually involved in the light from many different scatters while the discussion above is limited to the light from a single scatter, therefore the phase problem of scattering light from different scatters should be considered. Note that there is phase factor  $\varphi_k$  in Equation (2.48), which makes the light from different

scatters (e.g., the Raman scattered light caused by different molecules) not coherent, thus the Raman scattering intensity from molecules or solid systems is the algebraic sum of scattered light from each molecule or lattice vibrations.

The macroscopic theory of light scattering provides many satisfying explanations to the mechanism of light scattering and explores the features of the light scattering spectrum. But there are some problems related with the microscopic physical mechanism, such as the intensity of Stokes and anti-Stokes scattering and some selection rules. The classical theory cannot be applied here, so a microscopic theory is needed.

## 2.3 Microscopic Theory of Light Scattering

The microscopic theoretical description of light scattering can be based on quantized field theory [7], which corresponds to the particle collision model mentioned in Section 2.1. Whole scattering systems consist of quantized particles, namely light wave fields of incident and scattered beams are both quantized as photons and the scattering target consists of quantized particles or quasi-particles. The scattering process is the one in which the producing and annihilating of incident, scattered, and target particles are due to interactions between them.

If the photons involved in light scattering are the photons of visible frequency, the description of incident and scattered light does not necessarily use photons but rather classical electromagnetic waves; nevertheless, target particles are still regarded as quantized particles. Therefore, production and annihilation of target particles are equal to the quantum state change of target particles. This kind of theoretical form is the so-called non-relativistic one of quantized field theory, the so-called quantum mechanics. As the quantum mechanics theory can illuminate the mechanics and basic features of visible light scattering, moreover, quantized field theory is beyond the theoretical basics of most readers of this book. In addition, this book is mainly concerned with the visible and basic Raman scattering, so discussion will be based on quantum mechanics theory only.

### 2.3.1 Differential Scattering Cross Section and Quantum Transition Probability

Figure 2.11 exhibits the quantum mechanics description of vibration light scattering, in which the real and broken lines represent the real and virtual energy levels transition, respectively. In Figure 2.11 the process of light scattering is graphically represented to show that after the target particles are irradiated by incident light, they are transited from the initial quantum state to the middle one and then transited to the end state continuously, in which the energies of the initial and end states may or may not be equal. The scattered light is radiatively accompanied by the transition from the middle to the end states, of which the transition energy being equal and not equal are the Rayleigh and Raman scatterings, respectively. Moreover, the energy of the initial state, being lower or higher than the end state, is only the Stokes and anti-Stokes scattering, respectively.

From Equation (2.21), the differential cross section  $\frac{d^2\sigma}{dE_1 d\Omega}$  is directly proportional to the transition probability  $R$ , therefore it is clear that the solving of the transition probability  $R$  plays a key rule in obtaining a differential cross section and understanding light scattering by the quantum mechanics theory.

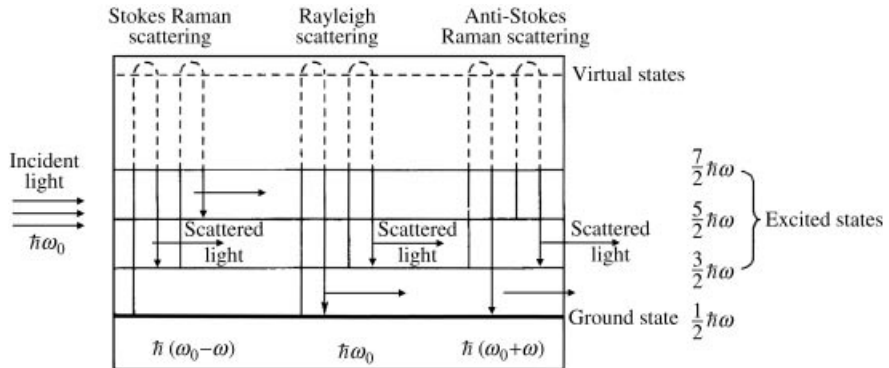


**Figure 2.11** The quantum mechanics description of vibration light scattering. Reprinted from S.-L. Zhang, *Raman Spectroscopy and Low-dimensional nanoscale Semiconductors*, Science Press, (2008)

### 2.3.2 Scheme of Quantum Transition Probability and Time Dependent Perturbation Theory for Vibration Light Scattering [8]

In a light scattering event, the transition probability  $R$  caused by the interaction between incident light and target particles can be obtained by solving the time-dependent Schrodinger equation:

$$\hat{H}(t)\psi(\mathbf{r}, t) = i\hbar \frac{\partial}{\partial t} \psi(\mathbf{r}, t) \quad (2.58)$$

where  $\hat{H}(t)$ s is the time-dependent Hamiltonian operator and  $\psi(\mathbf{r}, t)$  is the wave function describing the system quantum state. Assuming that the Hamiltonian operator can be written as

$$\hat{H}(t) = \hat{H}_0 + \hat{H}'(t) \quad (2.59)$$

then  $H_0$  and  $\hat{H}'(t)$  are Hermitian operators, which are unrelated and related to  $t$ , respectively. The time-dependent Hamiltonian equation can be revised as

$$\{\hat{H}_0 + \hat{H}'(t)\}\psi(\mathbf{r}, t) = i\hbar \frac{\partial}{\partial t} \psi(\mathbf{r}, t) \quad (2.60)$$

The eigenfunction  $\varphi_n(\mathbf{r})$  and eigenvalue  $\varepsilon_n$  of  $\hat{H}_0$  can be obtained from the stationary Schrodinger equation:

$$\hat{H}_0\varphi_n(\mathbf{r}) = \varepsilon_n\varphi_n(\mathbf{r}) \quad (2.61)$$

In a light scattering event,  $\hat{H}_0$  and  $\hat{H}(t) = \hat{H}_0 + \hat{H}'(t)$  are the Hamiltonian operators which do not exist and do exist the interaction between light and target particles, respectively. The  $\hat{H}'(t)$  reflecting interaction between the light and target particles can be seen as a perturbation of the system; in other words,  $\hat{H}'(t)$  is a small quantity compared with  $\hat{H}_0$ .

Therefore, we can use time-dependent perturbation methods to solve the time-dependent Schrodinger equation.

In the time-dependent perturbation method,  $\psi(\mathbf{r}, t)$  is expanded with a time-relative eigenfunction system of  $\hat{H}_0$ :

$$\phi_n(\mathbf{r}, t) = \varphi_n(\mathbf{r}) \exp(-i\epsilon_n t/\hbar), \quad (2.62)$$

then

$$\psi(\mathbf{r}, t) = \sum_n C_n(t) \phi_n \quad (2.63)$$

Obviously,  $C_n(t)$  is the wavefunction of  $\psi(\mathbf{r}, t)$  in the coordinate system with  $\varphi_n$  as basic vectors and also represents the probability at the state  $\varphi_n$  of the perturbed system  $\psi(\mathbf{r}, t)$ . Then the  $|C_n(t)|^2$  represents the transition probability from the initial state  $\varphi_k$  to the state  $\varphi_n$ . Therefore, from  $C_n(t)$  can be obtained the transition probability  $R$ .

Based on the perturbation method,  $\hat{H}'(t)$  can further be divided into 0, 1, 2, 3... orders of perturbation and thus  $C_n(t)$  can be written as

$$C_n(t) = C_n^{(0)}(t) + C_n^{(1)}(t) + C_n^{(2)}(t) + \dots \quad (2.64)$$

In Equation, (2.64) the wave function  $C_n^{(0)}(t)$  is one of no perturbation, which can be assumed as the  $k^{th}$  eigenstate  $\varphi_k(\mathbf{r})$  of  $\hat{H}_0$ . By solving the time-dependent Schrodinger equation, we obtain the wave function corresponding to the first-order perturbation:

$$C_n^{(1)}(t) = \frac{1}{i\hbar} \int_0^t \exp(i\omega_{nk}t) H'_{nk} dt, \quad (2.65)$$

The matrix element in Equation (2.65) is

$$H'_{nk}(t) = \langle \varphi_n(\mathbf{r}) | H'(t) | \varphi_k(\mathbf{r}) \rangle \quad (2.66)$$

$$\omega_{nk} = (\epsilon_n - \epsilon_k)/\hbar \quad (2.67)$$

Thus, the transition probability from the state  $\varphi_k(\mathbf{r})$  to the state  $\varphi_n(\mathbf{r})$  is expressed as

$$R_{nk}(t) = \frac{1}{\hbar^2} \left| \int_0^t \exp(i\omega_{nk}t) H'_{nk} dt \right|^2 \quad (2.68)$$

Below will be discussed the light scattering features of atoms, molecules, and general matter by using the microscopic theory already mentioned above.

### 2.3.3 Quantum Mechanical Description of Atom Light Scattering [8]

As shown in Section 2.2.2, atoms can be treated as systems with electrons moving around a nucleus and electron motion can be described by harmonic oscillation. The light scattering of atoms results from the scattering of bound electrons in the atoms.

First, we assume the electric field of the incident light does not change in the atomic region, that is, the incident electric field  $E$  is treated as a space-uniformed field, and amplitude  $E_0$  is

not a function of coordinate  $r$ . In this way, the electric field could be expressed as

$$\mathbf{E} = \mathbf{E}_0 \cos \omega_0 t \quad (2.69)$$

The electrical potential induced by the electric field is

$$\chi = -\mathbf{E} \cdot \mathbf{r} \quad (2.70)$$

Considering that the electron displacement  $\mathbf{r}$  will yield electric moment  $\mathbf{P}$ , which has a relation

$$\mathbf{P} = -e\mathbf{r} \quad (2.71)$$

then,  $\hat{H}'(t)$  can be expressed as

$$\hat{H}'(t) = -e\chi = e\mathbf{E} \cdot \mathbf{r} = -\mathbf{P} \cdot \mathbf{E} = -\mathbf{P} \cdot \mathbf{E}_0 \cos \omega_0 t \quad (2.72)$$

By setting Equation (2.72) into Equation (2.65), we have

$$C_{nk}^{(1)}(t) = -\frac{\mathbf{P}_{nk} \cdot \mathbf{E}_0}{2\hbar} \left\{ \frac{\exp [i(\omega_{nk} + \omega_0)t] - 1}{\omega_{nk} + \omega_0} + \frac{\exp [i(\omega_{nk} - \omega_0)t] - 1}{\omega_{nk} - \omega_0} \right\} \quad (2.73)$$

and the transition matrix element  $\mathbf{P}_{nk}$  in Equation (2.73) is

$$\mathbf{P}_{nk} = \langle \varphi_n(r) | \mathbf{P} | \varphi_k(r) \rangle \quad (2.74)$$

Hence, the transition probability of the atom light scattering is

$$R_{nk}(t) = \frac{|\mathbf{P}_{nk} \cdot \mathbf{P}_0|^2}{4\hbar^2} \frac{\sin^2[(\omega_{nk} - \omega_0)t/2]}{[(\omega_{nk} - \omega_0)t/2]^2} \quad (2.75)$$

### 2.3.4 Quantum Mechanical Theory of the Light Scattering Due to Molecule Vibrations

Section 2.3.2 described the mechanism of molecule light scattering from the view of classical theory. The light scattering of molecule vibrations is described as the action of an external electric field  $\mathbf{E}$ , where the vibration around the equilibrium position of atoms or ions in molecules induces a macroscopic polarization  $\mathbf{P}(\mathbf{r}, t)$ , as expressed by Equation (2.48). The radiation caused by  $\mathbf{P}(\mathbf{r}, t)$  is the scattered light of molecular vibrations.

From Section 2.3.3 the transition matrix element of atom electric polarization  $\mathbf{P}$  in Equation (2.74) was replaced by the induced electric moment of molecule vibrations  $\mathbf{P}^G$ . By using Equation (2.26), the matrix elements of  $\mathbf{P}^G$  can be obtained:

$$\begin{aligned} \mathbf{P}_{nk}^G &= \langle \varphi_n(r) | \mathbf{P}^G | \varphi_k(r) \rangle = \langle \varphi_n(r) | \mathbf{a} \cdot \mathbf{E} | \varphi_k(r) \rangle \\ &= \langle \varphi_n(r) | \alpha | \varphi_k(r) \rangle \cdot \mathbf{E} \end{aligned} \quad (2.76)$$

We introduce the notation  $[\alpha_{ij}]_{nk}$ , representing the polarization transition matrix element in Equation (2.76):

$$[a_{ij}]_{nk} = \langle \varphi_n(\mathbf{r}) | \alpha_{ij} | \varphi_k(\mathbf{r}) \rangle \quad (2.77)$$

As electric susceptibility  $\alpha$  is a real number, thus  $\alpha$  is a symmetrical matrix, so among nine of the components of susceptibility components, there are only six independent ones, as shown as Equation (2.77):

$$\begin{aligned} [\alpha_{xx}]_{nk} &= \langle \varphi_n(\mathbf{r}) | \alpha_{xx} | \varphi_k(\mathbf{r}) \rangle \\ [\alpha_{yy}]_{nk} &= \langle \varphi_n(\mathbf{r}) | \alpha_{yy} | \varphi_k(\mathbf{r}) \rangle \\ [\alpha_{zz}]_{nk} &= \langle \varphi_n(\mathbf{r}) | \alpha_{zz} | \varphi_k(\mathbf{r}) \rangle \\ [\alpha_{xy}]_{nk} &= \langle \varphi_n(\mathbf{r}) | \alpha_{xy} | \varphi_k(\mathbf{r}) \rangle \\ [\alpha_{xz}]_{nk} &= \langle \varphi_n(\mathbf{r}) | \alpha_{xz} | \varphi_k(\mathbf{r}) \rangle \\ [\alpha_{yz}]_{nk} &= \langle \varphi_n(\mathbf{r}) | \alpha_{yz} | \varphi_k(\mathbf{r}) \rangle \end{aligned} \quad (2.78)$$

### 2.3.5 Quantum Mechanical Explanation of Light Scattering

#### 2.3.5.1 Light Scattering Mechanism

From Equation (2.76) if susceptibility  $\alpha$  is the constant  $C$ , it can be removed from the integration. As  $\varphi_n(\mathbf{r})$  and  $\varphi_k(\mathbf{r})$  are orthogonal wave functions, we have

$$[\alpha]_{nk} = \begin{cases} C & n = k \\ 0 & n \neq k \end{cases} \quad (2.79)$$

which represents the occurrence and non-occurrence, respectively, of transitions between the same ( $n = k$ ) and different ( $n \neq k$ ) energy levels.

Light scattering implies that  $\alpha$  is not a constant. In this case, the  $[\alpha]_{nk} \neq 0$  at  $n = k$  or  $n \neq k$  indicates the occurrence of Rayleigh and Raman scatterings, respectively.  $[\alpha]_{nk} \neq 0$  means that the molecular susceptibility  $\alpha$  is changed and this change originates from small vibrations around their equilibrium position of atoms or ions in molecules. These small vibrations can be considered as fluctuations in the statistics, which indicates that the fluctuation is the light scattering origin and explores the origin of light scattering at the level of microscopic motion based on quantum mechanics. In the light scattering of atoms, the electron moment  $\mathbf{p}$  plays the same role as  $\alpha$  in molecular scattering. The change of electron position  $\mathbf{r}$  in atoms results in the change in  $\mathbf{p}$ , inducing the light scattering of atoms. Such a change can also be seen as a fluctuation in the statistics. Therefore, the fluctuation mechanism of light scattering interpretations is also the one of atomic light scattering.

#### 2.3.5.2 Rayleigh, Stokes and anti-Stokes Scattering

The condition for solving Equation (2.75) is  $\omega_0 + \omega_{nk} > 0$ , in which  $\omega_{nk}$  is expressed by Equation (2.67). There are three cases satisfying this condition:

- When  $\omega_n = \omega_k$ , we have  $\omega_0 + \omega_{nk} = \omega_0$ , meaning the initial and final states are at the same energy level.

- When  $\omega_n < \omega_k$ , we have  $\omega_0 + \omega_{nk} < \omega_0$ , meaning that the initial state is at the lower energy level compared to that of the final state, which also means that the frequency of scattered light is lower than that of the incident light.
- When  $\omega_n > \omega_k$ , we have  $\omega_0 + \omega_{nk} > \omega_0$ , which means that the initial state is at the higher energy level compared to that of the final state, which implies that the frequency of scattered light is higher than that of the incident light.

Obviously, the above three cases correspond to the Rayleigh scattering, Stokes, and anti-Stokes scattering, respectively.

### 2.3.5.3 Selection Rule

From Equations (2.75)–(2.77), there is at least one of  $[\alpha_{ij}]_{nk}$  not equivalent to 0. The transition from vibration state  $|\varphi_k(\mathbf{r})\rangle$  to vibration state  $|\varphi_n(\mathbf{r})\rangle$  is possible and the transition probability  $R_{nk}(t)$  will not be equal to 0, meaning that Raman scattering is possible, that is, the system is Raman-active. This is only the micro-theoretical mention of the selection rule.

In group theory,  $[\alpha_{ij}]_{nk} \neq 0$  demands that the triple product of  $\varphi_n(\mathbf{r})\alpha_{ij}\varphi_k(\mathbf{r})$  represents a full symmetry, thus the selection rule can be derived from spatial symmetry. The selection rule is very important for research of crystal Raman scattering. Loudon have finalised strict group theoretic derivations and discussions on the selection rule in crystal [9]. Some works have detailed depictions of this [10].

### 2.3.5.4 Intensity of Stokes and anti-Stokes Scattering

It is well-known that the particle population of occupying energy levels in equilibrium obeys the Boltzmann distribution. The description in Figure 2.11 shows that the Stokes and anti-Stokes Raman scattering correspond respectively to the transitions from a low energy level to a higher one or reverse. So the respective intensities of Stokes and anti-Stokes Raman scattering  $I_{k,s}$  and  $I_{k,As}$  can be expressed as

$$I_{k,s} \propto 1/[1 - \exp(-\hbar\omega_k/k_B T)] \quad (2.80)$$

$$I_{k,As} \propto 1/[\exp(+\hbar\omega_k/k_B T) - 1] \quad (2.81)$$

where  $k_B$  and  $T$  are the Boltzmann constant and absolute temperature, respectively. Thus the intensity ratio of Stokes and anti-Stokes scattering is

$$I_{k,s}/I_{k,As} \propto \exp(\hbar\omega_k/k_B T) \quad (2.82)$$

Under normal circumstance,  $\exp(\hbar\omega_k/k_B T)$  is much larger than 1. In this way, quantum theory correctly explains the question of why the intensity of Stokes scattering is larger than that of anti-Stokes scattering, which has been demonstrated to be impossible using classical theory.

In the above discussion, we have assumed the level energy as having an infinitely narrow value and the particle population at this level as not distributed. Obviously, this is not the case and the level energy  $E$  has a width of  $\Delta E$  and the particle population at this level is distributed. This shows that the radiation yielded by the transition between energy levels always has a broadening frequency and the intensity of every monochrome spectral component varies with frequency. These result in the existence of the width and line shape for spectra. This is the common phenomena in spectroscopy and more detail can be found in the references [11, 12].

## References

- [1] Rayleigh, L. (1871) *Phil. Mag.*, **XLI**, 274, 447.
- [2] Brillouin, L. (1922) *Ann. Phys. (Paris)*, **17**, 88.
- [3] Smekal, A. (1923) *Naturwiss.*, **11**, 873.
- [4] Jackson, J.D. (1998) *Classical Electrodynamics*, 3rd edn, John Wiley & Sons.
- [5] Long, D.A. (1977) *Raman Spectroscopy*, McGraw-Hill International Book Company, New York.
- [6] Svelto, O. (1998) *Principles of Lasers*, 4th edn, Springer.
- [7] Srednicki, M.A. (2007) *Quantum Field Theory*, Cambridge University Press.
- [8] Landau and, L.D. and Lifshitz, L.M. (1981) *Quantum Mechanics (Non-Relativistic Theory)*, 3rd edn, Butterworth Heinemann.
- [9] Loudon (1963) *Proc. Roy. Soc. (London) A*, **275**, 218.
- [10] Sherwood, P.M.A. (1972) *Vibrational Spectroscopy of Solids (Monographs on Physical Chemistry)*, Cambridge University Press, Cambridge.
- [11] Born, M. and Wolf, E. (1999) *Principle of Optics*, Cambridge University Press, Cambridge.
- [12] Bates, D.R. and Bederson, B. (1957) *Adv. Atom. Mol. Opt. Phy.*, **11**, 331.

# 3

## Experimental Foundation of Raman Spectroscopy

### 3.1 Generality of Raman Spectral Measurements

Experiments of Raman spectroscopy are to record the variation of Raman scattering signals with one or more variables. To obtain good results, fundamental knowledge of Raman spectral measurements is necessary to learn.

#### 3.1.1 Essential Object Measured by Conventional Raman Spectra

Chapter 2 discussed how the differential scattering cross section  $\frac{d\sigma}{d\Omega dE}$  contains the information of scattering events and is a basic physical quantity to be measured in scattering experiments. This enables us to record the variation of scattering density  $I$  in a solid angle  $d\Omega$  and energy interval  $E$  to  $E + dE$ . The energy of Raman spectra is usually expressed by frequency  $\omega$  or wavenumber  $\text{cm}^{-1}$ , thus such measured spectrum is named the frequency spectrum. Using the CCl<sub>4</sub> Raman spectrum, shown in Figure 1.5 as an example, Figure 3.1 shows the relationship between the parameters of Raman frequency spectrum and differential scattering cross section  $\frac{d\sigma}{d\Omega dE}$ .

#### 3.1.2 Features of Raman Spectra

The Raman spectrum has some spectral features that are similar to those of common spectra mentioned in Section 1.3. The mechanism of Raman scattering is different from common spectra and thus the Raman spectrum possesses have special features yet.

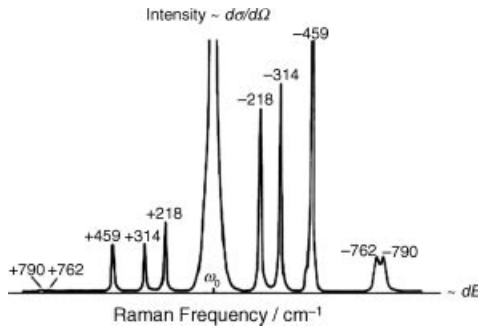


**Figure 3.1** Correlation between differential scattering cross section  $\frac{d\sigma}{d\Omega dE}$  and Raman frequency spectrum. Reprinted from S.-L. Zhang, *Raman Spectroscopy and Low-dimensional nanoscale Semiconductors*, Science Press, (2008)

### 3.1.2.1 Characteristics Related to the Energy of Excitation Sources

In scattering experiments with excitation sources such as visible light, neutrons, and X-rays, the corresponding energies  $E$  are  $10^0$ ,  $10^{-2}$ , and  $10^3$  eV, respectively, of which the corresponding energy uncertainties  $\Delta E/E$  are  $10^{-8}$ ,  $10^{-4}$ , and  $10^{-2}$ , respectively (Table 1.1). According to the uncertainty principle, the corresponding time uncertainty  $\Delta\tau$  values are

$$\text{Visible light} \approx 10^{-8} \text{ s}$$

$$\text{Neutron} \approx 10^{-10} \text{ s} \quad (3.1)$$

$$\text{X ray} \approx 10^{-17} \text{ s}$$

Since the actual measurement is always performed in a duration between  $-\tau$  and  $\tau$ , and  $I(t_0)$  is the intensity of Raman scattering at time  $t_0$ , then the actual measured intensity is an average one of time expressed as

$$\langle I(t_0) \rangle = \frac{1}{2\tau} \int_{-\tau}^{\tau} I(t' + t_0) dt' \quad (3.2)$$

The characteristic time of atom movements is usually  $10^{-12}$  second. When compared to the characteristic time listed above, the recorded intensity in neutron and visible scattering experiments must be a time-average one, while in X-ray scattering it is an immediate one. In static scattering experiments, the measurement process takes a long time and the recorded results must be time-average ones, even for X-ray scattering. Thus, the spectral intensities obtained by routine Raman scattering are always the time-average result.

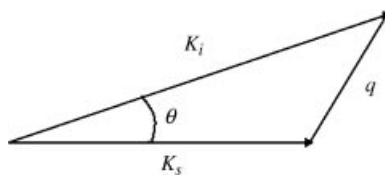


**Figure 3.2** Schematic diagram of the momentum conservation of incident light momentum  $\mathbf{k}_i$ , scattering light momentum  $\mathbf{k}_s$ , and scattered object momentum  $\mathbf{q}$ . Reprinted from S.-L. Zhang, *Raman Spectroscopy and Low-dimensional nanoscale Semiconductors*, Science Press, (2008)

### 3.1.2.2 Characteristics Related to the Momentum (Propagated Direction) of Incident and Scattered Light

If  $\mathbf{k}_i$ ,  $\mathbf{k}_s$ , and  $\mathbf{q}$  mark the momentums of the incident light, scattered light, and scattered object, respectively, and according to the law of momentum conservation should show the relation

$$\mathbf{k}_i = \mathbf{k}_s + \mathbf{q} \quad (3.3)$$

which is illustrated in Figure 3.2.

In Figure 3.2, the directions of  $\mathbf{k}_i$ ,  $\mathbf{k}_s$ , and  $\mathbf{q}$  represent the propagation direction of the incident light, scattered light, and scatter object, respectively. The angle  $\theta$  is the included angle between propagated directions of incident and scattered light. The back scattering experimental geometry is mostly used in solid scattering experiments, in which the propagation direction of scattered and incident light is the opposite. Figure 3.2 shows that the scatter wave vector  $\mathbf{q}=0$ , meaning that only the scattered object of  $\mathbf{q}=0$  is excited.

It is well-known that the energy of vibrations of molecules and phonons in solids is from  $3 \times 10^{12}$  to  $3 \times 10^{13}$  Hz and the energy of visible light is about  $6 \times 10^{14}$  Hz, therefore the energy change of scattered light relative to incident light can be ignored in the visible Raman scattering of molecules and solids. That means  $k_i \approx k_s$  and thus the scattered wave vector  $q$  can be expressed approximatively as

$$q \approx 2k_i \sin \frac{\theta}{2} \quad (3.4)$$

This indicates that in back scattering experiments on phonons, the scattering spectra are only from so-called long-wavelength phonons of  $q \approx 0$ .

### 3.1.2.3 Characteristics Related to the Polarization of Incident and Scattered Light

As mentioned in Chapter 2, Raman spectra possess a close relation with the polarizability of light. That is why a Raman spectrum will vary with the polarizations of incident and scattered light, which distinguishes characteristics of Raman spectra from those of common spectra. The Raman spectra measured by plane or circular polarized light are called plane or circular polarized Raman spectra, respectively.

Since a direction must be related to a geometric space, the polarized Raman spectra are dependent on the experimental geometric configuration, as defined in Figure 3.3.

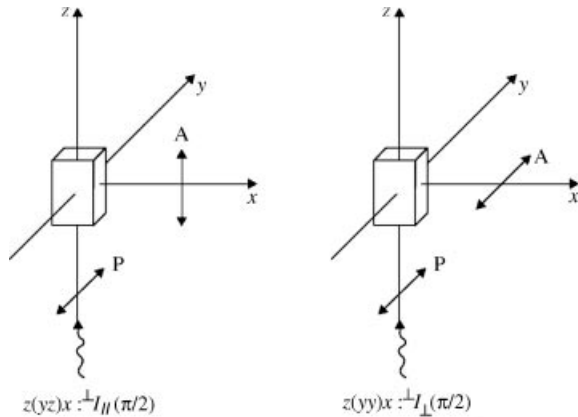


**Figure 3.3** Diagram of Raman experimental geometry configuration in the orthogonal coordinate system [1]. Reprinted from S.-L. Zhang, *Raman Spectroscopy and Low-dimensional Nanoscale Semiconductors*, Science Press, (2008)

To describe the geometric configuration of polarized Raman spectral experiments, we need to introduce a marking notation based on the Cartesian coordinate system as follows:

$$G_1(G_2 G_3)G_4 \quad (3.5)$$

where  $G_1$  and  $G_2$  denote the propagated and polarized directions of the incident light, respectively, while  $G_3$  and  $G_4$  represent the propagated and polarized directions of the collected scattered light, respectively.

Moreover, to describe a polarized scattering experiment, we define a scattering plane included by propagating directions of incident light,  $G_1$ , and the collected correction of scattered light,  $G_4$ , which are considered as essential plane in experiments. The polarization directions of perpendicular and parallel to the scattering plane are denoted by  $\perp$  and  $\parallel$ , respectively, while the nature of light is denoted by  $n$ .

- Intensity expression of polarized Raman spectra

To represent the intensity of polarized Raman spectra measured under various polarized light conditions, we introduced a marking symbol as

$$\perp I \parallel (\theta) \quad (3.6)$$

In the above expression, the sign at the upper left and lower right of  $I$  mark the polarization direction of the incident light and collected scattered light, respectively.

#### 3.1.2.4 Characteristic Quantity Related to Polarized Spectra

In common Raman spectra, we can extract the frequency, intensity, line shape, and line width spectral parameters. In polarized Raman spectra, there are more spectral parameters to be obtained, such as the polarized selection rule, depolarized ratio, and Raman optical activity (ROA).

- Polarization selection rule

In Section 2.2.1, it was shown that the polarizability tensor  $\alpha$  reflects the property of the medium itself, that is, each vibration mode of a medium has respective  $\alpha$  with respective symmetry. For example, the polarizability tensors of vibration modes with different symmetry for ZnO crystals with  $C_{6v}$  point group symmetry have forms as follows: [2]

$$\begin{aligned}\alpha'(A_1(z)) &= \begin{bmatrix} \alpha'_{11} & 0 & 0 \\ 0 & \alpha'_{22} & 0 \\ 0 & 0 & \alpha'_{33} \end{bmatrix}, \\ \alpha'(E_1(-x)) &= \begin{bmatrix} 0 & 0 & -\alpha'_{13} \\ 0 & 0 & 0 \\ \alpha'_{13} & 0 & 0 \end{bmatrix}, \\ \alpha'(E_1(y)) &= \begin{bmatrix} 0 & 0 & 0 \\ 0 & 0 & \alpha'_{13} \\ 0 & \alpha'_{13} & 0 \end{bmatrix}, \\ \alpha'(E_2) &= \begin{bmatrix} 0 & \alpha'_{12} & 0 \\ \alpha'_{12} & 0 & 0 \\ 0 & 0 & 0 \end{bmatrix}, \quad \alpha'(E_2) = \begin{bmatrix} \alpha'_{12} & 0 & 0 \\ 0 & -\alpha'_{12} & 0 \\ 0 & 0 & 0 \end{bmatrix}.\end{aligned}$$

According to Equation (2.26)

$$\mathbf{P} = \alpha \cdot \mathbf{E}$$

If the polarized direction of incident light, that is, electromagnetic field  $\mathbf{E}$  is fixed, the polarizability tensor  $\alpha$  is known, and the polarized direction of induced dipole moment is  $\mathbf{P}$ , then the scattering light can be induced and its polarization can be predicated by Equation (2.26). This rule is named as the polarization selection rule, which helps us to select an experimental configuration and to assign a certain vibration mode by polarized Raman spectra.

In 1966, Damen *et al.* applied the polarization selection rule to a sample [2]. Figure 3.4 shows their observed polarized Raman spectra at configuration of right-angle scattering for ZnO crystal with  $C_{6v}$  point group. According to the polarization selection rule, the frequency and symmetry character of the fundamental modes have been determined, of which the fundamental vibration modes are two  $E_2$  modes at  $101\text{ cm}^{-1}$  and  $437\text{ cm}^{-1}$ , two  $A_1$  modes at  $381\text{ cm}^{-1}$  (transverse) and  $574\text{ cm}^{-1}$  (longitudinal), and two  $E_1$  modes at  $407\text{ cm}^{-1}$  (transverse) and  $583\text{ cm}^{-1}$  (longitudinal).

In 1967, Porto *et al.* published the polarized Raman spectra of the materials  $\text{TiO}_2$ ,  $\text{MgF}_2$ ,  $\text{ZNF}_2$ ,  $\text{FeF}_2$ , and  $\text{MnF}_2$ , all of which belong to the  $D_{4h}$  point group [3]. Their work exhibited

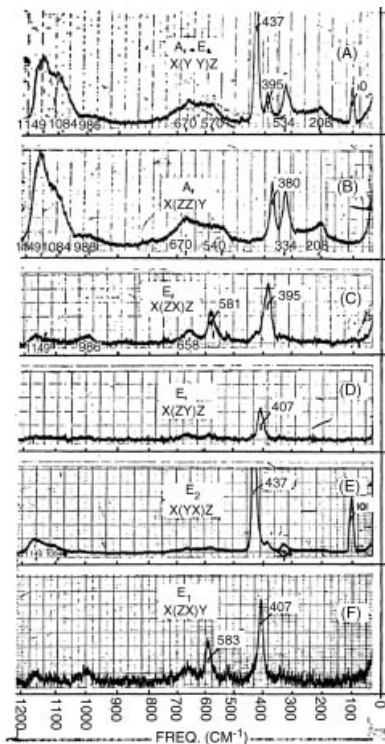


**Figure 3.4** Raman spectra of ZnO crystal measured in the right-angle geometric configuration for various polarization and propagation directions of incident and observed scattered light at room temperature, with 488 nm excitation [2]. Reprinted from T. C. Damen, S. P. S. Porto, and B. Tell, Raman Effect in Zinc Oxide, *Phys Rev*, 142 (1966) with permission of the American Physical Society

the application of the polarized selection rule further and confirmed the similarity of Raman spectral features for the same symmetric materials.

- Depolarization degree and symmetry

In Section 2.2.4, polarization characteristics of scattered light showed that spatial orientations of scattered objects are random, such as the molecules in gas and liquid, and the polarized direction of measured scattered light may differ from that of incident light, that is, even though the incident light is plane-polarized, the scattered light can be non-polarized light. To describe such polarization changes quantitatively, we defined a physical quantity of depolarization ratios, which is defined as the intensity ratios of two polarized Raman spectra. The depolarization ratios usually have the three forms  $\rho_n(\theta)$ ,  $\rho_{\perp}(\theta)$ , and  $\rho_s(\theta)$ , and according to the intensity symbol expression of polarized Raman spectra shown in Equation (3.6), they can be expressed as, respectively:

$$\rho_n(\theta) = \frac{nI_{\parallel}(\theta)}{nI_{\perp}(\theta)} \quad (3.7)$$

$$\rho_n(\theta) = \frac{\perp I_{\parallel}(\theta)}{\perp I_{\perp}(\theta)} \quad (3.8)$$

$$\rho_n(\theta) = \frac{\parallel I_{\perp}(\theta)}{\perp I_{\perp}(\theta)} \quad (3.9)$$

where  $\theta$  is the included angle between propagating directions of incident light and the corrected direction of scattered light.

Using Equations (2.55) and (2.48), the depolarization ratios can be expressed by using the special average of the second-order product of the components  $\alpha'_{ij}$  of derivative polarizability  $\mathbf{a}'$  [1]. For the molecules of random orientations in space, the non-zero spatial average of the second-order product of  $\alpha'_{ij}$  is

$$\overline{(\mathbf{a}'_{xx})^2} = \overline{(\mathbf{a}'_{yy})^2} = \overline{(\mathbf{a}'_{zz})^2} = \frac{1}{45}(45\alpha^2 + 4\gamma^2) \quad (3.10)$$

$$\overline{(\mathbf{a}'_{xy})^2} = \overline{(\mathbf{a}'_{yz})^2} = \overline{(\mathbf{a}'_{zx})^2} = \frac{1}{45}\gamma^2 \quad (3.11)$$

$$\overline{(\mathbf{a}'_{xx}\mathbf{a}'_{yy})} = \overline{(\mathbf{a}'_{yy}\mathbf{a}'_{zz})} = \overline{(\mathbf{a}'_{zz}\mathbf{a}'_{xx})} = \frac{1}{45}(45\alpha^2 - 4\gamma^2) \quad (3.12)$$

and others are zero.

On the right side of the above equations,  $\alpha$  and  $\gamma$  are the measures of polarizability and anisotropy, respectively, which are named as the mean polarizability and anisotropic rate, respectively, and are expressed as

$$\alpha = \frac{1}{3}(a'_{xx} + a'_{yy} + a'_{zz}) \quad (3.13)$$

$$\gamma^2 = \frac{1}{2} \left[ (a'_{xx} + a'_{yy})^2 + (a'_{yy} + a'_{zz})^2 + (a'_{zz} + a'_{xx})^2 + 6(a'_{xy})^2 + 6(a'_{yz})^2 + 6(a'_{zx})^2 \right] \quad (3.14)$$

where  $\alpha$  and  $\gamma$  don't change under rotation of coordinate systems.

As an example, we can write down the depolarization degrees by the derivative polarizability for the configuration shown in Figure 3.2 as

$$\rho_n\left(\frac{\pi}{2}\right) = \frac{\overline{(\mathbf{a}'_{zx})^2} + \overline{(\mathbf{a}'_{xy})^2}}{\overline{(\mathbf{a}'_{yx})^2} + \overline{(\mathbf{a}'_{yy})^2}} = \frac{6\gamma^2}{45a^2 + 7\gamma^2} \quad (3.15)$$

$$\rho_{\perp}\left(\frac{\pi}{2}\right) = \frac{\overline{(\mathbf{a}'_{zy})^2}}{\overline{(\mathbf{a}'_{yy})^2}} = \frac{3\gamma^2}{45a^2 + 4\gamma^2} \quad (3.16)$$

$$\rho_s\left(\frac{\pi}{2}\right) = \frac{\overline{(\mathbf{a}'_{yz})^2}}{\overline{(\mathbf{a}'_{yy})^2}} = \frac{3\gamma^2}{45a^2 + 4\gamma^2} \quad (3.17)$$

Chapter 2 showed that the expression of derivative polarizability is determined by the symmetry of scattered objects. Therefore, Equations (3.15)–(3.17) indicate that the polarization status and symmetry of scattered objects such as molecules and phonons can be extracted from the depolarization ratio. As a result, measurement and analysis of the depolarization ratio becomes a powerful method in symmetry classification. For example, according to Equations (3.15)–(3.17), the depolarization ratio  $\rho_n(\theta) = \rho_{\perp}(\theta) = \rho_s(\pi/2) = 0$  means that the anisotropic rate is zero and the scattered light is totally polarized. While  $\rho_{\perp}(\theta) = \rho_s(\pi/2) = 3/4$  and  $\rho_n(\theta) = 6/7$  indicate that the mean polarizability is zero and the scattered light is totally depolarized. When  $\rho_{\perp}(\theta)$  and  $0 < \rho_s(\pi/2) < 3/4$ , and  $0 < \rho_n(\theta) < 6/7$ , the scattered light is partially polarized.

- Raman optical activity (ROA)

The Raman scattered light intensity of right and left circularly polarizations for a chiral object is different, which is named as the Raman optical activity (ROA) and was first observed by Buckingham and Bogaard in 1973 [4].

ROA can be observed in a number of forms. For instance, in scattered circular polarization (SCP) experiments, the incident light is linearly polarized and differences in circular polarization of the scattered light are measured. In dual circular polarization (DCP), both the incident and the scattered light are circularly polarized, either in phase (DCPI) or out of phase (DCPII).

For the object's sensitive to chirality, such as some liquid crystals and biomolecules, ROA is a useful probe. For example, the Barron group [5] reported a ROC study on the polypeptide in a model  $\beta$ -sheet conformation and believed that the study provides a useful representation of the structural relationships among the polypeptide and protein states considered in their study. Figure 3.5 shows one of their observed ROC spectra.

### 3.1.3 Technological Keys of Raman Spectral Measurements

Chapters 1 and 2 show that, on the one hand, the intensity of Raman scattering is very weak with  $10^{-6}\text{--}10^{-12}$  of the incident light; on the other hand, the intensity of Rayleigh scattering is several thousand times of that of Raman scattering and sometimes a strong photoluminescence superimposed on Raman scattering bands will appear. These are the fundamental difficulties in a measurement of Raman spectra and there are mainly two ways to solve these problems.

One is to increase the power density of samples and the receiving efficiency of the scattering signal. Chapter 2 clarified that the Raman scattering intensity is proportional to the quadratic power of the electric field strength of incident light  $E$ , that is, proportional to the power density of incident light on samples, which is not an obstacle if a laser is used as the light source. Thus, enhancing the intensity of the scattering signal of the detector becomes the first choice in technology, rather than increasing the power of the light source only.

Another way is to decrease the intensity of stray light. With present-day photo-detectors, it is possible to detect a single photon, therefore if the laser is used as the light source, another technique is to enhance the signal-to-noise ratio of the Raman signal to stray light, rather than increasing the absolute intensity of the Raman signal.

In following sections, we will discuss ways of solving the two technological problems mentioned above, from the two viewpoints of experimental apparatus and measurements.

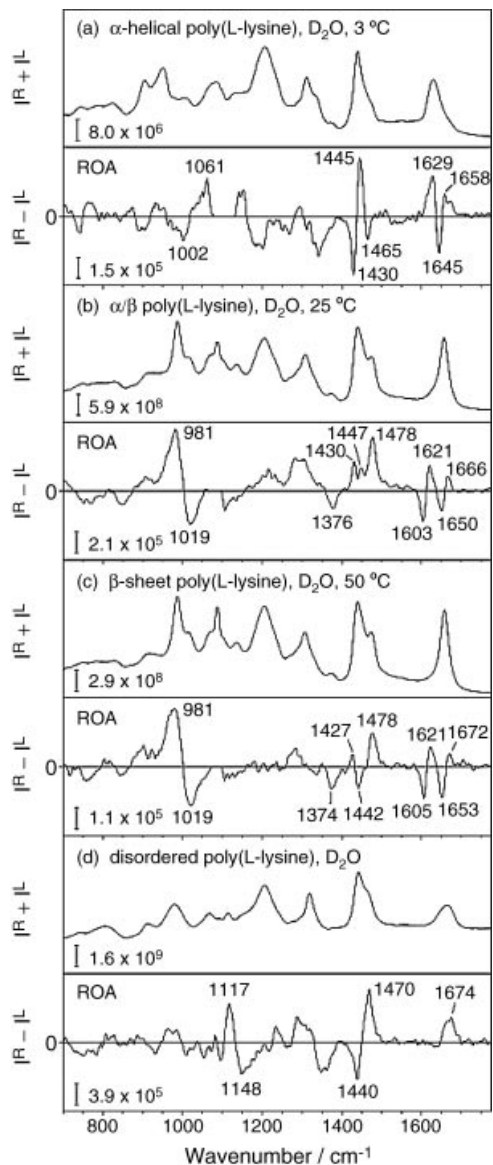


**Figure 3.5** Backscattered Raman and ROA spectra of poly(L-lysine) in  $D_2O$  at  $pD$  11.4 and  $\sim 3^\circ\text{C}$  (a),  $25^\circ\text{C}$  (b), and  $50^\circ\text{C}$  (c) corresponding to  $\alpha$ -helical, intermediate, and  $\beta$ -sheet states, respectively, and at  $pD$  3.0 and  $20^\circ\text{C}$  (d) corresponding to the disordered state [5]. Reprinted from Iain H. McColl, et al., A New Perspective on  $\beta$ -Sheet Structures Using Vibrational Raman Optical Activity: From Poly(L-lysine) to the Prion Protein, *J. Am. Chem. Soc.* 125, 10019 (2003) with permission of American Chemical Society

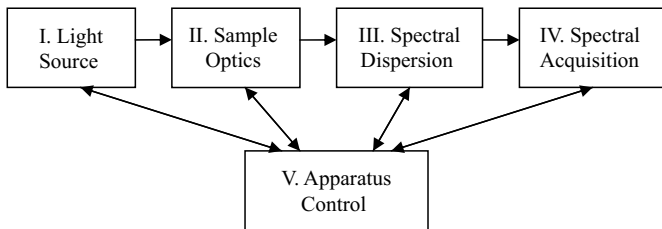


**Figure 3.6** Layout of Raman spectrometer. Reprinted from S.-L. Zhang, *Raman Spectroscopy and Low-dimensional nanoscale Semiconductors*, Science Press, (2008)

## 3.2 Experimental Apparatus

The experimental apparatus for Raman spectral measurement is called a Raman spectrometer. As shown in Figure 3.6, it usually consists of five parts: light source, sample optics, spectral dispersion, spectral acquisition, and apparatus control.

The core part of a Raman spectrometer is the spectral dispersion. This can be the diffraction grating, Michelson interferometer, or Fabry-Perot interferometer, of which the first and last two belong to the dispersion and interference type of spectrometers, respectively. Nowadays, the grating Raman spectrometer is used widely, so we will describe it in more detail, and the other two types of interfered spectrometers will be introduced in the last section of this chapter.

Various types of commercial Raman spectrometers have been developed widely. Commercial spectrometers are required generally to fit a variety of applications and be easy to use, thus it is impossible for them to fulfill the requirements of some special or extra-high performance measurements. This means we need to design a special Raman spectrometer ourselves for our special requirements. Of course, a deep understanding of the working principle, structure, and component performances of instruments would be of benefit, not for the good application of present spectrometers but also the design of special Raman spectrometers. In this section, we will introduce the Raman spectral apparatus in detail. First, we will introduce Raman apparatus parts, as shown in Figure 3.6. Second, we will discuss the common optical factors related to each element of Raman apparatus parts. Finally, instructions for designing a Raman spectrometer will be given.

### 3.2.1 Light Source [6]

As lasers began to be used as excited light sources, an understanding of the basic features of lasers is required. Because of the high concentration of emission energy in one photon state (optical mode), that is, high degeneracy of main photons, the laser processes have many properties, which are described below.

#### 3.2.1.1 Monochromaticity

The monochromaticity of light is indicated by its spectral line width,  $\Delta\lambda$ . If the consistency of wavelength is good and the line width is narrow, such light processes good monochromaticity. We usually introduce the relative line width,  $\Delta\lambda/\lambda$ , to describe the monochromaticity.

Good monochromaticity is an important advantage of the laser. For example,  $\Delta\lambda/\lambda$  of the He-Ne laser is  $\sim 10^{-11} \sim 10^{-13}$ , while the  $\Delta\lambda/\lambda$  at low temperature of discharge spectral line

$^{86}\text{Kr}$  at 605.7 nm is  $\sim 8 \times 10^{-7}$ , which was the usual standard of length in history and is lower by 4~6 orders of magnitude than that of monochromaticity of the He-Ne laser.

### 3.2.1.2 Directionality

The direction of the light source is described by the diverging angle  $2\theta$  of a beam or the solid angle  $\Delta\Omega = (2\theta)^2$ . The solid angle of an ordinary beam  $\Delta\Omega = 4\pi$ , when it is near to the diffraction limit determined by the exit aperture of lasers, that is,  $2\theta = \lambda/d$ , where  $d$  is the diameter of the beams. For example, the solid angle of the single-mode He-Ne laser is  $2\theta = 10^{-3}$ , meaning its  $\Delta\Omega$  is only  $10^{-6}$  radian.

### 3.2.1.3 High-Brightness

The above two properties make the brightness of lasers very high. Ordinary lasers after convergence can easily reach a brightness of  $10^6$  times the brightness of the sun's surface.

### 3.2.1.4 Polarization

The laser is formed in an optical resonance cavity and thus has a high degree of polarization; for example, the gas laser gives an excellent plane polarized light with an ideal degree of polarization.

### 3.2.1.5 Coherency

There are two kinds of coherency: time coherency and space coherency. Time coherency is when two beams are emitted from the same source at the same instant, and then superposed onto the same point. Space coherency is when two beams are emitted from the same source, but at different times, and are then superposed onto one point. If they do or not produce an interference fringe after superposition, they are considered as coherent or non-coherent, respectively, of which the interference scale is denoted by the coherence time  $\tau_c$  and coherency length  $L_c$ , respectively.

Lasers possess time and space coherency simultaneously. For example, the  $\tau_c$  and  $L_c$  of 605.7 nm spectra line of  $\text{Kr}^{86}$  at low temperatures are  $2.5 \times 10^{-9}$  s and of  $7.5 \times 10$  cm, respectively, while the frequency stabilization and spatial coherency of an ordinary He-Ne laser are  $\tau_c = 1.3 \times 10^{-4}$  and  $L_c = 4 \times 10^6$  cm, respectively.

### 3.2.1.6 Gaussian Features of Beam

The laser beam possesses Gaussian features. Since the propagation, convergence, and collimation of light are based on the understanding of light beam features, we will introduce the common knowledge of the Gaussian beam below.

No matter how the laser is constructed, whether with a stable spherical cavity or with an unstable spherical cavity, the electric field of the fundamental mode of lasers can be expressed as

$$E(x, y, z) = [A_0/w(z)] \exp\{-(x^2 + y^2)/w^2(z)\} \exp\{ik[z + (x^2 + y^2)/2R(z)] - i\varphi(z)\} \quad (3.18)$$

where  $A_0$  is the constant for beams,  $w(z)$ ,  $R(z)$ , and  $\varphi(z)$  are the beam diameter, with radius of curved face with equal phase and phase shift, respectively. Equation (3.18) expresses the features of the Gaussian beam where the laser is not the usual plane wave or the uniform spherical wave. The virtual index part in Equation (3.18) represents the shape of the wave face and its change, as well as the distribution of the wave amplitude and the amplitude

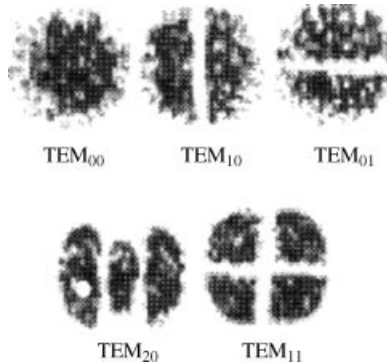


**Figure 3.7** The intensity distribution at the cross section of Gaussian beams for the fundamental mode and high-order modes [7]. Reprinted from S.-L. Zhang, *Raman Spectroscopy and Low-dimensional nanoscale Semiconductors*, Science Press, (2008)

changing in the propagating wave. Figure 3.6 shows the features of the Gaussian beam in the propagated wave.

Let  $\rho = (x^2 + y^2)^{1/2}$  as the distance away from the optical axis of a laser, then the amplitude of the Gaussian beam can be expressed as

$$[A_0/w(z)] \exp[-\rho^2/w^2(z)] \quad (3.19)$$

Equation (3.19) means the amplitude of the Gaussian beam is reduced with increasing distance from the optical axis and appears as a Gaussian distribution. The largest amplitude is at  $\rho = 0$ . The  $A_0/w(z)$  is the center amplitude. When  $\rho = w(z)$ , the amplitude is reduced to  $1/e$  of its center amplitude and thus the radius of beam is called  $w(z)$ .

However, the Gaussian beam has different orders of modes, that is, the first-order (fundamental) and high-order modes. The intensity distribution at the cross section of Gaussian beams do and do not continue for the fundamental mode and high-order modes, respectively, as shown in Figure 3.7. In spectral measurements, it is better to use the fundamental mode of the laser.

- In the propagating path, a Gaussian beam displays a divergence Gaussian spherical wave and the beam radius,  $w(z)$ , is changing, as shown in Figure 3.8. The beam radius is minimum at  $z = 0$ , which is called the lumbar size and denoted as  $w_0$ . We define the divergent angle as  $2\theta = dw(z)/dz$ . When  $z$  is infinite, the divergent angle at far field  $\theta = \lambda/v\pi w_0$ .

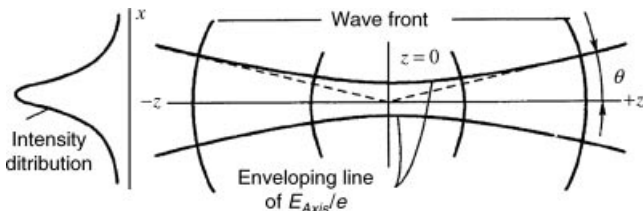


**Figure 3.8** Features of the Gaussian beam in the propagated path [7]. Reprinted from Y.-H. Zhou and T.-H. Sun, *Laser physics*, (1991) with permission of the Peking University Press

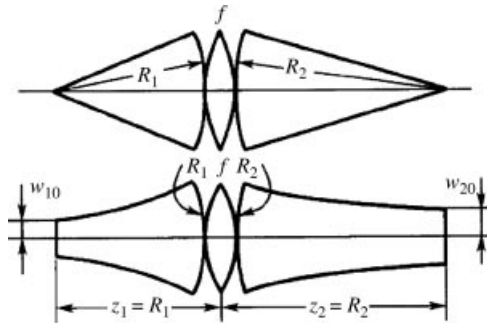


**Figure 3.9** The Gaussian beam transformed through a lens [7]. Reprinted from Y.-H. Zhou and T.-H. Sun, *Laser physics*, (1991) with permission of the Peking University Press

- The transforming and propagating law of a Gaussian beam is similar to that of an ordinary spherical wave. Its transformation through a thin lens can be expressed as

$$\frac{1}{R_2} = \frac{1}{R_1} - \frac{1}{f} \quad (3.20)$$

where  $R_2$  and  $R_1$  are the curvature radius of the equal-phase face of the lens before and after transforming, and  $f$  is the focal length. Figure 3.9 presents a Gaussian beam transforming through a lens. Practically, we use the imaging formula of thin lens in geometrical optics to deal with the transformation and propagation of Gaussian beams passing through lenses.

### 3.2.1.7 Types of Lasers

- According to the output wavelength of lasers, the laser is classified into two types: visible and invisible. For the invisible laser, there are still various types, such as, X-ray, ultraviolet, infrared, and THz lasers.
- For the time characteristics of output power, lasers are divided into two categories: continuous and pulse. The output power of pulse lasers is very huge at transient times.
- The working medium of lasers varies and thus are categorized as the solid-state lasers, liquid lasers, gas lasers, and semiconductor lasers.
- Regarding the difference of pump (energy supply), lasers are divided into optically pumped lasers, electric excitation lasers (gas discharge/power injection), and chemical lasers.

We have listed some kinds of lasers used in Raman spectral measurement and their performances are listed in Appendix I.

### 3.2.2 Sample Optics

The function of sample optics is to create the illumination of excitation light, collection of scattered light, and environments of measured samples. We will introduce the elements in sample optics according to the three functions mentioned above.

Sample optics should achieve the following basic requirements. For example, the excited light on the samples should have the highest power density possible but should not degenerate or destroy that sample. The scattered light from the sample can be collected

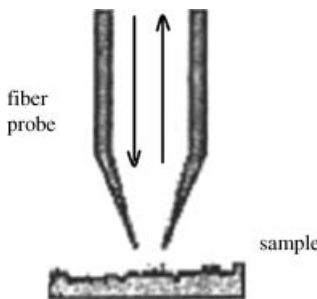


**Figure 3.10** An aperture optical fiber probe

and entered into the spectrometer at its greatest extent. Below we will introduce some of the ways to achieve the above.

The elements traditionally used in sample optics are lenses and mirrors. Recently, non-lens elements have become increasingly used, of which the aperture and apertureless optical fiber and metal probe are the most popular. Figure 3.10 shows an aperture probe. The application of probes helped the birth of new Raman spectroscopic branches, such as near-field and tip-enhancement Raman microscopy, which will be described in Chapter 4.

### 3.2.2.1 Illumination of Excitation Light

As mentioned above, the laser is good light source with good monochromaticity, high-brightness and high percent polarization, but it is not enough to produce a good spectral measurement. For example, gas lasers, such as  $\text{Ar}^+$  lasers, produce some radiation other than the frequency of the laser, that is, so-called plasma lines and some semiconductor lasers has strong luminescence around the laser line. In Appendix I, the wavelengths of some plasma lines have been listed, together with laser lines.

- Improvement of the monochromaticity of excitation light

Because there is a correspondence between Raman scattering frequency  $\omega_s$  and excitation light frequency  $\omega_i$ , a multiple frequency light source will generate multiple frequency scattered light. This will result in the depression of the signal-noise ratio of Raman spectra. Therefore, the improvement of the monochromaticity of excitation light is first required. The pre-monochromator and optical filter can reduce the excitation light intensity of unrequired wavelengths.

In addition, because the energy of lasers is basically concentrated in 80% of the section area of the laser, a small aperture set in the illumination optics is a convenient and cheap way to prevent stray light becoming mixed in the laser beam.

- Attenuation of light intensity

In Raman spectral experiments, we need to prevent the intensity of light from damaging samples due to the heating effect of lasers. The attenuated elements of light intensity are needed and these usually are a neutral filter or a lens of expanded beam.

- Change of light polarization

In the measurement of polarized spectra, the polarized property of illuminating light needs to be changed or improved.

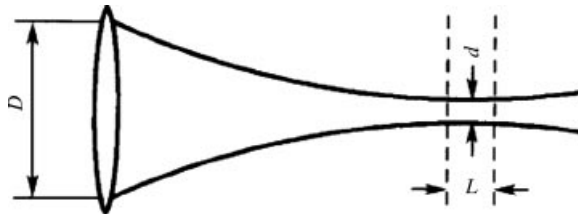


**Figure 3.11** Laser beam focused by a thin lens [7]. Reprinted from S.-L. Zhang, *Raman Spectroscopy and Low-dimensional nanoscale Semiconductors*, Science Press, (2008)

The change of polarization direction can use a polarization rotator or  $\lambda/2$  wave plate. The function of the former is dependent on light wavelength  $\lambda$  and can be used only for a specific wavelength  $\lambda$ .

In the measurement of Raman spectra of circular polarized light, we need to obtain the circular polarized intensity ratio  $\Delta (= I_R - I_L / (I_R + I_L))$ , where  $I_R$  and  $I_L$  are the intensity of Raman scattered light excited by right- and left-circular polarized light, respectively. Therefore, it should have the right- and left-rotated polarized light and that can be obtained from a plane polarized laser by using a photoelastic modulator or optical modulator

- Increase of light power density on samples

The increase of power density of illuminating light on samples is produced by using the directing and focusing elements. The directing elements of beams are used for guiding light beam towards the samples, of which the elements usually are glass prisms or dielectric mirrors.

The function of focusing elements is to decrease the diameter  $d$  and vertical depth  $L$  of the beam. Figure 3.11 shows a focusing lens and optical path, by which the relation between the diameter  $d$  and length  $L$  of lumbar and diameter  $D$  of the lens can be expressed as

$$d \approx \frac{4\lambda f}{\pi D} \quad (3.21a)$$

$$L \approx \frac{16\lambda}{\pi} \left( \frac{f}{D} \right)^2 \quad (3.21b)$$

From Equations (3.4) and (3.5), when the light wavelength  $\lambda = 500.0$  nm,  $D = 10$  mm,  $f = 50$  mm, and  $d = 0.003$  mm, we have  $D/d = 3 \times 10^3$ . This means that, on the one hand, the power density is  $3 \times 10^6$  times of that before focusing and, on the other hand, it will raise the spatial resolution of spectra.

- Change of illuminated faculae shape

The focusing elements usually are the lens or lens group. If two cylindrical lenses are used, as shown in Figure 3.12, the faculae on samples will be rectangular, which matches the shape of the incident slit and allows the scattered light to just pass through the slit. As a result, the collecting efficiency of scattered signal increases and the quantum of stray light entering the spectrometer decreases simultaneously.

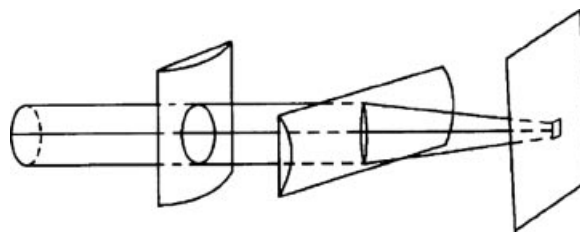


**Figure 3.12** Focused laser beam by using two cylindrical lenses. Reprinted from S.-L. Zhang, *Raman Spectroscopy and Low-dimensional nanoscale Semiconductors*, Science Press, (2008)

### 3.2.2.2 Collection of Scattered Light

The functions of the scattered light collection element is to make the scattered light enter the spectral dispersion part with high efficiency, while entry of stray light is as little as possible.

- High efficient collection of scattering light

This requires that the relative aperture of collecting lenses or mirror is large enough.

- Suppression of stray light

The suppression of stray light is achieved by using various types of optical filters, such as a narrow band filter, a notch filter, an edge filter, and pre-monochromator. All of filters must reduce the Raman signal to a certain degree when they reduce the stray light, for example, the pre-monochromator decreases the power of right excitation light by as much as 70–90 %. The notch filter has a higher passing efficiency for the main light beam but its bandpass is broader, resulting in it not being suitable for the measurement of low wavenumber spectra.

- Fixing of scattering light polarization

In the measurement of polarized spectra, the polarized property of scattered light also needs fixing, of which the method is to put an analyzer in the collected optical path.

### 3.2.2.3 Sharing of Excitation and Collection Optical Elements

The optical element used for excitation light illumination and scattered light collection in the spectrometer can be shared, as with an optical microscope. In fact, the optical microscope has been widely used with the spectrometer, as shown in Figure 3.13 [8].

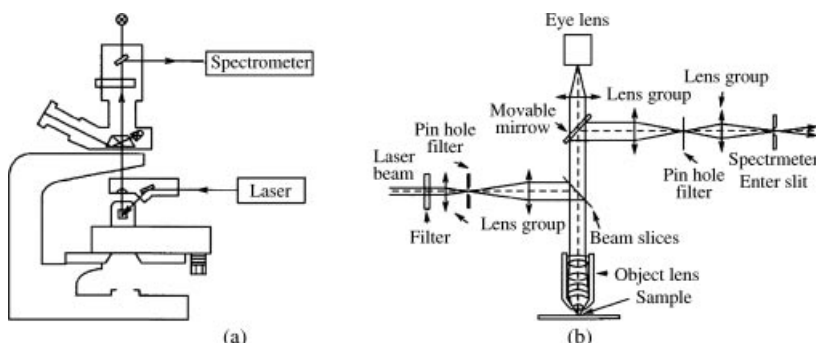


**Figure 3.13** Structure and optical path of a typical Raman microscope [8]. Reprinted from S.-L. Zhang, *Advanced Scientific Instrument*, (1993)

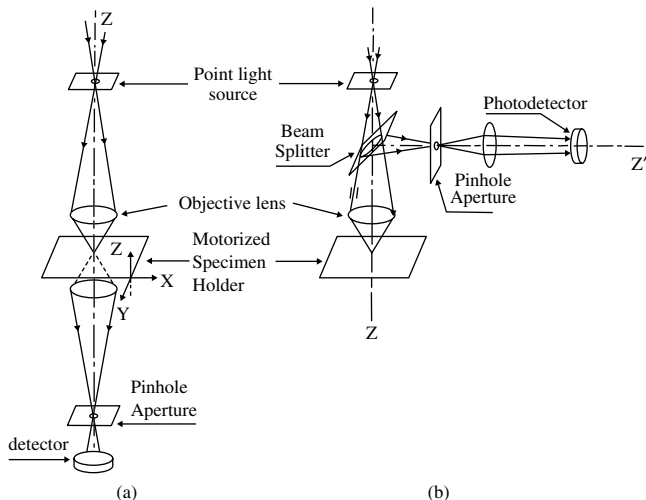


**Figure 3.14** Transmit (a) and reflect (b) confocal microscope optical paths [8]. Reprinted from S.-L. Zhang, Advanced Scientific Instrument, (1993)

### 3.2.2.4 Confocal Optical Path

It is well-known in optical imaging theory that only the image of the object on the optical axis can obtain an ideal optical image without aberration. If the object point and image point on the axis conjugate each other, it is called “confocal,” of which the essential characteristic is the illumination and detection aperture conjugated by two pinholes [9,10]. The effect of a space filter on the illuminated point and detection point is amplified to improve spatial resolution and also to reject stray light from out-of-focus regions. The traditional transmit or reflect confocal optical microscope with pinholes has been used in confocal spectrometers, of which the optical path is shown in Figures 3.14(a) and (b). A no-pinhole confocal Raman microscope optical path is shown in Figure 3.15, in which the slit and pixel of CCD play a role similar to pinholes [11].

The introduction of confocal optical paths in Raman spectrometer results in the improvements not only for plane resolution but also for depth. Figure 3.16 shows a resolution comparison between common and confocal micro-spectra.

The micro-Raman spectrometer, as shown in Figure 3.13, can only perform backscattered experiments on opaque samples, which will produce a strong stray light background and so is a shortcoming of this kind of spectrometer.

### 3.2.2.5 Environments of Measured Samples

At present, the sample environment of Raman spectral experiments makes it possible to change from an atmospheric environment to the electrical field, magnetic field, high pressure, and high temperature, and so on.

## 3.2.3 Spectral Dispersion

The spectral dispersion part is the core of the Raman spectrometer. Its main function for the grating spectrometer is to decompose the scattered light with energy (i.e., wavelength or frequency) in the spatial domain.

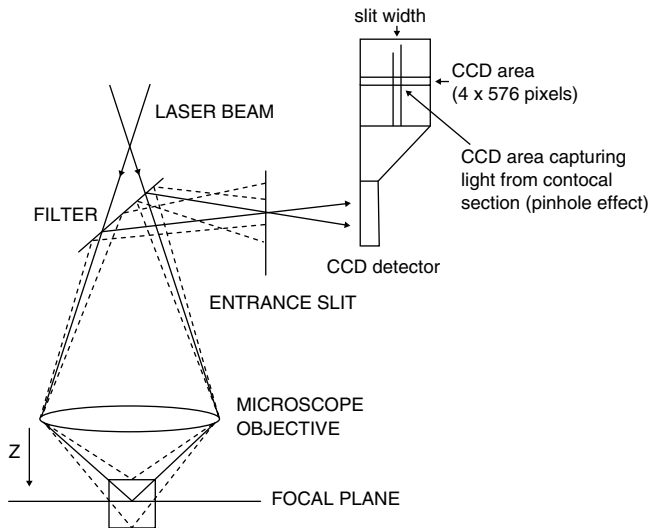


**Figure 3.15** Confocal optical path with no pinhole [11]. Reprinted from S.-L. Zhang, Raman Spectroscopy and Low-dimensional nanoscale Semiconductors, Science Press, (2008)

The spectral dispersion part mainly consists of a window (slit), a collimator, a grating, and a converging lens, as shown in Figure 3.17. The figure shows that  $a_1$  and  $a_2$  are the incident and exited slits or windows,  $F_1$  and  $F_2$  are the collimator and converging lenses with focal lengths of  $f_1$  and  $f_2$ , respectively,  $D$  is the lens diameter, and  $G$  is a grating.

### 3.2.3.1 Slits

On the incident and outgoing plane of the spectral dispersion part, there must be windows to allow entry of incident light and outgoing of spectral lines. On the incident plane a narrow strip window called a slit is opened, as shown in  $a_1$  in Figure 3.17. On the exit plane, a window marked by  $a_2$  in the figure can be a slit or a rectangular window, of which the former

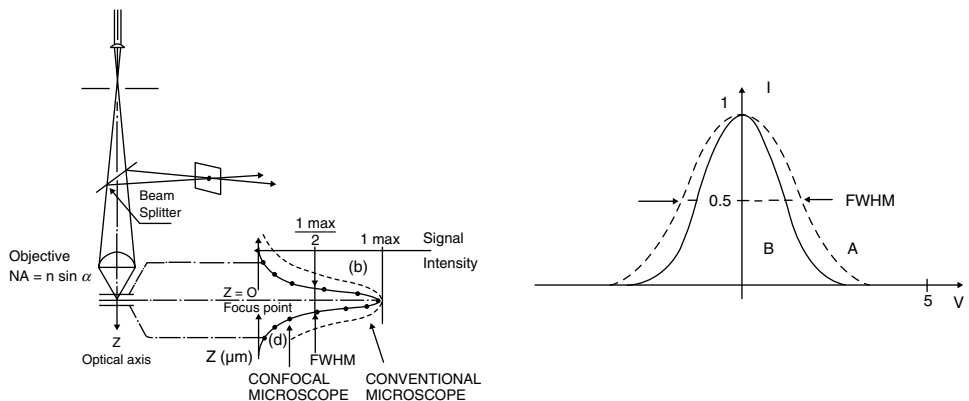


**Figure 3.16** Resolution comparison between common (dashed line) and confocal (solid line) micro-spectra [8]. Reprinted from S.-L. Zhang, Advanced Scientific Instrument, (1993)

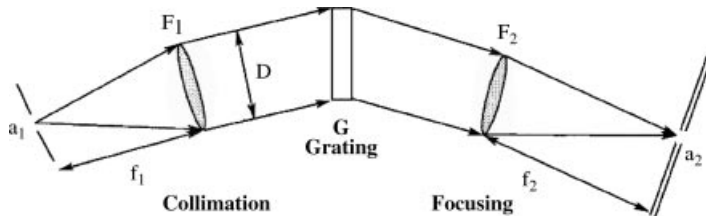


**Figure 3.17** Structure of the spectral dispersion part. Reprinted from S.-L. Zhang, Raman Spectroscopy and Low-dimensional nanoscale Semiconductors, Science Press, (2008)

only allows a narrow wavelength range of spectrum to exit while the latter allows a spectrum with a wider range of wavelengths to pass through. Correspondingly, these spectral apparatuses are called the spectrograph and spectrometer, respectively.

The geometry width of slits or windows in spectrometers corresponds to the spectral width, which will be described in Section 3.3.1.

### 3.2.3.2 Collimator

The function of the collimator is to have the scattered light coming from an incident slit transferred into a parallel beam of light that can then illuminate the grating uniformly and efficiently.

### 3.2.3.3 Converging lens

The converging lens is used to make the scattered light dispersed at various angles to converge at the outgoing slit, as shown in Figure 3.15.

The collimator and converging lens can use the lens or mirror. The aluminum plated mirror has a wider spectral bandpass compared to the glass lens and is more widely used.

### 3.2.3.4 Dispersion

Spectral dispersion in grating spectrometers is finalized by using a grating.

- Diffraction and grating equation of grating

A grating is a periodic structure formed by parallel strips of equal width and equal spacing and can split and diffract light into several beams traveling in different directions. Figure 3.18(a) illustrates the structure and optics of a transparent grating, where  $a$ ,  $d$ , and  $\theta$  are the groove width, constant, and diffracting angle of the grating, respectively. Based on the principles of diffraction of a single light beam and interference of multiple light beams, the grating diffracted intensity for the transparent grating,  $I(\theta)$ , can be expressed as [12]

$$I(\theta) = I_0 (\sin \alpha / \alpha)^2 \cdot (\sin N\beta / \sin \beta)^2 \quad (3.22)$$

and

$$\begin{aligned} \alpha &= \pi a \sin \theta / \lambda \\ \beta &= \pi d \sin \theta / \lambda \end{aligned}$$

where  $\lambda$  and  $I_0$  are the wavelength and intensity of incident light, respectively;  $N$  is the total number of the grooves in the illuminated area of the grating; and  $\theta$  is the diffraction angle.  $(\sin \alpha / \alpha)^2$  and  $(\sin N\beta / \sin \beta)^2$  are relative to the diffraction of a light beam from a single slit

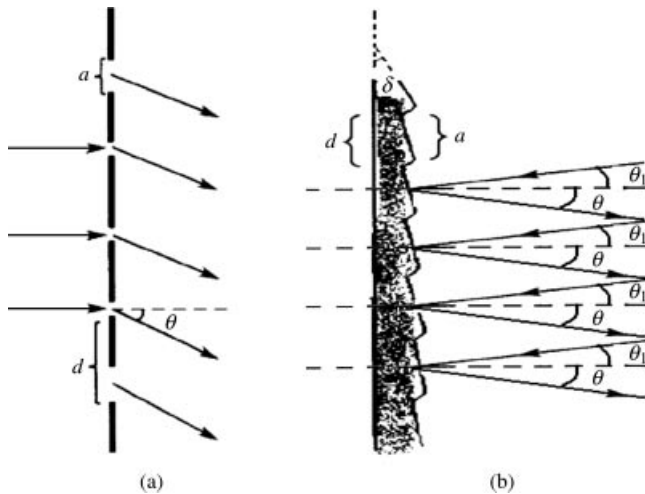


**Figure 3.18** Structure and optics for transparent (a) and reflecting plane (b) gratings. Reprinted from S.-L. Zhang, *Raman Spectroscopy and Low-dimensional nanoscale Semiconductors*, Science Press, (2008)

of a grating and the interference of light beams from multiple slits and, correspondingly, are named the single slit diffraction factor and multiple slits the interference factor, respectively.

- Main maximum, secondary maxima and grating equation of grating

Ignoring the single slit diffraction factor  $(\sin \alpha/\alpha)^2$ ,  $I(\theta)$  will be induced purely by the multiple slit interference factor, and the corresponding intensity,  $I(\theta)_{\text{Coh}}$ , can be expressed as

$$I(\theta)_{\text{Coh}} = I_0 (\sin N\beta / \sin \beta)^2 \quad (3.23a)$$

At  $\beta = k\pi$ , the  $I(\theta)_{\text{Coh}}$  maxima are expressed as

$$d(\sin \theta) = k\lambda \quad (3.23b)$$

This equation is the famous grating equation. The light beam of  $k = 0$  is directly transmitted (or reflected for the reflection grating) and is called the zero-order maximum.

At  $k \neq 0$ , the diffraction angle  $\theta$  corresponding to the incident light of different  $\lambda$  has different values and thus the incident light of different  $\lambda$  is diffracted in a different direction in space. The maxima of different  $\lambda$  constructs a so-called spectrum and the spectrum formed by different  $k$  is named the  $k$ -order spectrum. For different values of  $k$ , the diffraction angle  $\theta$  for the same wavelength of  $\lambda$  is different and thus localizes different spatial regions, which produce a different order of spectra, as shown in Figure 3.19.

At  $\beta = (k + 0.5)\pi/N$ , where  $\beta$  is not an integral multiple of  $\pi$ , many secondary maxima will appear, which are also known as grating satellites.

The secondary maximum intensity  $I(\theta)_{\text{Coh, Secd}}$  is calculated for  $N = 10^5$ , which is used in most spectrometers today and the calculated result is presented in Figure 3.20(a). Table 3.1

**Table 3.1** Wavenumber and intensity relative to main maximum for some orders of secondary maxima

Order	1st	10th	100th	190th	380th
Relative wavenumber away from main maximum	0.3	2.6	26	50	100
Intensity relative to main maximum	0.4	$10^{-3}$	$10^{-5}$	$3 \times 10^{-6}$	$7 \times 10^{-7}$

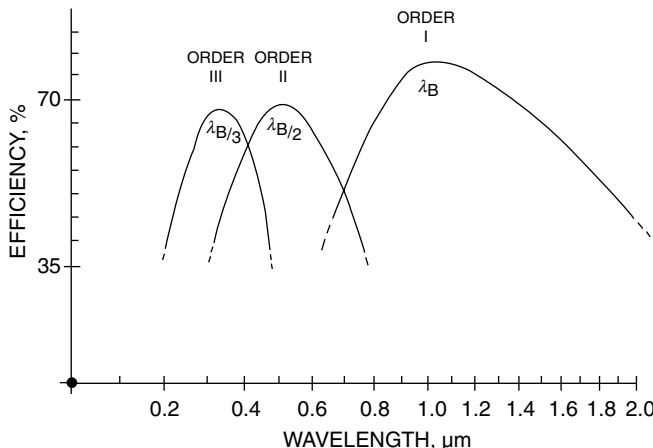


**Figure 3.19** Different order ( $k = I, II$  and  $III$ ) of grating spectra [12c]

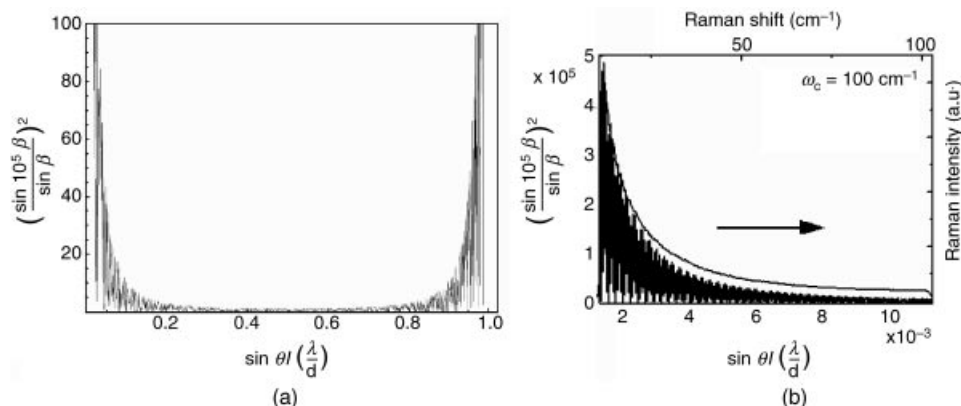


**Figure 3.20** Calculated  $I(\theta)_{Coh,Secd}$  for  $N = 10^5$  (a) and comparison between calculated and experimental results for spectra of  $11\text{--}100\text{ cm}^{-1}$  (b). In (b), the black fluctuating pattern and solid lines stand for the calculated and experimental date, respectively. Reprinted from B. Shuang, C. X. Wang, L. Xia, et al., Stray light in low wavenumber Raman spectra and secondary maxima of grating diffraction, *J. Raman Spec.* Online article DOI: 10.1002/jrs.2990, John Wiley & Sons (2011)

lists the secondary maximum wavenumbers and corresponding intensities relative to main maxima in the region near to the main maximum. Table 3.1 indicates quantitatively that the influence of secondary maxima on the spectrum constructed by the main maximum can be ignored for ordinary spectra such as absorption, reflection, and emission spectra. But for scattering spectrum, the situation is different from the ordinary spectra just described, as there must exist two components, Rayleigh and Raman scattering simultaneously and the intensity of Raman scattering is only  $1/10^{6\sim 12}$  order of magnitude of that of Rayleigh scattering. Thus, Table 3.1 indicates that the secondary maxima of Rayleigh scattering will surpass the Raman signal in the region lower than  $50\text{ cm}^{-1}$ , even for a strong Raman signal. A comparison between the calculated secondary maxima and measured L-Cystine Raman has been made, as shown in Figure 3.20(b). The comparison shows a good match between calculated and experimental data, giving the above argument on strong stray light in the low wavenumber region of Raman spectra quantitative confirmation. The above discussion explores an important point that the performance of stray light suppression in the low wavenumber region is very important for Raman spectrometers.

- Types of grating and blazing grating

The present gratings are made of a reflecting substrate, as shown in Figure 3.18(b), which is named the reflecting grating. The surfaces of grating substrates can be plane or curved and, correspondingly, they are named as plane and curved surface gratings. The gratings are also divided into two types of curved and holographic gratings, due to their different production methods. The holographic grating is made by the photoetching of interference fringe images formed by two intersecting coherent plane lights. The holographic grating is more uniform, with no stray light from ghost lines and is low cost, and so on. At present, almost all spectrometers use holographic reflecting plane gratings. Regardless of the kind of grating, the relationship between the angles of the diffracted beams, the grating spacing, and the wavelength of incident light, that is, the grating equation, can be applied to any grating with the same spacing, because the phase relationship between light scattered from adjacent elements of the grating remains the same. Thus, it is straightforward to show that the light beam is incident at an angle  $\theta_i$ , as shown in Figure 3.18(b), and the grating equation becomes

$$d(\sin \theta_i - \sin \theta) = k\lambda \quad (3.23c)$$

The grating equation offers only the main maximum direction of the  $k$  order. The relative intensity of different  $k$  order main maxima is determined by the intensity distribution of a single slit diffraction factor  $(\sin \alpha/\alpha)^2$ .

For a reflecting grating with  $a$ , included angle between the grating and the glove planes,  $\delta$ , when the main maximum direction of a certain  $k$  order coincides with the direction of maximum intensity from single slit diffraction factor  $(\sin \alpha/\alpha)^2$ , this  $k$  order intensity approaches a maximum value. It is considered that the grating is a blazing grating at blazing wavelength  $\lambda_B$ . From Equation (3.23c), the blazing condition can be expressed as

$$2d \sin \delta \cos(\theta_i - \delta) = k\lambda_B \quad (3.24)$$

- Dispersion rate of grating

The dispersion rate of a grating describes the dispersive grade of different wavelengths diffracted by gratings. It is defined as the change of the dispersion angle  $\beta$  with wavelength  $\lambda$ , that is, the angle dispersion rate  $D_\theta = d\theta/d\lambda$ , which can be expressed from the grating Equation (3.23):

$$D_\theta = d\theta/d\lambda = (m/d)/\cos \theta \quad (3.25)$$

The larger the angle of the dispersion rate is, the larger the separation of the spectral line will be. Actually, when  $\theta$  is not large,  $\cos \theta$  will not change much and thus  $D_\theta$  tends to a constant. Therefore, the dispersion can be regarded as uniform for a grating.

- Working wavelength range of gratings

According to Equation (3.6), it is obvious that both the incident angle and diffracted angle cannot be above  $90^\circ$  and then the upper limitation of  $\lambda_m$  is determined by the grating constant  $d$  and diffracted order  $m$ . This means that the grating has a limitation of working wavelength. Thus the measurement in a different wavelength range requires the grating of different  $d$ , meaning the measurements at long- and short- wavelength ranges need the grating to have small and large  $d$ , respectively.

- Free spectral range of gratings

It has been shown in Figure 3.19 that the spectra of  $k$  order and  $(k+1)$  order overlap, resulting in the spectral measurement in this overlapped region becoming impossible. The non-overlapped region is known as the free spectral region. Based on experience, when grating constant  $d > 2\lambda$ , the free spectral region  $\lambda_{\text{Free}}$  of a blazing grating is determined by the equation

$$\frac{2\lambda_B}{2k+1} < \lambda_{\text{Free}} < \frac{2\lambda_B}{2k-1} \quad (3.26)$$

where  $k$  and  $\lambda_B$  are the order and blazing wavelength of the grating, respectively. In the free spectral region, the spectral intensity relative to the maximum are usually larger than 0.4.

### 3.2.3.5 Number of Gratings in Spectrometer

The grating number in a spectrometer can be more than 1 and the corresponding optical paths have multiple modes.

- Single grating type

The most commonly used optical paths for single grating types have three modes, Littrow, Abert, and Czerny–Turner, as shown in Figure 3.21.

- Multiple grating type

The spectrometer can be constructed with more than one grating, forming a double or a triple grating monochromator, and so on. The two gratings in a double monochromator can work in the dispersion addition or dispersion subtraction modes. Figure 3.22 shows the optical paths of the dispersion addition mode for a double monochromator of plane arrangement (a) and a triple monochromator of plane (c) and stereoscopic arrangement (d). Figure 3.22(b) is the scheme of a double monochromator of dispersion subtraction mode.

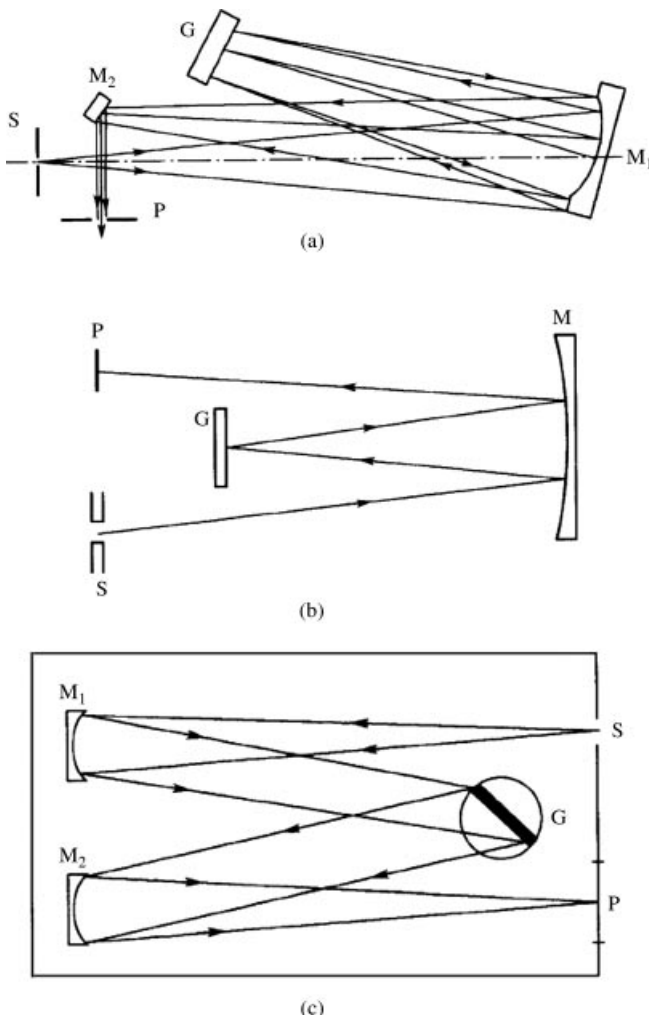


**Figure 3.21** Optical paths of monochromator with Littrow (a), Abert (b), and Czerny–Turner (c) modes, where S, P, M, and G represent the incident slit, exit slit, grating, and mirror, respectively. Reprinted from S.-L. Zhang, *Raman Spectroscopy and Low-dimensional nanoscale Semiconductors*, Science Press, (2008)

The additional mode of dispersion will increase the angle dispersion rate. This results in an increase of the spectral resolution and the improvement of the signal to noise ratio of spectra in the low wavenumber region near the Rayleigh line. Of course, the Raman signal is weakened by several orders of magnitude at the same time. Figure 3.23 shows the change of intensity along with the frequency in the single, double, and triple monochromators. Figure 3.23 shows that increasing the dispersion restrains the intensity Rayleigh line and at the same time the intensity of Raman scattering is also decreased.

The dispersion subtraction mode cannot increase the resolution rate but will suppress stray light and raise the ability to detect low wavenumbers. The CCD detected spectrometer

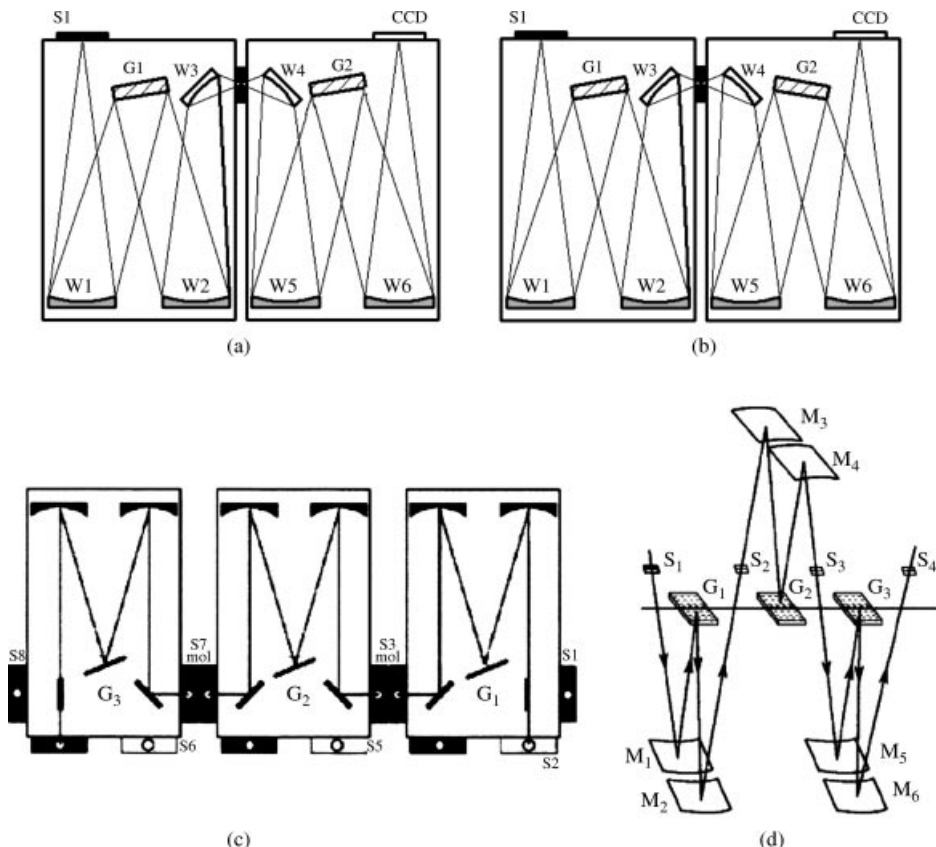


**Figure 3.22** Optical paths of double grating monochromator working at dispersion addition (a) and subtraction (b) modes and the dispersion additive triple grating monochromator of plane arrangement (c) [12a] and a triple monochromator of stereoscopic arrangement (d) [12b]: G – Grating; M – Mirior; S – Slit

of three gratings often adopted the dispersion subtraction mode for its former two monochromators.

- The monochromator and polychromatic spectrometer

When an instrument is equipped with more gratings in a monochromator, as shown in Figure 3.24, it is called a polychromator. The polychromatic spectrometer can be worked over a wider wavelength region by using one spectrometer.

### 3.2.4 Spectral Acquisition

A very weak Raman signal requires a high efficient acquisition, which is first determined by efficient detection of the optical signal. Optical signal detection in spectrometers is classified into two types: the single channel and multiple channel detections, which correspond to the spectral acquisition in a narrow and broad wavelength range in each acquired time, respectively.

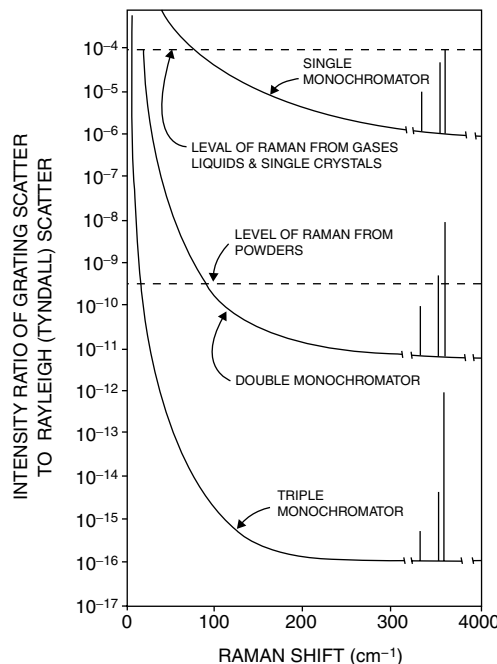


**Figure 3.23** Intensity variation of scattered lights for the single (a), double (b), and triple (c) grating spectrometers [12c]

The early detection of spectral signals was achieved by the photographic dry plate based on the photochemistry effect, of which the detection efficiency is very low, although it is multiple channel detection. In the middle of the last century, the photomultiplier tube (PMT) and charge-coupled device (CCD) were introduced in spectrometers, which solved the problem of weak spectral signal detection. PMT and CCD are both based in the photoelectric effect but they belong to different types of devices and detection methods; the former and latter are the vacuum tubes of single channel detection and the semiconductor devices of multiple channel detection, respectively.

PMT utilizes the secondary emission of electrons produced on the photoelectric cathode due to illumination. Figure 3.25 shows the structure and working principle of the PMT,

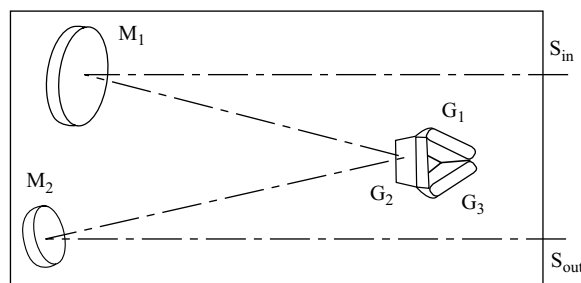


**Figure 3.24** Polychromator optical path, where  $G$ ,  $M$ , and  $S$  are gratings, mirrors, and slits, respectively

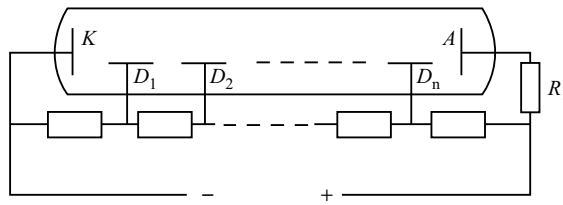


**Figure 3.25** Diagram of a PMT. Reprinted from S.-L. Zhang, *Raman Spectroscopy and Low-dimensional nanoscale Semiconductors*, Science Press, (2008)

which are constructed from a glass vacuum tube, in which there is a photocathode **K**, several dynodes  $D_1, D_2, \dots, D_n$ , and an anode **A**. The photocathode **K** is a layer of thin film deposited on the window of tube. When incident photons strike the photocathode, the photoelectrons are produced due to the photoelectric effect. These electrons are directed by focusing the electrode towards an electron multiplier, where electrons are multiplied due to secondary emission.  $10^6\text{--}10^8$  of electrons will be produce and they give rise to a negative pulse signal and a voltage drop on the load resistance  $R_l$ , which can be coupled into the photon counter to subsequently process signals.

CCD is a semiconductor dynamic shift register of different states represented by charge quantity. The CCD structure is shown in Figure 3.26. Each unit can store a certain amount of charge represented the sampling value of the signal. Under the command control of a clock signal, these units can transfer charge one by one along a fixed orientation. Until all of the units are used up, a high speed clock, and then a slower clock swiftly read out the charge information in the CCD and send it to a standard A/D converter.

CCD is usually composed of a group of regular metal-oxide-semiconductor (MOS) capacitor array, input, and output circuit. Therefore, CCD can complete multiple channel detection by up to more than 1000 channels at the same time. As a result, CCD does not only save large sampling times comparing with PMT but can improve greatly the signal/noise ratio due to the huge sampling times of spectral signals in a shorter time. Moreover, the CCD also allows the spectrometer to process the imaging capability. Now CCD has become the leader in spectral detection.

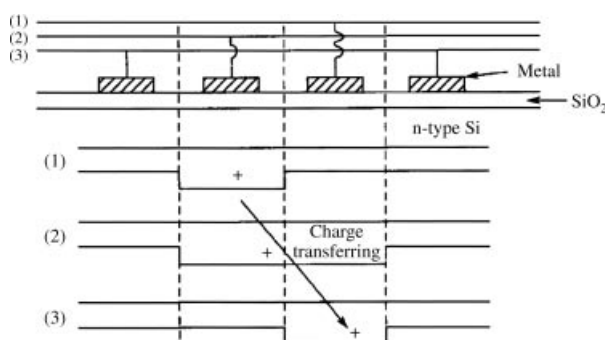


**Figure 3.26** Graphical representation of a CCD structure. Reprinted from S.-L. Zhang, *Raman Spectroscopy and Low-dimensional nanoscale Semiconductors*, Science Press, (2008)

The optic-electron devices always produce a small current, even without incident photons, so is called the dark current. To decrease the value and fluctuation of the dark current, the detectors need to be placed in low and stable temperatures, thus they are always placed in a structure with magnetic shielding and a constant low temperature.

The processing of acquired spectral data also plays an important role in acquired efficiency. The processing of photographic dry plates and optoelectric detectors, such as PMT and CCD, use the optical method such as the reading microscope and other electronic methods, respectively. Nowadays, high-performance computers and advanced computing technology make it possible to do the measurement of the high time-and space-resolved spectra data processing and analysis.

### 3.2.5 Apparatus Control

The function of apparatus control is to make the spectrometer run correctly according to the requirements of spectral measurement. The computer has become a core component in controlling the apparatus, which enables the operation and control of spectrometers to become more automatic and easy.

### 3.2.6 Common Optical Factors Related to the Multi-Elements in Spectrometers

To satisfy the requirements of spectral measurement, it is important to make each element in the instruments separately satisfy the experimental requirements. However, since some optical factors occur together in various elements, attention should also be paid to the overall design and running of spectrometers. We will list these factors and discuss their solutions below.

#### 3.2.6.1 The Common Factors Related to the Geometric Optics

For a good spectrometer, it should be ensured that the energy of the laser can excite the sample with the correct power density and the energy of scattered light should pass through the incident slit of the spectrometer to hit the grating with no energy loss. For these requirements, except for each element satisfying the above requirements individually, geometric optic matching of adjacent optical elements is a key factor.

The first kind of matching is the co-axis. This requires that the optical axes of all elements are aligned along the same axis, so that it is impossible for light to be lost.

The second kind of matching is illustrated in Figure 3.27. Figures 3.27(a) (b) and (c) represent the convergent lens, collecting lens group, and grating area, respectively.

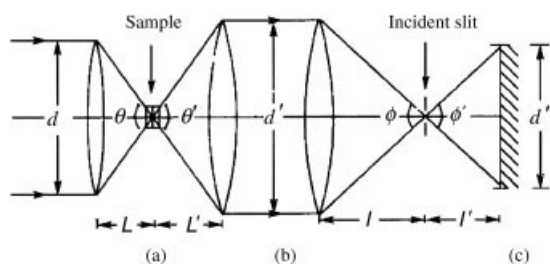


**Figure 3.27** Second type of matching. Reprinted from S.-L. Zhang, *Raman Spectroscopy and Low-dimensional nanoscale Semiconductors*, Science Press, (2008)

**Table 3.2** Transmitted and applied wavelength ranges of optical materials

Material	Transmit range ( $\mu\text{m}$ )	Applied wavelength range ( $\mu\text{m}$ )
Common grass	0.4–3	0.4–0.8
Special grass	0.3–3	0.3–0.8
Quartz	0.2–3.5	0.2–2.7
LiF	0.12–6	0.7–5.5
CaF <sub>2</sub>	0.12–9	5–9
NaCl crystal	0.2–17 (Absorption at 3.2 and 7.1 $\mu\text{m}$ )	3.16
KCl crystal	0.2–21	8–16
KBr crystal	0.21–28	15–28

The matching requires that the corresponding solid angles  $\theta$  and  $\theta'$  of (a) and (b), as well as  $\phi$  and  $\phi'$  of (b) and (c) are equal, respectively. If the  $d$ ,  $d'$ , and  $d''$  are the diameters of elements  $a$ ,  $b$ , and  $c$  also, the  $L$ ,  $L'$  and  $l$ ,  $l''$  are the distance between respective elements and their focusing points, respectively, and the above matching condition can be expressed as

$$\begin{aligned} d/L &= d'/L' \\ d'/l &= d''/l'' \end{aligned}$$

Obviously, from Figure 3.27 we see that the matching guarantees maximum efficiency in the transfer process of optical energies. Moreover, it makes the scattered light illuminate the whole area of the grating and does not overflow. As a result, the largest resolution can be obtained and also at the same time does not create any stray light due to overflowing.

### 3.2.6.2 The Factors Related to Physical Optics

Due to the refraction rate  $n$  of materials of the optical elements used, the responsibility of optical elements to light performance, such as wavelength, polarization, transmission, and reflection and so on, is different. For example, the working wavelength range of optical elements made by different materials varies, as listed in Table 3.2

- Dispersive effect

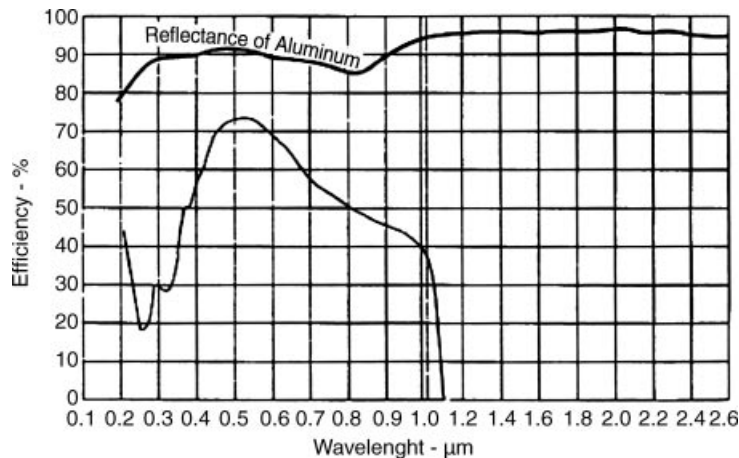
Due to the different refraction rate  $n$  of materials, the responsibility of light intensity on different wavelengths will be different, that is, the so-called dispersive effect.

Figure 3.28 shows the dependence of diffraction rate of a grating of aluminum substrate on wavelengths for the incident light of 45° polarization. The figure clearly shows that the efficiency of gratings is dependent on the incident light wavelength, although the reflection rate of aluminum is almost independent of the wavelength under the same illumination.

Dispersive effects also occur in a photoelectric detector, due to the responsive efficiency of photoelectric materials used in detectors of different light wavelengths, as shown in the Figures 3.29(a) and (b).

- Polarization effects

It is well-known that the optical elements made by the anisotropy crystals are obviously dependent on the polarization of light and thus their response efficiencies are related to the polarization property of light. Besides, polarization effect can also appear in other optical elements not made by crystalline materials.



**Figure 3.28** Dependence of diffraction efficiency of aluminum substrate grating and reflectance of aluminum on light wavelength [12c]

Figures 3.30(a) and (b) show the diffraction efficiency curves for the 1800 curve line/mm holograph grating and the 1200 ruled line/mm at 500 nm curve grating with blazed wavelength of 500 nm in the Littrow optical path. In Figure 3.30, O,  $E_{\perp}$ , and  $E_{\parallel}$  represent the natural, vertical polarization, and parallel polarization light, respectively. Figure 3.30 indicates clearly that the diffraction efficiency is dependent on the polarization of incident light, except for that of the wavelength.

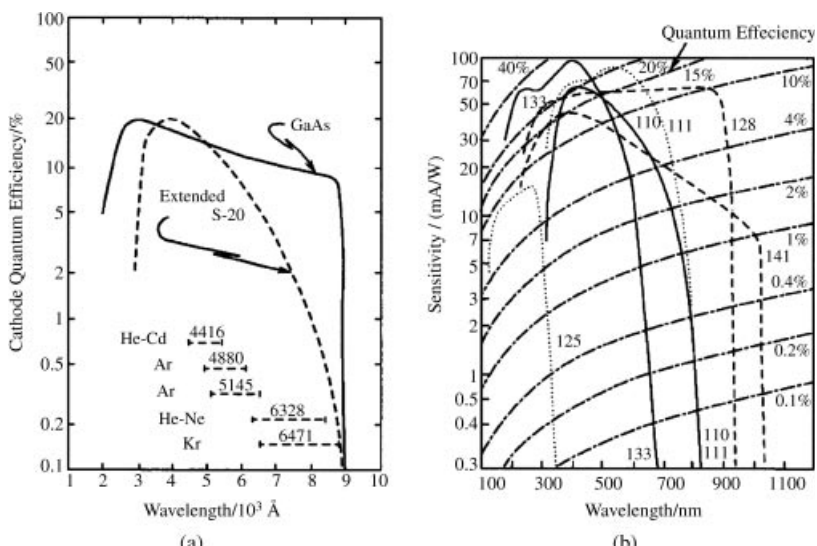


**Figure 3.29** Dispersion effects of the cathode materials used in a PMT. The marks of material in (b) are: 110 = multi-alkali (S20); 111 = multi-alkali; 125 = CsTe; 128 = GaAs; 133 = bi-alkali; 141 = GaInAs, such as GaAs, CsTe, GaInAs, and alkali (a and b) [12c]

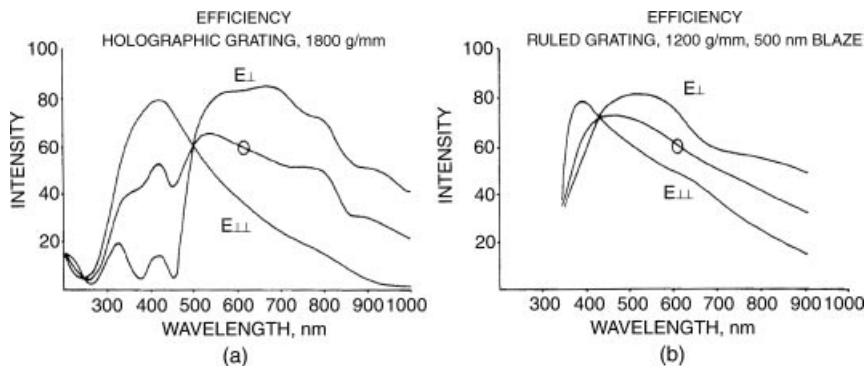


**Figure 3.30** Dependence of grating diffraction efficiency on different polarized light [12c]

Since the use of materials in windows and optic-electronic elements in photoelectric detectors vary, their responsive efficiencies on light polarization are different. Figure 3.31 shows such responsive efficiency on the light polarization for a PMT [12c].

### 3.2.7 Design of Raman Spectrometers

The discussion in Sections 3.2.1 and 3.2.2 has given foundation for the design and application of Raman spectrometers. In the following we will give some information that is helpful in its design.

#### 3.2.7.1 Optical Path

In the experiments of common Raman spectra, first we look at the selection and design of Raman spectrometers. The design involves the selection and alignment of the elements in

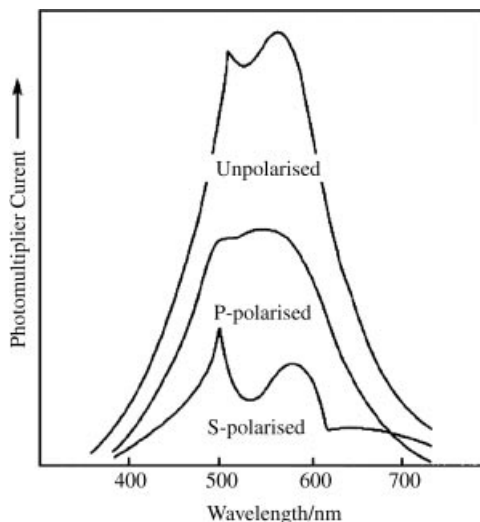


**Figure 3.31** Polarization effects of detecting efficiency for a PMT [12c]

the instruments, that is, so-called optical path design. The optical path belongs to instruments that can be made according to the content of Sections 3.2.2 and 3.2.3.

Due to the polarization effect of gratings and detectors, the spectrometer used for polarized Raman spectral measurement must allow the polarized scattering light to be transformed into isotropic light before it arrives at the grating, so that the intensities of different polarized scattered lights can be correctly compared and then reliable polarized physical quantities such as depolarization degree and ROA can be obtained. Isotropization is achieved by transferring the polarized light into a circular polarized light. That is usually performed by adding a polarization disturbing device or  $\lambda/4$  wave plate in the front or behind the incident slit, of which the latter is only effective for specific  $\lambda$ , while the former is not.

### 3.2.7.2 Spectral Date Amendment

Due to the dispersion effects mentioned above, advanced Raman spectrometers should have the automatic amendment function for spectral intensity, which is very important, especially for measurements in the wide-wavelength range. The amendment is realized by using an intensity response curve of spectrometers, like many commercial luminescence spectrometers have done. The intensity response or dispersion curve of instruments can be obtained by measuring and calculating with a standard spectral lamp as the light source of which the luminescent intensity dispersion is known. If there is no standard spectral lamp, an incandescent lamp can be used with a high stable power supply as the light source. In this method, the spectral intensity response curve is obtained by using the theoretical calculation for recorded spectrum. The spectral response function of spectrometers with frequency as a unit is defined as

$$S(v) = I(v)/\Phi(v) \quad (3.27)$$

where  $I(v)$  corresponds to apparent spectral intensity displayed in the spectrograph with wavenumber shift between  $v$  and  $v + \Delta v$ , and  $\Phi(v)$  represents a real spectral intensity in spectrometers with wavenumber shift between  $v$  and  $v + \Delta v$ .  $\Phi(v)$  can be expressed as

$$\Phi(v) = \alpha \times E(v) \times T(v) \times \Delta v = \alpha \times e(v) \times B(v) \times R(v) \times \Delta v \quad (3.28)$$

where  $\alpha$  is the scale factor;  $E(v)$  is intensity of emission spectrum of a standard tungsten lamp;  $T(v)$  is transmittance of the outer optical path of the spectrograph; and  $R(v)$  is reflectivity of an aluminum mirror in the outer optical path in the experiment. We can assume that  $T(v) = R(v)$ ,  $\Delta v$  is the bandpass of spectrometers,  $e(v)$  is the emission of a tungsten lamp, and  $B(v)$  is the spectral intensity of black body radiation. In principle,  $\Delta v$  is the function of  $v$ , but in most software of spectrometers it does not change with the frequency  $v$ . Therefore, Equation (3.28) can be simplified as

$$\Phi(v) = \alpha' \times e(v) \times B(v) \times R(v) \quad (3.29)$$

and

$$B(v) = (2\pi\hbar c^2 v^5) / (\exp(\hbar cv/kT) - 1) \quad (3.30)$$

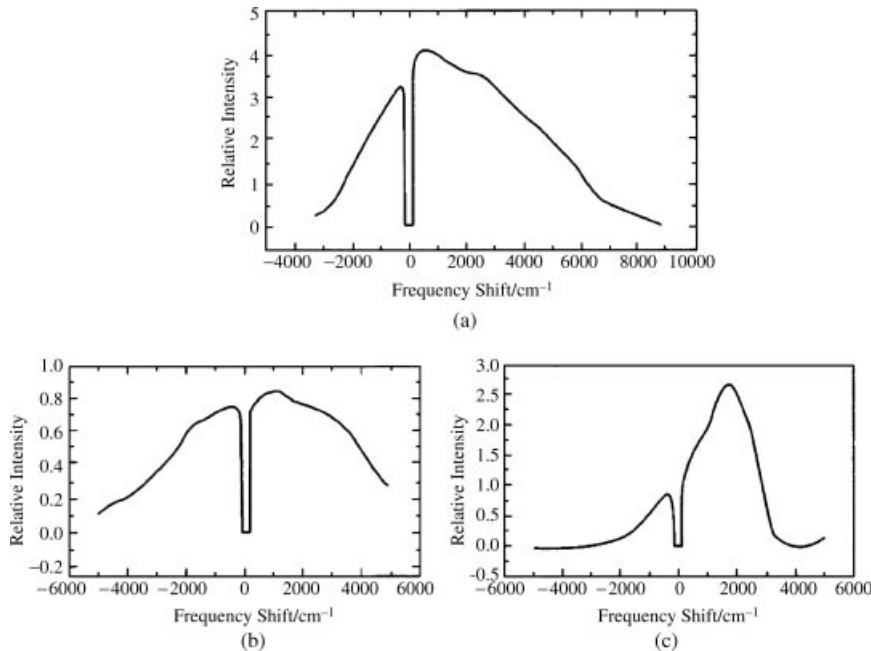


**Figure 3.32** Intensity response curve of a microscopic spectrometer with 515, 633, and 785 notch filters in the frequency (wavelength) range of 25,430 cm<sup>-1</sup> (393 nm)–11,430 cm<sup>-1</sup> (875 nm). Reprinted from S.-L. Zhang, *Raman Spectroscopy and Low-dimensional nanoscale Semiconductors*, Science Press, (2008)

Let  $B'(v)$  be monochrome energy density of black body radiation:

$$B'(v) = (8\pi h v^3)/c^3(\exp(hcv/kT) - 1) \quad (3.31)$$

where  $c$  is the velocity of light, and from the table we can obtain values of  $e(v)$  and  $R(v)$ . Hence, we have

$$S(v) = \alpha'' \times I(v)/[e(v) \times R(v) \times B(v)] \quad (3.32)$$

Using a tungsten lamp as the light source, in the frequency (wavelength) range of 25,430 cm<sup>-1</sup> (393 nm)–11,430 cm<sup>-1</sup> (875 nm) with the notch filters at 515, 633, and 785 nm in a microscope spectrometer, the spectral intensity response curve obtained by the above method is shown in Figure 3.32, in which the dips are induced by the notch filter.

### 3.3 Main Performance Parameters of Raman Spectrometers

Understanding the performance of spectrometers is a prerequisite for choosing a spectrometer correctly but also for measuring spectra with high quality.

The performance of spectrometers should satisfy the requirements to record spectra correctly, that is, the instrument should have the ability to provide the characteristic

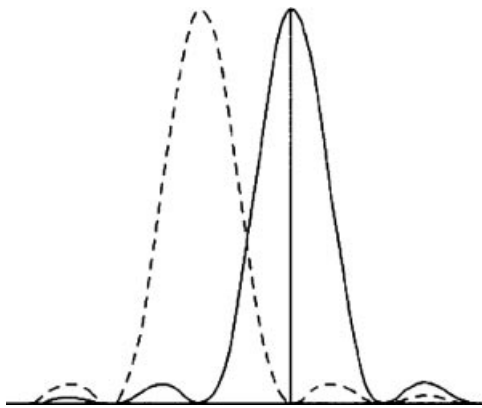


**Figure 3.33** Rayleigh criterion. Reprinted from S.-L. Zhang, *Raman Spectroscopy and Low-dimensional nanoscale Semiconductors*, Science Press, (2008)

parameters mentioned in Chapter 1 to achieve this. This ability is related to the performances of the instrument components. Therefore, we will introduce several important performance parameters of Raman spectrometers, together with the performance description related to the instrument components.

### 3.3.1 Spectral Resolution Rate

The spectral resolution rate indicates the ability of resolving two spectral peaks. This means that when two spectral peaks are close or partly overlap, as shown in Figure 3.33, how do we judge whether they are distinguishable? However, this judgment depends on the person involved. Thus, a criterion called the Rayleigh criterion was introduced artificially. The Rayleigh criterion mentions that when the vertical line of one peak falls to the smallest point of the first neighboring peak, the two peaks are considered to be distinguishable.

#### 3.3.1.1 Line Dispersive Rate

The dispersive rate is one of the most important parameters of spectrometers and directly related to the resolution of measured spectra. The angular dispersion rate defined in Section 3.2.2,  $D_\theta$ , represents the separated angle of two spectral lines at  $\lambda$  and  $\lambda + \Delta\lambda$ , which must be provided for each grating. However, a large angular rate cannot guarantee discrimination of two spectral lines when they are very close. The separated distance of two spectral lines,  $dl$ , in spectral measurements are dealt with by the introduction of a line dispersion rate  $dl/d\lambda$ , which is defined as

$$D_l = dl/d\lambda = f_1 d\beta/d\lambda = f_1 D_\theta \quad (3.33)$$

where  $f_1$  is the focal length of the collimating lens in the spectrometer and  $d\beta$  represents the angular dispersion of the gratings. Therefore the line dispersive rate can be obtained from Equation (3.33).

The dispersive rate of spectrometers is usually evaluated by the reciprocal of the line dispersion rate,  $d\lambda/dl$ . It represents the covered wavelength range within the unit distance,

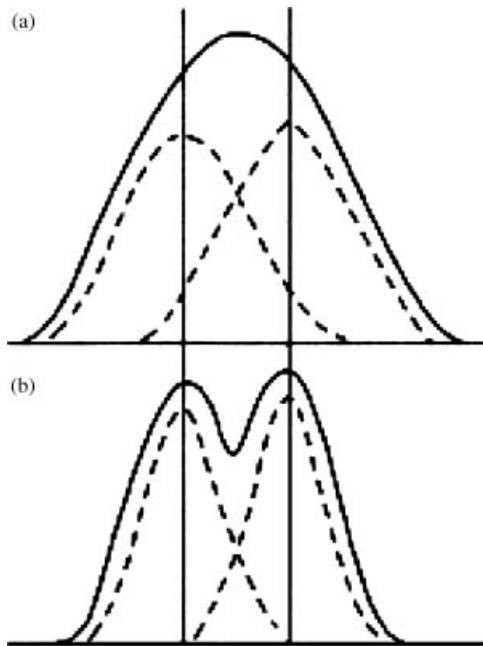


**Figure 3.34** Diagram of resolution of two spectral lines at different line width. Reprinted from S.-L. Zhang, *Raman Spectroscopy and Low-dimensional nanoscale Semiconductors*, Science Press, (2008)

that is, the unit spectral width. The smaller the value of  $D_l$ , the better the spectral dispersion of the spectrometer.

### 3.3.1.2 Chromatic Resolution Rate

The resolution of two spectral lines is also dependent on spectral line shape and line width, which can originate from the sample and/or the experiment, of which the latter can be the restriction of the instrument's performance and/or experimental parameter selection. Figure 3.34(a) shows that it is possible to resolve two spectral lines. However, in Figure 3.34(b), they overlap and become undistinguishable, because of their broad line width. Thus, whether two peaks can be distinguished is decided not only by how far apart they are, but also by the characteristics of their shape and width.

Therefore one introduce a parameter called the chromatic resolving rate to evaluate the ability to tell two lines apart which is defined as

$$R \equiv \frac{\lambda}{d\lambda} = \frac{v}{dv} = \frac{\omega}{d\omega} \quad (3.34)$$

where  $v$  and  $\omega$  represent the frequency and angular frequency, respectively.

### 3.3.1.3 Main Factors Relevant to Spectral Resolution Rate

From the above discussion, the factors relevant to spectral resolution rates are mainly the grating and the focus length of collimation and correction lens. The resolution of measured spectra is still relative to the slit and CCD type detector.

**Table 3.3** Dependence of resolving capability of spectrometers on the height and width of incident slits

Height of incident slits (mm)	Width of incident slits ( $\mu\text{m}$ )	Resolving capability (nm)
2	10	0.01
5	10	0.01
10	15	0.01
20	20	0.02

- Slit and resolution rate

The width of slits will affect the resolving capability of spectrometers. If the slit is infinitely narrow, the corresponding line width  $a_0$  is the diffracted width, which can be expressed as

$$a_0 = f_2 \lambda / D \quad (3.35)$$

where  $f_2$  and  $D$  are the focal length of the focusing lens and the diameter of the collimating beam, as in Figure 3.17. When the slit is close to infinitely narrow, the chromatic resolving rate of the spectrometer can be expressed as

$$R_0 = \frac{\lambda}{d\lambda} = \frac{\lambda D_\theta}{d\theta} = \frac{\lambda D_\theta}{\varphi} = DD_\theta \quad (3.36)$$

For a slit width of  $\Delta L$ , the corresponding spectral width of slits,  $\Delta f'$ , can be expressed as

$$\Delta f' = (d\lambda/dl)\Delta L \quad (3.37)$$

The spectral line shape at the exit plane of the spectrometer is not a straight line and thus increasing the slit height will reduce the resolving capability. Therefore, there exists a better combination of slit width and height for resolving capability. Table 3.3 lists the dependence of resolving capability of spectrometers on the width and height of incident slits.

### 3.3.2 Reading

#### 3.3.2.1 Display of Reading

The two display modes for reading displays are wavelength or wavenumber. Historically, these displays are determined by the grating driving type. The linear reading with the sine or cosine function relation will show the wavelength or wavenumber reading, respectively. Since recent advances in computers and calculation technology, the deriving method of gratings is no longer directly related to the reading method.

#### 3.3.2.2 Reading Accuracy and Repeatability

The ability to read the smallest wavelength/wavenumber value in one scanning and get the smallest deviation of reading values in multiple scannings is defined as reading accuracy and repeatability, respectively. These are determined by the linearity and precision of elements, especially the accuracy of the rotating base and rotating reading of gratings.

### 3.3.3 Suppressing Level of Stray Light

In Section 3.2.3, it was shown that there exists strong stray light in the low wavenumber region of Raman spectra. Therefore, the suppressing level of stray light in the low wavenumber region becomes a peculiar performance parameter for Raman spectrometers. The parameter  $\eta_{\Delta\nu}$  represents the suppressing level of stray light and is defined as

$$\eta_{\Delta\nu} = I_{(v_0+\Delta\nu)}/I_{v_0} \quad (3.38)$$

where  $v_0$  and  $I_{v_0}$  are the wavenumber and intensity of the Rayleigh line, and  $I_{(v_0+\Delta\nu)}$  is the Rayleigh line intensity at  $v_0 + \Delta\nu$ . Usually,  $\Delta\nu$  is set as  $20\text{ cm}^{-1}$ . When  $\eta_{(\Delta\nu=20\text{ cm}^{-1})}$  is greater than  $10^{-4}$ , it is possible to measure stronger Raman spectra from gas, transparent liquid, and crystals. The suppressing level of stray light in the low wavenumber region is usually evaluated by observing the low wavenumber Raman spectral line of L-Cystine.

## 3.4 Experimental Measurements

To obtain a Raman spectrum of high quality, it is necessary to adjust the instrument, preparing a good sample and running the instrument correctly, and so on.

### 3.4.1 Adjustment of Spectrometers

Because the Raman spectrometer is a precision instrument, keeping it in good condition is very important. First, the spectrometer should be placed on a rigid and vibration-proof platform in a room that is temperature stabilized, dust-free, and moisture proof. However, any changes in the above conditions, for instance, room temperature changes, incorrect usage, and time overuse and so on, will result in the spectrometer not being in a good-quality state. At this time, it is necessary to examine the instrument's performance and make adjustments so that the instrument retains its good performance. The adjustments required are mainly concentrated in sample optics and spectral dispersion parts of spectrometers.

#### 3.4.1.1 Adjustment of the Sample Optics Part

The adjusting of sample optics is mainly related to the issue of geometry optics mentioned in Section 3.2.2. The sample optics shown in Figure 3.35 illustrate sample optics adjustment. For example, to obtain a micro-sample optic, we only need to add a half reflecting and half transmitting mirror in the correcting optical path between the sample and in the microscope,  $L_s$ .

There are two optical paths that need to be adjusted separately: one is for laser illumination and another for scattered light collection, as shown in Figure 3.35, from laser to sample and from sample to the first convergence mirror of the spectrometer,  $M_s$ , respectively.

First, a collimated beam is required that is used as a reference light beam (RLB) in the adjustment. This reference light beam can be a laser beam with a small beam diameter and diverging angle, which can be achieved by collimation and then passes through a fine-holed diaphragm. Two dashed lines in Figure 3.35 labeled  $RLB_1$  and  $RLB_2$  are for the adjustment of scattered light collection and laser illumination optics, respectively.  $RLB_1$  is setup through link two center points of incident slit and first mirror of monochromator.  $RLB_2$  is a parallel line and crosses at sample position with  $RLB_1$  in its first and last parts, respectively. The adjustment procedure is making all optical units in sample optics coaxial with the reference light beam.

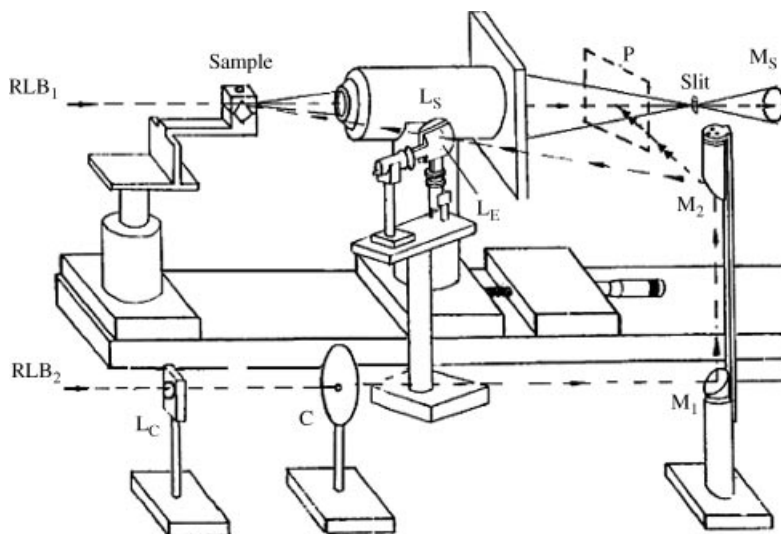


**Figure 3.35** Diagram of adjustment for sample optics:  $L_C$ ,  $L_E$ , and  $L_S$ : Expanse, Illuminating, and Collecting lenses;  $C$ : Small holder;  $M_1$  and  $M_2$ : Reflecting mirrors;  $M_S$ : First convergence mirror of spectrometer;  $P$ : Half reflecting and half transmitting mirror;  $RLB_1$  and  $RLB_2$  are the reference light beams for illuminating and collecting optics, respectively

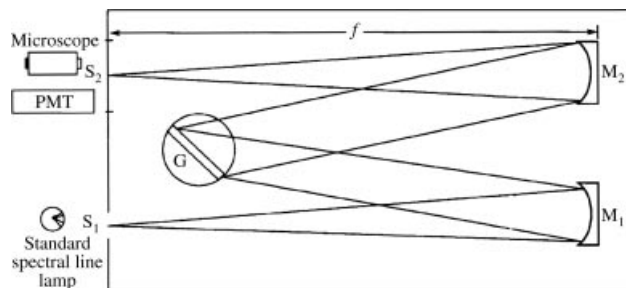
#### 3.4.1.2 Adjusting of the Spectral Dispersion Part

The first thing in the adjustment of the spectral dispersion part is to judge whether the adjustment is needed. This judgment is based on checking if the standard spectral lines can be recorded correctly with the accuracy accredited by the instrument. The standard spectral lines can be found in Appendix II of this book.

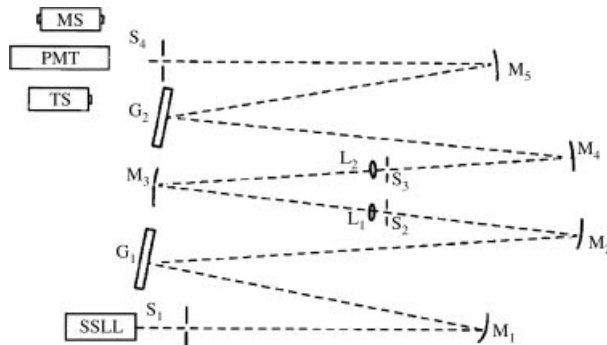
- Adjustment of monochromator

Figure 3.36 is a scheme used for the adjustment of a monochromator.

The checking and adjustment process require us to set the parameters of slits  $S_1$  and  $S_2$  as listed in the instrument manual and to choose a standard spectral line nearest to the blazing wavelength as the light source. Then we need to check if the readout wavelength values of



**Figure 3.36** Diagram of monochromator adjustment:  $G$  is grating;  $S_1$  and  $S_2$  are incident and exit slits, respectively, and  $M_1$  and  $M_2$  are the mirrors, respectively. Reprinted from S.-L. Zhang, Raman Spectroscopy and Low-dimensional nanoscale Semiconductors, Science Press, (2008)



**Figure 3.37** Diagram of double monochromator adjustment:  $G_1$  and  $G_2$  represent two gratings;  $M_1 \sim M_5$  are five concave mirrors;  $S_1$  and  $S_4$  are incident and exit slits, respectively.  $S_2$  and  $S_3$  are middle slits; MS and TS are microscope and telescope, respectively; SSLL is a standard spectral line lamp. Reprinted from S.-L. Zhang, *Raman Spectroscopy and Low-dimensional nanoscale Semiconductors*, Science Press, (2008)

the standard spectral line fit the standard values with the accuracy required by *manual* book and then to decide if the adjustment is still needed. The monitor used for adjustment can be a microscope and/or photoelectron devices such as PMT and CCD. The former benefits from previous adjustment.

According to the degree of reading value deviations from the standard ones, the adjustment should be done first for mirrors  $M_1$  and  $M_2$ , then for the grating  $G$ . This adjustment could be repeated many times. The adjusted result should keep the errors small and balance distributed for various spectral lines.

- Adjusting of double monochromator

Figure 3.37 is a sketch of the optical path in a double monochromator.

The double monochromator is constructed by the connection of two monochromators, and the adjustment can be done first for the second monochromator and then for the first monochromator. When adjusting the second monochromator, the first monochromator is set as a narrow-band filter by opening the slits. When adjusting the first monochromator, the second spectrometer is seen as an exit slit of the first spectrometer by closing the exit slits of the second monochromator to as narrow as possible. The above steps can be done repeatedly until they meet the requirements of instrument performance. Finally, two monochromators should be synchronized, enabling the same standard spectral line to pass from the first and second monochromator simultaneously.

### 3.4.2 Preparing of Samples

The preparation of a good sample is very important for obtaining a high-quality spectrum. Here we introduce some special preparation of samples.

#### 3.4.2.1 Liquid Samples

Figure 3.38 shows a capillary sample prepared for liquid measurement *in the geometry of z(xz)x*. The capillary has a plane bottom, so that the incident light can be fully utilized. The image of the lit part of the liquid fits the strip incident slit, which keeps the loss of scattered

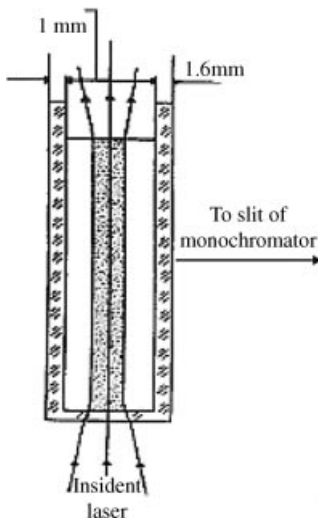


**Figure 3.38** Diagram of special prepared capillary tube for liquid samples [13]. Reprinted from S.-L. Zhang, *Raman Spectroscopy and Low-dimensional nanoscale Semiconductors*, Science Press, (2008)

light from samples to a minimum. As a result, scattered light is used efficiently and the SNR of spectra increases.

#### 3.4.2.2 Powder Samples

If the powder sample is pressed to a bulk-like plate, the scattering efficiency will increase as the number of scatters increases.

#### 3.4.2.3 Chemical Samples

The placing of chemical molecules on a substrate with a rough surface is a very important improvement in Raman spectral measurement. Such obtained spectra are called surface-enhanced Raman spectroscopy (SERS), which implies a new branch of Raman spectroscopy.

### 3.4.3 Improvement of Optical Path

It was mentioned in Section 3.2.2, sample optics should achieve:

- (1) the illuminating light on the sample at the highest power density;
- (2) no additional stray light from samples; and
- (3) preventing the illuminating light from going through the slit of the spectrometer.

To match the above requirements, the Brewster angle incidence of a laser beam to samples, as shown in Figure 3.39, is a good method for solid plate samples. In the figure, the angle between the incident laser beam and the normal line of sample surface is set as the Brewster angle  $\varphi_B$ . It is well known that  $\varphi_B$  is defined by

$$\tan \varphi_B = n_2/n_1 \quad (3.39)$$

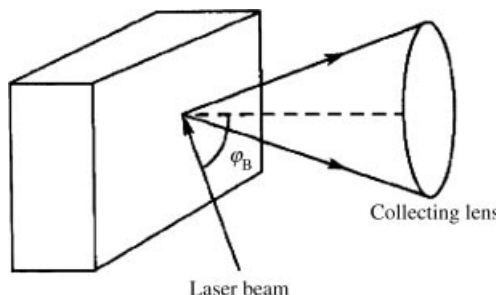


**Figure 3.39** Incident optical path with Brewster angle incidence. Reprinted from S.-L. Zhang, *Raman Spectroscopy and Low-dimensional nanoscale Semiconductors*, Science Press, (2008)

where  $n_2$  and  $n_1$  are the refraction index of the sample and air, respectively. At the Brewster angle, if the polarization direction of incident light is parallel to the incident plane, that is, the plane formed by the direction of incident light and the normal line of sample surface, all of the incident light must go into the sample and no light is reflected from the surface of the sample. As a result, it fits all of three of the requirements listed above.

Such an arrangement of laser incidence with the Brewster angle is especially suitable for an opaque solid plate sample. If  $n_2$  is large enough, at the Brewster angle the incident light beam within the sample almost equals the normal incidence and the optical path is similar to the backscattering path and almost no stray light is produced, which is impossible in common backscattering configurations.

### 3.4.4 Choice of Scanning Parameters

Sections 3.3.1–3.3.3 only discuss the optimization of “hardware” of instruments. Also, the above discussion clarifies that the influence of the spectrometer technical parameter on the spectral measurement is manifold and correlative. Therefore, for the hardware utilization of the spectrometer to reach a high level and to obtain a good measured result, it is necessary to make a good choice of scanning parameters (i.e., design good “software”).

The correct choice of scanning parameters of the spectrometer relies on a prior understanding of the features of spectra to be measured and the influence of spectrometer parameters on spectral features. The spectral features are mainly the frequency coverage of whole spectra and the frequency, width, and intensity of each spectral peak, as well as the features of possible noise spectra. Such spectral features can be obtained from references or analyses. Otherwise, it should be obtained by a speedy pre-scanning in a large wavelength range for the sample to be measured. In this section, we will discuss the choice of scanning parameters.

#### 3.4.4.1 Wavelength and Power of Lasers

The choice of laser wavelengths and power are related to the utilization of the resonant effect, avoiding photoluminescence disturbance and preventing heat damage and temperature effects of samples. Usually, the power of the exciting laser should be as smaller as possible, as long as the spectra can be recorded.

#### 3.4.4.2 Grating

For a commercial spectrometer, the grating choice is mainly based on the match between the covering wavelength regions of spectra and grating.

#### 3.4.4.3 Width and Height of Slits

Section 3.3.1 mentioned that the width and height of slits affect the resolving capability of spectrometers. If the spectral width of slits is larger than predicted spectral width of the samples, the line width and resolution of recorded spectra cannot be better than the spectral width of slits.

Moreover, the width and height of slits are also relative to the flux of light incident into and exiting off the spectrometer and thus affect its sensitivity.

#### 3.4.4.4 Scanning Time

The continuous scanning time is decided by the signal to noise ratio (SNR). The intensity of a random signal in stray light is proportional to  $1/\sqrt{n}$ , of which  $n$  represents times of repeating sampling and thus a large  $n$  implies the increasing of SNR and the high-quality spectra to be recorded.

The increase in scanning time can be done in two ways: increasing the repeating times of scanning for whole spectra and the sampling time at each step, which are more suitable for the case of a stable or unstable spectral signal, respectively.

### 3.5 Data Processing of Recorded Raman Spectra

In the measurement of Raman spectra, although the sample is prepared as well as possible, the spectrometer is adjusted carefully, and the scanning parameter is chosen well, the recorded “original spectrum” is often a spectrum consisting of many sub-spectra. The sub-spectra in the original spectrum usually consists of three parts from the sample, the instrument, and disturbance of the environment; the last two are the ones that produce the noise. The spectra from samples can also be classified into two types: real spectra and noise spectra, of which the latter is induced by impurities and defects in the sample. Therefore, to utilize observed spectra, first we has to process the original spectral data, which is discussed below.

The real spectra and noise spectra are similar to the so-called “true value” and “error” discussed in experiment textbooks, respectively. But there is a difference between these, for example, the object processed in the experiment textbook is a sole variable such as length, electric quantity, and temperature and the sub-spectra discussed here is the function of certain variables such as frequency, polarization, and temperature, and so on. Therefore, spectral data processing is more complicated than common data processing. However, the data processing principle and method mentioned in experiment textbooks is still the foundation of the processing of Raman spectral data.

The analysis for the component and its feature of “original spectra” are the foundation of data processing. In this section, we will discuss this subject further.

#### 3.5.1 Component and Corresponding Spectral Character of Original Spectra

##### 3.5.1.1 Spectra from Spectrometer Instrument Itself

- Incorrect spectral features from instrument structure

Due to the readout error and/or the intensity dispersive effect of spectrometer elements mentioned in Section 3.2.6, the wavelength/wavenumber and intensity values of original spectra will not reflect their real values correctly, which will be more serious for the spectra

covering a wide wavelength range, such as for Raman spectra of a wider wavenumber region, multi-phonon and various wavelength excitation, and so on.

- Noise spectra caused by impropriety of instrument adjustment

When adjustment and calibration of the spectrometer is inaccurate, an additional spectral line will appear in the measured spectra and/or the frequency will shift. The additional spectral line and frequency shift is the same for each spectra, thus it is a kind of noise spectra belong to the systematic error type.

- Electrical noise spectra from the instrument

There is an intrinsic noise mainly coming from an electronic circuit and an electrophotonic detector (electrophotonic diode, Photo Multiplier Tube, and CCD), as mentioned in Section 3.2.5. The spectral characteristic of such noise spectra is random.

### *3.5.1.2 Spectra from Sample*

The sample mentioned here is the one prepared specially for spectral measurement. Except for the object to be studied, the sample often includes the substrate, container, solution, and so on. The sake of clarity, we called the object to be studied the specimen.

- Real Raman spectra

The ideal sample must be pure, just containing the component we wish to study. The real spectra mentioned here are the spectra from the specimen, which is required to obtain the desired experimental measurement and is the base data for identification and research.

- Raman spectra from non-specimen

Objects different from the components of the specimen can be seen as impurities or defects. For example, unreacted raw materials and intermediate products in the preparation of samples are only some of the impurities. Of course, the substrate, container, and any solution surrounding the sample can also be considered as “impurities.” Also, the structure defects of materials are a kind of defect spectra of the non-specimen.

Because of exposure to air for a long time or any other mistakes in conservation, the sample will be contaminated or/and have deteriorated. For example, if the sample is exposed to air for a long time it will be oxidized; the materials could become another material completely. Such cases are common and occur easily for nanomaterials. The spectra from these changes can be seen as impurity spectra.

Sometimes the spectra from specimens will include non-Raman spectra, such as the photoluminescence spectra excited by the laser. Since the intensity of photoluminescence spectra is several orders of magnitude greater than that of Raman spectra, Raman spectra are overlapped easily.

The non-specimen spectra have a common feature. Their spectra characteristic is the same as the spectral characteristic of impurities or defects at source. For example, for a nanosilicon sample with impurity  $\text{SiO}_2$ , the characteristic of impurity spectra only matches the characteristic spectrum of  $\text{SiO}_2$ .

### *3.5.1.3 Disturbed Spectra from Environment*

When the experiment is performed under external condition, such as high temperature, electromagnetic field, and high pressure and so on, the corresponding disturbed spectra will

often appear. For example, if the temperature is high, black-body radiation of the sample and the heating furnace will appear in the frequency range of the measured Raman spectra and become disturbed spectra with the characteristics of black-body radiation. Disturbance spectra from the environment will include the following spectra.

- Disturbed spectra from non-excited light

First, non-excited light mostly originates from the noise light in lasers, such as the plasmon line in a gas laser. In addition, when the shielding for light is not enough, the non-excited light will include natural light and illumination lamp light.

- Disturbance spectra caused by change of experimental environment conditions

If a sample is measured over a long time, it is difficult to guarantee constant conditions and these changes will affect the measurement result. For example, a change in environmental temperature will lead to a drift in the Raman spectra, the background of Raman spectra varies with the intensity of environmental light, the change of electromagnetic field caused by environmental or commercial power will make the noise of spectra to increase, and any vibration of the spectrometer can lead to unstable spectra. Spectra produced by all of these factors become part of noise spectra. The characteristics of these spectra are random and usually slow to change.

- Disturbance spectra from cosmic rays

In an experiment, a spectral line from a cosmic ray is easy to observe. The obvious characteristic of a cosmic ray is a sharp line and its extreme high intensity without a fixed frequency position.

### **3.5.2 Elimination and Decrease of Noise Spectra**

Based on the analysis of components and their spectral characters in the original sample, noise spectra can be decreased and even eliminated through methods used according to the features of the sub-spectra.

#### *3.5.2.1 Correction of Intensity Dispersion*

The first amendment for original spectra is the distortion of spectral features induced by intensity dispersion of the instrument itself, which is critical for a wide wavenumber range of Raman spectra. The correction can be reached by using the intensity dispersion curve of spectrometers described in Section 3.2.7.

#### *3.5.2.2 Smoothing and Fitting*

If the fluctuation is large and the signal to noise ration is also large in the original spectra, it will be difficult to read out the spectral parameters correctly, such as peak number, shape, and width. The fluctuation superimposed on original spectra is often random. Therefore, elimination and decrease can be done by the spectral smoothing method. Nowadays the operation of spectral smoothing can be done by computer software; most commercial Raman spectrographs have incorporated this software into their software. Usually the smoothing can be performed with fitting simultaneously. Figure 3.40 (see color Plate 2 for the original Figure 3.40) shows an example where the spectra have been smoothed and spectral peaks have been worked out by fitting.

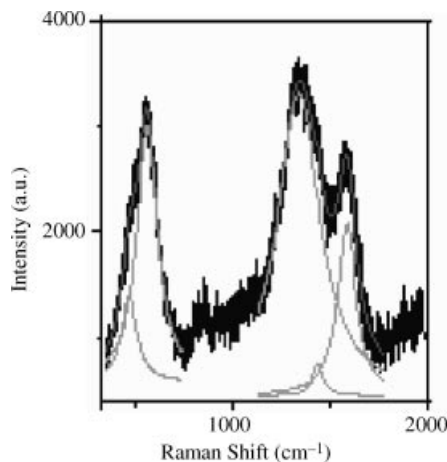


**Figure 3.40** A sample of smoothing and fitting: original (black), smoothed (red), and fitting (green) spectra. Reprinted from S.-L. Zhang, *Raman Spectroscopy and Low-dimensional nanoscale Semiconductors*, Science Press, (2008)

Close attention should be paid to every smoothing method, by a transformation in mathematics but this cannot ensure the smoothed spectra are reasonable. Therefore, the smoothing should be operated based on physical considerations.

### 3.5.2.3 Direct Deduction

The spectral smoothing process cannot eliminate and decrease any unreal components with non-random fluctuations in original spectra. For non-random fluctuant noise spectra, the deduction of such spectral components is needed.

- Disturbance spectra from cosmic rays

As shown in Figure 3.41(a), the original spectra of GaN nanoparticles include many thin and tall peaks, which are typical of cosmic ray spectra; hence we can delete them directly by deduction methods. After deduction, the spectral data in deduced positions are vacant

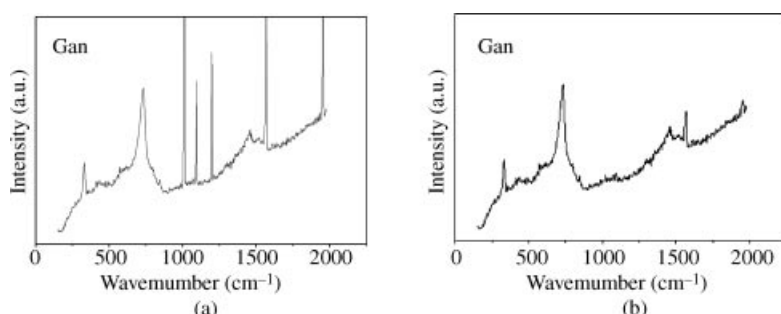


**Figure 3.41** Showing of deducting of cosmic ray: Original (a) and real (b) spectra of GaN nano particles. Reprinted from S.-L. Zhang, *Raman Spectroscopy and Low-dimensional nanoscale Semiconductors*, Science Press, (2008)

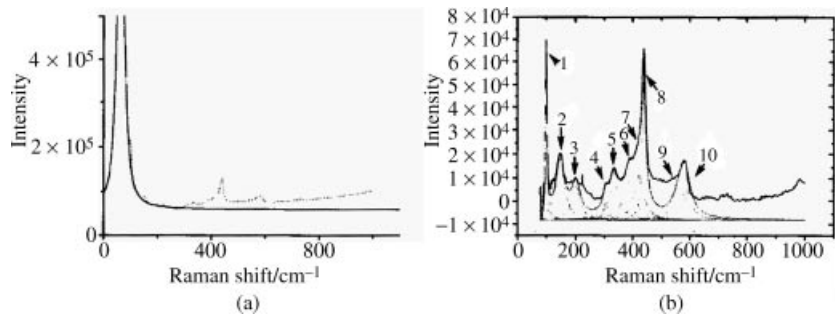


**Figure 3.42** Original (a) where, the undertone spectral line has been amplified by  $10^5$  and real (b) Raman spectra of ZnO NPs. Reprinted from S.-L. Zhang, *Raman Spectroscopy and Low-dimensional nanoscale Semiconductors*, Science Press, (2008)

and need to be filled with new spectral date so that the spectra are continuous. Figure 3.41 (b) is a real spectrum of GaN nanoparticles after removing the cosmic ray.

- Disturbance spectra from Rayleigh scattering

The background from Rayleigh scattering is strong, which always covers the real spectra in the low-wavenumber region. Figure 3.42(a) shows the original Raman spectra of ZnO nanoparticles (NPs); in this spectrum we can see that the Rayleigh spectral line is stronger than  $10^6$  photon count per second so that the weaker Raman scattering lines are invisible. After deduction of the Rayleigh spectral line, the real spectrum with about  $10^4$  photons numbers per second appears, as shown in Figure 3.42(b).

- Disturbance spectra from impurities

Figure 3.43(a) is an original spectrum of an SiC nanorods (NRs). Except for a continuous background spectrum from photoluminescence, it shows a large difference in the characters of bulk SiC spectrum and cannot be considered as the real spectrum of SiC

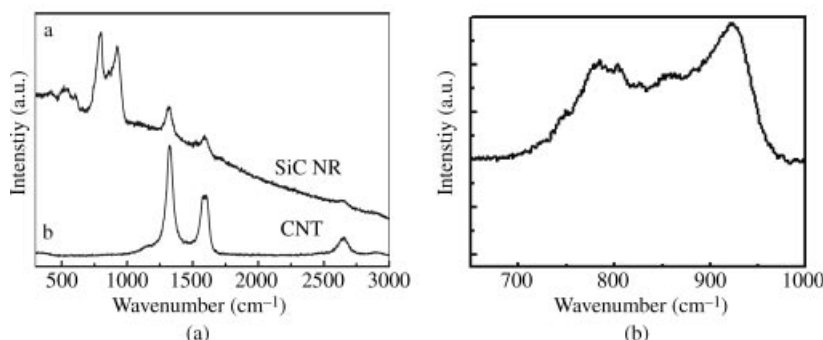


**Figure 3.43** (a) Observed original spectrum of SiC NRs (b) Real Raman spectrum of SiC NRs [14]. Reprinted from S.-L. Zhang, *Raman Spectroscopy and Low-dimensional nanoscale Semiconductors*, Science Press, (2008)

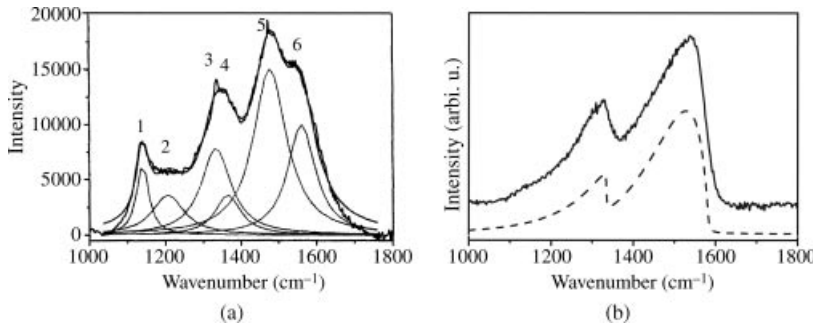


**Figure 3.44** Original (a) and real (b) Raman spectra of a diamond film sample [15]. Reprinted from S.-L. Zhang, *Raman Spectroscopy and Low-dimensional nanoscale Semiconductors*, Science Press, (2008)

NRs. Considering the SiC NR sample studied is made by the reaction of carbon nanotube (CNT) and SiO steaming, the sample may contain some unreacted CNT; thus the original spectrum may be a Raman spectrum of SiC NRs mixed with CNT. After deducting the Raman spectra of CNT, as shown in Figures 3.43(a and b), and the photoluminescence background, the real spectrum of SiC NRs appears, as shown in Figure 3.43(b).

- Spectral fitting and assigning

When the origin of sub-spectra is unknown, the real spectra of a specimen can be obtained based on the composition of the original spectrum, as described in Ref. [12]. The authors of Ref. 12 obtained an original Raman spectrum of a diamond film sample, shown as the solid line in Figure 3.44(a); which shows a large difference to the typical Raman spectra of diamond. To obtain the real spectrum of the specimen, they performed the spectral fitting for the original spectra by seven sub-spectra with a Gaussian line shape, shown as a dashed line in Figure 3.44(a). After these seven fitted sub-spectra are assigned and impurity spectra are removed, the real spectra of nanodiamond with nanographite are deduced, as shown in Figure 3.44(b).

In spectral fitting, the selection of line shapes plays a key role. The selection is usually from one of the Gaussian, Lorenzian, and Fano line-shape functions.

### 3.5.3 Acquisition of Spectral Parameters

The spectral parameter is the foundation of spectroscopic research and application. This parameter can be worked out only after obtaining correct measurements and a real spectrum as described above.

The spectral parameter is acquired mostly by spectral fitting. Figure 3.45(a) shows the spectra of ZnO nanoparticles (NPs) excited by different wavelengths of lasers. Through spectral fitting by computer, the Raman frequencies of each phonon mode and the average value of spectral frequency were acquired, as shown in Table 3.4. Table 3.5 shows the standard deviation from average values of each phonon mode. Figure 3.45(b) drew the dependence of Raman shift on excited energy and exhibits clearly that the frequency of different phonon modes do not change with the excited wavelength.

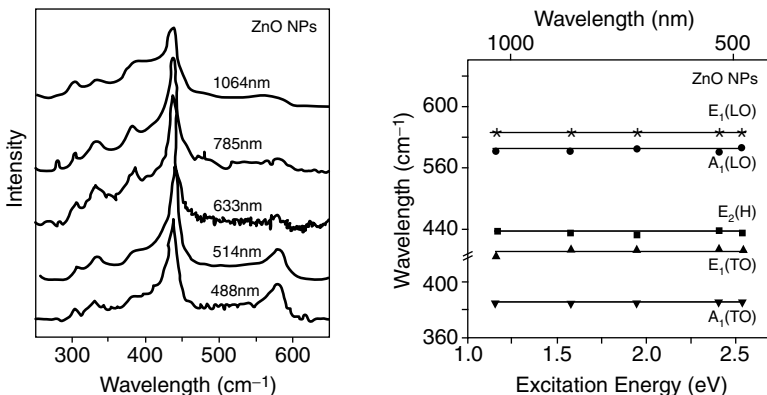


**Figure 3.45** Spectra excited by various wavelengths of laser (a) and the dependence of Raman shift on excited energy (b) for ZnO NPs [16]. Reprinted from S.-L. Zhang, *Raman Spectroscopy and Low-dimensional nanoscale Semiconductors*, Science Press, (2008)

**Table 3.4** Raman frequency  $\omega$  of phonon modes exited at various wavelengths for ZnO NPs

Phonon mode		A <sub>1,T</sub>	E <sub>1,T</sub>	E <sub>2(H)</sub>	A <sub>1,L</sub>	E <sub>1,L</sub>
$\omega/\text{cm}^{-1}$	at 488 nm	386.1	423.7	437.3	572.0	582.4
	at 514 nm	385.9	425.4	439.4	569.7	583.0
	at 633 nm	385.4	423.8	438.2	571.8	582.0
	at 785 nm	383.7	423.4	436.8	568.7	583.6
	at 1064 nm	385.0	420.7	437.8	569.0	582.7
	Average	385.4	423.0	437.9	570.2	582.9

**Table 3.5** The standard deviation from average values of each phonon frequency for ZnO NPs

Phonon mode		A <sub>1,T</sub>	E <sub>1,T</sub>	E <sub>2(H)</sub>	A <sub>1,L</sub>	E <sub>1,L</sub>
$\Delta\omega/\text{cm}^{-1}$	at 488 nm	+0.7	+0.7	-0.6	+1.8	-0.5
	at 514 nm	+0.4	+1.4	+1.5	-0.5	+1.1
	at 633 nm	0	+0.8	+0.3	+1.6	-0.9
	at 785 nm	-0.7	+0.4	-1.1	-1.5	+0.7
	at 1064 nm	-0.4	-3.3	-0.1	-1.2	-0.2
	Standard	0.59	1.88	0.99	1.56	0.84

### 3.6 A Typical Example of Vibration Raman Spectra – Raman Spectrum of CCl<sub>4</sub>

In this section, we will give a practical example of Raman spectral measurements. The used sample consists of molecules of CCl<sub>4</sub>, which remains a liquid under normal conditions and the CCl<sub>4</sub> molecule has a random spatial orientation in the liquid. In the following, the relationship between the structure, symmetry, vibration mode, and Raman spectra will be given.

### 3.6.1 The Structure and Symmetry of $\text{CCl}_4$ Molecule [17]

A  $\text{CCl}_4$  molecule consists of one carbon atom and four chlorine atoms, with the structure as shown in Figure 3.46(a), from which we can see that four chlorine atoms and one carbon atom occupy the four vertexes and the center of a regular tetrahedron, respectively.

It is well known that if a body coincides with itself after a series of operations, such as the rotation around an axis of itself, inversion or both of the two operations, these operations are called symmetric operations. The rotation axis and rotation-inversion axis of the  $\text{CCl}_4$  molecule is shown in Figure 3.46(b), where a  $\text{CCl}_4$  molecule has 24 symmetrical operations, including motionless operation. The 24 symmetrical operations are classified into five kinds of symmetry elements

$$E, 3C_2^m, 8C_3^j, 6iC_2^p, 6iC_4^m$$

The definition of the above symbols is

$E$ : motionless;

$C_n$ : rotation axis, subscript  $n$  means the rotation angle is  $2\pi/n$ ;

$i$ : inversion;

$m$ : rotation axis along with the coordinate axes of  $x, y, z$ ;

$j$ : rotation axis, the azimuth of the axis is the one of the body diagonal passed through the oriental point 0.  $j = 1, 2, 3, 4$ ;

$p$ : rotation axis, the azimuth of the axis overlaps the lines linked to the mid-points of the two opposite seamed edges and pass the center point  $O$  of a cube,  $p = a, b, c, d, e, f$ ;

+ or -: clockwise or anticlockwise.

The number before each symbol expresses the number of symmetrical operations.

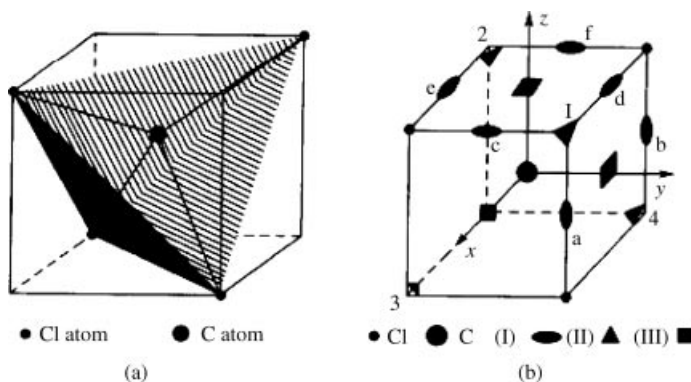


**Figure 3.46** Sketch of molecular structure (a) and symmetry elements. Reprinted from S.-L. Zhang, L.-L. Liu, Z.-X. Run and Z. Dan, *Raman Spectroscopy of vibrations*, Eds. Z.-Q. Wang and S. Wu, Peking University Press, 1998. (b) of  $\text{CCl}_4$  [17]. Reprinted from S.-L. Zhang, L.-L. Liu, Z.-X. Run and Z. Dan, *Raman Spectroscopy of vibrations*, Eds. Z.-Q. Wang and S. Wu, Peking University Press, 1998

### 3.6.2 The Vibration Modes and Polarized Raman Spectra of $\text{CCl}_4$ Molecules

The vibration freedom of a molecule containing  $N$  atoms is  $3N-3$ , of which  $N \geq 3$ . Thus a  $\text{CCl}_4$  molecule having four atoms has nine normal vibration modes. The nine modes can be classified into four categories, as shown in Figure 3.47(a). And these four categories can be classified into symmetric and anti-symmetric modes due to the difference of inverse symmetry. In the above four categories, the first category is symmetrical vibration while the others are anti-symmetric vibrations.

Generally speaking, one kind of vibration has only one basic vibration Raman line. Of course, considered the perturbation caused by the coupling between vibrations, it is possible that the spectral line will split into more than one line. The number of vibration modes for each kind of vibration corresponds to the degeneracy degree of energy levels in quantum mechanics. Thus, if a kind of vibration has  $g$  vibration modes, we call it a  $g$  fold degenerative.

Figure 3.47(b) is the polarized Raman spectra of  $\text{CCl}_4$ . Two of the weakest spectral lines at  $762$  and  $790\text{ cm}^{-1}$  are caused by the splitting of the spectral line at  $773\text{ cm}^{-1}$ . The spectral line at  $773\text{ cm}^{-1}$  originated from the coupling of the two vibrations corresponding to the spectral lines at  $314$  and  $459\text{ cm}^{-1}$  and then the coupling results in the split of the spectral line at  $763\text{ cm}^{-1}$ .

The depolarization degree  $\rho_s(\pi/2)$  obtained from the experimental results shown in Figure 3.47(b) are listed in Table 3.6, along with their theoretical values, which shows a good match. According to the description of depolarization degree mentioned in Section 3.1.2, the results listed in Table 3.6 indicate clearly that the vibration modes at  $278\text{ cm}^{-1}$  and  $314\text{ cm}^{-1}$  are fully depolarized and the vibration mode at  $419\text{ cm}^{-1}$  is fully polarized.

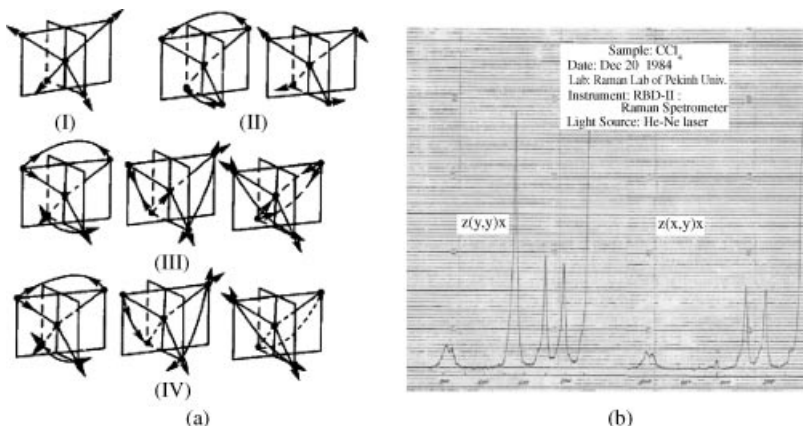


**Figure 3.47** Atomic vibration fashion (a) and polarized Raman spectrum. Reprinted from S.-L. Zhang, L.-L. Liu, Z.-X. Run and Z. Dan, *Raman Spectroscopy of vibrations*, Eds. Z.-Q. Wang and S. Wu, Peking University Press, 1998. (b) of  $\text{CCl}_4$  [17]. Reprinted from S.-L. Zhang, *Raman Spectroscopy and Low-dimensional nanoscale Semiconductors* (in Chinese), Science Press, Beijing, 2008

**Table 3.6** Values of frequencies and depolarization degree  $\rho_s(\pi/2)$  for vibration modes of  $CCl_4$  [18]

Symmetry of vibration modes Raman frequencies	Anti-symmetry $278\text{ cm}^{-1}$	Anti-symmetry $314\text{ cm}^{-1}$	Symmetry $459\text{ cm}^{-1}$
$\rho_s(\pi/2)$	Theoretical 0.75	Theoretical 0.75	0.00
	Experimental 0.74	Experimental 0.73	0.02

## 3.7 Interference Spectrometer and Fourier Transform Optics

Between 1970 and 1980, the interference spectrometer begun to enter research and applied field of light scattering spectra. There are two types of interference spectrometers: the Fourier Transform (FT) spectrometer and the Michelson interference spectrometer, which belong to the interference and dispersive types of spectrometers, respectively. In this section, the interference spectrometers will be introduced.

### 3.7.1 Fourier Transform (FT) Spectrometer [18]

#### 3.7.1.1 Michelson Interferometer

The core part of FT spectrometers is the Michelson interferometer, the structure of which is shown in Figure 3.48. In the figure we can see that an incident light beam with intensity  $I_0$

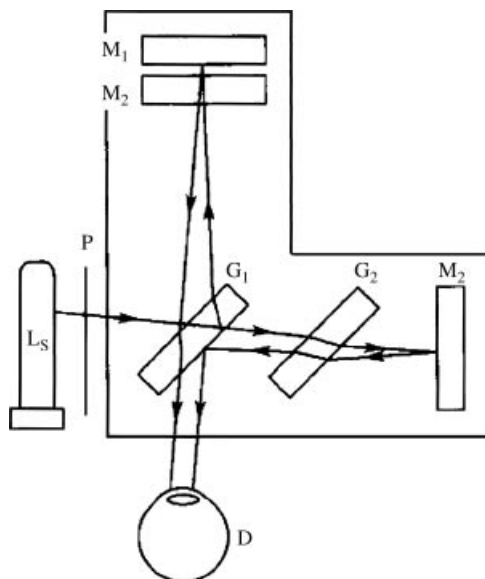


**Figure 3.48** Structure diagram of Michelson interferometer:  $L_s$ : light source;  $P$ : Ground glass;  $G_1$ : beam splitter;  $G_2$ : Compensation plate;  $M_1$ : Movable mirror;  $M_2$ : Fixed mirror;  $D$ : Detector [18]. Reprinted from Z. Kaihua and Z. Xihua, Optics, (1983) with permission of the Peking University Press

and wavelength  $\lambda$  (frequency  $v$ ) splits into transmitted and reflected beams with equal intensity by a beam splitter  $G_1$ , of which the reflected beams from the movable mirror  $M_1$  and fixed mirror  $M_2$  produce an optical path difference of  $\Delta = 2d$  and the corresponding phase difference is

$$\delta = 2\pi\Delta/\lambda = 2\pi v\Delta \quad (3.40)$$

The interfered intensity detected by detector  $D$  for two interfered light beams is

$$I = I_0(1 + \cos \delta) = I_0[1 + \cos(2\pi v\Delta)] \quad (3.41)$$

In the above equation, the first item reflects the background of the detector and is a constant, which can be neglected in the discussion. Thus we have

$$I = I_0 \cos \delta = I_0 \cos(2\pi v\Delta) \quad (3.42)$$

Obviously, Equation (3.42) indicates that the light intensity will change with phase difference  $\delta$  or with the optical path difference  $\Delta$ . The maximum light intensity detected by the detector  $D$  appears at  $\Delta = 0, 1/v_1, \dots, (n-1)/v_1, n/v_1, (n+1)/v_1, \dots$ , where  $n$  is the integral number of 0, 1, 2, ... . Therefore, the light intensity  $I$  from the Michelson interferometer will vary with the optical path difference  $\Delta$  and period  $1/v_1$ , as shown Figure 3.49(a).

For polychromatic light, Equation (3.42) indicates that when the mirror  $M_1$  does not move, the optical path difference  $\Delta$  is fixed but the phase difference  $\delta$  will vary for different colored light, that is, the incident light frequency  $v$ . According to Equation (3.42), the  $I$  of light beams of different frequencies after passing through the Michelson interferometer will interfere with each other. If the incident light consists of two beams of monochromatic light with frequencies  $v_1$  and  $v_2$ , at  $v_1\Delta = n$ , the interfered intensity of light of  $v_1$  reaches maximum, while at  $v_2\Delta = n - 1/2$ , the interfered intensity of light of  $v_2$  is minimum. When  $\Delta = 1/2(v_1 - v_2)$ , the maximum intensities of  $v_1$  and  $v_2$  overlap and the contrast of interference pattern reaches minimum. While  $\Delta = 1/(v_1 - v_2)$ , the intensities of  $v_1$  and  $v_2$  light are both at maximum, and the contrast of interference pattern reaches maximum. Figure 3.49(b) shows the light intensity variation of two monochromatic lights of  $v_1$  and  $v_2$  passed through a Michelson interferometer with optical path difference  $\Delta$ .

If the light source is a light with a continuous frequency  $v$  and spectral brightness distribution  $B(v)$ , its interfered intensity passing through the Michelson interferometer at frequency  $v$  within a interval  $dv$  is

$$B(v) \cos(2\pi v\Delta) dv \quad (3.43)$$

Obviously, the total interference intensity detected by the detector is

$$I(\Delta) = \int_0^{\infty} B(v) \cos(2\pi v\Delta) dv \quad (3.44)$$

Mathematically, the above equation is only the Fourier integration of light source spectral brightness  $B(v)$ . Figure 3.49(c) shows a sketch of a variety of interference

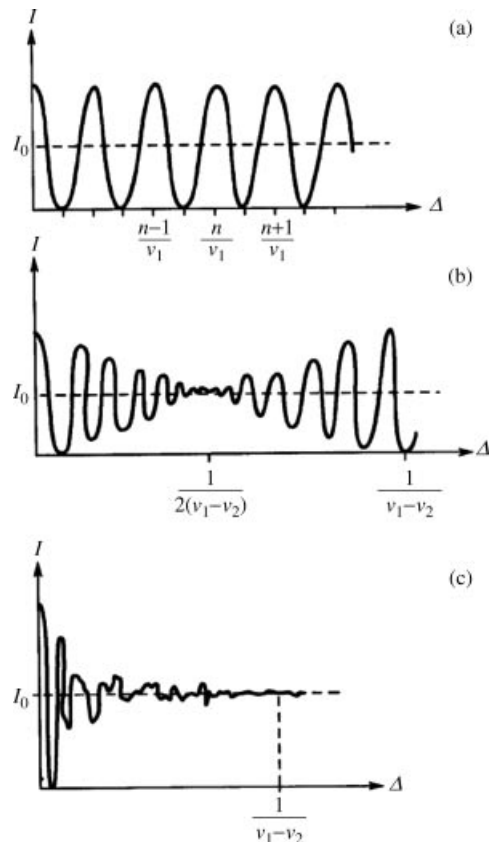


**Figure 3.49** Variety of light intensity  $I$  emitted from Michelson interferometer with optical path difference  $\Delta$  [19]. Reprinted from S.-H. Lv and Y.-K. Zhu, Experimental Technique of Modern Physics (I), High Education Press, (1991)

intensity  $I(\Delta)$  with optical path difference  $\Delta$  for continuous light of frequencies in the interval  $v_1$  and  $v_2$ .

### 3.7.1.2 Fourier Transform (FT) Spectrometer

By using the conversation of Fourier integration of Equation (3.44), we can obtain the frequency distribution of light source spectral brightness  $B(v)$ , that is, the spectrum of incident light:

$$B(v) \propto \int_0^{\infty} I(\Delta) \cos(2\pi v \Delta) d\Delta \quad (3.45)$$

Therefore, a new type of spectrometer without a grating can be designed for the Michelson interferometer and FT techniques, which is the reason why the Michelson interferometer spectrometer is called an FT spectrometer.

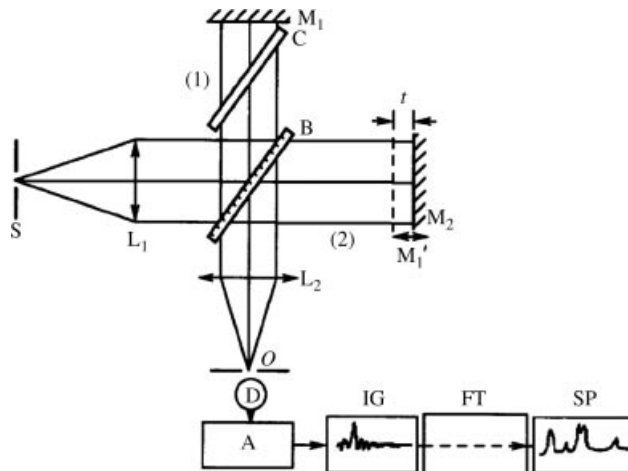


**Figure 3.50** Sketch of Fourier Transform (FT) spectrometer structure:  $S$  is light source;  $C$  is compensation board;  $L_1$  and  $L_2$  are collimating and focus lenses of light beam;  $D$  is the optical detector;  $A$ : Amplifier;  $IG$ : Interference figure;  $FT$ : Fourier transformation calculation;  $SP$ : Spectral display [19]. Reprinted from S.-H. Lv and Y.-K. Zhu, Experimental Technique of Modern Physics (I), High Education Press, (1991)

The calculated amount of FT is huge; only from when computer technology was fully developed in the 1980s did the FT spectrometer reach the stage of practical commercialization. Therefore, high-performance computers and advanced computing technology is crucial in FT spectrometry, which makes it possible that the time-domain spectrum transfers into the frequency spectrum and the measurement of high time-resolved spectra and real-time data processing and analysis. Figure 3.50 shows the structure and component of an FT spectrometer. Its main components are described below:

- Light source

The light source of FT spectrometry is mostly an Nd: YAG NIR laser with a wavelength of 1064 nm instead of the traditional visible light laser. In recent years, the diode pumped solid state Nd: YAG laser has been developed with a longer wavelength of 1064 nm to 1300 nm.

- Michelson interferometer

The Michelson interferometer is a key component of the FT spectrometer, which we were already discussed. The driving of the movable mirror is by a step motor. The beam splitter is a half-reflection and half-transmission optic plate coated with dielectric film. The compensation board is necessary for polychromatic light.

- Detection, amplification and data processing system

Optical detector  $D$  is a liquid nitrogen cooling Ge diode or InGaAs detector with a better response in the near infrared range. The detected interference light signal is amplified to make FTs in data processing systems, thus the spectra of light source is obtained.

### 3.7.1.3 Characteristics of FT Spectrometer

The major improvement in the key component of spectrometers is to replace gratings with Michelson interferometers.

Since movable mirrors driven by a motor move with speed  $v$  in a Michelson interferometer, the optical path difference  $\Delta$  must be the function of time  $t$  and can be written as

$$\Delta = 2d = 2vt \quad (3.46)$$

As a result, according to Equation (3.45), the direct measured  $B(v)$  is a function of time. This implies that the Michelson interferometer moves the light source brightness spectra  $B(v)$  with a frequency into the time domain. Unlike the Michelson interferometer, the function of the grating is to decompose a light spectrum with frequency (wavelength) in geometrical space. Therefore the spectra measured by using a grating and a Michelson interferometer are the spatial domain and time-domain spectra, respectively. Thus, the above characteristics of an FT spectrometer make it suitable to time-resolve spectra. FT spectra still have other characteristics, such as:

- Resolution with no diffraction restriction

The spectrometer with the spatial dispersive grating is restricted by the diffraction effect, but the FT spectrometer does not have this restriction. Its resolution can be improved become unrestricted by increasing optical path difference  $\Delta$ .

- Big light flux

In the grating spectrometer, the width of the slits is always decreased by more than one monochromator to increase the resolution, which lowers the light flux. The light flux of FT spectrometers is dependent of the size of the mirrors in the interferometer. Therefore, at the same resolution, the light flux of FT spectrometers is several hundred times better than that of grating spectrometers.

- High signal to noise ratio (SNR)

In the FT spectrometer, noise signal is not affected by the direct current (DC) signal of the FT, thus it can easily be eliminated. The effect of stray light is usually under 0.05%.

- Short acquisition time of spectra

The measurement of the whole spectral band by the FT spectrometer can be completed in one go, implying the acquisition spectra can be created in a short time.

- Application for Raman spectroscopy

Since the wavelength of light sources in the FT spectrometer is always in the near infrared range, such as 1064 nm, this avoids disturbance to Raman spectra from visible fluorescence. Of course, due to the intensity of Raman scattering being inversely proportional to the fourth power of incident light wavelength, the intensity of Raman scattering from near infrared light excited FT spectrometry will be lower than that obtained by grating spectrometers.

### 3.7.2 Fabry-Perot Coherent Spectrometer [18]

The Fabry-Perot coherent spectrometer is mainly used to measure Brillouin scattering spectra and thus is always called the Brillouin scattering spectrometer.

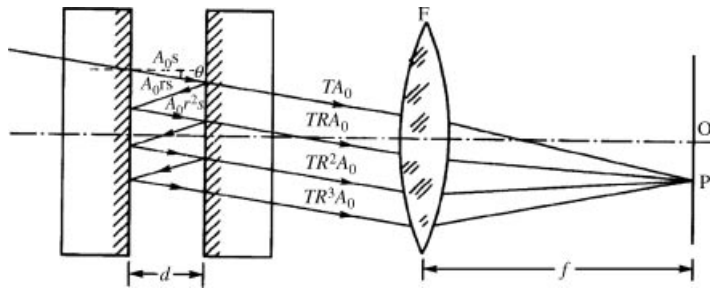


**Figure 3.51** Structure diagram of Fabry-Perot interferometer:  $d$  is the distance between two plates;  $f$  is the focus length of lens;  $R$  and  $T$  are the reflectivity and transparency of parallel plates, respectively, and  $A_0$  is the amplitude of incident light [18]. Reprinted from S.-H. Lv and Y.-K. Zhu, *Experimental Technique of Modern Physics (I)*, High Education Press, (1991)

### 3.7.2.1 Fabry-Perot Interferometer

The core part of the Fabry-Perot coherent spectrometer is the Fabry-Perot interferometer, the structure of which is shown in Figure 3.51. It consists of two glass or quartz flat plates, which are exactly parallel to each other. Its surface flatness is better than 1/50 wavelength. The plate surface is coated with metal or dielectric film with 98% high reflection. In Figure 3.51, the distance  $d$  between two plates is always between several millimeters and several centimeters.

The incidence light beam with an angle  $\theta$  relative to the normal line of the plate is reflected many times between the two plates before exiting. The optical path difference between the two adjacent transmitted light beams is

$$\Delta = 2n_0d \cos \theta \quad (3.47)$$

where  $n_0$  is the refractive index of the medium between the two plates. When  $\Delta$  is integral times of wavelength  $\lambda$ , equal inclination interference occurs, which is expressed as

$$2n_0d \cos \theta = n \cdot \lambda \quad (3.48)$$

In the above equation,  $n$  represents an integral.

When monochromatic light with frequency  $\lambda$  enters, an interference pattern on the back focus plane appears as a series of concentric circles; the radius of the  $n$ th order circle is

$$r = f\theta_n \quad (3.49)$$

$\theta_n$  is the incident angle of the  $n$ th order interference pattern.

Since the incident angle is very small, only several tens of millimeters to several centimeters,  $n$  will be in the range of  $10^3 \sim 10^5$ .

### 3.7.2.2 Performance of Fabry-Perot Interferometer

- Angular dispersion

The result by the differential calculation of Equation (3.48) is

$$n \cdot d\lambda/d\theta = 2n_0d \sin \theta \quad (3.50)$$

Because  $\theta$  is approximated to zero, the angular dispersion of the Fabry-Perot interferometer can be considered as

$$D_\theta = d\theta/d\lambda = 1/(\theta\lambda) \quad (3.51)$$

The above equation indicates that the angular dispersion is independent of  $d$ , and at  $\theta = 0$ ,  $D_\theta \rightarrow \infty$ .

- Reciprocal of linear dispersion

The reciprocal of linear dispersion of the Fabry-Perot interferometer is

$$d\lambda/dl = \theta\lambda/f = 0.1\lambda/f^2 \quad (3.52)$$

If the distance away from the circle's center is 1 mm,  $f = 50$  cm,  $\lambda = 500$  nm, and reciprocal linear dispersion  $d\lambda/dl$  is 0.002 nm/mm. For a grating spectrometer with a focus length of 3 m and a 1200 g/mm grating, the reciprocal of linear dispersion  $d\lambda/dl = 0.13$  nm/mm. The latter is 65 times smaller than that of the former. Therefore, the Fabry-Perot interferometer gives a very high spectral resolution.

- Free spectral range

The calculated free spectral range for adjacent orders, that is, the spectra of  $\Delta n = 1$  is

$$\Delta\nu = 1/2\theta \quad (3.53)$$

If  $d = 1$  cm, the free spectral range is  $\Delta\nu = 0.5$  cm<sup>-1</sup> and thus the Fabry-Perot interferometer processes a very small free spectral range.

- Resolving power

The resolving power of the Fabry-Perot interferometer:

$$R_0 = nF \quad (3.54)$$

$F$  is the fineness coefficient defined as the ratio of free spectral range  $\Delta\nu$  to spectral full width at half maximum (FWHM)  $\delta\nu$ , which is used to describe the fineness of the interference pattern and the dependence of the reflectivity of flat plates in Fabry-Perot interferometers. This dependence is listed in Table 3.7.

From the above discussion, we learn that the outstanding advantage of the Fabry-Perot interferometer is the extreme high resolution and the main disadvantage is the narrow free spectral range. Therefore, in the field of light scattering, people always use it to measure Brillouin scattering, which is why it is called the Brillouin spectrometer. Sometimes the Fabry-Perot interferometer combines with a grating spectrometer to exploit both of their

**Table 3.7** Relation between the reflectivity and fineness coefficient for Fabry-Perot interferometer

Reflectivity	0.60	0.70	0.80	0.90	0.95	0.98	1.00
Fineness coefficient	6	9	14	30	60	155	$\infty$

advantages to the full, for example, acoustic phonon Raman spectra of superlattices as close as  $1\text{ cm}^{-1}$  from the Rayleigh line have been captured by using this combination.

### 3.7.3 Spectrometers and Fourier Transform Optics

From the discussion in this section, we can understand that the cores of the grating spectrometer, Fabry-Perot (Brillouin scattering) spectrometer, and FT spectrometer, are the dispersive grating, the Fabry-Perot interferometer, and the Michelson interferometer, respectively. The grating spectrometer is based on the diffraction mechanism and the Fabry-Perot and FT spectrometers are based on the interference mechanism. The spectra directly measured by the grating spectrometer and the Fabry-Perot spectrometer is spatial dispersive, while the spectra directly measured by the FT spectrometer the time dispersive. All of these three types of spectrometers can be described based on FT optics.

## References

- [1] Zhang, Shu-Lin (2008) *Raman Spectroscopy and Low-dimensional Nano-semiconductors*, Science Press, Beijing.
- [2] Damen, T.C., Porto, S.P.S., and Tell, B. (1966) *Phys. Rev.*, **142**(66), 570.
- [3] Porto, S.P.S. and Wood, D.L. (1962) *J. Opt. Soc. Am.*, **52**, 251.
- [4] Barron, L.D., Bogaard, M.P., and Buckingham, A.D. (1973) *J. Am. Chem. Soc.*, **95**, 603.
- [5] McColl, I.H., Blanch, E.W., Gill, A.C., et al. (2003) *J. Am. Chem. Soc.*, **125**, 10019.
- [6] Siegman, A.E. (1986) *Lasers*, University Science Books.
- [7] Zhou, Y.-H. and Sun, T.-H. (1991) *Laser Physics*, Peking University Press, Beijing.
- [8] Zhang, S.-L. (1993) *Adv. Sci. Instrum.*, **4**, 47.
- [9] Puppels, G.J., de Mul, F.F.M., Oho, C., Greve, J., Arndt-Jarin, D.J., and Jovin, T.M. (1990) *Nature*, **347**, 301.
- [10] Tabakasblat, R., Meier, R.J., and Kip, B.J. (1992) *Appl. Spectrosc.*, **46**, 60.
- [11] Williams, K.P.J., Pitt, G.D., Batchelder, D.N., and Kip, B.J. (1994) *Appl. Spectrosc.*, **48**, 232.
- [12] The technical documents of PI (a), J-Y (b) and Spex 1403 (c) instruments.
- [13] Zhang, S.-L., Liu, L.-L., and Zhou, H.D. (Dec. 26 1985) Holder of Raman Spectra, Patent of Practical New-Type No: 85200108.8 Patent Office of P.R. China.
- [14] Zhang, S.-L., Zhu, B.-F., Huang, F., et al. (1999) *Solid State Commun.*, **111**, 647.
- [15] Yan, Y., Zhang, S., Hark, S.K., et al. (2004) *Chn J. Light Scattering*, **16**, 131.
- [16] Zhang, S.-L., Zhang, Y., Liu, W., et al. (2006) *Appl. Phys. Lett.*, **89**, 063112.
- [17] Zhang, S., Liu, L.-L., Run, Z.-X., and Dan, Z. (1998) *Raman Spectroscopy of Vibrations* (eds Z.-Q. Wangand S. Wu), Peking University Press, Beijing, pp. 80–95.
- [18] Zhao, K. and Zhong, X. (1983) *Optics*, Peking University Press, Beijing.
- [19] Lv, S.-H. and Zhu, Y.-K. (eds) (1991) *Experimental Technique of Modern Physics (I)*, High Education Press, Beijing.

# 4

## Introduction to Modern Raman Spectroscopy I- New Raman Spectroscopic Branch Classified Based on Spectral Features

After the change from conventional light sources to the laser, objects studied by Raman spectra have been greatly expanded. This expansion has enabled many new Raman spectral phenomena and regular patterns to be discovered in the last several decades. As a result, modern Raman spectroscopy has gradually developed and matured to its current form. Modern Raman spectroscopy can be described from two different angles, one from spectroscopic features and regular patterns of Raman spectra and the other from studied targets of Raman spectra. In this chapter, modern Raman spectroscopy will be briefly described from the aspect of spectroscopic phenomenon and regular patterns. Based on spectroscopic features, traditional Raman spectroscopy can only record the relationship of spectral intensity of molecular vibrations on frequencies, that is, the frequency spectra of visible excited, linear, first-order, non-resonant, spontaneous, atmospheric conditions, non-polarized, macroscopic, and far-field. In contrast, modern Raman spectroscopy has developed into a different kind of spectroscopy that includes the frequency and image spectroscopy of non-visible excited, non-linear, high-order, resonant, extra conditions, polarized, transient, microscopic, stimulated, and near-field. This new-style Raman spectroscopy is mainly contributed to the introduction of the laser into Raman spectrometer and thus it is named laser Raman spectroscopy often. In this chapter, the new-style Raman spectroscopic branches mentioned above will be briefly described.

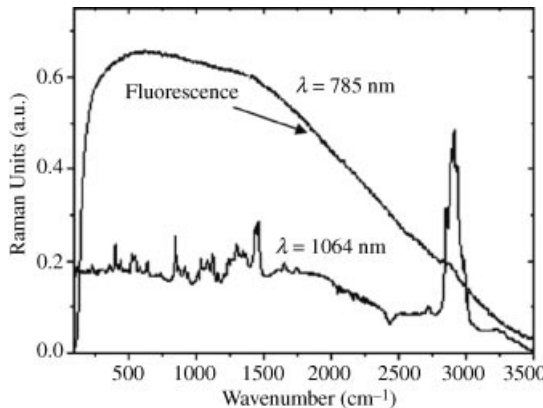


**Figure 4.1** Raman spectra of chocolate acquired with laser excitation wavelengths of 1065 and 785 nm, respectively [1]. Reprinted from S.Wartewig and R. Neubert, Pharmaceutical applications of Mid-IR and Raman spectroscopy, Advanced Drug Delivery Reviews, 57, 1144 (2005) with permission of Elsevier

#### 4.1 Non-visible Excited Raman Spectroscopy

The wavelength range of a laser used in Raman spectrometer has expanded from the visible to the invisible range, such as X-ray, ultraviolet (UV) and infrared (IR) and so on. With more available laser light sources, Raman spectroscopy is no longer restricted to visible light excitation and has gradually evolved into non-visible (such as IR, UV, and X-ray, etc.) excited Raman spectroscopy. On the one hand, non-visible excitation are preferred as the excitation sources for some objects, for example, X-ray excitation can be applied in electron Raman spectra and in medical diagnosis. On the other hand, non-visible excitation has the ability to prevent fluorescence and luminescence spectra interference Raman spectra and therefore their usage is sometimes required. IR Raman spectra, including the near- and far-IR sub-branches (NIR and FIR), were developed in the early 1960s and were the most used non-visible excited Raman spectra, due to their avoidance of disturbance of Raman spectra by visible fluorescence in the case of luminescent molecules and biological samples with fluorescent markers. Figure 4.1 shows the Raman spectra of chocolate acquired with laser excitation at the wavelengths of 1065 and 785 nm, demonstrating that there is no fluorescence appearing in its NIR 1065 nm excited spectrum. UV excitation is also widely used for semiconductors with a high electronic gap and in some biological samples. The UV excited Raman spectra are more sensitive at the surface area of a sample because the penetration depth of UV light in matter is shallower. Li *et al.* [2] reported that observed UV Raman spectra clearly showed that the phase transition initially took place at the surface regions during phase transition of ZrO<sub>2</sub> from the tetragonal phase to the monoclinic phase as calcinations temperatures elevated, as shown in Figure 4.2.

#### 4.2 Resonant Raman Spectroscopy (RRS) [3]

The frequencies of vibrations in molecules and solids (i.e., phonons in crystal lattices) are in the frequency range from  $3 \times 10^{12}$  to  $3 \times 10^{13}$  Hz, respectively and the frequencies of

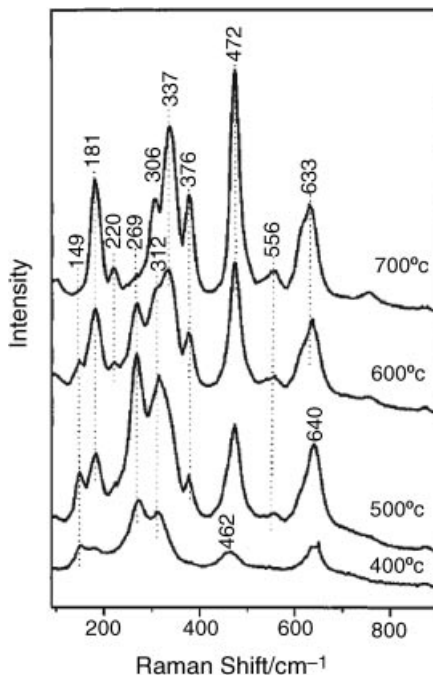


**Figure 4.2** UV Raman spectra of unpressed powder  $\text{Zr}(\text{OH})_4$  calcined at 400, 500, and 700 °C [2]. Reprinted from M. Li, Z. Feng, G. Xiong, et al., Phase transformation in the surface region of zirconia detected by UV Raman spectroscopy, *J. Phys. Chem. B*, 105, 8107 (2001) with permission of the American Chemical Society

visible light is about  $6 \times 10^{14}$  Hz, therefore the visible light cannot directly excite the vibrations in crystals and molecules but can only excite their electrons. In conventional Raman scattering processes, as mentioned in Section 2.4.1 and described in Figure 2.11, the electronic transition induced by the incident laser is a virtual one whose momentum in transition processes is not conserved, resulting in the scattering efficiency being very low. Once the energy of the incident laser is adjusted to match the energy that is required for a real electronic transition of the molecule or crystal, the so-called resonant Raman scattering (RRS) occurs. Because the energy of the electron transition differs from one material to another, the RRS was not widely used in the past. After 1970, the laser technology with a tunable wavelength and a narrow line width was gradually developed, and the RRS has evolved into an important branch of Raman spectroscopy.

The RRS usually implies the resonance of incident light with a real rather than a virtual electron energy level of materials. Since the width of electron energy levels is widened, RRS can be achieved using lasers with a certain wavelength range around the electron energy level; as a result, the RRS is divided into in-, at-, or near- resonance.

#### 4.2.1 Advantage, Shortage and Application of RRS

The main advantage of the RRS over traditional Raman spectroscopy is the high scattering efficiency, which is usually  $10^6$  fold of conventional Raman scattering. Therefore, the original weak Raman scattering can possibly be observed in an RRS experiment.

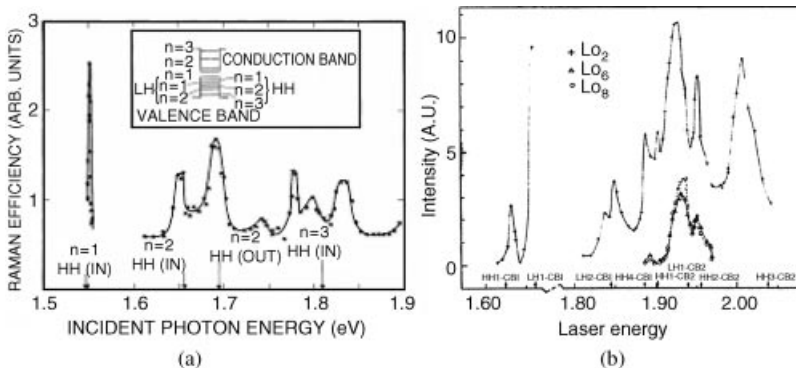


**Figure 4.3** Profile of resonant Raman spectra to figure out the electronic energy structures [4,5]. (a) Reprinted from J. E. Zucker, A. Pinczuk, D. S. Chemla, et al., Raman scattering resonant with quasi-two-dimensional excitons in semiconductor quantum wells, *Phys. Rev. Lett.*, 51, 1293 (1983) with permission of the American Physical Society. (b) Reprinted from S.-L. Zhang, T. A. Gant, M. Delaney, et al., Resonant behaviour of GaAs LO phonons in a GaAs-AlAs superlattice, *Chn. Phys. Lett.*, 5, 113 (1988)

Since the RRS is associated with the electronic energy transition, another advantage is that it can selectively excite objects with various electronic energy levels, that is, RSS processes the advantage of selective excitation in samples. The main disadvantages of RRS are the increase of fluorescence background due to the real electron transition and photodegradation of samples due to the increased energy of incident laser light.

The important development for RRS application is to take advantage of selective excitation. For example, the biomolecules containing chromophores have the charge-transfer transitions of the metal complex that can enhance metal-legend stretching modes, as well as some of modes that are associated with the legends. Therefore, a Raman spectral study on such biomolecules such as hemoglobin can provide structural information about the local state of the chromophores.

If the electronic energy structure is well defined, its electronic energy structure can be extracted by the profile of the RRS, despite the spectra only being generated from electron vibrations. Small-sized materials with size confined effects, such as superlattices and nanomaterials are such examples. Figure 4.3 shows two examples, in which the electronic energy levels of superlattices are worked out from their RRS profiles [4,5].

It is well known that the electronic energy level of nanomaterials is well defined and dependent of sample size, thus RRS can be selectively excite certain sizes of such particles. This has been applied in many nanomaterials, such as carbon-nanotubes [6] and Si nanowires [7], and so is called resonant size-selection Raman scattering.

#### 4.2.2 Incoming and Outgoing Resonances

In RRS, if the energy of the incident laser is adjusted to make either the incident light or the scattered light match the energy required for an electronic transition of the molecule or crystal, the former and latter are called in-coming and out-going resonances, respectively. However, in most materials, the incoming and outgoing electronic resonances are sufficiently broad that they cannot be distinguished.

### 4.2.3 Double Resonant Raman Scattering (DRRS) [8]

The double resonant Raman scattering (DRRS) is closely related to incoming and outgoing resonances. In DRRS processes, in addition to these resonances, the elementary excitation makes a real transition. DRRSs are much stronger than single resonances. They are, however, only observed under very specific experimental conditions: The energetic difference between two electronic bands needs to equal a phonon energy, which makes the DRRS realized for distinct excitation energies.

Figure 4.4 depicts a one-dimensional model of DRRS, where two linear bands with different Fermi velocities  $V_1$  and  $V_2$  crossing at the Fermi level. Even though such electronic dispersion is rare, a double resonant transition event can happen through a wide variety of excitation energies in addition to single resonances. The first step of a double resonant transition event for the particular incident laser energy  $E_1$  is to create an electron-hole pair at the  $k$  point matching the energy difference between the conduction and the valence band ( $i \rightarrow a$ ). It is obvious for a monotonically increasing phonon dispersion  $\omega_{\text{ph}}(q)$  that there is a  $(\omega_{\text{ph}}, q)$  combination, which can scatter the electron to a state in the second band ( $a \rightarrow b$ ). This is the phonon, in which double resonant transition occurs. Once the electron is elastically scattered back by the lattice defects ( $b \rightarrow c$ ), it recombines and conserves  $k$  in the process ( $c \rightarrow i$ ). For a larger incoming photon energy, a larger phonon quasi-momentum is required for this transition and hence a different phonon energy, if the phonon band is dispersive. The DRRS also occurs when two phonons are emitted at twice the amount of energy where quasi-momentum is conserved by equal and opposite  $q$  of the two emitted phonons, that is, it is not defect-induced.

The DRRS was only observed under specific experimental conditions: the energetic difference between two electronic orbits is or can be adjusted to the phonon energy by

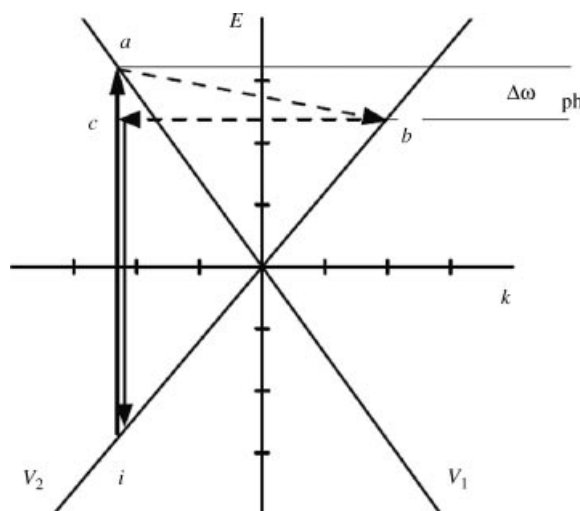


**Figure 4.4** Raman double resonance in one dimension for linearly dispersive bands with Fermi velocities  $V_1$  and  $V_2$  [8]. Reprinted from C. Thomsen and S. Reich, Double Resonant Raman Scattering in Graphite, *Phys Rev Lett*, 85, 5214 (2000) with permission of the American Physical Society

choosing the correct parameters of materials or by applying electric or magnetic fields, uniaxial stress, and so on [9–12], suggesting that DRRS conditions can only be achieved for distinct excitation energies.

In 2002, R. Saito *et al.* [13] confirmed that the above model, as suggested in [8], could be further extended to other phonon branches for predicting other dispersive phonon modes in graphite and identifying other dispersive phonon modes that have been previously observed in Resonance Raman experiments of  $sp_2$  carbons. Recently, Zhenhua Ni *et al.* [14] reported an experimental observation of an abnormally strong  $G$  band resonance, confirming that the normal  $G$  band was a double resonant event with the right laser energy for the particular stacking geometry of graphite layers.

### 4.3 High-Order/Multiple-Phonon Raman Spectroscopy (MPRS)

Two terminologies of high-order Raman scattering and multiple-phonon Raman scattering (MPRS) are described as the same physical event, in which merely the introduction of the described models is different.

In 1966, MPRS was invented based on the observation of RRS. Figures 4.5a and b show the MP Raman spectra of CdS [15,16].

One feature of MPRS spectra is that it is usually observed with RRS, resulting in Raman peaks of the multiple-phonon often overlapping the photoluminescence peak, which can be clearly seen in Figure 4.5b. Another feature of MPRS spectra is that it displays similar spectral features to hot luminescence (HL).

#### 4.3.1 Polarizability Model and High-Order Raman Scattering

In Chapter 2, it is described that light scattering originates from the radiation of electric dipole moment  $\mathbf{P}$  induced by incident light  $\mathbf{E}$ . The relationship between  $\mathbf{P}$  and  $\mathbf{E}$  has a linear relationship under weak  $\mathbf{E}$  and can be expressed by Equation (2.26), that is

$$\mathbf{P} = \alpha \cdot \mathbf{E}$$

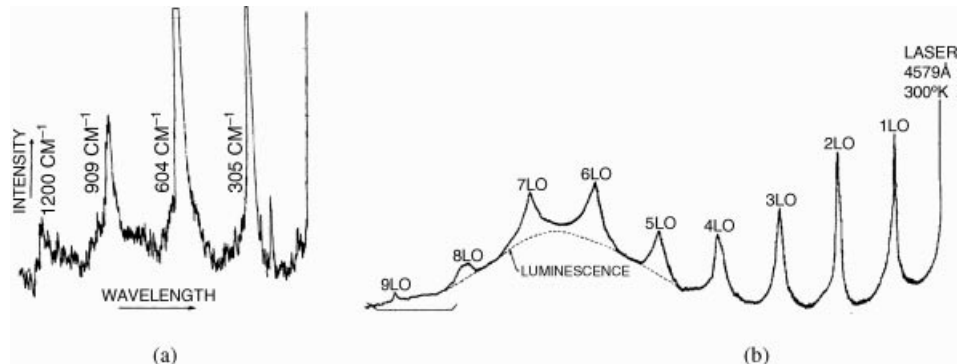


**Figure 4.5** Resonant MP Raman spectra of CdS (a) [15]. Reprinted from R. C. C. Leite and S. P. S. Porto, Enhancement of Raman Cross Section in CdS due to Resonant Absorption, *Phys. Rev. Lett.*, 17, 10 (1966) with permission of the American Physical Society and (b) [16]. Reprinted from R. C. C. Leite, J. F. Scott and T. C. Damen, Multiple-Phonon Resonant Raman Scattering in CdS, *Phys. Rev. Lett.*, 22, 780 (1969) with permission of the American Physical Society

In the above Equation,  $\alpha$  is polarizability, which reflects the property of the medium itself. The  $\alpha$  is the function of nuclear coordinate  $r$  of atoms and can be expressed as the Taylor expansion in normal coordinate  $Q$ . The corresponding component  $\alpha_{ij}$  of  $\alpha$  expanded to the second order can be expressed as

$$\begin{aligned}\alpha_{ij} = & (\alpha_{ij})_0 + \sum_k \left( \frac{\partial \alpha_{ij}}{\partial Q_k} \right)_0 Q_k + \frac{1}{2} \sum_{k,l} \left( \frac{\partial^2 \alpha_{ij}}{\partial Q_k \partial Q_l} \right)_0 Q_k Q_l \\ & + \left( \frac{\partial^3 \alpha_{ij}}{\partial Q_k \partial Q_l \partial Q_m} \right)_0 Q_k Q_l Q_m + \dots\end{aligned}\quad (4.1)$$

$Q_k$ ,  $Q_l$ , and  $Q_m$  are normal coordinates of the vibration modes with frequency of  $\omega_k$ ,  $\omega_l$ , and  $\omega_m$ , respectively, and the sum is extended to all the normal coordinates; the symbol  $(\alpha_{ij})_0$  depicts the value at the equilibrium position. The Raman scatterings related to the items of the first, second, and third orders of normal coordinate  $Q$  in the above expansion are the first, second, and third orders of Raman scatterings and correspond to the single, double, and three phonon Raman scatterings, respectively.

It is well known that the scattered intensity is related to the electronic polarizability tensor. While the Taylor expansive coefficients of polarizability,  $(\partial \alpha_{ij}/\partial Q_k)_0$ ,  $(\partial^2 \alpha_{ij}/\partial Q_k \partial Q_l)_0$  and  $(\partial^3 \alpha_{ij}/\partial Q_k \partial Q_l \partial Q_m)_0$  ..., inversely decrease with expansive order, which is one of the reasons why MP Raman spectrum was observed in resonant scattering and was usually overlapped by photoluminescence peaks.

### 4.3.2 Lattice Relaxation Model and MPRS

Raman scattering involves the molecular vibration or the elementary excitation in solids such as phonons and so on. The single phonon (SP) Raman scattering is such a process, in which a single phonon is involved, while higher order Raman scattering includes more than one phonon. This is the reason why higher order Raman scattering is also named multiple phonon (MP) scattering.

In lattice dynamics, the occurrence of MPRS is considered due to lattice relaxation [17]. One important aspect of lattice relaxation is that the electron transition can be accompanied by the simultaneous emission or absorption of a number of phonons. Such a transition is either a radiate or non-radiate electronic transition and involves the processes of MP Raman scattering and HL radiation. The energy levels and optical processes of SP- and MP-scattering, as well as HL, are shown in Figures 4.6a–c, respectively.

### 4.3.3 MPRS and Hot Luminescence

MPRS and HL display similar spectral features, although their optical processes are different, as shown in Figure 4.6.

For phonon Raman scattering, if the duration of an intermediate virtual state in the resonant or near-resonant electron transition is larger than the period of lattice vibrations, the lattice relaxation results in MP Raman scattering. Therefore, the MPRS is an instantaneous two-photon direct process and HL is a two-step process depending on the relaxation of the excess population in the intermediate states, and they can be distinguished by using the transient time spectra [18]. Otherwise, since MPRS can be viewed as a one-step coherent

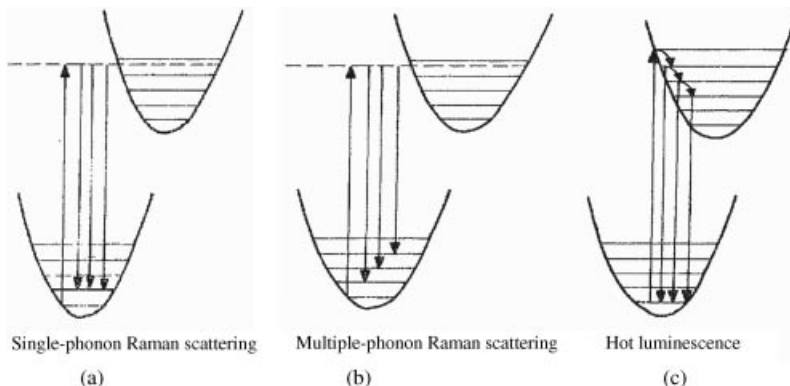


**Figure 4.6** Representation of the energy levels and optical processes of SPRS (a), MPRS (b), and HL (c). The lower and upper parabolas represent a ground and excited electronic state, respectively, where the solid and dashed lines denote the phonon and virtual electron transition states, respectively. The straight and curved arrows represent the absorption and emission of light and non-radiated transition of an electron, respectively

process, the spectrum is precisely correlated with the incident light in terms of the energy and polarization [19]. Accordingly, Zhang *et al.* [20] successfully distinguished MPRS and HL for observed overtone spectrum of a  $(\text{CdTe})_2(\text{ZnTe})_4/\text{ZnTe}$  short-period-superlattice multiple quantum, shown in Figure 4.7. Table 4.1 lists the depolarization ratios and frequencies of the multi-phonon of  $(\text{CdTe})_2(\text{ZnTe})_4/\text{ZnTe}$  short-period-superlattice multiple quantum well. Table 4.1 shows that the polarization memory is not lost and the highest order still remain polarized. Moreover, the overtone frequencies are a strict integer multiple of the first-order one. Therefore, the spectrum can only be viewed from the coherent scattering of Raman process and excludes the possibility of the overlap from HL [20].

#### 4.3.4 Two-Phonon Raman Scattering

In the SP Raman scattering process, the phonon is either created or destroyed. While in the MP Raman scattering process, the creation and destruction of phonons are complicated.

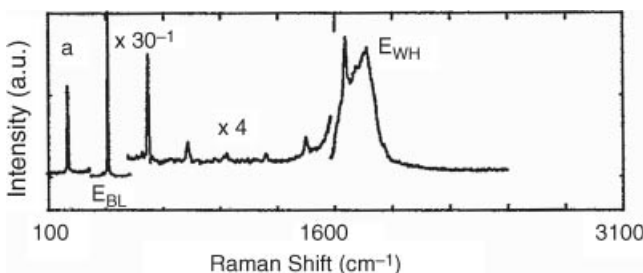


**Figure 4.7** The observed overtone spectrum of  $(\text{CdTe})_2(\text{ZnTe})_4/\text{ZnTe}$  short-period-superlattices multiple quantum well [20]. Reprinted from S. L. Zhang, *et al.*, Multiphonon Raman Scattering Resonant with two kinds of excitons in a  $(\text{CdTe})_2(\text{ZnTe})_4/\text{ZnTe}$  short-period-superlattice multiple quantum well, *Phys. Rev. B*, 47, 12937 (1993)

**Table 4.1** Depolarization ratios ( $I_{dp}$ ) and frequencies of multi-phonon of  $(CdTe)_2(ZnTe)_4/ZnTe$  short-period-superlattices multiple quantum well [20]. Reprinted from S. L. Zhang, et al., Multiphonon Raman Scattering Resonant with two kinds of excitons in a  $(CdTe)_2(ZnTe)_4/ZnTe$  Short-Period-superlattice multiple quantum well, Phys. Rev. B47, 12937 (1993)

$E_{in}$ (eV)	1 LO	2 LO	3 LO	4 LO	5 LO	6 LO	7 LO	8 LO	
2.41	$\omega$	209.5	420	630	836	(1040)	1244	1454	1658
	$I_{dp}$	2.5	1.7	1.6	2	1.6	2	2	1.5

Thus, in the MPRS study, two-phonon Raman scattering has been widely studied and has provided a better understanding of the MPRS mechanism. In this section we discuss two-phonon Raman scattering.

For two-phonon scattering, two phonons are both created (giving a Stokes component in the scattered light), one is created and the other is destroyed (giving a Stokes or anti-Stokes component), or both photons are destroyed (giving an anti-Stokes component). These results in two distinct types of second-order Raman spectra and they give rise to a line spectrum and a continuous spectrum, respectively [21].

#### 4.3.4.1 Two-Phonon Line Spectrum

The double phonon line spectrum is generated by the process in which light has undergone two successive SP Raman scatterings, as shown in Figure 4.8a.

The two-phonon line spectrum is due to processes in which light has undergone Raman scattering from two created phonons with frequencies  $\omega_0$  and  $\omega'_0$ , as shown in Figure 4.8a. It is essential that SP Raman scattering is independent for two phonons, and the frequency shifts occur in the two-phonon line spectrum as the sum and the difference of the shifts occurs in the SP spectrum. It is not necessary for the intermediate state shown in Figure 4.8a to conserve the

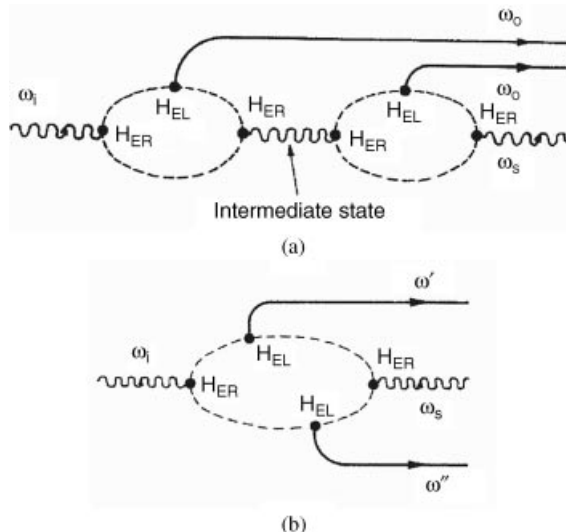


**Figure 4.8** Scattering processes for the two-photon line spectrum (a) and continuous spectrum (b)

energy. However, the total wave vector in this state must be the same as the one in the initial state. This conservation law forces the wave vector of the first phonon ( $\omega_0$ ) to be small and leads to the line nature of the resulting Raman spectrum. Since the process depends on two successive Raman scattering events, which must both take place within the crystal volume, the scattering efficiency for the two-phonon line spectrum increases when the crystal size increases.

#### 4.3.4.2 Two-Phonon Continuous Spectrum

The double-phonon continuous spectrum is a scattering process in which the light interacts with a pair of phonons in a single event, as shown in Figure 4.8b. We focus on the case where both photons are created. There is no restriction on the photon wave vectors, other than the requirement that their sum should equal to the change in wave vector of the scattered photon and the phonon wave vectors can range over the entire Brillouin zone. Since the photon wave vectors are negligible compared to the Brillouin zone dimensions, the wave vector conservation in this case requires that the wave vectors of the two phonons should be equal and opposite. The continuous frequency distribution displayed by the scattered photons is thus proportional to a weighted density of lattice states, in which two phonons of equal and opposite wave vector are present. The weighing is due to the frequency and wave vector dependence of the interactions that are involved in the scattering process. The second-order continuous spectrum is generated from a single scattering event and the scattering efficiency is therefore independent of the crystal size, as that in the SP. The Raman effect leads to an experimental solution for resolving the two-phonon line and continuous spectra in cases where the continuum has sharp features or where the lines are broad.

#### 4.3.4.3 Two-Phonon Raman Spectrum and Phonon Density of State (PDOS)

In two-phonon Raman scattering, any spectral structure must reflect the frequency dependency of the combined density of states of phonon pairs with equal and opposite wave vectors, or the frequency dependence of the interaction that gives rise to the transition.

If only a part of the two-phonon Raman spectrum is investigated, in which two phonons are created with  $\omega(\mathbf{q}) = \omega(-\mathbf{q})$ , the relevant phonon density of states is obtained from the phonon dispersion curves constructed by adding all pairs of phonon branches together at each wave vector  $\mathbf{q}$ . At each  $\mathbf{q}$  on the two-phonon dispersion curves, the total wave vector of the two-phonon states is effectively zero and every state is Raman active as far as the wave vector conservation rule is concerned, suggesting that two-phonon Raman scattering in crystals is no longer constricted by the wave vector selection rule  $q = 0$  and thus it can happen at any value of  $q$ . This results in a reduced Raman spectra, defined as the observed Raman spectrum divided by the factor  $(n_B + 1)^2$  (where  $n_B$  is the Bose-Einstein occupation factor), being a reflection of the phonon density of states (PDOS). Figure 4.9 shows the comparison between the measured two-phonon reduced Raman spectrum and PDOS for Ge [22].

### 4.4 Raman Spectroscopy under Extreme Conditions

In traditional Raman spectroscopy, the samples can only be measured in an atmospheric environment. However, modern Raman spectral experiments are not constrained to the atmospheric environment, such as normal temperature, pressure, and other external conditions. The Raman spectra can be easily acquired from the samples under conditions of high temperature, high pressure, external electrical field, and magnetic field and so on.

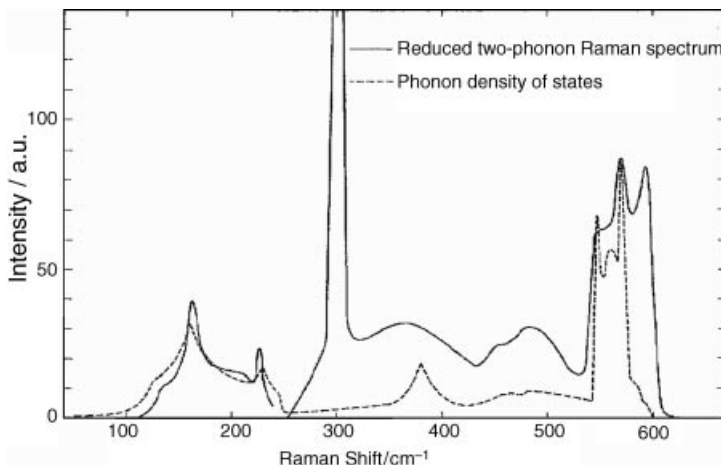


**Figure 4.9** Comparison between the measured reduced two-phonon Raman spectrum and calculated phonon density of states for Ge [22]. Reprinted from B.A. Weinstein and M. Cardona, Second-Order Raman Spectrum of Germanium, *Phys. Rev. B*, 7, 2545 (1973) with permission of the American Physical Society

Thus, many new types of Raman spectroscopy branches have been created, such as high temperature-, high pressure-, external electrical field-, and strong magnetic field- Raman spectroscopy. All these types of Raman spectroscopy branches are formally grouped as “extra-condition Raman spectroscopy.”

The change in the sample’s testing environment helps to expand Raman spectroscopy to more research and industrial fields. For example, measuring the Raman spectra dynamically as a function of temperature and pressure has been applied successfully *in situ* for the investigations of dehydration, solid state phase transformation, and composition changes. Figure 4.10 shows the Raman spectra of ZrO<sub>2</sub> measured under temperatures ranging from room temperature to 2023 K. Based on the change of Raman spectra with changing temperature, the author found that ZrO<sub>2</sub> were converted from monoclinic crystals to tetragonal crystals at approximately 1440 K [23].

For the pressure Raman spectra, Fredéric Decremps *et al.* [24] measured the pressure dependence of the zone-center phonons ( $E_2$ ,  $A_1$ , and  $E_1$ ) for the wurtzite structure ZnO as shown in Figure 4.11, which shows that around 8.7 GPa, the disappearance of all Raman peaks reflects the onset of the wurtzite-rocksalt structural transformation in excellent agreement with the previous high-pressure studies.

## 4.5 Polarized Raman Spectroscopy (PRS)

In Section 1.2, we briefly mentioned that Raman scattered light is essentially polarized, so that the polarized spectra in Raman spectroscopy play an important role. The occurrence and intensity of spectral lines vary with the change of polarization of the incident laser and the measured scattered light. Section 1.2 also mentioned that the features of polarized Raman spectra are closely related to the space symmetry of scattered objects and vibration modes, which are represented by so-called Raman tensors listed in Appendix III. Based on group

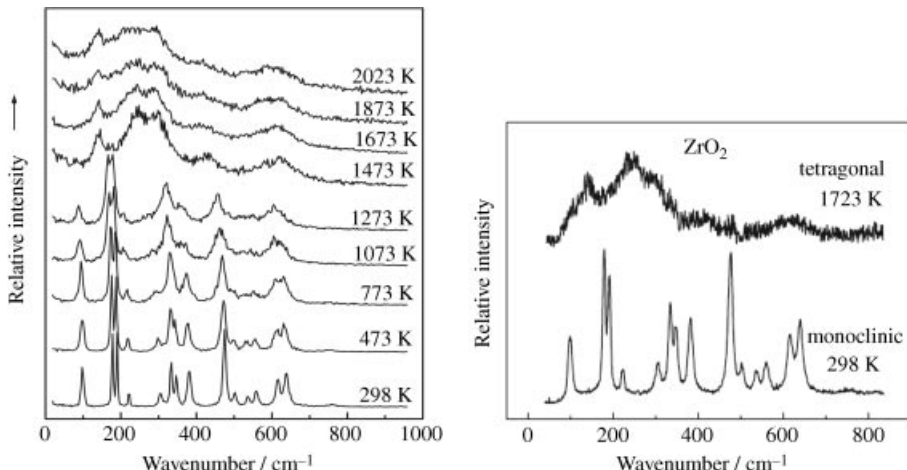


**Figure 4.10** Raman spectra of  $\text{ZrO}_2$  measured under temperatures ranging from room temperature to 2023 K [23]. Reprinted from J.-L. You, et al, Temperature Dependence of the Raman Spectra and Phase Transition of Zirconia, *Chin.Phys.Lett*, 18, 991 (2001) with permission of the Chinese Physical Society

theory analysis and Raman tensors, the polarized features of Raman spectra can provide information on the measured object regarding the spatial symmetry and the Raman modes of the object, by using physical quantities such as the polarized selection rule, depolarization degree, and Raman optical activity (ROA) and so on, as described in Section 3.1. Such information leads to a better understanding of molecular shapes, crystal structures, and the macromolecular orientation in crystal lattices and so on. Because the laser is an excellent polarized light source, the measurement of polarized Raman spectra using the laser as the light source has become popular and in recent years, polarized Raman spectroscopy has turned into an important branch of modern Raman spectroscopy.

## 4.6 Time-Resolved (Transient) Raman Spectroscopy (TRRS)

Time-resolved Raman spectroscopy (TRRS) is a basic branch of modern Raman spectroscopy. The TRRS can be used to study the dynamic processes in materials or chemical compounds. In principle, the TRRS can be used to study any process in which the properties naturally change in a material or after certain excitation such as light illumination. Recently, TRRS has developed various means, such as time-resolved anti-Stokes Raman spectroscopy, which allows direct monitoring of vibration relaxation dynamics as it only probes the vibrating excited molecules [25].

### 4.6.1 Technology of TRRS [26]

The development and application of TRRS mainly relies on the advancement of two technologies: pulse light source and fast signal detection. The light source bottleneck was resolved when the short pulse laser with narrow line width was invented. Traditionally, the

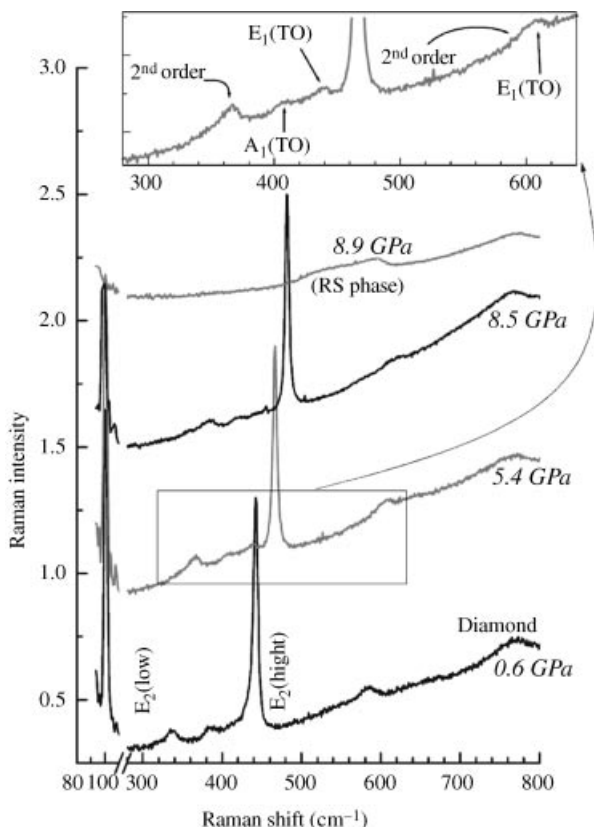


**Figure 4.11** Raman spectra of single-crystalline ZnO under different hydrostatic pressures in the backscattering geometry. The spectra are shifted upward for clarity [24]. Fig 1 in F. Decremps, J. Pellicer-Porres, A.M. Saitta, et al, High-pressure Raman spectroscopy study of wurtzite ZnO, Phys. Rev. B, 65, 092101 (2002) with permission of the American Physical Society

excitation light source was a picosecond, cavity dumped dye laser synchronously pumped by a mode-locked argon ion or Nd:YAG laser. In recent years, dye laser technology has been superseded by solid-state lasers, Ti:sapphire in particular. Even though the specialized photodetector, such as streak cameras or avalanche photodiodes, can detect picoseconds or even femtoseconds transients in real-time, alternative detection techniques are still needed for extremely high speed. Among such techniques, the pump-probe techniques based on the auto- or cross-correlation of two beams of femtosecond pulses are most promising and widely used. If the “sample” is a nonlinear crystal used for sum-frequency generation, this technique can determine the shape and relative arrival time of two short pulses. Figure 4.12 shows a typical pump-probe arrangement of a Raman spectra set-up by Hochstrasser group [26]. In Figure 4.12, a moderately high repetition rate Nd:YAG laser was used. The laser consists of an oscillator amplifier design, which provides a versatile source of both pump and probe radiation. The oscillators and amplifiers run at rep rates up to 20 Hz. A pulse from the oscillator train is isolated by a Pockels cell before being amplified three times.

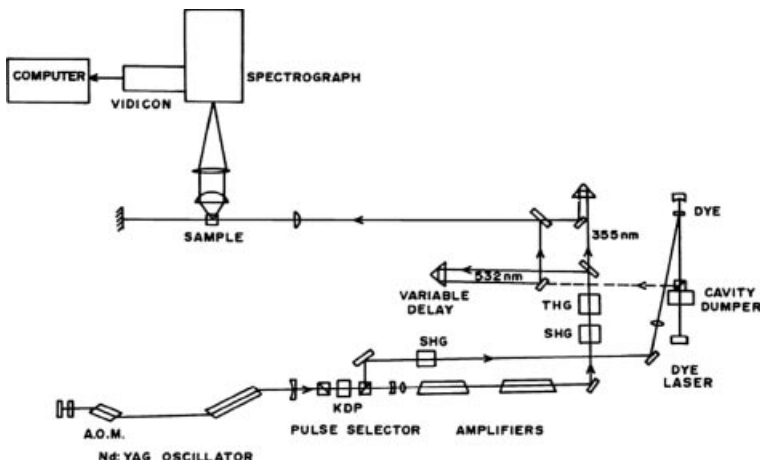


**Figure 4.12** Picosecond time-resolved Raman spectrometer. The passively and actively (by an acousto-optic modulator) mode-locked oscillator produces pulse trains from which single pulses are selected, expanded, and amplified. The rejected pulse trains can be used to pump a dye laser. Harmonics of the Nd:YAG laser are generated at 532 nm and 355 nm. The 532 nm pulse is delayed with respect to the 355 nm and probes in the sample region are excited by the 355 nm pulse. Raman scattering is collected, dispersed, and imaged on a cooled SIT vidicon. Data is transferred to a microcomputer for processing [26]. Reprinted from C.K. Johnson, G.A. Dalickas, S.A. Payne, et al., Picosecond timescale Raman processes and Spectroscopy, Pure and Appl. Chem., 57, 195 (1985) with permission of International Union of Pure and Applied Chemistry

#### 4.6.2 Development and Application of the TRRS

During the last three decades, the TRRS has evolved to study the processes that occur on a time scale as short as  $10^{-14}$  seconds and provides a reliable basis for elucidating the elementary physical and chemical processes taking place at the molecular level of biological systems [27,28]. For example, Matousek and Stone [29] reported an application of TRRS for the diagnosis of breast calcifications by detecting and identifying the chemical composition of calcified material within a clinically relevant depth of 16-mm-thick chicken tissue, demonstrating that the TRRS has great potential for advancing the diagnosis of human breast cancer *in vivo* in conjunction with traditional techniques, such as mammography or ultrasound techniques.

#### 4.7 Space-Resolved Micro-Raman Spectroscopy and Raman Microscopy [30,31]

When the spectroscope is used in the optical path of Raman spectrometers, the sampling point becomes very small. Therefore, the sampling point of the measured Raman spectra can be spatially resolved, leading to so-called space-resolved Raman spectroscopy. Since the sampling point can be located and moved precisely with monitoring by the CCD during the measuring process, the operational mode of the Raman spectroscopy is significantly changed from the recording of the variation of Raman spectral intensity with frequency

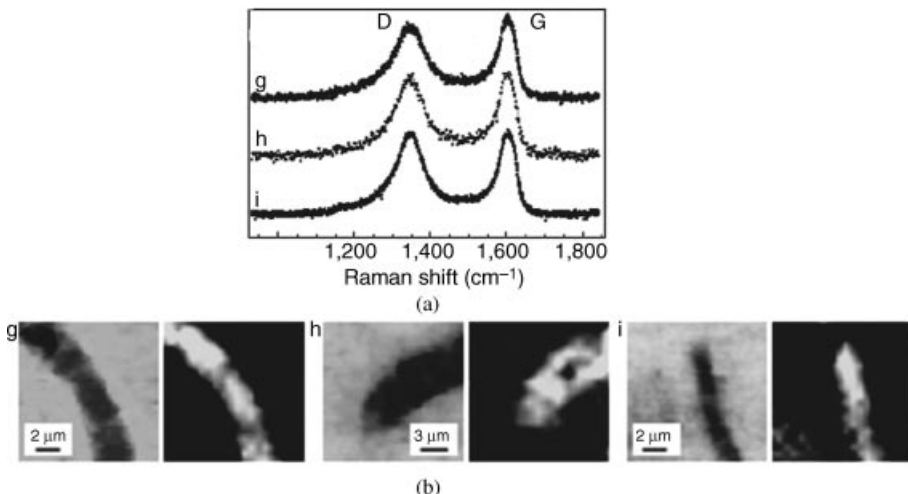


**Figure 4.13** (a) Raman spectra of the microbes in regions g, h, and i in a fossil sample (b) Raman microscopic image used the Raman G line (left) and optical microscopic images (right) of the microbes [32]. Reprinted from J. W. Schopf, A. B. Kudryavtsev, D. G. Agresti, et al., *Laser-Raman imagery of Earth's earliest fossils*, *Nature*, 416, 73 (2002) with permission of Nature Publishing Ltd

(i.e., frequency spectrum) to the recording of the intensity change of the Raman spectral line at a fixed frequency with spacial points (i.e., spectral line imaging or photography). To emphasize the function of imaging and photographing of the space-resolved Raman spectroscopy, a new technical word “Raman spectroscope” was introduced.

In Raman spectroscope, the Raman image results from using the Raman scattering light as the image or photographic light source. If the characterized Raman line of objects is chosen as the light source, the resulting image processes the selective nature of objects and can be used to identify and distinguish different materials and structures, which is a rare characteristic in other imaging technology. One of such examples is shown in Figure 4.13, where Schopf *et al.* [32] used Raman imaging to identify the microbes in regions g, h, and i of a fossil sample. The Raman characteristic G line at about  $1600\text{ cm}^{-1}$  of carbon in these regions was used to form a selective image with micrometer scale. This study has pushed the estimated time of origin of life ahead by  $7.7 \sim 35$  billion years. Furthermore, any Raman scattering light can be the light source in Raman spectrometers. For example, the light from the coherent anti-Stokes Raman scattering (CARS) and stimulated Raman scattering (SRS) have been used as light sources of Raman spectrometers. These Raman spectrometers possess some new features, due to the introduction of new types of Raman scattering light, which we will describe in the following related sections.

#### 4.8 Surface-Enhanced Raman Spectroscopy (SERS)

In 1974, with the development of sample preparation methods, for example, a monolayer of pyridine adsorbed on an electrochemically roughened silver electrode, Fleischmann and coworkers reported an unexpectedly strong Raman signal with an enhancement of  $10^6$  fold compared with the signal from pyridine molecules in the absence of metal substrate [33].

This newly discovered spectrum was named surface-enhanced Raman scattering (SERS). Shortly after, the Van Duyne group made an important contribution to SERS [34]. In fact, the SERS has achieved a genuine enhancement of a Raman signal level of up to  $10^{14}$  orders of magnitude, even at the single-molecule level. Because of this high sensitivity, SERS has pushed Raman spectroscopy to the single live cell and bio-molecule level.

However, the heterogeneity of metallic SERS substrates creates variability of electromagnetic field enhancement across the surface, forming the so-called “hot spots.” These hot spots limit the utility of the SERS technique and render quantitative measurements unreliable. Moreover, because the regular SERS is still in the far-field spectra, it is impossible to produce the spectra with nanoscale spatial resolution. The above shortcomings have been largely overcome by the development of the tip-enhancement Raman spectra.

#### 4.8.1 Sample Substrates in SERS

In SERS, the sample substrate is critical. At the beginning of SERS development, only Ag, Au, and Cu were used as sample substrates. Nowadays, a range of diverse metals and alloys are routinely selected as the sample substrates [35–42]. Furthermore, the sample substrate can be molded into the order nanostructures. Figure 4.14 exhibits an order nanoparticle array substrate of platinum fabricated by the E-beam technique, of which the particles are 40 nm in diameter and are spaced 150 nm apart [43]. Figure 4.15 shows the SERS spectra of pyridine adsorbed on different metal nanowires with the solution of 0.01 M KCl + 0.01 M Py.

#### 4.8.2 Enhancement Mechanism of SERS

When SERS was discovered, Fleischmann *et al.* proposed the theoretical explanation that the signal enhancement of spectra is due to a large number of molecules from the increased

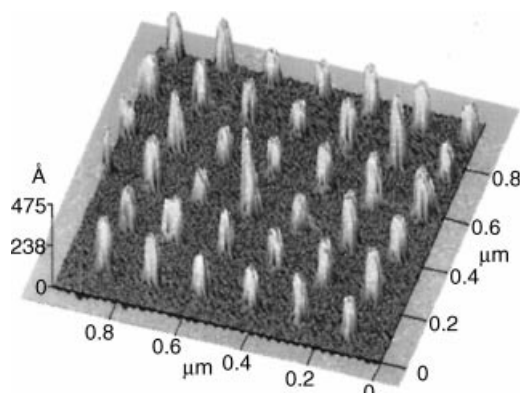


**Figure 4.14** (a) Raman spectra of pure pyridine, pyridine solution, and pyridine adsorbed on noble metal and transition metal surfaces at open circuit potentials and (b) the dependence of the frequencies of the  $v_1$  vibration of selected metal on the electrode potential (\*) The band at  $932\text{ cm}^{-1}$  is the total symmetric stretching vibration of  $\text{ClO}_4^-$  in the bulk solution. The exciting wavelength is  $632.8\text{ nm}$  [44]. Fig 1 in N. Félidj, J. Aubard, G. Lévi, et al., Controlling the optical response of regular arrays of gold particles for surface-enhanced Raman scattering, *Phys. Rev. B*, 65, (2002) with permission of the American Physical Society

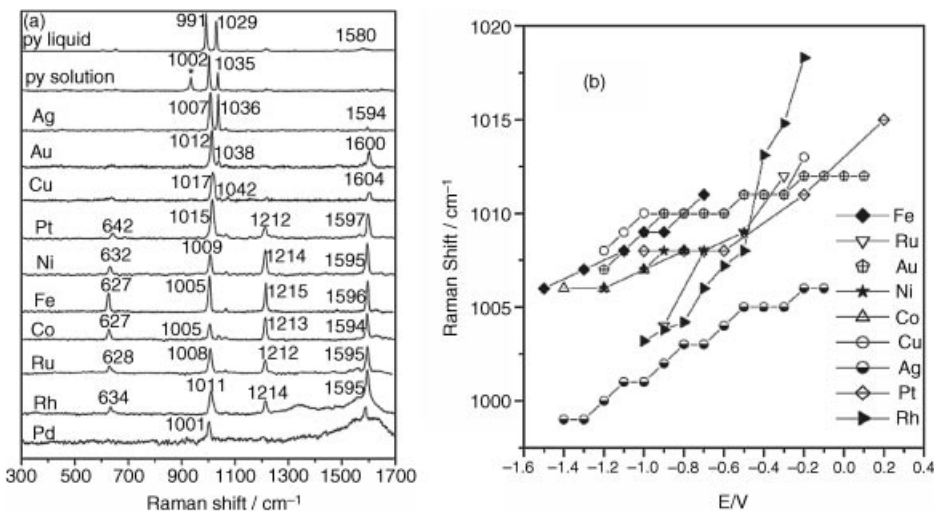


**Figure 4.15** (a) Raman spectra of pure pyridine, pyridine solution, and pyridine absorbed on noble metal and transition metal surfaces at open circuit potentials, and (b) the dependence of the frequencies of the  $v_1$  of selected metals on the electrode potential. (\*) The band at  $932\text{ cm}^{-1}$  is the total symmetric stretching vibration of  $\text{ClO}_4^-$  in bulk solution. The exciting wavelength is  $632.8\text{ nm}$  [44]. Reprinted from Z.-Q. Tian, B. Ren, and D.-Y. Wu, Surface-Enhanced Raman Scattering: From Noble to Transition Metals and from Rough Surfaces to Ordered Nanostructures. *J. Phys. Chem. B*, **106**, 9463 (2002) with permission of the American Chemical Society

surface area on the rough electrode. In 1977, Van Duyne and Creighton found that the enhanced signal in SERS was so strong that it could not be explained by an increase in surface area alone [34]. Since then, the mechanism of SERS has been subject to much debate and several different interpretations have been proposed. At present, it is generally accepted that the enhancement is the product of two mechanisms of electromagnetism (EM) and chemical transfer (CT).

The EM mechanism is determined by many effects, such as surface plasmon resonance, image field effect, lighting rod effect, particle coupling effect, and fractal structures. The CT mechanism is determined by effects, such as metal-to-molecule, molecule-to-metal, potential effect, coverage effect, and substrate effect. Kneipp *et al.* [44] have given a detailed description of the SERS-enhancement mechanism. Although SERS is still the far-field spectra, the enhancement mechanism essentially involves the near-field optics and nanoscale optics. Due to these two nascent and non-traditional scientific fields, the enhance mechanism of SERS is not completely clear to date.

## 4.9 Near-Field Raman Spectroscopy (NFRS)

Section 3.2.2 showed that conventional optical lenses are used to illuminate the samples and the collection of scattered light from samples in traditional Raman spectrometers. Generally, the illumination and collection optics have to be placed at some distance from the sample, that is, in the far-field region away from the sample. Therefore, the observed Raman

spectra possess all the far-field properties, of which the spectral resolution has to be restricted by the diffraction limitation.

When the samples are illuminated and/or the spectral signals of samples are collected in near-field (NF), the diffraction limit of the resolution is no longer apparent. The first description of the NF optical microscope appeared in 1928 [45]. Since then, many attempts to create such a microscope have been attempted. Until 1984, the first NF optical microscope, that is, the scanning NF optical microscope (SNOM) was built. After this, in 1994, the first NF Raman spectrometer (NFRS) was built in [46].

### 4.9.1 NF Optics and Diffraction Limit

#### 4.9.1.1 Near Field

In Section 2.2.1, we used the electrical dipole model based on classical electrodynamics to discuss the electromagnetic wave in the far-field region where the distance of the observed point away from dipole,  $R$ , is much larger than the electromagnetic wavelength  $\lambda$  (i.e.,  $R \gg \lambda$ ). In this section, we still use the same model as in Section 2.2.1 to discuss the electromagnetic wave in the NF region of  $\lambda \ll R \gg d$ , where  $d$  is the size of dipole.

The complete expression of polar coordinates for an electromagnetic field is

$$\begin{aligned} E_R &= 2(p_0 \cos \theta / R^3)(1 + ikR) \exp(ikR) \\ E_\theta &= (p_0 \sin \theta / R^3)(1 + ikR - k^2 R^2) \exp(ikR) \\ E_\phi &= (p_0 \sin \theta / R^3)(ikR - k^2 R^2) \exp(ikR) \end{aligned} \quad (4.2)$$

where  $p_0$  is the oscillated amplitude of dipole;  $k = \omega/c$  stands for the amplitude of wave vector  $\mathbf{k}$  ( $\omega$  is frequency of electromagnetic wave and  $c$  is the light velocity); and  $\theta$  is the included angle between  $\mathbf{R}$  and  $\mathbf{P}$ . At  $R \gg \lambda$  and  $R \ll \lambda$ , Equation (4.2) can be approximated. At the far-field region of  $R \gg \lambda$  and  $d \ll \lambda$ , only the term with  $1/R$  should be taken into account, the resultant electromagnetic field is expressed as

$$\begin{aligned} E_R &= 0 \\ E_\theta &= B_\phi = (k^2 P_0 \sin \theta / R) \exp(ikR) \end{aligned} \quad (4.3)$$

In the NF region of  $\lambda \ll R \gg d$ , the electromagnetic field can be expressed approximately as

$$\begin{aligned} E_R &= 2 P_0 \cos \theta / R^3 \\ E_\theta &= P_0 \sin \theta / R^3 \\ B_\phi &= (ik) P_0 \sin \theta / R^2 \end{aligned} \quad (4.4)$$

From the above expressions, the features of an electromagnetic field in the far- and NF are very different.

#### 4.9.1.2 Intensity Feature with $R$

In the far-field, the intensity of a traveling wave decreases with  $1/R$  and is equivalent to zero at  $\theta = 0$  and  $2\pi$ , where  $\theta$  is the included angle between the propagation direction of the field and the orientation of the dipole. In the NF, the intensity of a traveling wave decreases rapidly with  $R^3$  and reaches the maximum value at  $\theta = 0$  and  $2\pi$ , which is opposite to that in the far-field. Based on intensity variation related to  $R$ , the far- and near- fields are called the propagating and evanescent fields, respectively.

#### 4.9.1.3 Intensity Feature Along with the Propagation Direction $r$

The magnetic field strength  $\mathbf{B}$  is not the transverse field in the far- and near-fields, while the electrical field  $\mathbf{E}$  is the transverse field in the far-field and the transverse and longitudinal in the near field.

#### 4.9.1.4 Radiated Power

The time averaged radiation power in unit solid angle  $d\Omega$ ,  $dP/d\Omega$ , can be written as:

$$dP/d\Omega = (c/3\pi) \operatorname{Re} [R^2 \mathbf{n} \cdot \mathbf{E} \times \mathbf{B}] \quad (4.5)$$

where “Re” represents the taking of real part and  $\mathbf{n}$  is the direction of wave vector  $\mathbf{k}$ , that is, the propagating direction of electromagnetic field. In the far-field:

$$dP/d\Omega = (c/3\pi)k^4 p_0^2 \sin \theta \quad (4.6)$$

The total radiation power with no relation to the phases of  $P_0$  components is

$$P = ck^4 P_0^2 / 3 \quad (4.7)$$

In the NF region, since  $\mathbf{B}$  has only an imaginary part, we have

$$dP/d\Omega = P = 0 \quad (4.8)$$

From the above description, it can be seen that the far field is the radiation field and NF is the non-radiation field. Therefore, the far- and near-fields are also called the radiation and non-radiation fields, respectively. Based on the above, we can see from the NF region that the electrical field  $\mathbf{E}$  is the quasi-electrostatic field and the magnetic strength  $\mathbf{B}$  is smaller than the electrical field  $\mathbf{E}$  with  $k(2\pi R/\lambda)$ . Therefore, the electromagnetic field in the NF region is mainly the quasi-state electrostatic field and at the dipole surface of  $R \approx d$  there is only a quasi-state electrostatic field. Figure 4.16 illustrates the spatial feature of an electrical field  $\mathbf{E}$ .

#### 4.9.1.5 Breakthrough of Diffraction Limit

It is well known that the resolution of an optical image system, such as the microscope, telescope, or camera, is restricted by the so-called diffraction limit rule. The diffraction limit  $d_{\text{dif}}$  of a microscope is expressed as

$$d_{\text{dif}} = 0.77 \lambda_0 / n \sin \theta \quad (4.9)$$

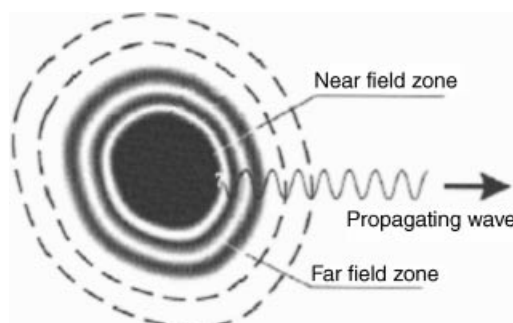


**Figure 4.16** Schematic representation of the spatial feature of electrical field  $\mathbf{E}$

where  $\lambda_0$  is the wavelength in a vacuum;  $n$  is the refractivity of the object space, that is, the space between lens and sample;  $\theta$  is the semi-aperture angle of the object in space; and  $n \sin\theta$  is called the numerical aperture (NA). Obviously, due to the restriction of the diffraction limit, the best resolution of optical image systems cannot exceed  $\lambda_0/2$ .

The optical wave field can be expressed as

$$\mathbf{E}(\mathbf{r}, t) = E_0(x, y, z) \exp [i(k_x x + k_y y + k_z z - \omega t)] \quad (4.10)$$

where  $\mathbf{r}$  and  $t$  are the spatial coordinate and time at the observed point, respectively, and  $E_0(x, y, z)$  is the amplitude of electrical field. The field described by Equation (4.10) is obviously a propagating field along the three directions of  $x, y, z$ . It has been proven in quantum physics that if any component of wave vector, say  $k_z$ , can be larger than the module of wave vector  $\mathbf{k}$ , the breakthrough of diffraction limit of resolution can be achieved. In this case, the  $k_z$  must be an imaginary number, that is:

$$k_z = i k_z \quad (4.11)$$

Thus,  $\mathbf{E}(\mathbf{r}, t)$  is expressed as

$$\mathbf{E}(\mathbf{r}, t) = E_0(x, y, z) \exp [i(k_x x + k_y y - \omega t) - k_z z] \quad (4.12)$$

The optical wave field expressed by Equation (4.12) is obviously propagating on the  $(x, y)$  surface of objects, while it exponentially decays in the  $z$  direction perpendicular to the source surface. Equation (4.12) also provides the condition of the breakthrough of diffraction limit and indicates that super-resolution imaging and detection can only be achieved in the NF.

## 4.9.2 NF Optical Techniques and Microscope

### 4.9.2.1 Key Techniques of NF Optics

The above section indicates that there is no diffraction limit in the NF, so the induced and accepted optical signals are not restricted by the diffraction limit. Therefore, the key to NF optical devices depends on the production and pickup of optical signals in the NF region and coupling of these non-radiated NF optical signal to the detectors usually placed in the far-field region. Figure 4.17 shows a principle design satisfying such requirements, where the function of a probe is the optical excitation of objects and/or detection of NF optical signals

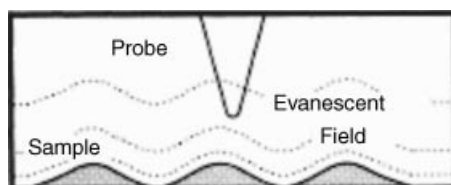


**Figure 4.17** A principle design of an NF optical device. Reprinted from S. L. Zhang, Near-field microscope and its application, Science Press, 2003

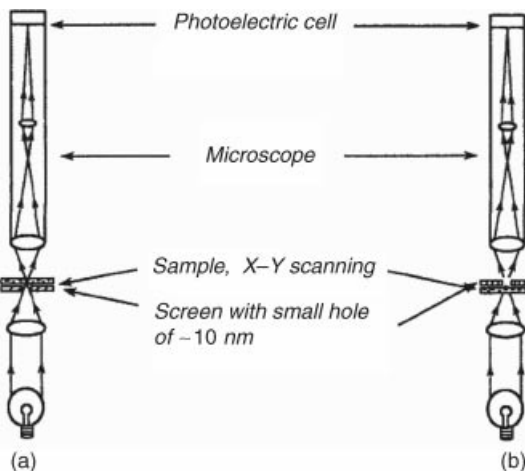


**Figure 4.18** Scheme of the NF microscope conceived by Synge. (a) Illuminating mode, (b) Collecting mode [49]. Reprinted from S. L. Zhang, *Near-field microscope and its application*, Science Press, 2003

from objects. When the probe is a tiny optical fiber or metal tip, the resolution limit is only restricted by the size of the probe.

#### 4.9.2.2 NF Optical Microscope

In the great effort to realize NF optical devices, the NF optical microscope has become the basis of NF Raman spectroscopy (NFRS).

The NF optical microscope was first proposed by E.H. Synge in 1928, based on an illuminator with a small pin-hole and special collective element, as shown in Figure 4.18. Synge pointed out the technological keys to achieving such a device are a very intense light source, a small pin-hole, and a moving probe in the perpendicular and parallel directions on the sample surface in the order of nm. Now it is clear that the idea proposed by Synge is correct but it was not within experimental capability at that time. Moon and O'Keefe [47] put forward their suggestions on the super-resolution optical microscope in 1950 and 1956, respectively. In 1972, Ash and Nichols [48] successfully set up the first NF microscope, using microwaves of 3 cm wavelength as the light source.

The development of the scanning tunnel microscope (STM) provides the key technique for the NF optical device. In 1984, the Pohl [50] group applied the technique of STM into the NF optical device and demonstrated that the image can achieve sub-wavelength resolution with visible light. Afterwards the NF scanning optical microscope (NSOM) and SNOM were innovated by Pohl [50] and Lewis [51], respectively. A sub-wavelength-sized aperture made from a quartz crystal rod [50] or metal pipette [51] served as a nanoscale light source and the transform element, respectively. Their work offers the basis for various objects with spatial resolution at the nanometer scale. Figures 4.19a and b show the structure scheme of NSOM and the medium-resolution records of a grating constant of 400 nm (width of groove = width of strip = 200 nm) grating. In Figure 4.19, the grating is heavily distorted but can still be clearly recognized.

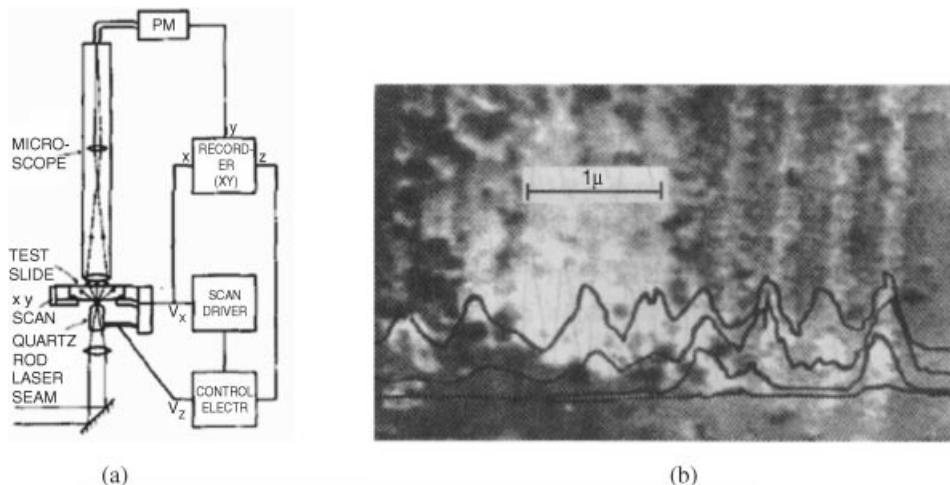


**Figure 4.19** (a) The structure of the first NSOM and (b) the medium-resolution records of a grating constant 400 nm (the width of groove=the width of strip=200 nm) grating [50]. Reprinted from S. L. Zhang, *Near-field microscope and its application*, Science Press, 2003

In 1989, Reddick *et al.* [52] provided an image comparison taken with PSTM, STM, and SNOM for a holographic grating of line spacing 1.17  $\mu\text{m}$ , as shown in Figure 4.20, confirming that the super-resolution ability using a photon is similar to that using an electron. The typical optics of NF microscope is shown in Figure 4.21.

#### 4.9.3 NF Raman Spectrometer and Microscope

Due to the similarity between the NF microscope and the conventional microscope used in Raman microscope, the NF Raman microscope was quickly developed. In 1994, Tsai *et al.* [53] reported the first NF Raman spectroscopic work, in which their scheme of the experimental setup is shown in Figure 4.22. After one year of their first report, the first NF Raman image was published and this is shown in Figure 4.23 [54].

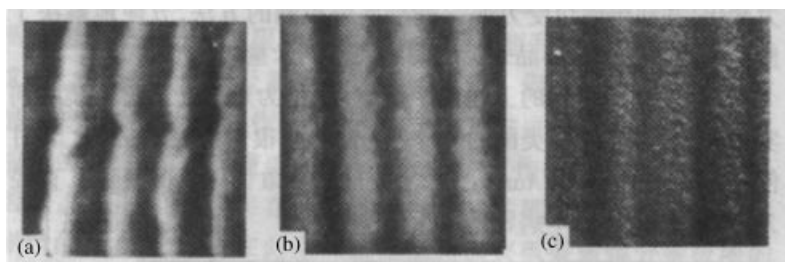


**Figure 4.20** Image comparing a holographic grating of line spacing 1.17  $\mu\text{m}$  taken with (a) SNOM (b) STM, and (c) SEM [52]. Reprinted from S. L. Zhang, *Near-field microscope and its application*, Science Press, 2003

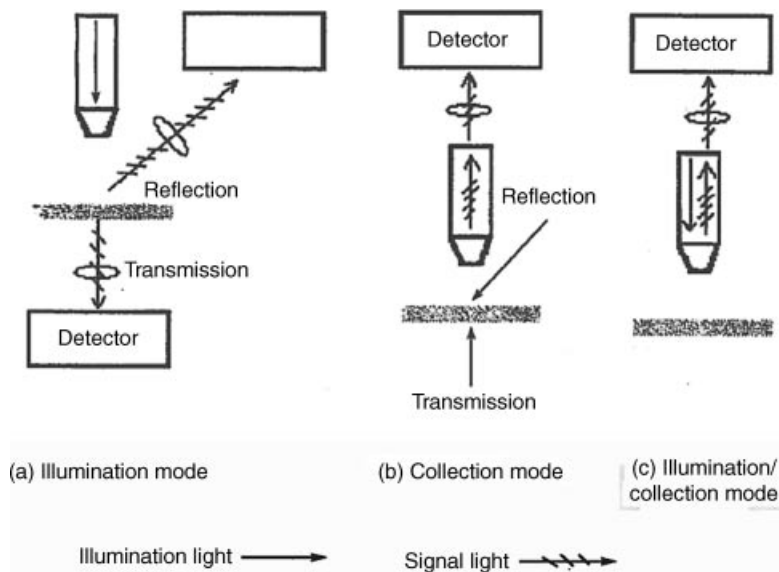


**Figure 4.21** Some typical optics of NF microscopes [49]. Reprinted from S. L. Zhang, Near-field microscope and its application, Science Press, 2003

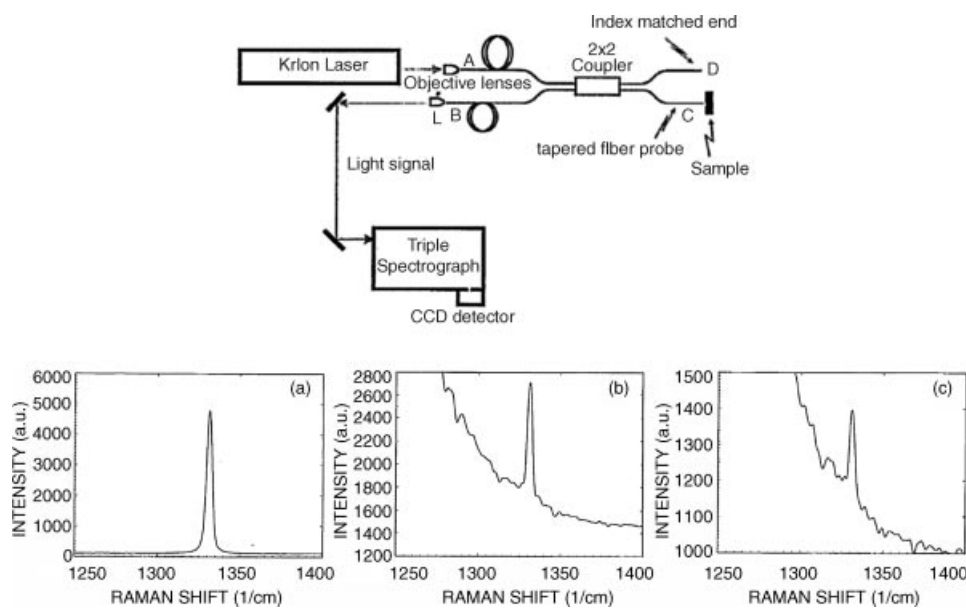


**Figure 4.22** NF Raman experimental setup (UP line) and spectra (down line) (a) Raman spectrum generated from a diamond sample using a conventional Raman microprobe. (b) and (c) are the Raman spectra generated from the same diamond sample by using a flat end and a tapered fiber, respectively, as emitter and collector [53]. Reprinted from D. P. Tsai, A. Othonos, M. Moskovits, et al., Raman spectroscopy using a fiber optic probe with subwavelength aperture, *Appl. Phys. Lett.* 64, (1994) with permission of the American Institute of Physics

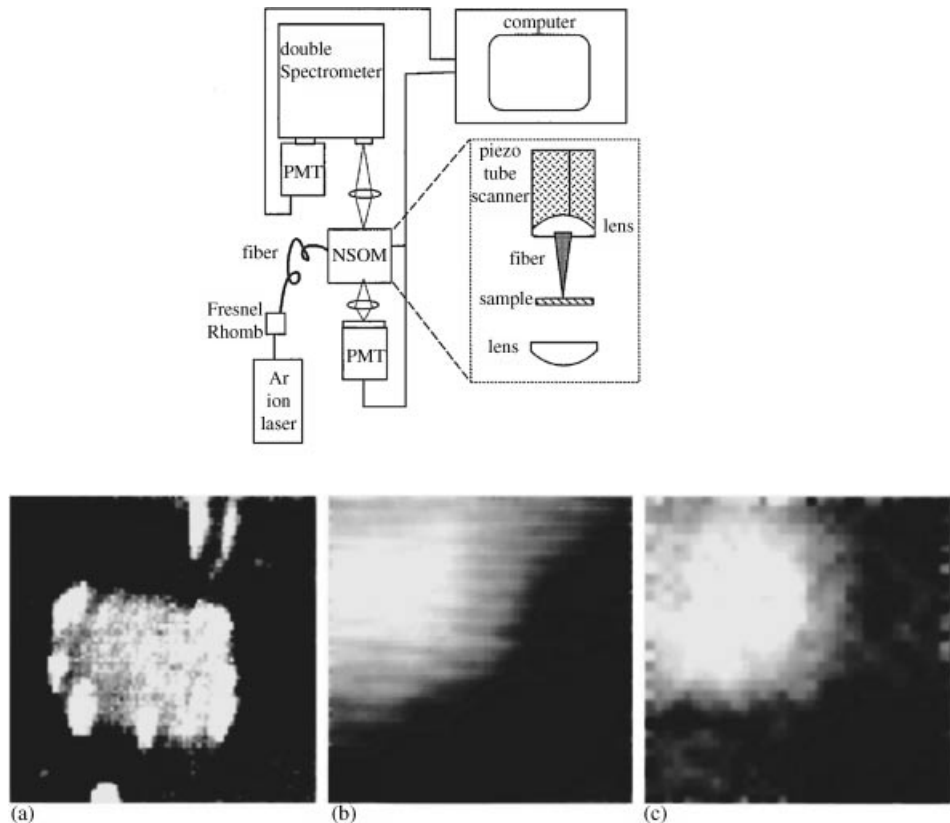


**Figure 4.23** Upper panel: NF Raman experimental configuration; Lower panel: Images of Rb-doped KTP sample. (a)  $10 \mu\text{m}^2$  topographic image with a gray scale range of 17 nm; (b) and (c)  $4 \mu\text{m}^2$  images of the same corner of an Rb-doped region. (b) Transmission image with a gray scale range of 460–550 nW. (c) Raman image with a gray scale range of 18–22 counts obtained in the near field [54]. Reprinted from M.A. Paesler, H.D. Hallen, Raman imaging with near-field scanning optical microscopy, *Appl. Phys. Lett.* 67, 2483 (1995) with permission of the American Institute of Physics

Section 3.1.3 mentioned that the major difficulty in Raman spectral measurement is the weak intensity of Raman scattering light, while the intensity of stray light, such as Rayleigh scattering and photoluminescence signals, which can be superimposed onto Raman spectral bands, are usually very strong. This section also described that the technological key to solving the above problems is to increase the signal-to-noise ratio of the Raman signal against the stray light S/N ratio. To raise the S/N ratio of the NF microscope, there is a specific problem in further increasing the transforming efficiency from the non-radiated NF light into far-field radiated light, which guarantees the information carried by NF light to arrive at far-field optical elements and then be detected and recorded. The apertureless Raman spectrometers, by using metal tips, has a high S/N ratio, while the S/N ratio and the successful rate of aperture NF Raman spectrometer are

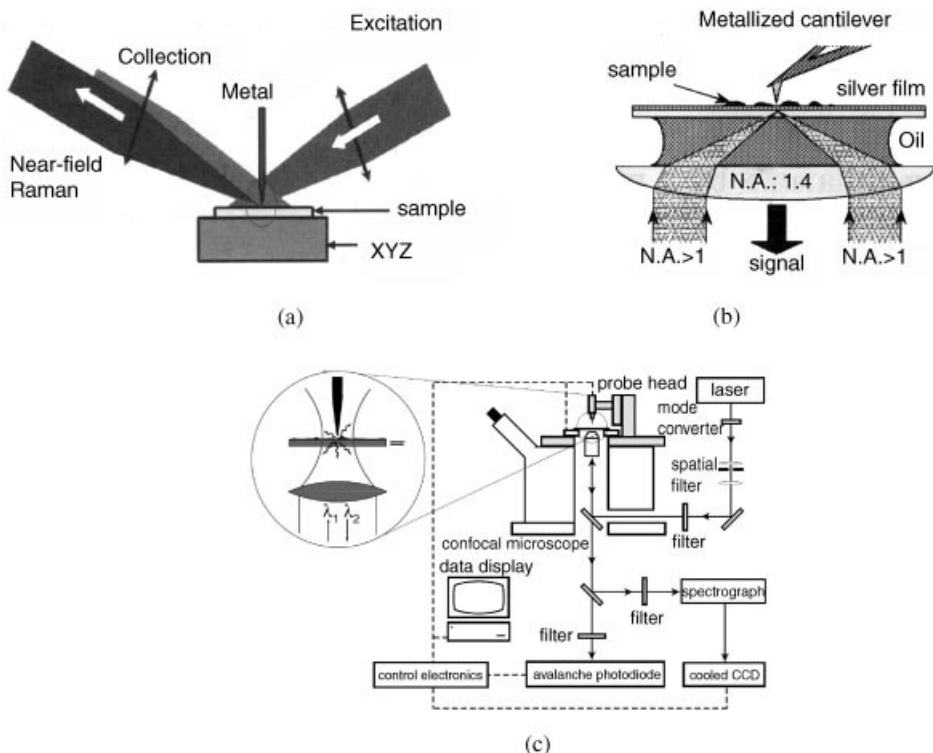


**Figure 4.24** The optics of apertureless Raman spectrometers by using metal tip (a). Reprinted from N. Hayazawa, Y. Inouye, Z. Sekkat, et al., Near-field Raman scattering enhanced by a metallized tip, *Chem Phys Lett*, 335, 369 (2001) with permission of Elsevier. Cantilever (b) [55]. Fig 4 in A. Hartschuh, N. Anderson, and L. Novotny, Near-Field Rama Spectroscopy of Individual Single-walled Carbon Nanotubes, *Intl. J. Nanoscience*, 3, 371 (2004) with permission of the World Scientific Publishing Company, and a complete apparatus (c) [56]

very low. Especially, the application of apertureless metal tips makes enhances the Raman intensity by about  $10^6$  fold. Figure 4.24 shows the optics of apertureless Raman spectrometers, in which the metal tip is used, the cantilever used in atomic force microscope, and a typical complete apparatus are shown in (a), (b), and (c), respectively. The NF Raman microscope shown in Figure 4.24(c) is based on an inverted optical microscope fitted with an  $x$ ,  $y$ -stage for raster-scanning samples and on-axis illumination. The laser light is reflected using a dichroic beam splitter and focused onto the sample surface using a microscope objective with a high numerical aperture. To obtain a tight focal spot at the sample surface, a sharp Au tip is placed into the focal region at a constant height of approximately 1–2 nm from the sample surface by means of a shear-force feedback mechanism. Raman scattered light is collected with the microscope objective, transmitted by the same dichroic beam splitter, and then detected.

Because the use of a sharp metal tip obtains a high spatial resolution and also provides a large enhancement of the optical signal, such kind of tip-enhanced Raman spectroscopy

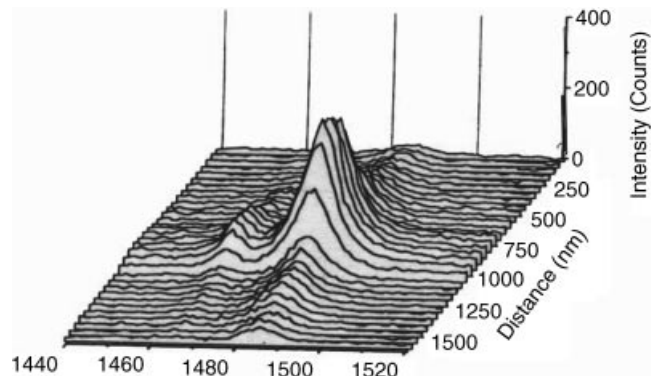


**Figure 4.25** Resonance Raman spectra of a polydiacetylene nanocrystal as a function of position across the sample with sub-wavelength resolution [57]. Reprinted from D. A. Smith, S. Webster, M. Ayad, et al., Sub-micron spatial resolution Raman spectroscopy and its application to stress mapping in silicon, *Ultramicroscopy*, 61, 247 (1995) with permission of Elsevier

has been further developed. To further raise the S/N ratio, the more efficient Raman scattering processes also need to be applied, such as:

- (1) Shorten the incident wavelength, as Raman cross section  $\propto 10^4$ ;
- (2) Resonant Raman scattering;
- (3) Surface-enhanced Raman scattering (SERS) with the total enhancement factor of  $10^{14\sim 15}$ ;
- (4) Coherent anti-Stokes scattering (CARS) with the frequency higher than the fluorescence frequency, which can avoid the disturbance of visible fluorescence background.

#### 4.9.4 NF Raman Spectroscopy and Microscopy

With the gradual improvements in NF Raman spectrometer and the NF Raman microscope, higher spatial resolutions ( $<10\text{ nm}$ ) and better quality spectra and images have been obtained. NF Raman spectroscopy and microscopy have become powerful tools for exploring the properties of matter on the scale approaching that of semiconductor quantum structures.

In 1995, Smith *et al.* presented an NF Raman spectra of line-scanning with sub-wavelength resolution for a polydiacetylene nanocrystal sample, as shown in Figure 4.25, with the spatial resolution at sub-wavelength [57]. The function of the spatial distribution of physical parameters extracted from FF Raman spectra can also be performed in NF Raman spectra with sub-wavelength resolution. In 1998, Webster *et al.* [58] published on the variation with the scale of 150 nm of residual deformation stress across the scratch lines on scratched silicon by NF Raman spectra, as shown in Figure 4.26.

#### 4.10 Tip-enhanced Raman Spectroscopy (TERS)

Raman spectroscopy is a powerful tool, due to the wealth of information obtained from Raman spectra. However, Raman scattering signals are relatively weak compared to other spectral signals such as photoluminescence and fluorescence. Moreover, the spatial

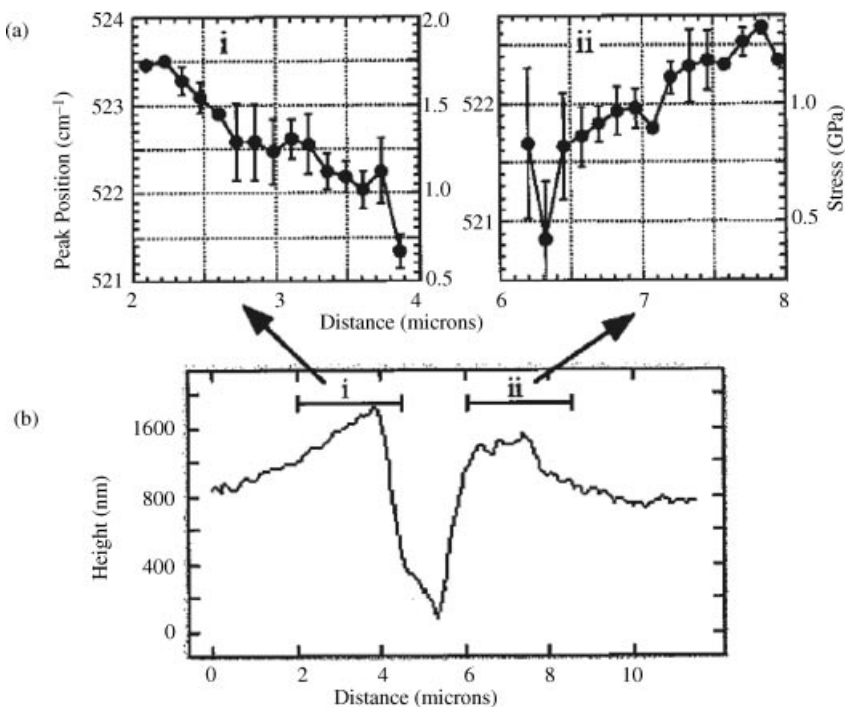


**Figure 4.26** (a) Central wave number of the silicon Raman peak shown as a function of distance across the scratch. Data represent the average of three adjacent lines of pixels and the error bars show the standard error. The right-hand vertical axis in (ii) shows the residual stress in the silicon calculated from the shift in frequency of the Raman band assuming a relationship of  $0.5 \text{ GPa}/\text{cm}^{-1}$ . (b) A topographic cross section of the scratch obtained from the shear-force image. The horizontal bars labeled i and ii indicate the regions from which the data in (a) were obtained [58]. Reprinted from S. Webster, D. N. Batchelder, and D. A. Smith, Submicron resolution measurement of stress in silicon by near-field Raman spectroscopy, *Appl. Phys. Lett.*, 72, 1478 (1998) with permission of the American Institute of Physics

resolution of conventional Raman spectra is also restricted within the half wavelength due to the diffraction limit, which also exists in other spectra. The problem of the weak signal has been partially overcome through the invention of surface-enhanced Raman scattering (SERS), which offers signal enhancement by several orders of magnitude over conventional Raman scattering. However, the spatial resolution in SERS remains at the same scale as that in conventional Raman scattering. With the emergence of near-field Raman spectra (NFRS), the breakthrough of the diffraction limit of spatial resolution was achieved, but the signal intensity in the NFRS was still very weak. Based on the emergence of the above two Raman spectral technologies of NFRS and SERS, a new Raman spectroscopy, called the tip-enhanced Raman spectroscopy (TERS) was been developed, in which a metal tip is used for the excitation of illuminating light and the collection of scattered light. TERS overcomes the above major weakness in conventional Raman scattering, gathering and producing strong Raman signals and excellent spatial resolution, only limited by the tip apex size and shape. Besides these advantages, the TERS does not need special sample preparation and generates signal enhancement with equal strength at every sample location, not as in the SERS where

there exists so-called hot spots. Therefore, the topographic information correlated with the spectroscopic data can be faithfully generated in TERS [59,60].

#### **4.10.1 Earliest Theoretical Conception and Instrument Development of TERS**

Based on studies of localized surface plasmons, in 1985 Wessel discovered that an electric field can be both highly enhanced and confined in the presence of some metal nanostructures, implying that the Raman intensity of molecules in close proximity to such structures will scale approximately with the fourth power of the electric field enhancement factor [61]. Furthermore, the optical spatial resolution limit can be broken with the use of the scanning tip in the NF. Wessel's discovery provided a theoretical basis for TERS. However, it took fifteen years after his initial finding to overcome all the technological difficulties for creating a practical setup to achieve his concept. Based on the technology from the SERS and the NFRS, the first TERS experimental apparatus was created independently by the Zenobi group [62], Anderson [63], and Kawata *et al.* [64] in 2000.

TERS can be considered as an alternative to the SERS and the apertureless NFRS using metal tips. The tip configurations in normal spectroscopy and TERS are shown in Figures 4.27a and b, respectively (see color Plate 3 for the original Figure 4.27). The prototype tip in Figure 4.27b illuminates the sample through the apex of an Ag-coated AFM tip that is placed in direct contact with samples and collects the scattered Raman signals. The observed normal and TER spectra of a flat layer of brilliant cresyl blue dispersed on a glass slide are shown in Figure 4.27c.

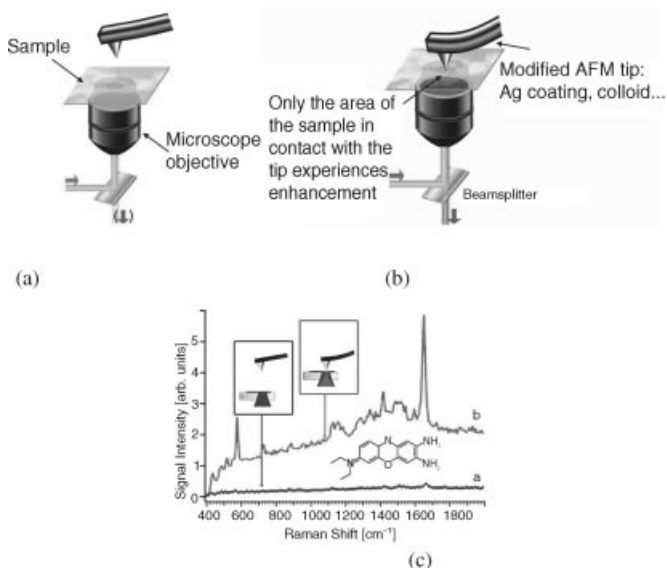


**Figure 4.27** Tip configurations of Normal (a), tip enhanced (b) silver coated tip probes with 10–15 nm thickness, and observed Raman spectra (c) correspondingly [62]. Reprinted from R. M. StrÖckle, Y. D. Suh, V. Deckert, et al., Renato Zenobi, Nanoscale chemical analysis by tip-enhanced Raman spectroscopy, *Chem. Phys. Lett.*, 318, 131 (2000) with permission of Elsevier

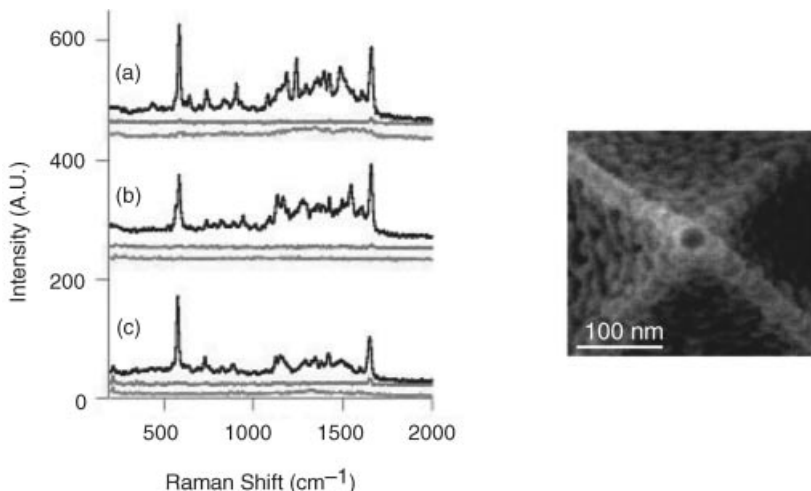


**Figure 4.28** Left: The Raman spectra of brilliant cresyl blue thin film acquired with tip in contact (black) and retracted (green traces) are shown for Ag coated (a)  $\text{SiO}_2$ , (b)  $\text{SiO}_x/\text{SiN}$ , and (c)  $\text{AlF}_3/\text{SiN}$  tips. The orange traces are the tips' spectra collected after the experiments. Right: High-quality SEM image of an Ag-coated tip used in the experiments [65]. Reprinted from B.-S. Yeo, T. Schmid, W. Zhang, et al., Towards rapid nanoscale chemical analysis using tip-enhanced Raman spectroscopy with Ag-coated dielectric tips, *Anal. Bioanal. Chem.*, 387, 2655 (2007) with permission of Springer

In TERS, the design and manufacture of tip probes determines the signal enhancement of Raman scattered light from the sample and the nanometer spatial resolution is limited only by the tip apex size and shape. Therefore, the tip probe is the heart of the TERS instrument. In tip design, the material plays an important role. To give strong TERS signals, the materials with low refractive indices such as  $\text{SiO}_2$ ,  $\text{SiO}_x$ , and  $\text{AlF}_3$  are suitable for supporting platforms of Ag films at 488 nm illumination, as shown in Figure 4.28 (see color Plate 4 for the original Figure 4.28) [65]. 70–80 X of the observed enhancement with net enhancements of  $>10^4$  has been achieved in a brilliant cresyl blue test analysis using Ag-coated tips made from or pre-coated with low refractive index materials. The significant enhancement of the Raman signals generated by the tips is found in all tested samples. These findings are crucial steps towards the use of TERS as a robust technique for rapid imaging with nanometer spatial resolution.

The optical configuration that is related to the illumination of tips is also another factor, which significantly affects the enhanced efficiency. To date, there are various types of designs, as shown in Figure 4.29; the designs for the transmission mode (a) and the side-illumination modes are suitable for opaque samples (b) and (c).

To obtain high enhanced efficiency, it is necessary for the tip to be controlled to approach the sample surface as closely as possible. Figure 4.30 shows a TER spectra from a few ( $<10$ ) BCB molecules (see color Plate 5 for the original Figure 4.30). Figure 4.30b shows that the peak at  $585 \text{ cm}^{-1}$  was greatly enhanced after the tip approached the sample surface.

TERS is still developing and has not yet achieved an ideal level, but more than  $10^6$  times of enhancement of Raman signal [67] and 4 nm of spatial resolution [68] have been reported.

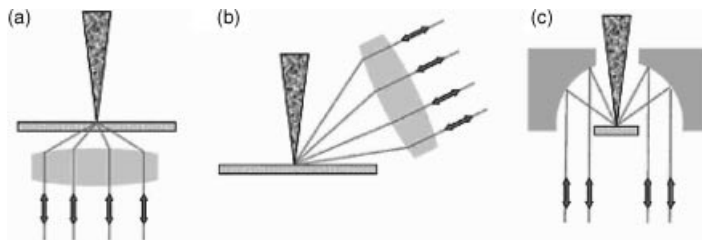


**Figure 4.29** Three optical configurations for the illumination of the TERS tip. (a) bottom illumination using an inverted microscope, (b) side illumination with a long working distance objective, and (c) illumination with a parabolic mirror [60]. Reprinted from B.-S. Yeo, J. Stadler, T. Schmid, et al., Tip-enhanced Raman Spectroscopy – Its status, challenges and future directions, *Chemical Physics Letters* 472, 1–13 (2009) with permission of Elsevier

As one of the Raman microscopic branches, if the metal probe of TERS is scanned over a sample, nanometer spatially resolved topography and optical images of the sample can be obtained simultaneously. Recently, an entire TERS system was placed in a stainless steel chamber, which was filled with the desired gases or evacuated to ultrahigh vacuum, demonstrating that TERS under ultra-conditions can be performed [69,70].

#### 4.10.2 Enhancement Mechanism of TERS

To date, the enhancement mechanism of TERS is not completely understood. Several interpretations have been proposed. One of the enhancement mechanisms is the so-called electromagnetic (EM) mechanism. In this mechanism, it is considered that the incident EM field is locally amplified and confined by the tip. The related effects are usually distinguished as the surface plasmon resonance, substrate (mirror charge) effect, and lightning rod effect.

Classical electromagnetic theory predicts that surface plasmon enhancement can be generated at the metallic tip apex when the wavelengths of the excitation laser and surface plasmons coincide. This gives rise to an enhanced electric field that occurs on the sample substrate in SERS. The most common experimental application of this mechanism is the use of AFM tips coated with a noble metal film, generally Ag or Au [71–74]. For example,

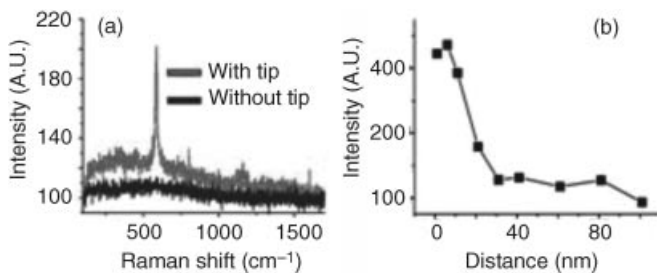


**Figure 4.30** (a) TERS spectra from a few (<10) BCB molecules and (b) dependence of Raman intensity on tip-sample distance [66]. Reprinted from B.-S. Yeo, J. Stadler, T. Schmid, et al., Tip-enhanced Raman Spectroscopy – Its status, challenges and future directions, *Chemical Physics Letters* 472, 1–13 (2009) with permission of Elsevier

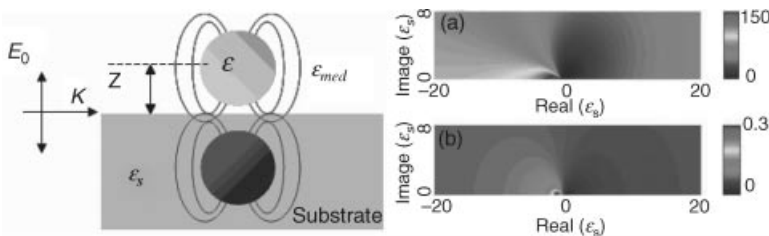


**Figure 4.31** Image dipole (left) and calculated influence of the substrate on the electric field enhancement (right): (a) Enhancement map at the tip apex as a function of the substrate permittivity. Tip radius  $r=20\text{ nm}$ , tip length  $l=1000\text{ nm}$ , tip angle  $\alpha=15^\circ$ , and tip-substrate distance  $1\text{ nm}$ . (b) Effective polarizability map of a dipole  $1\text{ nm}$  above an infinitely large substrate as a function of the permittivity of the substrate [78]. Reprinted from W. Zhang, X. Cui and O. J. F. Martin, Local field enhancement of an infinite conical metal tip illuminated by a focused beam, *J. Raman Spectrosc.*, **40**, 1338 (2009) with permission of John Wiley and Sons

a glass fiber tip with a single gold nanoparticle attached to its apex can be used [75,76]. Noguez reported that multipolar plasmon resonances are induced as the nanoparticle approaches the substrate [77].

In the SERS, the enhancement is dependent on material properties and geometrical parameters of sample substrates when the tip and the illumination wavelength are fixed, which are called the substrate effect in the TERS. This effect can be well explained by considering the role of the image dipole [78]. When the metal is close to a perfect mirror (i.e., a perfect conductor), the image tip becomes similar to the real tip and the field enhancement remains high. Moreover, according to this enhancement map, IR light can always be used to obtain reasonable enhancement, since all metals become good conductors in this wavelength region. Figure 4.31 shows a dipole image and the calculated influence of substrates on electric field enhancement (see color Plate 6 for the original Figure 4.31).

Regarding the lightning rod effect, when a sharp metal tip is illuminated by light of a different polarized direction to the tip shank, an increase in the local surface charge density occurs at its apex. The EM field at the tip apex is both enhanced and confined. Both the polarization of the incident field and the presence of geometrical singularities at the tip can increase the local charge density. Kneipp *et al.* [79] investigated the electromagnetic enhancement effects of metal colloids on the Raman scattering of SWNTs and reported the enhancement in the order of  $10^{12}$ . Figure 4.32 shows the lightning rod effect (see color Plate 7 for the original Figure 4.32).

Another mechanism is the so-called the chemical enhancement (CE) mechanism that originally occurs in SERS [81,82]. It is well known that many molecules have their lowest lying electronic transitions in the UV range, that is, they are colorless, making them weak Raman scattering signals in visible Raman experiments. However, when they are bound to a metal surface, the Fermi level of the surface tends to fall between the highest occupied molecular orbital and lowest unoccupied molecular orbital levels of the molecules. Charge transfer is now possible between molecule and metal or vice versa, with approximately half of the energy required for electronic excitation, compared to an isolated molecule. Therefore, chemical absorption serves as a channel to give more intermediate states for visible light Raman scattering. Hence, chemical enhancement can be considered as a form

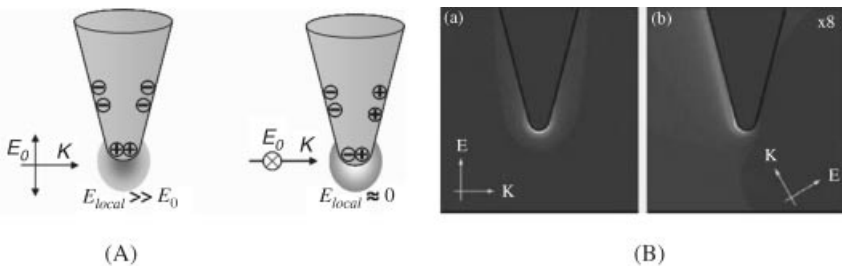


**Figure 4.32** Lightning rod effect showing the polarization direction of the incident radiation. (A) Physical picture and (B) calculated field distribution at a sharp Au tip with a diameter of 5 nm. (a) Field distribution for an incident electric field vector parallel to the tip shaft showing localization of the electric field at the tip apex. (b) Field distribution for an incident electric field oriented non-parallel to the tip shaft. The field is no longer confined to the tip apex [80]. Reprinted from N. Anderson, A. Hartschuh, and L. Novotny, Near-field Raman Spectroscopy, *Materialtoday*, 8, 50 (2005) with permission of Elsevier

of resonance Raman scattering, which contributes to the overall enhancement by approximately  $10\text{--}10^3$ .

For sharp metal tips, except for the key role mentioned above, there is another use for propagating the high spatial frequency components of Raman scattered light, that is, the subwavelength information in the far-zone. This makes the sharp metal tip act as an antenna to radiate EM wave.

Due to the features of huge intensity enhancement, nanoscale resolution, and good homogeneity of Raman signal from samples, TERS represents many exciting advancements, especially in Raman spectral measurements of weak signal and small objects.

## 4.11 Non-linear and Coherent Raman Spectroscopy (NLRS)

Non-linear Raman spectroscopy (NLRS) is one branch of nonlinear optics (NLO), which expresses the behavior of light in nonlinear media.

### 4.11.1 Nonlinear optics (NLO) [83]

Section 2.2.1 showed that the electrical field of optical wave,  $\mathbf{E}$ , is expressed as

$$\mathbf{E} = -\frac{\omega^2 p \sin \theta}{c^2 r} \cos(\omega t - \mathbf{k} \cdot \mathbf{r}) \mathbf{e}_E \quad (4.13)$$

where  $p$  is the amplitude of polarization  $\mathbf{P}$ ;  $\omega$ ,  $c$ , and  $\mathbf{k}$  are the frequency, velocity, and wave vector of light, respectively;  $k = \omega/c$  stands for the amplitude of  $\mathbf{k}$ ;  $\mathbf{r}$  is the position vector; and  $\mathbf{e}_E$  and  $\theta$  represent the unit vector of polarization direction (along with the direction normal to  $\mathbf{r}$ ) of  $\mathbf{E}$  and included plane of  $\mathbf{r}$  and  $\mathbf{P}$ , respectively. In classical electrodynamics,  $\mathbf{P}$  can be considered as an oscillating electric dipole moment, as shown in Figure 2.6, which is the radiated origin of light. If the induced dipole moments of the material respond instantaneously

to an applied electric field, the dielectric polarization (dipole moment per unit volume)  $\mathbf{P}(t)$  at time  $t$  in a medium can be written as a power series of electrical field  $\mathbf{E}(t)$ :

$$\mathbf{P}(t) = \mathbf{a}^{(1)} \cdot \mathbf{E}(t) + \mathbf{a}^{(2)} \cdot \mathbf{E}(t)^2 + \mathbf{a}^{(3)} \cdot \mathbf{E}(t)^3 + \dots \quad (4.14)$$

Here, the coefficients  $\mathbf{a}^{(i)}$  are the  $i$ th order susceptibilities of the medium, which is a  $(i+1)$  order of tensor and reflects the property of medium itself. The optics induced by  $i=1$  or  $i \geq 2$  of  $\mathbf{a}^{(i)}$  are named as linear or nonlinear optics, respectively.

In nonlinear optics, the superposition principle no longer holds. A number of nonlinear optical phenomena can be described as frequency-mixing processes with coherence properties. The frequency-mixing processes will induce the second, third, and high harmonic generation (SHG, THG, and HHG); the sum and difference frequency generation (SFG and DFG); the optical parametric amplification, oscillation, and generation (OPA, OPO, OPG), and so on. There are also other nonlinear processes, of which the most well known are the Kerr effect (KLM), self-focusing, four-wave mixing (FWM), two-photon absorption and chaos in optical systems, and so on. In some optical processes, the medium has a linear response to light, but the properties of the medium are affected by other causes, which are also categorized as nonlinear optics, such as the Pockels effect, of which the refractive index is affected by a static electric field.

Since the  $\mathbf{a}^{(i)}$  decreases with the increase of order  $i$ , the decrease is approximately proportional to  $(10^{10} \text{ V/cm})^{-1}$ . Therefore, the electric field  $\mathbf{E}$  in nonlinear optical effects must be as high as  $10^5 \sim 10^6 \text{ V/cm}$ , meaning that the power density of light must be  $10^7 \sim 10^9 \text{ W/cm}^2$ . However, in widely used light sources, such as sunlight, mercury vapor lamp, xenon lamp, and so on, none meets the above requirements, for example, the intensity of sunlight is only  $10 \text{ V/cm}$ . As a result, in history only a few nonlinear optical effects such as Kerr Effect and Pockels Effect were observed. When the laser with the power density of  $10^9 \text{ W/cm}^2$  and high coherency was created, a great number of nonlinear optical effects were observed, studied, and broadly used.

#### 4.11.2 Nonlinear Raman Spectroscopy (NLRS)

Nonlinear Raman spectroscopy (NLRS), as one of the branches of the nonlinear optical effects, has grown rapidly in last several decades. In 1962, two years after the invention of the laser, the first NLRS and the simulated Raman spectra appeared [84]. Since then, many NLRS have appeared, such as SRS, CARS, gain and loss Raman scattering, Raman Kerr Effect, and coherent Stokes Raman scattering (CSRS), and so on.

The NLO effects including NLRS can be categorized into three types. The first category is nonlinear attenuation and reinforcement caused by a light field directly, such as two-phonon or multiple-phonon absorption, gain and loss Raman scattering, and SRS. The second one is concentrated around the change of the refractive index due to a strong field, of which the samples are the Pockels Effect, Kerr Effect, two-phonon Kerr Effect, Raman Kerr Effect, self-action effect, and so on. The third are related to nonlinear polarization of media and the resultant frequency, polarization direction, or traveling direction change compared to those of the original electromagnetic field. For example, the second, third, and high harmonic generation (SHG, THG, and HHG), the sum and difference frequency generation (SFG and DFG), the optical parametric amplification, oscillation, and generation parameter, and

coherent Stokes and anti-Stokes Raman scattering (CSRS and CARS), belong to NLRS. NLRS, SRS, and CARS were the first observed and most popular, therefore, they will be introduced in a separate section.

## 4.12 Coherent Anti-Stokes Raman Scattering (CARS)

In 1965, Maker and Terhune [85] Published the first essay on Coherent anti-Stokes Raman Scattering (CARS), which they discovered when they used a pulsed ruby laser to investigate the third-order response of several materials and thus were called simply “three wave mixing experiments.” The name, coherent anti-Stokes Raman spectroscopy was created almost ten years later by Begley *et al.* in 1974 [86]. Because of CARS good features, it is one of the most widely used and rapidly developing nonlinear Raman effects.

### 4.12.1 Principle and Experiment of CARS

#### 4.12.1.1 Principle

When two beams of coherent light with frequencies  $\omega_1$  and  $\omega_2$  travel in a medium and due to nonlinear effects, a new coherent light with a new frequency  $\omega_3$  is generated, in which  $\omega_3$  is related to  $\omega_1$  and  $\omega_2$  and is expressed as

$$\omega_3 = \omega_1 + (\omega_1 - \omega_2) \quad (4.15)$$

The corresponding momentums satisfy

$$k_3 = k_1 + (k_1 - k_2) \quad (4.16)$$

If there is an elementary excitation of frequency  $\omega_M$  in the medium and  $\omega_M$  is expressed as

$$\omega_M = \omega_1 - \omega_2 \quad (4.17)$$

then Equation (4.15) can be rewritten as

$$\omega_3 = \omega_1 + \omega_M = \omega_{AS} \quad (4.18)$$

The above energy and momentum relationship are shown in Figure 4.33.

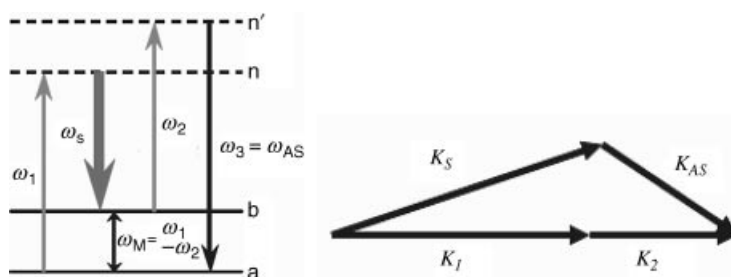


**Figure 4.33** Energy and momentum diagram for the CARS process:  $\omega_s$  is the Stokes scattering frequency of elementary excitation  $\omega_M$  induced by incident light  $\omega_1$

Obviously, if  $\omega_1$  and  $\omega_M$  are regarded as the frequencies of incident and elementary, respectively, the frequency  $\omega_3$  is only the frequency of anti-Stokes Raman scattering. The scattering described above results from interactions between coherent light beams, and accordingly it is called coherent anti-Stokes Raman scattering (CARS). In practical experiments, the frequency  $\omega_2$  is set by a continuously tuning laser to guarantee  $\omega_M = \omega_1 - \omega_2$ .

#### 4.12.1.2 Spectroscopic Features and Application

From the above analysis, we can summarize that CARS has the following spectroscopic features, which are different from those in common Raman spectroscopy:

First, the CARS process is non-stimulated but a new resonance scattering with elementary excitations (such as phonons) of  $\omega_M$  rather than electrons occur in the traditional Raman resonance scattering. Therefore, CARS possesses high excitation efficiency and spectral contrast inherent to chemical species, resulting in not requiring natural or artificial fluorophores and high excitation power, which prevent heating effects, such as burning and photo-bleaching.

Second, the coherent scattering nature of CARS results in high directionality, high monochromaticity, and signal generation only from the focal volume, which benefits the application of spectral imaging.

Third, the CARS signal frequency is higher than one-photon fluorescence, with little scattering and absorption of the near-IR excitation beam, allowing easy detection in the presence of a strong fluorescent background and reducing photo damage to samples.

However, CARS also has shortcomings, for example, a huge background signal from normal Raman scattering impedes its effective detection and wider application.

#### 4.12.1.3 Experiment

In connection with the advantages and shortcomings of CARS, many technological ways have been developed to record the information hidden in the CARS signal, in which the optimization of the laser source and improvements of detection methods are used. Some of these are listed below:

- Forward detected CARS (F-CARS)

The forward CARS (F-CARS) signals are generally very strong and can sometimes be observed by the naked eye. The signal is detected in the phase-matched direction and is selected by a set of spectral filters.

- Backward detected CARS (Epi-CARS)

The Epi-CARS signal is accompanied by a strong non-resonant background, which may overshadow weak signals of interest. When the detection is performed in the backward direction, the no-resonant signal is completely eliminated [87].

- Broadband CARS [88]

The essential feature of broadband CARS is the use of a single, ultra-broadband pulsed laser, which simultaneously provides all three photons necessary to produce the CARS signal. It can enable rapid analysis of multiple Raman bands when compared to spontaneous Raman spectroscopy, while providing the full fingerprint region Raman-equivalent spectrum.

- Polarized CARS (P-CARS)

Based on the polarized features of excited and scattered light in CARS [89], the polarized Raman spectral technology in traditional Raman spectroscopy is used and called Polarized CARS (P-CARS).

- Time-resolved CARS

Time-resolved CARS employs pulse lasers excitation and time-scale delay detection between the excitation and probe pulses. Time-resolved CARS allows for the complete suppression of non-resonant signals [90].

- Interferometric CARS (iCARS)

By interference of the CARS signal by a sample with a local oscillator CARS signal, it is possible to selectively image the real and imaginary part of the third-order nonlinear susceptibility.

In interferometric CARS (iCARS) the local oscillator is generated by an optical parametric amplifier, which is coherent with the CARS signal and is combined in a Mach-Zehnder interferometer. This technique gives a clear interferometric differentiation between the resonant CARS signal and the non-resonant four-wave-mixing signal and can selectively image the real and imaginary part of third-order nonlinear susceptibility [91].

#### 4.12.2 CARS Spectra

Begley *et al.* [86] reported a CARS spectral experiment. Figures 4.34a and b show their experimental apparatus and measured spectra. They demonstrated a number of potential advantages of CARS over conventional spontaneous Raman scattering. These advantages include over  $10^5$  higher conversion efficiency, considerably reduced average required powers (1–2 mW compared to 1 W), and extremely good rejection against background fluorescence of nearly nine orders of magnitude. In addition, the use of available pulsed high peak power tunable lasers allows Raman spectra to be readily carried out without the use of a monochromator or expensive sensitive detectors.

As mentioned above, CARS is resonant with vibrations rather than electrons in the medium. It is well known that the population of vibration states follows the temperature dependent Boltzmann distribution. Therefore, CARS carries the intrinsic temperature dependence and is a popular technique for monitoring the temperature of hot gases and flames, especially in harsh combustion environments. In most cases, the probed molecule is nitrogen, as it is a chemically inert and majority species abundant in all air-fed combustion environments with theoretically well-described spectral data. However, it is limited in fuel-rich hydrocarbon flames, because one of the Swan bands of  $C_2$  radicals occurs in the same spectral region as the CARS signal at around 473 nm. Malarski *et al.* recently reported that this limitation was overcome by using the dual-pump CARS technique with an annular phase matching geometry [92]. Figure 4.35 shows the spectra average taken in the equivalence ratio of a pure nitrogen and pure oxygen  $\phi = 2.3$  flame at a height of 13 mm and the relation of temperature versus height measured by the standard CARS and the

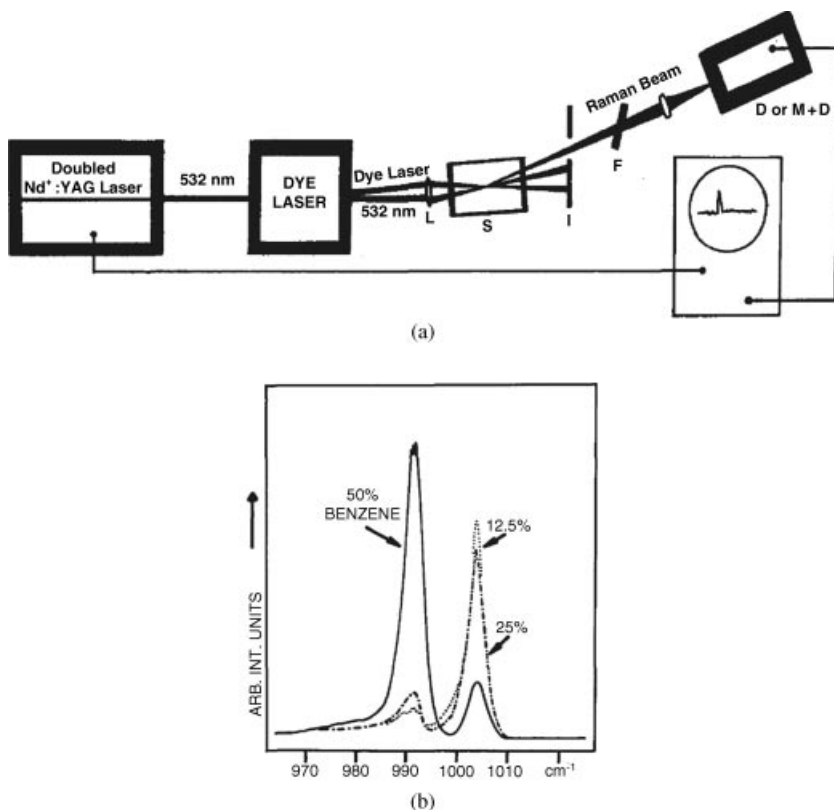


**Figure 4.34** (a) CARS apparatus, where  $L$  is lens,  $S$  is sample cell,  $I$  is the aperture,  $F$  is the interference filter centered at the anti-Stokes frequency, and  $D$  is the detector. (b) CARS spectra of benzene-toluene mixtures [86]. Reprinted from R. F. Begley, A. B. Harvey, and R. L. Byer, Coherent anti-Stokes Raman spectroscopy, *Appl Phys Lett*, 25, 387 (1974) with permission of Institute of Applied Physics

dual-pump CARS method, indicating that dual-pump CARS method leads to erroneous temperatures below the real temperature of the flame.

A recently published broadband CARS work is shown in Figure 4.36 [93]. The broadband CARS setup was used for the double-quadrature spectral interferometry (DQSI). Figure 4.36a shows the experimental setup, in which all three electrical fields of the CARS process are generated in a single pulse by a Ti: Sapphire laser oscillator (KM Labs) operating at 90 MHz, providing approximately 20-fs pulses with 120 nm of bandwidth centered at 800 nm. The CARS signal from this apparatus can be acquired *in situ* on a sub-second time scale. The resultant spectra is shown in Figure 4.36b, where (a) shows temperatures dependence of spectra and (b) real-time and *in situ* monitoring spectra, where the sample is baked for 10 min at 150 °C, then continuously exposed to the focused near-IR beam for the next 10 min and the spectra were taken after 0, 16, and 32 s and 10 min of near-IR exposure with an integration time of 500 ms.

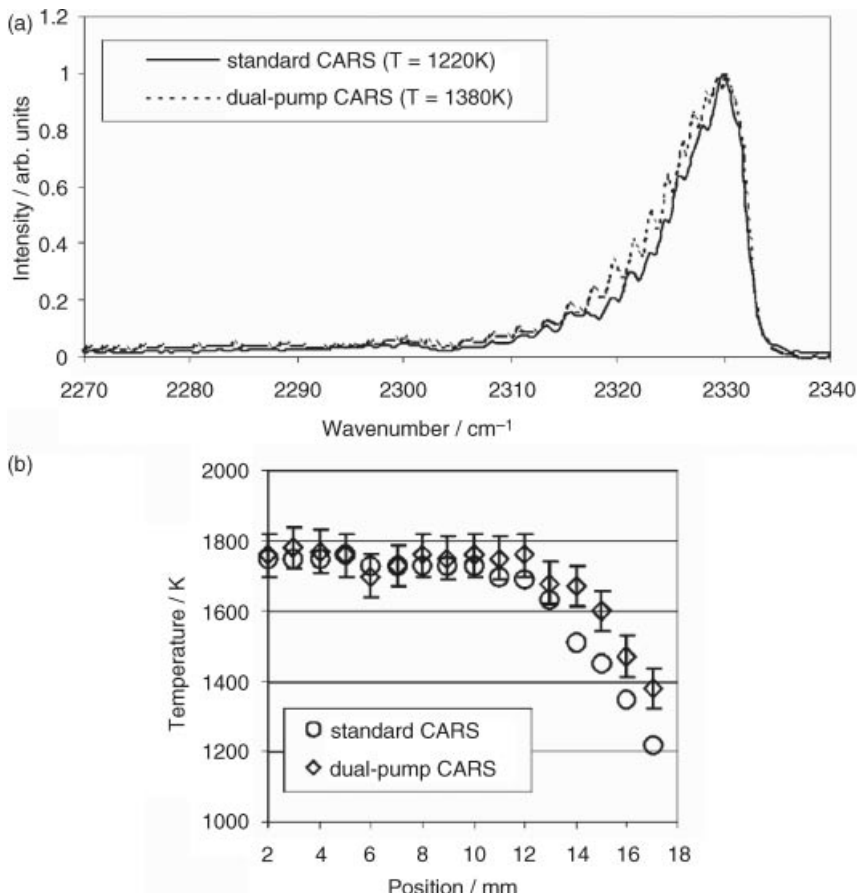


**Figure 4.35** (a) Spectra averaged over 90 laser shots taken in the equivalence ratio of pure nitrogen and pure oxygen  $\phi = 2.3$  flame at a height of 13 mm and (b) temperature versus height simultaneously measured in the flames with  $\phi = 2.3$  with the standard CARS and the dual-pump CARS method [92]. Reprinted from A. Malarski, F. Beyrau and A. Leipertz, Interference effects of C<sub>2</sub>-radicals in nitrogen vibrational CARS thermometry using a frequency-doubled Nd:YAG laser, *J. Raman Spectro.*, 36, 102 (2005) with permission of John Wiley and Sons

In polarized light CARS, the pump and Stokes beams can have arbitrary linear polarization states and the CARS emitted signal is analyzed along two perpendicular directions [94]. Figure 4.37 exhibits a measured result of polarization CARS (see color Plate 8 for the original Figure 4.37).

For pulse laser excited CARS, it has been demonstrated that a femtosecond-oscillator-based system CARS, combined with narrowband pulse lasers and time-delayed detection, is background-free. Figure 4.38 is a sample of this technology for a neat solution of benzene [95]. From Figure 4.38, it is clear to see that the strong broadband signal at zero probe delay is a mixture of both resonant signal and the non-resonant (NR) background. The NR contribution is spectrally broad. Due to its instantaneous nature, the NR-four-wave

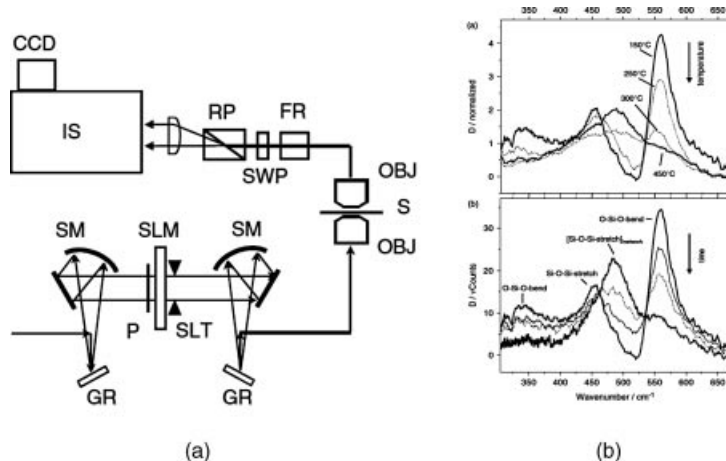


**Figure 4.36** (a) Experimental setup for broadband DQSI CARS: GR, grating; SM, spherical mirror; P, polarizer; SLM, spatial light modulator; SLT, slit; OBJ, microscope objective; S, sample; FR, Fresnel rhomb; SWP, short-wave pass filter; RP, Rochon prism; IS, imaging spectrometer; CCD, two-dimensional charge-coupled device. (b) CARS spectra of HSQ [93]. Reprinted from A. G. Caster, S. Kowarik, A. M. Schwartzberg, et al., *Observing hydrogen silsesquioxane cross-linking with broadband CARS*, *J. Raman Spectrosc.* 40, 770–775 (2009) with permission of John Wiley and Sons

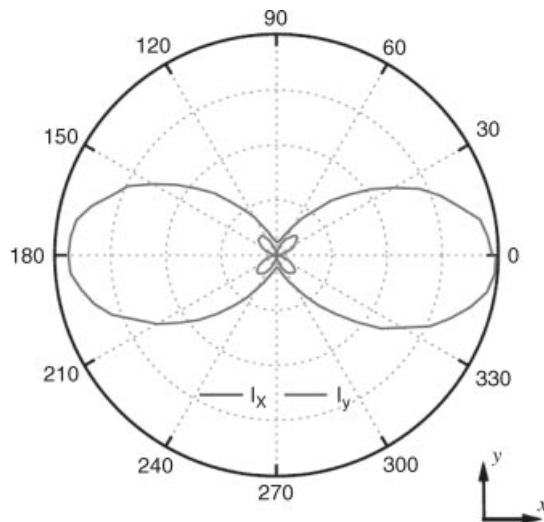


**Figure 4.37** CARS polarization responses  $I_x$  and  $I_y$  (represented as polar plots) for pure water when the Stokes linear polarization is set parallel to the x-axis and the pump linear polarization rotates from 0° to 360° [94]. Reprinted from F. Munhoz, et al., *Raman depolarization ratio of liquids probed by linear polarization coherent anti-Stokes Raman spectroscopy*, *J. Raman Spectrosc.* 40, 775 (2009) with permission of John Wiley and Sons

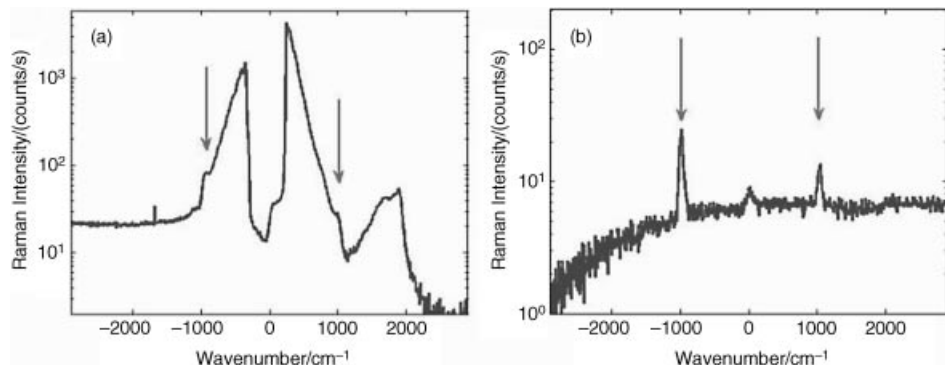


**Figure 4.38** CARS-CSRS spectrogram of a neat solution of benzene: for 0 ps (a) and 0.6 ps (b) probe pulse delays [95]. Reprinted from J. Peng, D. Pestov, M.O. Scullya, et al., Simple setup for hybrid coherent Raman microspectroscopy, *J. Raman Spectrosc.*, 40, 795 (2009) with permission of John Wiley and Sons

mixing (FWM) signal rapidly decays when the delay between the two pulses is increased. On the other hand, the long-living resonant contribution stands out [Figure 4.38b]. Two narrowband blue- and red-shifted lines (pointed by arrows) are CARS and coherent Stokes Raman scattering (CSRS) components of the scattered radiation corresponding to the ring-stretching mode at  $992\text{ cm}^{-1}$ . Even though the time delay of the probe pulse is accompanied by attenuation of the coherent Raman signal, it still drastically improves the signal-to-background ratio.

#### 4.12.3 CARS Microscopy (SRS)

The CARS microscope developed the most rapidly and drew the most attention in the CARS research field.

##### 4.12.3.1 History of CARS Microscopy and Micro-Spectroscopy

In 1982, Duncan *et al.* constructed the first CARS microscope by using CARS lines as the light source of the Raman image instrument [96]. Its scheme is shown in Figure 4.39. In 1999, a large improvement in the CARS microscope was made by Xie [97], who changed the non-collinear system to a collinear system and the picosecond visible laser to a femtosecond (FS)[61] near IR laser. He successfully observed the first image of a single biological cell, which is shown in Figure 4.40 (see color Plate 9 for the original Figure 4.40). After this initial work, Xie's group continuously published more works and maintained the leading position in the CARS microscopy field.

##### 4.12.3.2 Application of CARS Microscopy

The CARS microscope possesses intrinsic advantages of CARS and used similar technology as in CARS spectra. CARS microscopy can, in principle, be used for all applications, which require images with vibration contrast as would be obtained with a Raman microscope. The vibration contrast means a chemically-selective imaging modality, and provides microscopic contrast without the need of labels, making it a powerful tool in biological and medical fields, including lipid metabolism, organelle transport *in vivo*, and viral disease.

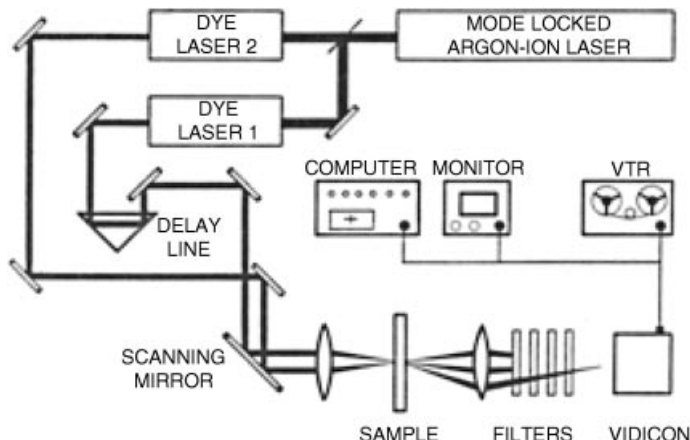


**Figure 4.39** The first CARS image spectrometer [96]. Reprinted from M. D. Duncan, J. Reintje, T.J. Manuccia, Scanning coherent anti-Stokes Raman microscope, *Optic Lett.*, 7, 350 (1982) with permission of The Optical Society of America

## 4.13 Stimulated Raman Scattering (SRS)

The process of Raman scattering can be considered as the loss of incident light  $\omega_0$  and the gain of scattering light  $\omega_s$  in medium. It is obvious that when the gain exceeds the loss, Stimulated Raman Scattering (SRS) occurs. SRS is actually a combination of a Raman process and stimulated emission and was first observed by Woodbury and Ng in 1962, soon after the laser was employed as the light source of Raman spectrometers [98].

### 4.13.1 Principle and Features of SRS

The SRS is one of the third-order nonlinear optical (NLO) effects, which is the result of employing two photons of the Raman pump ( $\omega_{\text{pump}}$ ) and the Raman probe ( $\omega_{\text{probe}}$ ).

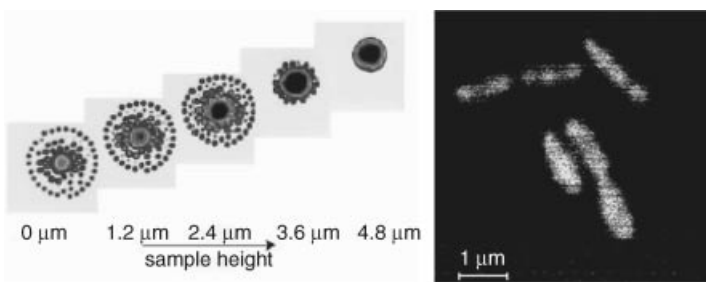


**Figure 4.40** The first image of single biological cells by s CARS microscope [97]. Reprinted from A. Zumbusch, G. R. Holton and X. Sunney Xie, Three-Dimensional Vibrational Imaging by Coherent Anti-Stokes Raman Scattering, *Phys. Rev. Lett.*, 82, 4142 (1999) with permission of the American Physical Society

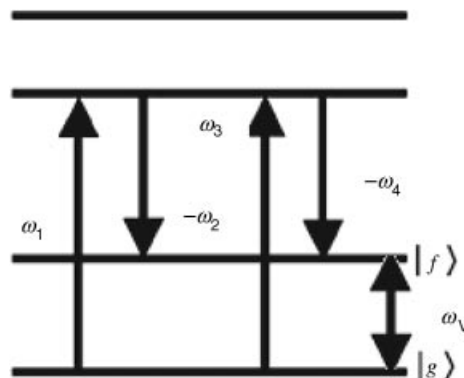


**Figure 4.41** Illustration of SRS energy-level diagram

When the two optical fields simultaneously meet on a sample with molecular vibration frequency ( $\omega_v$ ) equal to ( $\omega_{\text{pump}} - \omega_{\text{probe}}$ ), the attenuation of the Raman pump occurs and the gain in the Raman probe at a frequency corresponding to the difference between the Raman pump and molecular vibration ( $\omega_v = \omega_{\text{pump}} - \omega_{\text{probe}}$ ) is observed. SRS is obviously a four-wave mixing process and can be understood by the use of an energy level diagram, as illustrated in Figure 4.41, in which  $\omega_1 = \omega_3 = \omega_{\text{pump}}$  and  $\omega_2 = \omega_{\text{probe}}$ . In the SRS process, the corresponding momentum fits the phase matching condition:

$$k_1 - k_2 - k_1 = -k_4 \quad (4.19)$$

The above phase matching condition results in the emission of a photon coherently with the probe photon and thereby not affected by any spontaneous process (fluorescence). This is in distinct contrast with CARS, which requires specific three pulse phase matching, thus making signal detection difficult.

SRS possesses the characteristics of the stimulated radiation, for instance, there is a sharp threshold for the stimulation and the scattered light exhibits the features of coherency, directivity, mono-chromaticity, high intensity, and so on. In the SRS process, most of the power of the stimulated light is converted to radiation with frequency ( $\omega_{\text{pump}} \pm n\omega_v$ ) ( $n = 1, 2, 3, \dots$ ). Accordingly, SRS can be employed as a new way of generating lasers with variable frequencies. In SRS, most incident radiation with the frequency  $\omega_{\text{pump}}$  is converted to that of the first Stokes frequency  $\omega_{\text{pump}} - \omega_v$ . If the first vibration energy level  $\omega_v$  is significantly distributed, SRS can provide an important approach for the measurement of the vibration state lifetime. The output light of the SRS exhibits conjugation properties in its phase, which can be used to modify aberrations and degradation of lasers, obtaining the light with almost no diffraction limitation.

#### 4.13.2 Spectroscopy of SRS

The spectra are one of major applications of SRS. As with Raman spectroscopy, the SRS has much variation, in which many types of SRS are originated mainly from application of various kinds of laser sources.

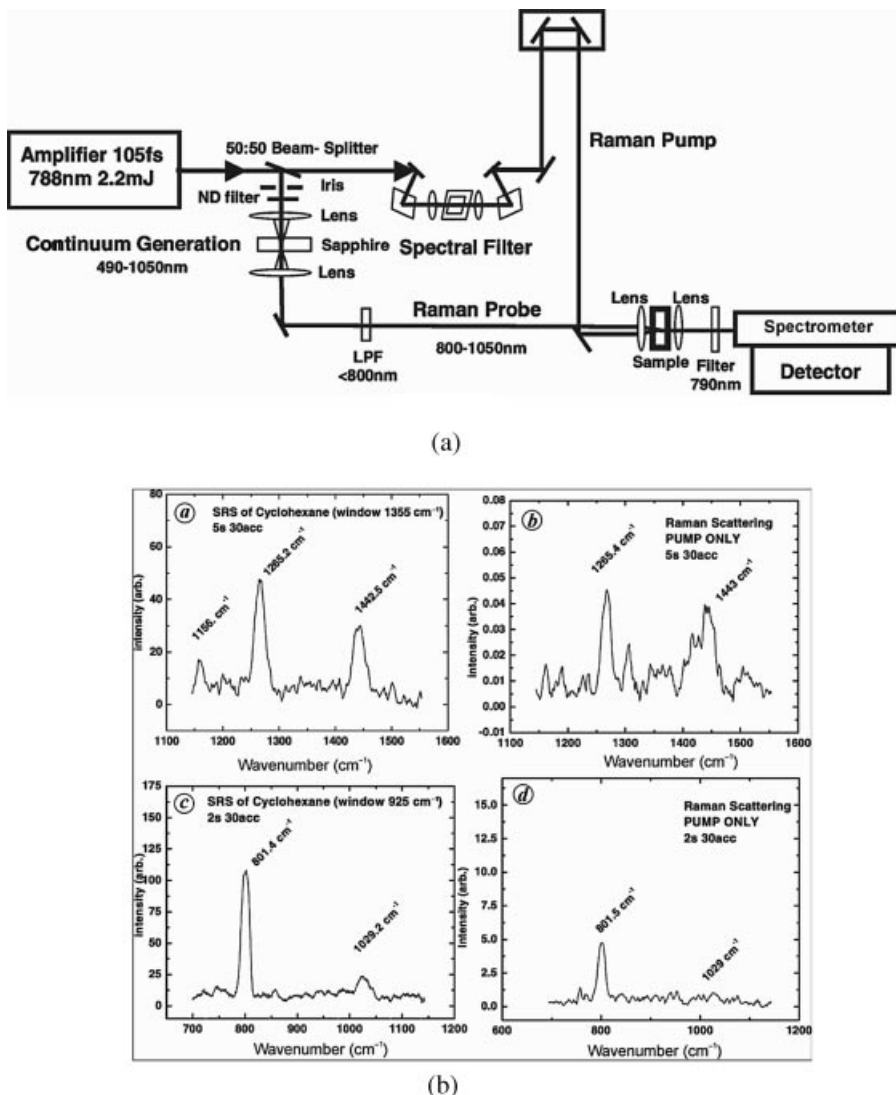


**Figure 4.42** Structure drawing of SRS spectrometer (a) and recorded SRS and spontaneous Raman spectra of cyclohexane (b): Pump  $\rightarrow \lambda$  central at 787.78 nm, BW =  $17.54\text{ cm}^{-1}$ , energy =  $1.25\text{ }\mu\text{J}$ , beam diameter =  $24.7\text{ }\mu\text{m}$ . **a, b.** Probe  $\rightarrow$  energy =  $0.43\text{ nJ}$  at 880 nm, beam diameter =  $12.5\text{ }\mu\text{m}$ . **c, d,** Probe  $\rightarrow$  energy =  $0.62\text{ nJ}$  @ 880 nm, beam diameter =  $12.5\text{ }\mu\text{m}$  [99]. Reprinted from B. Mallick, A. Lakshmanan, V. Radhalakshmi et al., Design and development of stimulated Raman spectroscopy apparatus using a femtosecond laser system, Current Science, 95, 1551 (2008)

A SRS experimental spectrometer using an fs laser system is shown in Figure 4.42a [99]. This system employs the generation of two NIR pulses: a ps narrow bandwidth ( $5\text{--}20\text{ cm}^{-1}$ ) Raman pump pulse centered at 787 nm, and an fs broadband continuum Raman probe pulse (800–1050 nm), providing the Stokes field covering vibrations in the range  $300\text{--}2500\text{ cm}^{-1}$ ,

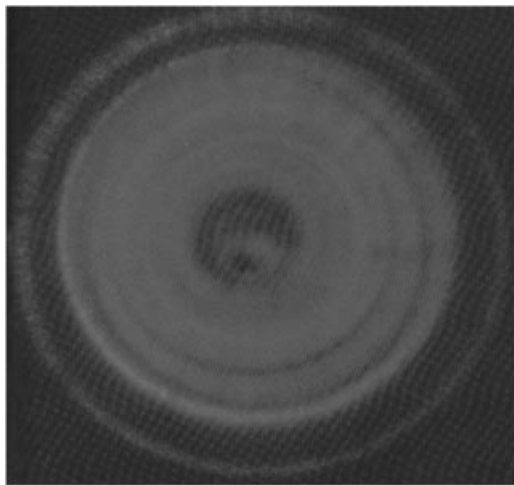


**Figure 4.43** An angle-dependent Raman spectrum of SRS [103]. Reprinted from S.-L. Zhang, *Raman Spectroscopy and Low-dimensional Nano-semiconductors*, Science Press (2008)

from a 105 fs laser source. When the two fields overlap spatially and temporally on the sample, we can observe gain features on top of the probe beam. The ratio of the probe spectrum for the Raman pump on and off, gives the gain spectrum. Use of a long duration ps pulse as a Raman pump ensures a good spectral resolution. Figure 4.42b shows a comparison between spontaneous Raman and SRS spectra of cyclohexane measured by the above setup.

Moreover, if an fs laser pulse propagates through a molecular medium, it excites a molecular coherence in any Raman-active molecular vibration mode, provided the pulse has temporal features faster than the vibration period, which is called impulsive stimulated Raman scattering (ISRS) [100–102]. ISRS is a general material response and occurs even in the absence of any direct resonant transitions that might be excited by the pulse. ISRS can be used to generate and control coherent phonons and other low frequency modes. Moreover, the pulse reshaping of an intense ultrafast pulse propagating through a molecular gas can allow the excitation of Raman coherence that the unshaped laser pulse was incapable of exciting via ISRS.

To illustrate the direction selectivity of IRS, we show an angle dependent Raman spectrum of IRS in Figure 4.43 (see color Plate 10 for the original Figure 4.43).

#### 4.13.3 Microscopy of SRS

Based on the above discussion, it is natural for us to anticipate that the spectral lines of SRS can play a similar role in developing a new kind of imaging technique, as has happened in other Raman scattering research fields. In 2008, a three-dimensional multiphoton vibration imaging technique was based on SRS and first developed by Xie's group [104].

The SRS microscopy has a major advantage over previous coherent Raman techniques. For example, SRS microscopy allows mapping of molecular species in three dimensions and has the ability to follow their dynamics in living cells and organisms based on the features of their Raman spectra, leading to a new approach for studying pharmacokinetics *in situ*. So far, there

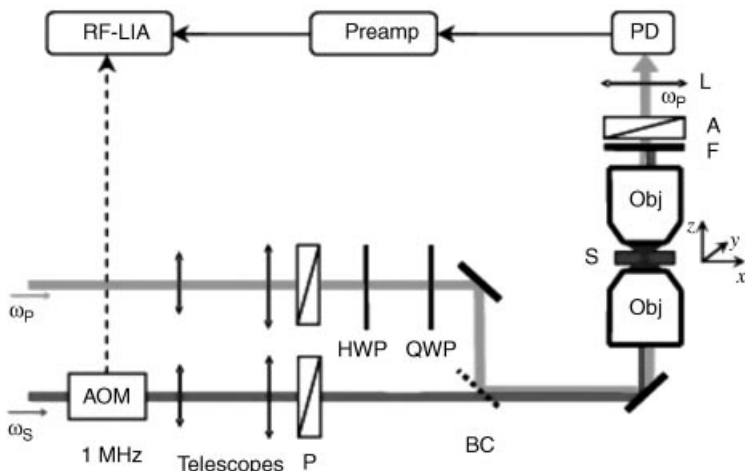


**Figure 4.44** Schematic of the SRS microscope configured for SRL detection. (P, polarizer; HWP/QWP, half/quarter-wave plate; BC, dichroic beam combiner; Obj, objective lens; F, filter; A, analyzer; L, lens; S, sample; AOM, acoustooptical modulator; PD, photodiode detector; Preamp, pre-amplifier; RF-LIA, radio-frequency lock-in amplifier. [104]. Reprinted from P. Nandakumar, A. Kovalev and A. Volkmer, Vibrational imaging based on stimulated Raman scattering microscopy, *New J. Phys.* 11 (2009) with permission of the Institute of Physics

are a variety of biomedical applications by SRS, such as differentiating distributions of omega-3 fatty acids and saturated lipids in living cells, imaging of brain and skin tissues based on intrinsic lipid contrast, and monitoring drug delivery through the epidermis.

Although the amplified laser system generates a large SRS signal, its excessive peak power results in sample damage and its low repetition rate limits the image acquisition speed. These drawbacks of the amplified laser system make it unsuitable for bio-imaging. The Xie group took a different approach, using a high repetition rate (76 MHz) picosecond pulse trains with more than three orders of magnitude lower peak power. The pump beam for SRL is provided by a synchronously pumped, tunable optical parametric oscillator (OPO) and the Stokes beam is provided by a 1064-nm mode-locked Nd:YVO<sub>4</sub> oscillator. A 7-ps pulse width is chosen because its frequency bandwidth offers optimal spectral resolution ( $3 \text{ cm}^{-1}$ ). Besides the features above, they also adopted other techniques and incorporated a stimulated Raman Lose (SRL) microscope, as shown in Figure 4.44 (see color Plate 11 for the original Figure 4.44).

The SRL microscope was first used to monitor the uptake of omega-3 fatty acids in living human lung cancer cells through SRL image and micro-spectroscopy [104]. Later, A SRL work of a self-assembled layer of 2.4  $\mu\text{m}$  polystyrene beads on a cover slip surrounded by water was published. Figure 4.45 (a) and (b)(see color Plate 12 for the original Figure 4.45) [105] shows an image acquired within  $\sim 90$  s at a Raman shift of  $2904 \text{ cm}^{-1}$  the Raman spectrum covering CH-stretching vibration range. The observed SRS spectrum qualitatively reproduces the characteristic features of the corresponding parallel-polarized spontaneous Raman spectrum,  $I''_{\text{Raman}} (\omega_p - \omega_S)$ , of bulk polystyrene, which is also shown for comparison. Authors concluded that at the power levels used in the study strong coherent

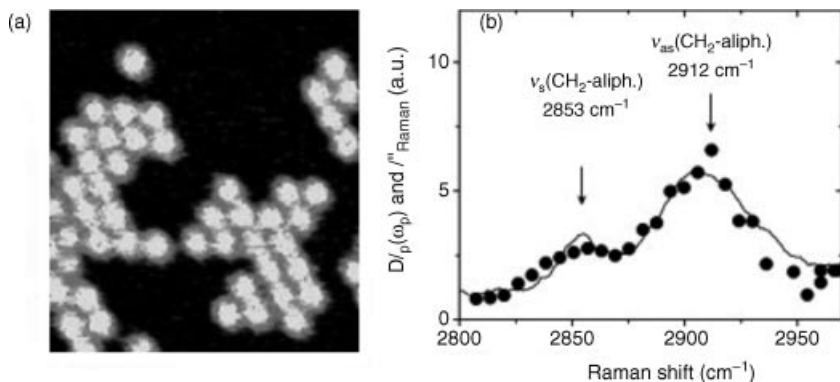


**Figure 4.45** SRS microscopy of a polystyrene bead. (a) SRL image of self-assembled  $2.4 \mu\text{m}$  polystyrene beads in water recorded with pump and Stokes beams at  $716 \text{ nm}$  and  $904 \text{ nm}$ , corresponding to a Raman shift of  $2904 \text{ cm}^{-1}$ . The average power of each beam was  $5 \text{ mW}$ . The image size measures  $23.1 \mu\text{m} \times 25.6 \mu\text{m}$  ( $140 \times 155$  pixels) with a pixel dwell time of  $4 \text{ ms}$ . (b) Measured SRL spectrum (filled circles) of a single  $2.4 \mu\text{m}$  polystyrene bead recorded with the Stokes wavelength at  $901 \text{ nm}$  and the pump wavelength tuned from  $711$  to  $719 \text{ nm}$ . The average power of each beam was  $10 \text{ mW}$ . Both the aliphatic symmetric  $v_s(\text{CH}_2)$  and anti-symmetric  $v_{as}(\text{CH}_2)$  Raman modes of polystyrene at  $2853$  and  $2912 \text{ cm}^{-1}$ , respectively, are clearly resolved. Shown for comparison as a solid line is the parallel-polarized spontaneous Raman spectrum  $I_{\text{Raman}}^{||}$  of bulk polystyrene [105]. Reprinted from P. Nandakumar, A. Kovalev and A. Volkmer, Vibrational imaging based on stimulated Raman scattering microscopy, *New J. Phys.* **11** (2009) with permission of the Institute of Physics

interaction effects are not present. Consequently, the recorded image pixel intensities in figure 4.45 (a) are interpreted as being linearly proportional to the number densities of  $v_{as}(\text{CH}_2)$  Raman modes of polystyrene inside the focal volume.

## References

- [1] Wartewiga, S. and Neubert, R. (2005) *Adv. Drug Deliv. Rev.*, **57**, 1144.
- [2] Li, M., Feng, Z., Xiong, G. *et al.* (2001) *J. Phys. Chem. B*, **105**, 8107.
- [3] Martin, R.M. and Falicov, L.M. (1983) in *Light Scattering in Solids I*, vol. **8**, Topics in Applied Physics (ed. M. Cardona), Springer, Berlin, p. 79.
- [4] Zucker J.E., Pinczuk, A., Chemla, D.S. *et al.* (1983) *Phys. Rev. Lett.*, **51**, 1293.
- [5] Zhang S.-L., Gant, T.A., Delaney, M. *et al.* (1988) *Chn. Phys. Lett.*, **5**, 113.
- [6] Rao, A.M., Richter, E., and Bandow, S. (1997) *Science*, **275**, 187.
- [7] Zhang, S.-L., Ding, W., Yan, Y. *et al.* (2002) *Appl. Phys. Lett.*, **81**, 4446.
- [8] Thomsen, C. and Reich, S. (2000) *Phys. Rev. Lett.*, **85**, 5214.
- [9] Jahncke, CL., Paesler, MA., and Hallen, HD. (1995) *Appl. Phys. Lett.*, **67**, 2483.
- [10] Smith, D.A., Webster, S., Ayad, M. *et al.* (1995) *Ultramicroscopy*, **61**, 247.
- [11] van Hulst, N.F. and Moers, M.H.P. (1996) *IEEE Eng. in Med. & BioMagazine*, **15**, 51.
- [12] Jahncke, CL., Hallen, HD., and Paesler, MA. (1996) *J. Raman Spec.*, **27**, 579.
- [13] Saito, R., Jorio, A., Souza Filho, A.G. *et al.* (2002) *Phys. Rev. Lett.*, **88**, 027401.

- [14] Ni, Z., Liu, L., Wang, Y. *et al.* (2009) *Phys. Rev. B*, **80**, 125404.
- [15] Leite, R.C.C. and Porto, S.P.S. (1966) *Phys. Rev. Lett.*, **17**, 10.
- [16] Leite, R.C.C., Scott, J.F., and Damen, T.C. (1969) *Phys. Rev. Lett.*, **22**, 780.
- [17] Huang, K. (1985) *Adv. Science of China Physics*, **1**, 1.
- [18] Shen, Y.R. (1974) *Phys. Rev. B*, **9**, 622.
- [19] Takagahara, T. (1980) in *Relaxation of Elementary Excitation*, vol. **18** Springer Series in Solid-State Sciences (eds R. Kubo and E. Hanamura), Springer-Verlage, New-York, p. 45.
- [20] Zhang S.L., Hou, Y.T., Shen, M.Y. *et al.* (1993) *Phys. Rev.*, **B47**, 12937.
- [21] Loudon, R. (1964) *Adv. Phys.*, **13** (52), 423.
- [22] Weinstein, B.A. and Cardona, M. (1973) *Phys. Rev. B*, **7**, 2454.
- [23] You, J.-L. *et al.* (2001) *Chn. Phys. Lett.*, **18**, 991.
- [24] Decremps, F., Pellicer-Porres, J., Saitta, A.M., Chervin, J.-C., and Polian, A. (2002) *Phys. Rev. B*, **65**, 092101.
- [25] Nakabayashi, T., Okamoto, H., and Tasumi, M. (1997) *J. Phys. Chem. A*, **101**, 7189.
- [26] Johnson, C.K., Dalickas, G.A., Payne, S.A., and Hochstrasser, R.M. (1985) *Pure and Appl. Chem.*, **57**, 195.
- [27] Hamaguchi, H. (1987) in *Vibrational Spectra and Structure*, vol. **16** (eds J.R. Durig), Elsevier, Amsterdam, p. 227.
- [28] Hamaguchi, H. and Gustafson, T.L. (1994) *Ann. Rev. Phys. Chem.*, **45**, 593.
- [29] Matousek, P. and Stone, N. (2007) *J. Biomed. Opt.*, **12**, 024008.
- [30] Delhayé, M. (1982) in *Proceedings of the 8th International Conference on Raman Spectroscopy* (eds J.L. Lascombre and P.V. Huang), John Wiley & Co., Chichester, p. 233.
- [31] Narita, Y., Tadokoro, T., Ikeda, T. *et al.* (1998) *Appl. Spectrosc.*, **52**, 301.
- [32] Schopf, J.W., Kudryavtsev, A.B., Agresti, D.G. *et al.* (2002) *Nature*, **416**, 73.
- [33] Fleischmann, M., Hendra, P.J., and McQuillan, A.J. (1974) *Chem. Phys. Lett.*, **26**, 163.
- [34] Jeanmaire, D.L. and Van Duyne, R.P. (1977) *J. Electroanal. Chem.*, **84**, 1.
- [35] Qian, X., Peng, X.H., Ansari, D.O. *et al.* (2008) *Nat. Biotechnol.*, **26**, 83.
- [36] Tian, Z.Q., Ren, B., and Mao, B.W. (1997) *J. Phys. Chem. B*, **101**, 1338.
- [37] Cai, W.B., Ren, B., Li, X.Q. *et al.* (1998) *Surf. Sci.*, **406**, 9.
- [38] Ren, B., Xu, X., Li, X.Q. *et al.* (1999) *Surf. Sci.*, **427**, 157.
- [39] Zou, S., Weaver, M.J., Li, X.Q. *et al.* (1999) *J. Phys. Chem. B*, **103**, 4218.
- [40] Cao, P.G., Yao, J.L., Ren, B. *et al.* (2000) *Chem. Phys. Lett.*, **316**, 1.
- [41] Yao, J.-L., Xu, X., Wu, D.-Y. *et al.* (2000) *Chem. Commun.*, 1627.
- [42] Seinfeld, J.H. and Pankow, J.F. (2003) *Annu. Rev. Phys. Chem.*, **54**, 121.
- [43] Felidj, N., Aubard, J., Levi, G., *et al.* (2002) *Phys. Rev. B*, **65**, 075419.
- [44] Tian, Z.-Q., Ren, B., and Wu, D.-W. (2002) *J. Phys. Chem. B*, **106**, 9463.
- [45] Synge, E.H. (1928) *Phil. Mag.*, **6**, 356.
- [46] Tsai, D.P., Othonos, A., Moskovits, M., and Uttamchandani, D. (1994) *Appl. Phys. Lett.*, **64**, 1768.
- [47] Moon, R.J. (1950) *Science*, **112**, 389.
- [48] Ash, E.A. and Nichols, G. (1972) *Nature*, **237**, 510.
- [49] Zhang, S.L. (2003) *Near-Field Microscope and its Application*, Science Press, Beijing.
- [50] Pohl, D.W., Donk, W., and Lanz, M. (1984) *Appl. Phys. Lett.*, **44**, 651.
- [51] Lieberman, K., Harush, S., Lewis, A., and Kopelman, R. (1990) *Science*, **247**, R59.
- [52] Reddick, R.C., Warmack, R.J., and Ferrell, T.L. (1989) *Phys. Rev. B*, **39**, 767.
- [53] Tsai, D.P., Othonos, A., Moskovits, M., and Uttamchandani, D. (1994) *Appl. Phys. Lett.*, **64**, 1768.
- [54] Paesler, M.A. and Hallen, H.D. (1995) *Appl. Phys. Lett.*, **67**, 2483.
- [55] Hayazawa, N., Inouye, Y., Sekkat, Z., and Kawata, S. (2001) *Chem. Phys. Lett.*, **335**, 369.
- [56] Hartschuh, A., Anderson, N., and Novotny, L. (2004) *Intl. J. Nanoscience*, **3**, 371.
- [57] Smith, D.A., Webster, S., Ayad, M. *et al.* (1995) *Ultramicroscopy*, **61**, 247.
- [58] Webster, S., Batchelder, D.N., and Smith, D.A. (1998) *Appl. Phys. Lett.*, **72**, 1478.
- [59] Yeo, B.-S., Stadler, J., Schmid, T. *et al.* (2009) *Chem. Phys. Lett.*, **472**, 1.

- [60] Kiefer, W. (Editor-in-Chief) (2009) *J. Raman Spectrosc.*, **40**, 1335–1457.
- [61] Wessel, J. (1985) *J. Opt. Soc. Am. B*, **2**, 1538.
- [62] StrÖckle, R.M., Suh, Y.D., Deckert, V., and Zenobi, R. (2000) *Chem. Phys. Lett.*, **318**, 131.
- [63] Anderson, M.S. (2000) *Appl. Phys. Lett.*, **76**, 3130.
- [64] Hayazawa, N., Inouye, Y., Sekkat, Z., and Kawata, S. (2000) *Opt. Commun.*, **183**, 333.
- [65] Yeo, B.-S., Schmid, T., Zhang, W., and Zenobi, R. (2007) *Anal. Bioanal. Chem.*, **387**, 2655.
- [66] Yeo, B.-S., Mädler, S., Schmid, T. *et al.* (2008) *J. Phys. Chem. C*, **112**, 4867.
- [67] Kudelski, A. (2008) *Talanta*, **76**, 1.
- [68] Yeo, B.-S., Stadler, J., Schmid, T. *et al.* (2009) *Chem. Phys. Lett.*, **472**, 1.
- [69] Steidtner, J. and Pettinger, B. (2008) *Phys. Rev. Lett.*, **100**, 236101.
- [70] Steidtner, J. and Pettinger, B. (2007) *Rev. Sci. Instrum.*, **78**, 103104.
- [71] Sackrow, M., Stanciu, C., Lieb, M.A., and Meixner, A.J. (2008) *ChemPhysChem*, **9**, 316.
- [72] Neugebauer, U., Schmid, U., Baumann, K. *et al.* (2007) *ChemPhysChem*, **8**, 124.
- [73] Yeo, B.-S., Zhang, W., Vannier, C., and Zenobi, R. (2006) *Appl. Spectrosc.*, **60**, 1142.
- [74] Hayazawa, N., Watanabe, H., Saito, Y., and Kawata, S. (2006) *J. Chem. Phys.*, **125**, 244705.
- [75] Kalkbrenner, T., Håkanson, U., and Sandoghdar, V. (2004) *Nano. Lett.*, **4**, 2309.
- [76] Kalkbrenner, T., Ramstein, M., Mlynek, J., and Sandoghdar, V. (2001) *J. Microsc.*, **202**, 72.
- [77] Noguez, C. (2007) *J. Phys. Chem. C*, **111**, 3806.
- [78] Zhang, W., Cuib, X., and Martin, O.J.F. (2009) *J. Raman Spectrosc.*, **40**, 1338.
- [79] Kneipp, K., Kneipp, H., Corio, P. *et al.* (2000) *Phys. Rev. Lett.*, **84**, 3470.
- [80] Anderson, N., Hartschuh, A., and Novotny, L. (2005) *Material Today*, **8**, 50.
- [81] Campion, A. and Kambhampati, P. (1998) *Chem. Soc. Rev.*, **27**, 241.
- [82] Otto, A. (1984) *Topics Appl. Phys.*, **54**, 289.
- [83] Boyd, R.W. (2008) *Nonlinear Optics*, 3rd edn, Academic Press, Burlington.
- [84] Woodbury, E.J. and Ng, W.K. (1962) *Proc. IRE.*, **50**, 2367.
- [85] Maker, P.D. and Terhune, R.W. (1965) *Phys. Rev. A*, **137**, 801.
- [86] Begley, R.F., Harveyt, A.B., and Byer, R.L. (1974) *Appl. Phys. Lett.*, **25**, 387.
- [87] Volkmer, A., Cheng, J.X., and Xie, X.S. (2001) *Phys. Rev. Lett.*, **023901**, 87.
- [88] Caster, A.G., Kowarik, S., Schwartzberg, A.M. *et al.* (2009) *J. Raman Spectrosc.*, **39**, 770.
- [89] Cheng, J.-X., Book, L.D., and Xie, X.S. (2001) *Optics Lett.*, **26**, 1341.
- [90] Cheng, J.X., Volkmer, A., Book, L.D., and Xie, X.S. (2001) *J. Phys. Chem. B*, **105**, 1277.
- [91] Marks, D.L. *et al.* (2004) *Appl. Phys. Lett.*, **85**, 5787.
- [92] Malarski, A., Beyrau, F., and Leipertz, A. (2005) *J. Raman Spectrosc.*, **36**, 102.
- [93] Lepetit, L., Cheriaux, G., and Joffre, M. (1995) *J. Opt. Soc. Am. B*, **12**, 2467.
- [94] Munhoz, F., Brustlein, S., Gachet, D. *et al.* (2009) *J. Raman Spectrosc.*, **39**, 775.
- [95] Peng, J., Pestov, D., Sculley, M.O., and Sokolov, A.V. (2009) *J. Raman Spectrosc.*, **39**, 795.
- [96] Duncan, M.D., Reintje, J., and Manuccia, T.J. (1982) *J. Optic Lett.*, **7**, 350.
- [97] Zumbusch, A., Holtom, G.R., and Xie, X.S. (1999) *Phys. Rev. Lett.*, **82**, 4142.
- [98] Woodbury, E.J. and Ng, W.K. (1962) *Proc. IRE*, **50**, 2367.
- [99] Mallick, B., Lakshmanan, A., Radhalakshmi, V., and Umapathy, S. (2008) *Current Scirnce*, **95**, 1551.
- [100] Weiner, A.M., Leaird, D.E., Wiederrecht, G.P., and Nelson, K.A. (1991) *J. Opt. Soc. Am. B*, **8**, 1264.
- [101] Weiner, A.M., Leaird, D.E., Wiederrecht, G.P., and Nelson, K.A. (1990) *Science*, **247**, 1317.
- [102] Bartels, R.A., Backus, S., Murnane, M.M., and Kapteyn, H.C. (2003) *Chem. Phys. Lett.*, **374**, 326.
- [103] Zhang, Shu-Lin (2008) *Raman Spetroscopy and Low-imensional Nano-semiconductors*, Science Press, Beijing.
- [104] Freudiger, C.W., Min, W., Saar, B.G. *et al.* (2008) *Science*, **332**, 1858.
- [105] Nandakumar, P., Kovalev, A., Volkmer, A. (2009) *New J. Phys.* 11 033026.

# 5

## Introduction to Modern Raman Spectroscopy II- New Raman Spectroscopic Branch Classified Based on Applied Objects

In traditional Raman spectroscopy, due to the restrictions of excited light intensity, the observation of objects is limited mainly to chemical molecules. In modern Raman spectroscopy, observations have expanded to all matter that is able to interact with light. In this chapter we will briefly introduce the various branches classified by objects studied by modern Raman spectroscopy.

### 5.1 Common Spectroscopic Basis Related to the Study and Application of Raman Spectroscopy

The objects studied by modern Raman spectroscopy fall into two categories: molecular bonds and elementary excitations mainly.

Compared with other kinds of spectra, the advantages of modern Raman spectra are excellent spectral features such as sharp spectral lines, which make the spectra easily distinguished and applied. Moreover, in contrast with other techniques, such as X-Ray diffraction and various electronic microscopes, samples used for modern Raman spectral measurements can be less than the order of  $\mu\text{g}$  in quantity, no special preparation is required, and studies can be carried out *in situ* without destroying the sample. Therefore Raman spectroscopic technique is a very effective one in the field of material study and application.

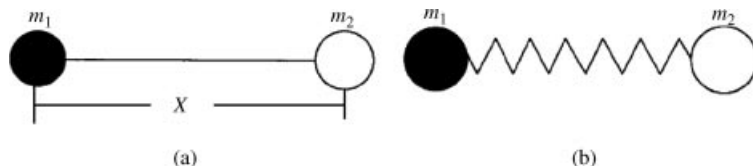


**Figure 5.1** Scheme of molecular structure (a), and spring model (b)

### 5.1.1 Raman Spectral Feature of Molecular Bonds

Besides chemical molecules, molecular bonds also exist in other fields, such as in biology, medicine, pharmacy, and environmental science and so on. Therefore, Raman spectral features of molecular bonds are the basis of study and application in many fields.

Figure 5.1a shows the structure of a simple molecule-double atomic molecule, where \$m\_1\$ and \$m\_2\$ are the atomic masses and \$x\$ is the distance between the atoms. The vibration energy of the bonds is related to the above parameters as well as the charges in objects. To describe bond vibrations, we use a model of a double atomic molecule and a vibrating spring, as shown in Figure 5.1b. It is well known that the energy of the vibrating spring at harmonic vibration can be expressed as

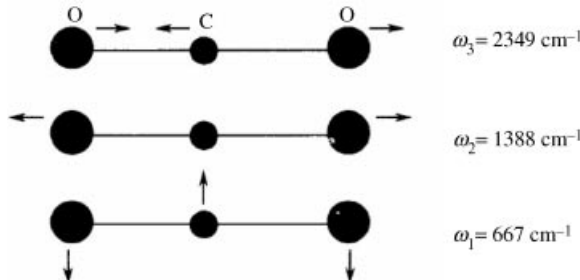
$$E = (1/2)\mu x^2 = \hbar\omega \quad (5.1)$$

where \$\mu = m\_1 m\_2 / (m\_1 + m\_2)\$ is the reduced mass of two atoms with masses \$m\_1\$ and \$m\_2\$; \$\hbar\$ is the Planck constant, and \$\omega\$ is the vibration frequency, of which \$\omega\$ represents the Raman frequency in Raman spectral measurements.

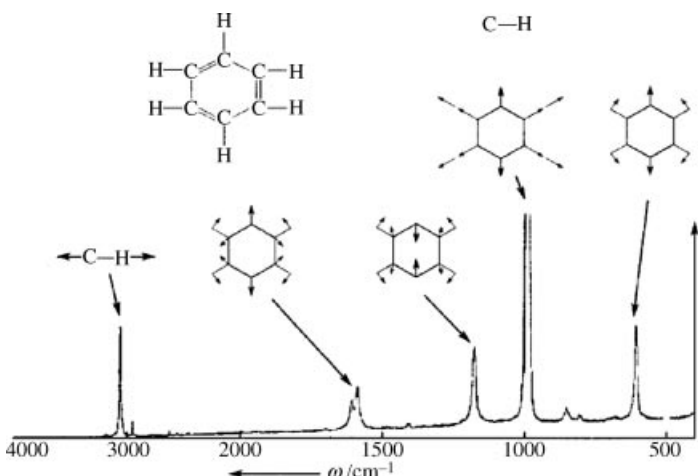
Figure 5.2 shows vibration models of a three-atom linear chain molecule consisting of O–C–O and corresponding Raman frequencies of different vibration modes, confirming that the Raman frequencies of O–C–O molecules vary for different vibration modes.

Figure 5.3 shows more complex chemical bonds and their Raman spectra, in which the vibration modes and corresponding frequencies of a single C–H bond and benzene ring by constitution of C–H bonds can be seen. In Table 5.1 the Raman vibration frequencies of some molecular groups in organic molecules and inorganic molecules are listed [1].

The above discussion indicates that the vibration frequency is related to the property of atoms or ions, their position in space, and their vibration modes. Therefore, the matter of



**Figure 5.2** Vibration modes of a three-atom linear chain molecule consisting of O–C–O and corresponding Raman frequencies of different vibration modes



**Figure 5.3** Dependence of vibration frequency on C–H bond and benzene ring consisting of C and H atoms

different components, microstructures, and inner atom or ion motion modes can produce Raman spectra with different characteristics, and vice versa. Thus Raman spectroscopy is an effect analysis and research tool for study at the molecular level.

### 5.1.2 Raman Spectral Features of Elementary Excitations

An elementary excitation is a kind of quasi-particle, which includes phonons, electrons, excitons, magnetons, spinons, polaritons, and so on. Raman spectra of elementary excitations are the basis of Raman spectroscopy of matter in a condensed state. The widest elementary excitation involved in Raman spectroscopy is the phonon, which will be used as a typical example of elementary excitations in the following discussion.

The phonon is a quasiparticle characterized by the quantization of the lattice vibrations of solids. The relation of phonon energy  $\hbar\omega$  with its momentum  $\hbar q$ , that is, the relation between frequency  $\omega$  and wavevector  $q$ , is called the dispersion relation. Moreover, due to the nature of its periodic structure, the spatial symmetry is a fundamental property, which plays a key role together with dispersion relations in solid Raman spectroscopy. The dispersion relation and symmetry of matter is the common basis of condensed matter Raman spectroscopy.

Since silicon and diamond possess the same crystal structure and symmetry, the dispersion curves are similar, as shown in Figures 5.4a and b. Thus their Raman spectra will have similar features but their frequencies will be different because of their different masses, as confirmed by Figure 5.4c.

Materials with different components and microstructures can possess huge differences in chemical, physical, and biological properties, for which accurate identification is necessary and important. The above discussion shows that the features of Raman spectra are related to the componential atoms or ions and their geometric structures, that is, microstructures including spatial distances and their position within molecules. Therefore, Raman spectroscopy is an important tool in material identification. In Table 5.1, Raman frequencies of some bonds/groups in molecules (a) and some phonons in crystals are listed.

**Table 5.1** Raman frequencies of some bonds and groups of molecules (a) and some phonon modes of crystals (b)

(a) Raman frequencies of some bonds and groups in molecules

Chemical bonds	Region of vibration frequency/cm <sup>-1</sup>
O—H	3730–3500
O—H (association)	3520–3100
N—H	3550–3420
N—H (association)	3500–3100
≡C—H	3310–3200
=C—H	3100–3000
—C—H	3000–2800
—S—H	2600–2550
C≡N	2255–2220
C≡C	2250–2100
C=O	1820–1680
C=C	1900–1500
C=N	1680–1610
N=N, aliphatic substituent	1580–1550
N=N, aromatic substituent	1440–1410
(C—)SO(—C)	1070–1020
C=S	1250–1000
(CH <sub>2</sub> )δ <sub>a</sub> (CH <sub>3</sub> )	1470–1400
δ <sub>s</sub> (CH <sub>3</sub> )	1380
CC, aromatics	1600, 1580, 1500, 1450, 1000
CC, alicyclics, and aliphatic chains	1300–600
O—O	900–845
S—S	550–430
Se—Se	330–290
C(aromatic)—S	1100–1080
C(aliphatic)—S	790–630
C—Cl	800–550
C—Br	700–500
C—I	660–480
δ <sub>s</sub> (CC), aliphatic chains	400–250
C <sub>n</sub> , n = 3 ... 12	
n > 12	2495/n
=CH <sub>2</sub>	3080±10 2975±10
 $\begin{array}{c}   \\ =\text{C}-\text{H} \end{array}$	 3020±10
 $\begin{array}{c}   \\ -\text{C}-\text{H} \\   \end{array}$	 2890
S—H	~2580
Si—H	~2240
C <sub>6</sub> H <sub>6</sub>	1625–1575 1520–1480
C=O (anhydride)	1860–1800 1800–1750
C=O (esters)	1760–1720
C=O (aldehydes)	1725–1715

**Table 5.1** (Continued)

## (a) Raman frequencies

Chemical bonds	Region of vibration frequency/cm <sup>-1</sup>
C=O (ketone)	1720–1705
C=O amide-type	1690–1650
C=O (1)R-CO-NH <sub>2</sub>	1630–1620
C=O (2) R-CO-NHR'	1680–1640
	1570–1530
C=O (3) R-CONR'R''	1650
C-O Saturated ethers	1150–1070 580–540
	1120–1010

## (b) Raman frequencies of some phonon modes in crystals

Phonon Modes	Raman Frequency (cm <sup>-1</sup> )				
	Rutile Structure				
	TiO <sub>2</sub>	MgF <sub>2</sub>	ZnF <sub>2</sub>	FeF <sub>2</sub>	MnF <sub>2</sub>
B <sub>1g</sub>	143	92	70	73	61
E <sub>g</sub>	447	295	253	257	247
A <sub>1g</sub>	612	410	350	340	341
B <sub>2g</sub>	826	515	522	496	476
Zincblende Structure					
Longitudinal mode	GaP	InP	GaAs	ZnS	ZnTe
	402	345	292	352	208
Transverse mode	367	304	269	271	177
Spiauterite Structure					
E <sub>1L</sub>	BeO	ZnO	CdS	ZnS	AgI
	1097	591	307	356	124
A <sub>1L</sub>	1081	579	305	356	124
E <sub>1T</sub>	722	413	243	280	106
A <sub>1T</sub>	678	380	234	280	112
E <sub>2,high</sub>	684	444	256	280	112
E <sub>2,low</sub>	338	101	43	55	17
Diamond Structure					
F <sub>2G</sub>	Si	Ge	Diamond		
	520	300	1333		
Flat Hexagonal Structure					
Graphite					
E <sub>2G2</sub>			1582		
E <sub>2G1</sub>			42		

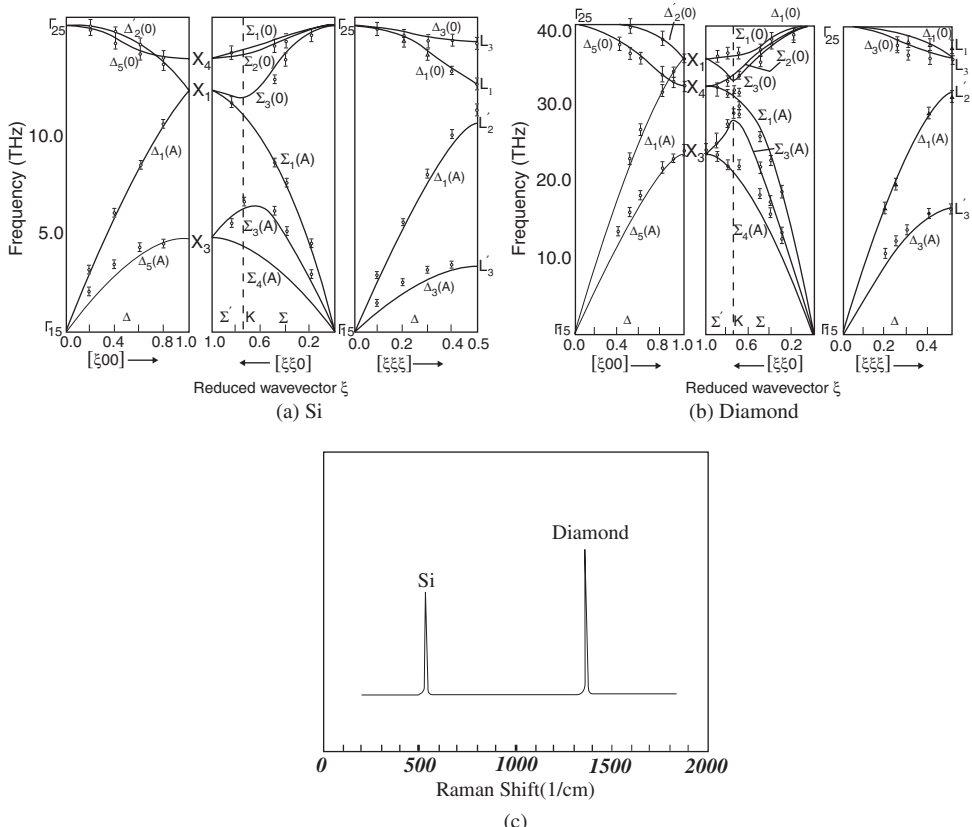


**Figure 5.4** Dispersion curves of (a) silicon, (b) diamond, and (c) Raman spectra of silicon and diamond [2]. Reprinted from W. Weber, Adiabatic bond charge model for the phonons in diamond, Si, Ge, and a-Sn, Phys. Rev. B, 15, 4789–4804 (1977) with permission of the American Physical Society

## 5.2 Chemistry Raman Spectroscopy

Chemistry Raman spectroscopy is related to chemical bonds, which were the subject of earliest studies in Raman spectroscopy and is still applied widely today.

Chemistry Raman spectroscopy is often applied in the identification of structures and properties of new synthetic inorganic and organic chemical materials. For example, at the end of the 1980s, a new type of liquid crystal lateral chain polymer poly-2,5-bis (p-methoxybenzoyloxy) styrene was synthesized [3]. This new liquid crystal polymer broke through the traditional theory, as a flexible spacer is necessary in a liquid crystal lateral chain polymer and thus is an innovative result [4]. Of course, the verification of molecular structure for this new liquid crystal was important and Raman spectra gave such verification. Figures 5.5a and b show the molecular structure of methoxy

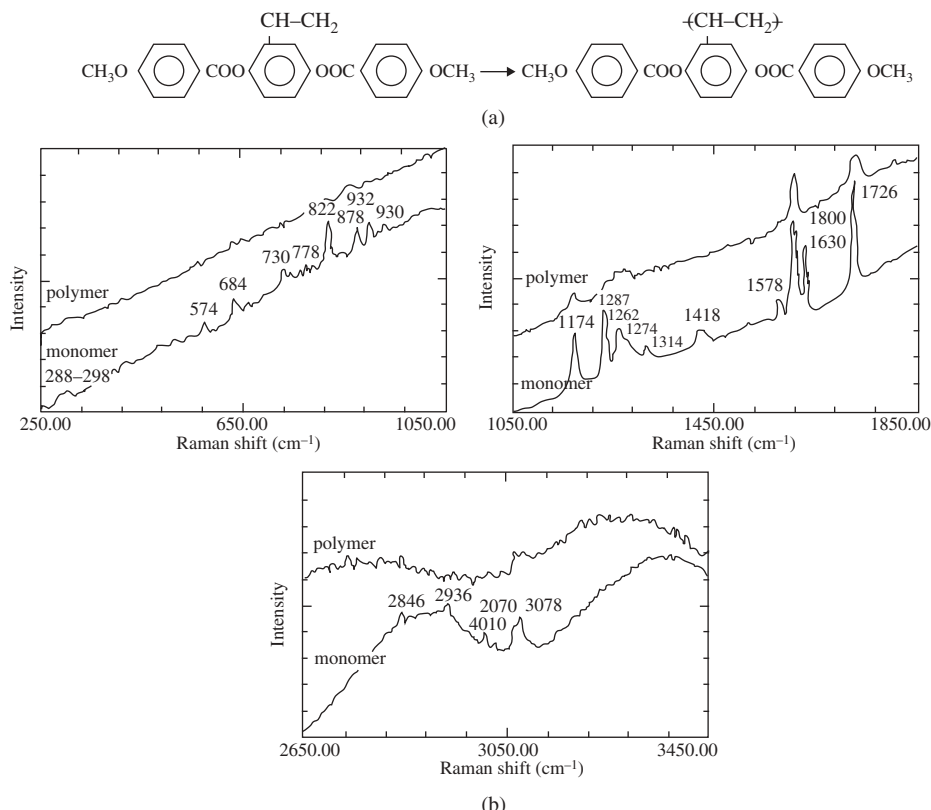


**Figure 5.5** (a) Molecular structure of methoxy chain-terminating-monomer- and poly-2,5-bis (p-methoxybenzoyloxy) styrene and their polymerization processes; (b) Raman spectra of a monomer and polymer [4]. Reprinted from S.-L. Zhang, W. Meng, Q.-F. Zhou, et al., *Acta Polymerica Sinica*, 3, 370 (1991)

chain-terminating-monomer- and poly-2,5-bis (p-methoxybenzoyloxy) styrene and its polymerization process and the Raman spectra of monomer and polymer, respectively.

The analysis shown in Figure 5.5 found that the characteristic Raman spectra of the vinyl group in the monomer changed more in the polymer, especially for the Raman line corresponding to the C=C bonds of the vinyl group, which disappeared completely in the polymer. In contrast, the Raman spectra of the rest of the group did not present any substantial differences between the monomer and the polymer. These experimental facts showed that the vinyl group of the monomer was transferred to the polymeric backbone, while the chemical structure of the mesogenic unit in the monomer remained after polymerization. The above Raman spectral results confirm the success of the synthesis of a liquid crystal side chain polymer, without a flexible spacer between the mesomorphic unit and the molecular main chain.

## 5.3 Condensed Matter Raman Spectroscopy

Condensed matter is any material with a condensed state phase structure, which appears whenever the number of constituents in a system is extremely large and the interactions between the constituents are strong. The most familiar condensed forms of matter are solids and liquids. Many biological systems exist in a liquid form but are not classified as condensed matters in our discussion here.

The Raman spectral research on solids is the earliest and widest used since the emergence of modern Raman spectroscopy. The example of the first laser Raman spectrum was a ruby crystal [5]. Since then, semiconductors have been the most studied and applied objects in condensed matter Raman spectroscopy. To date, almost all elementary excitations in bulk and nanoscale semiconductors, such as electrons, photons, phonons, holes, excitons, magnons, spinons, polaritons, polaron, plasmon, and so on have been investigated.

Raman spectroscopic studies have involved many properties of condensed matter, of which some results will be introduced below.

### 5.3.1 Microstructure and Symmetry

The microstructure of solids has the spatial arrangement of atoms or ions in solids. The order of the arrangement of the atoms and ions in the long range of lattices possesses some particle properties, such as spatial symmetry, long range order, and crystallization. In contrast, if the arrangement is disordered, the matter is non-symmetrical, with long range disorder and so is amorphous. Section 2.2.4 mentioned that the microstructures and vibration modes with the same symmetry will have similar Raman spectral features. Therefore Raman spectroscopy can play an important role in identification of solid structures and their symmetry.

Diamond and graphite are both constructed of carbon atoms, while their microstructure and symmetry are different, belonging to diamond and hexagonal structures, respectively, as shown in Figure 5.6. Differences in microstructure will result in a huge difference in physical and chemical properties, for example, diamond processes great rigidity and chemical stability, while graphite does not. Moreover, their Raman spectral features are different, as shown in Figure 5.6b. The Raman features of diamond and graphite are also very different, with Raman peaks of diamond and graphite at 1332 and  $1580\text{ cm}^{-1}$ , respectively. The identification of the structural phase for carbon materials is important, in which Raman spectrum can reliably identify diamond from other carbon materials. In fact, the Raman spectral method has become the most authorized criterion in precious stone identification.

### 5.3.2 Phase Transition

The change of external conditions, such as temperature, pressure, electric field, and magnetic field, can cause microstructure change in matter, that is, so-called “phase transition” appears. Raman spectroscopy is an important method for studying phase transition. For instance, although sharing the same component silicon, crystal and amorphous silicon have totally different microstructures with long- and short- range orders, respectively. Figure 5.7 shows the characteristic Raman spectra of crystalline and amorphous silicon, which shows that the difference of spectral features is obvious from the position or width of the Raman peaks. Thus Raman spectroscopy has become an important identification method in the preparation and study of silicon materials.

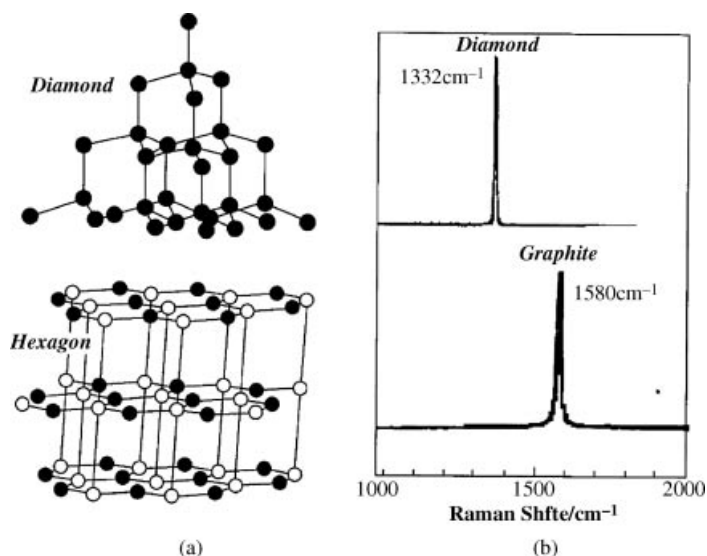


**Figure 5.6** Diamond and hexagonal crystal structures (a) and Raman spectra of diamond and graphite

In the past, most studies of the ferroelectric phase transition of KDP were performed by Raman spectroscopy. Before the use of this method, researchers adopted the proton kinetics mechanism (proton tunneling) to explain the ferroelectric phase transition of KDP. In 1968, a ferroelectric soft mode in the low frequency Raman spectral region of  $\leq 150\text{ cm}^{-1}$  was observed. In the early 1980s, more Raman spectral results confirmed that the KDP ferroelectric phase transition is originated from the order-disorder mechanism of the distortional tetrahedron of  $\text{PO}_4$  rather than the proton kinetics mechanism. Above the temperature of phase transition,  $T_c$ , the Raman modes  $\leq 150\text{ cm}^{-1}$  observed in the  $X(Y, X)Y$  configuration is the release mode of local distortional tetrahedron of  $\text{PO}_4$  rather than the proton-lattice ferroelectric soft mode. Figure 5.8 shows a Raman spectra obtained in a

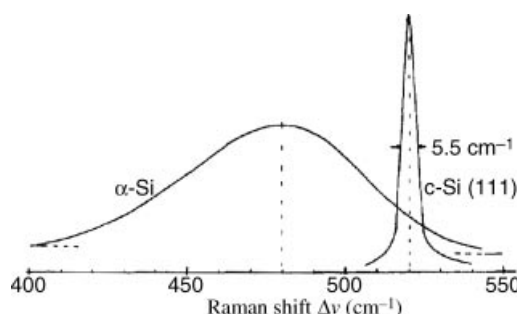


**Figure 5.7** Raman spectra of crystalline (c-Si) and amorphous (a-Si) [6]. Reprinted from S. Vepiek, et al., Properties of polycrystalline silicon prepared by chemical transport in hydrogen plasma at temperatures between 80 and 400 degrees, *J. Phys. C: Solid State Phys.*, 14, 295 (1981) with permission of the Institute of Physics

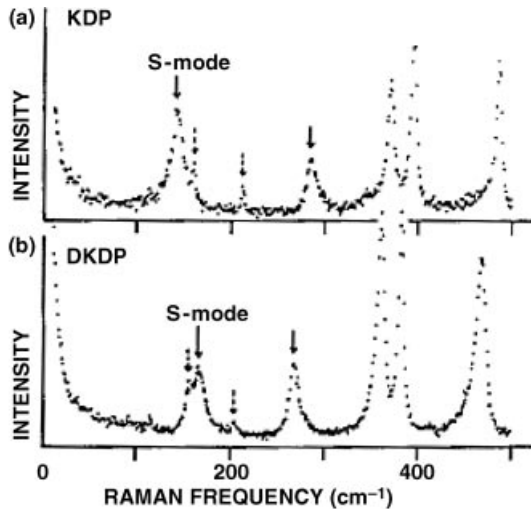


**Figure 5.8** Raman spectra obtained under the  $Z(X, Y)\bar{Z}$  geometric configuration for  $\text{KH}_2\text{PO}_4$  at  $T = 100.0\text{K}$  (a) and  $\text{KD}_2\text{PO}_4$  at  $T = 213.6\text{ K}$ , respectively [7]. Reprinted from Y. Tominaga, Proceedings of the IXth International Conference on Raman Spectroscopy, Tokyo Japan, August 27-September 1, 1984

ferroelectric phase transition study under the  $Z(X, Y)\bar{Z}$  geometric configuration and at below  $T_c$ . In Figures 5.8a and b, the Raman spectra of  $\text{KH}_2\text{PO}_4$  are at  $T = 100.0\text{ K}$  and  $\text{KD}_2\text{PO}_4$  at  $T = 213.6\text{ K}$ , respectively.

Section 5.1 indicated that Raman spectral features such as frequency and linewidth are correlated with component, structure, and physical and chemical parameters. Therefore it is natural that the physical parameters of objects can be extracted by Raman spectra.

$\text{NiSi}$  is a new material used in CMOS devices, but at high temperatures will transfer into the  $\text{NiSi}_2$  phase with a higher resistivity, which means it cannot be used in devices. With improved procedures of temperature stability of  $\text{NiSi}$ , Shao *et al.* [8] found that by using Raman spectra, as shown in Figure 5.9, the  $\text{Ni}/\text{Zr}/\text{Ni}/\text{Si}$  structure involving the metal  $\text{Zr}$  can raise the transition temperature of  $\text{NiSi}$  ( $650^\circ\text{C}$ ) to that of  $\text{NiSi}_2$  (above  $800^\circ\text{C}$ ), extending the stable temperature region of the  $\text{NiSi}$  sheet. However, the  $\text{Ni}/\text{Co}/\text{Ni}/\text{Si}$  structure containing the metal  $\text{Co}$  does not improve the temperature stability of the  $\text{NiSi}$  sheet. Therefore it was verified that the  $\text{Ni}/\text{Zr}/\text{Ni}/\text{Si}$  structure formed by doping  $\text{Zr}$ , instead of the more expensive noble metal  $\text{Pt}$  in  $\text{NiSi}$ , can improve the temperature stability from  $600^\circ\text{C}$  to more than  $800^\circ\text{C}$  under original low resistance, making it possible to use the new material in device technology.

### 5.3.3 Physical Parameters

The different physical parameters of materials result in different Raman spectral features. For example, the stress caused by lattice mismatch, impurities, and defects and so on will usually result in a shift of Raman frequency. Therefore Raman spectra can be used to measure these physical parameters.

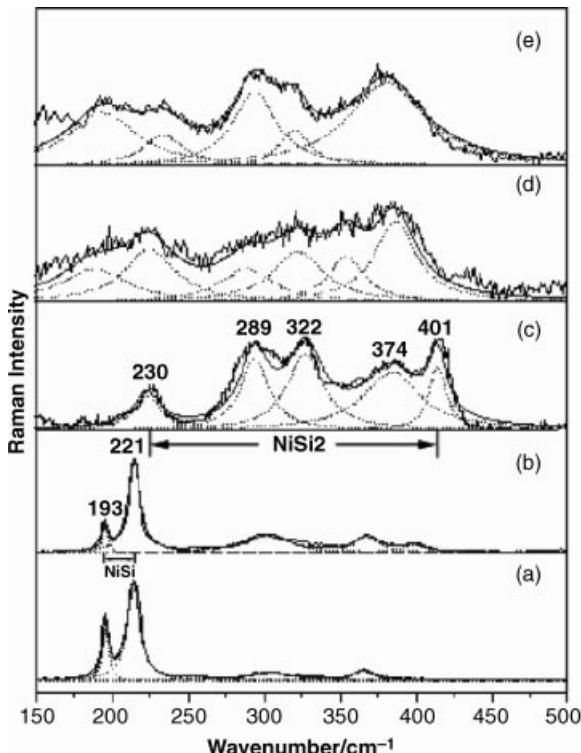


**Figure 5.9** Observed (solid line) and fitted (dashed line) Raman spectra of samples Ni/Zr/Ni/Si/650 (a) Ni/Zr/Ni/Si/800, (b) Ni/Zr/Ni/Si/850, (c) Ni/Co/Ni/Si/650, (d) Ni/Co/Ni/Si/800, (e) excited at 633-nm laser [8]. Reprinted from J. Shao, et al., Raman spectral study on the thermal stability of Ni/Zr/Ni/Si and Ni/Co/Ni/Si structures, *J. Raman Spectrosc.*, 37, 951 (2006)

In physical parameters, the local stress and microstress in semiconductor materials and microelectronic devices are hard to measure using traditional techniques but it is easier with Raman microscope. For example, chemical vapor deposited  $\text{Si}_3\text{N}_4$  films on silicon substrates in devices has an intrinsic tensile stress of about  $9.23 \times 10^8 \text{ N/m}$ . These films are known to introduce large stresses in the silicon substrate, especially at the film edges. Through the variation of the Raman frequency of silicon as a function of the position on the sample, the local stress distribution over the whole location can be obtained. Figure 5.10 shows a Raman shift  $\Delta\omega$  and corresponding stress  $\sigma'_{11}$  (assuming uniaxial stress along the  $x'$  axis) in silicon near and beneath a 9.4-mm-wide  $\text{Si}_3\text{N}_4/\text{poly-Si}$  line. The stress is obtained by using two analytical stress models: uniaxial stress and planar stress.

Understanding microscale stress characterization of integrated circuits and micro-electromechanical system (MEMS) structures is essential for the successful design and operation of such devices. Wu *et al.* measured the Raman spectra at fixed point A of a single-crystal silicon cantilever in the straining process, and the result is shown in Figure 5.11. The linear fitting result is also plotted in Figure 5.2. The slope of the fitted line is  $-0.002163$ , so accordingly the coefficient  $C_{\text{Si}}$  is  $-462$ , which is close to the theoretical value  $-434$ . Therefore, value  $-434$

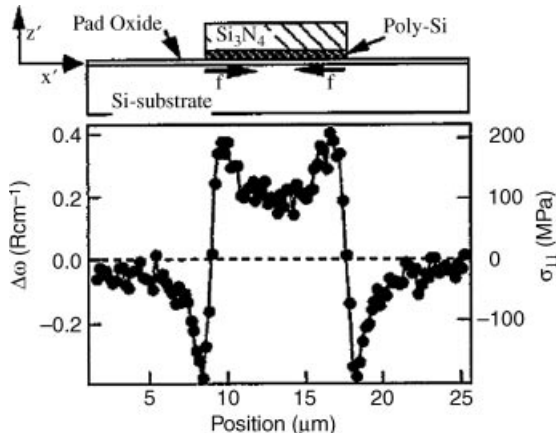


**Figure 5.10** Raman shift  $\Delta\omega$  and corresponding stress  $\sigma'_{11}$  (assuming uniaxial stress along the  $x'$  axis) in silicon near and beneath a 9.4-mm-wide  $\text{Si}_3\text{N}_4/\text{poly-Si}$  line. A example is shown at the top of the figure [9]. Reprinted from I. De Wolf, H. E. Maes, and S. K. Jones, Stress measurements in silicon devices through Raman spectroscopy: Bridging the gap between theory and experiment, *J. Appl. Phys.* 79, 148 (1996) with permission of the American Institute of Physics

was used in the succeeding measurements [3], using Raman spectroscopy to measure the stress in single-crystal silicon and the result is shown in Figure 5.11. The figure shows the experimental relation between Raman frequency and stress of single-crystal silicon.

### 5.3.4 Low-Dimensional and Nanoscale Structures

The development of Raman spectral techniques that are described in Chapters 3 and 4 makes Raman spectroscopy a standard tool for the characterization and study of low-dimensional

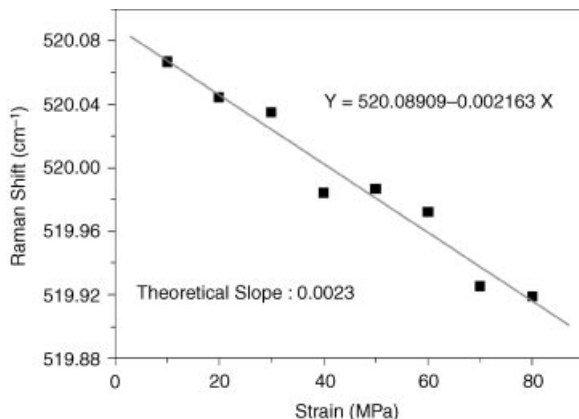


**Figure 5.11** Raman spectroscopy measurement of strained single-crystal silicon cantilever [10]. Reprinted from X. Wu, J. Yue, T. Rena, L. Liu, Micro-Raman spectroscopy measurement of stress in silicon, *Microelectronics Journal*, 38, 87 (2007) with permission John Wiley and Sons

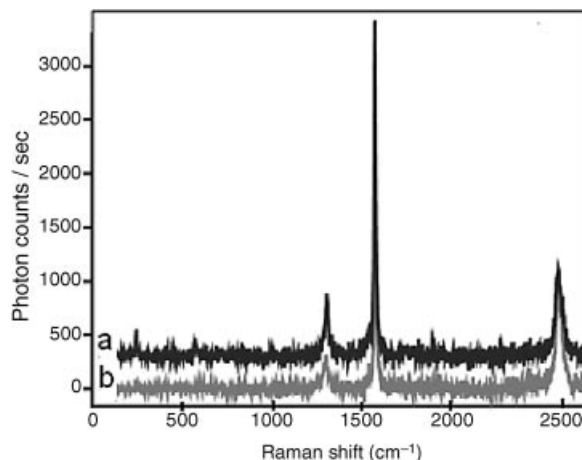


**Figure 5.12** TERS spectra of an individual SWNT with (a) and without (b) a sharp Au tip present for an acquisition time of 210 ms (graph offset for clarity) [11]. Reprinted from N. Anderson, A. Hartschuh, and L. Novotny, Near-field Raman spectroscopy, *Materials Today*, 50 (2005) with permission of John Wiley and Sons

and nanoscale structures and has obtained many achievements, which will be described in Part II of this book. Here are listed some examples to show the detected ability of Raman spectra for low-dimensional and nanoscale structures.

For example, TERS spectra of an isolated single wall carbon nanotube (SWNT) have been measured, as shown in Figure 5.12, of which the typical enhancement factors are in the order of  $10^3$ – $10^4$ .

Moreover, NF Raman spectroscopy has been used to study SWNTs within dense samples. Figure 5.13 shows a NFRS investigation compared with far-field Raman spectra for an SWNT sample (see color Plate 13 for the original Figure 5.13).

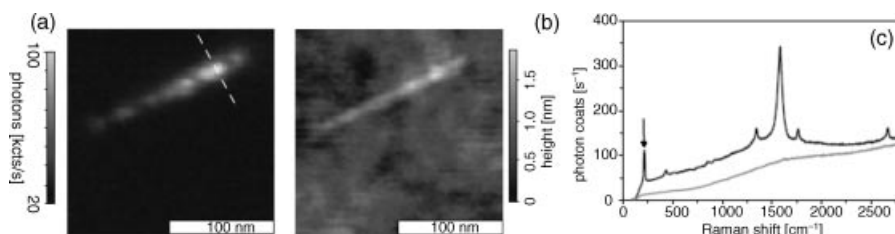


**Figure 5.13** (a) NF Raman image from G band of carbon, (b) topographic image, (c) near-field Raman spectrum detected on top of the SWNT at the position marked in (a) (NF (black line) and far-field (blue line)) [12]. Fig 4 in A. Hartschuh, N. Anderson, and L. Novotny, Near-Field Raman Spectroscopy of Individual Single-walled Carbon Nanotubes, *Intl. J. Nanoscience*, 3, 371 (2004) with permission of the World Scientific Publishing Company

## 5.4 Biological and Medical Raman Spectroscopy

The main advantage of Raman spectroscopy applied in biological and medical samples is its ability to obtain spectra of aqueous samples, because Raman signals of water are weak. Especially, the emergence of modern Raman spectroscopy has meant that biological and medical Raman spectroscopy has become one of the main branches.

As in all scientific studies, the basic research is also very important in biological and medical Raman spectroscopy. This includes two aspects, one is the characteristic spectra of biosome and another is theoretical models related to biological systems and structures. Basic research by Raman spectroscopy has been applied to include various objects existing in organisms related to medicine. Such objects in a biological organism mainly include molecules and tissues, such as protein, lipid, nucleic acid (DNA/RNA), DNA strands, collagen, carotenoids, calcium phosphate, and cholesterol. Raman spectroscopy has covered objects related to medicine, such as eye lenses, cataracts, hemoglobin, breast tissue and cancer, gallstones and kidney stones, brain tissue and brain tumors, lung tissue, lymph nodes, atherosclerosis, sclerosis and arteries, oncogenes, germs, viruses, bacteria and cells.

Before 1995, research results of biological and medical Raman spectroscopy have been summarized in the literature [13–15]. Since then, accompanied with many new developments in modern Raman spectroscopic techniques, many significant results in biological and medical Raman spectroscopy have been published. These cover many aspects, such as cancer identification (oral, skin, breast, cervical, colorectal); *in vivo* studies of skin, bone transdermal drug transfer, bone (composition, mechanics, and disease), soft dental tissue, teeth, intravascular atherosclerosis; studies of the eye (lens, fluids) and the structure, dynamics, and functions of drugs. Recently, some new summaries were published [16–18] but in this chapter we only introduce some results of biological and medical Raman spectroscopy on a sample.

### 5.4.1 Sample Preparation

Good sample preparation and special measuring equipment are important for biological and medical Raman spectral measurement.

Figure 5.14 shows sample preparation technology for a DNA SERS measurement. Before and after silver nanoparticles of coding functional DNA are linked to aggregate, a strong SERS signal is not obtained and is obtained, respectively [19].

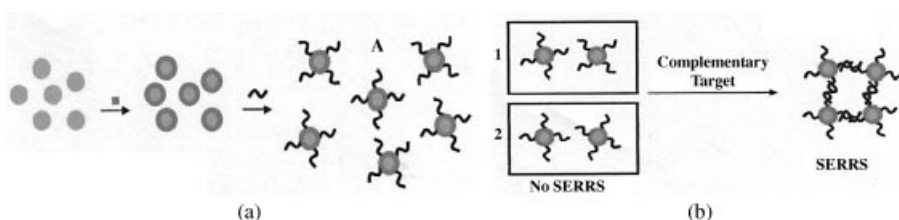


**Figure 5.14** A sample preparation technology for DNA SERS measurement. Silver nanoparticles of coding functional DNA not linked (a) and linked (b) to aggregate [19]. Reprinted from D. Graham, K. Flanlds, E. Smith, New approaches to misanalysis using nanoparticles and SERRS, Proceeding of ICORS, Eds: R. Withnall and B. Chowdhry, 17th–22nd August, 2008

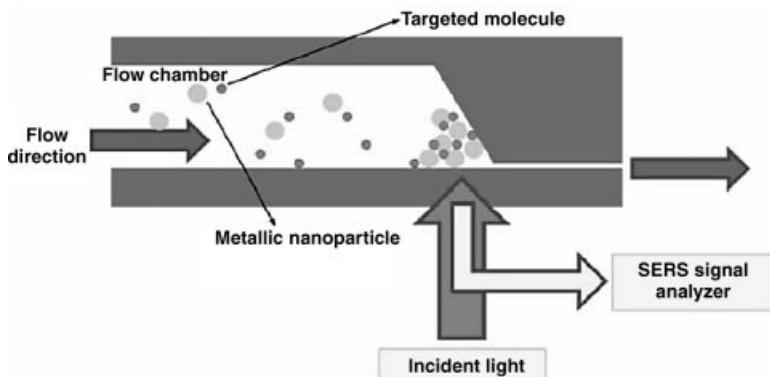


**Figure 5.15** Diagram of an optofluidic device with aggregated nanoparticle-SERS active clusters at the step structure [17]. Reprinted from A. Q. Liu, et al., Label-free detection with micro optical fluidic systems (MOFS), *Anal Bioanal Chem*, 391, 2443 (2008) with permission of Springer

Liu *et al.* [17] studied a micro-optical fluidic system, as shown in Figure 5.15. The depth of the nanochannel is smaller than the size of the nanoparticles. Thus nanoparticles are trapped and aggregated. The equipment provides an SERS measured platform for different cellular biophysics, such as cell mass detection, cell Young's modulus and so on.

A Raman spectral measurement setup of a single nucleotide was suggested by the Kneipp group. Figure 5.16 illustrates the idea of such rapid sequence bases upon surface-enhanced RS from a single DNA bases. Single nucleotides are cleaved and attached to colloidal silver or gold clusters, which flow through the laser focus and are detected in order of cleavage.

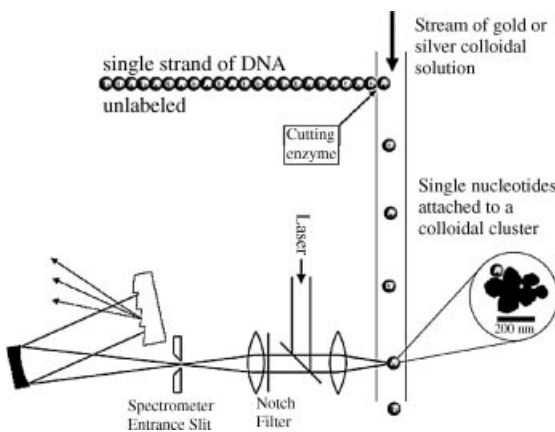


**Figure 5.16** An ideal Raman spectroscopy measurement setup of a single nucleotide [20]. Reprinted from K. Kneipp, et al., Surface-enhanced Raman scattering and biophysics J. Phys.: Condens. 14, R597 (2002) with permission of the Institute of Physics

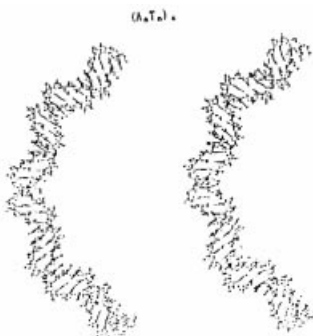


**Figure 5.17** Molecular structure of abnormal DNA extracted from Raman spectrum [21]. Reprinted from G. A. Thomas and W. L. Peticolas, Fluctuations in Nucleic Acid Conformations. 2. Raman Spectroscopic Evidence of Varying Ring Pucker in A-T Polynucleotides, *J. Am. Chem. Soc.*, 105, 993 (1983) with permission of the American Chemical Society

#### 5.4.2 Raman Spectra of Organic Molecules and Tissues

The extraction of an abnormal form of DNA molecular structure in a typical sample can be observed with Raman spectrum combining molecular model calculations. At the start of the 1980s, through an experimental Raman spectral study combined with theoretical calculations for curved DNA and DNA with pyrimidine and B/I, Thomas and Peticolas extracted its molecular structure, as shown in Figure 5.17.

Raman microscope has been applied to biological samples from earliest times. Figure 5.18 show the vibration Raman spectra by a Raman microscope for a single photoreceptor cells frozen at 77 k.

During the development of new Raman spectral technology, such as NFRS, TERS, and CARS, the measurements of DNA molecules were important [23,24]. For example, in 2007, Domke *et al.* [24] published a TERS spectra of DNA bases adsorbed at Au(111), as shown in Figure 5.19 (see color Plate 14 for the original Figure 5.19). The figure shows the spectra of sub-monolayers of the four DNA bases, adenine, guanine, thymine, and cytosine, adsorbed homogeneously at Au(111) in picomole quantities shown respectively. The purine and pyrimidine bases of the nucleic acids are absorbed at wavelengths shorter than 280 nm.

Since the local analysis by TERS is easy to perform, DNA/RNA sequencing and single RNA strands have been investigated by TERS and the results indicate that it is distinguishable in spectroscopy [25–27]. Figure 5.20 shows an AFM topography image (a) and TERS spectra (b) of single RNA strands where eight spots in (a) show the positions where the TERS measurements were made (see color Plate 15 for the original Figure 5.20).

The TERS spectrum of a single tobacco mosaic virus particle has been published [28] and Figure 5.21 shows the result of this investigation where (A) is the AFM image of the investigated virus particle and (B) is the TERS spectra excited by a 568.2 nm laser of the virus particle recorded at various positions (see color Plate 16 for the original Figure 5.21).

Since the spectrum of individual bases can be measured as the TERS tip moves along the biopolymer, the TERS can be used to sequence DNA or RNA [26]. Alginate films, which are used to model the extracellular polymeric substances of biofilms as well as other biological samples, were also studied recently by TERS [28].

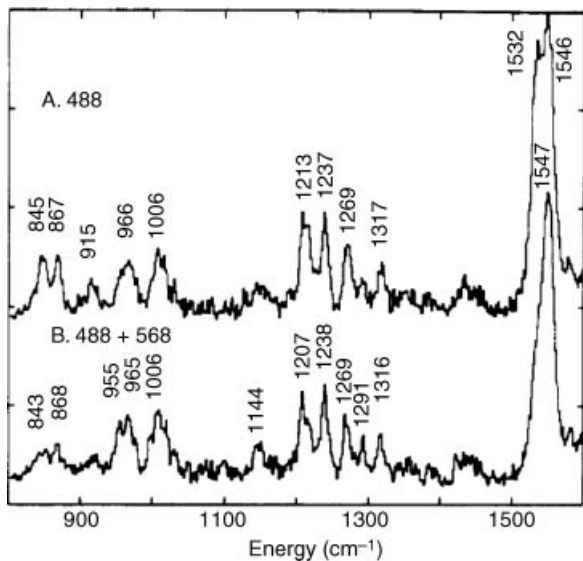


**Figure 5.18** Raman microscope spectra of 500-nm angelfish rods. Spectrum A was taken with a 488-nm probe. Spectrum B was recorded at 488 nm with the addition of a coaxial 568-nm pump [22]. Reprinted from B. Barry and R. Mathies, Biochemistry, Raman Microscope Studies on the Primary Photochemistry of Vertebrate Visual Pigments with Absorption Maxima from 430 to 502 nm, *Biochemistry*, 26, 59 (1987) with permission of the American Chemical Society

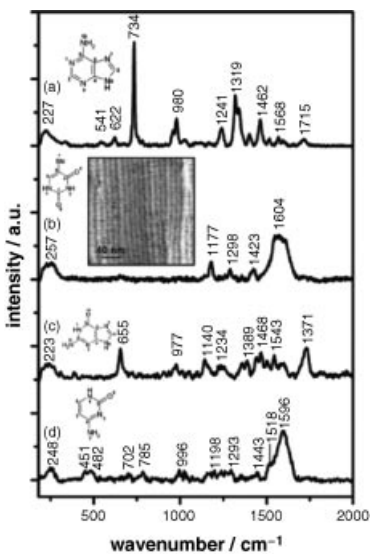


**Figure 5.19** TERS spectra (background-corrected) of DNA bases adsorbed at Au(111): (a) adenine; (b) thymine; (c) guanine; (d) cytosine; normalized to 1 s integration time at 2 mW incident power. Inset shows an example of an STM image of a thymine self-assembled monolayer of Au(111) recorded after 12 h adsorption with an Au probe [24]. Reprinted from K. Domke, D. Zhang, and B. Pettinger, Tip-Enhanced Raman Spectra of Picomole Quantities of DNA Nucleobases at Au(111), *J. Am. Chem. Soc.* 129, 6708 (2007) with permission of the American Chemical Society

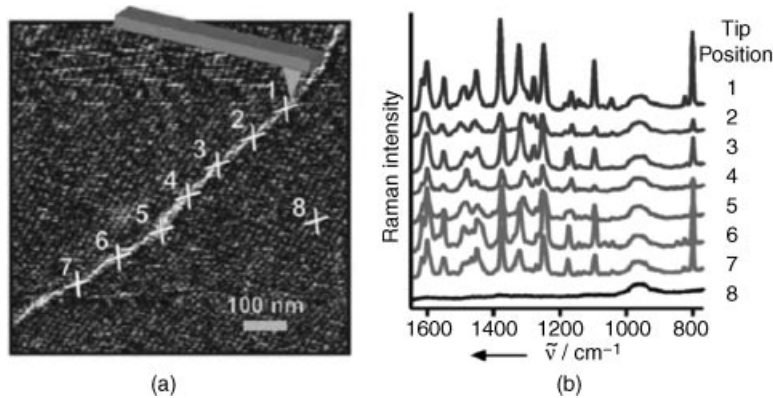


**Figure 5.20** AFM topography image (a) and TERS spectra (b) of a polycytosine homopolymer. Eight spots are shown corresponding to the positions where TERS measurements were taken. (b) The TERS spectra taken at the eight positions [27]. Reprinted from Elena Bailo and Volker Deckert, Tip-Enhanced Raman Spectroscopy of Single RNA Strands: Towards a Novel Direct-Sequencing Method, *Angew. Chem. Int. Ed.*, 47, 1658 (2008) with permission of John Wiley and Sons

Concerning SERS investigation of biological samples, Figure 5.22a shows an image of the dark field reflection mode of living Tu686 cells and H520 cells marked with ScFv-conjugated gold nanoparticles. Figure 5.22b is a SERS spectra of single cells shown by the arrow and associated surface polaron image of single cancer cells [29].

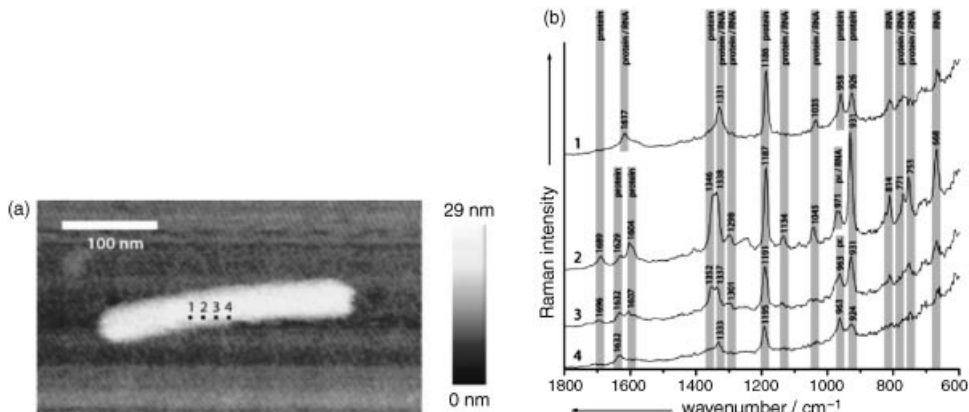


**Figure 5.21** TERS investigations of a single tobacco mosaic virus particle. (a) AFM image of the investigated virus particle. The positions of the TERS tip in respect to the virus particle are marked. (b) The TERS spectra of the virus particle recorded at various positions [28]. Reprinted from D. Cialla, T. Deckert-Gaudig, C. Budich, et al., Raman to the limit: tip-enhanced Raman spectroscopic investigations of a single tobacкомosaic virus, *Journal of Raman Spectroscopy*, 40, 240 (2009) with permission of John Wiley and Sons

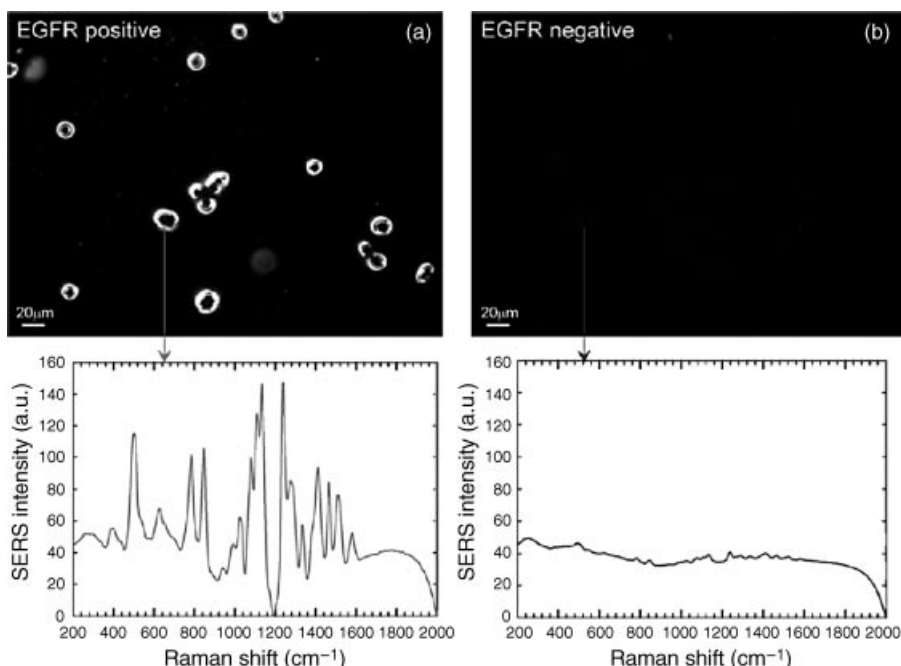


**Figure 5.22** Image of dark field reflection mode of living Tu686 cells and H520 cells marked with ScFv-conjugated gold nanoparticles; SERS spectra of single cells showed by the arrow [29]. Reprinted from X.-M. Qian and S. M. Nie, Single-molecule and single-nanoparticle SERS: from fundamental mechanisms to biomedical applications, *Chem. Soc. Rev.*, 37, 912 (2008) with permission of the Royal Society of Chemistry

The observation of live and single biological cell was long awaited. In 1999, it was realized by the Xie group, first by CARS and then by SRS [30,31]. Figure 5.23 shows the SRL images of unstained human HL60 cells in an aqueous environment. (see color Plate 17 for the original Figure 5.23).

#### 5.4.3 Raman Spectra of Dynamic Process of Biomedical Objects

Raman spectral research of dynamic processes and properties of biomedical samples are related to the application of Raman spectroscopy, especially in medical applications such as diagnostics, monitoring, and treatment of disease.

In 1983, Ozaki *et al.* reported *in situ* Raman spectral research on age-related structural changes in the lens proteins of a normal mouse lens, as shown in Figure 5.24. The figure shows that the Raman spectrum of an ICR-strain mouse lens nucleus showed virtually no change in the 550–850 and 900–1800 cm<sup>-1</sup> regions as the mouse aged.

As shown in Figure 5.25, the Nie group reported a SERS investigation of *in vivo* cancer targeting (see color Plate 18 for the original Figure 5.25). The photographs show a laser beam focusing on the tumor site and on the location of the liver (top), and Raman spectra obtained from the tumor and the liver locations by using (a) targeted and (b) non-targeted nanoparticles (lower).

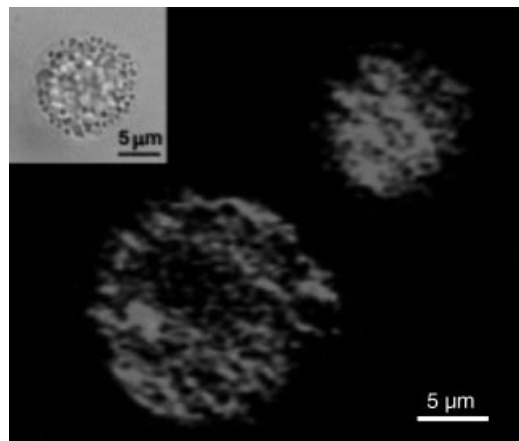


**Figure 5.23** SRL images of unstained human HL60 cells in an aqueous environment. The size of the image is  $38.3\text{ }\mu\text{m} \times 33.6\text{ }\mu\text{m}$  ( $200 \times 170$  pixels). The pump and Stokes beams were at 746.5 and 852 nm with powers of 7.5 and 30 mW, respectively. The corresponding Raman shift was  $1659\text{ cm}^{-1}$  on resonance with the C=C stretching vibrations. The image pixel dwell time was 10 ms [31]. Reprinted from P. Nandakumar, A. Kovalev and A. Volkmer, Vibrational imaging based on stimulated Raman scattering microscopy, *New J. Phys.* 11, 033-026 (2009) with permission of the Institute of Physics

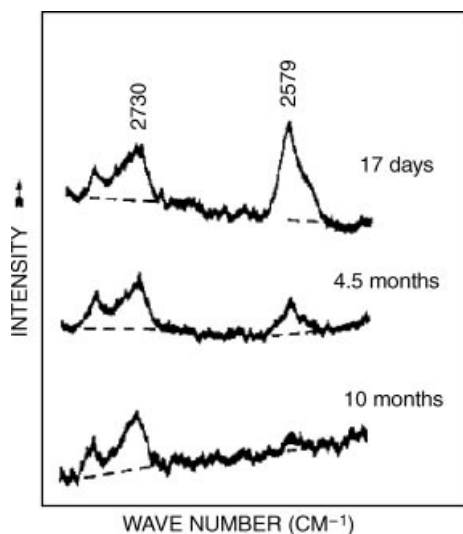


**Figure 5.24** Raman spectra in the region of  $2500\text{--}2800\text{ cm}^{-1}$  of ICR-strain mouse lens nuclei (17 days and 4.5 and 10 months old) [32]. Reprinted from Y. Ozaki, et al., Structural changes in the lens proteins of hereditary cataracts monitored by Raman spectroscopy, *Biochemistry*, 22, 6254 (1983) with permission of the American Chemical Society

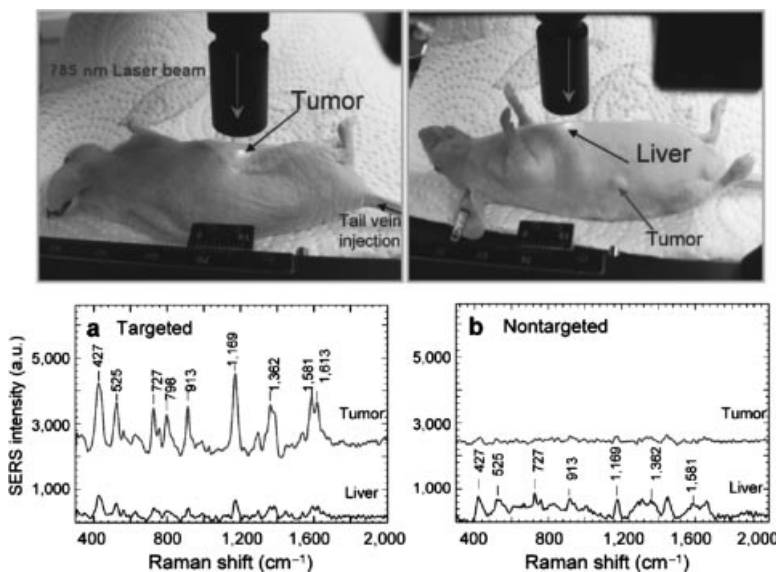


**Figure 5.25** *In vivo* cancer targeting and surface-enhanced Raman spectra. Top: Photographs of a laser beam focused to the tumor site or to the anatomical location of liver. Lower: Raman spectra obtained from the tumor and the liver locations by using (a) targeted and (b) non-targeted nanoparticles [29]. Reprinted from X.-M. Qian, et al., *In vivo: tumor targeting and spectroscopic detection with surface-enhanced Raman nanoparticle tags*, *Nat. Biotechnol.*, 26, 83 (2008) with permission of Nature Publishing Group

Because of the high density of  $\text{CH}_2$  oscillators in lipids, exceptionally high CARS signals are obtained from lipid-containing specimens. When dynamics on the seconds to minutes timescale are relevant to the imaging application, the much higher scanning speed of CARS makes it the chosen method. For example, CARS imaging has been used for high-speed, selective imaging of neutral lipid droplets (LDs) in unstained live fibroblast cells, for the understanding of dynamic distribution of lipid droplets in cell cultures. Figure 5.26 shows one of such results. The images are the polarized CARS (P-CARS) images taken on 3T3-L1

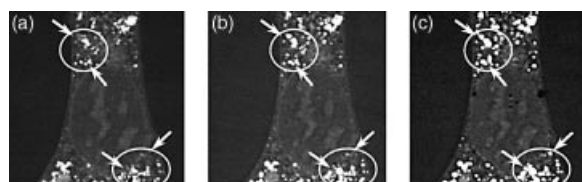


**Figure 5.26** P-CARS images of 3T3-L1 cells at different stages of differentiation, (A) 0 h (growth stage), (B) 48 h, and (C) 192 h, after adding the induction media. All the images were taken at  $2845\text{ cm}^{-1}$  [33]. Reprinted from J.-X. Cheng, E. O. Potma, X. S. Xie, Coherent anti-Stokes Raman scattering correlation spectroscopy: probing dynamical processes with chemical selectivity, *J. Phys. Chem. A* 106, 8561 (2002) with permission of the American Chemical Society

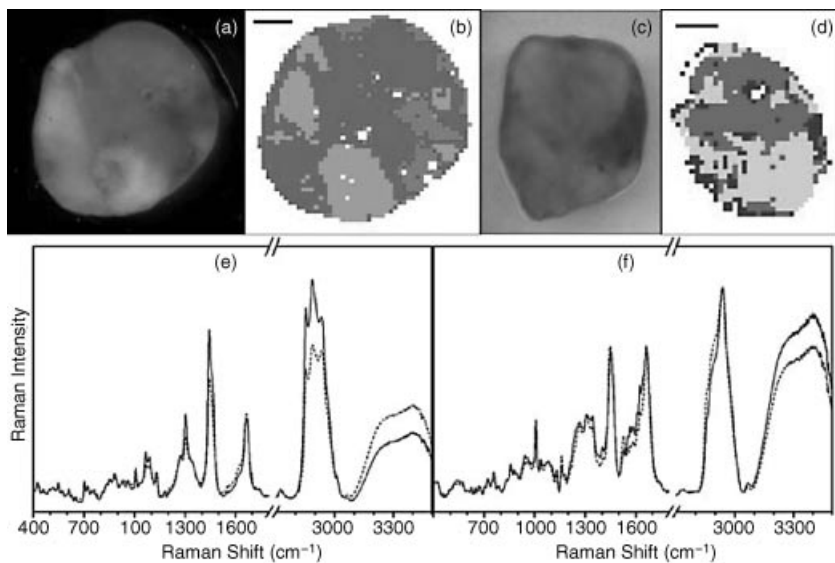


**Figure 5.27** Photographs of Raman imaging of non-dried normal brain tissue (a, b) and a brain metastasis of lung cancer (c, d). Raman images were segmented into three clusters by k-means cluster analyzes. Raman spectra of the light green (solid in (e)), dark green (dashed in (e)), red (solid in (f)), and orange clusters (dashed in (f)), are due to proteins, lipids, hemoglobin, carotene, and water differing throughout the spectra [34]. Reprinted from C. Kraft, G. Steiner, C. Beliteis, Salzer, Disease recognition by infrared and Raman spectroscopy, *R. J. Biophoton.* 2, 13 (2009) with permission of John Wiley and Sons

cells at different stages of differentiation at  $2845\text{ cm}^{-1}$ . Figure 5.26 indicates an intermediate stage, that is, the removal of cytoplasmic lipid droplets after addition of the induction medium. The reduction of lipid droplets was attributed to increased activity of hormone sensitive lipase, the enzyme responsible for hydrolyzing intracellular triglyceride and sterol esters [33(b)].

Figure 5.27 shows Raman images and Raman spectra that were collected from non-dried tissues from the same system (see color Plate 19 for the original Figure 5.27). They found that normal brain tissue can clearly be distinguished from a brain metastasis of lung cancer by different spectral contributions due to protein, lipids, water, hemoglobin, and carotene. Brain metastases of malignant melanomas were sensitively detected, because the spectral contributions of the pigment melanin were resonantly enhanced. In Figure 5.27, spectra of clusters of light green and dark green are represented by solid and dashed lines. The spectra of lung cancer metastasis to the brain red and orange clusters are represented by dashed and solid lines, respectively.

#### 5.4.4 Raman Spectra in Pharmacology

The structure/activity relationships (SAR) has become part of the discovery process of drugs. Figure 5.28 shows a comparison of trend and activity for two types of drug molecules.

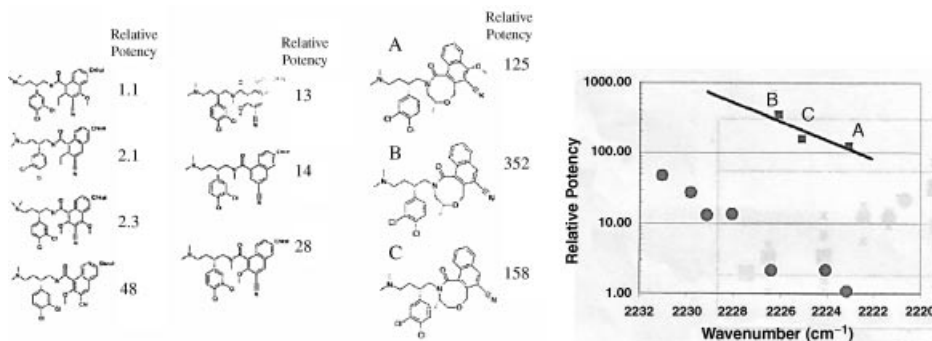


**Figure 5.28** Comparison of trend and activity for two types of drug molecules [35]. Reprinted from D. Pivonka, Applications of Raman spectroscopy in pharmaceutical drug discovery, Proceeding of ICORS 2008, Eds: R. Withnall and B. Chowdhry, 17th–22nd August, 2008

## 5.5 Geology and Mineralogy Raman Spectroscopy

In 1969, when laser Raman spectroscopy was first developed, Griffith pointed out specifically that Raman spectroscopy could be usefully applied for the identification of minerals and provision of structural information [36]. Since then, geology and mineralogy became important applied fields of solid Raman spectroscopy, leading geology and mineralogy Raman spectroscopy to be developed as an independent branch.

In this branch, the Raman spectral application for fluid inclusions is a typical and distinct example. Fluid inclusions are microscopic bubbles of liquid and gas trapped within crystals. These inclusions formed during the process of the earth's generation, containing so much dissolved solids that when it cooled, crystals of halite, sylvite, gypsum, and hematite were formed. Thus, fluid inclusions trapped in such a time capsule the size of a micrometer can provide much information, including the conditions existing during the formation of the enclosed mineral. Figure 5.29 shows the micro-Raman spectra of molecular water in two fluid inclusions (a) and (b) of olivine. The photographic images show the positions of laser focal spots of  $1\text{--}2 \mu\text{m}$  [39,40]. The result indicates that the water in the fluid inclusion is derived from a mantle magma source instead of contaminated crust.

Fortunately Raman microscopy makes the research on fluid inclusions easy to perform. In 1982, Dubessy *et al.* published a study on the electrolytes dissolved in the aqueous phase of fluid inclusions [37]. To date, many valuable research results [38–40] and review papers [41,42] have been published.

In the Raman spectrum of a fluid inclusion in a sample, except for some strong Raman peaks such as the strongest peak of quartz is at  $466 \text{ cm}^{-1}$  and relatively strong lines occurring at  $128$ ,  $206$ ,  $1082$ , and  $1160 \text{ cm}^{-1}$ , a weak band at  $\sim 1230 \text{ cm}^{-1}$  near the  $\text{CO}_2$  spectral peak was observed. Figure 5.30 shows the enlarged spectra of this weak band and illustrates a crowded spectrum containing the peaks of quartz at  $1160$  and  $1230 \text{ cm}^{-1}$ , the peak of disordered graphite at  $1350 \text{ cm}^{-1}$ , and many other peaks, which confirms that Raman spectra of fluid inclusions can provide a lot of information.

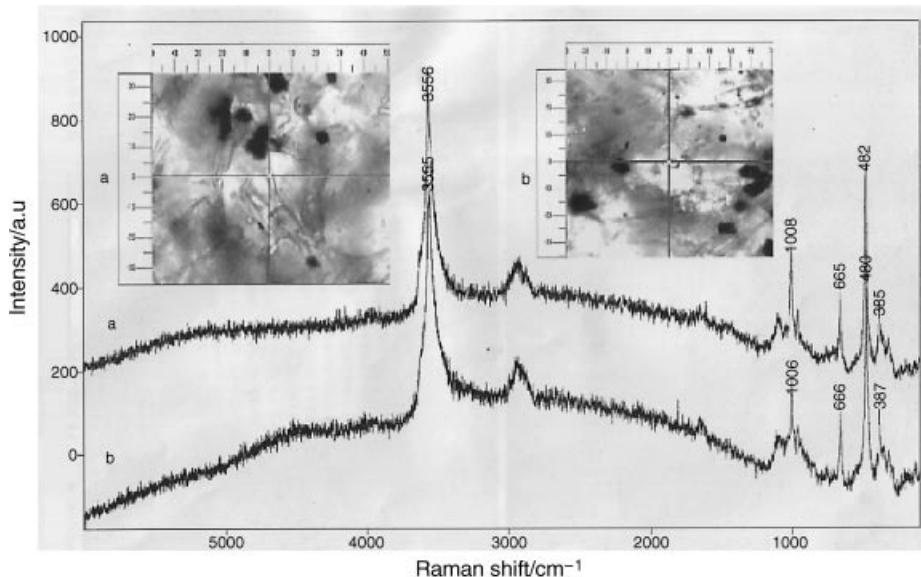


**Figure 5.29** Micro-Raman spectra of molecular water in two fluid inclusions (a) and (b) of olivine. The photographic images show the positions of laser focal spots of  $1\text{--}2\ \mu\text{m}$  [40]. Reprinted from J. A. Shao, et al., Discovery of molecular water in fluid inclusion of olivine, *Acta Petrologica Sinica*, 16, 127 (2001)

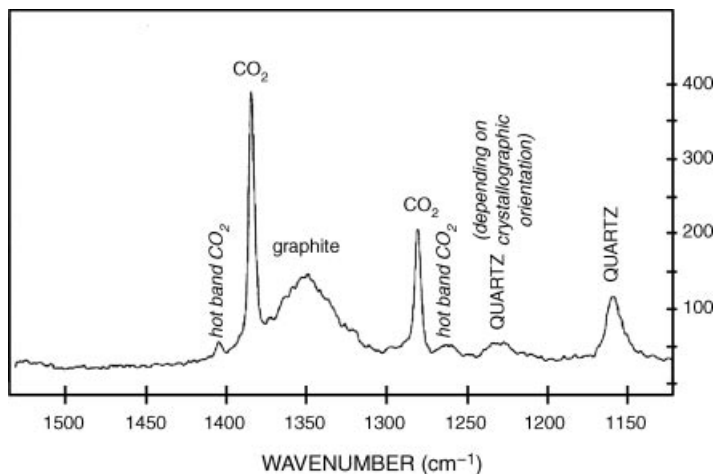


**Figure 5.30** Raman spectra around the  $\text{CO}_2$  Fermi diad of a fluid inclusion [43]. Reprinted from Ernst A.J. Burke, Raman microspectrometry of fluid inclusions, *Lithos*, 55, 139 (2001) with permission of Elsevier

## 5.6 Art and Archeology Raman Spectroscopy

The enormous strides in Raman instruments have made Raman spectroscopy widely used at the arts/science interface. The Raman spectroscopic study of art and archaeological matter has become popular since the pioneering work of Professor Robin Clark in the mid-1980s. To date, art and archaeology Raman spectroscopy allows conservation scientists to record molecular and elementary excitation spectra of minute samples or directly from the art and archaeological matter. Recently, Raman spectroscopy in this field has published some valuable reviews [44–47]. In the following, we present few examples to illustrate Raman spectral power in answering key questions about art and archaeological objects.

Figure 5.31 shows one of the works of the Clark group. The figure shows Raman spectrum of the black paint on an ancestral Puebloan sherd from the Wallace Ruin, Colorado, USA, showing bands attributable to carbon black ( $1584$  and  $1341\text{ cm}^{-1}$ ) and magnetite ( $672\text{ cm}^{-1}$ ) [48].

Chemical molecular Raman spectra are suitable to directly analyze art objects, including colorants. Figure 5.32 shows a Raman spectral analysis of the colored regions of a porcelain card (see color Plate 20 for the original Figure 5.32). The Raman spectra identified the various colorants used: (a) Bright blue: Prussian blue; (b) Dark blue: Ultramarine; (c) Red: Vermilion; (d) Yellow: Chrome yellow; (e) White: White lead.

In 2007, Colomban and Tournie [50] reported the first *in situ* Raman study of a stained glass window in the upper chapel of the Sainte-Chapelle, Paris, as shown in Figure 5.33 (see color Plate 21 for the original Figure 5.33). The results differ from those presented in the Corpus Vitrearum Medii Aevi (obtained by visual inspection) and therefore demonstrate the need for updating these reports with modern methods such as *in situ* Raman spectroscopy.

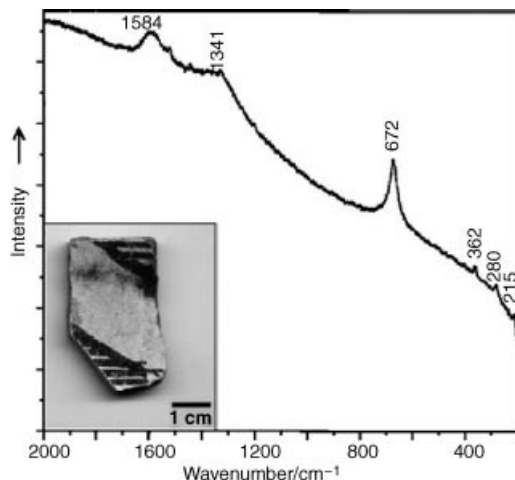


**Figure 5.31** Raman spectrum of the black paint on an ancestral Puebloan sherd (inset) [48]. Reprinted from J. Weerd, G.D. Smith, S. Firth and R.J.H. Clark, Identification of black pigments on prehistoric Southwest American potsherds by infrared and Raman microscopy, *J. Archaeol. Sci.* 31, 1429 (2004) with permission of Elsevier

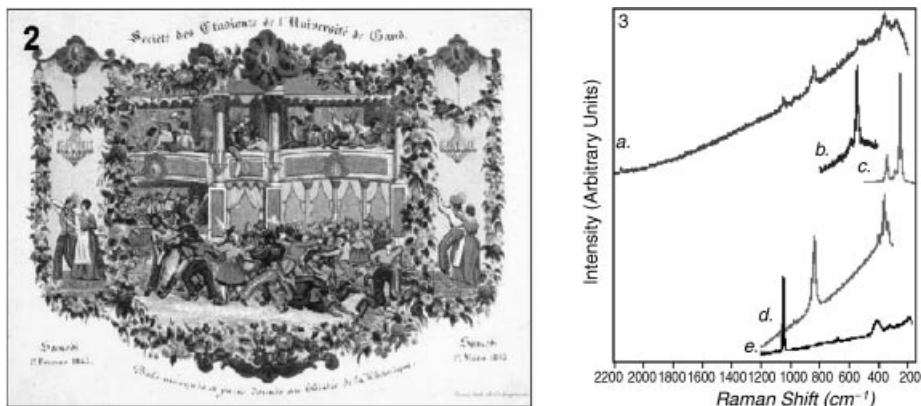


**Figure 5.32** Raman spectra (3) of colored regions of porcelain card (2) [49]. Reprinted from P. Vandenabeele and L. Moens, *The application of Raman Spectroscopy for the Non-destructive Analysis of Art Objects, Proceedings of 15th World Conference on Non-Destructive Testing, 15–21 October 2000*

## 5.7 Industry Raman Spectroscopy

Unlike conventional techniques, such as UV-VIS spectra, NIR spectra, or chromatography, Raman spectroscopy possesses greater advantages such as non-contact and non-destructive measurement, no special preparation, and small sample quantities down to Picomoles, as well as high chemical selectivity, and easy reading of spectra and so on. Therefore Raman spectroscopy has become an emergent method for monitoring industrial processes.

The Raman spectral techniques used in industrial processes are manifold, but are all based on Raman spectroscopic study of chemical molecules and solid elementary excitations. The above basic research results from information on the component, contaminant,

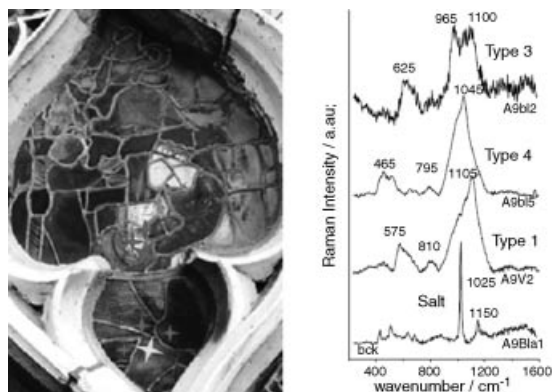


**Figure 5.33** Rose window panes and its Raman spectra [50]. Reprinted from P. Colombar and A. Tournie, *On-site Raman identification and dating of ancient/modern stained glasses at the Sainte-Chapelle, Paris*, *Journal of Cultural Heritage*, 8, 242 (2007) with permission of Elsevier

microstructure, crystalline morphology, and related function of matter. Due to the rapid development of industrial Raman spectroscopy, it is difficult to describe it completely, so only some prominent applications will be mentioned here.

### 5.7.1 Chemical and Pharmaceutical Industry

The application of Raman spectroscopy in the chemical and pharmaceutical industries is a logical development in the application of chemistry Raman spectroscopy.

The applications in the chemical and pharmaceutical industries are mainly molecular identification and polymer morphology, such as the degree of crystallization, size of crystals, and crystal orientation of a polymers. Obvious differences between the spectra indicate it to be a good method for monitoring production to obtain excellent quality. In fact, in the polymer synthesis industry, Raman techniques have become an alternative monitoring method to traditional ones [51].

The pharmaceutical industrial process includes numerous steps, such as the screening of new drugs, crystallization, polymorphic form ID, hydrate/solvate, drying and coating of non-destructive tablets and so on. The monitoring and control of this process is typical of applications of industrial Raman spectroscopy. In the production process of pharmaceuticals, Raman spectroscopy offers many benefits, such as the identification of raw materials, the quantitative determination of active substances in different formulations, and supporting polymorphic screenings and chemical development process scale-up. Figure 5.34a shows the setup for quantitative analysis of active components in commercial pesticide formulations. One of the monitored results by using this setup is shown in Figure 5.34b, in which the product of chemigram was verified [52].

### 5.7.2 Electronic and Semiconductor Industry

Raman spectroscopy is an established technique for the characterization and analysis of failure and defects in semiconductors. The Raman microscope and fiber probe are

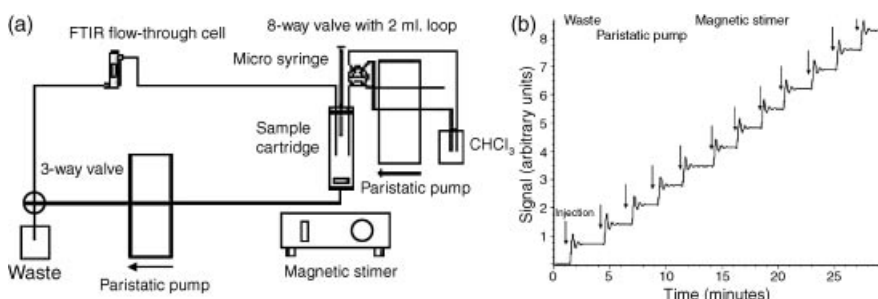


**Figure 5.34** (a) Layout of setup for quantitative analysis of active components in commercial pesticide formulations. (b) Chemigram obtained from peak-area measurement between  $1027$  and  $1017\text{ cm}^{-1}$ , with a baseline correction established in  $2000\text{ cm}^{-1}$ , for 12 consecutive Malathion standard injections [52]. Reprinted from S. Morel and F. Adar, *Refined Raman Spectroscopy: Bringing New Insight into Industrial Processes, Optics & Photonics News* 16, 42–46 (2005) with permission of The Optical Society of America

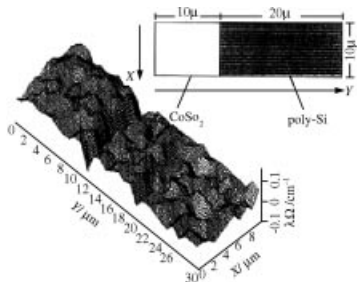


**Figure 5.35** A three-dimensional image of stress distribution at the micrometer scale for a CoSi electrode in an IC using a Si characteristic Raman spectral line [53]. Reprinted from G. Quintás, S. Armenta, S. Garrigues, et al., Mid-infrared and Raman spectrometry for quality control of pesticide formulations, *Trends in Analytical Chemistry*, 24, 772 (2005) with permission of Elsevier

particular ways for observing and investigating local strain in very small micro-electronic devices, which is a serious difficulty. Such information can be easily obtained by the Raman band shift of materials. Figure 5.35 show a three-dimensional Raman image of stress distribution with a micrometer-scaled for a CoSi electrode in an integrated circuit (IC). From this image, the micro-stress distribution of CoSi in an IC is visible, which is hard to acquire using other techniques and provides some information to improve the production technology [53].

### 5.7.3 Food Industry

In the food industry, much information related to food is needed to ensure food quality and safety. Quality control requires powerful analytical tools for learning about the various compounds in a food.

Raman spectroscopy provides structural information about the changes in proteins, water, and lipids of meat food that occur during deterioration. Therefore, Raman spectroscopy has been successfully correlated with traditional quality methods commonly used to determine quality of meat (such as protein solubility, apparent viscosity, water holding capacity), DMA content, peroxide values, fatty acid composition among others, and the saturation in oils and fats. This also includes various ingredients such as additives, and biopolymers such as emulsifiers, stabilizers, carbohydrates, and thickeners. In some cases, this correlation Raman analysis with chemometric analysis has been carried out. Up to date, Raman spectroscopy data can predict the results obtained by traditional quality methods used in the study of meat and thus elucidate if this spectroscopic technique can be used as a tool to assess meat quality. All these possibilities and advantages offered by Raman spectroscopy provide an adequate on-line tool in the food industry [54].

As an example, Figure 5.36 exhibits the possibility of Raman spectra to monitor techniques in the food industry. In Figures 5.36a and b, a FT-Raman spectrum of a sunflower oil margarine and the peak height ratio  $\nu(\text{C}=\text{C})/\delta(\text{CH}_2)$  against the iodine values (IV) of seven commercial margarines from Raman spectra are shown, indicating the ability to monitor quality by this method.

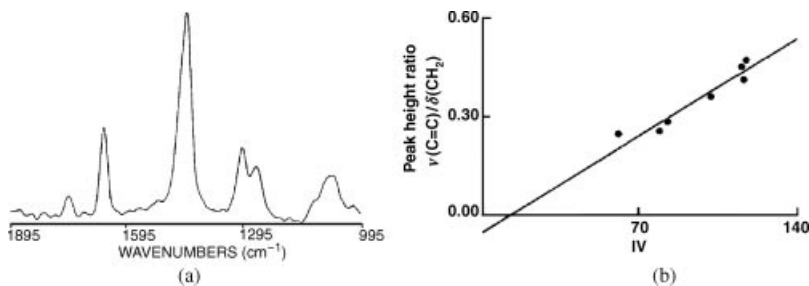


**Figure 5.36** (a) FT-Raman spectrum of sunflower oil margarine; (b) the peak height ratio  $\nu(C=C)/\delta(CH_2)$  against the iodine values (IV) of seven commercial margarines from Raman spectra [54]. Reprinted from B-B Li, F. Huang, S. L. Zhang, et al., Micro-Raman spectroscopic study of two-dimensional stress distribution in poly-Si induced by Patterns, *Semicond. Sci. Technol.* 13, 364 (1998)

## 5.8 Raman Spectroscopy in National Security and Judicature

In national security and judicature, Raman spectroscopy was applied in much earlier times, although the details were not generally known due to its sensitivity.

Raman spectroscopy in national security mostly involves the identification of hazardous materials such as explosives. Raman spectral applications in judicature include the identification of illegal drugs, forgeries (such as documents, currency notes, bank checks, coupons), paint and fiber analysis, distinguishing between natural and artificial diamonds/gems and inks and so on. In the following we show some examples.

Since Raman spectroscopic allows identification of extremely small amounts of a sample, a certain police department in UK checked out cocaine from the finger of a suspect who had sold it two weeks earlier. The characteristic Raman peaks of cocaine helped to gain a conviction.

Figure 5.37 shows an example of identification of handwriting on a document brought before a Chinese court. The court wished to know whether the date had been altered on a

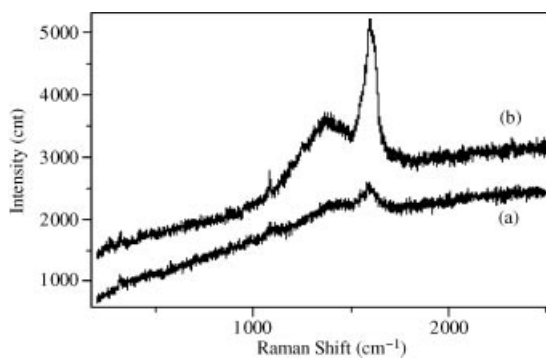


**Figure 5.37** Raman spectra of writings in a bank draft of horizontal line above "5" character (a) and another "5" writing (b) [55]. Reprinted from H. Sadeghi-Jorabchi, P.J. Hendra, R.H. Wilson, et al., Determination of the Total Unsaturation in Oils and Margarines by Fourier Transform Raman Spectroscopy, *JAOCs*, 67, 483 (1990) with permission of Springer

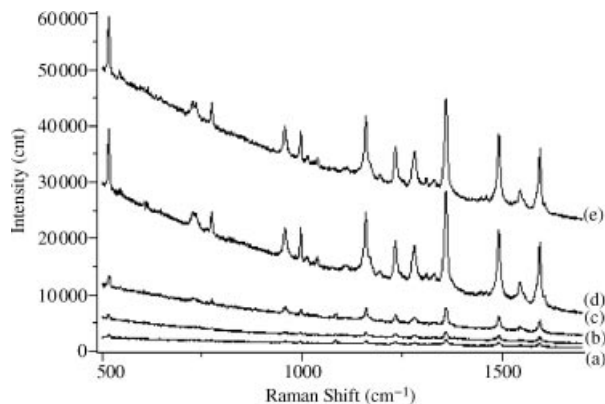


**Figure 5.38** Raman spectra of same seal generated in different years (a) 2006 (b) 2005 (c) 2004 (d) 2003 (e) [55]. Reprinted from KE Wei-Zhong and H. Hang, Applications of Raman Spectroscopic Technique on the Expert Testimony, *Chin. J. Light Scattering*, **8**, 136 (2008) with permission of the Carnegie Mellon University

bank drift. Figure 5.37a shows horizontal writing above “5” and (b) another character “5.” Due to the sharp difference between Raman spectral features of the two “5” characters, it verified that the bank drift was altered.

Another example is the identification of the date of seals. Figure 5.38 shows the Raman spectra of seals generated in different years. Since the Raman spectrum of the tested seal matched that of 2003, it was concluded that the seal was not generated in 2006, as declared by the company.

## References

- [1] Long, D.A. (1977) *Raman Spectroscopy*, McGraw-Hill International Book Company, New York.
- [2] Pandey, B.P. and Dayal, B. (1973) *J. Phys. C Solid State Phys.*, **6**, 2943.
- [3] Weber, W. (1977) *Phys. Rev.*, **15**, 4789.
- [4] Zhang, S.-L., Meng, W., Zhou, Q.-F., and Zhu, X.-L. (1991) *Acta Polymerica Sinica*, **3**, 370.
- [5] Porto, S.P.S. and Wood, D.L. (1962) *J. Opt. Soc.*, **52**, 251.
- [6] Vepiek, S., Iqbal, Z., Oswald, H.R., and Webb, A.P. (1981) *J. Phys. C: Solid State Phys.*, **14**, 295.
- [7] Tominaga, Y. (August 27-Sreptember 1 1984) *Raman Spectral Study on Ferroelectric Phase Transition of KH<sub>2</sub>PO<sub>4</sub>*. Proceedings of the IXth International Conference on Raman Spectroscopy, Tokyo, Japan, p. 38.
- [8] Shao, J., Lu, J., Huang, W. et al. (2006) *J. Raman Spectrosc.*, **37**, 951.
- [9] De Wolf, I., Maes, H.E., and Jones, S.K. (1996) *J. Appl. Phys.*, **79**, 148.
- [10] Wu, X., Yue, J., Rena, T., and Liu, L. (2007) *Microelectr. J.*, **38**, 87.
- [11] Anderson, N., Hartschuh, A., and Novotny, L. (2005) *Mater. Today*, 50.
- [12] Hartschuh, A. and Anderson, N. (2004) *Intl. J. Nanoscience*, **3**, 371.
- [13] Spiro, T. (1975) *Proc. R. Soc. Lond. A*, **345**, 89.
- [14] Zhang, S.L. (1995) *Chn J. Light Scattering*, **7**, 47.
- [15] Yue, K. (1996) *Chn. J. Light Scattering*, **8**, 113, 174.
- [16] Neugebauer, U., Schmid, U., Baumann, K. et al. (2007) *ChemPhysChem*, **8**, 124.

- [17] Liu, A.Q., Huang, H.J., Chin, L.K. *et al.* (2008) *Anal. Bioanal. Chem.*, **391**, 2443.
- [18] Kraft, C., Steiner, G., Beleites, C., and Salzer, R. (2009) *J. Biophoton.*, **2**, 13.
- [19] Graham, D., Flanlds, K., Smith, E., *et al.* (2008) Proceeding of ICORS (eds R. Withnall and B. Chowdhry), 17th–22nd August, London, UK, p. 6.
- [20] Kneipp1, K., Kneipp, H., Itzkan, I. *et al.* (2002) *J. Phys.: Condens.*, **14**, R597.
- [21] Thomas, G.A. and Peticolas, W.L. (1983) *J. Am. Chem. Soc.*, **105**, 993.
- [22] Barry, B. and Mathies, R. (1987) *Biochemistry*, **26**, 59.
- [23] Rasmussen, A. and Deckert, V. (2006) *J. Raman Spectrosc.*, **37**, 311.
- [24] Domke, K., Zhang, D., and Pettinger, B. (2007) *J. Am. Chem. Soc.*, **129**, 6708.
- [25] Dieringer, J.A., Lettan, R.B., Scheidt, K.A., and van Duyne, R.P. (2007) *J. Am. Chem. Soc.*, **129**, 16249.
- [26] Bailo, E. and Deckert, V. (2008) *Angew. Chem. Int. Ed.*, **47**, 1658.
- [27] Bailo, E. and Amgew V.D. (2008) *J. Chem. Int. Ed.*, **47**, 1658.
- [28] Schmid, T., Messmer, A., Yeo, B.S. *et al.* (2008) *Anal. Bioanal. Chem.*, **391**, 1907.
- [29] Qian, X.-M. and Nie, S.M. (2008) *Chem. Soc. Rev.*, **37**, 912.
- [30] Zumbusch, A., Holtom, G.R., and Xie, X.S. (1999) *Phys. Rev. Lett.*, **82**, 4142.
- [31] Nandakumar, P., Kovalev, A., and Volkmer, A. (2009) *New J. Phys.*, **11**, 033026.
- [32] Ozaki, Y., Mizuno, A., Itoh, K. *et al.* (1983) *Biochemistry*, **22**, 6254.
- [33] Cheng, J.-X., Potma, E.O., and Xie, X.S. (2002) *J. Phys. Chem. A.*, **106**, 8561.
- [34] Kraft, C., Steiner, G., Beleites, C., and Salzer, R. (2009) *J. Biophoton.*, **2**, 13.
- [35] Pivonka, D. (2008) *Application of Raman Spectroscopy in Pharmaceutical Drug Discovery*, Proceedings of ICORS (eds R. Withnall and B. Chowdhry), 22nd August, London, UK, p. 26.
- [36] Griffith, W. (1969) *Nature*, **224**, 264.
- [37] Dubessy, J., Audeoud, D., Wilkins, R., and Kosztolanyi, C. (1982) *Chem. Geol.*, **37**, 137.
- [38] Karim, D. and Hong, H. (2010) *J. Am. Sci.*, **6**, 30.
- [39] Shao, J.A. *et al.* (2000) *Sci. Geol. Sinica*, **9**, 159.
- [40] Shao, J.A. *et al.* (2001) *Acta Petrologic Sinica*, **16**, 127; (2002) **16**, 275; (2003) **16**, 449.
- [41] Burke, E.A.J. (2001) *Lithos*, **55**, 139.
- [42] Chen, Y. and Burke, E.A.J. (2009) *Geo. Rev.*, **55**, 851.
- [43] Burke, E.A.J. (2001) *Lithos*, **55**, 139.
- [44] Vandenabeele, J. (2004) *J. Raman Spectrosc.*, **35**, 607.
- [45] Edwards, H.G.M. and Chalmers, J.M. (eds) (2005) *Raman Spectroscopy in Archaeology and Art History*, RSC Analytical Spectroscopy Series. Springer Verlag, Berlin.
- [46] Vandenabeele, P., Edwards, H.G.M., and Moens, L. (2007) *Chem. Rev.*, **107**, 675.
- [47] Clark, R.J.H. (2007) *J. Mol. Struct.*, **834–836**, 74.
- [48] Weerd, J., Smith, G.D., Firth, S., and Clark, R.J.H. (2004) *J. Archaeolog. Sci.*, **31**, 1429.
- [49] Vandenabeele, P. and Moens, L. (15–21 October 2000) *Identification and Classification of Natural Organic Binding Media and Varnishes by Micro-Raman Spectroscopy*. Proceedings of 15th World Conference on Non-Destructive Testing, Rome.
- [50] Colombari, P. and Tournie, A. (2007) *J. Cultural Heritage*, **8**, 242.
- [51] Morel, S. (June 2005) Optics and Photonics News, p. 42.
- [52] Quintás, G., Armenta, S., Garrigues, S., and dela Guardia, M. (2005) *Trends Anal. Chem.*, **24**, 772.
- [53] Li, B.-B., Huang, F., Zhang, S.L. *et al.* (1998) *Semicond. Sci. Technol.*, **13**, 634.
- [54] Sadeghi-Jorabchi, H., Hendra, P.J., Wilson, R.H., and Belton, P.S. (1990) *JAOCs*, **67**, 483.
- [55] Wei-Zhong, K.E. and Heng, H. (2008) *Chn. J. Light Scattering*, **8**, 136.

## **Part II**

# **Study of Nanostructures by Raman Spectroscopy**

# 6

## General Knowledge of Nanostructures

### 6.1 Nanostructure, Characteristic Length, and Dimension

#### 6.1.1 Nanostructure

It is well known that the object with a macro-scale ( $>$  visible wavelength  $\approx \mu\text{m}$ ) structure obeys the law of classical physics, while the object with a micro-scale (sub-atomic scale  $\approx 0.01 \text{ nm}$ ) is described by quantum physics, indicating that the size of objects will exercise significant influence over the object property. An object with intermediate size between macro- and micro-scales is usually named as a nanostructure. Therefore, the nanostructure is directly related to size-scale, so “small size” is the basic feature of nanostructures. Since the macro-object is seen as being of infinite size in physics, so the “small size” is also seen as being of “finite size.”

Such a defined nanostructure is still macroscopic in geometry, but a series of quantum mechanical phenomena appear, such as separate electron energy levels. In other words, a nanostructure is a localized so-called “mesoscopic world” between macro- and micro-worlds, so is also called a mesoscopic structure in much of the literature.

#### 6.1.2 Characteristic Length

Whether an object can be considered a nanostructure is dependent of which property of objects that you are concerned, and so the practical scale of nanostructure judgment varies. This judgment scale is named the “characteristic length.” Important characteristic lengths are the dephasing length  $L_\varphi$ , defused length  $L_D$ , Bohr radius of electronic (exciton)  $r_e$ , de Broglie wavelength of particle  $\lambda_D$ , and wavelength of electromagnetic radiation  $\lambda$ .

The dephasing length  $L_\varphi$  is the most basic one in characteristic lengths.  $L_\varphi$  is defined by such a length. With this length an electron suffered by inelastic scattering still holds a memory of the phase at the start point of scattering.  $L_\varphi$  is expressed as

$$L_\varphi = (D\tau_\varphi)^{1/2} \quad (6.1)$$

where  $D$  is the diffusion coefficient and  $\tau_\phi$  is the dephasing time.  $D$  in a three- dimension system is expressed as

$$D = v_F l / 3 \quad (6.2)$$

where  $v_F$  is the Fermi speed and  $l$  is the mean free path of elastic scattering.  $L_\phi$  is seen as a straight line between the start and end points of scattering, that is, the average straight distance between two inelastic scatterings. Thus,  $L_\phi$  must be smaller than  $l$ . For example,  $l$  of a normal metal at liquid helium temperature is about  $10^{-1}$  cm, but corresponding,  $L_\phi$  is only  $10^{-5}$  cm.

Under different conditions, the size of characteristic lengths can vary. For example, de Broglie wavelength of the electrons in conduction bands can be from 10 to 100 nm. In addition, the electron Bohr radius in hydrogen atoms is only 0.05 nm, while the Bohr radius of the conduction electrons in GaAs is about 10 nm. Therefore, the judgment scale of nanostructures is not a unified one and is dependent on the object of interest and the conditions surrounding it.

### 6.1.3 Low-dimension Structure

A macroscopic object is usually defined as a system where its size scale is infinite in three dimensions. However, the size of a real object is always limited and then if the size of object is much larger than the characteristic length in three dimensions, this object can only be the macroscopic one. Correspondingly, if the size of the structure is less than the characteristic length in one, two, or three dimensions, it is named a two-, one-, or zero-dimensional structure, respectively, which are all considered low-dimensional structures.

## 6.2 Nanomaterials

Nanostructures are related to various scientific and technologic fields, for example, the viral assembly is included in nanostructures in some literature. The nanostructures in material sciences and technologies are always called nanomaterials.

Nanomaterials possess morphological features of nanoscale and, especially, special properties stemming from their nanoscale. Nanomaterial is the main form embodied in the nanostructures.

### 6.2.1 Nanomaterial in Nature

Nanomaterials already exist in the nature, for example, the huge super magnetic particles that aggregate in the oceans. The colloids and the raw materials of China ink existed a thousand years ago are all nanomaterials.

### 6.2.2 Artificial Nanomaterials

The nanomaterials of interest at present are mostly artificial ones, which are prepared based on modern nanotechnologies. To date, artificial nanomaterial has developed into a huge family, of which some important ones are the multiple layer (ML) nanofilm, gradient multi-layer (GML) nanofilm, nanocages, nanowires, nanocomposites, nanofabrics, nanofibers,

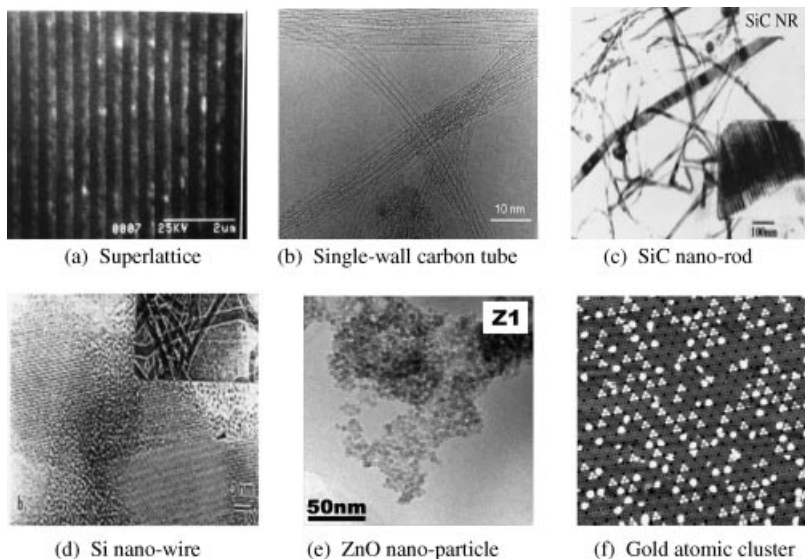


**Figure 6.1** Electron micrographs of some typical nanomaterials. Reprinted from Shu-Lin Zhang, Raman Spectroscopy and Low-dimensional nanoscale Semiconductors (in Chinese), Science Press, Beijing, 2008

nanoflakes, nanoflowers, nanofoams, nanomeshes, nanoparticles, nanopillar, nanopin film, nanoplatelets, nanorings, nanorods, nanoshells, and so on. Some nanomaterials have different names in different fields, such as in semiconductor science and technology the nanoparticle, nanowire, and multiple layer nanofilm are named as quantum dot, quantum wire, and quantum well (superlattices), as their excitons, electrons, or holes are confined in three, two, and one dimensions, respectively. Figure 6.1 shows some typical nanomaterials, which are introduced below.

#### 6.2.2.1 Quantum Wells and Superlattices

Figure 6.1a is an electron micrograph of a multiple quantum well (MQW)/superlattice (SL) sample. The figure clearly shows a multiple layer structure of the sandwich type. If the electronic band-gaps of alternating layers of materials are not equal, a quantum well will form: large and small band-gap semiconductor layers become the barrier and well layer, respectively. The electrons and holes are localized in the well layers and barrier layers, respectively. The sizes of parallel and perpendicular SLs and QWs to the layer plane of are infinite and nanoscale, respectively. Correspondingly, the movement of electrons along and perpendicular to the layer plane are free and confined and, therefore, the superlattice structure is a typical one of two-dimensional nanomaterial.

#### 6.2.2.2 Quantum Wire and Quantum Dots by Photolithography on QW Base

If a wire-like groove is formed along one or two directions in the plane layer of a quantum well, by a method such as photolithography, a new electronic barrier layer will be formed in these one or two directions, respectively. As a result, a two-dimensional quantum well will become a one-dimensional quantum wire and zero-dimensional quantum dots

with confinement effects on electrons and phonons in two and three dimensions, respectively.

By using different growth techniques, the quantum well shape can have square and sinusoidal patterns. In addition, if the two alternating layer of material of SLs are constructed by different atoms (ions) or components, the different types of SLs can be formed, for example, the two elements superlattices of A/B-type Ge/Si SLs, three elements superlattices of AB/CB-type GaAs/AlAs SLs, and quaternary elements superlattices of AB/CD-type CdSe/ZnTe SLs.

#### *6.2.2.3 Nanotubes, Nanorods, Nanowires, and Coaxial Cables*

Nanotubes, nanorods, nanowires, and nanocoaxial cables are all one-dimensional materials. For wire-shaped nanomaterials, if its aspect ratio is small, it is named a nanorod, otherwise a nanowire. The nanocoaxial cable is constructed from a core surrounded with a nanotube. Figures 5.1b–d are the transmission electron microscopic images of single-walled carbon nanotube, SiC nanorod, and silicon nanowire samples.

The single-walled carbon nanotube is constructed by curling of a single molecular layer of graphite sheet (graphene). Therefore, it is a strictly one-dimensional quantum structure, as the two-direction perpendicular to the tube axis is strictly confined.

#### *6.2.2.4 Nanoparticle and Cluster*

Figures 6.1e and d show the electron micrographs of ZnO nanoparticles and gold clusters, respectively.

A cluster has its own special features and is usually composed of only a few atoms or molecules and its size is generally 1 nm or less, meaning it is smaller than other nanomaterials. The cluster is a relatively stable aggregate and represents the initial form of condensed matters and processes with different properties from that of single atoms and bulk solids. Moreover, the structure of clusters consists of a central atom surrounding by other atoms and a process Mackay icosahedron with a five-fold symmetry that does not exist in bulk crystals. Especially, there are so-called “magic number” sequences for clusters and a relatively stable cluster occurs only with such magic numbers, which means that the cluster size must be same exactly for same kind of cluster.

### **6.3 Properties of Nanostructures**

The above discussion indicates that the nanostructure is a bridge to link bulk and atom-molecular structures. In nanostructures, many properties in bulk materials and atoms or molecules are altered. For example, the properties of bulk materials are not related to sample sizes; however, the properties of nanostructures are often size-dependent. It induces many unique properties different from that in bulk materials, resulting in wide applications and becoming a hot topic in the world today. The unique properties of nanostructures have many manifestations, some of which are introduced below.

#### **6.3.1 Manifestation in Physical Property**

##### *6.3.1.1 Phase Structure*

Solids can turn into liquids at room temperature, for example, gold nanoparticles melt at much lower temperatures ( $\sim 300^\circ\text{C}$  for 2.5 nm size) than gold slabs ( $1064^\circ\text{C}$ ) [1].

### 6.3.1.2 Mechanical Properties

Copper nanoparticles smaller than 50 nm are considered super hard materials that do not exhibit the same malleability and ductility as bulk copper. Metallic nanowires are much stronger than corresponding bulk metals [2,3].

### 6.3.1.3 Optical Properties

A copper nanostructure alters from an opaque substance to a transparent one. Silicon nanoparticles change from usually yellow gold and gray to red in bulk silicon. Gold nanoparticles appear deep red to black in solution.

### 6.3.1.4 Conductivity

Semiconductor silicon in nanostructures become conductors.

### 6.3.1.5 Magnetic Properties

Super-paramagnetism has been observed in magnetic nanomaterials.

## 6.3.2 Manifestation in Chemical Properties

The important alteration of chemical properties in nanostructures is in the application in catalysts and cells.

### 6.3.2.1 Catalysts

Many chemical materials inert at normal scales, such as gold, can serve as a potent chemical catalyst at nanoscales.

### 6.3.2.2 Cells

Lithium, lithium titanate, and tantalum nanoparticles are being applied in lithium ion batteries. Silicon nanoparticles have been shown to dramatically expand the storage capacity of lithium ion batteries during the expansion/contraction cycle.

Silicon nanoparticles are also used in new forms of solar energy cells. Thin film deposition of silicon quantum dots on the polycrystalline silicon substrate of a photovoltaic (solar) cell increases voltage output by as much as 60% through the fluorescing of incoming light prior to capture.

## 6.3.3 Crystallography of Different Nanomaterials

For nanomaterials formed by different growth methods, their crystallography properties can be different.

A self-organized growth method requires the binding energy to be minimized in the growth process, thus the crystallographic unit cell, lattice constant, and symmetry of nanomaterials prepared by this method are similar to corresponding bulk materials.

The lattice constancy and symmetry of unit cells in the growth direction of a quantum well/superlattice is different from corresponding bulk materials. For example, the lattice constant in the growth direction of GaAs/AlAs superlattices  $L$  is expressed as

$$L = n_1 a_1 + n_2 a_2 \quad (6.3)$$

where  $a_1$  and  $a_2$  are the bulk lattice constants of GaAs or AlAs, respectively;  $n_1$  and  $n_2$  are the number of single atomic layers of GaAs and AlAs in superlattices, respectively. From Equation (6.3), it is obvious that the lattice constant in the growth direction of GaAs/AlAs superlattices is different from those of GaAs and AlAs.

Section 6.2.2 shows that the cluster is not usually solid and its crystallographic structure does not belong to any of the crystallographic structures in solids.

## 6.4 Finite Size and Specific Surface

Section 6.1.1 mentioned that the basic features of the nanostructure is its small size. Section 6.3 described that many new properties do not appear in corresponding bulk materials and much of the fascination of nanostructures stems from these unique properties. These new properties of nanostructure are mainly originated by the small size of the structure. The influence of small size on the properties of objects is fundamentally embodied by finite size effect (FSE) and specific surface effect. For example, finite size impacts not only on the physical quantity of energy and so on but physical law such as the momentum conservation law.

### 6.4.1 Potential Well and Quantum Confinement Effect

The important result induced by FSE is the quantization of energy in nanostructures, that is, appearing so-called quantum confinement effect (QCE).

#### 6.4.1.1 Potential Well [4]

The quantum confinement effect is directly relative to the potential well in materials. To clarify QCE, we introduce the description of a one-dimensional potential well, which will not lose any essential objects from a three-dimensional well.

#### 6.4.1.2 One-Dimensional Square Potential Well

For a one-dimensional square potential well, the profile of the potential is shown in Figure 6.2a. The potential profile  $V(z)$  can be expressed as

$$V(z) = \begin{cases} V_0 & -a/2 \leq z \leq a/2 \\ 0 & -a/2 \geq z \geq a/2 \end{cases} \quad (6.4)$$

where  $V_0$  and  $a$  are the height and width of the potential well, respectively.

#### 6.4.1.3 One-dimensional Parabolic (Harmonic Oscillator) Potential Well

Figure 6.3a represents the electric potential profile of a one-dimensional parabolic potential well, which is a good model for the potential well in real bulk materials. The mathematical formulation of a parabolic potential well can be expressed as

$$V(x) = \frac{1}{2}Kx^2 \quad (6.5)$$

where  $K$  represents the force constant. Because the harmonic oscillation potential is proportional to the square of the distance  $x$  between two atoms of the oscillator, the parabolic

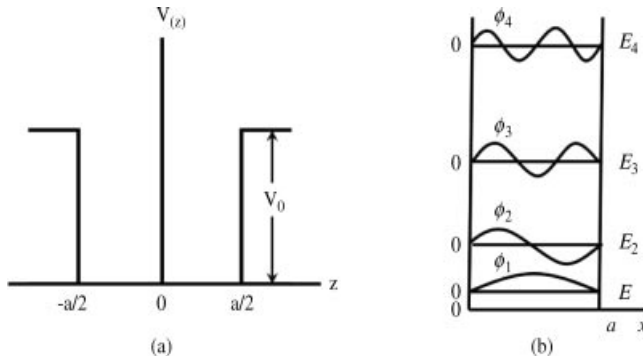


**Figure 6.2** The potential profile (a) and the energy levels and corresponding wave functions in a well (b) for a one-dimensional square potential well [4]. Reprinted from J.-Y. Zeng, Quantum Mechanics Volume I (in Chinese), Third Edition, Science Press, Beijing, 2006

potential well is also called a harmonic oscillator potential well. If the reduced mass and intrinsic oscillating vibration frequency are marked as  $\mu$  and  $\omega_0$ , respectively, we have

$$K = \omega_0^2 / \mu \quad (6.6)$$

thus

$$V(x) = \frac{1}{2\mu} \omega_0^2 x^2 \quad (6.7)$$

#### 6.4.1.4 Quantum Confinement

If the well height  $V_0$  is finite and the particle energy has an appropriate energy compared with well height  $V_0$ , this particle can be imagined as, such as tunneling through the walls of the potential well. In bulk semiconductors, an electron-hole pair is typically bound within a characteristic length called the Bohr radius of excitons. If the height  $V_0$  of the potential

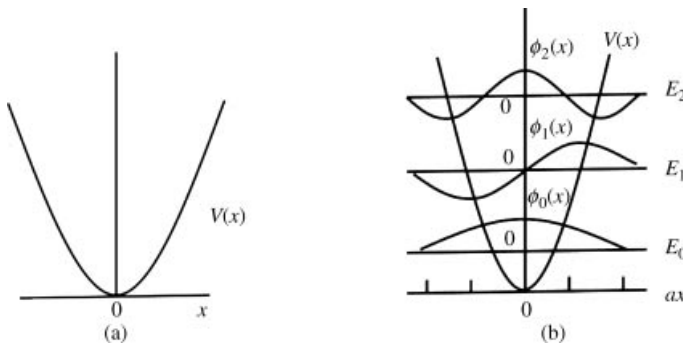


**Figure 6.3** The potential profile (a) and the energy levels and corresponding wave functions in a well (b) for a one-dimensional parabolic (harmonic oscillator) potential well [4]. Reprinted from J.-Y. Zeng, Quantum Mechanics Volume I (in Chinese), Third Edition, Science Press, Beijing, 2006

well rises and approaches infinite, the energy levels and corresponding wave functions of particles (such as electrons, phonons, etc.) in the potential well will be as shown in Figure 6.2b, that is, the movement in the  $z$  direction is confined and the energy of particles splits into separated levels from continuous energy in bulk materials [5,6], which are named the quantum confinement effect (QCE). The energy gap of separate levels increases with the narrowing of well width  $a$ . The energy levels of confined electrons can be expressed as

$$E_n(k) = E_n + \frac{\hbar^2 k^2}{2m} \quad (6.8)$$

where the subscript  $n$  is the marker of splitting level;  $E_n$  is the value of splitting energy levels  $n$ ;  $k$  is the electron momentum; and  $m$  is the electron mass. The electron energy  $E_n$  of a one-dimensional square potential well is expressed as

$$E_n = \frac{n^2 (\pi \hbar)^2}{2m} \frac{1}{a^2} \quad (6.9)$$

For a two-dimensional well, if the Fermi level  $E_F \ll E_2$  and  $(E_2 - E_1) \gg K_B T$ , the movement in the  $z$  direction of electrons with two-dimensional sub-band energy of  $n = 1$  is frozen, meaning electron motion is in the plane and thus the system is two-dimensional. When the energy level with  $n > 1$  is also occupied, it is called a quasi-two-dimensional system. From Equation (6.9), it can be seen that when the well width  $a \rightarrow \infty$ ,  $E_n = 0$  and the energy difference of adjacent energy levels  $\Delta E_n$  becomes large with the decreasing of well width  $a$ . Therefore, under the same temperature conditions, the formation of a two-dimensional system is easier, which indicates that reduction of dimensions directly correlates with the size of systems.

Similar to the square well above, the energy level distribution and the corresponding wave function for a one-dimensional parabolic potential well can be as shown in Figure 6.3b. The mathematical formulation of quantified harmonic oscillator energy  $E_n$  in a parabolic potential is

$$E_n = \left( n + \frac{1}{2} \right) \hbar \omega_0 \quad (6.10)$$

The QCE will lead to new electronic properties that are not present in bulk semiconductors and thus many new semiconductor devices were developed in past few decades. Another effect of QCE appears in optics. For example, the color feature of colloidal quantum dots changes with size. The larger the dot, the redder (lower energy) it is in the fluorescence spectrum.

The phonons in nanostructures are considered to be localized in a phonon potential well. The results originated from QCE on electrons can also appear for the phonon in nanostructures.

Finally, we would point out that the quantum well/superlattice structure is the first artificial object to exemplify a one-dimensional square potential well.

## 6.4.2 Breaking of Translation Symmetry and Invalidation of Momentum Conservation Law

### 6.4.2.1 Translation and Translation Symmetry

A translation implies the sliding of an object. In physics, translational symmetry is the invariance of a system under any translation. Translation symmetry of an object means that a

particular translation does not change the object. For example, the laws of physics are translation invariant if they do not distinguish at different points in space.

#### 6.4.2.2 Momentum Conservation and Size-scale

Translation symmetry/invariance of a physical system is equivalent to possess the momentum conservation. In addition, translation invariance is closely related to space properties and implies that, at least in one direction, the object is infinite.

Therefore, when the size of nanostructure is very small and it cannot be considered as infinite, translation symmetry will break down and the momentum conservation law will be invalid or relaxed. The momentum conservation law plays a key role in lattice dynamics and visible Raman scattering of phonons.

#### 6.4.3 Uncertainty Principle and Momentum Diffusion

The uncertainty principle is a statement of the relation between position and momentum of matter in quantum physics, which mentions that the root mean square deviation of position and momentum from its mean values,  $\Delta x$  and  $\Delta p$ , satisfy the following inequality:

$$\Delta x \Delta p \geq \frac{\hbar}{2} \quad (6.11)$$

where  $\hbar$  is Planck's constant. It is obviously that when an object size  $x$  is very small, the measure deviate value of  $x$ ,  $\Delta x$ , must also be very small. Thus, from Equation (6.11), the momentum deviation  $\Delta p$ , that is, momentum uncertainty will be very large, meaning the momentum is diffusive rather than of fixed value and the degree of diffusion increases with decrease in size.

The above implies that the momentum of a nanostructure will no longer be a fixed value, unlike that in bulk materials of large size.

#### 6.4.4 Specific Surface

An important aspect induced by the small size of a nanostructure is that the ratio of surface area to volume increases greatly, of which the characteristic parameter of a specific surface is defined as

$$\text{Specific surface} \equiv \text{surface area (m}^2\text{)}/\text{mass (g)} \quad (6.12)$$

The specific surface increases rapidly with decreasing particle diameter  $d$ . For example, for copper, when  $d = 20 \text{ nm}$ , the specific surface area =  $33 \text{ m}^2/\text{g}$ , and when  $d = 2 \text{ nm}$ , the specific surface =  $330 \text{ m}^2/\text{g}$ . Moreover, when  $d$  decreases and the specific surface increases, the number of surface dangling bonds or/and unsaturated bonds increases quickly compared with that within the object. This feature is important and of practical value in science and technology. For example, it means a number of nanomaterials can be developed into very efficient detector materials, adsorbents, and catalysts. In addition, the increase of a specific surface area plays a critical role in maximizing the amount of absorbed radiation, reducing the incipient melting temperature, and increasing the tremendous driving force of diffusion, especially at elevated temperatures.

## 6.5 The Study of Nanostructure

Section 6.2.1 showed that the nanostructure such as the raw materials of China ink, stick-soot carbon, already existed one thousand years ago; however, the nanostructure study in the scientific sense only started one hundred years ago.

### 6.5.1 Short History of Study

The establishment of colloid chemistry in 1861 marked the beginning of nanostructure study in the scientific sense; although the study was limited from the conventional macroscopic angle.

The first observation and size measurement of nanostructures were made by using an ultra-microscope that employed the dark field method. The results were published in 1914 [7].

In 1962, Kubo published his study of ultrafine particles of metal and noted the finite size effect. Then he proposed the quantum confinement theory known as the Kubo theory. This indicates the beginning of research from the microscopic view [5]. In 1970, Ezaki and Tsu proposed a concept of the semiconductor superlattice [6], indicating the starting of two-dimensional structure study. In 1971, Cho finished the preparation of the semiconductor superlattice by molecular beam epitaxy (MBE), implying the birth of the first artificial crystal structure that does not exist in nature [8]. In 1984, Birringer *et al.*, at the Saarland University of Germany, prepared a block body sample of a metal nanoparticle by *in situ* pressing in a vacuum chamber and found many new features [9]. Based on the experimental results, they proposed a theory on singularity of the interface structure of nanomaterials.

Since the 1980s, extensive research on nanostructures has made tremendous progress in various aspects accompanying the appearance of large numbers of nanomaterials. The studies on C<sub>60</sub>, porous silicon, carbon nanotubes, Si nanomaterials, and graphene and so on are typical and historical events reflect the research boom. Existing study has showed that nanostructures, in particular nano-semiconductors, appear as many novel phenomena and obey new physical laws, resulting in being applied in many technological and industrial fields.

### 6.5.2 Short Introduction of Study Ways

The aim of nanostructure study is mainly to learn about their appearance, including topography, size, and size-distribution and so on, as well as inner properties, including energy, momentum, and movement law and so on of nanoscale objects.

The ways adopted to study the appearance nanostructures are by using electron scanning/transmission and atomic force microscopes. Spectroscopy excited by visible light, infrared light, ultraviolet light, X-ray, and electron beam and so on and involved with absorption, emission, luminescence, and scattering spectra, are used to research inner properties of nanostructures.

Spectroscopy, as an efficient way of nanostructure study, was adopted early. For example, in 1974, Dingle *et al.* first observed QCE by using absorption optical spectrum, as shown in Figure 6.4 which exhibits that the change in the number and energy values of energy levels with well width L<sub>z</sub> (i.e., the thickness of GaAs layer) for a confined carrier in

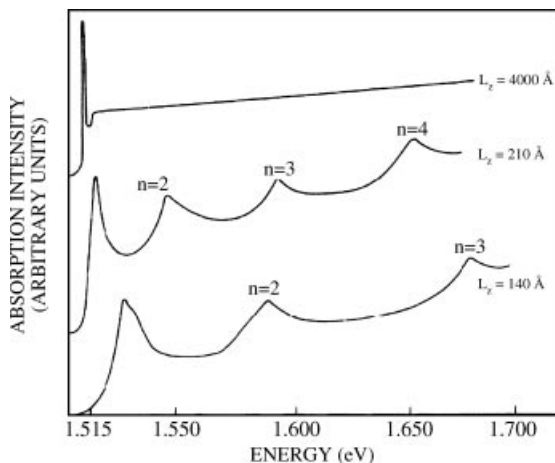


**Figure 6.4** Absorption spectra of  $\text{Al}_x\text{Ga}_{1-x}\text{As}-\text{GaAs}-\text{Al}_x\text{Ga}_{1-x}\text{As}$  heterostructures with quantum well width  $L_z$  [10]. Reprinted from R. Dingle, W. Wiegmann and C. H. Henry, Quantum States of Confined Carriers in Very Thin  $\text{Al}_x\text{Ga}_{1-x}\text{As}-\text{GaAs}-\text{Al}_x\text{Ga}_{1-x}\text{As}$  Heterostructures, *Phys. Rev. Lett.*, **33**, 827–830 (1974) with permission of the American Physical Society

a  $\text{Al}_x\text{Ga}_{1-x}\text{As}-\text{GaAs}-\text{Al}_x\text{Ga}_{1-x}\text{As}$  quantum well structure, is consistent with theoretical prediction and thus demonstrates QCE experimentally.

## References

- [1] Zhang, S.L. (2008) in *Raman Spectroscopy and Low-dimensional Nanoscale Semiconductors* (in Chinese) Science Press. Beijing.
- [2] Imry, Y. (2006) *Introduction to Mesoscopic Physics*, 2nd edn, Oxford University Press, Oxford.
- [3] Cao, G. (2004) *Nanostructures & Nanomaterials: Synthesis, Properties & Applications*, Imperial College Press, London.
- [4] Zeng, J.-Y. (2006) *Quantum Mechanics*, Vol. 1 (in Chinese), 3rd edn, Science Press, Beijing.
- [5] Kubo, R. (1962) *J. Phys. Soc. Jpn.*, **17**, 975.
- [6] Esaki, L. and Tsu, R. (1970) *IBM J. Res. Dev.*, **14**, 61.
- [7] Zsigmondy, R. (1914) in *Colloids and the Ultramicroscope*, J. Wiley and Sons, New York.
- [8] Cho, A.Y. (1971) *Appl. Phys. Lett.*, **19**, 467–468.
- [9] Birringer, R., Gleiter, H., Klein, H.P., and Marquardt, P. (1984) *Phys. Lett. A*, **102**, 365–369.
- [10] Dingle, R., Wiegmann, W., and Henry, C.H. (1974) *Phys. Rev. Lett.*, **33**, 827–830.

# 7

## Theoretical Fundamentals of Raman Scattering in Solids

The crystallographic structure of nanomaterials formed by the self-organized growth method is consistent with that of solids, as was described in Section 6.3.3. Concerning other nanomaterials not formed by the self-organized growth method, such as the super-lattice prepared by molecular beam epitaxy (MBE), the crystallographic structure is still partially consistent with the composition of its solid material. Therefore, we need to have knowledge of the theoretical fundamentals of Raman scattering in solids before discussing Raman scattering in nanostructures, which is discussed in this chapter.

In light scattering theory, as discussed in Chapter 2, the scattering of objects concerns atoms and molecules, in order to explore the scattering mechanism clearly. However, the scattering objects in this present study mostly involve condensed matter including solids, liquids, and organisms and so on, which consist of many atoms and molecules. The Raman scattering theory in solids can be seen as a supplement and generalization of the Raman scattering theory described in Chapter 2.

A solid is made up of atoms or molecules arranged in space. To show this arrangement, it can be visualized that the atoms or molecules occupy the points of the lattice, forming the “crystal lattice.” If the crystal lattice displays a periodic arrangement, then it has a long-range order and the corresponding solid is a crystal, otherwise it is a non-crystal, an amorphous solid. Figures 7.1(a) and (b) show the atom array structures of crystalline and amorphous silicon viewed from its (110) surface, which are generated by a computer and are a good match as those in experiments [1].

The interaction between light and solids occurs between light and so-called “elementary excitation” in the solids. In Raman scattering within solids, the most important elementary excitation is the phonon, that is, the quantum of lattice vibration. Lattice vibration not only interrelates with Raman scattering, but also with other physical properties, such as thermology, photology, electroylogy, superconductivity, magnetology, and phase transition and so on in solids. In this chapter, we mainly discuss Raman scattering of lattice vibrations

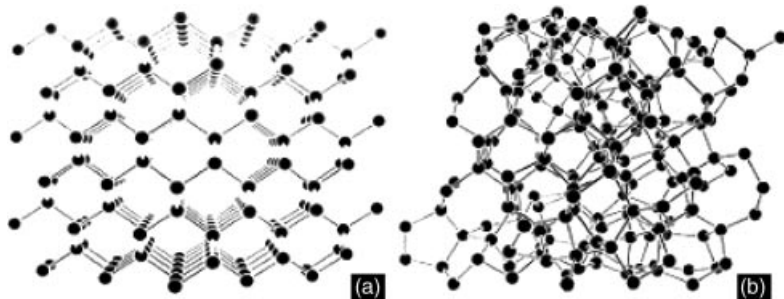


**Figure 7.1** Sketch of atom array structure generated by computer for crystalline (a) and amorphous (b) silicon viewed from its (110) surface [1]. Reprinted from K. Winor, Structural and vibrational properties of a realistic model of amorphous silicon, *Phys. Rev. B*, 35, 2366–2374 (1987) with permission of the American Physical Society

and so will only introduce lattice dynamics and the Raman scattering theory of lattice vibrations.

## 7.1 General Knowledge of Lattice Dynamics [2–6]

The solid physical properties, including lattice vibrations, can be studied by solving the Newton equation used in classical mechanics or the Schrödinger equation used in quantum mechanics. However, due to there being such a large number of atoms and molecules in solids, it is impossible to solve any motion equation exactly. Even with computer technology being so advanced, we can only solve the system involving atomic numbers of  $10^2 \sim 10^3$  order of magnitude. Therefore, we have to make a reasonable approximation for motion equations and then derive a simplified equation that can be solved. To date, solid Raman scattering theory is performed based on these simplified equations mostly.

### 7.1.1 Simplification of Motion Equation and Lattice Dynamics

The total Hamilton of crystals  $H$  can be expressed as

$$\mathcal{H} = - \sum_i \frac{P_i^2}{2M_i} + \sum_j \frac{p_j^2}{2m_j} + \mathcal{H}_{\text{int}}(\mathbf{R}, \mathbf{r}) \quad (7.1a)$$

where the first and second terms represent the kinetic energy of the atomic nucleus and electrons in the system, respectively, in which  $M_i$ ,  $m_j$ , and  $P_i$ ,  $p_j$  represent mass and momentum of the atomic nucleus and electrons, respectively; the third term is the total interacting energies between different atomic nuclei, different electrons, and atomic nuclei and electrons, and  $\mathbf{R}$  and  $\mathbf{r}$  represent space coordinates of atomic nuclei and electrons, respectively.

#### 7.1.1.1 Separation for the Inner and Outer Layer Electrons in Atoms and Ion Core

First, we can separate the electrons in solids into two types: the inner and outer layer electrons. The inner electrons are within the full shell of atoms, which is made up of an “ion

core” (the atomic nucleus) together with the atomic nucleus. The outer electrons are in the unfilled shell, which are named as valence electrons and play a key role in the formation of electron energy bands in solids.

### 7.1.1.2 Born–Oppenheimer (Adiabatic) Approximation and the Separating of Ion Core from Electrons

The mass of the atomic nucleus (ion core) is much larger than that of electrons (valence electrons) and thus the vibration frequency of the atomic nucleus is less than  $10^{13}$  Hz, while the vibration frequency of electrons is about  $10^{15}$  Hz, which indicates that the energy difference between the atomic nucleus and electrons is  $2 \sim 3$  orders of magnitude. In quantum mechanics, the energy exchange between the atomic nucleus and electrons is considered as not occurring, implying they have the so-called “adiabatic status.” Therefore, we introduce an adiabatic approximation, the so-called Born–Oppenheimer approximation. In adiabatic approximation, the motion of the atomic nucleus can be separated from electron motion. Regarding the motion of electrons, the atomic nucleus is thought to remain in its present position, so the motion of the atomic nucleus is in the static state relative to the electrons. So we do not need to consider the instant distribution of electrons and can think of the atomic nucleus as only suffering an effective potential of electrons  $\Phi(r)$ . The resulting Hamilton  $\mathcal{H}$  of the system can be written as the summation of the independent atomic nucleus (ion core) Hamilton  $\mathcal{H}_{ion}$  and electron Hamilton  $\mathcal{H}_e$ , namely:

$$\mathcal{H} = \mathcal{H}_{ion}(\mathbf{R}) + \mathcal{H}_e(\mathbf{r}, \mathbf{R}_0) \quad (7.1b)$$

Let  $\chi(r)$  and  $\varphi_n(R, r)$  be the wave function of the electrons and nucleus, respectively. In the above equation,  $\mathbf{r}$  is the electron coordinate and  $R$  and  $R_0$  are the coordinates of the atomic nucleus at immediate and stable positions, respectively. Under the adiabatic approximation, the wave function of the system can be written as the product of the wave functions of the atomic nucleus and electrons:

$$\psi(\mathbf{R}, \mathbf{r}) = \varphi_n(\mathbf{R}, \mathbf{r})\chi(\mathbf{r}) \quad (7.2)$$

where  $n$  represents the energy level. Now the Schrödinger equation of the system is

$$[\mathcal{H}_{ion}(\mathbf{R}) + \mathcal{H}_e(\mathbf{r}, \mathbf{R}_0)]\varphi_n(\mathbf{R}, \mathbf{r})\chi(\mathbf{r}) = E\varphi_n(\mathbf{R}, \mathbf{r})\chi(\mathbf{r}) \quad (7.3)$$

By using the separation of variables for the above equation, we can respectively obtain Schrödinger equations of the atomic nucleus and electrons:

$$\mathcal{H}_e(\mathbf{r}, \mathbf{R}_0)\varphi_n(\mathbf{R}, \mathbf{r}) = E_n\varphi_n(\mathbf{R}, \mathbf{r}) \quad (7.4)$$

and

$$[\mathcal{H}_{ion}(\mathbf{R}) + E_n]\chi_v(\mathbf{r}) = E_{n,v}\chi_v(\mathbf{r}) \quad (7.5a)$$

$E_n$  in Equation (7.4) is the Eigen energy with the electron being in the state to play a role in the effective potential  $\Phi(x)$  in Schrödinger Equation (7.5a), thus Equation (7.5a) can be re-written as

$$[\mathcal{H}_{ion}(\mathbf{R}) + \Phi(\mathbf{R})]\chi_v(\mathbf{r}) = E_{n,v}\chi_v(\mathbf{r}) \quad (7.5b)$$

Equation (7.4) is the electron equation with an atom at position  $\mathbf{R}$ . Equation (7.5) is the motion equation of atomic nucleus under the effective potential  $\Phi(x)$  of elections.  $\Phi(x)$  is determined

by the energy of a certain stationary state. To resolve Equation (7.4) requires electron motion theory, while to resolve Equation (7.5) requires lattice dynamics. The solving of Equation (7.4) can be obtained from the information of energy band structures of electrons in solids, while the solving of Equation (7.5) will show the relation between the frequency  $\omega$ , mode number, momentum  $q$  (i.e., dispersion relation), and the VDOS. Therefore, Equation (7.5) is closely correlated with light scattering and the Raman spectrum.

#### 7.1.1.3 Mean Field Approximation and Single Electron Theory

The electron concentration in semiconductors is about  $10^{23}/\text{cm}^3$  so to solve Equation (7.4) is not possible. Thus the so-called mean field approximation has been introduced, in which the interaction between electrons in solids is ignored and the motion of each electron is considered to be in a mean field formed by other electrons and the nucleus. As a result, the solving of many electrons is simplified into the solving of a single electron. The mean field approximation is also called the single electron approximation or Hartree–Fock approximation. The build-up of electron energy band theory is based solely on this single electron approximation.

#### 7.1.1.4 Small Vibration and Harmonic Approximation

As long as the absolute temperature is not below zero, the atomic nucleus cannot attach to the lattice point and can only move around the point within lattice. If this movement is a “small movement,” we can adopt a so-called harmonic approximation to describe it, that is, the atomic nucleus movement is seen as a harmonic vibration in the vicinity of the lattice point.

### 7.1.2 Classical Mechanics Theory-Lattice Waves

The harmonic vibration of the crystal lattice is typically a small vibration in classical mechanics theory, which can be described as follows.

If there are  $N$  atoms in the system, the equilibrium position of the  $n$ -th lattice point is  $R_n$  and the displacement of departure against  $R_n$  is described by  $u_n$ , the position of the atom at time  $t$  can be written as

$$\mathbf{R}_n(t) = \mathbf{R}_n + \mathbf{u}_n(t) \quad (7.6)$$

If the displacement vector is to be expressed by its components,  $N$  atoms have  $3N$  components of equilibrium position vectors  $R_i$  ( $i = 1, 2, \dots, 3N$ ) and  $3N$  components of displacement vectors  $u_i$  ( $i = 1, 2, \dots, 3N$ ).

The canonical equation can be used to discuss lattice vibration [7]. First, we need the potential function  $V$  of the system.  $V$  is the function of displacement  $u_i$  and can be expressed by the Taylor's series expansion of displacement  $u_i$  as

$$V = V_0 + \sum_{i=1}^{3N} \left( \frac{\partial V}{\partial u_i} \right)_0 u_i + \frac{1}{2} \sum_{i=1, j=1}^{3N} \left( \frac{\partial^2 V}{\partial u_i \partial u_j} \right)_0 u_i u_j + \dots \quad (7.7)$$

In the above equation, the subscript 0 indicates that the labeled function takes the value at the equilibrium position. Let the potential at resting state be  $V_0 = 0$  and  $\left[ \frac{\partial V}{\partial u_i} \right]_0 = 0$ . Since we are

only concerned with the small vibration, the potential  $V$  can be taken to the square of  $u_i$ , so we have

$$V = \frac{1}{2} \sum_{i=1, j=1}^{3N} \left( \frac{\partial^2 V}{\partial u_i \partial u_j} \right)_0 u_i u_j \quad (7.8)$$

Second, we need the kinetic energy  $T$  of the system of  $N$  atoms, which can be written as

$$T = \frac{1}{2} \sum_{i=1}^{3N} M_i \dot{u}_i^2 \quad (7.9)$$

In order to simplify the above equations, the potential and kinetic energy functions should not merge, so we use the normal coordinate  $Q_i$  ( $i = 1, 2, \dots, 3N$ ) to replace the displacement coordinate  $u_i$  and the relation between them is expressed by the following orthogonal transformation relations:

$$\sqrt{m_i} u_i = \sum_{j=1}^{3N} a_{ij} Q_j \quad (7.10)$$

Thus, in the form of normal coordinates:

$$T = \frac{1}{2} \sum_{i=1}^{3N} \dot{Q}_i^2 \quad (7.11)$$

$$V = \frac{1}{2} \sum_{i=1}^{3N} \omega_i^2 Q_i^2 \quad (7.12)$$

The coefficient in Equation (7.12) is expressed as a square form  $\omega_i^2$ , indicating that it is positive and the atoms are in equilibrium at the lattice points.

We can obtain the Lagrangian function  $L = T - V$  and so the corresponding canonical momentum  $P_i$  is

$$P_i = \frac{\partial L}{\partial \dot{Q}_i} = \dot{Q}_i \quad (7.13)$$

Thus the Hamilton of system is expressed as

$$\mathcal{H} = T + V = \frac{1}{2} \sum_{i=1}^{3N} \left( p_i^2 + \omega_i^2 \dot{Q}_i^2 \right) \quad (7.14)$$

The canonical motion equation is

$$\ddot{Q}_i + \omega_i^2 Q_i = 0 \quad (7.15)$$

Equation (7.15) has  $i = 1, 2, \dots, 3N$ , and canonical motion equations have no correlation with each other and have  $3N$  independent solutions. As a result, the solution of a many-body system becomes that of a single-body system. Any solution of canonical coordinates is a

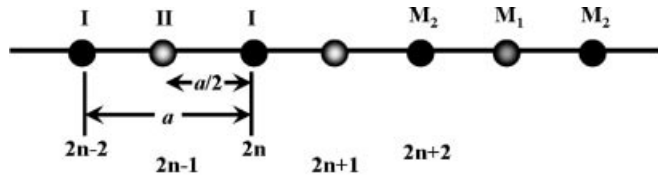


**Figure 7.2** One-dimensional diatomic linear chain model. Reprinted from S.-L. Zhang, Raman Spectroscopy and Low-dimensional nanoscale Semiconductors, Science Press, (2008)

harmonic function, thus the solution to Equation (7.15) is

$$Q_i = A_i \sin(\omega_i t + \varphi_i) \quad (7.16)$$

The corresponding displacement  $u_i$  is

$$u_i = \frac{1}{\sqrt{m_i}} \sum_{j=1}^{3N} a_{ij} A_j \sin(\omega_j t + \varphi_j) \quad (7.17)$$

We can see from Equations (7.16) and (7.17) that each vibration solution of the equations expressed by canonical coordinate  $Q_i$  is not only the vibration of a certain atom but also the vibration caused by all of the atoms in the system. This collective vibration is the “vibration mode.” The vibration mode joined by all atoms in the system processes a characteristic of wave and thus the lattice vibration is named the “lattice wave” in classical mechanics.

### 7.1.3 Lattice Vibration of One-dimensional Double Atom Chain [2,3]

As mentioned above, there are a great number of atoms in a crystal, so the calculation of lattice dynamics for a three-dimensional solid crystal is impossible practically. However, in order to gain a basic knowledge of lattice dynamics, we designed a one-dimensional linear chain to model an imaginary crystal so that we could perform a “strict” calculation of lattice dynamics.

#### 7.1.3.1 Newton Equation and its Solution – Optical and Acoustic Lattice Wave

The structure of a one-dimensional double atom linear chain is shown in Figure 7.2. This type of structure can be considered as a one-dimensional double atom crystal. There are two atoms in one primitive cell, of which two atoms are labeled I and II with masses  $M_1$  and  $M_2$ , respectively. In Figure 7.2, label  $a$  is the lattice constant, the distance between atoms is  $a/2$ , and the atoms in the chain are labeled as  $2n - 1$ ,  $2n$ , and  $2n + 1$ , and so on. This only considers the motion along atom chains, that is, in the longitudinal direction. Considering that atoms only have an elastic interaction between their neighbors, the interaction force can be written as

$$F = -f\delta \quad (7.18)$$

where  $f$  is a force constant; and  $\delta$  is the relative displacement of atoms. For instance, the relative displacement of atom I at  $2n$  and atom II at  $2n + 1$  is  $\delta_{2n}$  and  $\delta_{2n+1}$ , respectively, expressed as

$$\begin{aligned} \delta_{2n} &= 2u_{2n} - u_{2n+1} - u_{2n-1} \\ \delta_{2n+1} &= 2u_{2n+1} - u_{2n+2} - u_{2n} \end{aligned} \quad (7.19)$$

According to the Newton equation, we can write the motion equations of atoms I and II as

$$\begin{aligned} M_1 \ddot{u}_{2n+1} &= -f(2u_{2n+1} - u_{2n} - u_{2n+2}) \\ M_2 \ddot{u}_{2n} &= -f(2u_{2n} - u_{2n+1} - u_{2n-1}) \end{aligned} \quad (7.20)$$

In the two equations above, when they include a  $N$  primitive cell, that is, contain  $N$  atom I and atom II, Equation (7.20) becomes a simultaneous equation of  $2N$  equations; the formal solution of the equations is

$$\begin{aligned} u_{2n} &= Ae^{i(\omega t - naq)} \\ u_{2n+1} &= Be^{i(\omega t - (n+1/2)aq)} \end{aligned} \quad (7.21)$$

Substituting the above formal solutions into the motion Equations (7.20), we have

$$\begin{aligned} -M_1\omega^2 B &= f \left( e^{\frac{1}{2}iaq} + e^{-\frac{1}{2}iaq} \right) A - 2fB \\ -M_2\omega^2 A &= f \left( e^{\frac{1}{2}iaq} + e^{-\frac{1}{2}iaq} \right) B - 2fA \end{aligned} \quad (7.22)$$

The above equations have no correlation with  $n$ , meaning the motion equations are independent of the specific position of primitive cells. All simultaneous equations can be attributed to the same pair of equations, so Equation (7.22) can be considered a linear homogeneous equation with unknown numbers A and B:

$$\begin{aligned} (M_2\omega^2 - 2f)A + 2f \cos(aq/2)B &= 0 \\ 2f \cos(aq/2)A + (M_1\omega^2 - 2f)B &= 0 \end{aligned} \quad (7.23)$$

The existing condition of the above solution is that the coefficient determined in Equation (7.23) is equal to 0:

$$\begin{vmatrix} M_2\omega^2 - 2f & 2f \cos(aq/2) \\ 2f \cos(aq/2) & M_1\omega^2 - 2f \end{vmatrix} = 0 \quad (7.24)$$

$\omega^2$  can be obtained from Equation (7.24) as

$$\omega^2 = f \frac{M_1 + M_2}{M_1 M_2} \left\{ 1 \pm \left[ 1 - \frac{4M_1 M_2}{(M_1 + M_2)^2} \sin^2(aq/2) \right]^{1/2} \right\} \quad (7.25)$$

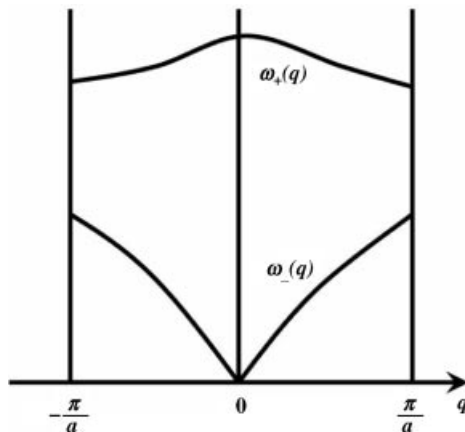


**Figure 7.3** Dispersion relation of acoustic and optical waves in one-dimensional diatomic chain crystal. Reprinted from S.-L. Zhang, *Raman Spectroscopy and Low-dimensional nano-scale Semiconductors*, Science Press, (2008)

Substituting  $\omega_+$  and  $\omega_-$  back into Equation (7.23), we obtain the solution of A and B:

$$\left(\frac{B}{A}\right)_+ = -\frac{M_2\omega_+^2 - 2f}{2f \cos(aq/2)} \quad (7.26)$$

$$\left(\frac{B}{A}\right)_- = -\frac{M_2\omega_-^2 - 2f}{2f \cos(aq/2)} \quad (7.27)$$

From Equation (7.21), we know that the phase difference between adjacent primitive cells, that is, the phase difference between the same type of atoms in the adjacent primitive, is  $aq$ . Obviously, if we change  $aq$  with integer times  $2\pi$ , there will be no difference in the vibration of all atoms and this indicates the value of wave vectors if they are in following limited range:

$$-\frac{\pi}{a} < q \leq \frac{\pi}{a} \quad (7.28)$$

This limited range is only the “first Brillouin zone” of a one-dimensional double atom chain, in which there are two lattice wave solutions for any wave vector  $q$ , with the frequencies  $\omega^+$  and  $\omega^-$  given by Equation (7.25). The lattice wave has the same properties of amplitude and phase as a common wave, but the amplitude ratio and phase difference of atoms I and II is fixed and determined by Equations (7.26) and (7.27), thus the term “Brillouin zone” will only means the first Brillouin zone.

Figure 7.3 shows the variation curve of lattice wave frequency  $\omega^+$  and  $\omega^-$  with wave vector determined by Equation (7.25), which is the dispersion curve of the lattice wave. The lattice wave  $q \approx 0$  is very important in solving actual problems, especially in the light scattering of a crystal. In order to understand the properties of a lattice wave, we will discuss these properties in a one-dimensional double atom chain at  $q \approx 0$ , That is, the long wave limitation.

- Lattice wave of  $\omega_-$

It can be seen from Equation (7.25) and Figure 7.3 that when  $q \rightarrow 0$ ,  $\omega \rightarrow 0$ , we have

$$\frac{4M_1M_2}{(M_1 + M_2)^2} \sin^2(aq/2) \ll 1 \quad (7.29)$$

We solve the radical expression in Equation (7.25) with  $q^2$  and have

$$\omega_- \approx \frac{a}{2} \sqrt{\frac{2f}{M_1 + M_2}} q \quad (7.30)$$

Equation (7.30) shows that lattice wave  $\omega_-$  is proportion to  $q$ , meaning that the lattice wave of  $\omega_-$  is like the elastic wave in the media and thus lattice wave of  $\omega_-$  is called an acoustic wave. When  $q \rightarrow 0$ ,  $\omega \rightarrow 0$ , and from Equation (7.27) we have

$$\left(\frac{B}{A}\right)_- \rightarrow 1 \quad (7.31a)$$

It means that for a long acoustic wave, the motion of two kinds of atoms in a primitive cell is the same, with no difference in amplitude and phase of vibrations.

- Lattice wave of  $\omega_+$

For lattice wave of  $\omega_+$ , when  $q \rightarrow 0$ , the frequency approaches a finite value expressed as

$$\omega_+ \rightarrow \sqrt{2f \left/ \left( \frac{M_1M_2}{M_1 + M_2} \right) \right.} \quad (7.32)$$

Substituted the above value of  $\omega_+$  into Equation (7.26), and letting  $\cos(aq/2) \rightarrow 0$ , we have

$$\left(\frac{B}{A}\right)_+ \rightarrow -\frac{M_2}{M_1} \quad (7.31b)$$

When  $q \rightarrow 0$ , it can be seen from Equation (7.25) that the phase of vibration is the same for same kind of atoms, that is, the lattice formed by same kind of atoms vibrate as a rigid body. Thus, Equation (7.31b) shows that when  $q \rightarrow 0$ , the vibrations of these two kinds of atoms (e.g., atoms I and II) have an opposite phase and thus the lattice wave of  $\omega_+$  is called an optical wave. In the vibration process of the optical wave, atoms I and II vibrate relatively while their mass centers do not vary, as shown in Figure 7.4.



**Figure 7.4** Sketch of lattice vibration of optical wave formed by atoms I and II in one-dimensional diatomic chain. Reprinted from S.-L. Zhang, Raman Spectroscopy and Low-dimensional nanoscale Semiconductors, Science Press, (2008)



**Figure 7.5** Born–Karman boundary conditions for one-dimensional diatomic chain [8]. Reprinted from S.-L. Zhang, *Raman Spectroscopy and Low-dimensional nanoscale Semiconductors*, Science Press, (2008)

#### 7.1.3.2 Periodicity Condition – a Limitation on Taken Values of Wave Vectors

The chain length of a one-dimensional diatomic chain, as shown in Figure 7.2, is modeled as infinite and all atoms move in the same way according to motion in Equation (7.20). However, it is impossible for a chain to be of infinite length, and also the situation of atoms at two ends of a chain are different from those in the middle of the chain, meaning the motion equation being too complex to resolve. In order to prevent the above difficulties, Born and Karman suggested a model for a one-dimensional diatomic chain, in which a cyclic chain with  $N$  primitive cells is used to simulate a one-dimension finite chain with  $N$  primitive cells, as shown in Figure 7.5 [8]. Although the cyclic chain contains a limited number of atoms, it makes all the primitive cells equal at the same time. Because the number of  $N$  is very large, the motion along the ring can still be seen as the motion of a one-dimensional linear chain and thus Equation (7.20) still holds. This model means that the phase part of the standard solution (Equation 7.21) follows the condition

$$e^{-iN\alpha q} = 1 \quad (7.33)$$

Thus, the wavevector is expressed as

$$q = \frac{2\pi}{Na} K \quad (7.34)$$

where  $K$  is an integer

Since the range of  $q$  is  $(-\pi/a, +\pi/a)$ ,  $K$  can only be taken at different integer values  $K$  within  $(-N/2, +N/2)$ . Thus,  $q$  has  $N$  different values in a one-dimensional chain composed of  $N$  atoms. Because each  $q$  corresponds to two wave vectors, there will be  $2N$  different wave vectors. The number  $2N$  of wave vectors are only the motion freedom number of chains, which proves that the Born–Karman cyclic chain can obtain all of the vibration modes within the chain.

The Born–Karman circular chain model means a periodicity boundary condition, so the Born–Karman cyclic chain model is also called the Born–Karman boundary condition.

If we extend a one-dimensional double atom chain into a three-dimensional system, it is possible in principle to perform a lattice dynamics calculation of a real crystal. However, the calculation quantity is still large and, in the past, most of the calculations of three-dimensional crystal lattice dynamics were based on phenomenological models, to be discussed in the next section.

Although the above description is based on the one-dimensional linear chain model, the derived results, such as the features of acoustic and optical lattice waves and the possibility of the accepted range for the wave vector value, still have universal significance.

### 7.1.4 Quantum Mechanical Theory – Phonon

According to the relation between classical mechanics and quantum mechanics [9], as long as we consider the canonical momentum  $P_i$  and normal coordinate  $Q_i$  as a pair of non-commute and conjugate operators of quantum mechanics and write  $P_i$  as a quantum mechanics operator  $-i\hbar \frac{\partial}{\partial Q_i}$ , the canonical equation in classical mechanics will be transformed to the wave equation in quantum mechanics, expressed as

$$\sum_{i=1}^{3N} \frac{1}{2} \left( -\hbar^2 \frac{\partial^2}{\partial Q_i^2} + \omega_i^2 Q_i^2 \right) \psi(Q_1, Q_2 \cdots Q_{3N}) = E \psi(Q_1, Q_2 \cdots Q_{3N}) \quad (7.35)$$

Since Equation (7.35) is the motion equation of  $3N$  independent harmonic vibration modes; there exists a motion equation for each normal coordinate  $Q_i$ , expressed as

$$\frac{1}{2} \left( -\hbar^2 \frac{\partial^2}{\partial Q_i^2} + \omega_i^2 Q_i^2 \right) \varphi_{n_i}(Q_i) = \varepsilon_i \varphi_{n_i}(Q_i) \quad (7.36)$$

The energy  $\varepsilon_i$  and corresponding wave function  $\varphi_{n_i}(Q_i)$  for each vibration mode are expressed as

$$\varepsilon_i = \left( n_i + \frac{1}{2} \right) \hbar \omega_i \quad (7.37)$$

$$\varphi_{n_i}(Q_i) = \sqrt{\frac{\omega}{\hbar}} \exp\left(-\frac{\xi^2}{2}\right) H_{n_i}(\xi) \quad (7.38)$$

In Equation (7.38),  $\xi = \sqrt{\frac{\omega}{\hbar}} Q_i$  and  $H_{n_i}$  is the Hermitian polynomial. The energy  $\varepsilon_i$  and wave function  $\varphi_{n_i}(Q_i)$  for the Eigen state of the system are

$$E = \sum_{i=1}^{3N} \varepsilon_i = \sum_{i=1}^{3N} \left( n_i + \frac{1}{2} \right) \hbar \omega_i \quad (7.39)$$

$$\psi(Q_1, Q_2 \cdots Q_{3N}) = \prod_{i=1}^{3N} \varphi_{n_i}(Q_i) \quad (7.40)$$

The Eigen energy of the vibration state of normal coordinate  $Q_i$  described by Equation (7.38) is shown in Equation (7.37), and the unit of energy  $\varepsilon_i$  shown in Equation (7.37) is expressed by  $\hbar \omega_i$ . In quantum mechanics, energy unit  $\hbar \omega_i$  is seen as an energy quantum and is called a “phonon.” When the subscript of  $\varphi_{n_i}(Q_i)$  is  $n_i = 0$ , the system is at its lowest state, and has energy  $1/2 \hbar \omega_i$ , which indicates that the system is in the so-called ground state and thus  $n_i \neq 0$  means the system is in the excited state with  $n_i$  phonons.

Unlike an electron, a phonon cannot exist isolated from a solid. Moreover, the momentum  $q$  of a phonon does not need to be conservative in its interactive process with another object. A phonon is an excited unit of atomic collective motion in solids and so is called as elementary excitation, that is, a phonon is a quasi-particle. A phonon is, in fact, a boson and thus there is no limit on the number that can occupy an energy level and the average occupation number at energy level of  $\hbar\omega_i$  follows the Bose–Einstein distribution:

$$n_i(\mathbf{q}) = \frac{1}{e^{\hbar\omega_i(\mathbf{q})/k_B T} - 1} \quad (7.41)$$

where  $k_B$  is the Boltzmann constant and  $T$  is absolute temperature.

### 7.1.5 Electron-Phonon Interaction [5]

In the theory of single electrons mentioned in Section 7.1.1, the electrons in a crystal lattice move in the periodic potential field formed by the crystal lattice. The lattice vibration reflects the deviation of atoms (or ions) from the lattice point, which will destroy the periodic potential field and thus the electrons will be affected by the new potential field. Therefore, in order to know the energy band of the electrons, we must consider the interaction between the crystal lattice vibration (phonon) and the electron. In the phonon scattering process induced by visible light, the energy difference between light and a phonon is about three orders of magnitude and thus they cannot interact and induce the visible light scattering directly. Therefore, the visible light scattering must recur as an intermediary agent, which is only the electron. Thus, the light scattering of crystal lattice vibration also involves this electro-phonon interaction. As a result, the total Hamilton  $H$  of light scattering not only includes Hamilton  $\mathcal{H}_{ion}(\mathbf{r}_i, \mathbf{R}_j)$  of the atomic core and Hamilton  $\mathcal{H}_e(\mathbf{r}_i, \mathbf{R}_j)$  of electrons, but also the Hamilton  $\mathcal{H}_{e-ph}(\mathbf{r}_i, \delta\mathbf{R}_j)$  of the electron-phonon interaction, meaning that Equation (7.1b) should be re-written as

$$\mathcal{H} = \mathcal{H}_{ion}(\mathbf{R}_j) + \mathcal{H}_e(\mathbf{r}_i, \mathbf{R}_j) + \mathcal{H}_{e-ph}(\mathbf{r}_i, \delta\mathbf{R}_j) \quad (7.42)$$

Light scattering of a crystal lattice vibration usually occurs at  $q \approx 0$  and thus the electron-phonon interaction is important for the light scattering of crystal lattice vibrations (phonons) under long wavelength conditions. In the following we will discuss the electron-phonon interaction in the approximation of long wavelength for the transverse acoustic (TA), longitudinal acoustic (LA), transverse optical (TO), and longitudinal optical (LO) phonons.

### 7.1.6 Electrons-Acoustic Phonon Interaction

An acoustic phonon represents the entire motion of atoms in solids, so it can change the crystal shape, resulting in a change in the energy of electrons in the energy band. The energy of an electron with the effective mass at energy band side  $m^*$  and wave vector  $\mathbf{k}$  can be expressed as

$$\varepsilon_k = \varepsilon_c + \frac{\hbar^2 k^2}{2m^*} \quad (7.43)$$

In the above equation,  $\varepsilon_c$  is the potential energy in the periodic potential field, without taking into account lattice vibration. A lattice vibration in solids will induce deformation of crystals,

then the lattice constant  $a$  and crystal volume  $V$  will change and then the electron energy at the band side will change with a changed quantum  $\delta\epsilon$  expressed as

$$\delta\epsilon = \left(\frac{\partial\epsilon}{\partial V}\right)\delta V = V\left(\frac{\partial\epsilon}{\partial V}\right)\frac{\delta V}{V} = a_c \frac{\delta V}{V} \quad (7.44)$$

In the above equation,  $a_c$  is the deformation potential induced by the change of volume, which is induced by the displacement of atoms and is a short-range interaction.

#### 7.1.6.1 Piezoelectric Electrons-Acoustic Phonon Interaction

In non-centro-symmetrical crystals, such as ZnO, CdS, and CdSe, strain can induce a macro-electric polarization field  $\mathbf{E}$ , which is known as the piezoelectric effect. In the medium with permittivity  $\epsilon$ , when the strain is small, the electric field induced by strain is linear and can be expressed as

$$\mathbf{E} = \hat{\mathbf{e}}_m \cdot \mathbf{e}/\epsilon \quad (7.45)$$

where  $\hat{\mathbf{e}}_m$  is the proportional coefficient caused by strain and is called the electricity tensor. Because the deformation tensor is a two-order tensor,  $\hat{\mathbf{e}}_m$  is a three-order tensor. The strain discussed above is static strain and can be worked in the strain field induced by acoustic phonon vibration. The strain energy of an acoustic phonon is  $i\mathbf{q} \cdot \Delta\mathbf{R}$ , so the macro-electric polarization field induced by an acoustic phonon can be written as

$$\mathbf{E}_{pe} = i\hat{\mathbf{e}}_m \cdot \mathbf{q} \cdot \delta\mathbf{R}/\epsilon \quad (7.46)$$

In the above equation,  $\mathbf{q}$  and  $\delta\mathbf{R}$  is the wave vector of phonons and atom displacement, respectively. The scalar potential induced by the longitudinal component of the electric potential is

$$\phi_{pe} = -i\mathbf{q} \cdot \mathbf{E}_{pe}/(iq^2) \quad (7.47)$$

So, the Hamilton of piezoelectric electrons-acoustic phonons is

$$H_{pe} = -|e|\phi_{pe} = (|e|/q^2\epsilon_\infty)\mathbf{q} \cdot \hat{\mathbf{e}}_m \cdot (\mathbf{q} \cdot \delta\mathbf{R}) \quad (7.48)$$

#### 7.1.6.2 Deformation Potential Interaction of Electron-Optical Phonon

The optical vibration cannot induce macro-strain, but can be regarded as induced by micro-strain in primitive cells. Like acoustic phonons, there are two ways to affect the energy of electrons. In non-polar crystals, it is caused by the change bond length and bond angle to affect the energy of electrons. This is similar to the deformation potential interaction of acoustic phonons and thus known as the deformation potential interaction between electrons and optical phonons.

Supposing the distance between two atoms in the primitive cell is  $a_0$ , and these two atoms are related to the phonons at the center of the Brillouin zone with a displacement  $\mathbf{u}$ , strain potential of the electron-optical phonon interaction can be defined as

$$\mathcal{H}_{e-\Delta p} = D_{n,k}(\mathbf{u}/a_0) \quad (7.49)$$

The proportional coefficient  $D_{n,k}$  is the strain potential of an optical phonon at energy band  $E_{n,k}$ . This strain potential is independent of the phonon wave vector  $\mathbf{q}$  and thus is a short-range interaction.

### 7.1.6.3 Fröhlich Interaction

In polar crystals, when the atoms of carrying charge undergo a relative displacement, a macroscopic electrical field will be generated. This macroscopic electrical field will interact with the electrons. This is a long-range Coulomb interaction, that is, the so-called Fröhlich potential. Similar to the strain electrical field of an acoustic phonon, a long wavelength LO vibration can cause macroscopic polarization; if we define  $\mathbf{u}_{LO}$  as the relative displacement between cation and anion, the induced electrical field is

$$\mathbf{E}_{LO} = -F\mathbf{u}_{LO} \quad (7.50)$$

In the above equation

$$F = -[4\pi N\mu\omega_{LO}^2(\varepsilon_{\infty}^{-1} - \varepsilon^{-1})]^{1/2} \quad (7.51)$$

where  $\mu$  is reduced mass of the primitive cell and is defined by  $1/\mu = \sum_i 1/M_i$ ;  $M_i$  is the mass of the  $i$ th atom;  $i$  represents the number of atoms in a primitive cell;  $N$  is the number of primitive cells in unit volume;  $\omega_{LO}$  is frequency of a phonon, and  $\varepsilon_{\infty}$  and  $\varepsilon$  are the dielectric constants of high and low frequency, respectively. The electrical field can be showed by the scalar potential; for longitudinal scalar potential  $\phi_{LO}$  of  $\mathbf{E}_{LO}$  is

$$\phi_{LO} = (F/iq) u_{LO} \quad (7.52)$$

The Hamilton of the long-range Coulomb interaction is

$$\mathcal{H}_F = -e\phi_{LO} = (ieF/q) u_{LO} \quad (7.53)$$

From Equation (7.53), the Fröhlich interaction  $H_F$  is inversely proportional to wave vector  $q$ , which is totally different from the strain interaction of the electrons-acoustical phonon that has no correlation with  $q$ .

Unlike polar crystals, TO phonons generate traverse electrical fields, which can interact with photons directly and thus produces far-infrared spectra.

### 7.1.6.4 Electrons-Phonon Interaction at Big Wave Vectors

Interaction between electrons and phonons at large wave vectors correlates with the electrons and phonon at and near the boundaries of the Brillouin zone, which is important in non-direct light absorption and hot electron process. Raman scattering of multi-phonons and nano-semiconductors also correlate with the scattering of phonons at the boundaries of the Brillouin zone.

There exists some differences for the electron-phonon interaction between a large wave vector (near the boundary of the Brillouin zone) and a small wave vector (near the center of the Brillouin zone). For the phonons at the boundary of the Brillouin zone, there is no long-range electrical field and so is independent of the phonon wave vector, which is different from a piezoelectric and a Fröhlich interaction.

**Table 7.1** Types of electron-phonon interaction involving TA, LA, TO, and LO phonons with long wavelength for non-polar Si and polar GaAs [5]. Reprinted from P. Y. Yu and M. Cardona, *Fundamentals of Semiconductors*, Third Edition, (2001) with permission of Springer

Phonon	Si		GaAs	
	Conduction band	Valence Band	Conduction band	Valence Band
TA	DP <sup>a</sup>	DP	PZ	DP, PZ
LA	DP	DP	DP, PZ	DP, PZ
TO		DP		DP
LO		DP	F	F

<sup>a</sup> DP, PZ, and F represent the deformation potential, piezoelectric interaction and Fröhlich interaction.

Taking Si and GaAs as an example, we now introduce the types of electron-phonon interactions involved with TA, LA, TO, and LO phonons with long wavelengths, as shown in Table 7.1.

## 7.2 Microscopic Model of Lattice Dynamics

As mentioned in the beginning of this chapter, the strict calculation of crystal lattice dynamics in bulk solids is impossible and the calculation of crystal lattice dynamics in bulk solids basically relies on the phenomenological model.

In the phenomenological theory of crystal lattice dynamics, there are two types of modeling for crystals. One of them is the so-called microscopic model based on atoms (ions) in crystals and the other is the macroscopic model based on the crystal as a continuous medium. In the microscopic models, the interactions between atoms (or ions) are often simulated in different ways, resulting in different practical modes, such as the force constant model, shell model, bond model, and bond charge model and so on. The macroscopic models are set up based on continuous medium dynamics and classical electromagnetic field theory, for which there are the dielectric continuum model and continuous elastic model and so on. All of the above models are abstracted from specific crystals; therefore, different models have their own best application to the object.

In 1912, Born and von Karman proposed the first phenomenological model for performing the calculation of crystal lattice dynamics [8]. The classic masterpiece of phonon physics “Theory of crystal lattice dynamics” developed Born and von Karman’s model are very successful. Although their model is successful in fitting to the experimental dispersion curve, it does not provide information on the nature of the bonds and does not show a deep understanding of physical processes of lattice dynamics microscopically. In the 1950s, the models involving ions and electrons appeared, in which the shell model and bond-charge model are the most representative. The Huang equation is a typical representation of macroscopic models, which will be introduced below.

### 7.2.1 Crystal Lattices Dynamics of 3-dimension Crystal

#### 7.2.1.1 Newton Equation of 3-Dimensional Crystals

Section 7.1.3 described crystal lattices dynamics equations of one-dimensional double atoms chains. Now we write a crystal lattice dynamics equation of a three-dimension

crystal as

$$M_\alpha \ddot{u}_{\alpha,ik} = - \sum_{\beta,j\gamma} \phi_{\alpha\beta,ik;j\gamma} u_{\beta,j\gamma} \quad (7.54)$$

where  $i, j$  and  $\kappa, \gamma$  are the labels of primitive cells and the atoms in the cell, respectively; and  $a, \beta$  are the Cartesian coordinates of displacement  $\mathbf{u}$ . The  $\phi_{\alpha\beta,ik;j\gamma}$  represents the force along the  $\alpha$  direction suffered by an  $(i, k)$  atom when the  $(j, \gamma)$  atom has a displacement along the  $\beta$  direction.

Supposing the trial solution of Equation (7.54) is

$$u_{\alpha,ik} = M_k^{-\frac{1}{2}} u_{\alpha,k}(\mathbf{q}) \exp(-i\omega t + i\mathbf{q} \cdot \mathbf{R}_i) \quad (7.55)$$

where  $\mathbf{R}_i$  is the lattice vector;  $\mathbf{q}$  is the wave vector; and  $M_k$  is the mass of atom  $k$ . Substituting Equation (7.55) into Equation (7.54), we have

$$\omega^2 u_{\alpha,k}(\mathbf{q}) = \sum_{\beta\gamma} D_{\alpha\beta,k\gamma}(\mathbf{q}) u_{\beta\gamma}(\mathbf{q}) \quad (7.56)$$

In which

$$D_{\alpha\beta,k\gamma}(\mathbf{q}) = (M_k M_\gamma)^{-\frac{1}{2}} \sum_{R_i - R_j} \phi_{\alpha\beta,ik;j\gamma} \exp(-i\mathbf{q} \cdot (\mathbf{R}_i - \mathbf{R}_j)) \quad (7.57)$$

is the dynamics matrix, and summarizing for  $R_i - R_j$  means that the summation is for all lattice vectors.

The Eigen value of the dynamics matrix in the above equation is the square of phonon frequency  $\omega^2$ . Acquiring phonon frequency  $\omega$  implies that we obtain the basic information of the phonon dispersion relation and vibration density of state (VDOS) and so on, which are needed for the study of Raman scattering.

### 7.2.1.2 Solving of Crystal Lattice Dynamics Equation

The calculation of crystal lattice dynamics is attributed to the calculation of the dynamics matrix  $D_{\alpha\beta,k\gamma}(\mathbf{q})$ . The key to calculating  $D_{\alpha\beta,k\gamma}(\mathbf{q})$  is to obtain the “force constant”  $\phi_{\alpha\beta,ik;j\gamma}$ . This calculation is complex, thus many simplified models have been introduced for such a calculation.

## 7.2.2 Force Constant Model

### 7.2.2.1 Short Introduction

The force constant model only involves mechanical force between atoms. Born and Karman proposed the first force constant model [8], in which they supposed that atoms were solid balls and were connected to each other with springs, the spring constants determined by fitting experiment data. Born fitted the experimental results of carbon and Si by a force constant model with two spring constants [10]. To date, the force constant model is still commonly used.

### 7.2.2.2 Calculated Examples of Force Constant Model

Based on the force constant model, the authors of Ref. [11,12] performed the group theoretical analysis of symmetry and calculation of oscillation frequency for high-temperature

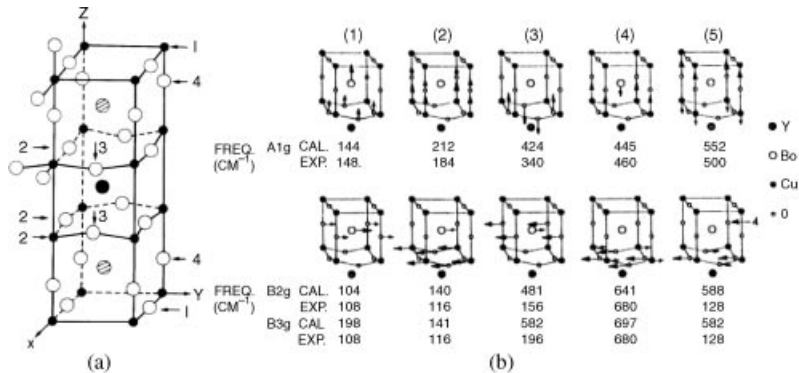


**Figure 7.6** Unit cell structure and the results of symmetry analysis based on group theory and the vibration mode frequency calculated based force constant model for high temperature superconductor  $\text{YBaCu}_x\text{O}_{7-x}$ ; CAL and EXP indicate that the date are from calculation and experiment, respectively [11,12]. Reprinted from S.-L. Zhang, *Raman Spectroscopy and Low-dimensional nanoscale Semiconductors*, Science Press, (2008)

superconductor  $\text{YBaCu}_x\text{O}_{7-x}$ . Figure 7.6(a) is a diagram of the unit cell of  $\text{YBaCu}_x\text{O}_{7-x}$  possessed orthorhombic structure with point group symmetry  $P_{2h} - mmm$ .

- Dynamics matrix

By marking the force constant between atoms  $i_1$  and  $i_2$  by  $f_s$  and an unit vector along the direction of  $i_1$  and  $i_2$  by  $x_s$ , as well as introducing a tensor  $T_{\alpha\beta}^s = x_{s\alpha}x_{s\beta}f_s$ , based on the definition of  $D_{\alpha\beta,i_1i_2}$  in Equation (7.57), the dynamics matrix with  $i_1 \neq i_2$  should be

$$\begin{aligned} D_{\alpha\beta,i_1i_2} &= \left[ T_{\alpha\beta}^s / (M_{i_1}M_{i_2}) \right]^{\frac{1}{2}} \exp[-i\mathbf{q} \cdot (\mathbf{r}_i - \mathbf{r}_j)] + D_{\alpha\beta,i_1i_2}^0 \\ D_{\alpha\beta,i_1i_2} &= T_{\alpha\beta}^s / M_{i_1} + D_{\alpha\beta,i_1i_2}^0 \\ D_{\alpha\beta,i_1i_2} &= T_{\alpha\beta}^s / M_{i_2} + D_{\alpha\beta,i_1i_2}^0 \end{aligned} \quad (7.58)$$

In the above equation,  $\mathbf{r}_i$  and  $\mathbf{r}_j$  are the position vector of atoms  $i$  and  $j$ , respectively, and the superscript “0” indicates initial value. By labeling the force constant of bond angle between atoms  $i_1$ ,  $i_2$  and  $i_3$  as  $f_b$ , and the position vectors of atoms 1, 2, and 3  $\mathbf{r}_1, \mathbf{r}_2$ , and  $\mathbf{r}_3$ , we have

$$\begin{aligned} \mathbf{r}_{12} &= \mathbf{r}_1 - \mathbf{r}_2 \\ \mathbf{r}_{32} &= \mathbf{r}_3 - \mathbf{r}_2 \\ \mathbf{x}_n &= \mathbf{r}_{12} \times \mathbf{r}_{32} \end{aligned} \quad (7.59)$$

Moreover, we construct two vectors  $\mathbf{x}_{b1}$  and  $\mathbf{x}_{b2}$  with the directions  $\mathbf{r}_{12} \times \mathbf{x}_n$  and  $\mathbf{r}_{32} \times \mathbf{x}_n$ , as well as the lengths  $1/r_{12}$  and  $1/r_{32}$ , respectively.

With tensor  $T_{\alpha\beta}^b = x_{b,\alpha}x_{b,\beta}f_b$ , at  $i_1 \neq i_2$ , we have

$$\begin{aligned} D_{\alpha\beta,i_1i_2} &= \left[ T_{\alpha\beta}^b / (M_{i1}M_{i2})^{\frac{1}{2}} \right] \exp[-i\mathbf{q} \cdot (\mathbf{r}_i - \mathbf{r}_j)] + D_{\alpha\beta,i_1i_2}^0 \\ D_{\alpha\beta,i_1i_2} &= T_{\alpha\beta}^b / M_{i1} + D_{\alpha\beta,i_1i_2}^0 \\ D_{\alpha\beta,i_1i_2} &= T_{\alpha\beta}^b / M_{i2} + D_{\alpha\beta,i_1i_2}^0 \end{aligned} \quad (7.60)$$

At  $i_1 = i_2$ :

$$D_{\alpha\beta,i_1i_2} = T_{\alpha\beta}^b / M_{i2} \exp[-i\mathbf{q} \cdot (\mathbf{r}_i - \mathbf{r}_j)] + D_{\alpha\beta,i_1i_2}^0 \quad (7.61)$$

If  $T_{\alpha\beta}^b = x_{b_2\alpha}x_{b_2\beta}f_b$  and  $T_{\alpha\beta}^b = x_{b_1\alpha}x_{b_1\beta}f_b$ , we can work out the contribution of  $f_b$  to  $D_{\alpha\beta,i_3i_2}$ ,  $D_{\alpha\beta,i_3i_3}$ ,  $D_{\alpha\beta,i_2i_2}$ ,  $D_{\alpha\beta,i_1i_3}$ ,  $D_{\alpha\beta,i_1i_1}$

- Calculation and result of dynamics matrix

The calculation of the dynamics matrix can be performed by a group theory analysis program. Before making such a calculation, we usually make some approximation for force constants, which are:

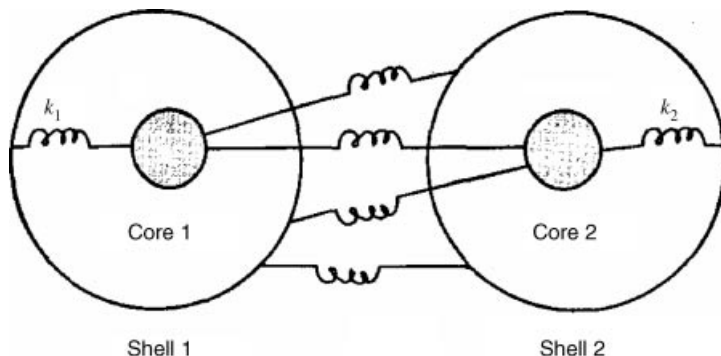
- (1) The interaction between nearest atoms is only considered;
- (2) Two kinds of force constants are considered. One is that an atom suffers a force along the direction of connection line when the atom is moving along the bond direction by a unit displacement; another is that the torque suffered by atoms due to the bond angle between three atom changes, which is marked by  $f_b$ .
- (3) The force constants are determined only by the space and bond angle between atoms.

Figure 7.6(b) is a diagram of the results of vibration modes analysis and Raman frequency calculation of high-temperature superconductor  $\text{YBaCu}_x\text{O}_{7-x}$ , by using a program of group theory symmetry analysis.

The results show that, for wave vector  $\mathbf{q} = 0$ , there are four vibration modes with frequencies of 0, in which there are three acoustic modes and the remaining one is the vibration mode with the vibration of the Cu(1) atom in  $\text{YBaCu}_x\text{O}_{7-x}$ , which is along the  $b$ -axis of crystals. Figure 7.6(b) exhibits the vibration mode and corresponding frequency of  $A_{1g}$ ,  $B_{2g}$ , and  $B_{3g}$  symmetry phonons. In Figure 7.6(b), the calculated frequency  $\omega_{cal}$  and experimental frequency  $\omega_{exp}$  are also marked. The comparison between calculations and experimental results indicates that only a few calculated values are close to the experimental values. This may show that, on the one hand, the model is too simple and, on the other hand, the experiment was too simplistic. However, there is still a significant achievement in the analyses of the vibration mode and its symmetry.

### 7.2.3 Shell Model

In many cases, the force constant mode seems simpler, in which the atoms are seen as a whole. However, even for non-polar covalence semiconductors such as Si and Ge, their valence electron is not localized in the ion core and so cannot be seen as “pure” atoms and



**Figure 7.7** Diagram of shell model and its typical interactions between two deformable atoms [13]. Reprinted from P. Y. Yu and M. Cardona, *Fundamentals of Semiconductors* (Third Edition), (2001) with permission of Springer

described by a force constant mode. Thus, Cochran proposed a so-called shell model, as shown in Figure 7.7 [13]. The atom in the shell model was assumed to be built up by a rigidity ion core surrounded by the valence electron shell, which moves relatively to the ion core.

In the shell model, the interaction of two atoms in a primitive cell is represented by a spring in Figure 7.7. One of the important features of the shell model is that it includes the long-range Coulomb interaction between atoms. This interaction originated from the interaction of an induced dipole, which is induced by the movement of the shell with an electric charge relative to the ion core. After the introduction of the long-range interaction, the short-range interaction can be localized between atoms of nearest or second nearest, and so on. Cochran used the shell model to fit the phonon dispersion curve of Ge with five tunable parameters. Later, Dolling and Cowley expanded the short-range interaction to the second nearest atoms, and fitted the phonon dispersion curve of Si with the shell model of eleven parameters [14].

The main dispute over the shell model is that the valence electron distribution in the semiconductors of diamond and zincblende structures is not a ball shell. As a result, there is no clear physical meaning for the parameters determined by the shell model, which means the model cannot be used in other applications other than for the fitting of a phonon dispersion curve. The most serious problem of the shell model was pointed out by Phillips [15,16], who saw that the model separated two valence electric-charges of two atoms in a covalent bond artificially. However, a covalent electron is allocated two atoms in time and two valence charges spend their time partly on both atoms.

#### 7.2.4 Bond Models

Valence electrons in semiconductors with diamond and zincblende structures form a highly oriented bond. These valence electrons are important for understanding the properties of these kinds of semiconductors. Especially, they play an important role in determining vibration frequency. For instant, the vibration properties of molecules formed by valence bonds is analyzed by using these valence force fields. Their phonon dispersion curve can be

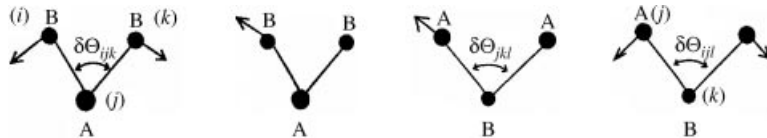


**Figure 7.8** Configurations of bond bending in the crystal with two atoms A and B in unit cell [17]. Reprinted from P. Y. Yu and M. Cardona, *Fundamentals of Semiconductors* (Third Edition), (2001) with permission of Springer

effectively calculated only by a few valence force fields for the molecules with primitive cells including two atoms A and B, as shown in Figure 7.8.

Musgrave and Pople studied the lattice dynamics of diamond in terms of the bond model [18]. Figure 7.9 shows a phonon dispersion curve of a zincblende type semiconductor CdS, which was obtained by using the valence force field model with eight tunable parameters by Nusimovici and Birman [19].

Keating introduced a simple scheme of the valence force field model [20]. There are only two parameters in his model for covalence semiconductors, while adding a charge parameter for ion compounds. Because Keating's model is simple and meaningful in physics, it is widely used in the study of the elastic and static properties of covalent compound semiconductors.

### 7.2.5 Bond Charge Model

Section 7.1.1 described the concept that the atomic nucleus and inner shell electron can be considered together as an ion core and the valence electrons are isolated from this ion core.

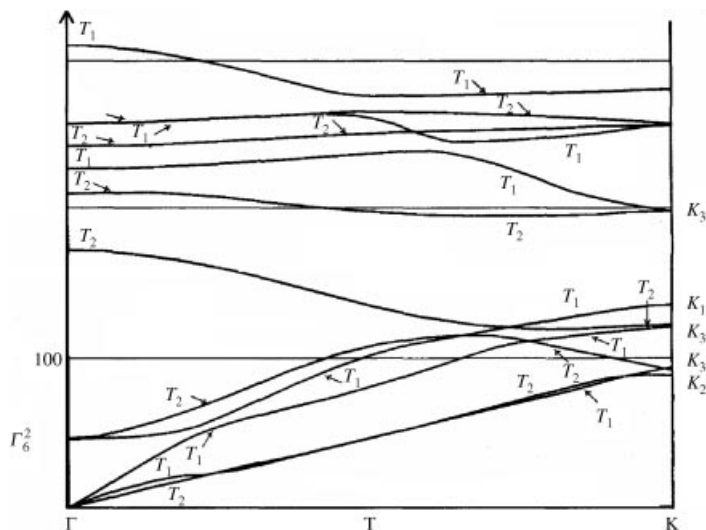


**Figure 7.9** Phonon dispersion curves of CdS obtained by valence force field model with eight adjustable parameters [19]. Reprinted from M. A. Nusimovici and J. L. Birman, *Lattice Dynamics of Wurtzite: CdS*, Phys. Rev., 156, 925 (1967) with permission of the American Physical Society

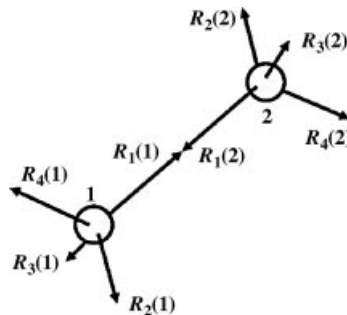


**Figure 7.10** Bond charge model simulated for diamond structure [22]. Reprinted from R. M. Martin, Dielectric Screening Model for Lattice Vibrations of Diamond-Structure Crystals, *Phys. Rev.*, 186, 871–884 (1969) with permission of the American Physical Society

However, an experiment of X-ray scattering showed that in covalent semiconductors, such as Si and diamond, the valence electrons will accumulate along the band direction and form the so-called bond charge [21].

Martin introduced a bond charge into the lattice dynamics calculations of semiconductors with a very simple phenomenological way [22]. Figure 7.10 shows a bond charge model, of which the specific object is a diamond structure. In this model, the bond charge and its position is marked by  $R_i(s)$ , where  $s = 1, 2$  is the label of atoms and  $i = 1 \sim 4$  is the label of charges. The four valence electrons of each atom are divided into two types: the localized bond charge and nearly free electrons. Each atom contributes four of  $1/2$  charges, which form four bonds with its neighbors. The bond charge is localized and thus no shielding is induced for ions. Assuming that the remaining  $4 \sim 2$  valence electrons of each atom are free and can shield the ions, the force to decide phonon frequency is:

- (1) Coulomb repulsion force between bond charges;
- (2) Coulomb attraction force between bond charges and ions;
- (3) Coulomb repulsion force between ions;
- (4) Non-Coulomb force between ions in the spring approximation.

Weber proposed the so-called adiabatic bond charge model (ABCM) shown in Figure 7.11 [17]. ABCM further improved the bound charge model proposed by Martin,

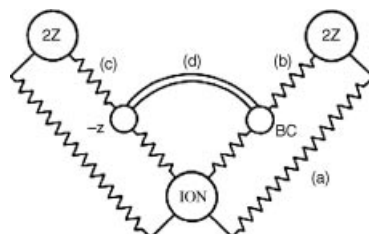


**Figure 7.11** ABCM proposed by Weber [17]. Reprinted from W. Weber, Adiabatic bond charge model for the phonons in diamond, Si, Ge, and *a*-Sn, *Phys. Rev. B*, 15, 4789–4804 (1977) with permission of the American Physical Society

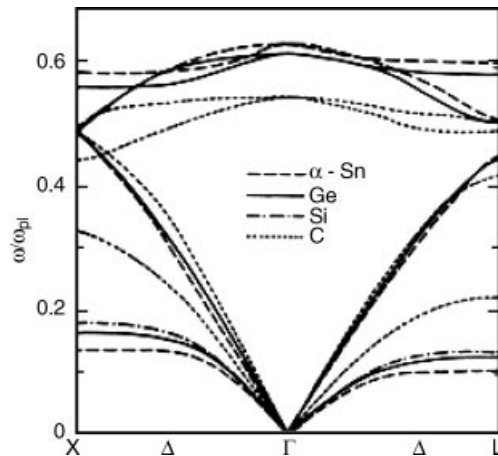


**Figure 7.12** Phonon dispersion curves of Si, diamond, Ge, and  $\alpha$ -Sn calculated by ABCM [17]. Reprinted from W. Weber, Adiabatic bond charge model for the phonons in diamond, Si, Ge, and  $\alpha$ -Sn, Phys. Rev. B, 15, 4789–4804 (1977) with permission of the American Physical Society

based on assimilating the advantages of the bond charge model, shell model, and the Keating model. The model has four adjustable parameters: the central force between ions  $\phi''_{i-i}$ ; the central potential between ion and bond charge  $\phi''_{i-bc}$ ; the Coulomb interaction between bond charges  $z^2/e$ ; and the bond bending parameter  $\beta$  of Keating's nuclear model.

### 7.2.6 Theoretical Phonon Dispersion Curves of Typical Semiconductors

Figure 7.12 shows the theoretical phonon dispersion curves of typical non-polar semiconductor Si, diamond, Ge, and  $\alpha$ -Sn, calculated by ABCM. Figures 7.13(a) and (b) are the

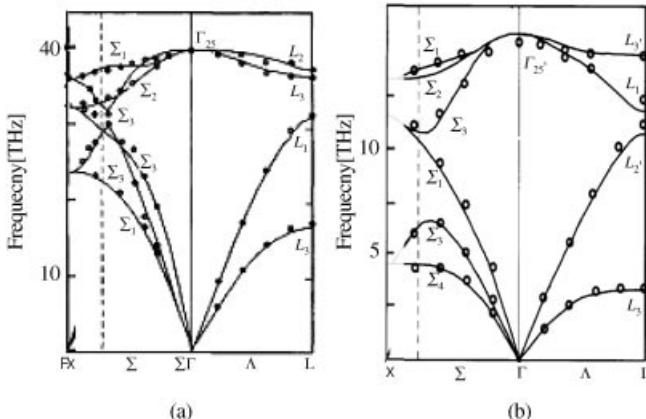


**Figure 7.13** Comparison of theoretical phonon dispersion curves calculated by ABCM with experimental data for Si (a) and diamond (b); where the circles are experimental data points [17]. Reprinted from W. Weber, Adiabatic bond charge model for the phonons in diamond, Si, Ge, and  $\alpha$ -Sn, Phys. Rev. B, 15, 4789–4804 (1977) with permission of the American Physical Society

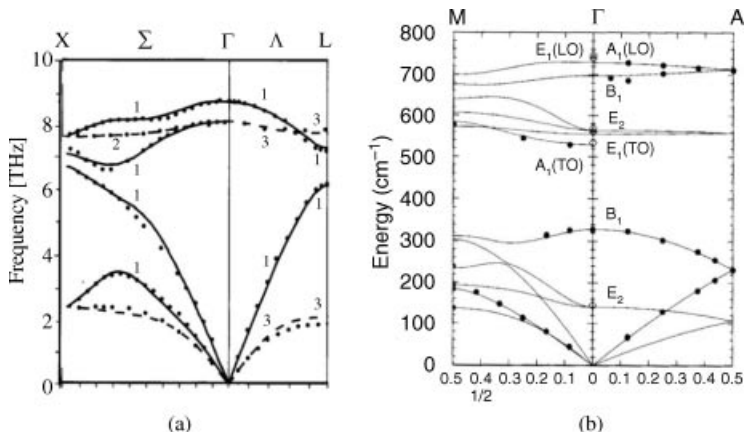


**Figure 7.14** Calculated phonon dispersion curves of the cubic zincblende polar GaAs (a) and the hexangular wurtzite structure semiconductor GaN. Reprinted from D. Strauch and B. Dordor, Phonon dispersion in GaAs, *J. Phys. Cond. Mater.*, 2, 1457–1474 (1990) with permission of the Institute of Physics. (b) where the experimental data are also shown by solid circles [23,24]. Reprinted from T. Ruf, J. Serrano, M. Cardona, et al., Phonon Dispersion Curves in Wurtzite-Structure GaN Determined by Inelastic X-Ray Scattering, *Phys. Rev. Lett.*, 86, 906–909 (2001) with permission of the American Physical Society

comparison of theoretical phonon dispersion curves with experimental data for Si and diamond. Figures 7.14(a) and (b) are the phonon dispersion curves of cubic zincblende polar GaAs and hexangular wurtzite structure semiconductor GaN, respectively, in which the experimental data used for comparison are also shown.

From Figures 7.12–7.14,, we see that the calculated dispersion curves fit the experimental data well, indicating that accuracy of the calculation is high. In addition, from Figures 7.12–7.14, we find the following features possessed by phonon dispersion curves:

- (1) The phonon dispersion curves of cubic symmetry Si, Diamond, and GaAs are similar; however, they are different from that of hexangular symmetry GaN, both in the number and feature of phonon modes.
- (2) In the center of the Brillouin zone, the LO and TO phonons of Si and GaAs with the same cubic crystal symmetry are degenerate and non-degenerate, respectively. This is because GaAs is an ionic crystals but Si is not. However, two TA branches of Si and GaAs are both degenerate. This is because these two lateral vibrations are indistinguishable for a crystal with cubic symmetry. As mentioned above, we can infer that if cubic symmetry is destroyed, the degeneracy will be increased.
- (3) All dispersion curves indicate that the acoustic phonon at  $q=0$ ,  $\omega \rightarrow 0$ , and near the region of  $q=0$ , will have near-linear dispersion curves. It is the manifestation of the elastic properties of acoustic phonon that are described in Section 7.1.3.
- (4) We also found that the energy of the LA phonon is higher than that of the TA phonon, meaning that the TA phonon is a shear deformation acoustic wave and the LA phonon is a longitudinal compression acoustic wave. This is because the energy change of shear

deformation is less than that of longitudinal compression, which results in the energy of the TA phonon being lower than the LA phonon.

- (5) The energy of the TO phonon is less than that of the LO phonon, as described in Section 7.1.

## 7.3 Macroscopic Model of Lattice Dynamics

### 7.3.1 Continuous Elastic Model [25]

An acoustic vibration will lead to a macroscopic strain in a crystal. The wavelength of an acoustic vibration is much longer than the lattice constant and the crystal can be considered as a continuous elastic medium.

The macroscopic strain in elastic media can be described by strain tensor  $e_\rho$ , of which there are six independent variables. The relation of displacement vector  $\mathbf{u}$  and strain tensor  $e_\rho$  is expressed as

$$e_\rho = \begin{cases} \partial u_\alpha / \partial x_\alpha & \alpha, \beta = x, y, z \\ \partial u_\alpha / \partial x_\beta + \partial u_\beta / \partial x_\alpha & \end{cases} \quad (7.62)$$

where the correspondence between subscript  $\rho$  (1, 2, 3, 4, 5, 6) and tensor index  $(\alpha, \beta)$  are as follows:

$\rho$	1	2	3	4	5	6
$(\alpha, \beta)$	xx	yy	zz	zy (yz)	xz (zx)	xy (yx)

The stress  $\sigma$  produced by the strain tensor is a second-order tensor and under reduced representation  $\sigma$  can be expressed as

$$\sigma_i = \sum_j C_{ij} e_j \quad (7.63)$$

where the elastic modulus  $C_{ij}$  is a forth-order tensor with 36 components. For crystals with cubic symmetry, there are only three independent variables  $C_{11}$ ,  $C_{12}$ , and  $C_{44}$ , so Equation (7.63) can be expressed as

$$\begin{aligned} \sigma_1 &= C_{11}e_1 + C_{12}(e_2 + e_3) \\ \sigma_2 &= C_{11}e_2 + C_{12}(e_1 + e_3) \\ \sigma_3 &= C_{11}e_3 + C_{12}(e_1 + e_2) \\ \sigma_4 &= C_{44}e_4 \\ \sigma_5 &= C_{44}e_5 \\ \sigma_6 &= C_{44}e_6 \end{aligned} \quad (7.64)$$

Now we consider a force along the  $z$  direction suffered in a small unit volume in crystals. According to Newton's second law, the motion equation along the  $z$  direction of this unit volume can be obtained as

$$\rho \frac{\partial^2 u_z}{\partial t^2} = F_z = \frac{\partial \sigma_3}{\partial z} + \frac{\partial \sigma_4}{\partial y} + \frac{\partial \sigma_5}{\partial x} \quad (7.65)$$

where  $u_z$  is the displacement;  $\rho$  is the mass density; and  $\sigma_3 = \sigma_{zz}$ ,  $\sigma_4 = \sigma_{yz}$ ,  $\sigma_5 = \sigma_{xz}$ ,  $\sigma_{ij}$  represent the force along the  $j$  direction of per unit area on the plane perpendicular to the  $i$  axis. Substituting Equations (7.62) and (7.63) into Equation (7.65), we obtain

$$\begin{aligned} \rho \frac{\partial^2 u_z}{\partial t^2} &= C_{44} \left( \frac{\partial^2 u_x}{\partial x^2} + \frac{\partial^2 u_y}{\partial y^2} + \frac{\partial^2 u_z}{\partial z^2} \right) + (C_{12} + C_{44}) \frac{\partial}{\partial z} \left( \frac{\partial u_x}{\partial x} + \frac{\partial u_y}{\partial y} + \frac{\partial u_z}{\partial z} \right) \\ &\quad + (C_{11} - C_{12} - 2C_{44}) \frac{\partial^2 u_z}{\partial z^2} \end{aligned} \quad (7.66)$$

With displacement of coordinates  $x$ ,  $y$ ,  $z$ , the motion equation in the  $x$ ,  $y$  direction can be obtained.

For acoustic vibration in crystals, it can be described using the plane wave form, that is

$$\mathbf{u}(\mathbf{r}, t) = \mathbf{u} e^{-i\mathbf{q} \cdot \mathbf{r} - i\omega t} \quad (7.67)$$

where  $\mathbf{u}$  is the amplitude and is a constant vector;  $\mathbf{q}$  is the wave vector; and  $\omega$  is the circular frequency of vibration. Assuming  $\mathbf{q}$  is along the  $z$  direction, then the acoustic wave propagates along the  $z$  direction. By substituting Equation 7.67 into the motion Equation (7.66), we be obtained three equations expressed as

$$\begin{aligned} -\omega^2 \rho u_z &= -C_{11} q^2 u_z \\ -\omega^2 \rho u_x &= -C_{44} q^2 u_x \\ -\omega^2 \rho u_y &= -C_{44} q^2 u_y \end{aligned} \quad (7.68)$$

where  $q$  is the magnitude of  $\mathbf{q}$ . We can see that the three equations are independent of each other. The first equation corresponds to the longitudinal wave, of which the vibration and the propagation directions are the same. The next two equations correspond to transverse waves with the vibration direction perpendicular to the propagation direction. From Equation (7.68), we obtain the relation between frequency and wave vector as

$$\omega = \sqrt{C_{11}/\rho q} \quad (7.69a)$$

$$\omega = \sqrt{C_{44}/\rho q} \quad (7.69b)$$

From the above equations, it can be seen that the acoustic wave frequency is proportional to the wave vector, of which the ratio coefficient is usually called the sound velocity and is different for longitudinal and transverse waves.

It should be noted that only when  $q$  is small, that is, the wavelength is relatively long, Equation (7.69) is effective. When  $q$  is close to the boundary of the Brillouin zone ( $q \approx \pi/a$ ),

Equation (7.69) no longer holds. At this point the wavelength is already equivalent to the lattice constant and so the continuous medium assumption is no longer effective. Strict calculations of lattice dynamics show that when  $q$  is near the boundary of the Brillouin zone,  $\omega$  is no longer a linear increase and increases more slowly.

We can see from the relation between  $\omega$  and  $q$  that the above result of the elastic continuous medium model is the same as that of a one-dimension diatomic chain. It means that for a long-wave length acoustic phonon, elastic continuous medium is a reasonable approximation.

### 7.3.2 Dielectric Continuous Model – Huang Equation

The atoms involved in the above lattice dynamics calculation are only electrically neutral ones, which is equivalent to non-polar semiconductors. However, there are only four non-polar semiconductors Si, Ge,  $\alpha$ -Sn, and diamond in nature; the rest are the polar semiconductors constructed by the ions with strong or weak iconicity, which are one part of ion crystals. In this section we will focus on the lattice vibration of ionic crystals.

In the discussion on the one-dimensional diatomic linear chain in Section 7.1.3, we pointed out that for the vibration of two atoms out of phase, that if these two atoms are positive and negative ions in the crystal, polarization and macroscopic electromagnetic fields will be generated, which must be taken into account for such lattice vibration of ionic crystals.

#### 7.3.2.1 Huang Equation [2,3]

As an example, we adopt a cubic crystal, including only a pair of ions with masses of  $M_+$  and  $M_-$  in one primitive cell, to discuss the optical (out-phase) vibration of ions in crystals. In a macro-small region, similar to the description of an effective inertial mass of unit volume – the density for an elastic motion, Huang introduced a macro-quantity  $\mathbf{W}$  for the optical type of motion, defined as

$$\mathbf{W} = \left(\frac{\mu}{\Omega}\right)^{\frac{1}{2}} (\mathbf{u}_+ - \mathbf{u}_-) \quad (7.70)$$

where  $\mu$  is the reduced mass defined as  $\frac{1}{\mu} = \frac{1}{M_+} + \frac{1}{M_-}$ ;  $\Omega$  is the primitive cell volume; and  $\mathbf{u}_+$  and  $\mathbf{u}_-$  are the displacement of positive and negative ions, respectively. Then Huang set up a motion equation of ionic crystals, later known as the “Huang equation.”

$$\ddot{\mathbf{W}} = b_{11}\mathbf{W} + b_{12}\mathbf{E} \quad (7.71)$$

$$\mathbf{P} = b_{21}\mathbf{W} + b_{22}\mathbf{E} \quad (7.72)$$

where  $\mathbf{P}$  is the macro-polarization and  $\mathbf{E}$  is the macroscopic electric field strength. The coefficients  $b_{ij}$  ( $i, j = 1, 2$ ) are not independent of each other, for example, the kinetic coefficient symmetry requires that  $b_{12} = b_{21}$ . The first equation is the kinetic equation of relative vibration of ions. The second equation considers the polarization generated by the relative displacement of positive and negative ions and additional macroscopic electric polarization. In the following, we will discuss the polarization problem of ion crystals in terms of the Huang equation.

- Electrostatic field

In the electrostatic field, the positive and negative ions will occur as relative displacement  $\mathbf{W}$ , resulting in  $\ddot{\mathbf{W}}$  in Equation (7.71) becoming 0 and then  $\mathbf{W} = -\frac{b_{12}}{b_{11}}\mathbf{E}$ .

Substituted the latter into Equation (7.72), we have

$$\mathbf{P} = (b_{22} - b_{12}^2/b_{11})\mathbf{E} \quad (7.73)$$

According to the electrostatic field theory,

$$\mathbf{P} = [\varepsilon - \varepsilon_0]\mathbf{E} \quad (7.74)$$

where  $\varepsilon$  is the dielectric constant and  $\varepsilon_0$  is the vacuum dielectric constant, thus we have

$$[\varepsilon - \varepsilon_0] = b_{22} - b_{12}^2/b_{11} \quad (7.75)$$

- High frequency electric field

When the electric field frequency is much higher than the lattice vibration frequency, the lattice displacement cannot follow the electric field changes and so  $\mathbf{W} = 0$ . Thus, from Equation (7.72) we have

$$\mathbf{P} = b_{22}\mathbf{E} \quad (7.76)$$

According to Equation (7.74), we obtain

$$[\varepsilon_\infty - \varepsilon_0] = b_{22} \quad (7.77)$$

where  $\varepsilon_\infty$  is the high-frequency dielectric constant. Substituting the above equation into Equation (7.74), we have

$$[\varepsilon - \varepsilon_\infty] = -b_{12}^2/b_{11} \quad (7.78)$$

and

$$\begin{aligned} -b_{11} &= \omega_0^2 \\ b_{12} = b_{21} &= [\varepsilon - \varepsilon_\infty]^{\frac{1}{2}} \omega_0 \\ b_{22} &= \varepsilon_\infty - \varepsilon_0 \end{aligned} \quad (7.79)$$

In the above equation,  $\omega_0$  is the frequency of the transverse long optical wave.

- Ionic polarization model [4]

The lattice vibrations in ionic crystals can also be studied for the atomic polarization from the microscopic view. As in the above discussion, we still use the cubic crystal as an example, in which the primitive cell contains only a pair of positive and negative ions. From the polarization of a positive and negative ion pair, it can be deduced not only for the Huang equation but also for four coefficients  $b_{ij}$  of the Huang equation, listed as

$$b_{11} = -\frac{f}{M} + \frac{(q^*)^2}{3\varepsilon_0\Omega\mu} \left/ \left( 1 - \frac{\alpha_+ + \alpha_-}{3\varepsilon_0\Omega} \right) \right. \quad (7.80)$$

$$b_{12} = b_{21} = \frac{q^*}{(\mu\Omega)^{1/2}} \left/ \left( 1 - \frac{\alpha_+ + \alpha_-}{3\varepsilon_0\Omega} \right) \right. \quad (7.81)$$

$$b_{22} = \frac{\alpha_+ + \alpha_-}{\Omega} \left/ \left( 1 - \frac{\alpha_+ + \alpha_-}{3\epsilon_0\Omega} \right) \right. \quad (7.82)$$

where  $f$  is the constant of positive and negative ions;  $q^*$  is the ion effective charge; and  $\alpha_+$  and  $\alpha_-$  are the polarization rate of positive and negative ions, respectively.

The Huang equation is the motion equation that includes the interactions between mechanical and electromagnetic and based on this equation we obtain not only the solution of acoustic wave vibrations but also the solution of optical wave vibrations. However, to make the Huang equation possible to apply to an entire crystal, the displacement must be independent of the primitive cell, which means that the equation describes only the lattice vibration at long wavelength limitation. That means the Huang equation is mainly applied in the calculation of long wavelength optical phonon of wave vector  $q \approx 0$ .

- Dispersion relation of long optical wave in ionic crystals [3]

By using the cubic crystal as an example, we use the Huang equation to calculate the frequency of a long optical wave. Because there are two kinds of long optical waves in a cubic crystal, that is, transverse and longitudinal waves, we use  $\mathbf{W}_T$  and  $\mathbf{W}_L$  to represent  $\mathbf{W}$  of transverse and longitudinal waves, respectively. Due to the different properties of transverse and longitudinal waves:

$$\nabla \cdot \mathbf{W}_T = 0 \quad (7.83a)$$

$$\nabla \cdot \mathbf{W}_L \neq 0 \quad (7.83b)$$

$$\nabla \times \mathbf{W}_L = 0 \quad (7.83c)$$

$$\nabla \times \mathbf{W}_T \neq 0 \quad (7.83d)$$

the electric field satisfies the following static electricity equation:

$$\nabla \cdot \mathbf{D} = \nabla \cdot (\epsilon_0 \mathbf{E} + \mathbf{P}) = 0 \quad (7.84a)$$

$$\nabla \times \mathbf{E} = 0 \quad (7.84b)$$

The adopted  $\mathbf{P}$  value of Equation (7.72) instead of that of Equation (7.84a), we have

$$\nabla \cdot (\epsilon_0 \mathbf{E} + b_{21} \mathbf{W} + b_{22} \mathbf{E}) = 0, \quad (7.85)$$

Thus,

$$\nabla \cdot \mathbf{E} = \frac{-b_{21}}{\epsilon_0 + b_{22}} \nabla \cdot \mathbf{W}, \quad (7.86)$$

Since  $\mathbf{W} = \mathbf{W}_L + \mathbf{W}_T$  and  $\nabla \cdot \mathbf{W}_T = 0$ ,  $\nabla \times \mathbf{W}_L = 0$ , we obtain

$$\nabla \cdot \mathbf{E} = \frac{-b_{21}}{\epsilon_0 + b_{22}} \nabla \cdot \mathbf{W}_L \quad (7.87)$$

Therefore an obvious solution is

$$\mathbf{E} = \frac{-b_{21}}{\epsilon_0 + b_{22}} \mathbf{W}_L \quad (7.88)$$

This solution is unique, as  $\mathbf{E}$  must be irrational. Substituting Equation (7.88) into Equation (7.71), we obtain

$$\ddot{\mathbf{W}}_T + \ddot{\mathbf{W}}_L = \left( b_{11} - \frac{-b_{12}^2}{\epsilon_0 + b_{22}} \right) \mathbf{W}_L + b_{11} \mathbf{W}_T \quad (7.89)$$

Because the decomposition of solenoidal and irrational parts of a vector equation is unique, we can make solenoidal and irrational parts of both sides of the equation equal. Therefore, the solenoidal part is

$$\frac{d\mathbf{W}_T^2}{dt^2} = b_{11} \mathbf{W}_T \quad (7.90)$$

According to the first formula of Equation (7.79), there will be

$$\omega_{TO}^2 = \omega_0^2 \quad (7.91)$$

and the irrational part is

$$\frac{d\mathbf{W}_C^2}{dt^2} = [b_{11} - b_{12}^2 / (\epsilon_0 + b_{22})] \mathbf{W}_T = \omega_{LO}^2 \mathbf{W}_L \quad (7.92)$$

and

$$\frac{d\mathbf{W}_L^2}{dt^2} = -[\epsilon/\epsilon_\infty] \omega_0^2 \mathbf{W}_L \quad (7.93)$$

Thus,

$$\omega_{LO}/\omega_{TO} = [\epsilon/\epsilon_\infty]^{\frac{1}{2}} \quad (7.94)$$

The above Equation is called the Lyddano–Sachs–Teller (LST) relation.

- Dispersion relation of longitudinal wave

The LST relation is the dispersion relation of longitudinal wave, which shows that:

- (1) Longitudinal wave frequency  $\omega_{LO}$  is independent of wave vector  $q$  and is a constant, meaning that the longitudinal wave dispersion relation is a horizontal straight line, as shown in Figure 7.15. This is due to the longitudinal polarization electric field being an irrational field similar to the electrostatic field, which results in there being no coupling between electromagnetic waves and longitudinal polar lattice vibration modes and thus the longitudinal wave still maintains the properties of mechanical vibration.
- (2) The electrostatic dielectric constant  $\epsilon$  is usually larger than the high frequency dielectric constant  $\epsilon_\infty$ . Thus, from the LTS relation, we know that the long LO wave frequency  $\omega_{LO}$  is always larger than the long optical transverse wave frequency  $\omega_{TO}$ ; this is because of the polarized electric field induced by the long optical wave in ionic crystals enhances the resilience of longitudinal waves and then the energy (frequency) of longitudinal wave increases. The magnitude of the polar electric field correlates

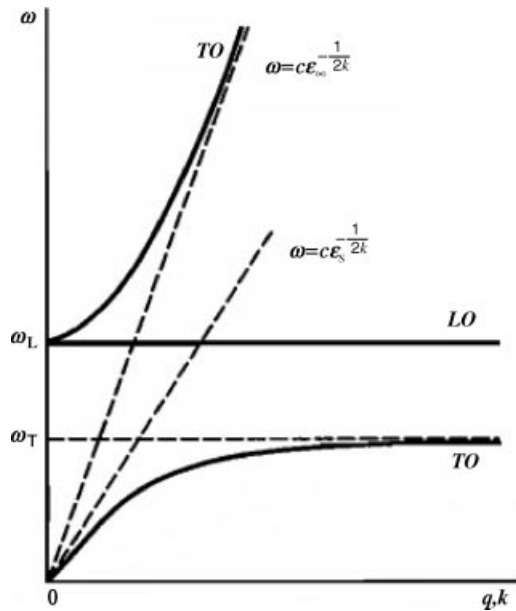


**Figure 7.15** Dispersion relation of polariton in double-ion cubic crystals [4]. Reprinted from S.-L. Zhang, *Raman Spectroscopy and Low-dimensional nanoscale Semiconductors*, Science Press, (2008)

with the effective charge of positive and negative ions, the larger the effective charge, the larger the difference of  $\omega_{LO}$  and  $\omega_{TO}$ . Thus we can use  $(\omega_{LO}^2 - \omega_{TO}^2)$  to estimate the ion charge  $q^*$ . Moreover, we can speculate for non-polar semiconductors such as diamond and Si that due to their  $q^* = 0$ ,  $\omega_{LO}$ , and  $\omega_{TO}$ , should degenerate, which explains the results shown in Figure 7.13.

- Dispersion relation of transverse wave

Using Equation (7.83a) and the transverse wave equation

$$\mathbf{E}_T = [\omega^2/\epsilon_0(q^2 - c^2 - \omega^2)] \mathbf{P} \quad (7.95)$$

we obtain dielectric constant  $\epsilon = q^2 c^2 / \omega^2$ , due to  $\epsilon = \epsilon_\infty + (\epsilon - \epsilon_\infty) / [1 - (\omega/\omega_T)^2]$ , thus we have the dispersion relation of a transverse wave:

$$q^2 c^2 / \omega^2 = \epsilon_\infty + (\epsilon - \epsilon_\infty) / [1 - (\omega/\omega_T)^2] \quad (7.96)$$

From the above equation, it can be seen that the frequency of a transverse wave is correlated with the value of wave vector  $q$ , but uncorrelated with its direction. For every permitted wave vector  $q$ , there are two solutions for Equation (7.96). For instance, when  $q = 0$ , the equation give the two solutions of  $\omega = 0$  and  $\omega = \omega_L$ . In Figure 7.15, we drew the dispersion curve of TO modes by two solid lines; the higher and lower ones are called high and low frequency branches, respectively. They are double degenerate and thus have four transverse vibration modes for each  $q$  value, of which two come from transverse mechanical vibration and two

from transverse electromagnetic field vibration. If the transverse mechanic vibration does not couple with the transverse electromagnetic field vibration, the frequency of mechanical vibration is  $\omega_T$ , which does not change with wave vector values, as shown by the level dashed line in Figure 7.15 and is only the solution of the Huang Equation (7.71) where there is no electric field  $E$ . The frequency of a transverse electromagnetic vibration is  $\omega = c\varepsilon_\infty^{-1/2}k$ , which is a straight line passing through the origin and with slope  $v = c\varepsilon^{1/2}$ , as shown by dashed lines in Figure 7.15 and the only the solution of Equation (7.72) that does not consider ion vibration. However, the transverse wave of polar lattice vibration can be coupled with electromagnetic waves of transverse polarization, resulting in the two dispersion curves, shown by the two dashed lines in Figure 7.15, changing to two dispersion curves expressed by the hyperbola in the figure.

### 7.3.2.2 Electromagnetic Dipole – Polariton

There is a vibration mode originated from the coupling of an elastic wave with an electromagnetic wave, which is not a pure lattice vibration and is known as polariton. A polariton possesses the properties of both mechanical and electromagnetic vibrations. As shown in Figure 7.15, when the wave vector is small, the low frequency branch possesses electromagnetic properties, while the high frequency branch possesses mechanical properties. When the wave vector is large, the high frequency branch of the polariton shows an obvious electromagnetic property, and the electromagnetic property of the low frequency branch of the polariton almost disappears, only exhibiting pure mechanical property. At present, the frequency of transverse polar lattice vibration  $\omega_T$  is equal to the intrinsic vibration frequency  $\omega_0$ .

The polariton predicted by Huang was proved in the material of GaP in 1965 [26].

## 7.4 Lattice Dynamics of Amorphous Matter [3]

At the beginning of this chapter, we pointed out that the structure of amorphous systems is long-range disorder but keeps short-range order, thus, there is no translation symmetry and the momentum  $\mathbf{q}$  is no longer a good quantum number. In this case, the concept of a lattice wave is no longer effective, but a series of intrinsic vibrations still exist and energy is still quantized, thus we can retain the concept of the “phonon,” and the phonon at this case is only an energy quantum with no “quasi momentum.” Therefore, in amorphous crystals, the dispersion relation of phonon frequency  $\omega(q)$  no longer exists, but the distribution of phonon number with frequency (i.e., phonon density of state, PDOS) still exists. The PDOS  $g(\omega)$  is defined as the phonon number in unit volume and unit frequency interval:

$$g(\omega) = \frac{dN}{d\omega} \quad (7.97)$$

where  $N$  is the number of phonons in the unit volume. Under most conditions, the PDOS of amorphous crystals is related to the dispersion curve of phonons of corresponding crystals  $\omega(q)$  [27] and is expressed as

$$g(\omega) = \sum_i \oint_S \frac{1}{|\nabla_q \omega_i(\mathbf{q})|} \frac{dS}{8\pi^3} \quad (7.98)$$

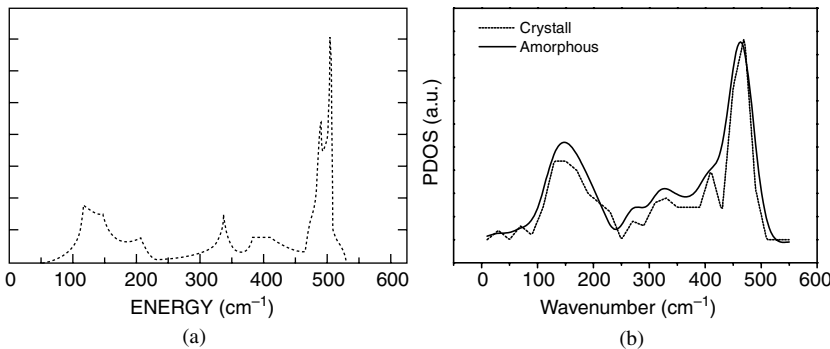


**Figure 7.16** (a) PDOS of amorphous silicon calculated by a phenomenological model [19]. Reprinted from J. E. Smith, Jr., M. H. Brodsky, B. L. Crowder, et al., Raman Spectra of Amorphous Si and Related Tetrahedrally Bonded Semiconductors, *Phys. Rev. Lett.*, 26, 642–646 (1971) with permission of the American Physical Society. (b) PDOS of crystalline (dashed line) and amorphous silicon (solid line) calculated by the first principle method (Gaussian convolution factor 2 cm<sup>-1</sup>)

where  $i = 1, 2, \dots, 3s$ ; and  $s$  is the atomic number in a primitive cell. Thus  $3s$  is the number of vibration modes and the integral area is the curved surface of  $\omega \equiv \omega(q)$  in the first Brillouin zone.

The PDOS  $g(\omega)$  can be obtained by the calculations of lattice dynamics. Figure 7.16(a) shows a PDOS of amorphous silicon calculated by a phenomenological model [19]; while in Figure 7.16(b) the PDOS of crystal (dashed line) and amorphous silicon (solid line) are calculated by the first principles method.

From Figure 7.16(b), we see that the difference between the PDOS of crystalline and amorphous crystals is not large. This is because in the calculations of crystalline crystal the interaction between atoms involves only neighboring ones, which is similar to the amorphous calculation and thus there is not much difference between both of them.

## 7.5 Raman Scattering Theories in Solids

In order to explore the essential features of Raman scattering theory, we now concentrate on single phonon non-resonant Raman scattering in solids. The solid state matter involved will be limited to those of non-conduction, non-magnetism, and non-absorption. Moreover, the elementary excitations in solids are mainly phonons. If the reader's interest in light scattering is other than mentioned above, please read Reference [28,29].

### 7.5.1 Introduction

#### 7.5.1.1 Basic Condition of the Occurrence of Raman Scattering

- Existence of spatial and temporal fluctuations of atoms in medium

If the atoms in medium are fixed and so not moving in space, the intensity of light scattered by such atoms can be calculated through the summing of the scattered light from each atom. For a perfect crystal with atoms and molecules arranged periodically

and the incident light wavelength much longer than the distance between atoms, the scattered light from atoms or molecules become interference secondary waves. Based on the interference principle of light [30,31], the superimposing result of these interference secondary waves from such atoms will mean no light appears in the direction deviated away from the direction of incident light, that is, so-called destructive interference appears. So no light appears in other than the incident direction of light, that is, occurrence the scattered light phenomenon will not occur. Of course, the coherent second wave also produces constructive interference; however, the effect of constructive interference only results in the reduction of light velocity. If we consider that the atoms and molecules are moving around their balance position with time, the above destructive interference will not occur and light scattering phenomena will appear.

The above discussion indicates for solids (more widely, for condensed matter) that if we neglect the fluctuation in space and time of atoms and molecules, there will be no light scattering phenomena, which means that the fluctuation of objects is the essential origin of light scattering.

- Matching of energy, wave vector, and polarization between phonon and light

The fluctuation in space and time of atoms and molecules can be represented by a lattice wave (phonon), thus light scattering is induced by the interaction between a phonon and light. However, the occurrence of the interaction between a phonon and light (photon) is possible only where the matching conditions of energy (frequency), wave vector, and polarization between a phonon and light are satisfied.

To illustrate the matching condition, we show the dispersion curves of a phonon and light in Figure 7.17, from which we see that the dispersion curve of light approaches close to the vertical coordinate axis as the light wave vector is very small. In Figure 7.17, the interaction between the phonon and light is represented by the crossing between the dispersion curves

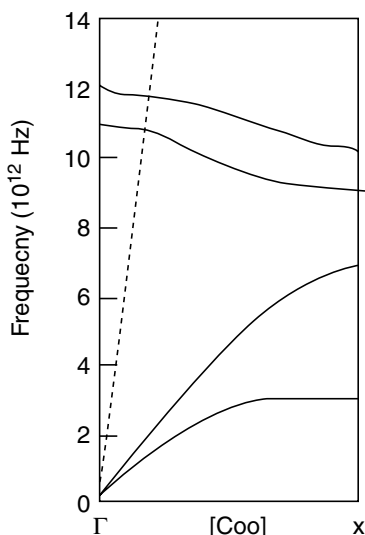


**Figure 7.17** Phonon (solid line) and light (dotted line) dispersion curves. The upper two and lower two branches in phonon dispersion curves are acoustic and optical, respectively

of the phonon and light. Therefore, from Figure 7.17 we see there is no such crossing for the dispersion curves of acoustic phonons, meaning the acoustic phonon in such crystals is non-Raman active, while for optical phonon, only long wavelength phonons with wave vector  $q \approx 0$  have an interaction with light, that is, are Raman active.

The frequency of phonons is about  $10^{12} \sim 10^{14}$  Hz, so only far-infrared light and THz waves can interact with a phonon. Therefore, as mentioned in Chapter 2, phonon Raman scattering must have the help of “intermediary,” that is, electrons. As a result, phonon Raman scattering involves the interaction of two systems: one is an energy band system of electrons in solids with many body effects involving excitons and so on, and the other is the phonon system with dispersion and anharmonic interaction.

### 7.5.1.2 Symmetry and Raman Scattering of Crystals

Symmetry is an important feature of all crystals. In addition to the translational symmetry already mentioned, crystals have rotation and inversion symmetries. The application of crystal symmetry can greatly reduce theoretical and experimental complexity in crystal Raman scattering. To convenient usage, Appendix IV provides the information of structures and its corresponding symmetries for some crystals.

In Sections 2.2.4 and 2.7.4, we demonstrated for mode  $k$  that Raman activity and the Raman selection rule of vibration modes are judged by whether it is zero or not for the derivative  $\alpha'_k(k)$  of the classical theory and polarization transition matrix element  $[\alpha_{ij}]_{nk}$  ( $i, j = x, y, z; n$ , and  $k$  are the marks of the end of initial quantum states) of quantum theory.  $\alpha'_k(k)$  and  $[\alpha_{ij}]_{nk}$  correspond to the so-called “Raman tensor.”

In Sections 2.2.4 and 2.7.4, we also discussed whether the Raman tensor is zero as determined by crystal symmetry. Therefore, any crystals with the same crystal symmetry must have the same number and symmetry of Raman vibration modes and the specific form of the Raman tensor must correspond to a specific polarization selection rule in Raman experiments. That means that if the spatial orientation of a crystal is fixed in an experiment, the Raman spectra with different symmetries will be detected by different geometric configurations in such experiments.

In order to facilitate the application of the Raman tensor, we have enumerated the Raman tensors with their symmetric attributes, and some applied examples of Raman tensors are shown in Appendix III. As an example, Figure 7.18 shows some polarized Raman spectra detected at different configurations for a ZnO crystal.

Because the normal coordinates can be used as the basic vectors of irreducibility representation of a crystal symmetry group, therefore, in Raman scattering theory, after writing out the interaction form by normal coordinates and obtaining the dynamic matrix of Raman scattering, we can perform the symmetry analysis of the vibration mode to learn the symmetric classification of these modes. As a result, we find their Raman activity and polar selection rule, and so on and the complexity in theory and experiment of Raman scattering becomes much simpler.

This book will not specifically described the basic principles and specific practices of the symmetry group of lattice vibration analysis, and if readers need to understand more on this, please read reference [4]. From the 1980s, the group theory symmetry analysis of lattice vibration modes was performed by using specific computer software.

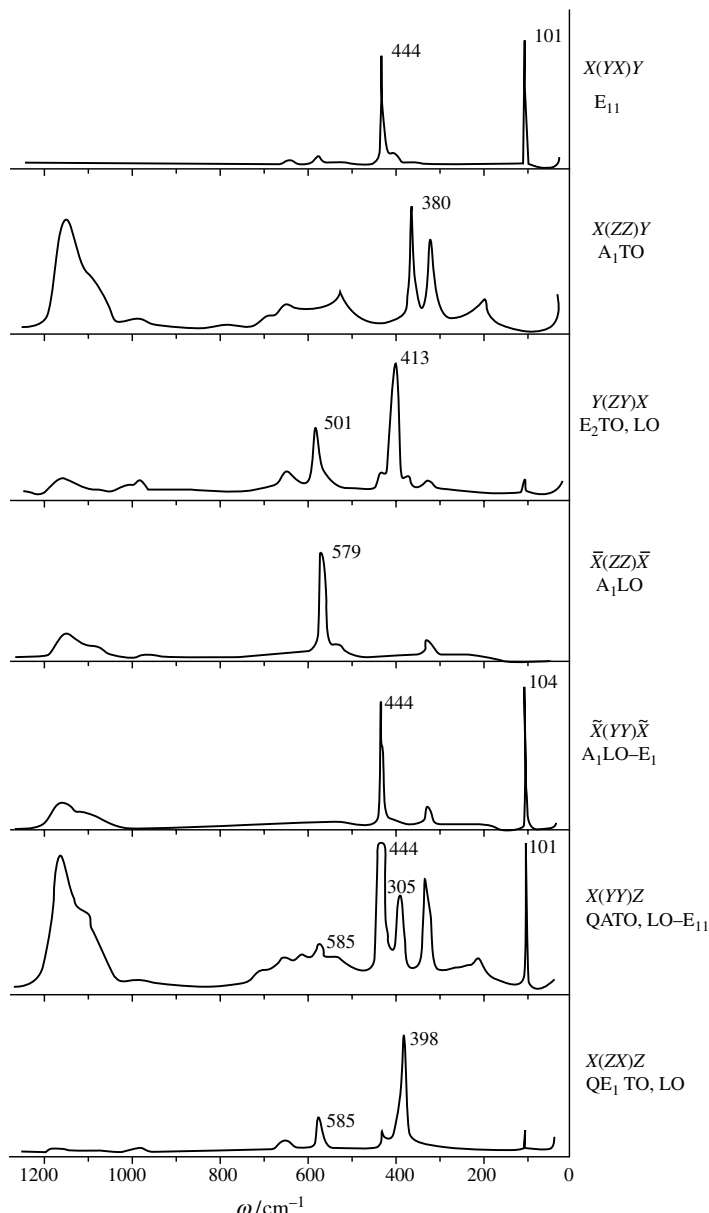


**Figure 7.18** Observed polarized Raman spectra at different geometric configurations of  $\text{ZnO}$  crystal [32]. Reprinted from T. C. Damen, S. P. S. Porto, and B. Tell, Raman Effect in Zinc Oxide, *Phys. Rev.*, 142, 570–574 (1966) with permission of the American Physical Society

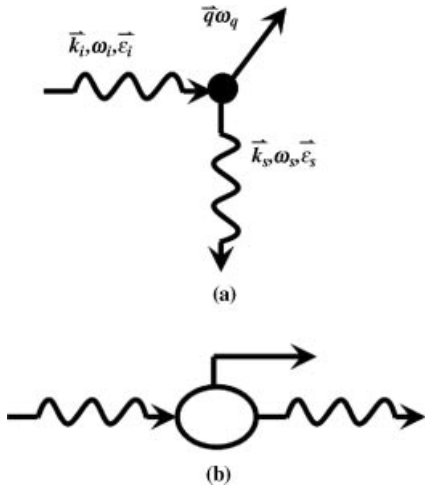


**Figure 7.19** (a) Raman scattering process in crystals; (b) interaction with important contributions in six possible interactions for scattering processes (a), where the wave-like and straight lines represent photons and phonons, respectively [33]. Reprinted from R. M. Martin, Theory of the One-Phonon Resonance Raman Effect, Phys. Rev. B, 4, 3676–3685 (1971) with permission of the American Physical Society

### 7.5.2 Microscopic Quantum Mechanical Description of Solid Raman Scattering [33]

We will now use the Raman scattering process of crystals shown in Figure 7.19(a) to introduce a simple quantum mechanics theory of Raman scattering. In the scattering process, the incident photon with frequency  $\omega_i$ , polarization  $\epsilon_i$ , and wave vector  $\vec{k}_i$  will transform to a scattered phonon with frequency  $\omega_f$ , polarization  $\epsilon_f$ , and wave vector  $\vec{k}_f$ . Meanwhile, a phonon of frequency  $\omega_q$ , polarization  $\epsilon_q$ , and wave vector  $\vec{q} = \vec{k}_f - \vec{k}_i$  is created. Equation (2.21) provides the Raman differential scattering section in quantum theory:

$$\frac{d^2\sigma}{dE_f d\Omega} = \frac{mk_f}{\hbar^2 j_{0Z}} N(\vec{k}_s) \sum_{n_i, n_f} P_{n_i} R(n_i, \vec{k}_i; n_f, \vec{k}_f; t) \quad (7.99)$$

The above equation can be simplified to

$$\frac{d^2\sigma}{dE_f d\Omega} \propto \sum_{n_i, n_f} P_{n_i} R(n_i, \vec{k}_i; n_f, \vec{k}_f; t) \quad (7.100)$$

where  $P_{n_i}$  is the probability of target particles with energy equivalent to the engine state energy of incident particles.  $R(n_i, \vec{k}_i; n_f, \vec{k}_f; t)$  represents the probability that in unit time,  $n_i$  incident particles localized at the engine state of engine energy  $E_i$  and momentum  $\hbar\vec{k}_i$  transit to the engine state of  $n_f$  scattered particles with energy  $E_f$  and momentum  $\hbar\vec{k}_f$ .

Equation (2.65) showed the transition probability from state  $\varphi_i(\mathbf{r})$  to  $\varphi_f(\mathbf{r})$ :

$$R_{if}(t) = \frac{1}{\hbar^2} \left| \int_0^t \exp(i\omega_{if}t) H'_{if} dt \right|^2 \quad (7.101)$$

where the matrix element is

$$H'_{if}(t) = \langle \varphi_i(\mathbf{r}) | H'(t) | \varphi_f(\mathbf{r}) \rangle \quad (7.102)$$

Obviously,  $R_{if}(t)$  is  $P_{n_i} R(n_i, \mathbf{k}_i; n_f, \mathbf{k}_f; t)$  in Equation (7.100). In phonon Raman scattering, this equation is equivalent to the scattering matrix elements  $W_{fi}$  in perturbation theory, in which a photon transmits from initial state  $i$  to final state  $f$  and at the same time produces a specific phonon.  $W_{fi}$  is the sum of direct photon–phonon and indirect photon–electron–phonon interactions. For visible Raman scattering, because of the incident light frequency  $\omega_i \gg$  frequency of phonons  $\omega_q$  and photons and phonons cannot directly couple, the former items are negligible. Therefore, light scattering is achieved by photon–electron–phonon interactions and its contribution to the lowest order of  $W_{fi}$  is

$$W_{fi} = \sum_{\lambda_1 \lambda_2} \frac{\langle 0; s, 1 | \mathcal{H}' | \lambda_1 \rangle \langle \lambda_2 | \mathcal{H}' | \lambda_1 \rangle \langle \lambda_1 | \mathcal{H}' | 0; i, 0 \rangle}{(E_{\lambda_2} - E_{0,i})(E_{\lambda_1} - E_{0,i})} \quad (7.103)$$

where  $\langle 0; i, 0 |$  expresses the electronic ground state with a photon in the state  $i$  and no phonon and the remaining are an analogy; the summation labels  $\lambda_1$  and  $\lambda_2$  cover all possible intermediate states. The total perturbation  $H'$  is the sum of the electronic–photon interaction  $\mathcal{H}_R$  and electron–phonon interaction  $\mathcal{H}_L$ :

$$\mathcal{H}' = \mathcal{H}_R + \mathcal{H}_L \quad (7.104)$$

where  $\mathcal{H}_R$  can be expressed specifically as

$$\mathcal{H}_R = \sum_{\mu} \left( -\frac{e}{m} \right) \left( \frac{2\pi\hbar}{Vn^2\omega_{\mu}} \right)^{1/2} \epsilon_{\mu} \cdot \mathbf{p} e^{i\mathbf{k}_{\mu} \cdot \mathbf{r}} a_{\mu} + c.c. \quad (7.105)$$

$a_{\mu}$  is the destruction operator of phonon at state  $\mu$ . And  $\mathcal{H}_L$  can be written as the form of electron operator:

$$\mathcal{H}_L = V^{-1} \sum_v \theta^v(\mathbf{r}) e^{i\mathbf{q}_{\mu} \cdot \mathbf{r}} b_v + c.c. \quad (7.106)$$

where  $v$  represents the summation for all phonon modes and wave vectors and  $\theta^v(\mathbf{r})$  is the interacting potential, of which the latter can be the deformation potential and Fröhlich potential, and so on. There are six possible configurations of  $H_R$  and  $H_L$  contributing to  $W_{fi}$ . Here we only consider the one shown in Figure 7.19(b).

In the adiabatic approximation, the electron part of a wave function can be written as

$$|\lambda, k\rangle = \sum_{c,v,k} \Phi_{k,cv}(\mathbf{k}) |\lambda, k\rangle = \sum_{c,v,k} U_{\lambda k,cv}(\mathbf{k}) \Phi_{k,cv}(\mathbf{k}) \quad (7.107)$$

where  $\Phi_{k,cv}(\mathbf{k})$  is an antisymmetric wave function of the Bloch state in valence electron band; and  $U$  is the correlation function of the electron and hole exciton. Substituting

Equations (7.105)–(7.107) into Equation (7.103), differential scattering section of Raman scattering is obtained, that is, Raman spectrum of a phonon. The strict calculation of differential scattering can be carried out by the First-principle (*ab initio*) method. However, such calculations for bulk matter is impossible due to the large quantity of data, even though computer technology is flourishing. Therefore it has to rely on the calculation of macroscopic models and, therefore, we will now introduce some macroscopic models of Raman scattering.

### 7.5.3 Dielectric Fluctuation Correlation Model of Raman Scattering

#### 7.5.3.1 Macroscopic Polarization and Dielectric Tensor

The light scattering of condensed matter constructed from abundant atoms or molecules can be described by a macro-quantity. Section 2.2.3 described macro-polarization. Section 2.2.2 discussed light scattering of a single atom by classical theory, where we pointed out that the electric dipole moment  $\mathbf{P}_i(\mathbf{r}, t)$  is determined by the external electric field  $\mathbf{E}$  through atom polarization  $\alpha$ . From the Equation (2.36) of macro-polarization, it can be seen that this is correlated with the position of atoms in condensed matter. If the array of atoms is regular and their movement is frozen, the macro-polarization  $\mathbf{P}(\mathbf{r}, t)$  is uncorrelated with  $\mathbf{r}$ . Similar to atom polarization, the macro-polarization  $\mathbf{P}$  induced by an electric field can be expressed as

$$\mathbf{P} = \frac{1}{4\pi} (\epsilon - 1) \cdot \mathbf{E} \quad (7.108)$$

where  $\epsilon = \{\epsilon_{\alpha\beta}\}$  is the dielectric tensor. The dielectric tensor  $\epsilon$  is a constant at the frequency of visible light and can be assumed as a scalar in liquid and cubic crystals, that is,  $\epsilon_{\alpha\beta} = \epsilon \delta_{\alpha\beta}$ .

In a medium with constant  $\epsilon$ , the only effect of polarization is to correct the wavelength  $\lambda_v$  and light velocity  $c_0$  in a vacuum. Within a medium,  $\omega = c \cdot k$ , while

$$c = c_0/n; \quad (7.109)$$

$$k = 2\pi/\lambda = 2\pi n/\lambda_v \quad (7.110)$$

where  $c_0$  is vacuum light velocity;  $n = \sqrt{\epsilon}$  is the index of refraction; and  $\lambda$  and  $\lambda_v$  represent light wavelengths in medium and vacuum, respectively.

#### 7.5.3.2 Dielectric Tensor Fluctuation and its Scattering Field

With an atom, a small vibration occurs with translation or rotation, that is, there is a fluctuation in space and time for the atom. Assuming that there is an instantaneous and localized relation between polarization and electric field, we have

$$\mathbf{P}(\mathbf{r}, t) = \frac{1}{4\pi} (\epsilon(\mathbf{r}, t) - 1) \mathbf{E}(\mathbf{r}, t) \quad (7.111)$$

Thus, the dielectric tensor  $\epsilon(\mathbf{r}, t)$  can be written as

$$\epsilon(\mathbf{r}, t) = \epsilon_0 + \delta\epsilon(\mathbf{r}, t) \quad (7.112)$$

where  $\epsilon_0$  is dielectric tensor at no fluctuation and  $\delta\epsilon(r, t)$  represents the fluctuation of the dielectric tensor. In the following we apply Maxwell equations to investigate the scattering field induced by  $\delta\epsilon(r, t)$  under the action of incidence light field  $E_0$ .

Since the studied material has been assumed to be non-magnetic, the total electromagnetic field can be expressed by the electric field  $E$ , electric displacement vector  $D$ , and magnetic field  $B$ . Assuming that  $E_0$  and  $B_0$  are the electric field and magnetic field of incidence light, respectively, and the electric displacement vector does not affect fluctuations in time and space, then  $D_0 = E_0 + 4\pi P_0$ . Obviously, the electric displacement vector  $D_0$  has no correlation with atom movement. Since  $E_0$ ,  $B_0$ , and  $D_0$  are physical quantities not affected by fluctuations in time and space, they must satisfy the Maxwell equation and the total electromagnetic field also satisfies this equation. As the function is linear,  $E'$ ,  $B'$ , and  $D'$  in the following equations also satisfy the Maxwell equation:

$$\begin{aligned} E &= E_0 + E' \\ D &= D_0 + D' \\ B &= B_0 + B' \end{aligned} \quad (7.113)$$

It can be found from Equation (7.113) that  $E'$  and  $B'$  are the scattering fields, and their Maxwell equation set are

$$\left\{ \begin{array}{l} \nabla \times E' = -\frac{1}{c} \dot{B}' \\ \nabla \times B' = \frac{1}{c} \dot{D}' \\ \nabla \cdot D' = 0 \\ \nabla \cdot B' = 0 \end{array} \right. \quad (7.114)$$

where

$$\begin{aligned} D' &= D - D_0 = E + 4\pi P - E_0 - 4\pi P_0 \\ &= (E - E_0) + 4\pi(P - P_0) = E' + 4\pi P' \end{aligned} \quad (7.115)$$

and

$$\begin{aligned} P' &= P - P_0 = \frac{1}{4\pi}(\epsilon(r, t) - 1)E(r, t) - \frac{1}{4\pi}(\epsilon_0 - 1)E_0 \\ &= \frac{1}{4\pi}(\epsilon_0 - 1)E' + \frac{1}{4\pi}\delta\epsilon \cdot E_0 + \frac{1}{4\pi}\delta\epsilon \cdot E' \end{aligned} \quad (7.116)$$

Since the fluctuation  $\delta\epsilon$  of  $\epsilon$  is very small and the induced scattering field  $E'$  is also very small, the item of second smallest in Equation (7.116) can be neglected, thus we have

$$P' = \frac{1}{4\pi}(\epsilon - 1)E' + \delta P \quad (7.117)$$

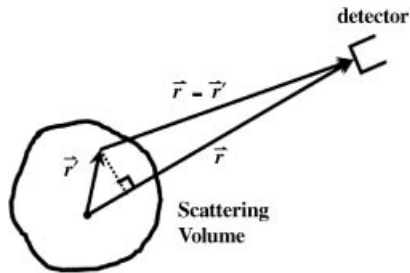


**Figure 7.20** Spatial configuration to detect the scattering field generated by dielectric fluctuations  $\delta\mathbf{P}$ . Reprinted from S.-L. Zhang, *Raman Spectroscopy and Low-dimensional nanoscale Semiconductors*, Science Press, (2008)

$$\delta\mathbf{P} = \frac{1}{4\pi} \delta\epsilon \cdot \mathbf{E}_0 \quad (7.118)$$

therefore

$$\mathbf{D}' = \mathbf{E}' + 4\pi\mathbf{P}' = \epsilon \cdot \mathbf{E}' + 4\pi\delta\mathbf{P} \quad (7.119)$$

Substituted  $\mathbf{D}'$  into the Maxwell equation set and combining the three former equations, an inhomogeneous wave equation of  $\mathbf{E}'$  is obtained as

$$\Delta\mathbf{E}' - \frac{1}{c^2} \ddot{\mathbf{E}'} = -4\pi \left( \frac{1}{\epsilon_0} \nabla(\nabla\delta\mathbf{P}) - \frac{1}{c^2} \delta\ddot{\mathbf{P}} \right) \quad (7.120)$$

where  $c = c_0/\sqrt{\epsilon}$  is the light velocity in the medium. Using the Hertz vector  $\mathbf{Z}$  in the solution of equation  $\nabla^2\mathbf{Z} - \frac{1}{c^2} \frac{\partial^2 \mathbf{Z}}{\partial t^2} = -4\pi\delta\mathbf{P}$ , by resolving Equation (7.120), the scattering field is

$$\mathbf{E}'(\mathbf{r}, t) \approx \frac{1}{C^2 r} \mathbf{e}_r \times \left[ \mathbf{e}_r \times \int dr^3 \delta\ddot{\mathbf{P}}(\mathbf{r}', t_{ret}) \right] \quad (7.121)$$

In the above equation,  $t_{ret}$  is the postponed time and is expressed as

$$t_{ret} = t - \frac{1}{c/n} |\mathbf{r} - \mathbf{r}'| \approx t - \frac{1}{c/n} + \frac{\mathbf{e}_r \cdot \mathbf{r}'}{c/n} \quad (7.122)$$

Its physical meaning is shown in Figure 7.20.

In solving the above scattering field, we neglect details of the solving process of inhomogeneous wave equations; the reader who interested in more detail can refer to reference 8 in chapter 2 of this book.

From scattered field Equation (7.121), it can be seen that the obtained scattered field  $\mathbf{E}'$  is considered only as electric dipole radiation and the scattering field is from the polarization fluctuation  $\delta\mathbf{P}$ . Therefore,  $\delta\mathbf{P}$  can be seen as the source of the scattered field, which also can be seen from the relation Equation (7.119) of  $\mathbf{D}'$  and  $\delta\mathbf{P}$ .

Because the time fluctuations of  $\delta\epsilon$  are lower than incident light frequency  $\omega_o$ , this can be approximated as

$$\delta\ddot{\mathbf{P}} = \frac{1}{4\pi} \delta\epsilon \cdot \ddot{\mathbf{E}} = \frac{-\omega_0^2}{4\pi} \delta\epsilon \cdot \mathbf{E} \quad (7.123)$$

Obviously, the polarization  $\mathbf{n}'$  of scattered wave is horizontal, that is,  $\mathbf{n}' \cdot \mathbf{e}_r = 0$ , thus, we obtain

$$\begin{aligned}\mathbf{n}' \cdot (\mathbf{e}_r \times (\mathbf{e}_r \times \delta\epsilon \cdot \mathbf{n}_0)) &= \mathbf{n}' \cdot (\mathbf{e}_r(\delta\epsilon \cdot \mathbf{n}_0)\mathbf{e}_r - \delta\epsilon \cdot \mathbf{n}_0) \\ &= -\mathbf{n}' \cdot \delta\epsilon \cdot \mathbf{n}_0 = -\delta\epsilon_{\alpha\beta}\end{aligned}\quad (7.124)$$

For component  $E' = \mathbf{n}' \cdot \mathbf{E}'$ , we have

$$E'(\mathbf{r}, t) = \frac{\omega_0^2 E_0}{4\pi c^2 r} \int d\mathbf{r}'^3 \delta\epsilon(\mathbf{r}', t_{ret}) e^{i(\mathbf{k}_0 \cdot \mathbf{r} - \omega t_{ret})} \quad (7.125)$$

### 7.5.3.3 Raman Scattering and Dielectric Fluctuation Correlation Function

- Differential scattering section and dielectric fluctuation correlation function

Chapter 2, according to classical electromagnetic theory, gives the expression of the differential scattering section equation for light scattering at  $\mathbf{r}$  with incidence electric field  $E_0$  along the  $z$  direction and scattered field  $\mathbf{E}'$  along the  $\mathbf{n}$  direction, which is

$$\begin{aligned}\frac{d^2\sigma}{d\Omega dE'} &= \frac{r^2}{N \langle E_{0,Z}^2 \rangle} \mathbf{n} \langle |E'(\mathbf{r})|^2 \rangle \\ &= \frac{r^2}{N \langle E_{0,Z}^2 \rangle} \mathbf{n} \langle E^*(\mathbf{r}, 0) E^*(\mathbf{r}, t) \rangle\end{aligned}\quad (7.126)$$

In the above equation, the mark  $\langle \dots \rangle$  expresses the average for time and space. Substituting the scattered field expression in Equation (7.121) into the above equation and using the translation invariance in time and space of the system, we have

$$\langle \delta\epsilon(\mathbf{r}', t) \delta\epsilon(\mathbf{r}'', t'') \rangle = \langle \delta\epsilon(0, 0) \delta\epsilon(\mathbf{r}'' - \mathbf{r}', t'' - t') \rangle \quad (7.127)$$

For the scattered wave of frequency  $\omega'$ , after introducing the wave vector

$$\mathbf{k}' = \frac{\mathbf{e}_r \omega}{c/n} \quad (7.128)$$

and the change amount expression of frequency and wave vector of a scattered wave relative to those of an incident wave is

$$\omega = \omega_0 - \omega', \quad (7.129)$$

$$\mathbf{k} = \mathbf{k}_0 - \mathbf{k}' \quad (7.130)$$

Then we have

$$\begin{aligned}\frac{d^2\sigma}{d\Omega d\omega'} &= \frac{1}{4\pi^2 \rho_0} \left( \frac{\omega_0}{C} \right)^4 \frac{1}{2\pi} \int_{-\infty}^{+\infty} dt e^{-i\omega t} \int d\mathbf{r}^3 e^{i\mathbf{k} \cdot \mathbf{r}} \langle \delta\epsilon_{\alpha\beta}(0, 0) \delta\epsilon_{\gamma\delta}(\mathbf{r}, t) \rangle \\ &= \frac{1}{4\pi^2 \rho_0} \left( \frac{\omega_0}{C} \right)^4 \frac{1}{2\pi} \int_{-\infty}^{+\infty} dt e^{-i\omega t} \int d\mathbf{r}^3 e^{i\mathbf{k} \cdot \mathbf{r}} G_{\alpha\beta\gamma\delta}(\mathbf{r}, t)\end{aligned}\quad (7.131)$$

In the above equation, we have quoted the definition of dielectric fluctuation correlation function  $G_{\alpha,\beta,\gamma,\delta}(\mathbf{r}, t)$  as [1]

$$G_{\alpha,\beta,\gamma,\delta}(\mathbf{r}, t) = \langle \delta\epsilon_{\alpha\beta}(0, 0) \delta\epsilon_{\gamma\delta}(\mathbf{r}, t) \rangle \quad (7.132)$$

where  $\rho_0 = N/V$  is the density of scatters.

The above derivation allows us to obtain a common result in light scattering. The generation of scattered light can be understood in terms of dielectric fluctuations and the differential scattering cross section can be expressed by the dielectric fluctuation correlation function.

- Spatial correlation function of dielectric fluctuations

For the scattering of crystals, the fluctuation is caused by atomic motion. The vibration amplitude of atoms in solids is small, therefore, the vibration is harmonic and the vibration mode can be described by normal coordinates. When taking into account the optical dielectric constant modulation by harmonic vibration modes, the dielectric tensor can also be expanded by normal coordinates and the expansion is only needs to take into account the first-order atomic displacement. Thus, when the atomic displacement of the  $j$ th vibration mode can be expressed with a normal coordinate  $Q_j(t)$ , the expression of the fluctuation of  $\epsilon_{\alpha\beta}(\mathbf{r}, t)$  has a simple form as

$$\delta\epsilon_{\alpha\beta}(\mathbf{r}, t) = \sum_{j=1}^{3N} R_{\alpha\beta}(\mathbf{r}, t) Q_j(t) \quad (7.133)$$

Unless the contribution from displacements of neighboring atoms cancel each other out due to local symmetry of atoms, such as the inversion symmetry, the first-order derivative,  $\partial\epsilon/\partial Q$ , is generally non-zero. By substituting Equation (7.133) into Equation (7.132) and using the statistical independent principle of different normal coordinates, we obtain

$$G_{\alpha\beta,\gamma\delta}(\mathbf{r}, t) = \sum_{j=1}^{3N} R_{\alpha\beta,\gamma\delta}(\mathbf{r}, j) \langle Q_j(0) Q_j(t) \rangle \quad (7.134)$$

where

$$R_{\alpha\beta,\gamma\delta}(\mathbf{r}, j) = \left\langle \frac{\partial\epsilon_{\alpha\beta}(0)}{\partial Q_j} \frac{\partial\epsilon_{\gamma\delta}(\mathbf{r})}{\partial Q_j} \right\rangle \quad (7.135)$$

These results show that for each particle, the relationship of space and time is separate; by using the nature of harmonic oscillator, we obtain

$$\langle Q_j(0) Q_j(t) \rangle = \frac{1}{2\omega_j} \{ n(\omega_j) e^{i\omega_j t} + [1 + n(\omega_j)] e^{-i\omega_j t} \} \quad (7.136)$$

where

$$n(\omega_j) = \exp(\hbar\omega_j/kT - 1)^{-1} \quad (7.137)$$

is the Bose–Einstein distribution.

The time correlation of Equation (7.136) is known, thus when we discuss the intensity of Raman scattering, we only need to consider the space correlation of the dielectric tensor. Thus, the spatial correlation functions of the dielectric fluctuation reflect only the spatial correlation of atomic displacement of normal modes. The space correlation function of dielectric fluctuation  $R(\mathbf{r}, j)$  reflects the space correlation of the regular mode only. So the correlated region of  $R(\mathbf{r}, j)$  is only the correlation region of the mode  $j$  (for simplification, it will be referred to as the correlation function). The results of Equations (7.134)–(7.136) have universal significance and can be applied to any vibration Raman scattering of solid or amorphous crystals, of which the only difference is the extended regions with different sizes. In the following, we will start from the correlation function to discuss Raman scattering spectra of crystals and amorphous crystals specifically.

## 7.5.4 Raman Spectra of Crystals and Amorphous Crystals [34]

### 7.5.4.1 Raman Spectra of Crystals

Due to lattice periodicity and translational invariance of crystals, the lattice vibration of crystals is similar to that of wave vibration in the infinite region. Correspondingly, the relation between the spatial correlation function  $R(\mathbf{r}, j)$  and its coordinate  $\mathbf{r}$  processes a sine relation with wavelength  $\lambda_j = 2\pi/q_j$  and the Raman scattering complies with the momentum conservation law (i.e., phonon wave vector selection rules). Thus, the mode  $j$  with frequency  $\omega_j$  has a definite wave vector  $\mathbf{q}_j$ . For the actual crystal, there are a variety of defects and damping of phonon coupling and so on, and the region associated by the correlation function is limited; however, it is still large enough when compared with wavelength and the crystal wave vector selection rule is still an effective approximation. The effect is only that the Raman spectrum of practical crystals is not sharp, tending to a broad signal.

### 7.5.4.2 Raman Spectra of Amorphous Crystals

As mentioned at the start of this chapter and shown in Figure 7.1(b), the atomic array in amorphous crystals has no periodicity in large regions and no long-range order; however, they are still in order of the range of 3–4 bond length and has short-range order. For example, the atoms in covalent bond crystals are composed of covalent bonds with saturation and directionality, in which Si is such a crystal with a regular tetrahedron structure. In amorphous Si, each Si atom is surrounded by four Si atoms and its bonds form a covalent bond; however, the length and bond angle of bonds are changed and thus the regular tetrahedron structure no longer holds, meaning that only the long-range order disappears. The range of the short-range order of amorphous Si usually is three or four bond lengths, which is 0.12–0.15 nm [28].

Since there is no long-range order in amorphous crystal, the translational symmetry reflecting crystal characteristics is lost, resulting in the correlation region between atoms becomes smaller and thus the localization of correlation function, that is, the coherence length of normal modes becomes shorter. For Raman scattering, we assume that when the coherence length is only one-tenth or less than the light wavelength, the vibration mode evolves into a localized mode, which will no longer be characterized by a single wave vector.

If we suppose  $\Lambda$  to represent the correlation region, the vibration eigen function can be expressed as

$$\exp(i\mathbf{q} \cdot \mathbf{r}) \exp(-\mathbf{r}/\Lambda) \quad (7.138)$$

that is, a plane wave factor  $\exp(i\mathbf{q} \cdot \mathbf{r})$  multiplied by a spatial decay factor  $\exp(-\mathbf{r}/\Lambda)$ . The factor  $\exp(-\mathbf{r}/\Lambda)$  plays a role in which the vibration eigen function is mixed with different  $\mathbf{q}$  states, which reflect  $\mathbf{q}$  to no longer be a good quantum number. Thus, for the  $j^{\text{th}}$  mode, Raman scattering appears as a wide, flat peak at around  $\mathbf{q}_j$ , as mentioned above. In the case of  $q\Lambda_j \ll 1$  ( $\Lambda_j$  is the correlation region of  $j$  mode), the spatial Fourier transform of the correlation function with a region of  $\Lambda_j$  possesses a limited form not related to  $\mathbf{q}$ :

$$\{R_{\alpha\beta,\gamma\delta}(\mathbf{r}, j)\}_q = A_{\alpha\beta,\gamma\delta}(j) \Lambda_j^3 \quad (7.139)$$

where  $A_{\alpha\beta,\gamma\delta}(j)$  is the optical coupling tensor, which characterizes the dielectric modulation strength and  $\Lambda_j^3$  is the volume of the coherent scope of modes.

According to the above, the light scattering correlation function of amorphous crystals is

$$G_{\alpha\beta,\gamma\delta}(\mathbf{q}, \omega) = \sum_{j=1}^{3N} A_{\alpha\beta,\gamma\delta}(j) \Lambda_j^3 \cdot (1/2\omega) \{n(\omega_j) \delta(\omega + \omega_j) + [1 + n(\omega_j)] \delta(\omega - \omega_j)\} \quad (7.140)$$

In a given Raman band,  $A(j)\Lambda_j^3$  is a constant independent of frequency. Thus the expression of Raman spectra can be written as

$$I_{\alpha\beta,\gamma\delta}(\omega) = \sum_b C_b^{\alpha\beta,\gamma\delta}(1/\omega)[1 + n(\omega)]g_b(\omega) \quad (7.141)$$

where  $g_b(\omega)$  is the state density of band  $b$ , and the summation is for all bands; the constant  $g_b(\omega)C_b^{\alpha\beta,\gamma\delta}$  is independent of band  $b$ ; and  $\alpha\beta, \gamma\delta$  represent the polarization of tensor determined by the geometric configuration of incident and scattering light. Equation (7.142) shows that Raman spectrum of amorphous crystals is determined jointly by the Bose-Einstein factor  $n(\omega)$ ,  $1/\omega$ , transition probability (dependent of  $C_b^{\alpha\beta,\gamma\delta}$ ), and VDOS  $g_b(\omega)$ .

Figure 7.21 copies shows the Raman spectrum of the optical vibration mode of Si shown in Figure 5.7. The figure shows that the Raman peak of the optical mode of crystalline Si is at  $520 \text{ cm}^{-1}$ , with a line width of  $5.5 \text{ cm}^{-1}$  and the Raman peak of the optical mode of amorphous Si is at  $480 \text{ cm}^{-1}$ , with a line width of  $70 \text{ cm}^{-1}$ , which obviously shows the difference in Raman spectral features of crystalline and amorphous crystals.

## 7.5.5 Phonon/Vibration Density of State (P/VDOS) and Bose Peak

From the above discussion, the amorphous spectra are directly dependent of the vibration/phonon density of state (V/PDOS). In this section we will discuss VDOS.

### 7.5.5.1 Phonon/Vibration Density of state (P/VDOS)

We have introduced the concept of PDOS in Section 7.4 and gave its definition expression in Equation (7.97). Here, it will be discussed from a broader statistical mechanics perspective.

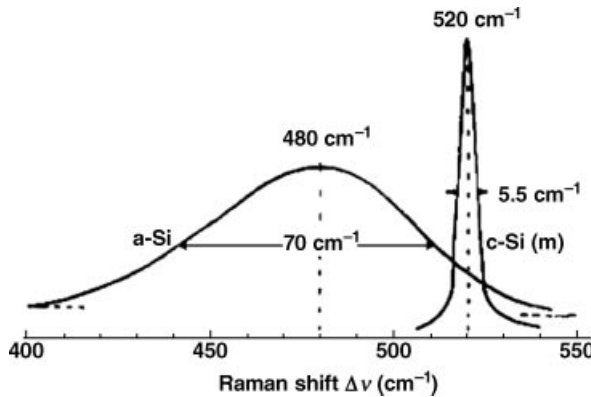


**Figure 7.21** Raman spectra of optical phonon of crystalline and amorphous Si [35]. Reprinted from S. Vepiek, Z. Iqbal, H. R. Oswald and A. P. Webb, Properties of polycrystalline silicon prepared by chemical transport in hydrogen plasma at temperatures between 80 and 4000 C, *J. Phys. C: Solid State Phys.*, 14, 295–308 (1981) with permission of the Institute of Physics

According to statistical mechanics, the thermodynamic function of an  $N$ -particle system is determined entirely by the energy level of the system. In a solid composed of  $N$ -particles, there are  $3N$  freedoms of motion. Section 7.2.5 shows that if we introduce normal coordinates, the  $3N$  motion freedom can become  $3N$  canonical modes. After a simple deduction, we can obtain the Helmholtz function of the system as [2]

$$F = U + \frac{1}{2} \sum_i \hbar\omega_i + kT \sum_i \ln(1 - e^{-\hbar\omega_i/kT}) \quad (7.142)$$

When  $N$  is very large, a VODS of the system,  $g(\omega)$ , can be introduced to express the number of vibration modes in the frequency range of  $\omega \sim \omega + d\omega$  and the following equation is established:

$$\int_0^{\infty} g(\omega) d\omega = 3N \quad (7.143)$$

By using  $g(\omega)$ , the summation in Equation (7.143) can be changed into the integral:

$$F = U + \frac{1}{2} \int_0^{\infty} \hbar\omega g(\omega) d\omega + kT \int_0^{\infty} \ln(1 - e^{\hbar\omega/kT}) g(\omega) d\omega \quad (7.144)$$

Thus the vibration density function  $g(\omega)$  of the system completely determines the thermodynamic properties. In crystals,  $g(\omega)$  can be obtained from dispersion relations through Equation (7.98). By using experimental methods, there are at least five ways to obtain information of VDOS, which are Raman scattering, specific heat capacity measurement, inelastic neutron scattering, inelastic X-ray scattering, and infrared absorption spectrum.

The above results are totally dependent on the periodicity of lattices and thus can be fully applied to crystals. In amorphous crystals, Equation (7.98) should not be effective, as there is no definite relation between wave vector  $\mathbf{q}$  and dispersion relation. Therefore, there are some problems for VDOS discussion of amorphous crystals by starting from the framework of present lattice dynamics [36].

#### 7.5.5.2 Vibration Density of State and Raman Scattering [36]

Section 7.5.3 showed that because there is no periodicity in amorphous crystals, the wave vector selection rule is destroyed, and Raman scattering includes the contribution of all modes, meaning that the Stokes Raman scattering spectrum of amorphous crystals is determined by Equation (7.141). If we assume the Raman coupling parameter  $C_b^{\alpha\beta,\gamma\delta}$  varies slowly and smoothly and so can be considered as a constant, we can define a reduced Raman spectrum  $I_R(\omega)$  from Equation (7.141) as

$$I_R(\omega) = \frac{I_{\alpha\beta,\gamma\delta}(\omega)}{(1/\omega)[1 + n(\omega)]} \quad (7.145)$$

where  $I_{\alpha\beta,\gamma\delta}(\omega)$  is an observed Raman spectrum and  $(1/\omega)[1 + n(\omega)]$  is only interrelated with temperature, therefore  $I_R(\omega)$  can be obtained by using Raman spectral measurements. Thus, according to Equation (7.141), we have

$$I_R(\omega) \propto g_b(\omega) \quad (7.146)$$

This indicates that the reduced Raman spectrum reflects the basic features of VDOS, indicating VDOS  $g(\omega)$  plays a key role in amorphous Raman spectra and Raman scattering is a useful way to study VDOS of amorphous crystals.

In Equation (7.141), the frequency correlated factors  $1/\omega$  and  $1 + n(\omega)$  change the contribution of  $g_b(\omega)$  to bands and obviously it contributes to the low frequency band.  $1 + n(\omega)$  is a heat distribution factor and appears in all Raman spectra. The factor  $1/\omega$  is strictly correct for the vibration spectrum in a large range of frequencies and is important, especially for the low frequency Raman spectrum. However, the latter is usually ignored, which is discussed below.

#### 7.5.5.3 Boson Peak

From the 1970s, some unique properties of amorphous crystals have been found experimentally. One of these is that there are some unique properties in low wave number Raman scattering of amorphous crystals. For example, in the polarized Raman spectra of vitreous silicon, there is a Raman peak in the range of  $20\text{--}100\text{ cm}^{-1}$ , as shown as in Figure 7.22(a), which is sometimes called the Bose peak. In the range of much lower frequency, the intensity of the Bose peak is much larger than that expected by the Debye theory, as shown in Figure 7.22(b) [37].

From experiments, there are four factors that contribute to Raman scattering of around  $5\text{--}100\text{ cm}^{-1}$ :

- (1) The tail in high wave number range from Brillouin scattering;
- (2) The tail at low frequency range from acoustic phonon scattering;
- (3) Quasi-elastic scattering;
- (4) Boson peak.

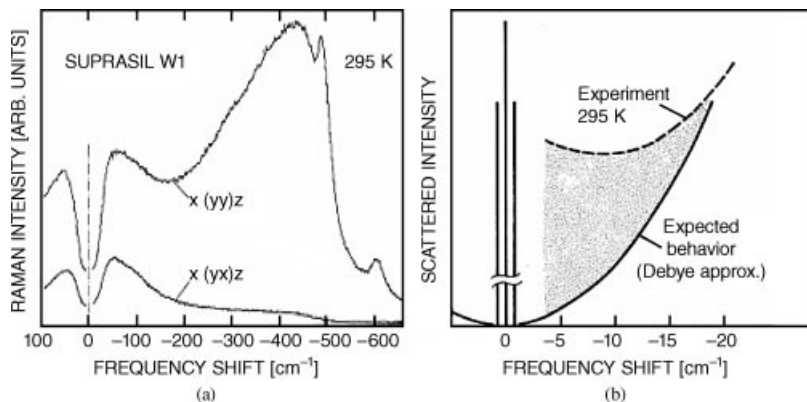


**Figure 7.22** (a) Polarized Raman spectrum of vitreous silica; (b) the scattered intensity comparison between experimental observation (dashed line) and the expectation by Debye theory (solid line) [37]. Reprinted from G. Winterling, Very-low-frequency Raman scattering in vitreous silica, *Phys. Rev. B*, 12, 2432–2440 (1975) with permission of the American Physical Society

where the second and third items are dominant and of most concern. We have already pointed out that a reduced Raman spectrum of an amorphous crystal has the Raman coupling parameter  $C_b^{\alpha\beta,\gamma\delta}$  multiplied by the vibration state density  $g_b(\omega)$ . The Boson peak was considered to be composed of the Raman coupling factor. However, in recent years it was found for many amorphous materials that the dependence of Raman coupling parameter in the vicinity of the Bose peak on Raman frequency are approximately linear, that is [38]:

$$C(v) = v/v_{BP} + B \quad (7.147)$$

where  $v_{BP}$  is the frequency of the Boson peak. By using  $B = 0$  or  $0.5$ , the amorphous crystals are classified into two types. General agreement is that the Bose peak in low-frequency Raman scattering is caused by the vibration state density, that is, there are the low-frequency modes of no Debye theory involved in low-frequency Raman scattering of amorphous crystals [37].

In different experiments, for many amorphous materials with different chemical composition and structure, they exhibit very similar properties of Bose peaks, which all originate from the VDOS. That is, they are from excess vibration modes beyond the Debye theory. The Bose peak, as a common characteristic sign of amorphous materials, has been increasingly accepted.

The Boson peak was even observed in liquid and has been the mutual property of amorphous crystal materials, so it must have a deep physical origin. In this section, we have introduced a rough view of the nature of amorphous material, but not enough to explain the origin of the Boson peak. The understanding of amorphous crystals in nature is still superficial compared to that of other crystals. To explore the origin of the Bose peak may be a breakthrough in understanding the nature of amorphous crystals. This issue has been discussed for thirty years in academic circles and many theories have been proposed [39–44]; however, there is still no conclusion.

However, some authors [45] recently found that the optical phonon Raman spectra of polar nano-semiconductors possess amorphous features, so the research of low frequency optical phonon Raman spectrum of polar nano-semiconductors may provide important information and revelations for research of the nature of the Boson peak.

## References

- [1] Winor, K. (1987) *Phys. Rev. B*, **35**, 2366–2374.
- [2] Born, K. and Huang, K. (1968) *Dynamical Theory of Crystal Lattices*, Oxford University Press, Oxford.
- [3] Kittel, C. (2005) *Introduction to Solid State Physics*, 8th edn, John Wiley & Sons, Inc, New York.
- [4] Sherwood, P.M.A. (1972) *Vibrational Spectroscopy in Solids*, Cambridge University Press, Cambridge.
- [5] Yu, P.Y. and Cardona, M. (2001) *Fundamentals of Semiconductors*, 3rd edn, Springer-Verlag, Berlin.
- [6] Zhang, S.L. (2008) *Raman Spectroscopy and Low-dimensional Nanoscale Semiconductors* (in Chinese), Science Press, Beijing.
- [7] Bradbury, T.C. (1981) *Theoretical Mechanics*, Krieger Publishing Co.
- [8] Born, M. and Karman, T.V. (1912) *Phys. Zeit.*, **13**, 271.
- [9] Shankar, R. (1994) *Principles of Quantum Mechanics*, 2nd edn, Springer-Verlag, Berlin.
- [10] Born, M. (1914) *Ann. Physik*, **44**, 605–642.
- [11] Zhang, S.L., Zhou, H.T., Meng, W. et al. (1988) *Solid State Commun.*, **66**, 657–660.
- [12] Zhang, S.L., Jin, Y., Guo, Z.A. et al. (1990) in *Progress in High Temperature Superconductivity*, vol. **22**(eds Z.X. Zhao, G.J. Cui, and R.S. Han), World Scientific, p. 83.
- [13] Cochran, W. (1959) *Proc. R. Soc. Lond. Ser. A*, **253**, 260–276.
- [14] Dolling, G. and Cowleg, R.A. (1966) *Proc. Phys. Soc. Lond.*, **88**, 463.
- [15] Phillips, J.C. (1968) *Phys. Rev.*, **166**, 832–838.
- [16] Phillips, J.C. (1968) *Phys. Rev.*, **168**, 905–911.
- [17] Weber, W. (1977) *Phys. Rev. B*, **15**, 4789–4804.
- [18] Musgrave, M.J.P. and Pople, J.A. (1962) *Proc. R. Soc. Lond A*, **268**, 474–484.
- [19] Smith, J.E., Brodsky, Jr., M.H., Crowder, B.L., Nathan, M.I. and Pinczuk, A. (1971) *Phys. Rev. Lett.*, **26**, 642–646.
- [20] Keating, P.N. (1966) *Phys. Rev.*, **145**, 637–645.
- [21] Yang, Y.W. and Coppens, P. (1974) *Solid State Commun.*, **15**, 1555–1559.
- [22] Martin, R.M. (1969) *Phys. Rev.*, **186**, 871–884.
- [23] Strauch, D. and Dordor, B. (1990) *J. Phys. Cordons. Mater.*, **2**, 1457–1474.
- [24] Ruf, T., Serrano, J., Cardona, M. et al. (2001) *Phys. Rev. Lett.*, **86**, 906–909.
- [25] Kelly, M.J. (1995) *Low-Dimensional Semiconductors: Materials, Physics, Technology, Devices*, Oxford University Press Co., New York.
- [26] Duval, E., Boukenter, A., and Achibat, T. (1990) *J. Phys.: Condens. Matter*, **2**, 10227–10234.
- [27] Kittel, C. (2005) *Introduction to Solid State Physics*, 8th edn, John Wiley & Sons, New York.
- [28] Cardona, M. (ed.) (1983) *Light Scattering in Solids* (2nd), Spring-Verlag.
- [29] Klingshirn, C.F. (2001) *Semiconductor Optics*, 3rd edn, Springer Press.
- [30] Hecht, E. (2001) *Optics*, 4th edn, Addison Wesley.
- [31] Born, M. and Wolf, E. (1999) *Principles of Optics*, 7th (Expanded) edn, Cambridge University Press, Cambridge.
- [32] Damen, T.C., Porto, S.P.S., and Tell, B. (1966) *Phys. Rev.*, **142**, 570–574.
- [33] Martin, R.M. (1971) *Phys. Rev. B*, **4**, 3676–3685.

- [34] Shuker, R. and Gammon, R.W. (1970) *Phys. Rev. Lett.*, **25**, 222–225.
- [35] Vepiek, S., Iqbal, Z., Oswald, H.R., and Webb, A.P. (1981) *J. Phys. C: Solid State Phys.*, **14**, 295–308.
- [36] Weaire, D.L. (1981) in *Amorphous Solids-Low-Temperature Properties* (ed. W.A. Phillips), Springer-Verlag, Berlin
- [37] Winterling F G. (1975) *Phys. Rev. B*, **12**, 2432–2440.
- [38] Surovtsev, N.V. (2001) *Phys. Rev. E*, **64**, 61102.
- [39] Winterling, G. (1975) *Phys. Rev. B*, **12**, 2432–2440.
- [40] Surovtsev, N.V. (2001) *Phys. Rev. E*, **64**, 61102.
- [41] Buchenau, U., Nücker, N., Dianoux, A.J. et al. (1986) *Phys. Rev. B*, **34**, 5665–5673.
- [42] Duval, E., Saviot, L., Surovtsev, N. et al. (1999) *Philos. Mag. A*, **79**, 2051–(2056.).
- [43] Orth, K., Schellenberg, P., and Friedrich, J. (1993) *J. Chem. Phys.*, **99**, 1–6.
- [44] Götze, W. and Mayr, M.R. (2000) *Phys. Rev. E*, **61**, 587–606.
- [45] Zhang, S.L., Shao, J., Hoi, L.S. et al. (2005) *Phys. Stat. Sol. (c)*, **2**, 3090.

# 8

## Theoretical Fundamentals of Raman Scattering in Nanostructures

The Raman scattering theory introduced in Chapter 7 is in connection with solids with infinite size, in which the size of studied objects does not pay attention to. However, the finite size of objects plays a key role in the study and application of nanostructures.

The earliest theoretical study on the phonon spectrum of finite sized crystals was by Fröhlich in 1949 [1], who considered a spherical sample constructed by double atoms, of which the radius is larger than the lattice constant but less than the infrared wavelength. In this model, he proved that the polarization inside the ball is uniform and found that a new optical mode emerges between the longitudinal and transverse optical phonon frequencies,  $\omega_L$  and  $\omega_T$ . This new mode induced by the finite size of materials was called the Fröhlich model and its frequency was labeled as  $\omega_F$ .

Ten years later, it was discovered that the infinite cycle of the crystal boundary conditions mentioned in Section 7.1.3 did not hold for the Coulomb force. This raised concerns about the finite size effect on lattice dynamics and light scattering theory [2]. At that time, the confirmation of these theoretical results was limited to the infrared spectrum and specific objects to be studied were often in the infrared spectrum.

The first Raman experiments of finite sized crystals were performed on a  $\text{KBr}_{1-x}\text{I}_x$  crystal with grain size 50 nm and the results were published in 1972 [3]. The first theoretical calculation of Raman scattering of a small sized crystal was published in 1973 [4]. Since then, lattice dynamics and Raman scattering theory of small sized crystals have been published continuously and become a new discipline.

As mentioned above, the study of Raman scattering of nanostructures started with theory first then the experiments soon followed. Many Raman features of nanostructures are also studied by theory first, thus the expected Raman features of nanostructures will be described along with the introduction of theory in this chapter.

Section 7.1.1 describes the structure of various types of nanomaterials as totally different. This leads to different types of material structures of finite size responding differently,

as described in Section 7.1.2. Therefore, the Raman scattering theory and theoretically expected Raman features of nanostructure materials (NM) will be introduced according to their structures in this chapter.

## 8.1 Superlattices

Section 7.1.1 showed that the superlattice (SL) is a “sandwich” layered structure. It grows along the direction perpendicular to the face of the substrate (usually marked as  $z$ ) to form a new crystal structure, whose symmetry and crystal lattice period are different from bulk materials which constitute the superlattice. The structural features of superlattices will result in a new type of dispersion and spectral feature for SL phonons, which are different from the features of component bulk materials.

First, along the growth direction  $z$ , the superlattice forms a phonon potential well [5], which is similar to an electron potential well. The continuous phonon energy changes to separate energy levels.

Second, the superlattice has a new crystal lattice period  $L = (n_1 + n_2) a$ , where,  $n_1$  and  $n_2$  are the monolayer numbers of atoms I and II that is constituted SL, respectively, and  $a$  is the bulk lattice constant of constituted materials in the SLs. The new lattice period leads to a Brillouin zone of  $0-1/a$  becoming a small Brillouin zone of  $0-1/L$  with the bulk dispersion curve then “folding” into the inside of the small Brillouin zone. Thus, the phonon energies of materials 1 and 2 “split” into  $n_1 + n_2$  energy levels in SLs, which is shown in Figure 8.1(b) for a sample of GaAs/AlAs SLs. From the figure, we can see that, on the one hand, the optical phonon modes in bulk materials “split” into  $n_1 + n_2$  modes. It is well known that the acoustic phonon dispersion curves of bulk GaAs and AlAs do not intersect with the photon dispersion curve (i.e., the acoustic phonons are not Raman active). However, in the GaAs/AlAs superlattice, the acoustic phonon dispersion curves through folding intersect with the photon dispersion curve, meaning that non-Raman active acoustic phonons in bulk GaAs and AlAs become Raman active in superlattices and can be observed in Raman spectra.

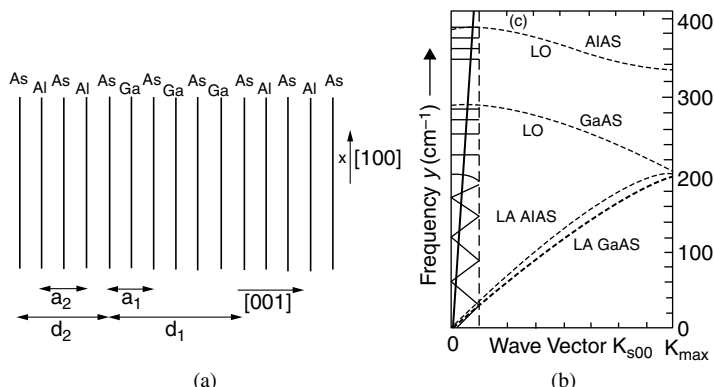


**Figure 8.1** Sketch of GaAs/AlAs superlattice structure (a) and dispersion curves of photon (oblique solid line) and longitudinal phonons of bulk GaAs and AlAs (dashed line) and superlattice (solid line) (b) [6]. Reprinted from B. Jusserand and M. Cardona, Ed. G. Güntherodt, *Raman Spectroscopy of Vibration in Superlattices in Light*, (1989) with permission of Springer

Third, along the growth direction of the superlattice, the translation symmetry is still retained, thus the conservation of momentum and the wave vector selection rule are also still maintained and the first-order Raman scattering still occur at the center of Brillouin zone.

Finally, there appears the interfaces in superlattice structures that do not exist in an ideal bulk material. These interfaces will produce related vibration modes, which is impossible to occur in corresponding bulk materials.

The sandwich layered structure of superlattices is deposited by the slabs of different materials. Thus, the theoretical model of slabs becomes the foundation of the superlattice theoretical model. Therefore, before lattice dynamics and light scattering theory of superlattices is introduced, we will briefly discuss the non-polar and polar slab theoretical model.

### 8.1.1 Non-Polar Semiconductor Slab Model [7]

The main points of the non-polar semiconductor slab are:

- (1) The slab consists of a thin layer of one or multiple unit cells.
- (2) As the layers of superlattices are considered to expand infinitely, the periodicity along  $x$  and  $y$  directions in the thin layers is still maintained. Thus, in these two directions, the position of atoms could be approximated by plane wave expansion and periodic boundary condition, similar to that in bulk materials.
- (3) In the  $z$  direction perpendicular to the thin layer plane, the plane wave expansion and periodic boundary condition cannot be used; however, the sequence along the  $z$  direction formed by primitive cells of bulk materials can be treated as a new unit cell.

Practical theoretical calculations are conducted based on the valence force field model introduced in Section 8.2. In the calculation, assuming that the force field is only related to the interaction (force constant) of the first neighbors, the bond–bond interaction (force constant  $\Delta\gamma$ ) and do not consider a Coulomb interaction between charges, the lattice potential energy can be expressed as

$$\Phi = \frac{1}{2} \sum_{ij} \lambda (dr_{ij})^2 + \frac{1}{3!} \sum_{iji'} rr_0^2 (d\theta_{iji'})^2 \quad (8.1)$$

where  $r_{ij}$  and  $\theta_{iji'}$  are the atomic distance and bond angle, respectively. The first summation covers all the first neighbor atoms  $ij$ , while the second summation covers all bond angles  $iji'$  of each atom.

As a calculated sample of the slab model, a slab of Si with thickness of 1–50 unit cells was calculated [7]. The calculated variation dependence of optical vibration frequency on slab thickness and calculated distribution dependence of vibration mode numbers in monolayers on frequency (i.e., phonon density of states (PDOS)) are shown in Figures 8.2(a) and (b), respectively. From Figure 8.2(a), the frequencies of vibration modes goes up quickly with increase in layer thickness and finally approaches the frequency of bulk silicon of  $520\text{ cm}^{-1}$ . Figure 8.2(b) shows:

- (1) For a thickness of 1–5 unit cells, the PDOS appears as the first maximum at  $480\text{--}490\text{ cm}^{-1}$ , which closes the peak frequency of the amorphous silicon Raman spectrum. The second maximum frequency is not so obvious and appears almost in the high-frequency range.

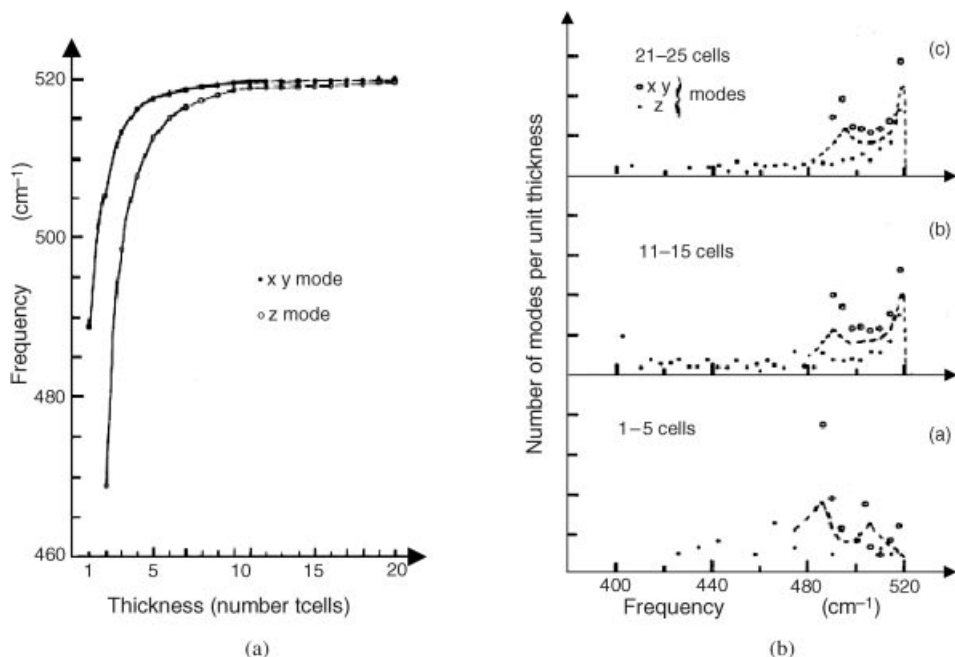


**Figure 8.2** (a) Dependence of calculated optical phonon frequency on slab thickness by slab model; (b) calculated frequency distribution of mode number (i.e., PDOS) in the unit cell for different thickness of slab by slab model, where • and ○ stands for x y and z modes, respectively. Reprinted from G. Kanallis, J. F. Morhange and M. Balkanski, Effect of dimensions on the vibrational frequencies of thin slabs of silicon, *Phys. Rev. B*, 21, 1543–1548 (1980) with permission of the American Physical Society

- (2) For a thickness of 11–15 unit cells, the second maximum mentioned above becomes more prominent than that of the first maximum.
- (3) For a thickness of 21–25 unit cells, the second maximum becomes much more prominent and the first maximum in the lower frequency range moves to a higher frequency range.

Figure 8.3 shows the Raman spectra of silicon samples by ion implantation and then laser annealing. Ion implantation converts crystalline Si into amorphous Si and laser annealing induces re-crystallization and decreasing amorphous composition, resulting in the change of Si crystallite size. Therefore, the spectra shown in Figure 8.3 could be used as an experimental result to compare with the calculated results of Figure 8.2. The comparison confirms that the calculated results are reliable and then two important findings for Raman spectral features of nanosilicon are obtained:

- (1) All the modes of the slab correspond to the specific phonon branch of bulk crystals, while their frequencies are lower than those of bulk crystal and the lowered quantity is related to layer thickness. The frequency of optical mode in thin slabs with a thickness of one unit cell is close to  $480 \text{ cm}^{-1}$  of amorphous Si and increases almost exponentially to approach the Raman frequency  $520 \text{ cm}^{-1}$  of bulk Si at point  $\Gamma$  (i.e., center) of the Brillouin zone.

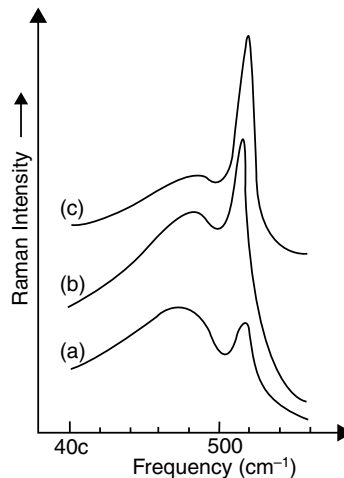


**Figure 8.3** Raman spectra of silicon treated with ion implantation and then laser annealing, where (a), (b), and (c) stand for the increase in re-crystalline grain size in turn. Reprinted from G. Kanallis, J. F. Morhange and M. Balkanski, Effect of dimensions on the vibrational frequencies of thin slabs of silicon, *Phys. Rev. B*, 21, 1543–1548 (1980) with permission of the American Physical Society

- (2) The varied features of bulk PDOS (i.e., the weight distribution function of frequency) with slab thickness shows that Raman spectral features of small size Si are similar to those of amorphous Si.

### 8.1.2 Ion Crystal Slab Model [8]

The earliest lattice dynamics calculation of the optical vibration mode in an ion crystal slab was accomplished by Fuchs and Kliewer [8]. Later, this became one of the foundational works of superlattice dynamics theory.

The scheme of the ion crystal slab model with finite thickness is shown in Figure 8.4. This slab is infinite in  $x$  and  $y$  directions and finite in the  $z$  direction of thickness  $L$ . In addition, the

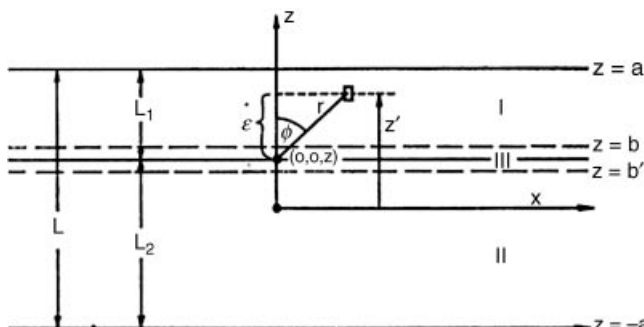


**Figure 8.4** Diagram of ion crystal slab model [8]. Reprinted from R. Fuchs and K. L. Kliewer, Optical Modes of Vibration in an Ionic Crystal Slab, *Phys. Rev.*, 140, A2076–2088 (1965) with permission of the American Physical Society

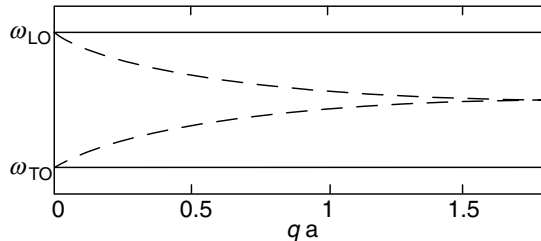


**Figure 8.5** The dispersion relation of vibration modes of ion crystal slab, where the solid line and dashed lines stand for TO and LO surface modes, respectively [6]. Reprinted from B. Jusserand and M. Cardona, *Raman Spectroscopy of Vibration in Superlattices*, in *Light Scattering in Solids*, Editors M. Cardona and G. Güntherodt, Springer-Verlag, (1989) with permission from Springer

wavelength  $\lambda$  must be larger than the distance between ions  $r_0$ , that is,  $\lambda = r_0$ , thus the ion position vector can be expressed as

$$\mathbf{x}(l,j) = \mathbf{x}(l) + \mathbf{x}(j) \quad (8.2a)$$

$$\mathbf{x}(l) = n_1 \mathbf{a}_1 + n_2 \mathbf{a}_2 + n_3 \mathbf{a}_3 \quad (8.2b)$$

where  $\mathbf{x}(l)$  is the position of the unit cell expressed by the basic vector  $\mathbf{a}_i (i=1, 2, 3)$  and  $n_i (i=1, 2, 3)$  is set as an integer, thus  $\mathbf{x}(j)$  is the position of the  $j$ th ion in the unit cell.

When the wavelength is larger than the lattice parameter (e.g., lattice constant  $a$ ) and the delay effect is ignored, Fuchs and Kliewer obtained a coupling integral equation based on lattice dynamics and electrodynamics, which contained both ion displacement and normal mode frequency [8]. The calculation showed that the normal mode has two kinds of vibrations with frequencies  $\omega_{TO}$  and  $\omega_{LO}$ , which are equivalent to frequencies of transverse optical (TO) and longitudinal optical (LO) modes at wave vector  $\mathbf{q}=0$  in infinite crystals, respectively. In addition, a new mode with no corresponding vibration mode in infinite crystals also appears, of which the frequency is between  $\omega_{TO}$  and  $\omega_{LO}$  and the amplitude decreases exponentially with the departure distance from two surfaces on both sides of the slab. Therefore this mode is called the “surface vibration mode.” The dispersion relation of these two kinds of modes is shown in Figure 8.5.

### 8.1.3 Lattice Dynamic Models of Semiconductor Superlattices [6,9]

Lattice dynamics of semiconductor superlattices developed based on solid theory. Therefore, similar to that in solid theory, it can also be classified as macroscopic and microscopic theory. For the former, we will focus on the superlattice elastic continuum model and continuous dielectric model-Huang equations, while for the latter, we will introduce the one-dimension linear chain model and the Huang-Zhu model.

#### 8.1.3.1 Elastic Continuum Model [6,10a]

The propagating behavior of acoustic waves in superlattices can be solved in terms of the elastic continuum medium equation setup by Rytov [11]. To describe simply but not lose universality, we only discuss the solution of the vibration along the superlattice growth direction (namely, the longitudinal wave), and mark the mediums of alternate

layers as A and B. Similar to Equation (7.67), the vibration in material A and B can be expressed as

$$\begin{aligned} u_A(z, t) &= u_A(z)e^{i\omega t} \\ u_B(z, t) &= u_B(z)e^{i\omega t} \end{aligned} \quad (8.3)$$

Based on motion Equation (7.64), we obtain the general solution

$$\begin{aligned} u_A(z) &= A_1 e^{i\alpha z} + A_2 e^{-i\alpha z} \\ u_B(z) &= B_1 e^{i\beta z} + B_2 e^{-i\beta z} \end{aligned} \quad (8.4)$$

where

$$\begin{aligned} \alpha &= \omega/v_{LA} \\ \beta &= \omega/v_{LB} \end{aligned} \quad (8.5)$$

where  $v_{LA}$  and  $v_{LB}$  are the longitudinal acoustic velocity of materials A and B, respectively. Thus we can express longitudinal wave displacement in superlattice A/B as

$$u(z) = \sum_m u_A(z-z_m) e^{i\alpha z_m} + \sum_n u_B(z-z_n) e^{i\alpha z_n} \quad (8.6)$$

where  $z_n$  and  $z_m$  are coordinates of the central point in the A and B layers and we set the central point of material A as the origin of the coordinates. In addition, at boundary  $z_i$ , the A and B layers should satisfy the displacement continuity condition:

$$C_{11,A} \frac{\partial u_A}{\partial z} \Big|_{z_i} = C_{11,B} \frac{\partial u_B}{\partial z} \Big|_{z_i} \quad (8.7)$$

and atomic displacement continuity condition:

$$u_A(z_i) = u_B(z_i) \quad (8.8)$$

Thus, we can obtain the dispersion relation (i.e., the relation between frequency  $\omega$  and wave vector  $q$ ) of longitudinal acoustic waves:

$$\cos(qd) = \cos\left(\frac{\omega d_A}{v_A}\right) \cos\left(\frac{\omega d_B}{v_B}\right) - \frac{1}{2} \left( \frac{\rho_B v_B}{\rho_A v_A} + \frac{\rho_A v_A}{\rho_B v_B} \right) \sin\left(\frac{\omega d_A}{v_A}\right) \sin\left(\frac{\omega d_B}{v_B}\right) \quad (8.9)$$

In the above equation,  $d_A$  and  $d_B$  are the thicknesses of layers A and B, respectively;  $d = d_A + d_B$  is the superlattice periods; and  $\rho_A$  and  $\rho_B$  are the densities of layers A and B, respectively. Thus Equation (8.9) can be expressed as

$$\cos(qd) = \cos\left[\omega\left(\frac{d_A}{v_A} + \frac{d_B}{v_B}\right)\right] - \frac{\varepsilon^2}{2} \sin\left(\omega \frac{d_A}{v_A}\right) \sin\left(\omega \frac{d_B}{v_B}\right) \quad (8.10)$$

In the above equation, the first and second items stand for the modulation for space and acoustic velocity, respectively, where

$$\varepsilon = \rho_B v_B - \rho_A v_A / (\rho_B v_B \rho_A v_A)^{1/2} \quad (8.11)$$

Since  $\varepsilon^2/2$  in III-V or II-VI chemical compounds are about  $10^{-2}$ , the second item in Equation (8.10) can be ignored. Thus we have

$$\cos(qd) = \cos\left[\omega\left(\frac{d_A}{v_A} + \frac{d_B}{v_B}\right)\right] \quad (8.12)$$

or

$$qd = \pm\omega\left(\frac{d_A}{v_A} + \frac{d_B}{v_B}\right) + 2m\pi \quad m = 0, \pm 1, \pm 2, \dots \quad (8.13)$$

The dispersion relation expressed above explores two important features of the acoustic phonon dispersion relation of superlattices:

- (1) Equation (8.13) shows the “folding” of bulk dispersion curves, which confirms theoretically the description related to dispersion curves in Section 8.1 and Figure 8.1.
- (2) If the second item of reflecting acoustic modulation in Equation (8.10) is not taken into account, the degeneracy of phonon energies at the center and boundary of the Brillouin zone occurs. The degeneracy energy  $\Omega_m$  is expressed as

$$\Omega_m = m\pi v/d \quad (8.14a)$$

If an acoustic velocity modulation item is added to Equation (8.13), the degeneracy mentioned above will split and the split value  $\Delta\Omega_m$  can be expressed as

$$\Delta\Omega_m \cong \pm\varepsilon\frac{v}{d}\sin\left[\frac{mv(1-\alpha)v_B - \alpha v_A}{2(1-\alpha)v_B - \alpha v_A}\right] \quad (8.14b)$$

where  $\alpha = \frac{v_B}{v_A + v_B}$  and the odd and even labels stand for the center or boundary of the Brillouin zone, respectively.

Figure 8.6 shows a calculated dispersion curve of a longitudinal acoustic phonon in a GaAs/AlAs superlattice by using Equations (8.10) and (8.12). The enlarged drawing in Figure 8.6 shows the split of  $A_1$  and  $B_2$  modes, taking into account acoustic modulation.

### 8.1.3.2 Dielectric Continuous Model

Similar to the application of the elastic continuum model for superlattices, the dielectric continuous model-Huang equation introduced in Section 7.3.2 can also be applied to superlattices. The specific application is introduced as follows:

First, we write down the dielectric constants of materials A and B in the A/B superlattice:

$$\begin{aligned} \varepsilon_A(\infty) &= \varepsilon_{\infty,A} \frac{\omega^2 - \omega_{LO,A}^2}{\omega^2 - \omega_{TO,A}^2} \\ \varepsilon_B(\infty) &= \varepsilon_{\infty,B} \frac{\omega^2 - \omega_{LO,B}^2}{\omega^2 - \omega_{TO,B}^2} \end{aligned} \quad (8.15)$$

where  $\varepsilon_{\infty,A}$  and  $\varepsilon_{\infty,B}$  are the high frequency dielectric constants of materials A and B.

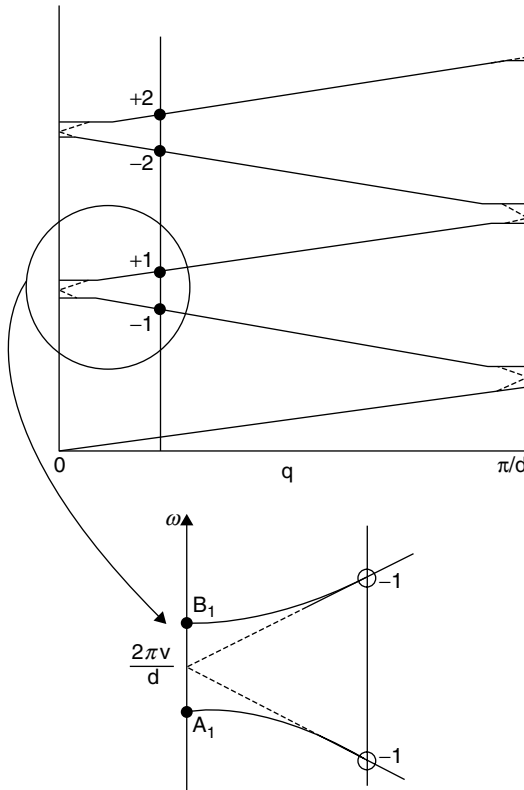


**Figure 8.6** Calculated dispersion curve of longitudinal acoustic phonon in GaAs/AlAs superlattice based on the elastic continuum medium model, where the solid and dashed lines represent the results that do and do not take into account acoustic modulation, respectively [10a]. Reprinted from C. Colvard, R. Merlin, M. V. Klein and A. C. Gossard, Observation of Folded Acoustic Phonons in a Semiconductor Superlattice, *Phys. Rev. Lett.*, 45, 298–301 (1980) with permission of the American Physical Society

Second, we introduce static electricity continuous conditions at the interface of the two materials:

$$\begin{aligned} E_{11,A}|_0 &= E_{11,B}|_0 \\ D_{z,A}|_0 &= D_{z,B}|_0 \end{aligned} \quad (8.16)$$

In the above equation, symbol “|<sub>0</sub>” indicates the values at the interface between the two materials.

Finally, by using the Huang equation and static electricity equation, the dispersion relation of optical phonon in superlattices can be obtained as

$$\cos(q_{\parallel}d) = \cosh(q_{\parallel}d_A)\cosh(q_{\parallel}d_B) + \frac{1}{2} \left[ \frac{\varepsilon_A}{\varepsilon_B} + \frac{\varepsilon_B}{\varepsilon_A} \right] \sinh(q_{\parallel}d_A)\sinh(q_{\parallel}d_B) \quad (8.17)$$

The modes, whose frequencies  $\omega_{LO,A}$ ,  $\omega_{TO,A}$ ,  $\omega_{LO,B}$ , and  $\omega_{TO,B}$  are equal to the frequencies of optical phonons of bulk materials A and B, are named as the confined optical modes or bulk-like modes, while the remaining mode is called a macroscopic interface mode. The features related to light scattering for these two kinds of modes are introduced below.

- Confined optical modes (bulk-like modes)

For A/B type superlattices, the vibration with  $\omega_{LO,A}$  in material B is

$$\begin{aligned}\varphi_B(z) &= 0 \\ E_B &= 0 \\ \mathbf{E}_{\parallel,A}|_0 &= 0 \\ \varphi_A(z)|_0 &= 0 \\ w_B &= 0\end{aligned}\tag{8.18}$$

The above equations indicate that the electrostatic potential  $\varphi_B(z)$ , electric field  $E_B$ , and optical reduced displacement  $w_B$  of bulk-like modes in layer B are all zero, indicating that the bulk-like modes of layer A are completely confined to layer A.

- Macroscopic interface mode

For the superlattices with different thickness ratio of two layers, such as  $(\text{GaAs})_{20}/(\text{AlAs})_{20}$  and  $(\text{GaAs})_{20}/(\text{AlAs})_{60}$ , (the subscript stands for the number of atoms in the monolayer), the dispersion relation calculated by using Equation (8.17) is shown in Figures 8.7(a)–(d). In Figure 8.7, symbols + (–) stand for the even or odd parity of the inversion of the electrostatic potential of macroscopic interface modes of  $(\text{GaAs})/(\text{AlAs})$  relative to the central plane of the GaAs well (AlAs barrier) with  $z$ , and the oblique line region is the region where the vibration mode can exist. From Figure 8.7 it can be seen that parities of  $d_{\text{GaAs}} \leq d_{\text{AlAs}}$  and  $d_{\text{GaAs}} > d_{\text{AlAs}}$  are opposite and there is no macroscopic interface mode in the central region for the superlattices with unequal GaAs and AlAs layer thicknesses.

In the case of  $\omega_{LO,B} > \omega_{TO,B}$ ,  $\omega_{LO,A} > \omega_{TO,A}$ , and  $\varepsilon_{\infty,A} \approx \varepsilon_{\infty,B}$ , the frequency of macroscopic interface modes at  $q_z = 0$  and  $q_{\parallel} \rightarrow 0$  is [9]

$$\begin{aligned}\omega_{+A}^2 &\approx \frac{1}{d} \left[ d_A \omega_{LO,A}^2 + d_B \omega_{TO,A}^2 \right] \\ \omega_{-A}^2 &\approx \frac{1}{d} \left[ d_B \omega_{LO,A}^2 + d_A \omega_{TO,A}^2 \right] \\ \omega_{+B}^2 &\approx \frac{1}{d} \left[ d_B \omega_{LO,B}^2 + d_A \omega_{TO,B}^2 \right] \\ \omega_{-B}^2 &\approx \frac{1}{d} \left[ d_A \omega_{LO,B}^2 + d_B \omega_{TO,B}^2 \right]\end{aligned}\tag{8.19}$$

#### 8.1.3.3 Linear Chain Model

- AB/BC type superlattices

In the upper part of Figure 8.8, the structural representation of a ternary AB/BC type superlattice constructed by atoms (ions) A, B, and C is shown. In this superlattice, the atomic

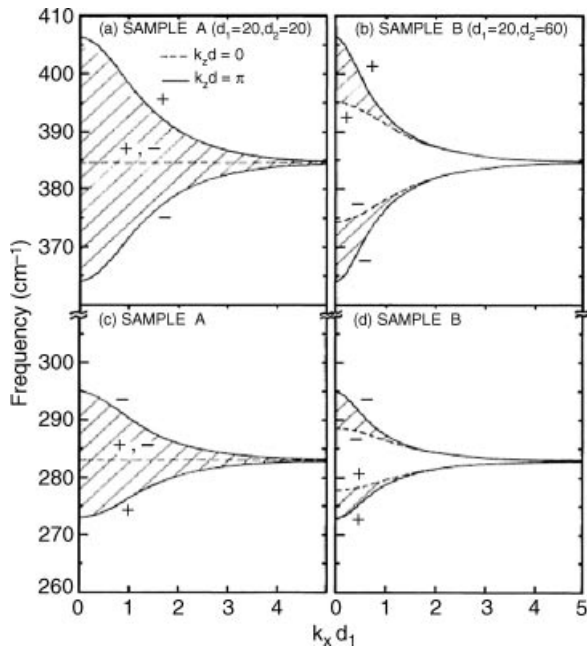


**Figure 8.7** The macroscopic interface mode dispersion relation of  $(\text{GaAs})_{d_A}/(\text{AlAs})_{d_B}$  superlattices: (a)  $d_A = d_B$  (b)  $3d_A = d_B$  [12]. Reprinted from A. K. Sood, J. Menendez, M. Cardona and K. Ploog, Interface Vibrational Modes in GaAs-AlAs Superlattices. *Phys. Rev. Lett.*, 54, 2115–2118 (1985) with permission of the American Physical Society

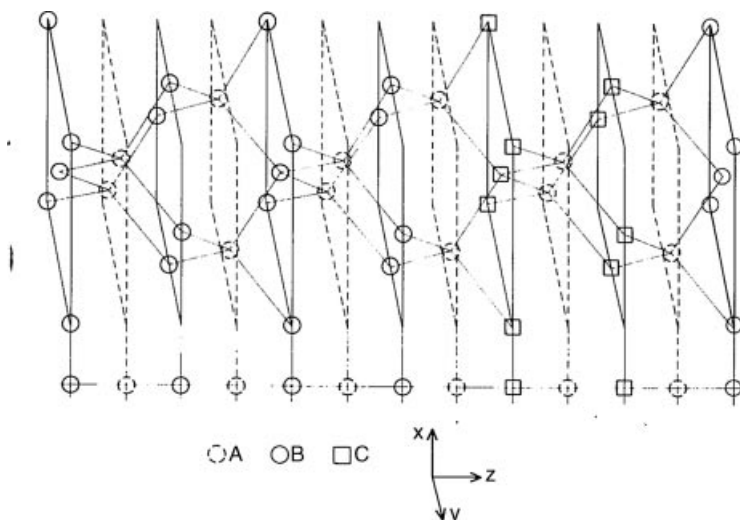


**Figure 8.8** Sketch of AB/CB superlattice structure (upper) and corresponding one-dimensional linear chain model (lower) [6]. Reprinted from C. Colvard, T. A. Gant, M. V. Klein, et al., Folded acoustic and quantized optic phonons in  $(\text{GaAl})\text{As}$  superlattices, *Phys. Rev. B*, 31, 2080–2091 (1985) with permission of the American Physical Society

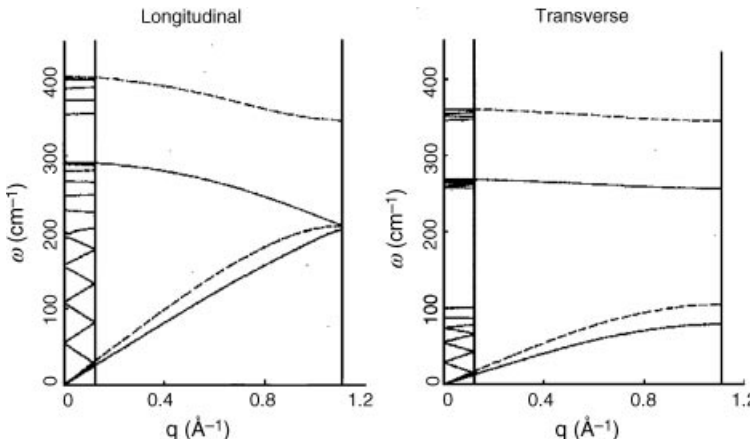


**Figure 8.9** Calculated longitudinal (a) and transversal (b) phonon dispersion curves of GaAs/AlAs superlattice by using linear chain model [10b]. Reprinted from C. Colvard, T. A. Gant, M. V. Klein, R. Merlin, R. Fischer, H. Morkoc and A. C. Gossard, Folded acoustic and quantized optic phonons in (GaAl)As superlattices, *Phys Rev B*, 31, 2080 (1985) with permission of the American Physical Society

movement in the  $x$ - $y$  plane vertical to growth direction  $z$  is whole and the vibration along the longitudinal direction  $z$  and transversal direction  $x$ - $y$  are not coupled. Therefore, when considering atomic motion along the  $z$  direction, the one-dimensional chain could be used to simulate it, as shown in the lower part of Figure 8.8. Therefore, the linear strain model discussed in Section 7.1.3 can be quoted directly.

Colvard *et al.* have used the linear chain model to calculate the dispersion relation of GaAs/AlAs AB/CB type superlattices, and the result is expressed as [13]

$$\cos(qd) = \cos(q_1 d_1) \cos(q_2 d_2) + \eta \sin(q_1 d_1) \sin(q_2 d_2) \quad (8.20)$$

where  $q_1$  and  $q_2$  are the wave vectors of the GaAs and AlAs layers, respectively, and  $\eta$  is expressed as

$$\eta = \frac{1 - \cos(q_1 d_1) \cos(q_2 d_2)}{\sin(q_1 d_1) \sin(q_2 d_2)} \quad (8.21)$$

Figure 8.9 shows calculated dispersion curves of longitudinal and transverse phonons of GaAs/AlAs superlattices by using the linear chain model. In the figure, the dashed and solid lines represent bulk and superlattice dispersion curves, respectively. The calculated results show again the folding (confinement) relation of phonon dispersion curves between bulk and superlattice.

- AB/CD type superlattices [14]

Figure 8.10(a) is a diagram of the structure and linear chain modeling of InAs/GaSb AB/CD-type superlattices. In the lower part of the figure, it can be seen that the interface bonds do not exist in layers. For example, the B-C(As-Ga) and A-D(In-Sb) bonds at the interface are different from the A-B(In-As) and C-D(Ga-Sb) bonds in the AB and CD layers, and

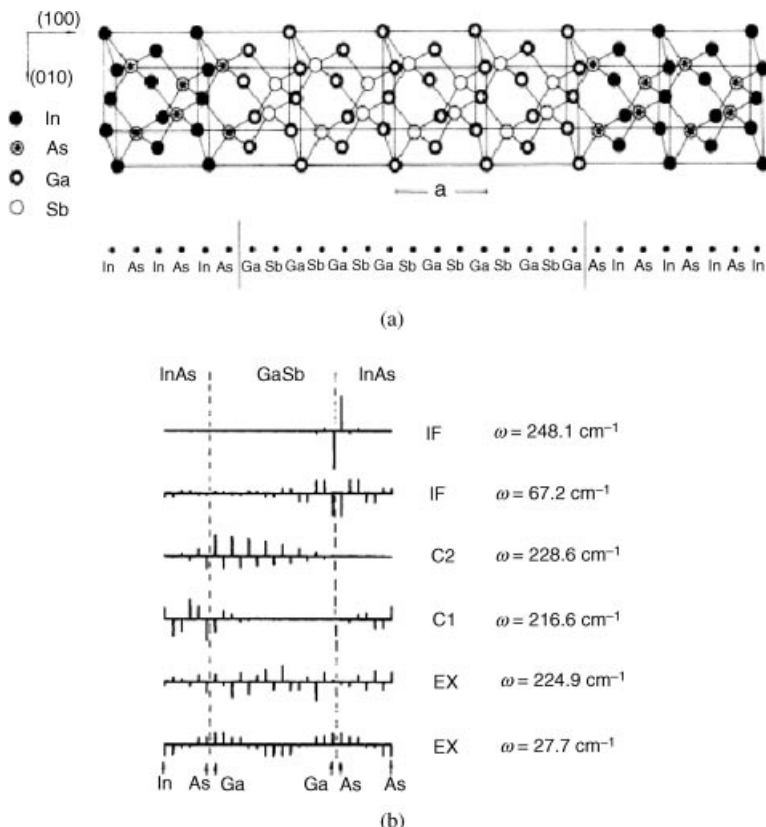


**Figure 8.10** Structure and linear chain modeling (a) and displacement mode and frequency of phonon modes (b) for InAs/GaAs AB/CD-type superlattices [14]. Reprinted from A. Fasolino, E. Molinary and J. C. Maan, Calculated superlattice and interface phonons of InAs/GaSb superlattices, *Phys. Rev. B*, 33, 8889–8891 (1986) with permission of the American Physical Society

different from those in AB/CB-type superlattices. For example, in GaAs/AlAs AB/CB-type superlattices, the Ga-As and Al-As bonds at the interface layer are the same as the Ga-As bond in AB (GaAs) layers and the As-Al bond in CB (AlAs) layers. Therefore, we expect that the AB/CD-type superlattices will show new vibration modes related to their interface bonds.

Fasolino used the linear strain model to calculate lattice dynamics of InAs/GaSb AB/CD-type superlattices, and the results are shown in Figure 8.10(b). In the figure, EX, C<sub>1</sub>/C<sub>2</sub>, and IF mark the expanded, confined, and interface modes, respectively. From the figure we can see that the displacement of two IF modes at the top are localized in the interfaces, which is a new type of mode appearing in the AB/CD-type superlattice and cannot appear in AB/CB type superlattices. The atoms of this interface mode only relate to atoms at the interface and are highly localized in the interface layer, thus it is called a “microscopic interface mode.”

### 8.1.3.4 Huang-Zhu Model [15a]

The Huang-Zhu model is the application and extension of the dipole lattice model of which the latter was published by Huang and Reys in 1951 [15b].

In the Huang-Zhu model, it is first assumed that there is a frequency difference between the intrinsic vibration mode frequencies  $\omega_{OA}$  and  $\omega_{OB}$  of the two layers of materials A and B:

$$\Delta\omega_0^2 = \omega_{OB}^2 - \omega_{OA}^2 \quad (8.22)$$

This frequency difference reflects that in a superlattice there exists a phonon potential well with a barrier height of  $\Delta\omega_0^2$ , which indicates that the materials A and B are constructed as superlattice structures. Then, with the eigen vibration mode  $|\mathbf{q}, j\rangle$  ( $j = 1, 2, 3$  stand for vibration modes LO, TO<sub>1</sub>, and TO<sub>2</sub>) of material A as the basis, the wave function of superlattice vibration (displacement) is expanded. Thus, for the  $i$ th atom in the superlattice with the period  $L = (n_A + n_B)a$  ( $a$  is bulk material lattice constant,  $n_A$  and  $n_B$  stand for the atom unit layer numbers of materials A and B), the vibration displacement wave function can be expressed as

$$\begin{aligned} \mathbf{u}(l; \mathbf{q}; i) &= \sum_{sj} a_{sj}(\mathbf{q}, i) |\mathbf{q}_s, j\rangle \\ &= \sum_{sj} a_{sj}(\mathbf{q}, i) \left[ N^{-3/2} e^{i\mathbf{q}_s \cdot \mathbf{r}(l)} \mathbf{e}^0(\mathbf{q}_s, i) \right] \end{aligned} \quad (8.23)$$

where  $\mathbf{q}$  is the phonon wave vector;  $N$  is the number of bulk primitive cells;  $\mathbf{e}^0(\mathbf{q}_s, i)$  is the unit polarization vector with wave vector  $\mathbf{q}_s$ , and  $i = 1, 2, 3, \dots, (n_A + n_B)$ .

Based on this wave function, by constituting the Hamiltonian of superlattices and solving the kinetic equation, we obtain the dispersion relation and displacement vector of the  $A_{n_A}/B_{n_A}$  superlattice.

The Huang-Zhu microscopic model is a great achievement. It explores many dynamic features and behaviors of superlattices, which were not known or understood originally, for example, of which some are related to Raman scattering directly:

- (1) The Huang-Zhu model verified that the macroscopic interface mode is a confined optical mode with order  $n = 1$ , which first explores the optical vibration nature of the macroscopic interface mode. Moreover, it verifies that the confined mode with  $n = 1$  does not exist and only the confined modes of  $n \geq 2$  can occur.
- (2) It is found that the bulk-like and macroscopic interface modes do and do not relate to propagation (wave vector) direction, respectively.
- (3) It is verified that the electrostatic Coulomb interaction plays an important role in the superlattice. For example, it makes the macroscopic interface mode rely on the wave vector  $\mathbf{q}$  (i.e., propagation) direction and the dipole forbidden polarization selection rule of Raman scattering in bulk materials is no longer effective in superlattices.
- (4) It reveals that the dielectric continuum model corresponds to the Huang-Zhu model without considering phonon dispersion. Figure 8.11 shows the dispersion relations of the macroscopic interface mode in an  $A_7/B_7$  superlattice calculated by the continuous dielectric model and the zero dispersive Huang-Zhu model.

### 8.1.3.5 Bond Charge Linear Chain Model [16]

Based on the bond charge model introduced in Section 7.2.5, Yip and Chang proposed a bond charge linear chain model, as shown in Figure 8.12. This model has two types: one

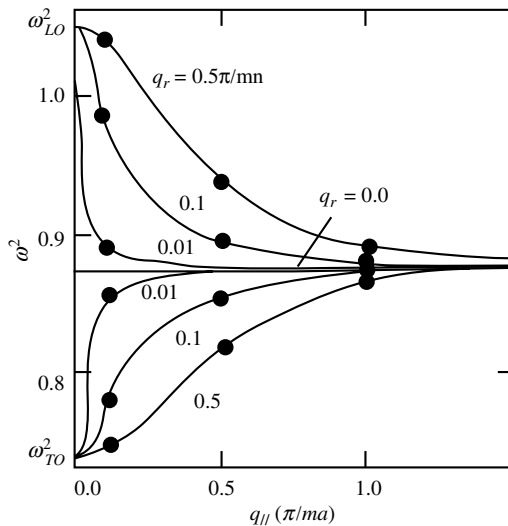


**Figure 8.11** Dispersion relations of the macroscopic interface mode in  $A_7/B_7$  superlattices calculated by the continuous dielectric model (solid lines) and the zero dispersive Huang-Zhu model (dots) [9]. Reprinted from K. Huang and B. Zhu, Dielectric continuum model and Frohlich interaction in superlattices, Phys. Rev. B, 38, 13377 (1988) with permission of the American Physical Society

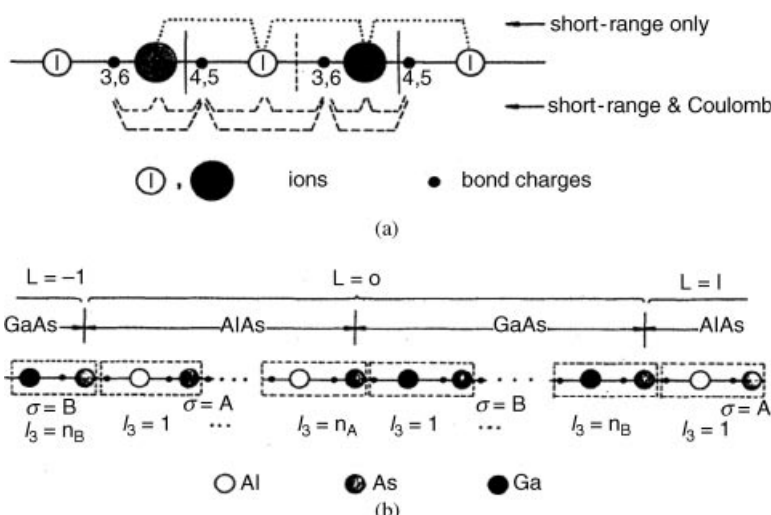


**Figure 8.12** Bond charge linear chain model (a) and bond charge linear chain model for an  $(n_A/n_B)$  GaAs/AlAs (001) superlattice (b), where  $L$  and  $l_3$  labels the superlattice unit cell and the principal layer, respectively [16]. Reprinted from S.-K. Yip and Y.-C. Chang, Theory of phonon dispersion relations in semiconductor superlattices, Phys. Rev. B, 30, 7037 (1984) with permission of the American Physical Society

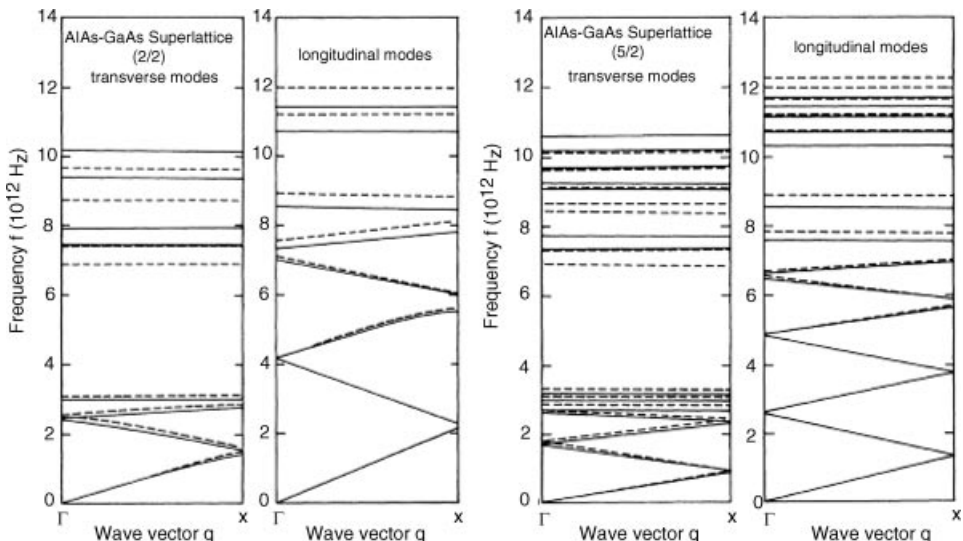


**Figure 8.13** Phonon dispersion curves along growth direction ( $q_{\parallel} = 0$ ) of  $(\text{GaAs})_2/(\text{AlAs})_2$  and  $(\text{GaAs})_5/(\text{AlAs})_2$  superlattices calculated by using the bond charge linear chain model, where dashed and solid lines are short-range interaction and Coulomb, respectively [16]. Reprinted from S.-K. Yip and Y.-C. Chang, Theory of phonon dispersion relations in semiconductor superlattices, *Phys. Rev. B*, 30, 7037 (1984) with permission of the American Physical Society

considers only short-range interactions between ions and the other considers both the short-range interaction and Coulomb interaction between ions. By using this model, they calculate phonon dispersion curves of  $(\text{GaAs})_2/(\text{AlAs})_2$ , and  $(\text{GaAs})_5/(\text{AlAs})_2$  superlattices, which are shown in Figure 8.13. The results indicate for optical phonons that there is more difference when taking the Coulomb force into account.

## 8.2 Nanostructure Materials

Section 6.2 described the finite size effect on energy, momentum, and symmetry and so on. Based on these effects, we will now introduce some qualitative expectations of Raman spectral features for nanostructure materials (NMs).

### 8.2.1 Common Raman Spectral Features of NMs

#### 8.2.1.1 Number of Raman Vibration Modes

First, because of the changing or reducing of symmetry, non-Raman active or degeneration modes in macroscopic crystal may develop into Raman active modes or restrict degeneration in NMs. Second, new phonon modes related to NM structures will be produced. For example, it has been mentioned that the NMs will occur crystallite interfaces in inner of NMs and possess huge specific surfaces, which do not occur within bulk materials, thus new

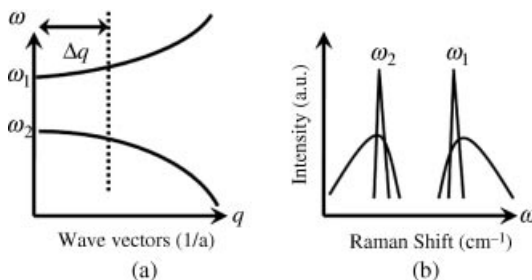


**Figure 8.14** Typical dispersion curves of bulk semiconductors (a) and expected Raman spectral features of NMs (b). Reprinted from S.-L. Zhang, *Raman Spectroscopy and Low-dimensional nanoscale Semiconductors*, Science Press, (2008)

vibration models related to the above new structures, such as the interface and surface modes, will be produced.

Therefore it can be expected for NMs that the number of vibration modes will usually increase.

#### 8.2.1.2 Frequency and Lineshape of Raman Spectra

Section 6.3.3 pointed out for NMs produced by self-organized growth method that crystal structures of nano- and bulk materials are basically the same, therefore the dispersion curve of NMs can borrow from that of bulk materials. However, Section 6.2 also mentioned that the finite size destroys the translation symmetry and momentum occurs diffusion with  $\Delta\mathbf{q} \approx \hbar/\Delta\mathbf{r}$  ( $\Delta\mathbf{r}$  is the size uncertainty), which leads to the relaxation of the wave vector selection rule of  $\mathbf{q} \approx 0$  in visible Raman scattering and then the phonons in the region of wave vector  $\Delta\mathbf{q}$  can join the Raman scattering process. In the following, we will discuss the expected Raman spectral features of NMs, qualitatively based on the dispersion curve of bulk materials.

Figure 8.14(a) shows a typical dispersion curve of semiconductors. Based on the wave vector selection rule of visible Raman scattering in bulk-materials,  $q \approx 0$ , Raman spectral can only originate from the phonons at  $q \approx 0$  and the Raman spectral peaks are the narrow spectral lines at  $\omega_1$  and  $\omega_2$ , as shown in Figure 8.14(b). However, all phonons of NMs in the momentum relaxation region  $\Delta q$  can participate in Raman scattering, thus their Raman spectral peaks become two spectral bands, as shown in Figure 8.14(b). These spectral bands show the features as:

- (1) When the slope rate of the bulk dispersion curve is not zero, the peak frequency will shift. The shift direction is up or down corresponding to the slope rate of  $> 0$  or  $< 0$ , respectively.
- (2) Since the phonons in the wave vector region  $\Delta q$  join Raman scattering, the spectral linewidth is broadened.
- (3) The non-zero slope rate of the bulk dispersion curve also leads to the appearance of asymmetrical spectral line shape. The “tail” of asymmetric bands appears in the high and low ends of the frequency corresponding to the slope rate of dispersion curves  $> 0$  and  $< 0$ , respectively.

### 8.2.1.3 Limitations of the Application of Bulk Phonon Dispersion for NMs

Before further discussion, we must point out that the application of bulk phonon dispersion for NMs is only approximate and thus the conditions of available application must be made clear. So we introduce an estimate, by using nano-Si as an example.

Hu and Zi performed a lattice dynamics calculation for nano-Si by using the cluster model and obtained the dependence of phonon dispersion curves and vibration density of states (VDOS) on sample sizes [13]. The results show that an Si nanocrystal larger than 2 nm still has a dispersion relation but with dispersive phonon energy. Figure 8.15(a) shows the calculated phonon dispersion relation of an Si nanocrystal containing 915 atoms (equal to size 3.27 nm). From the figure, we can see that the fashion of nano-Si dispersion relation is similar to the bulk one, but its phonon energy is dispersive and its momentum appears as discrete values.

The calculated nano-Si VDOS is shown in Figure 8.15(b). When comparing nano-Si to bulk-Si, it is found for nano-Si that the density of state in the low frequency range increases, while the peak of the density of state shifts down the high frequency range. The authors thought it to be the result of size confinement. Moreover, it also shows that there is only a small difference in the density of states between nano- and bulk-Si as a whole, which is similar to the calculated VDOS of amorphous and crystal Si described Section 7.4 and indicates that the reasons for the small difference in both cases are similar. The interactions between atoms involves only near neighbors in all calculations.

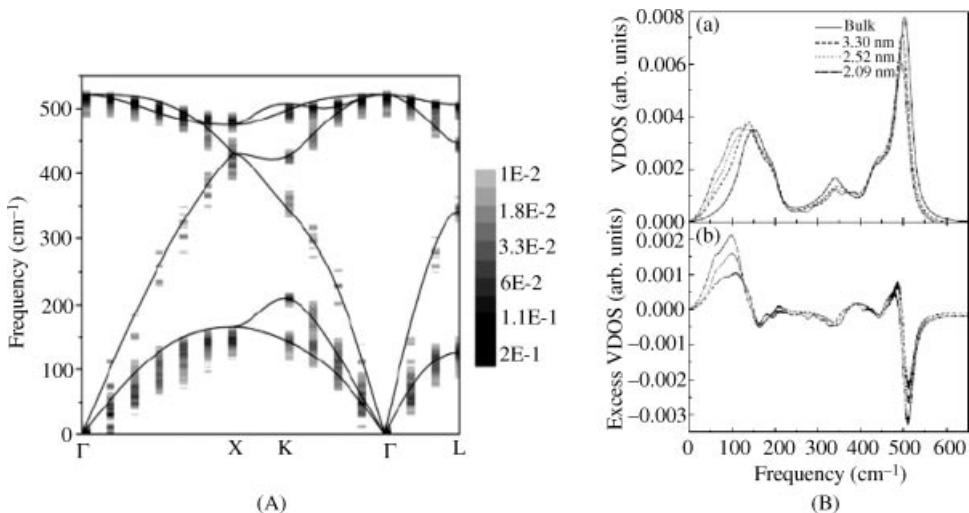


**Figure 8.15** Calculated dispersion relation of 3.27 nm nano-Si (A) and the differences between VDOS of nanocrystal with various sizes and bulk material. Reprinted from X. Hu and J. Zi, Reconstruction of phonon dispersion in Si nanocrystals, *J. Phys.: Condens. Matter* 14, L671–L677 (2002) with permission of the Institute of Physics. (B) where the solid line is bulk Si phonon dispersion curves [13]. Reprinted from X. Hu, et al., The vibrational density of states and specific heat of Si nanocrystals, *J. Phys.: Condens. Matter* 13, L835–L840 (2001) with permission of the Institute of Physics

### 8.2.2 Non-Polar Semiconductor Small Crystals [17]

To calculate the Raman spectra of non-polar semiconductor small crystals, Othman and Kawamura proposed a model as follows:

- (1) The coherence between normal vibration modes is limited in small crystals, that is, the system does not follow the breaking of the translation symmetry and wave vector selection rule.
- (2) The coupling between atomic vibration and light is achieved through the electron polarizability of materials.

Based on the dielectric fluctuation correlation theory of Raman scattering introduced in Section 7.5.3, the difference between small crystals and infinite crystals rests with the difference of the expanding regional scale of correlation functions. In infinite crystals, the space correlation function is

$$R(\mathbf{r},j) = \Lambda_j \exp(i\mathbf{q}_j \cdot \mathbf{r}) \quad (8.24)$$

where  $\Lambda_j$  is the space correlation amplitude of the  $j$ th mode and relies on the first-order differential coefficient of the optical dielectric constant relative to atomic displacement of  $j$ th normal mode. For small crystals, since the coherence of normal vibration modes is confined in small crystals, the space correlation function should be revised as

$$R(\mathbf{r},j) = C(\mathbf{r}) \Lambda_j \exp(i\mathbf{q}_j \cdot \mathbf{r}) \quad (8.25)$$

where  $C(\mathbf{r})$  is a modulation function that is introduced, based on the consideration of the limited coherence of normal vibration modes mentioned above. When  $\mathbf{r}$  reaches to the physical boundary of small crystals,  $C(\mathbf{r})$  goes down to zero monotonically.  $C(\mathbf{r})$  reflects the relaxation of the momentum conservation rule in the scattering process.

If it is assumed that the small crystals are spherical and there is no phonon damping in small crystals, the coherence of phonons must be perfect. Thus, its average correlation is proportional to the volume of the overlapping part of two spheres with diameter  $D$ , when they are separated by a distance between two sphere centers, that is, the volume of shaded area in Figure 8.16(a). Assumed that the small crystals are not the size-distributed ones, we have

$$C(\mathbf{r}) = \begin{cases} \frac{1}{2D^3}(2D^3 - 3D^2r + r^3) & r \leq D \\ 0 & r > D \end{cases} \quad (8.26)$$

Figure 8.16(b) shows the dependence of calculated Raman shift  $\Delta\omega$  and peak width  $\Gamma$  on particle sizes of small Si crystals based on the model. In the calculation, a further assumption was made that the space correlation  $\Lambda_j$  and Raman efficiency are constant in all normal modes, and phonon dispersion in the Brillouin zone is isotropic. In Figure 8.16(b), the solid and dot-dash lines stand for the results with the flat and no-size distribution, respectively. To confirm the reliability of the calculation, the experimental results and calculated results by using MC model are also shown in this figure [18]. The compared

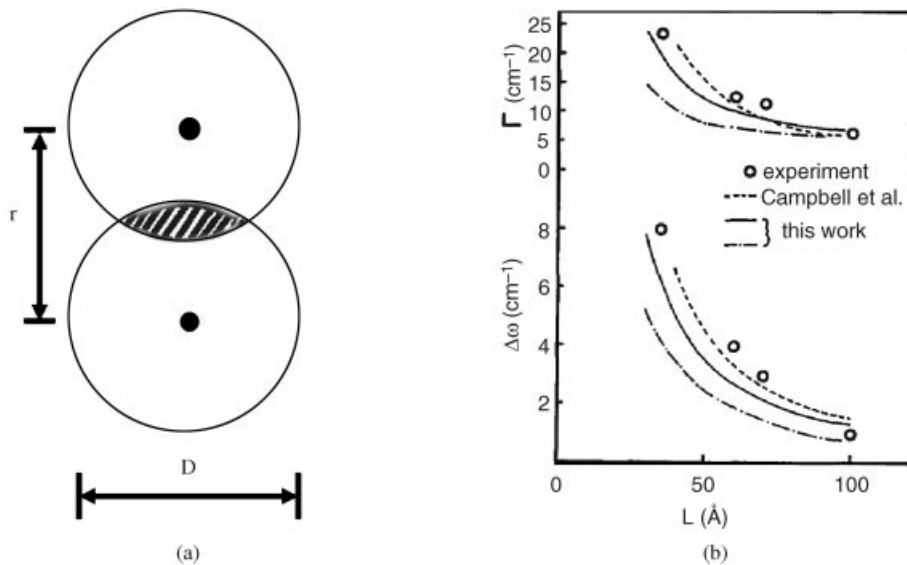


**Figure 8.16** Sketch of the correlation of non-polar semiconductor small crystals (a), and the dependence of calculated Raman shift  $\Delta\omega$  and peak width  $\Gamma$  on sizes of Si small crystals (b) [17]. Reprinted from N. Othman and K. Kawamura, Theoretical Investigation of Raman Scattering From Microcrystallites, Solid State Commun., 75, 711–718 (1990) with permission of Elsevier

results are good and thus we can draw important conclusions for Raman scattering of non-polar semiconductor small crystals:

- (1) The relaxation of momentum conservation plays an important role.
- (2) The phonon damping, surface mode, and crystal lattice expansion, have little influence on Raman scattering of small crystals, due to the calculation not taking them in account.

### 8.2.3 Polar Semiconductor Small Crystals [19]

Martin and Genzel discussed Raman spectra of powders composed of non-centrosymmetric polar semiconductor small crystalline particles using the Nyquist-theorem approach. They formulated a model to discuss Raman scattering, as described below:

- (1) There is an interaction between particles in the powder.
- (2) Each small crystal particle is completely described by a frequency-dependent complex dielectric function.
- (3) The crystal is assumed to be able to support a polarization wave, but the atomicity of small crystallites is in all other respects ignored.
- (4) The only mode with appreciable Raman activity is the one with uniform homogeneous polarization.
- (5) A power composed of interacting particles can support a plane wave –like s waves that have either transverse or longitudinal characters.
- (6) The powder layers composed of crystal particles behave as a homogeneous and isotropic medium optically.

Section 2.1.2, based on the classic theory of radiation, described the scattering light intensity  $E(\omega_1)$  radiated from an oscillating dipole induced by laser field  $E(\omega_i)$ , which can be expressed as

$$I(\omega_s) = \frac{V^2 n_s \omega_s^4}{2\pi c^3 R^2} \langle P^2(\omega_s) \rangle \quad (8.27)$$

where  $\langle P^2(\omega_s) \rangle$  is the mean square fluctuation of the  $\omega_s$  Fourier component of the dipole momentum  $P(\omega_s)$ , induced by laser field  $E(\omega_i)$  in unit volume;  $n_s$  is refractive index at frequency  $\omega_s$ ;  $c$  is light velocity;  $R$  is distance between measured point and dipole; and  $V$  is the volume of the sample. The fluctuations of macroscopic electric field  $\langle E^2(\omega_{ir}) \rangle$  and atomic displacement  $\langle Q^2(\omega_{ir}) \rangle$  will both lead to Raman scattering. A correlation item proportional to  $\langle EQ(\omega_{ir}) \rangle$  should also be included in  $\langle P^2(\omega_s) \rangle$ . Thus,

$$\langle P^2(\omega_s) \rangle = |E(\omega_i)|^2 [d_E^2 \langle E^2(\omega_{ir}) \rangle + 2d_E d_Q \langle EQ(\omega_{ir}) \rangle + d_Q^2 \langle Q^2(\omega_{ir}) \rangle] \quad (8.28)$$

Obviously, the contribution of electric field fluctuation relative to atomic displacement fluctuation to Raman scattering will change with the fraction of the total sample volume occupied by small crystal particles ( $f=0$  and 1 correspond to the sample behaving as a bulk material and the isolated particle, respectively) in different samples.

The results derived from the fluctuation spectra are summarized as:

(1) For transverse wave:

$$\langle E^2(\omega) \rangle = 0 \quad (8.29)$$

$$\langle Q^2(\omega) \rangle = \frac{\hbar}{2\pi\mu} [n(\omega) + 1] \frac{\omega\gamma}{(\omega_{ST}^2 - \omega^2)^2 + \omega^2\gamma^2} \quad (8.30)$$

$$\langle EQ(\omega) \rangle = 0 \quad (8.31)$$

(2) For longitudinal wave:

$$\langle E^2(\omega) \rangle = \frac{2fN\hbar}{\varepsilon_\infty^{av}} [n(\omega) + 1] \frac{(\omega_{SL}^2 - \omega_{ST}^2)\omega\gamma}{(\omega_{SL}^2 - \omega^2)^2 + \omega^2\gamma^2} \quad (8.32)$$

$$\langle Q^2(\omega) \rangle = \frac{\hbar}{2\pi\mu} [n(\omega) + 1] \frac{\omega\gamma}{(\omega_{SL}^2 - \omega^2)^2 + \omega^2\gamma^2} \quad (8.33)$$

$$\langle EQ(\omega) \rangle = - \left( \frac{fN}{\pi\mu\varepsilon_\infty^{av}} \right)^{1/2} \hbar [n(\omega) + 1] \frac{(\omega_{SL}^2 - \omega_{ST}^2)^{1/2}\omega\gamma}{(\omega_{SL}^2 - \omega^2)^2 + \omega^2\gamma^2} \quad (8.34)$$

where  $\omega_{SL}$  and  $\omega_{ST}$  are frequencies of longitudinal and transverse phonons, respectively, and are related to static and high frequency average dielectric constants  $\varepsilon_0^{av}$  and  $\varepsilon_\infty^{av}$ :

$$\omega_{SL}^2 / \omega_{ST}^2 = \varepsilon_0^{av} / \varepsilon_\infty^{av} \quad (8.35)$$

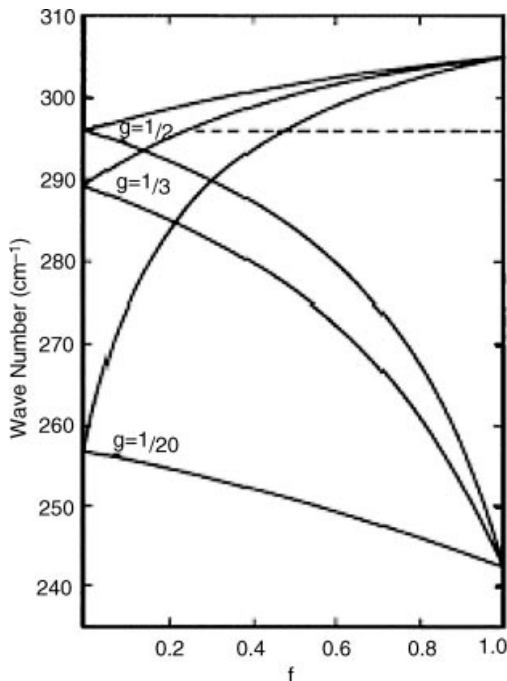


**Figure 8.17** Longitudinal phonon frequencies (upper) and transverse phonon frequencies (lower) of an MC powder as a function of the fraction  $f$  of the volume occupied by particles. The parameters are chosen to represent CdS for three different particle shape factors  $g$ . The dotted line indicates the observed frequency [19]. Reprinted from T. P. Martin and L. Genzel, Raman Scattering in Small Crystals, Phys. Rev. B, 8, 1630–1638 (1973) with permission of the American Physical Society

In the above equations, the transverse wave expression is equal to the longitudinal wave expression at  $f=0$ , especially  $\langle E^2 \rangle$  and  $\langle EQ \rangle$  are equal to 0 for two polarizations and  $\omega_{ST}$  and  $\omega_{SL}$  are also equal. The above results indicate that for an isolated sphere it is meaningless to distinguish whether its vibration mode is longitudinal or transverse. When  $f$  approaches 1,  $\omega_{ST}$  and  $\omega_{SL}$  in the fluctuation equation approach  $\omega_T$  and  $\omega_L$  of bulk materials. Obviously, the above result should be expected in physics.

The calculated dependence of longitudinal phonon frequencies  $\omega_{SL}$  (upper) and transverse phonon frequencies  $\omega_{ST}$  (lower) of CdS on fraction number  $f$  is shown in Figure 8.17. In the figure,  $g = 3$  corresponds to a sphere,  $g = 1/2$  is the appropriate shape factor along an axis perpendicular to an infinite needle, and  $g = 1/20$ , along an axis parallel to a long but finite needle. The fluctuation of longitudinal wave field is related to  $f$ , while the fluctuation of atomic displacement is not related to  $f$ , as shown by the dashed line in the figure.

The calculation results indicate that if a powder is composed of micro-crystal (MC) particles with the size being smaller than the incidence wavelength, they can be optically regarded as homogeneous materials with exact definitional longitudinal and transverse long

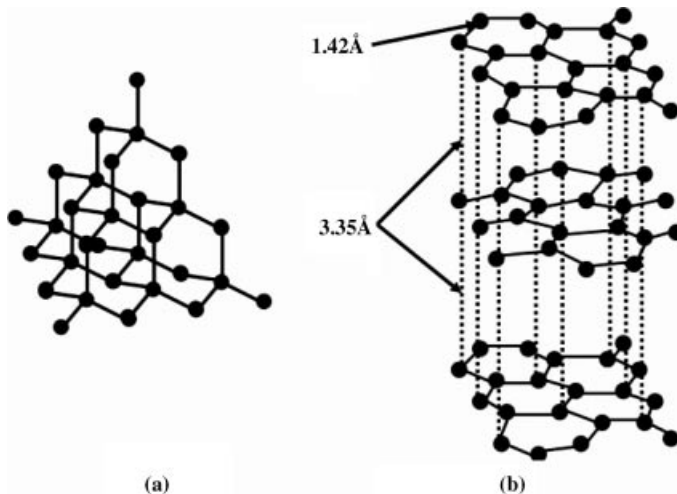


**Figure 8.18** Cubic structure of diamond (a) and hexagonal structure of graphite (b)

wave phonons. The phonon frequencies rely on the density of the powder sample and the shape of the particle, while the relative contribution to Raman scattering from electric field fluctuations and atomic displacements also relies on the density of powder samples.

#### 8.2.4 Carbon Nanostructures

The carbon family has many allotropes, such as diamond, graphite/graphene, and fullerenes. The carbon atoms are bonded together in a tetrahedral lattice arrangement in diamond, in sheets of hexagonal lattices in graphite/graphene, and in spherical, tubular, or ellipsoidal formations in fullerenes.

In crystallographic structures, the carbon family has two crystallographic structures: the cubic structure of diamond and the hexagonal structure of graphite, as shown in Figure 8.18. Graphite is a layered structure with weak coupling between layers, as shown in Figure 8.18 (b). In the graphite family, three-dimensional high purity crystal presents as highly oriented pyrolytical graphite (HOPG), while the monolayer graphite is called graphene.

Section 8.2.2 mentioned that lattice dynamics and Raman scattering of nanodiamond are based on its bulk dispersion curve, while the lattice dynamics of bulk diamond were introduced in Chapter 7. Therefore, in this section we will only discuss the Raman scattering theory of graphite nanostructures.

##### 8.2.4.1 Graphene – Monolayer Graphite

Graphene is a sheet of carbon atoms bound together by double electron bonds (called  $sp^2$  bonds) in a thin film only one atom thick. Graphene provides the structural basis of all other graphitic materials, from graphite itself to the fullerenes (carbon nanotubes, buckyballs, etc.). The discovery of graphene in 2004 [20] means that we now have access to materials of all dimensions, including zero-dimensional (quantum dots) and one-dimensional (nanowires, carbon nanotubes), and two-dimensional 2D (graphene).

Graphene as an atomic monolayer of graphite has two atoms per unit cell, thus having six phonon branches at the center of the Brillouin zone,  $q=0$ , that is

$$A_{2u} + B_{2g} + 2E_{1u} + 2E_{2g} \quad (8.36)$$

where the  $E_{1u}$  and  $E_{2g}$  modes represent the translational vibrations in the graphene plane;  $A_{2u}$  and  $B_{2g}$  modes are the ones with the movement direction of carbon atoms perpendicular to the graphene plane. The  $E_{2g}$  mode is a two fold degenerate optical vibration and the only mode with Raman activity. The vibration pattern and calculated phonon dispersion of graphene are shown in Figures 8.19(a) (b), and (c), respectively.

#### 8.2.4.2 Fullerenes – $C_{60}$ Buckyball

A fullerene is a molecule composed entirely of carbon, in the form of a hollow sphere, ellipsoid, or tube. Spherical fullerenes are also called buckyballs, of which the smallest member is  $C_{20}$  (unsaturated version of dodecahedrane) and the most common is  $C_{60}$ . Cylindrical tubes are called carbon nanotubes. Figure 8.20 shows the structures of buckminsterfullerene  $C_{60}$  and carbon nanotubes.

Buckyball- $C_{60}$ , as the first fullerene, was first prepared artificially in 1985 by Kroto *et al.*, [21], which can also be found in small quantities in soot. Since then, the structural variations on fullerenes have evolved well beyond the individual clusters themselves, such as  $C_{70}$ , “ball-and-chain” dimers, and fullerene rings and so on. However, we only pay attention to Buckyball- $C_{60}$  here.

The structure of a buckminster fullerene is a truncated icosahedron made of 20 hexagons and 12 pentagons, with a carbon atom at the vertices of each polygon and a bond along each polygon edge, as shown in Figure 8.20(a). The van der Waals diameter of a  $C_{60}$  molecule is about 1.01 nm. Each carbon atom in the structure is bonded covalently with three others.

$C_{60}$  is the most abundant fullerene. The most prominent feature of  $C_{60}$  is the  $I_h$  symmetry, the highest symmetry in molecules. This leads to it having only 46 vibration modes in 174 degrees of freedoms, which can be expressed as

$$2Ag + 3F_{1g} + 4F_{2g} + 6G_g + 8H_g + A_u + 4F_{1u} + 5F_{2u} + 6G_u + 7H_u. \quad (8.37)$$

of which  $8 H_g$  and  $2Ag$  modes of even state are Raman active and all the other odd state modes are silent or IR active.

For  $C_{60}$  in solid states, Yildirim and Harris studied the lattice dynamics by means of group theory and diagonalizing the dynamical matrix method [22]. In the representation to which the modes belong at  $q = 0$  (factor group  $T_h$ ), the translations are odd and odd under inversion, and the number of translation is given, respectively, by

$$A_u + E_u + 3T_u; \quad A_g + E_g + 3T_g \quad (8.38)$$

and the dispersion curve is shown in Figure 8.20(c).

#### 8.2.4.3 Single-Walled Carbon Nanotube – Curled into Cylindrical Graphene

The earliest carbon nanotubes, discovered in 1992, were the multi-walled carbon nanotubes [23], and single-walled carbon nanotubes (SWNTs) were first manufactured in

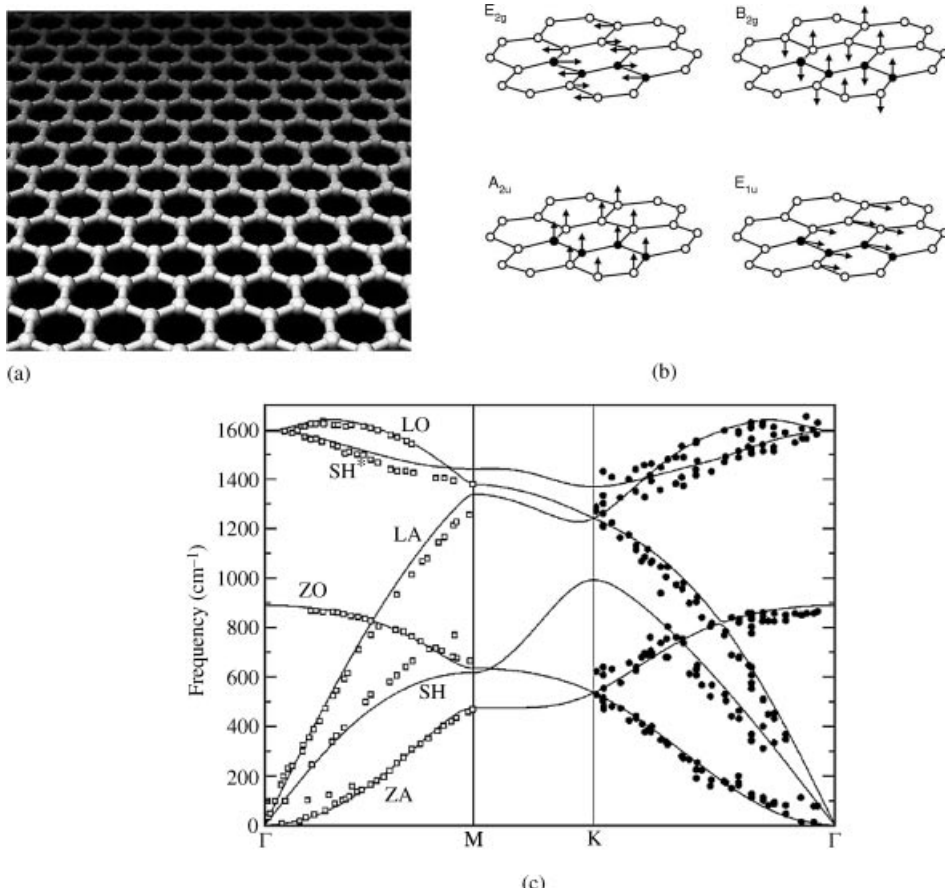


**Figure 8.19** Molecular structures (a), eigen vectors of phonons (b), and phonon dispersion relation (c) of a graphene sheet. In (c), the solid lines show the results of the ab initio force constant approach for the soft potential. The open squares represent the reflection electron-energy-loss spectroscopy (REELS) data and the solid circles correspond to the high-resolution electron-energy-loss spectroscopy (HREELS) data. The phonon branches are labeled as (mode/symmetry): out-of-plane transverse acoustic (ZA/A<sub>2u</sub>); in-plane transverse acoustic (SH/E<sub>1u</sub>); longitudinal acoustic (LA/E<sub>1u</sub>); out-of-plane transverse optic (ZO/B<sub>2g</sub>); in-plane transverse optic (SH\*/E<sub>2g</sub>); and longitudinal optic (LO/E<sub>2g</sub>) [29]. Reprinted from O. Dubay and G. Kresse, Accurate density functional calculations for the phonon dispersion relations of graphite layer and carbon nanotubes, *Phys Rev B*, 67, 035401 (2003) with permission of the American Physical Society

1993 [24, 25]. Since then, theoretical research on carbon nanotubes concentrated basically on SWNTs. In this section, we mainly discuss the work related to SWNTs.

- Structure of SWNT

A SWNT can be seen a graphene curled into a cylindrical shape, as shown in Figure 8.21. When we connect sites *O* and *A*, and *B* and *B'*, a carbon nanotube is constructed.

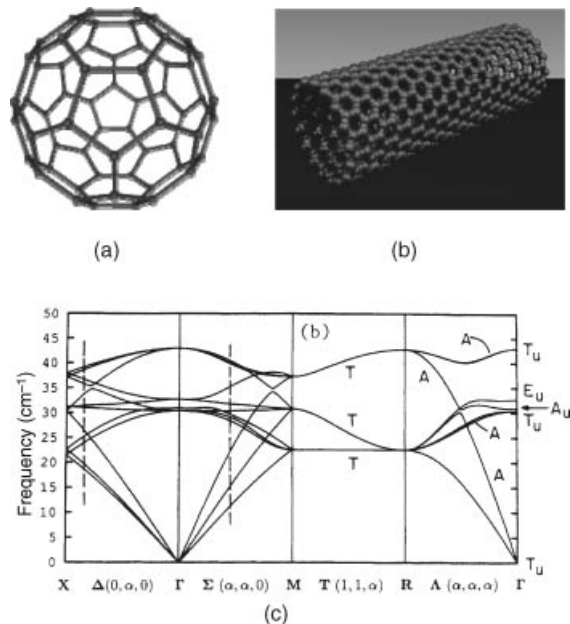


**Figure 8.20** The molecular structures of buckyball- $C_{60}$  (a) and carbon nanotube (b), as well as Harmonic phonon dispersion curves of solid  $C_{60}$  (c) [22]. Reprinted from T. Yildirim and A. B. Harris, Phys. Rev. B, 92, 7878 (1992) with permission of the American Physical Society

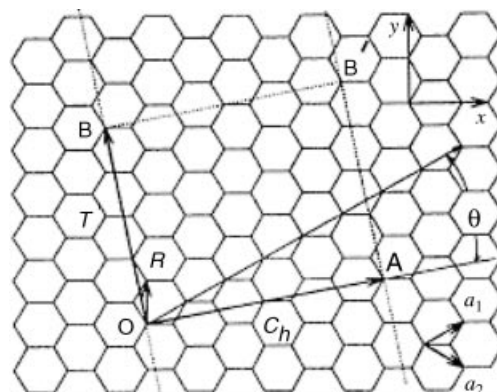


**Figure 8.21** Uncurled two-dimensional honeycomb lattice of graphene, corresponding to  $C_h = (4, 2)$ ,  $d = d_R = 2$ ,  $\mathbf{T} = (4, -5)$ ,  $N = 28$ ,  $R = (1, -1)$  [26]. Reprinted from R. Saito, G. Dresselhaus and M. S. Dresselhaus, *Physical Properties of Carbon Nanotubes*, (1998) with permission of the World Scientific Publishing Company

The rectangle  $OAB'B$  is defined as the unit cell of nanotubes.  $\vec{OA}$  and  $\vec{OB}$  define the chiral vector  $\mathbf{C}_h$  and the translation vector  $\mathbf{T}$  of nanotubes, respectively. The vector  $\mathbf{R}$  denotes a symmetric vector. Their definition expressions are expressed as

$$\begin{aligned}\mathbf{C}_h &= n\mathbf{a}_1 + m\mathbf{a}_2 \equiv (m, n) \\ (n, m \text{ are integral number}, 0 \leq |m| \leq n)\end{aligned}\quad (8.39)$$

$$\begin{aligned}\mathbf{T} &= t_1\mathbf{a}_1 + t_2\mathbf{a}_2 \equiv (t_1, t_2) \\ (t_1 \text{ and } t_2 \text{ and are integral number})\end{aligned}\quad (8.40)$$

$$\begin{aligned}\mathbf{R} &= p\mathbf{a}_1 + q\mathbf{a}_2 \equiv (p, q) \\ (p \text{ and } q \text{ are integral number})\end{aligned}\quad (8.41)$$

where  $\mathbf{a}_1$  and  $\mathbf{a}_2$  are unit vectors in real space in Figure 8.21 and have relations:

$$\begin{aligned}\mathbf{a}_1 \cdot \mathbf{a}_2 &= \mathbf{a}_2 \cdot \mathbf{a}_2 = a^2 \\ \mathbf{a}_1 \cdot \mathbf{a}_2 &= a^2/2\end{aligned}\quad (8.42)$$

where  $a = 0.144 \text{ nm} \times \sqrt{3} = 0.249 \text{ nm}$  is the lattice constant of the honeycomb-shaped structure.

The three vectors mentioned above can be used to express several physical parameters of carbon nanotubes, such as the diameter expressed as

$$d_t = L/\pi = |\mathbf{C}_h| = \sqrt{\mathbf{C}_h \cdot \mathbf{C}_h} = a\sqrt{n^2 + m^2 + nm} \quad (8.43)$$

The chiral angle  $\theta$  defined by the included angle between vectors  $\mathbf{C}_h$  and  $\mathbf{a}_1$  can be expressed as

$$\cos \theta = \frac{\mathbf{C}_h \cdot \mathbf{a}_1}{|\mathbf{C}_h||\mathbf{a}_1|} = \frac{2n+m}{2\sqrt{n^2+m^2+nm}} \quad (8.44)$$

As shown in Figure 8.22, the Brillouin zone of a carbon nanotube is represented by the line segment  $WW'$ , which is parallel to  $\mathbf{K}_2$ , where  $\mathbf{K}_1$  and  $\mathbf{K}_2$  are reciprocal vectors along the

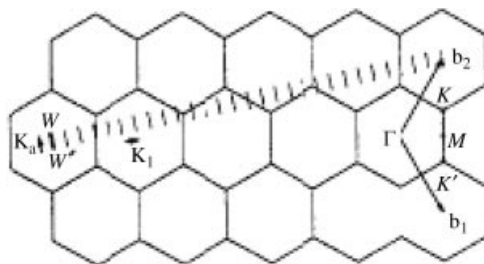


**Figure 8.22** The Brillouin zone of a carbon nanotube [27]. Reprinted from R. Saito, G. Dresselhaus and M. S. Dresselhaus, Physical Properties of Carbon Nanotubes, (1998) with permission of the World Scientific Publishing Company

nanotube axial direction (corresponding to  $\mathbf{C}_h$ ) and circle direction (corresponding to  $\mathbf{T}$ ), and can be expressed as

$$\mathbf{K}_1 = \frac{1}{N}(-t_2\mathbf{b}_1 + t_1\mathbf{b}_2) \quad (8.45)$$

$$\mathbf{K}_2 = \frac{1}{N}(m\mathbf{b}_1 - n\mathbf{b}_2) \quad (8.46)$$

where  $\mathbf{b}_1$  and  $\mathbf{b}_2$  are two-dimensional reciprocal vectors of graphite, respectively:

$$\begin{aligned}\mathbf{b}_1 &= \left( \frac{2\pi}{\sqrt{3}a}, \frac{2\pi}{a} \right) \\ \mathbf{b}_2 &= \left( \frac{2\pi}{\sqrt{3}a}, -\frac{2\pi}{a} \right)\end{aligned}\quad (8.47)$$

Carbon nanotubes can be classified into the chiral and non-chiral types, based on their symmetrical properties. The non-chiral type can be further classified into two types, the armchair and the zigzag types. Their specific structures are shown in Figure 8.23.

For a SWNT, the tube diameter is usually less than 2 nm, the tube wall is the monolayer graphite-graphene, and the ratio of diameter to length can be more than  $10^{-5}$ . Therefore, the influence of the “hat” shape structure at two ends of the nanotube can be ignored and so the carbon nanotube can be regarded as a typical one-dimensional tube-shaped structure with axial symmetry.

- Phonon dispersion relations of SWNTs [26]

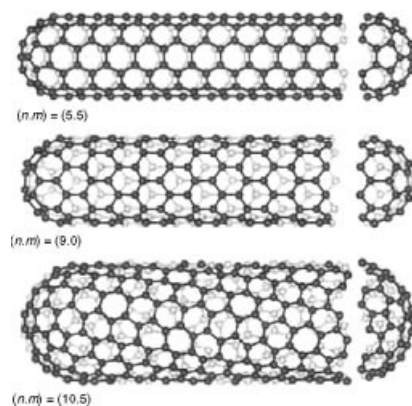


**Figure 8.23** Three types of carbon nanotube structure: armchair (upper), zigzag (middle), and chiral (lower) [27]. Reprinted from R. Saito, G. Dresselhaus and M. S. Dresselhaus, *Physical Properties of Carbon Nanotubes*, (1998) with permission of the World Scientific Publishing Company

The phonon dispersion relation of carbon nanotubes can be obtained in various ways, as follows:

### 1. Zone folding method

The structure in the radial direction of carbon nanotubes and the structure in the growth direction of superlattices are similar in symmetry. For example, carbon nanotubes also appear with new periodicity not existing in graphite, which is similar to that mentioned in Section 8.1 and results in the folding of the energy band. Therefore, at a first approximation, the dispersion relation of SWNTs  $\omega_{1D}^{mu}(k)$  can also be obtained by using the folding of the dispersion curve  $\omega_{2D}^m$  of two-dimensional graphite and the folding relation is similar to Equation (8.13):

$$\omega_{1D}^{mu}(k) = \omega_{2D}^m \left( k \frac{\mathbf{K}_2}{|\mathbf{K}_2|} + \mu \mathbf{K}_1 \right) \quad (8.48)$$

$$m = 1, \dots, 6; \quad \mu = 0, \dots, N-1; \quad -\pi/T < k \leq \pi/T$$

In the vibrations of graphene, there is a TA phonon mode at  $\mathbf{q} = 0$ , perpendicular to the graphite sheet with zero energy, which is as the labeled A<sub>2u</sub> branch in Figure 8.19(b) and shown in Figure 8.24(a). When the graphite sheet curls into a carbon nanotube, the above TA phonon mode in the graphite sheet becomes a radial breathing (RB) phonon with non-zero energy at  $\mathbf{q} = 0$ , as shown in Figure 8.24(b). However, in the dispersion relation, by using the folding method, the RM mode cannot exist. Therefore, the precise dispersion relation of SWNT needs to be based on complete lattice dynamics calculations.

### 2. Lattice dynamics calculation [26]

Below we describe the force constant method introduced in Section 7.2.2, to calculate phonon dispersion relations of SWNTs.

In general, if we label the coordinates of the  $i$ th carbon atom as  $u_i(x_i, y_i, z_i)$ , then the equations of motion for the displacement of the  $i$ th coordinates,  $u_i(x_i, y_i, z_i)$  for  $N$  atoms in the unit cell, are given by

$$M_i \ddot{\mathbf{u}}_i = \sum_j K^{(i,j)} (\mathbf{u}_j - \mathbf{u}_i) \quad (i = 1, \dots, N) \quad (8.49)$$

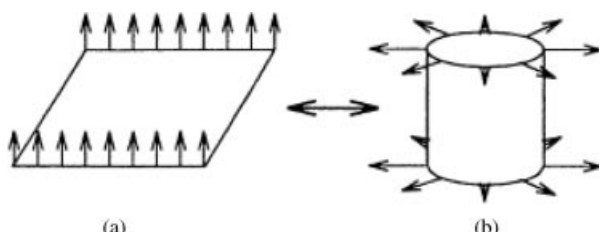


**Figure 8.24** Diagrams of the change from the vibration perpendicular to graphite sheet surface (a) to radial vibration of carbon nanotube. Reprinted from S.-L. Zhang, *Raman Spectroscopy and Low-dimensional nanoscale Semiconductors*, Science Press, (2008)

where  $M_i$  is the mass of  $i$ th atom and  $K^{(i,j)}$  stands for the  $3 \times 3$  force constant tensor between  $i$ th and  $j$ th atoms. The summation for  $j$  usually takes the  $i$ th atom with nearest neighbor or second-nearest neighbor, according to the approximation requirement. The normal mode displacement of the above equation can be expressed as

$$\mathbf{u}_i = \frac{1}{\sqrt{N_\Omega}} \sum_{\mathbf{q}'} e^{i(\mathbf{q}' \cdot \mathbf{R}_i - \omega t)} \mathbf{u}_{\mathbf{k}'}^{(i)} \quad (8.50)$$

Thus, motion Equation (8.49) changes to

$$\left( \sum_j K^{(i,j)} - M_i \omega^2 \right) \sum_{\mathbf{k}_1} e^{-i(\mathbf{q}' \cdot \mathbf{R}_i - \omega t)} \mathbf{u}_{\mathbf{k}'}^{(i)} = \sum_j K^{(i,j)} \sum_{\mathbf{k}'} e^{i(\mathbf{q}' \cdot \mathbf{R}_i - \omega t)} U_{\mathbf{k}'}^{(j)} \quad (8.51)$$

and it can be expressed further as

$$\left( \sum_j K^{(i,j)} - M_i \omega^2(\mathbf{k}) I \right) U_{\mathbf{k}}^{(i)} - \sum_j K^{(i,j)} e^{i\mathbf{k} \cdot \Delta\mathbf{R}_{ij}} U_{\mathbf{k}'}^{(j)} = 0 \quad (8.52)$$

$$i = 1, \dots, N$$

where  $I$  is the  $3 \times 3$  unit matrix,  $\Delta\mathbf{R}_{ij} = \mathbf{R}_i - \mathbf{R}_j$ , and according to solution conditions of Equation (8.52), we obtain the dynamic matrix:

$$D^{(i,j)}(\mathbf{k}) = \left( \sum_{j''} K^{(i,j'')} - M_i \omega^2(\mathbf{k}) I \right) D_{ij} - \sum_{j'} K^{(i,j')} e^{i\mathbf{k} \cdot \Delta\mathbf{R}_{ij'}} \quad (8.53)$$

The phonon dispersion curves and the respective PDOS for a (10,10) SWNT obtained by the folding procedure and lattice dynamics calculation are illustrated in Figure 8.25.

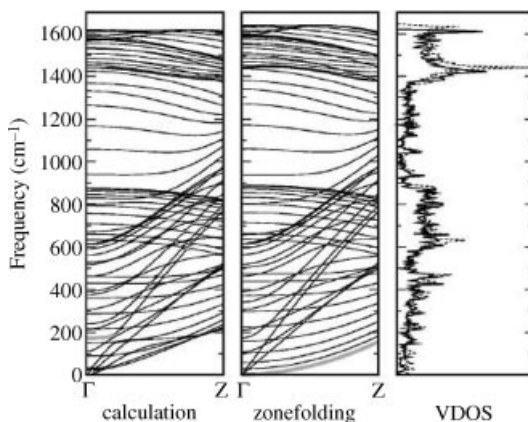


**Figure 8.25** Phonon dispersion relations and VDOS for the armchair (10,10) SWNT s. Gray thick lines show branches of the RBM. The VDOS panels show the VDOS for zone-folding (dashed line) and ab initio (solid line) calculations [29]. Reprinted from O. Dubay and G. Kresse, Accurate density functional calculations for the phonon dispersion relations of graphite layer and carbon nanotubes, *Phys Rev B*, 67, 035401 (2003) with permission of the American Physical Society

The large amount of sharp structure in the PDOS in Figure 8.25 reflects the many phonon branches and the one-dimensional nature of SWNTs relative to two-dimensional graphite arising from the quantum confinement of the phonon states into van Hove singularities. The two-dimensional PDOS shown in Figure 8.25 can be recovered by summing the one-dimensional PDOS for many SWNTs [27, 28]. The above allows the unique one-dimensional effects to be studied in detail and is more interesting in SWNTs, since a one-dimensional system blends the singular energy levels of molecules (delta functions in the PDOS) with the quasi-continuous behavior of solid-state systems along the nanotube axis.

Besides the van Hove singularities in the PDOS, carbon nanotubes exhibit other unusual aspects regarding their phonon dispersion relations, such as having four acoustic branches. In addition to the longitudinal acoustic and transverse acoustic modes, there are two acoustic twist modes for rigid rotation around the tube axis, which are important for heat transport and charge carrier scattering. Also important for coupling electrons to the lattice are the low-lying optical modes at the center of the Brillouin zone  $q=0$ . These modes include one with  $E_2$  symmetry expected at  $\sim 17\text{ cm}^{-1}$  (the squash mode), one with  $E_1$  symmetry, expected at  $\sim 118\text{ cm}^{-1}$ , and one with  $A$  symmetry (the radial breathing mode (RBM)) expected at  $\sim 165\text{ cm}^{-1}$  for a (10,10) SWNT. Of these three low-energy phonon modes, it is only the RBM with  $A$  symmetry, where all the carbon atoms are vibrating in phase in the radial direction.

In SWNTs, the G band is split into many features around  $1580\text{ cm}^{-1}$ , and the lower frequency RBM is usually the strongest features in SWNT Raman spectra. The RBM is a unique phonon mode, appearing only in carbon nanotubes and its observation in the Raman spectrum provides direct evidence that a sample contains SWNTs. The RBM frequency is inversely proportional to the tube diameter  $dt$  and is expressed as  $\omega_{\text{RBM}} = C/dt\text{ (cm}^{-1}\text{)}$ , where  $C$  is related to the effect of the substrate and tube–tube interactions. For example,  $C = 248\text{ cm}^{-1}\text{ nm}$  for isolated SWNTs on an  $\text{SiO}_2$  substrate [30].

### 8.2.5 Quantumwell Wires, Quantum Wires, and Nanowires – The Shape Effect of Samples

Quantum well wires, quantum wires, and nanowires are the nanostructures with asymmetric shapes. Except for the size confinement effect, there exists a shape effect in nanostructures, although it does not appear in bulk materials. It is usually considered that the size confinement effect exists in both polar and non-polar semiconductors and the shape effect occurs only in polar semiconductors. The reason for the latter is that the shapes do and do not have an influence on the long range Coulomb interaction and the deformation potential localized in the region of neighboring atoms, respectively. Therefore, the shape effect can only occur in polar nano-semiconductors with Coulomb interactions.

#### 8.2.5.1 Confined Optical Phonon Modes

Comas *et al.* [31] used the dielectric continuum model to analyze and calculate the shape effect on Rama scattering of GaAs quantum wire buried in AlAs; in that calculation the radius of the circular section is marked as  $r_0$  and the direction of axial is defined as  $z$ . The calculation is performed for the phonon with  $q_z = 0$  and propagating along the axial direction, and when  $r < r_0$  and  $n = 1, 2, 3$ , the transcendental equation of phonon mode

for GaAs quantum wire is expressed as

$$\begin{aligned} & \frac{(\varepsilon_{\infty}^{(1)} + \varepsilon_{\infty}^{(2)})}{2} [f_{n-1}(x)f_{n+1}(y) + f_{n-1}(y)f_{n+1}(x)] + \left(\frac{\beta_{LO}}{\beta_{TO}}\right)^2 \\ & \times \frac{\varepsilon_{\infty}^{(1)}}{y^2} R^2 \left[ f_{n-1}(x) + \frac{n}{x} f_n(x) \left( \frac{\varepsilon_{\infty}^{(2)}}{\varepsilon_{\infty}^{(1)}} - 1 \right) \right] f_{n+1}(y) = 0 \end{aligned} \quad (8.54)$$

where  $\varepsilon_{\infty}^{(i)}$  is the high frequency dielectric constant of material  $i$ ;  $f_n$  is Bessel function of first kind;  $\beta_{LO}$  and  $\beta_{TO}$  stand for the electric field of  $LO$  and  $TO$  modes;  $x = qr$ ;  $y = Qr_0$ ; and  $R^2 = \left(\frac{r_0}{\beta_{LO}}\right)^2 (\omega_{LO}^2 - \omega_{TO}^2)$  with the constriction condition

$$R^2 = x^2 - y^2 (\beta_{TO}/\beta_{LO})^2 \quad (8.55)$$

The calculated relation between the energy of  $LO$  and  $TO$  modes,  $\hbar\omega$ , and the diameter of quantum wire,  $r_0$ , are shown in Figure 8.26.

Figure 8.26 shows that when  $n = 0$ , there are pure longitudinal and transverse modes with complete decoupling. However, when  $n = 2$  and  $n = 3$ , the coupling of longitudinal and transverse modes occurs and the  $LO$  mode approaches the  $TO$  mode.

Mahan *et al.* [32] studied the long-range dipolar interactions in a cubic polar crystalline semiconductor nanowire. Based on considering the influence of the local field induced by dipole–dipole interactions, they calculated the correlation between the optical phonons and the aspect ratio of the wire ( $L/D$ ) of samples. The calculated bulk longitudinal and transverse phonon frequency  $\omega_{LO}$  and  $\omega_{TO}$  are expressed as [33]

$$\omega_{LO}^2 = \omega_0^2 + \omega_P^2 \frac{2(\varepsilon_z(\infty) + 2)}{9\varepsilon_z(\infty)} \quad (8.56)$$

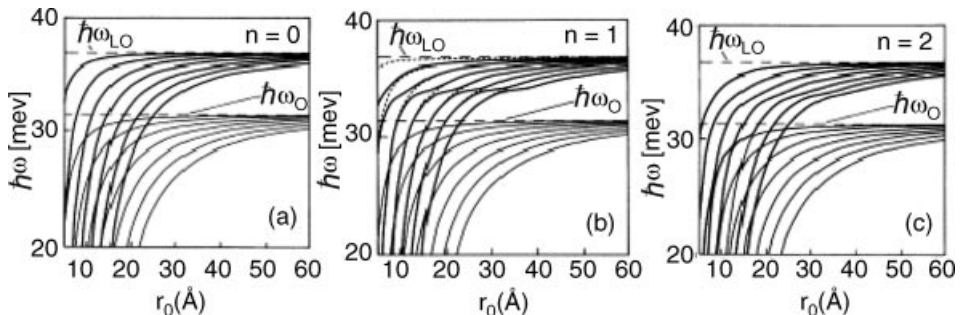


**Figure 8.26** The phonon energies of the first seven modes in an infinite cylinder with circular cross section as function of  $r_0$  for frequency region below and above  $\omega_0$ . The broken lines correspond to bulk  $LO$  and  $TO$  phonon energies. By comparison, the  $LO$  phonon decoupled modes are presented by dot-dashed lines in the case  $n = 1$  [31]. Reprinted from F. Comas, C. T. Giner and A. Cantarero, Optical phonons and electron-phonon interaction in quantum wires, *Phys. Rev. B*, 47, 7602–7605 (1993) with permission of the American Physical Society

$$\omega_{TO}^2 = \omega_0^2 - \omega_p^2 \frac{2(\varepsilon_z(\infty) + 2)}{9} \quad (8.57)$$

where

$$\varepsilon_z(\infty) = 1 + \frac{4\pi\alpha/V_0}{1 - 4\pi\alpha/3V_0} \quad (8.58)$$

is the high frequency (real) Lorenz–Lorentz dielectric constant;  $V_0$  and  $\alpha$  are the volume and polarizability of unit cell, respectively; and

$$\omega_p^2 = \frac{4\pi e^{*2}}{\mu V_0} \quad (8.59)$$

is the ion plasma frequency, where  $e^*$  is the Szigeti charge and  $\mu$  is the reduced mass of the ion pair. For optical phonons in nanowires,  $\varepsilon_{zz}(\omega)$  of electric constant in the  $zz$  direction is the same as that of bulk at pole and 0 points:

$$\begin{aligned} \omega_{TZ} &= \omega_{TO} \\ \omega_{LZ} &= \omega_{LO} \end{aligned} \quad (8.60)$$

In the  $xx$  direction, there is

$$\omega_{Tx}^2 = \omega_0^2 + \omega_p^2 \frac{(\varepsilon_x(\infty) + 2)}{9(\varepsilon_x(\infty) + 1)} \quad (8.61)$$

$$\omega_{Lx}^2 = \omega_0^2 + \omega_p^2 \frac{7(\varepsilon_x(\infty) + 2)}{9(\varepsilon_x(\infty) - 1)} \quad (8.62)$$

where

$$\varepsilon_x(\infty) = \frac{3\varepsilon_z(\infty)^z - 1}{\varepsilon_z(\infty) + 1} \quad (8.63)$$

For  $\omega_{Ty}$  and  $\omega_{Ly}$  in the  $yy$  direction, we only need to change the subscript  $x$  of the above equations to  $y$ .

The calculations indicate that the two LO and two TO phonon frequencies in the nanowire are sensitive to the aspect ratio of the wire. The two optic phonon modes in bulk cubic polar semiconductors split due to the long range dipolar interactions and the shape (wire geometry) of the sample. The  $\omega_{TZ}$ ,  $\omega_{LZ}$ ,  $\omega_{Tx}$ , and  $\omega_{Lx}$  of some representative polar semiconductors are listed in Table 8.1. From the table it can be seen that the shape effect makes the phonon split at  $q = 0$ .

### 8.2.5.2 Interface Phonon Modes

Based on the Huang-Zhu model, Zhu [37] calculated the interface mode of one-dimensional quantum well wires. The calculated results indicate that it is similar to two-dimensional features in many respects, for instance, the optical phonon modes can also be classified as confined and interface modes, and the interface mode also has hybrid features of bulk longitudinal and transverse modes.

Zhang and Xie [38] used the dielectric continuum model to calculate the interface phonon of quantum well wire consisting of a multi-layer hollow cylinder. Figure 8.27 draws

**Table 8.1** The bulk LO and TO Raman mode frequencies of cubic polar semiconductors [34,35], and the calculated mode frequencies  $\omega_{TZ}$ ,  $\omega_{LZ}$ ,  $\omega_{TX}$ , and  $\omega_{LX}$  for a nanowire as described in the text. The dielectric constant,  $\epsilon_z(\infty)$ , data is from [36]. Reprinted from G. D. Mahan, R. Gupta, Q. Xiong, C. K. Adu, and P. C. Eklund, Optical phonons in polar semiconductor nanowires, *Phys Rev B*, 68, 073402 (2003) with permission of the American Physical Society

Crystal	$\omega_{TO}(\omega_{TZ})/\text{cm}^{-1}$	$\omega_{LO}(\omega_{LZ})/\text{cm}^{-1}$	$\omega_{TX}/\text{cm}^{-1}$	$\omega_{LX}/\text{cm}^{-1}$
GaAs	268.6	292	290.2	292.7
GaP	367	403	399.5	404.3
ZnS	274	349	337.9	353.6
SiC	796	972	950.5	980.6
ZnSe	206	252	248.9	254.4
ZnTe	179	206	202.9	207.2
CdTe	140	171	167.3	172.4
AlP	440	501	494.2	503.6
InP	303.7	345	341.3	346.4
InSb	179	200	198.8	200.4
AlSb	319	340	338.2	340.8

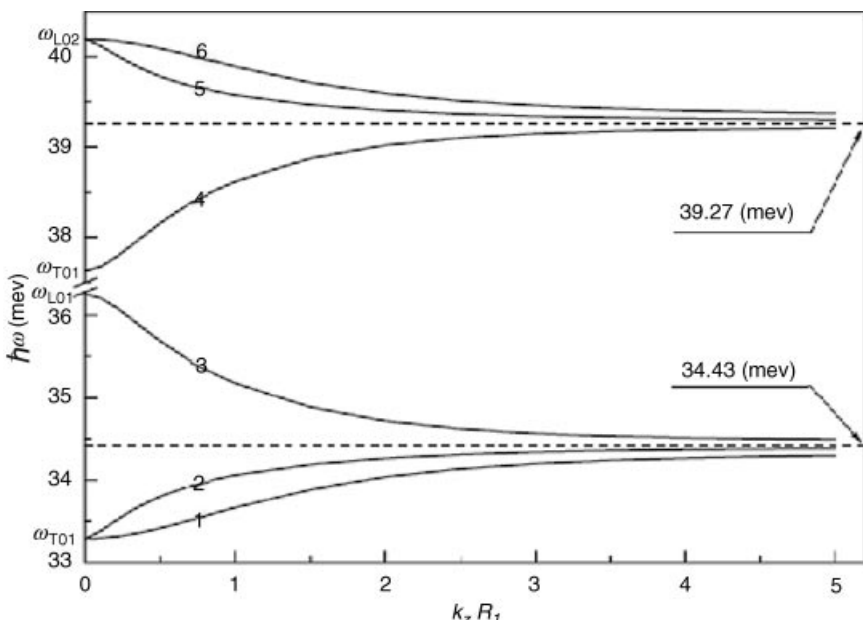


**Figure 8.27** Dispersion relation of interface modes with azimuthal quantum number  $m=0$  for  $\text{GaAs}/\text{Ga}_{0.6}\text{Al}_{0.4}\text{As}/\text{GaAs}/\text{Ga}_{0.6}\text{As}_{0.4}\text{Al}_{0.4}\text{As}$  four-layer quantum well wire (the layer thickness is 5 nm/5 nm/5 nm/ $\infty$ ) [38]. Reprinted from L. Zhang and H. J. Xie, Transfer Matrix Method for the FRÖHLICH Electron-Interface Optical Phonon Interaction in Multilayer Coaxial Cylindrical Quantum-Well Wires, *International journal of Modern Physics B*, 18, 379–393 (2004) with permission of the World Scientific Publishing Company

the dispersion relation of interface mode of GaAs/Ga<sub>0.6</sub>Al<sub>0.4</sub>As/GaAs/Ga<sub>0.6</sub>As<sub>0.4</sub>Al<sub>0.4</sub>As four-layer quantum well wire with a thickness of 5 nm/5 nm/5 nm/∞, respectively, where six interface modes are shown. These modes show obvious dispersion only at small phonon wave vector  $k_z$  and approach  $\omega_{TO_1}$ ,  $\omega_{LO_1}$ ,  $\omega_{TO_2}$ , and  $\omega_{LO_2}$  (1 and 2 stand for material GaAs and Ga<sub>0.6</sub>Al<sub>0.4</sub>As, respectively) of corresponding quantum well structure. When the  $k_z$  increases, the frequencies of 1, 2, 3 and 4, 5, 6 branches approach two fixed values of 39.72 and 34.43 meV, respectively.

### 8.3 Micro-Crystal Models

In Raman scattering study of small size semiconductors, some phenomenological theory has been widely applied, in which the Micro-crystal (MC) model is a famous one. The MC model is usually the single name for the RWL model and the space correlation model. Two models are suggested to explain measured frequency shift and line width broadening of Raman spectra due to their small size in semiconductors. However, the origins of the above spectral feature changes are different, specifically in these two models. The concern of the former is the phonon confinement induced by the small size of MC particles, while the problem of the latter is the phonon localization induced in the alloying process of  $Ga_{1-x}Al_xAs$ . The MC model has been applied widely and successfully by experimental researchers especially, but the questions for the model have been put forward by many researchers. In this section, we will introduce and review the MC model in more detail.

#### 8.3.1 Archetypes of MC Models

##### 8.3.1.1 RWL Model

The RWL model was originally proposed by Richter *et al.* in 1981, [18], which is the reason why the model is named as the “RWL model.” In 1986, Campheil and Fauchet further discussed and developed the RWL model [39]. Based on the Brillouin theorem, authors wrote down the wave function for a phonon of wave vector  $\mathbf{q}_0$  in an infinite crystal [39]:

$$\Phi(\mathbf{q}_0, \mathbf{r}) = u(\mathbf{q}_0, \mathbf{r})e^{-i\mathbf{q}_0 \cdot \mathbf{r}} \quad (8.64)$$

where  $u(\mathbf{q}_0, \mathbf{r})$  is the periodic function with the period defined by lattice constant and  $\exp(i\mathbf{q}_0 \cdot \mathbf{r})$  is a plane wave. Furthermore, they suggested that the wave function for a phonon of wave vector  $\mathbf{q}_0$  in a microcrystal of diameter  $L$  is

$$\Phi(\mathbf{q}_0, \mathbf{r}) = W(\mathbf{r}, L) \Phi(\mathbf{q}_0, \mathbf{r}) = \Phi'(\mathbf{q}_0, \mathbf{r})u(\mathbf{q}_0, \mathbf{r}) \quad (8.65)$$

where  $W(\mathbf{r}, L)$  is the phonon weighting function, which indicates that the microcrystal phonon wave function is a superposition of the Eigen function with  $\mathbf{q}$  vectors centered at  $\mathbf{q}_0$ . Expanding  $\psi'$  in a Fourier series:

$$\psi'(\mathbf{q}_0, \mathbf{r}) = \int d^3 q C(\mathbf{q}_0, \mathbf{r}) e^{i\mathbf{q} \cdot \mathbf{r}} \quad (8.66)$$

with Fourier coefficients  $C(\mathbf{q}_0, \mathbf{r})$  determined by

$$C(\mathbf{q}_0, \mathbf{q}) = \frac{1}{(2\pi)^3} \int d^3 q \psi'(\mathbf{q}_0, \mathbf{r}) e^{-i\mathbf{q} \cdot \mathbf{r}} \quad (8.67)$$

Since  $\psi'(\mathbf{q}_0, \mathbf{r})$  reflects the distribution of phonon density in the real space of MCs,  $C(\mathbf{q}_0, \mathbf{q})$  is the distribution function of phonon density in wave vector space. Moreover, Equation (8.66) of  $\psi'(\mathbf{q}_0, \mathbf{r})$  indicates that the phonon density distribution function in coordinate space can be expressed as the combination of plane waves with different wave vector (phonon momentum)  $\mathbf{q}$ , which reflects a new feature that the momentum of crystal particles is diffusive. The weight of contribution from the plane waves with different  $\mathbf{q}$  in the combination is different, which is determined by weighting function  $C(\mathbf{q}_0, \mathbf{q})$ . Thus the first order Raman spectrum can be expressed as

$$I(\omega) = \int \frac{d^3 q \cdot |C(\mathbf{q}_0, \mathbf{q})|^2}{[\omega - \omega(\mathbf{q})]^2 + (\Gamma_0/2)^2} \quad (8.68)$$

where  $\omega(\mathbf{q})$  is the phonon dispersion curve of corresponding bulk materials;  $\Gamma_0$  is the Raman line width of bulk material; and the integration range is the whole Brillouin zone.

The  $C(\mathbf{q}_0, \mathbf{q})$  takes the Gaussian function form at  $\mathbf{q}_0 = 0$  in Ref 18, namely

$$|C(0, \mathbf{q})|^2 = \exp(-q^2/4\alpha L^2) \quad (8.69)$$

where  $L$  is crystal particle size and  $\alpha$  is a modulus to adjust size parameter;  $\alpha$  is determined by the fitting of calculated results to experimental results. The authors of Ref. [39] pointed out that the weighting function  $W(\mathbf{r}, L)$  used in the original RWL model is the Gaussian function of  $\exp(-2r^2/L^2)$ , that is, the phonon vibration amplitude equals the peak amplitude  $1/e$  at the microcrystal boundary, and they assumed such confinement form had no physical reason.

In spherical crystal particles, Richter, *et al.* proposed the weighting function at  $\mathbf{q}_0 = 0$  is [18]

$$|C(0, \mathbf{q})|^2 \cong e^{-q^2 L^2/c} \quad (8.70)$$

Campbell and Fauchet suggested many kinds of weighting function  $W(\mathbf{r}, L)$  [39] and believe that Gaussian type distribution function expressed below is much better:

$$W(\mathbf{r}, L) = \exp(-4\pi \cdot r/L) \quad (8.71)$$

The above equation reflects that the phonon density is the symmetric distribution type and its value is strongest at the center and then approaches zero at the boundary. The wave function of Equation (8.65) assumes that crystal particles are spherical. For the irregular shapes of microcrystals, the difference of confined function is very small and so the induced error can be ignored.

Since the main contribution of integration comes from the center of the Brillouin zone, the phonon dispersion function used in the model usually adopts a simple form. For example, the phonon dispersion function of silicon is usually expressed in its one-dimensional form as

$$\omega(q) = \omega_0 \cdot \cos\left(\frac{a}{2}q\right) \quad 0 \leq q \leq \frac{\pi}{2a} \quad (8.72)$$

$$\omega(q) = \omega_0 \cdot \sin\left(\frac{a}{2}q\right) \quad \frac{\pi}{2a} \leq q \leq \frac{\pi}{a} \quad (8.73)$$

where  $a$  is the lattice constant and the integration region is simplified as  $0 - \pi/a$ .

- Spatial correlation (SC) model [40, 41]

In the Raman spectral investigation of anharmonicity and disorder-induced effects in  $Ga_{1-x}Al_xAs$  mixed crystals, Jusserand and Sapriel found that the Raman peak of the  $GaAs$  optical phonon in  $Ga_{1-x}Al_xAs$  appeared an asymmetric broadening with increasing Al component  $x$ . They proposed an elementary phenomenological model to interpret this phenomenon. In a one-dimensional model, they suggested that the Raman scattering light by the different contribution modes has a Lorentzian distribution around the frequency  $\omega(q)$  with the half-width  $\Gamma(q)$ , where  $q$  is equal to  $k/Q$ ,  $Q$  being the wave vector magnitude corresponding to the extremity of the Brillouin zone. The Raman intensity  $I(\omega)$  is thus a weighted sum of the contributed spectral lines:

$$I(\omega) = \int_0^1 P(q) \frac{\Gamma(q)/\pi}{[\omega - \omega(q)]^2 + \Gamma(q)^2} dq \quad (8.74)$$

where  $P(q)$  is the weight factor, which stands for probability of different mode contributions to spectra. Moreover, the authors assumed:

1. The optical branch,  $\omega(q) = \omega_0 - \beta q^2$ ;
2.  $r$  is independent of  $q$ ;
3. The distribution of the weighting factor  $P(q)$  is Lorentzian, with a half-width  $\alpha$ :

$$P(q) = \frac{2\alpha}{\pi} \frac{1}{q^2 + \alpha^2} \quad (8.75)$$

If we assume  $\Gamma(q)$  in Equation (8.74) is independent of  $q$  and  $p(q) = |C(0, q)|^2$  in Equation (8.75), the RWL and SC models are equivalent in form. Therefore we cannot distinguish the RWL and SC models in practical applications. In the following, we use the name “micro-crystal (MC) model” to represent the above two models.

### 8.3.2 Basic Assumptions of MC Models

We have mentioned that RWL and SC models were proposed based on the phonon confinement originating the small size of crystals and the phonon localization due to alloying and impurities. From the introduction of RWL and SC models, we find that they also make some assumption in physics and spectroscopy in the setting up of the models.

- Assumption in physics:
  - (1) In the region of small size and localized scale, the periodic arrangement of crystals basically exists, that is, the translation symmetry holds and momentum conservation is maintained.
  - (2) Based on the uncertainty principle, the small size or localized scale induces the momentum diffusion and the relaxation of wave vector selection rule  $q = 0$  in visible Raman scattering.
- Assumption in spectroscopy:  
From Section 8.3.1, we can understand that when scattering intensity Equation (8.74) was suggested, the authors of the SC model made specific assumptions, which should be considered as reasonable.

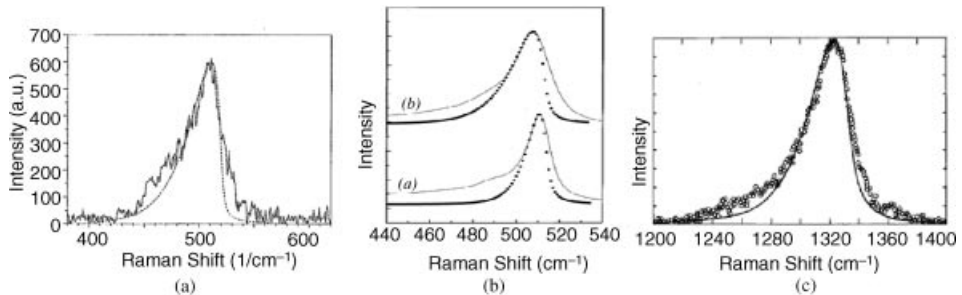


**Figure 8.28** Comparison between calculated Raman spectra by the MC model for porous silicon (a, dashed line.) [42] Reprinted from Z. Sui, P. P. Leong, I. P. Herman, et al., Raman analysis of light-emitting porous silicon. *Appl. Phys. Lett.*, 60, 2086–2088 (1992) with permission of the American Institute of Physics, Si nanowire (b, dotted line.) [43] Reprinted from B. Li, D. P. Yu and S. L. Zhang, Raman spectral study of silicon nanowires, *Phys. Rev. B*, 59, 1645–1648 (1999)., and nanodiamond (c, solid line) with corresponding experimental results [44]. Reprinted from M. Yoshikawa, Y. Mori, H. Obata, et al., Raman scattering from nanometer-sized diamond, *Appl. Phys. Lett.*, 67 (1995) with permission of the American Institute of Physics

### 8.3.3 Successful Application of MC Models

After the MC model was proposed, it was applied widely and successfully in various fields, such as in nano-semiconductors, ion implantation semiconductors, and alloy semiconductors. For example, Figure 8.28 shows a fitting result of the non-polar nano-semiconductors: porous silicon, Si nanowire, and nanodiamond, from which a good fit can be seen.

In the change of Raman spectral features induced by alloying and localization in polar nano-semiconductors, the MC model also achieves good results [45, 46] and Figure 8.29 exhibits two successful examples.

In the three factors of the MC model,  $W(\mathbf{r}, L)$ ,  $\omega(q)$ , and  $\Gamma_0$ , the practical expression of the phonon weighting function  $W(\mathbf{r}, L)$  plays a key role in the fit. To date, the selected expressions of weighting functions have had various forms varying from that in the original RWL model, in which the weighting function expressed by Equation (8.65) is widely used. In this equation, there are two adjustable parameters: one is the sample size  $L$  and the other is the strength limited parameter  $\alpha$ ; thus, by fitting we can obtain the parameters of the sample size and shapes and so on. For example, from the fitting result of porous silicon shown in Figures 8.30(a) and (b), we learn that the shape of porous silicon is not wire-like and there is a relation between the Raman shift and average size of porous silicon, respectively.

In fact, in many successful applications, the selection of the other two factors, that is, the dispersion relation  $\omega(q)$  and line width  $\Gamma_0$  in the model, is also different from those in the original RWL model. For example, Paillard, *et al.* proposed  $\bar{\omega}_0$  expressed as Equation (8.76) to replace traditional isotropic one-dimensional  $\omega(q)$  and reflect the anisotropy of three-dimensional phonon dispersion curves [47]:

$$\bar{\omega}_0 = \sqrt{\frac{1}{3} \left( S(\mathbf{q} = 0) - \sum_{\text{scoustic}} \omega_i^2 \right)} = \sqrt{522^2 - \frac{126100 \times q_r^2}{|q_r| + 0.53}} \quad (8.76)$$

with  $|q_r| < 0.5$

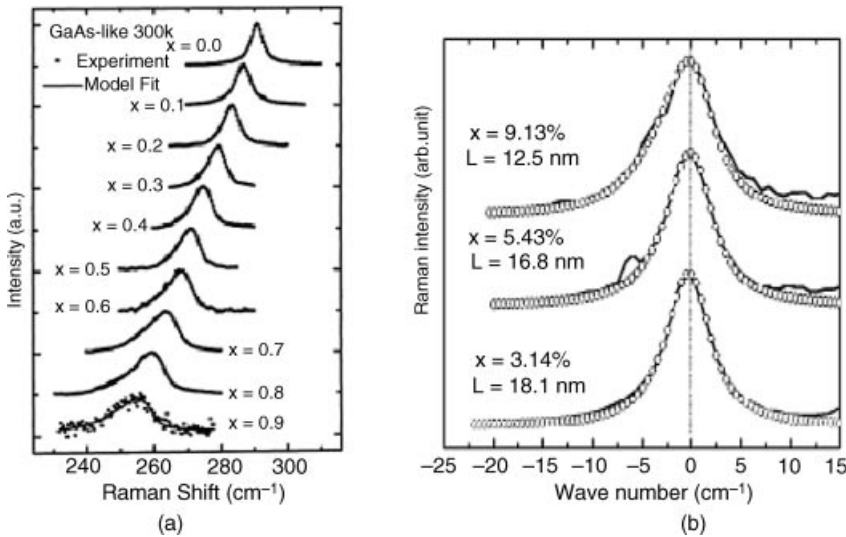


**Figure 8.29** The experimental Raman spectra of GaAs-like LO mode in  $\text{Ga}_{1-x}\text{Al}_x\text{As}$  alloy thin film (a) [45] and ZnSe-like LO mode in  $\text{Zn}_{1-x}\text{Be}_x\text{Se}$  alloy thin film (solid line) [46], and the calculated Raman spectra with composition parameter  $X$  based on the MC model. (a) Reprinted from Y. T. Hou, Z. C. Feng, M. F. Li and S. J. Chua, Characterization of MBE-grown  $\text{Ga}_{1-x}\text{Al}_x\text{As}$  alloy films by Raman scattering, *Surface and Interface Analysis*, 28, 163–165 (1999) with permission of John Wiley and Sons. (b) Reprinted from L. Y. Lin, C. W. Chang, W. H. Chen, Y. F. Chen, S. P. Guo and M. C. Tamargo, Raman investigation of anharmonicity and disorder-induced effects in  $\text{Zn}_{1-x}\text{Be}_x\text{Se}$  epifilms, *Phys. Rev. B*, 69, 075204 (2004) with permission of the American Physical Society

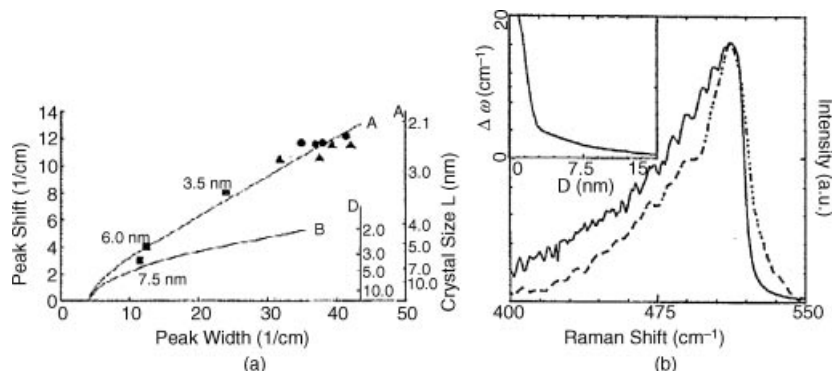


**Figure 8.30** Comparison between the experimental and the calculated (solid line) Raman spectra by the MC model for porous silicon [42,43]. In (a), A and B represent the calculations for the sphere and cylindricality porous silicon; in (b), the insert is the relationship between the Raman frequencies shift  $\Delta\omega$  and the average diameter  $D$  of porous silicon. (a) Reprinted from Z. Sui, P. P. Leong, I. P. Herman, et al., Raman analysis of light-emitting porous silicon, *Appl. Phys. Lett.*, 60, (1992) with permission of the American Institute of Physics. (b) Reprinted from S-L. Zhang, et al., Raman investigation with excitation of various wavelength lasers on porous silicon, *J. Appl. Phys.* 72, 4469 (1992)

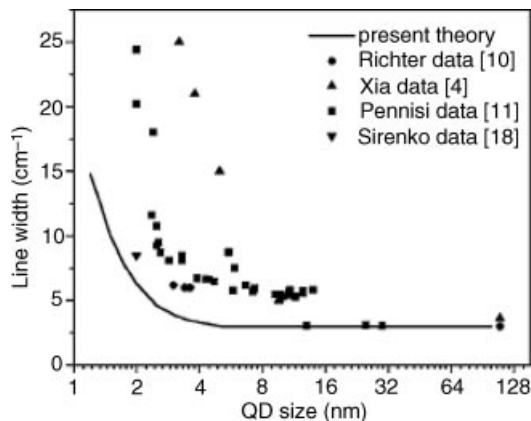


**Figure 8.31** Dependence of calculated line width by various authors on quantum dot size [48]. The number in [ ] in figure are the reference number in Ref 48. Reprinted from S. V. Novikov and G. G. Malliaras, Modified Raman confinement model for Si nanocrystals, *Phys. Rev. B*, 73, 033307 (2006) with permission of the American Physical Society

Moreover, as shown in Figure 8.31, the fitting results indicate that the spectral line width used in the model is related to sample size rather than the constant line width of the bulk crystal proposed in the original models.

Figure 8.32(a) clearly shows [49], for size-distributed nano semiconductors, that the calculation when taking the size distribution into account is better than that not taking it into account. Figure 8.32(b) [50] exhibits the effect of the size distribution to the fitting results.

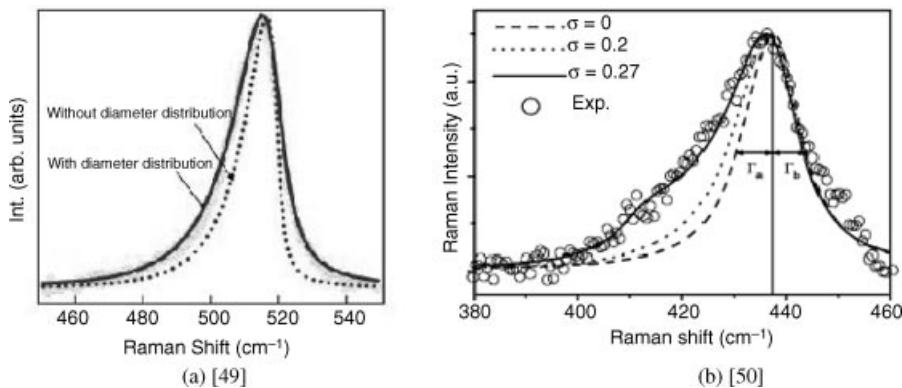


**Figure 8.32** Influence of taking and not taking sample size distribution into account when fitting results. (a) Reprinted from K. W. Adu, et al., Confined Phonons in Si Nanowires, *Nano Lett.*, 5, 409–414 (2005) with permission of the American Chemical Society. (b) Reprinted from K. F. Lin, H. M. Cheng, H. C. Hsu, et al., Band gap engineering and spatial confinement of optical phonon in ZnO quantum dots, *Appl. Phys. Lett.*, 88, 263117 (2006) with permission of the American Institute of Physics

The author of Ref. [50] introduced the size distribution function  $f(q) = \frac{1}{\sqrt{1 + \frac{q^2 \sigma^2}{2}}}$ . From the figure, it can be seen that when  $\sigma = 0$  (no size distribution), the fitting result is worse.

### 8.3.4 Correct Presentation and Application Extent of MC Model

The discussion in previous sections has indicated that for the application of the MC model to be a success, we have to make modifications to the Raman intensity formula of the MC model. That also concerns the correct presentation and suitable applied extent of the Raman intensity formula representing the MC model.

**8.3.4.1 Discussion of the validity of MC model based on the microscopic calculation**  
 Zi *et al.* used a microscopic bond polarizability model in the framework of partial-density approximation to obtain the Raman intensity with polarization  $\mu\nu$  under back scattering geometrics, expressed as [51]

$$I_{\mu\nu}(\omega) \propto [n(\omega) + 1] \sum_j \delta[\omega - \omega_j(q)] |\Delta\alpha_{\mu\nu}(j\bar{q})|^2 \quad (8.77)$$

where  $[n(\omega) + 1]$  is the Bose–Einstein factor. Zi *et al.* performed calculations for spheres of Si with different diameters with the maximum atom number up to 657. Since the vibration amplitude can be viewed as the envelope function, or weighting function described above, for an Si sphere consisting of 357 atoms (i.e., diameter  $L = 23.5$  Å), they calculated the vibration amplitudes from the ball center to the boundary (in the ball center, the vibration amplitude normalized to 1, which also represents the variation of the weighting function). The calculated vibration amplitudes are shown in Figure 8.33.

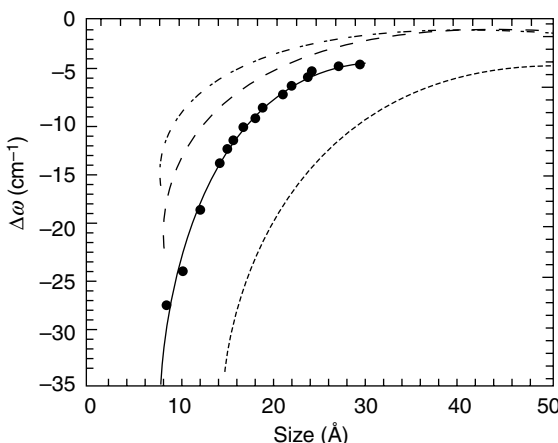


**Figure 8.33** Relation between the Raman frequency shifts with respect to the bulk LO phonon at point  $\Gamma$  and the size for spherical Si nanocrystals. The solid circles are the results calculated by the bond-polarizability model and the solid line is the fitted results. The results obtained by using the sinc weighting function (dashed line) and Gaussian weighting function with  $\alpha = 8\pi^2$  (dotted line) and  $\alpha = 9.67$  (dot-dashed line) are also plotted for comparison [51]. Reprinted from J. Zi, K. Zhang and X. Xie, Comparison of models for Raman spectra of Si nanocrystals, Phys. Rev. B, 55, 9263–9266 (1997) with permission of the American Physical Society

If the Raman frequency shift  $\Delta\omega$  is defined by

$$\Delta\omega = \omega(L) - \omega_0 \quad (8.78)$$

where  $\omega(L)$  is the Raman frequency of an Si sphere with size  $L$  and  $\omega_0$  is the LO or TO phonon frequency of the perfect Si crystal at the  $\Gamma$  point. In Figure 8.33, the Raman frequency shifts versus size for Si spheres obtained by the bond-polarizability model are given as solid circles. The Raman frequency shift  $\Delta\omega$  obtained by the bond-polarizability model is

$$\Delta\omega = -A(a/L)^\gamma \quad (8.79)$$

where  $A = 47.41 \text{ cm}^{-1}$  and  $\gamma = 1.44$ . The fitted results are given in Figure 8.33 as a solid line. In the figure, the results obtained by the MC model with different weighting functions are also given for comparison. It can be seen that the MC model cannot satisfactorily reproduce the Raman frequency shifts calculated by the partial-density approach and the bond-polarizability model. The MC model, with a sinc weighting function, gives relatively better agreement compared to that by a Gaussian function. Especially for small sized Si spheres, the MC model cannot give a satisfactory description for the weighting function and the Raman shift simultaneously.

However, Paillard *et al.* [52] believed that the MC model and bond polarizability model agree each other, as mentioned by Zi. As shown in Figure 8.34, they believe that when the

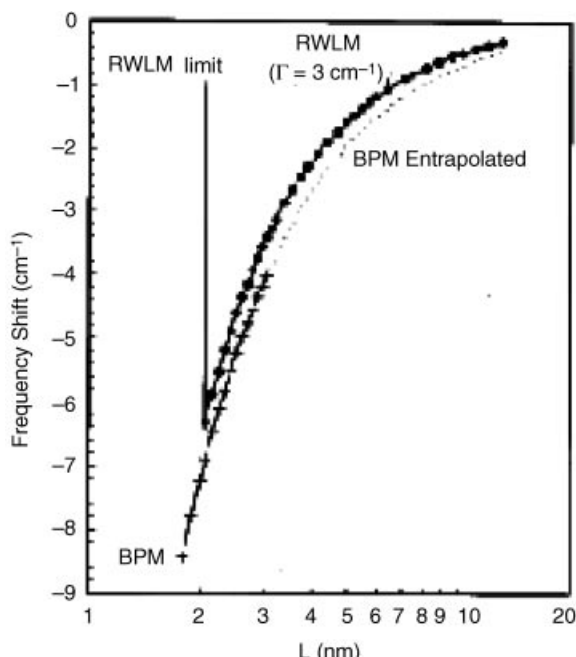


**Figure 8.34** Phonon frequency shifts using the MC model (RWLM) and the bond polarizability model (BPM). The MC model is limited to  $L > 2.2 \text{ nm}$ , while the bond polarizability model calculations stop at  $L \leq 3 \text{ nm}$  [52]. Reprinted from V. Paillard, P. Puech, M. A. Laguna, et al., Improved one-phonon confinement model for an accurate size determination of silicon nanocrystals, *J. Appl. Phys.*, 86, (1999) with permission of the American Institute of Physics

particle diameter is less than 2.2 nm, the bond polarizability may be more suitable. In addition, Adu *et al.* [49] pointed out that the adjustable parameter  $\alpha$  in the model (Equation (8.65)) is not sensitive to diameter over the range 4–25 nm.

#### 8.3.4.2 Discussion on factors and parameters related to MC mode

The discussions in the previous sections all involve the choice of factors and parameters of the model as well as the sample sizes. The factors of the MC model mainly contain the weighting function  $C(\mathbf{q}_0, \mathbf{q})$ , phonon dispersion curves,  $\omega(\mathbf{q})$ , and spectral line width  $\Gamma_0$ . We will discuss and analyze them one by one below.

- Weighting function  $C(\mathbf{q}_0, \mathbf{q})$

The weighting function  $C(\mathbf{q}_0, \mathbf{q})$  is the Fourier transformation of the phonon confinement function  $W(\mathbf{r}, L)$ , which reflects the size confinement of phonon wave function and is equivalent to the PDOS distribution in real space, which is related to the sample size  $L$ . Correspondingly,  $C(\mathbf{q}_0, \mathbf{q})$  reflects the occurring probability of the phonons with various wave vectors in the wave packet. The wave packet is formed by the superposition of various wave vector states caused by the size confinement of phonons. That is only the density distribution of various wave vector phonons in the wave vector space.

The confined wave function in an infinite potential well should be a stationary wave form. Superlattice theory also points out that the confinement effect on the phonon wave function is very strong, and is stronger than that of the electron wave function. The entering depth of confined phonon wave function in the potential barrier is only 1~2 atomic layers [16]. While the confinement expressed by the Gaussian function is much weaker, it cannot fully express the size confinement effect on phonons. This also reveals the physical origin of the discovery by Zi *et al.* that the weighting function formed by sinc function form is better than that formed by the Gaussian function [52].

Moreover, the specific confinement effect on different samples is varied. For example, when the sample size is distributed, the confined potential well could be more than 1 and the depth and shape of each potential well also could be different, implying that  $C(\mathbf{q}_0, \mathbf{q})$  has many expressions. Therefore, we should be very careful in adopting the weighting function form.

Based on the above analysis and discussion, it is expected that the weighting function  $C(\mathbf{q}_0, \mathbf{q})$  has various forms corresponding to various samples.

- Dispersion relation  $\omega(\mathbf{q})$

Section 8.3.1 mentioned that the dispersion relation  $\omega(\mathbf{q})$  in MC models adopted the corresponding bulk dispersion relations. However, it has also been mentioned that based on the uncertainty relation  $\Delta\mathbf{r}\Delta\mathbf{p} \leq \hbar/2$ , when the sample size  $\mathbf{r}$  becomes smaller, the uncertainty of the corresponding momentum  $\mathbf{p}$  (i.e., the wave vector  $\mathbf{q}$  for the phonons) must become larger, and the phonon dispersions are meaningless or do not exist. In Section 8.3.2, the calculation quoted by Zi *et al.* shows that the dispersion relation of the Si crystal particles of 2.8 nm still exist, but the energy is dispersive and the wave vector (i.e., the momentum) is separated.

Therefore, based on this main premise condition of the MC model is the effectiveness of bulk dispersion, and reasonability and validity rely on whether the system can have an applied bulk dispersion relation. That is, the so-called “bulk-like approximation” is valid for the system being studied.

- Line width  $\Gamma_0$

Most of previous calculations believe that the line width equals the summation of bulk material natural line width and measured instrument line width. It is well known for small size crystal that the line width  $\Gamma_0$  of nanosystems increases as size decreases and thus the above formulation for the line width cannot reflect the real case.

According to the above analysis and discussion, the MC model reflects the Raman scattering spectrum induced by the finite size effect in small sized systems. However, we need to simultaneously take notice of the applied conditions. First, only while the dispersion relation  $\omega(\mathbf{q})$  still exists, the MC model is available. In addition, since the choice of the weighting function  $C(\mathbf{q}_0, \mathbf{q})$  is largely influenced by sample conditions, it needs to choose different weighting function forms for different samples. Finally, the spectral line width  $\Gamma$  is also different for different samples.

### 8.3.5 Testing of MC Model Applied Conditions [53]

The previous subsection mentioned that the application of the MC model needed to satisfy certain conditions in the sample size and the choice of model parameters. In this section we introduce the testing of these conditions by using Si nanoparticles as an example. Testing was performed by fitting the theoretical Raman spectra calculated by using the MC model with observed Raman spectra for nearly uniform sized nanocrystalline (NC)-Si.

The example used in experiments is the Si nanowires (NWs), of which the TEM images of silicon wire samples are shown in Figure 8.35. From the low resolution TEM image in Figure 8.35(a) we can see the appearance of SiNWs, while in the high-resolution TEM shown in Figure 8.35(b), we observe that in Si NWs there are a lot of small crystal particles with complete crystal lattices. It has been verified [54] that the Si NWs consist of a collection of smaller crystalline particles due to the presence of abundant structural defects and the effective confined size is not the diameter of the wires, which indicates that the observed Raman spectrum is from such Si particles. Based on the resonant size selection effect [55, 56] and the incident laser energies, we can determine the size of particles from sized distributed Si NWs in the Raman spectral measurement simultaneously. The obtained sizes of Si particles are 0.8, 0.9, 1.2, and 2.1 nm from the Raman spectra excited at laser wavelengths of 488, 515, 633, and 785 nm, respectively.

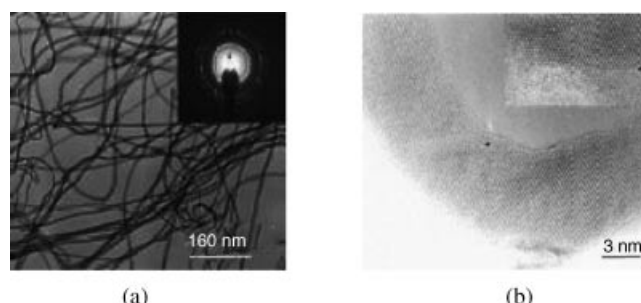


**Figure 8.35** Transmission electron microscope (TEM) images of Si nanowire at low resolution (a) and high resolution (b). Reprinted from S.-L. Zhang, *Raman Spectroscopy and Low-dimensional nanoscale Semiconductors*, Science Press, (2008)

**Table 8.2** Different choices for weighting function  $W(r, L)/C(\mathbf{q}_0, \mathbf{q})$ , dispersion curve  $\omega(q)$ , and line width  $\Gamma$  in the fitting of the MC model calculation [53]. Reprinted from S. L. Zhang, et al., Study on the applied limitation of the micro-crystal model for Raman spectra of nano-crystalline semiconductors, *J. Raman Spec.*, 39, 1578–1583 (2008)

Choice		I		II			III
		1	2	3	4	5	6
$W(r, L)$	Gaussian [18]	✓		✓	✓	✓	—
	Sinc [49]	—	✓	—	—	—	✓
$\omega(q)$	Bulk [18]	✓	✓	—	—	✓	—
	Paillard <i>et al.</i> [46]	—	—	✓	—	—	—
	Adu <i>et al.</i> [49]	—	—	—	✓	—	✓
$\Gamma_0$	Constant = $4.5 \text{ cm}^{-1}$	✓	✓	✓	✓	—	—
	Adjustable	—	—	—	—	✓	✓
Figure 8.36	—	a	b	c	d	e	f
							/

The fitting work is performed in three ways, as listed in Table 8.2. In the different choices, the combination used was different  $W(r, L)$ ,  $\omega(q)$ , and  $\Gamma_0$ , for example, choice I corresponds to that in which  $W(r, L)$  is Gaussian and the bulk  $\omega(q)$  and  $\Gamma_0 (= 4.5 \text{ cm}^{-1})$  were chosen. In method II, only one parameter was changed in each choice, as listed in choices 2–5. In method III,  $\omega(q)$  was chosen as suggested by Hu and Zi and the  $\Gamma_0$  was dependent on  $q$ , simultaneously, and  $W(r, L)$  was chosen in two functional forms, as listed in choices 6 and 7. The fitting results are shown in Figure 8.36, in which the calculated and observed Raman spectra are shown as solid and dotted lines and Figures 8.26 (a)–(f) correspond to choices 1–6, respectively.

From Figure 8.36(a), the result gives a bad fit for resonant spectra, that is, from the samples with nearly uniform size and good fit for the spectrum excited at 785 nm, the spectra is out of resonance and thus is from size-distributed samples. This indicates that choice 1 cannot obtain a good fit for the spectrum of the nearly uniform sized NC-Si and the better fit occurred in the size-distributed NC-Si. The latter only coincides with the recognized view that the MC model is suitable for size-distributed samples [57]. The similar phenomenon can be seen in all spectra excited at 785 nm in Figures 8.36(b)–(f), confirming the above argument. Figure 8.36(b) does not show obvious improvement when compared to Figure 8.36(a), reflecting that the different choices of  $W(r, L)$  do not have significant effects on the results. In Figures 8.36(c)–(e), the fitting results do not show any essential improvement when compared to Figures 8.36(a) and (b). The fitting results of choices 6 and 7 are similar and thus show the fitting result of choice 6 in Figure 8.36(f). Considering the only difference between choices 6 and 7 is the choice of weighting function  $W(r, L)$ , and the above similarity indicates again that the form of the weighting function has no significant influence. From Figure 8.36(f), at a glance, a better fit was obtained for all spectra excited at four wavelengths, except for the low wave number region around  $480 \text{ cm}^{-1}$ . It has been pointed out that an amorphous silicon oxide thin outer layer covers the surface of Si NW samples, which has a Raman band peak at  $480 \text{ cm}^{-1}$  [58]. If we consider that the Raman spectrum should deduct the component from the amorphous silicon oxide thin outer layer, the fit

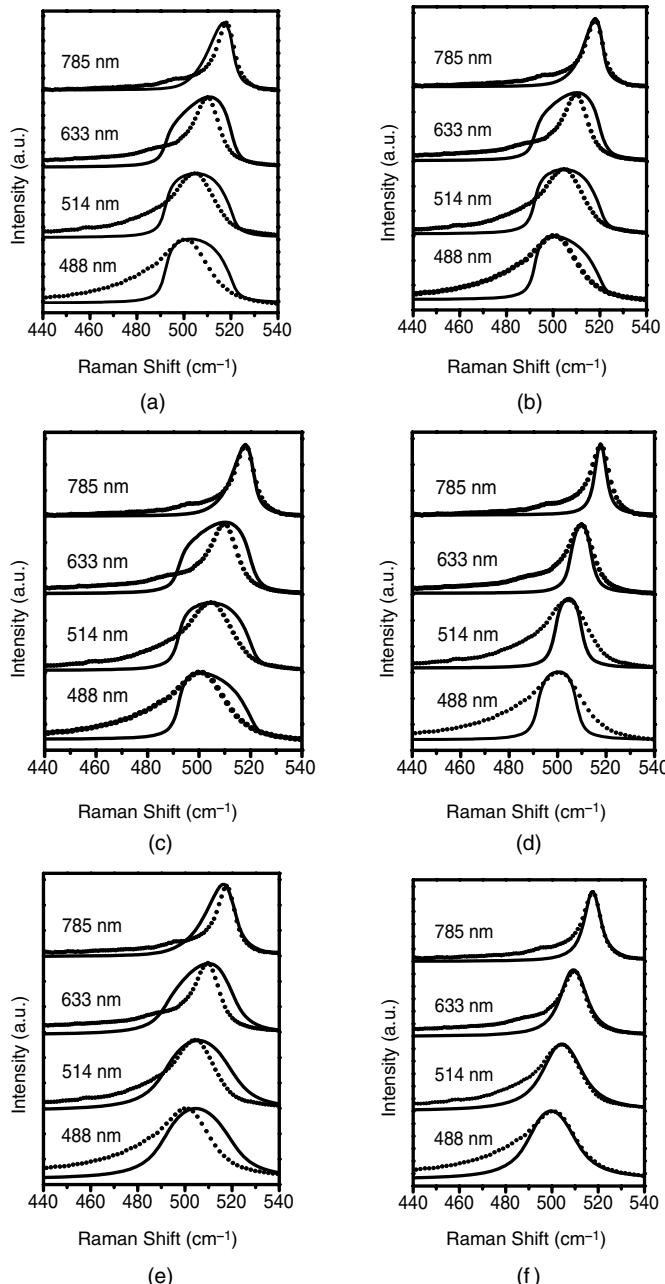


**Figure 8.36** Observed (dotted lines) and calculated (solid lines) Raman spectra by using the MC model, in which (a), (b), (c), (d), (e), and (f) correspond to choices 1, 2, 3, 4, 5, and 6 listed in Table 8.2, respectively, for NC-Si particles; Raman spectra excited at laser wavelengths of 488, 515, 633 and 785 nm from samples with sizes 0.8, 0.9, 1.2 and 2.1 nm, respectively [53]. Reprinted from S. L. Zhang, et al., Study on the applied limitation of the micro-crystal model for Raman spectra of nano-crystalline semiconductors, *J. Raman Spec.*, 39, 1578–1583 (2008)

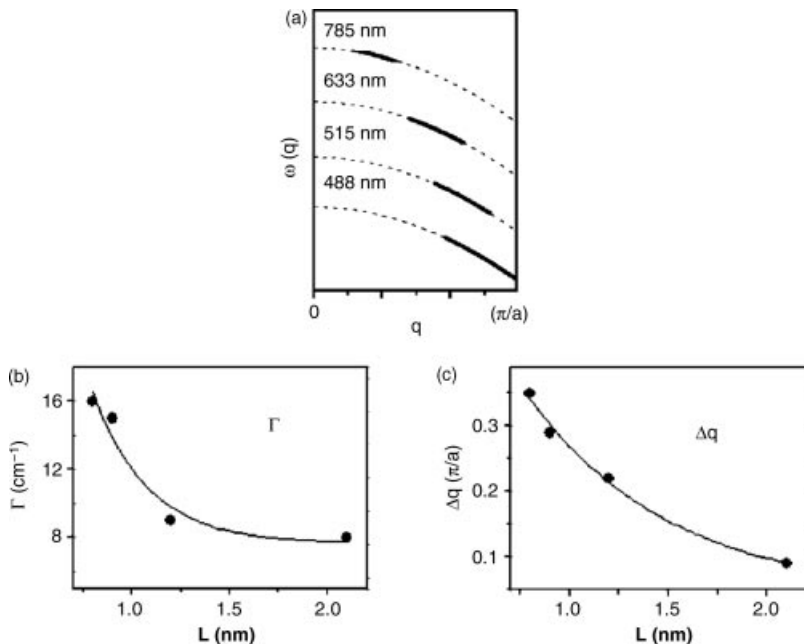


**Figure 8.37** The best fitted dispersion curve  $\omega_{\text{Eff}}(q)$  (thick solid lines) and corresponding bulk Si dispersion curve (dashed lines): (a) dependence of best fitted line width  $\Gamma(q)$ ; (b) wave vector range  $\Delta q$  of  $\omega_{\text{Eff}}(q)$  on sample size  $L$  for choice 8 in Table 8.2; where  $\pi/a$  is half the size of the Brillouin zone: Raman spectra excited at laser wavelengths of 488, 515, 633 and 785 nm from samples with sizes 0.8, 0.9, 1.2 and 2.1 nm, respectively [53]. Reprinted from S. L. Zhang, et al., Study on the applied limitation of the micro-crystal model for Raman spectra of nanocrystalline semiconductors, *J. Raman Spec.*, 39, 1578–1583 (2008)

shown in Figure 8.36(f) should be regarded as the best fit. This result confirms that the MC model is applicable if the dispersion curve and line width do not use the bulk crystal ones simultaneously. In other words, the choice of parameters  $\omega(q)$  and  $\Gamma_0$  based on the bulk-like approximation are not appropriate in the application of the MC model for nearly uniform-sized small NC-Si.

It will be possible in exploring the physical nature of the fitting results to learn that fitted dispersion curve and line width used is the best fit shown in Figure 8.36(f). The best fit dispersion curves here represent the frequency  $\omega$  and corresponding wave vector  $q$  of the scattered phonons, which are called the effective dispersion curve and labeled as  $\omega_{\text{Eff}}(q)$ . Accordingly, the best fitted line width is called an effective line width and labeled  $\Gamma_{\text{Eff}}(q)$ . The  $\omega_{\text{Eff}}(q)$ , the corresponding wave vector range  $\Delta q$  of  $\omega_{\text{Eff}}(q)$ , and the best fitting line width  $\Gamma_{\text{Eff}}(q)$  for the spectra from different sizes of nanocrystal Si particles are shown in Figures 8.37(a)–(c) with solid lines, respectively. The solid lines in Figures 8.37(b) and (c) were drawn by fitting of the least square method.

From Figure 8.37(a), it is found that  $\omega_{\text{Eff}}(q)$  is absent in the region near the Brillouin zone center, implying that the phonons at and near the center did not participate in the Raman scattering event for nearly uniform sized small Si crystallites. In fact, by closely examining the observed spectra shown in Figure 8.36, it can be seen that the above feature of  $\omega_{\text{Eff}}(q)$

coincides with the feature of observed Raman spectra: the scattering intensity from the phonons of  $520\text{ cm}^{-1}$  at and near  $q=0$  are obviously very weak for the spectra of samples with 0.8, 0.9, and 1.2 nm. The results presented here are contrary to the predication by the bulk-like approximation theory that Raman scattering is mainly from the phonons in the region near  $q=0$  for crystallites of small size.

From Figures 8.37(b) and (c), we find that the dependence of  $\Gamma_{\text{Eff}}(q)$  and  $\Delta q$  on  $L$  are exponential and can be expressed as

$$1.48 \times \exp(-L/0.29) \quad \text{for } \Gamma_{\text{Eff}}(q) \quad (8.80)$$

$$0.92 \times \exp(-L/0.72) \quad \text{for } \Delta q \quad (8.81)$$

From Equations (8.80) and (8.81), we observe that  $\Gamma_{\text{Eff}}(q)$  and  $\Delta q$  are, respectively, about  $\frac{0.04\pi}{a}$  and  $7.61\text{ cm}^{-1}$  at infinite  $L$ , which are basically consistent with  $\Delta q \approx 0$  and  $\Gamma_0 \approx 7\text{ cm}^{-1}$  in bulk-crystal Si, confirming the reliability of the two equations.

The exponential dependence of  $\Delta q$  on  $L$  is inconstant with the well-known linear dependence of  $\Delta q$  on  $L$  being  $\Delta q = \frac{2\pi}{L}$ , derived from the bulk-like approximation [59]. Moreover, from Equation (8.81), we find that when  $\Delta q$  approaches the value of bulk-crystal Si,  $L \approx 3.9\text{ nm}$ , implying that about 4 nm is the size limitation of the MC model based on the bulk-like approximation. This coincides with the disappearing size of the quantum confinement effect on electrons [60, 61] and phonons [62] of Si particles of  $4\sim 5\text{ nm}$ .

The above results and discussion indicate that the MC model is invalid for Si crystallites smaller than  $\sim 4\text{ nm}$ , if the dispersion curve  $\omega(q)$  and line width  $\Gamma(q)$  are chosen based on the bulk-like approximation. In addition, we discovered that the features of  $\omega(q)$  and  $\Gamma(q)$  within the best fit are different from those predicated by the bulk-like approximation. The above results indicate that the present modifications within the bulk-like approximation frame for the MC model is not appropriate and the microscopic theory is needed for very small crystallites.

## 8.4 Amorphous Feature and PDOS Expression of Nanostructure Raman Spectra

Section 8.1.1 introduced a theoretical calculation by a valence-force-field model with two parameters for a finite thickness of Si slab. The calculated results show that the calculated frequency distribution of mode number (i.e., PDOS, or say, phonon spectrum) exhibits the features of amorphous Si. These theoretical results are confirmed by observed Raman spectra of amorphization silicon treated with ion implantation and then laser annealing. This indicates that the Raman spectrum in nanostructures are related directly to the PDOS.

### 8.4.1 Finite Size Effects and Amorphous Feature of Nanostructure Raman Spectra

Because of the finite size effect, the translational symmetry in nanocrystals is broken down. Thus all vibration modes are allowed to contribute to the Raman-scattering. As a result, the Raman spectra should be related to their PDOS, meaning Raman spectra of nanostructures

should be amorphous-like. Based on this idea, a spectral calculation of polar SiC nanorods has been performed by using the amorphous crystal model and the results indicate it fits the experimental spectrum well [63].

The introduction above implies that the theoretical Raman spectra of nanocrystals could also be derived from the calculation of PDOS through the amorphous crystal model for both polar and non-polar nano-semiconductors.

#### 8.4.2 PDOS and Amorphous Raman Spectra

The Raman spectral calculation of amorphous crystals has been suggested by Shuker and Gammom and introduced in Section 7.5.4, which was expressed in Equation (7.141) as

$$I(\omega)_{\alpha\beta,\gamma\delta} = \sum_b C_b^{\alpha\beta,\gamma\delta}(1/\omega)[1 + n(\omega)]D_b(\omega) \quad (8.82)$$

where  $D_b(\omega)$  is the PDOS of the Raman band  $b$ ;  $n(\omega) = [\exp(\hbar\omega/kT)^{-1} - 1]^{-1}$  is the population of the phonons at frequency  $\omega$ ; and  $C_b$  is the weighting factor of the  $b$  band. Note that the model gives a direct relationship between Raman spectra and PDOS. The formula can be changed to a convenient form (7.146) for comparison between calculated and experimental results:

$$I(\omega)_R = D_w(\omega) \quad (8.83)$$

In the above equation,  $I(\omega)_R = \omega \times I(\omega)/[1 + n(\omega)]$  is called the reduced Raman spectra, which can be obtained from experimental spectra  $I(\omega)$ ; and  $D_w(\omega) = \sum_b C_b D_b(\omega)$  is called the weighted PDOS. We can set  $C_b$  as a constant to all the bonds, and note that experiments are conducted at room temperature and near  $500 \text{ cm}^{-1}$ , so  $D_w(\omega) \propto D(\omega)$  and  $I(\omega)_R \approx I(\omega)$ , so we have

$$I(\omega) \approx D(\omega) \quad (8.84)$$

Hence, we can calculate PDOS  $D(\omega)$  to obtain theoretical Raman spectrum and compare it with observed Raman spectra  $I(\omega)$  directly to verify the calculation and explain the experimental results.

In §7.4, it has been described that the calculation of PDOS in bulk semiconductors is by using expression (7.98) as

$$D(\omega) = \sum_s \int \frac{1}{\nabla_q \omega_s(q)} \frac{ds}{(2\pi)^3} \quad (8.85)$$

where  $s$  is the atomic number in primitive cells and  $\omega(\mathbf{q})$  is the phonon dispersion relation. The integration performs on the surface of the first Brillouin zone. The above expression shows that the PDOS calculation attributed as the calculation of  $\omega(\mathbf{q})$ .

The calculation of  $\omega(\mathbf{q})$  has been described in Chapter 7 by various models based on classical and quantum mechanics, while in nano-semiconductors, the calculation can be performed based on the first principle method, which will be introduced in Section 8.5.

## 8.5 First-Principles/*ab initio* Calculation of Nanostructure Raman Spectra

Section 7.1 mentioned that since a solid contains large amounts of atoms, it is impossible to solve motion equations. Therefore, we have to simplify the motion equation by reasonable approximation and propose phenomenological models, so that the calculation can be performed.

However, fast developing computer technology, high-speed processor and highcapacity memorizers make complex calculations possible. Moreover, since the development of scientific calculations based on density functional theory and scientific calculation software, directly solving motion equation becomes possible without any assumptions such as empirical models and fitting parameters. This means it is possible that the calculation of atomic and molecular structure can be made directly from the first principles of quantum mechanics, without using quantities derived from experiments as parameters. This simulation method is called the first principle or *ab initio* calculation. The *ab initio* calculation is suitable, especially for nanostructures, since its atom number is only around  $10^3$  orders of magnitude and the calculation results by the phenomenological model is invalid, as mentioned in Section 8.3.5.

In this section, we introduce *ab initio* calculations and several calculation examples.

### 8.5.1 *ab initio* Calculation

#### 8.5.1.1 *ab initio* Calculation Based on Quantum Mechanism [65]

The *ab initio* calculation and corresponding calculation software are established based on density functional theory. Its origin is the multi-body Schrodinger equation:

$$\hat{\mathcal{H}}\psi = -\frac{\hbar^2}{2m} \nabla^2 \psi + V(r)\psi = i\hbar \frac{\partial \psi}{\partial t} \quad (8.86)$$

Section 7.1 mentioned that during the adiabatic (Born–Oppenheimer) and the Hartree–Fock approximations, the multi-body Schrodinger equation finally changed into a single electron equation:

$$\hat{\mathcal{H}}\psi_e(r) = (T + V + E_{EX})\psi_e(r) = E\psi_e(r) \quad (8.87)$$

where the Hamiltonian contains mainly kinetic energy term  $T$ , Coulomb potential energy  $V$ , and exchange-correlation energy  $E_{EX}$ ; while  $\psi_e(r)$  can be expressed as

$$\psi_e(r_1, r_2, \dots, r_n) = \psi_1(r_1)\psi_2(r_2) \cdots \psi_n(r_n) \quad (8.88)$$

Considering the exchange symmetry of microscopic particles, we express the above equation as the Slater determinant:

$$\varphi(\mathbf{r}_1, \mathbf{r}_2, \dots, \mathbf{r}_n) = \frac{1}{\sqrt{N!}} \begin{vmatrix} \varphi_1(\mathbf{r}_1) & \varphi_2(\mathbf{r}_1) & \cdots & \varphi_N(\mathbf{r}_1) \\ \varphi_1(\mathbf{r}_2) & \varphi_2(\mathbf{r}_2) & \cdots & \varphi_N(\mathbf{r}_2) \\ & & \ddots & \\ \varphi_1(\mathbf{r}_N) & \varphi_2(\mathbf{r}_N) & \cdots & \varphi_N(\mathbf{r}_N) \end{vmatrix} \quad (8.89)$$

Mathematically, the solution of this equation depends on the equation coefficients and solution  $\psi(r)$  must be the function of coefficient  $V(r)$ , while, physically, the potential field in crystal depends on the electron number density, which is proportional to square of wave function mode:

$$\rho_e(r) = |\psi_e(r)|^2 \quad (8.90)$$

Therefore, a self-consistent wave function exists. It meets the mathematical solution of the equation and establishes the relation in physics. Therefore we can use an iterated operation to obtain its approximation solution.

From the introduction above we see that the *ab initio* calculation is established for solving electron motion theory, that is, it is suitable for solving the problems of electron energy band structure in semiconductors.

#### 8.5.1.2 Application of *ab initio* Calculation

- Application for the dispersion relation calculation of phonons [66]

The calculation of phonons is established as the correct calculation of ground state energy. The key of phonon calculation is to work out each component of the force constant matrix (Hessian matrix). In crystals, we assume the position of the  $l$ th atom can be expressed as

$$\mathbf{R}_l = \mathbf{R}_{ol} + \mathbf{r}_0 + \mathbf{u}(l) \quad (8.91)$$

where the first term of the equation is the position in the Bravais lattice of the unit cell, the second and third terms are the equilibrium position in the unit cell, and the displacement relative to equilibrium position of this atom.

The calculation of phonons is first based on the Schrodinger equation of multi-electron system motion. By using the iterated operation, the total energy of all fixed ions can be obtained, which is the Bron–Oppenheimer energy surface. Through solving the energy second derivative relative to atom equilibrium position of the Bron–Oppenheimer energy surface, the force constant matrix (Hessian matrix) is solved as

$$C_{st}^{\alpha\beta}(l, m) = \frac{\partial^2 E}{\partial u_s^\alpha(l) \partial u_l^\beta(m)} \quad (8.92)$$

The phonon frequency is the solution of the secular equation:

$$\det \left| \frac{1}{\sqrt{M_s M_t}} C_{st}^{\alpha\beta}(q) - \omega^2(q) \right| = 0 \quad (8.93)$$

where subscript  $s, t$  is the different kinds of atoms; parameter  $l, m$  is non-equivalence atoms; and  $\alpha, \beta$  is the Cartesian components.

Since one atom has three degrees of freedom of motion, the crystal containing  $N$  atoms has three  $N$  Eigen vibration frequencies. Considering the crystal has three translation degrees of freedom as a whole, then three of  $3N$  Eigen frequencies must

equal zero. As  $N$  is usually very large and about  $10^{23}$  orders of magnitude, we can ignore the difference between  $3N$  and  $3N-3$ . According to Equation (8.93), if it is worked out that phonon frequencies correspond to all wave vector  $q$  in first Brillouin zone,  $3N$  eigen vibration frequencies are solved. Then we can draw the distribution diagram of PDOS.

In practical calculations, we usually takes samples in the first Brillouin zone, that is, take certain amounts of wave vectors and then obtain their eigen frequencies. This enables us to obtain a distribution of phonon frequencies with wave vectors and thus the dispersion of the phonon is produced.

- Application for Si/Ge superlattices [67]

Qteishand and Molinari calculated the lattice dynamics of longitudinal mode in the Si/Ge superlattice by the *ab initio* method. The lattice constant of Ge differs from that of Si by 6%, thus the Si/Ge superlattice is the strained-layer superlattice. The calculation by the *ab initio* method is related to the atomic layer and so is helpful in identifying the physical features of Ge/Si superlattices at the atomic level.

Figures 8.38(a)–(c) are the calculated model and results for a  $\text{Ge}_4/\text{Si}_4$  superlattice orientation along (001), respectively. Figures 8.39(b) and (c) show the calculated dispersion curves and the change of longitudinal displacement amplitude along the  $z$  direction in a unit cell for phonons at point  $\Gamma$ .

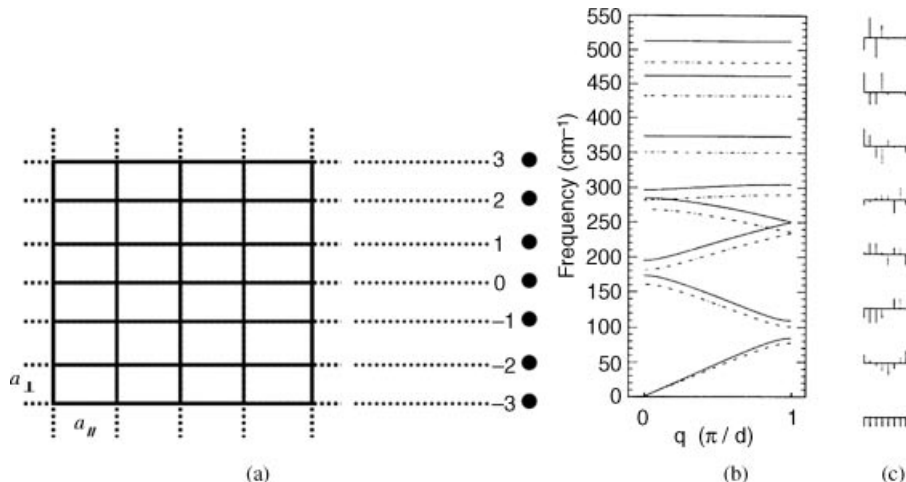


**Figure 8.38** (a) Geometry of the freestanding infinite crystal in the presence of biaxial strain in the (001) plane; (b) dispersion along [001] direction of longitudinal phonon for [001]-oriented  $\text{Si}_4\text{Ge}_4$  superlattices, where solid and dashed-dotted lines represent the lattice matching to Si and Ge substrates, respectively; (c) amplitude of longitudinal  $\Gamma$ -point phonon displacements as a function of the  $z$ -position of the (001) atomic planes in the unit cell. Reprinted from W. Liu, M. X. Liu and S. L. Zhang, Dependence of vibrational density of states and Raman spectra on size in non-polar and polar nano-crystalline semiconductors, *Physics Letters A*, 372, 2474–2479 (2008)

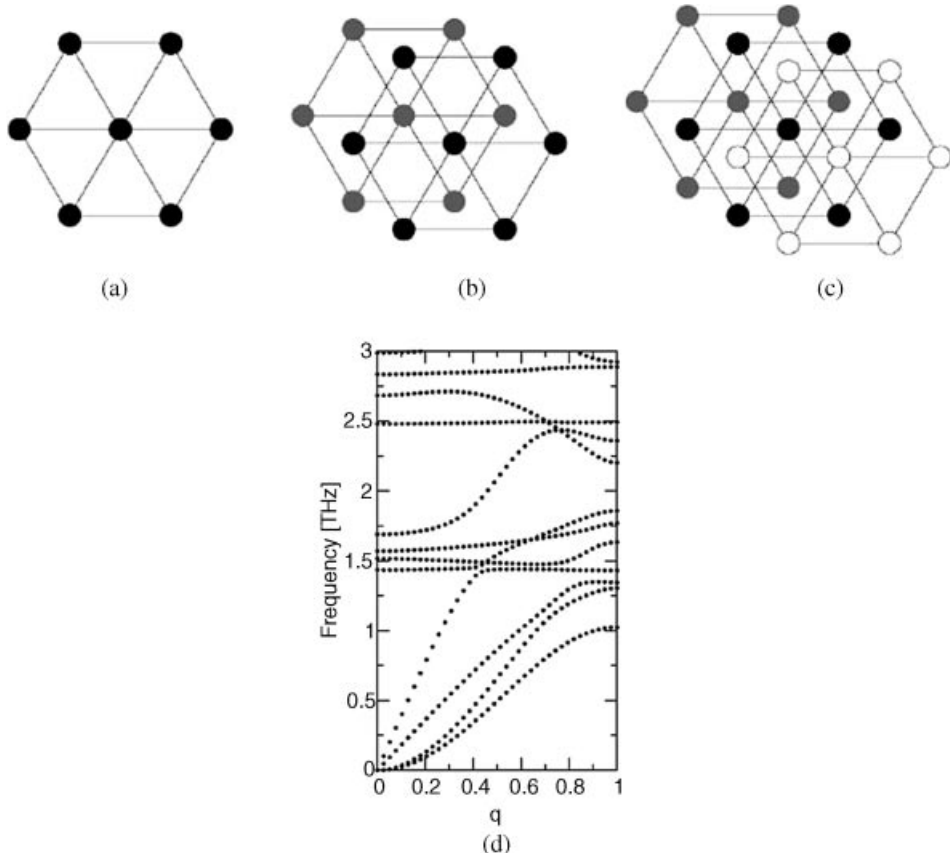


**Figure 8.39** Approximation for an Si [111] nanowire by a hexagonal-shaped cross section. Depicted are the placing of the first two layers as black spheres (a), the two middle layers in gray (b), and the last two layers as white spheres (c). (d) Some low frequencies of the phonon spectrum for an Si [111] nanowire. In (d),  $q$  refers to the reduced wave vector [68]. Reprinted from A. Qteish and E. Molinary, Phys. Rev. B, 42, 7090–7096 (1990) with permission of the American Physical Society

- Application for Si [111] nanowires [68]  
Thonhauser and Mahan used the classic dynamics theory to solve long wave optical phonon with amplitude  $Q_\mu$ . The dynamics equation is

$$\omega(q)^2 Q_\mu = \omega_0^2 Q_\mu + \omega_c^2 t_{\mu\nu}(q) Q_\nu - F_{\mu\nu\alpha\beta} q_\alpha q_\beta Q_\nu \quad (8.94)$$

The first term on the right comes from the short-range force of nearest neighbors and the second term is the long-range dipole interaction expressed as

$$t_{\mu\nu}(q) = 3q_\mu q_\nu / q^2 - \delta_{\mu\nu} \quad (8.95)$$

The calculation model is approximated by a hexagonal cross section and the calculated results are shown in Figures 8.39(a)–(d), respectively.

These results indicate that the eigen vectors for acoustic phonons are in agreement with the well-known boundary conditions of vanishing surface stress. In addition, the eigen vectors for the optical modes reveal that all displacements at the surface of the wire are zero.

### 8.5.2 Molecular Dynamic Calculation

The atomic number calculated by original *ab initio*/first principle calculation is still much limited. Thus ones introduced various calculated methods based on the first principle, of which the molecular dynamic calculation is used widely.

Molecular dynamic calculation is a simulation technique for computing classical many-body system, in which the nuclear motion of particles obeys the laws of classical mechanics. The molecular dynamic calculation provides a possibility for the computer simulation with limited calculation condition. This advantage has the calculation to be possible for a system with much more atoms.

The equation of motion for atomic system can be shown in many ways. In molecular dynamic, the usual form is the Lagrangian equation of motion:

$$\frac{d}{dt} \left( \frac{\partial \mathcal{L}}{\partial \dot{q}_k} \right) - \left( \frac{\partial \mathcal{L}}{\partial q_k} \right) = 0 \quad (8.96)$$

Where the Lagrangian function  $\mathcal{L}(q, \dot{q})$  is defined as  $\mathcal{L} = T - V$ . If we use Cartesian coordinates rather than generalized coordinates, the equation become:

$$m_i \ddot{r}_i = f_i \quad (8.97)$$

Where  $m_i$  is the mass of atom  $i$  and  $f_i$  is the force on that atom and equals minus gradient of potential. So after solving the differential equation, we can obtain the motion of each atom and further the material properties defined by the statistical mechanics of all the atoms.

#### 8.5.2.1 Cluster model of molecular dynamic calculation [69]

The calculation of PDOS in terms of the molecular mechanics simulation with the cluster model is introduced shortly as follows. First, a stable cluster structure should be produced. If the bulk crystal structure of calculated clusters is a face-centered cubic (FCC) lattice, all clusters were modeled initially using a network with cubically aligned atoms. The number of atoms in each cluster and corresponding cluster sizes are listed in Table 8.3, for Si, diamond SiC and InSb. The stable structures with minimum energy are obtained via geometry optimization. As a sample, the optimized cluster structures of various Si atomic number are shown in Figure 8.40. Secondly, Phonon frequencies are calculated based on the optimized structures. Then PDOS in histogram form is obtained by counting the number of phonon modes in a certain frequency interval. Finally, after PDOS is convoluted by a Gaussian function, the calculated Raman spectra is produced. Figure 8.41 show the convoluted and normalized PDOS, i.e., Raman spectra, of Si, diamond, SiC and InSb clusters [69].

To facilitate comparison with the observed Raman spectra, the PDOS bands should be classified, based on the correlation between the PDOS and phonon dispersion curve [64],

**Table 8.3** Number of atoms and corresponding size of Si, diamond, SiC, and InSb clusters [69]. Reprinted from S. L. Zhang, et al., Study on the applied limitation of the micro-crystal model for Raman spectra of nano-crystalline semiconductors, *J. Raman Spec.*, 39, 1578–1583 (2008)

Number of Atoms	Sizes (nm)	
	Si	Diamond
216	1.49	0.98
344	1.76	1.16
512	2.08	1.34
1000	2.57	1.69
1728	3.12	2.05
2198	3.39	2.23
		SiC
		InSb
512	2.12	2.42
730	2.40	2.75
1000	2.69	3.07
1332	2.97	3.39
1728	3.25	3.72
2198	3.53	4.04

we label in the acoustic phonon region of Si and diamond as the transverse acoustic-like (TA-like) band and longitudinal-acoustic-like (LA-like) band, and those in the optical phonon region as optical-like bands. Furthermore, for SiC and InSb, we divide optical-like bands into two subdivisions: transverse-optical-like (TO-like) and longitudinal-optical-like (LO-like) bands.

The theoretical and experimental dependence of Si optical phonon frequency on Si nanoparticle size are shown in Figure 8.42. From Figure 8.42, it can be seen that the agreement between calculated and observed results is pretty good.

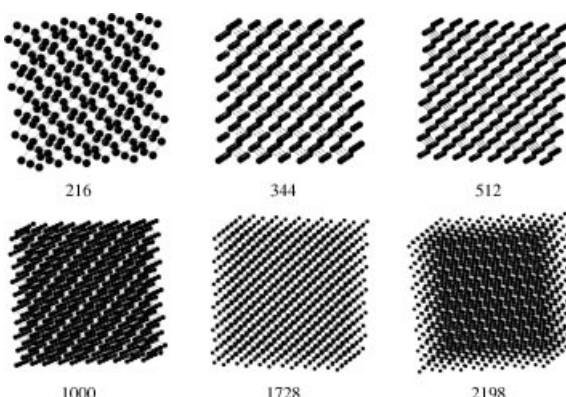


**Figure 8.40** Optimized Si cluster structures of various  $i$  atomic number [69]. Reprinted from T. Thonhauser and G. D. Mahan, Phonon modes in  $\text{Si}^{+111^{\ddagger}}$  nanowires, *Phys. Rev. B*, 69, 075213 (2004) with permission of the American Physical Society

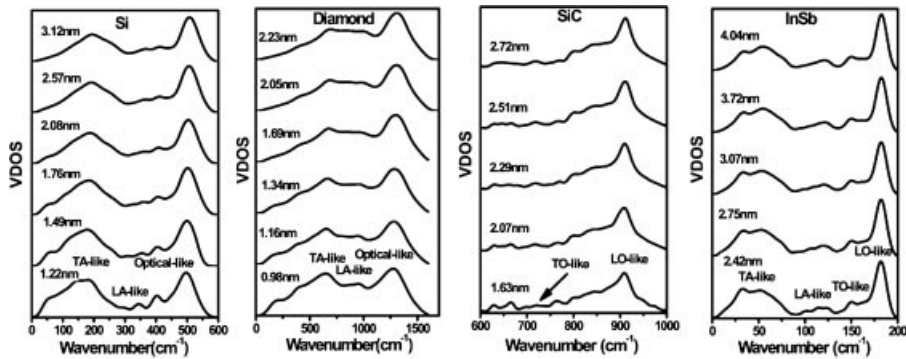


**Figure 8.41** Convolved and normalized PDOS of Si, diamond, SiC, and InSb clusters [69]. Reprinted from W. Liu, M. X. Liu and S. L. Zhang, Dependence of vibrational density of states and Raman spectra on size in non-polar and polar nano-crystalline semiconductors, Physics Letters A, 372, 2474–2479 (2008)

### 8.5.2.2 Molecular mechanics simulation with the empirical potential

This method gets help from the empirical pseudo-potential method in bulks, in which the structure and form factors in potential are determined by fitting experimental date. In the practical calculation it has introduced various models.

- Shell model

In the shell model, each ion is considered as a point core surrounded by a massless shell. The ion is accounted for by the force constant  $K$  in a spring potential:

$$V_s = \frac{1}{2}k_2r^2 \quad (5.98)$$

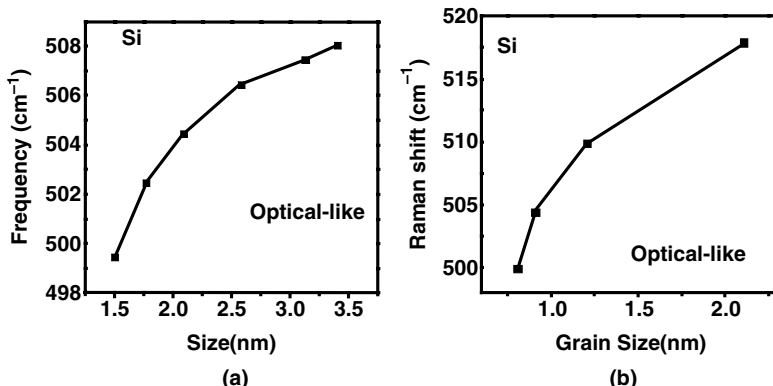


**Figure 8.42** The theoretical (a) and experimental (b) dependence of Si optical phonon frequency on sizes for Si nano-particles. Reprinted from W. Liu, M. X. Liu and S. L. Zhang, Dependence of vibrational density of states and Raman spectra on size in non-polar and polar nano-crystalline semiconductors, Physics Letters A, 372, 2474–2479 (2008)

**Table 8.4** Empirical parameters of interactions used in the calculation of ZnO NPs;  $O_s$  and  $O_c$  stand for the shell and core of O respectively, Zn<sub>c</sub> stands for Zn core

	A(eV)	r(Å)	C (eV × Å <sup>6</sup> )	k (eV × Å <sup>-2</sup> )	Charge ( e )
O <sub>s</sub> -O <sub>s</sub>	22772.92	0.1330	89.7564		Zn <sub>c</sub> 2.1
Zn <sub>c</sub> -O <sub>s</sub>	648.47	0.3529	0.1034		O <sub>s</sub> -3.49
O <sub>c</sub> -O <sub>s</sub>				54.6594	O <sub>c</sub> 1.39

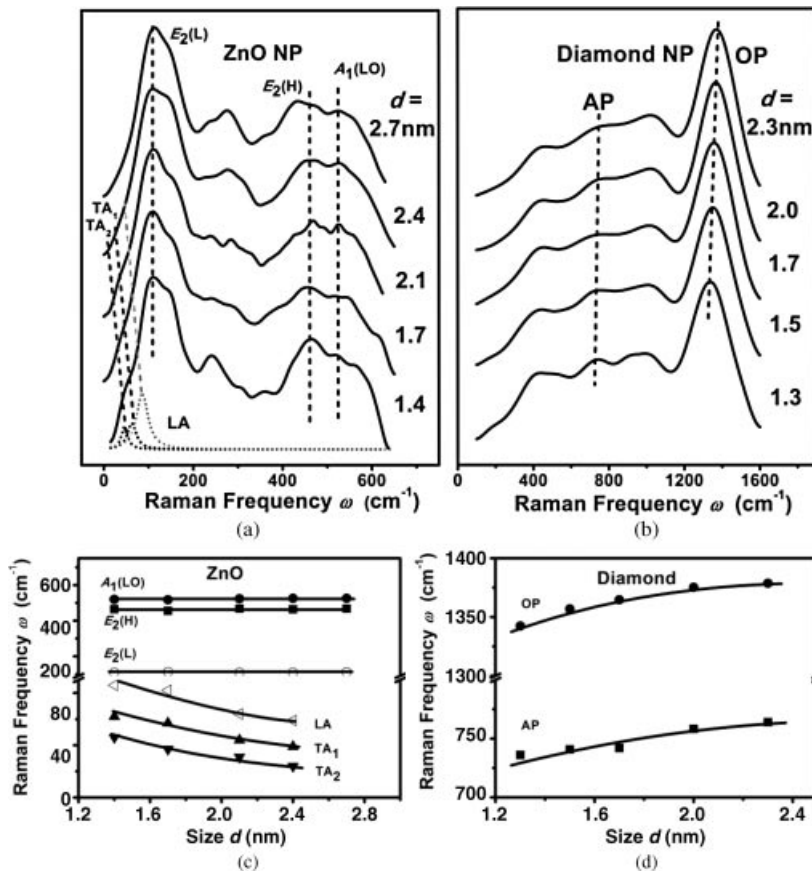


**Figure 8.43** Calculated Raman spectra with the assignment of phonon modes of ZnO (a) and diamond (b) NPs; calculated dependence of phonon frequency on sample size  $d$ 's for ZnO(c) and diamond (d) NPs. Where E<sub>2</sub>(L) and E<sub>2</sub>(H) are low and high frequency E<sub>2</sub> symmetry optical phonons, respectively; A<sub>1</sub>(LO) is longitudinal A<sub>1</sub> symmetry optical phonon; LA and TA (TA<sub>1</sub> and TA<sub>2</sub>) are longitudinal and transverse acoustic phonons, respectively; OP and AP are optical and acoustic phonons, respectively

The central force and short-ranged potential is described by Born-Mayer-Buckingham form:

$$V_r = a \exp(-r/r_0) - cr^{-6} \quad (5.99)$$

The potential parameters are obtained by the fitting to property the parameters corresponding to bulks. These parameters include the lattice constant, elastic and dielectric constant [70].

Shell model is pretty perfect in describing ionic crystal. We used this model to calculate ZnO nano-particles (NPs). Table 8.4 lists the model parameters representing the interatomic interaction in the lattice after fitting for ZnO. In the calculation, first, different sizes  $d$  of ZnO NPs were constructed according to the crystal structure. Then we make the geometry optimization and then calculated the vibration properties of each particle and finally gave out the PDOS. The final PDOS smoothed by a Gaussian function with a width of  $10\text{ cm}^{-1}$  to obtain Raman spectrum as shown in Figure 8.43a.

- Reactive empirical bond order model

The reactive empirical bond order (REBO) model introduced by Brenner etc. at 2002 [71], which are widely used in diamond simulation. So we use REBO to optimize and calculate five different sizes of diamond NPs. The final PDOS is smoothed by a Gaussian function with a width of  $10\text{ cm}^{-1}$  and  $5\text{ cm}^{-1}$  to obtain the Raman spectrum and is shown in Figure 8.43b. The calculated dependence of phonon frequency on sample sizes are shown in Figure 8.43c and d for ZnO and diamond NPs, respectively. After comparing of calculated results with experimental data [72–74], it is found that the calculated results agree very well with experimental ones for ZnO and diamond NPs both.

## References

- [1] Fröhlich, H. (1949) *Theory of Dielectrics*, Oxford University Press, Oxford.
- [2] Roseustock, H.B. (1961) *Phys. Rev.*, **121**, 416–424.
- [3] Nair, I.R. and Walker, C.T. (1972) *Phys. Rev. B*, **5**, 4101–4104.
- [4] Martin, T.P. and Genzel, L. (1973) *Phys. Rev. B*, **8**, 1630–1635.
- [5] Jusserand, B., Paquet, D., and Regreny, A. (1984) *Phys. Rev. B*, **30**, 6248.
- [6] Jusserand, B. and Cardona, M. (1989) in *Raman Spectroscopy of Vibration in Superlattices, in Light Scattering in Solids V* (eds M. Cardona and G. Güntherodt), Springer-Verlag, Berlin.
- [7] Kanallis, G., Morhange, J.F., and Balkanski, M. (1980) *Phys. Rev. B*, **21**, 1543–1548.
- [8] Fuchs, R. and Kliewer, K.L. (1965) *Phys. Rev.*, **140**, A2076–A2088.
- [9] Kelly, M.J. (1995) *Low-Dimensional Semiconductors: Materials, Physics, Technology, Devices*, Oxford University Press., New York.
- [10] (a) Colvard, C., Merlin, R., Klein, M.V., and Gossard, A.C. (1980) *Phys. Rev. Lett.*, **45**, 298–301; (b) Colvard, C., Gant, T.A., Klein, M.V., Merlin, R., Fischer, R., Morkoc, H., and Gossard, A.C. (1985) *Phys. Rev. B*, **31**, 2080–L-2091.
- [11] Retov, S.M. and Akust, Zh. (1956) *Sov. Phys. Acoust.*, **2**, 68.
- [12] Sood, A.K., Menendez, J., Cardona, M., and Ploog, K. (1985) *Phys. Rev. Lett.*, **54**, 2115–2118.
- [13] Hu, X. and Zi, J. (2002) *J. Phys.: Condens. Matter*, **14**, L671.
- [14] Fasolino, A., Molinary, E., and Maan, J.C. (1986) *Phys. Rev. B*, **33**, 8889–8891.

- [15] (a)Huang, K., Zhu, B.F., and Tang, H. (1990) *Phys. Rev. B*, **41**, 5825–5842; (b) Huang, K. and Huang, L. (1951) *Acta Phys. Sin.*, **8**, 207, *Chn. Physics*.
- [16] Yip, S.K. and Chang, Y.C. (1984) *Phys. Rev. B*, **30**, 7037–7058.
- [17] Othman, N. and Kawamura, K. (1990) *Solid State Commun.*, **75**, 711–718.
- [18] Richter, H., Wang, Z.P., and Ley, L. (1981) *Solid State Commun.*, **39**, 625–629.
- [19] Martin, T.P. and Genzel, L. (1973) *Phys. Rev. B*, **8**, 1630–1638.
- [20] Novoselov, K.S., Geim, A.K., Morozov, S.V. *et al.* (2004) *Science*, **306**, 666–669.
- [21] Kroto, H.W., Heath, J.R., O'Brien, S.C. *et al.* (1985) *Nature*, **318**, 162–163.
- [22] Yildirim, T. and Harris, A.B. (1992) *Phys. Rev. B*, **92**, 7878.
- [23] Iijima, S. (1991) *Nature*, **56**, 354.
- [24] Iijima, S. and Ichihashi, T. (1993) *Nature*, **363**, 603–605.
- [25] Bethune, D.S., Kiang, C.H., Vries, M.S. *et al.* (1993) *Nature*, **363**, 605–607.
- [26] Saito, R., Takeya, T., Kimura, T. *et al.* (1998) *Phys. Rev. B*, **57**, 4145–4153.
- [27] Dresselhaus, M.S., Dresselhaus, G., and Eklund, P.C. (1996) *J. Raman Spectrosc.*, **27**, 351.
- [28] Maultzsch, J., Reich, S., Thomsen, C. *et al.* (2004) *Phys. Rev. Lett.*, **92**, 075501.
- [29] Dubay, O. and Kresse, G. (2003) *Phys Rev B*, **67**, 035401.
- [30] Jorio, A., Saito, R., Hafner, J.H. *et al.* (2001) *Phys. Rev. Lett.*, **86**, 1118–1121.
- [31] Comas, F., Giner, C.T., and Cantarero, A. (1993) *Phys. Rev. B*, **47**, 7602–7605.
- [32] Mahan, G.D., Gupta, R., Xiong, Q. *et al.* (2003) *Phys. Rev. B*, **68**, 073402.
- [33] Comas, F., Cantarero, A., Giner, C.T., and Moshinsky, M. (1995) *J. Phys.: Condens. Matter*, **7**, 1789–1808.
- [34] Mooradian, A. and Wright, G.B. (1966) *Solid State Commun.*, **4**, 431–434.
- [35] Wilkinson, G.R. (1973) in *Raman Effect* (ed. A. Anderson), Dekker, New York.
- [36] Yu, P. and Cardona, M. (2001) in *Physics of Semiconductors*, Springer, New York.
- [37] Zhu, B.F. (1991) *Phys. Rev. B*, **44**, 1926–1929.
- [38] Zhang, L. and Xie, H.J. (2004) *International journal of Modern Physics B*, **18**, 379–393.
- [39] Campbell, I.H. and Fauchet, P.M. (1986) *Solid State Commun.*, **58**, 739–741.
- [40] Jusserand, B. and Sapriel, J. (1981) *Phys. Rev. B*, **24**, 7194–7205.
- [41] Parayenthal, P. and Pollak, F.H. (1984) *Phys. Rev. Lett.*, **52**, 1822–1828.
- [42] Sui, Z., Leong, P.P., Herman, I.P. *et al.* (1992) *Appl. Phys. Lett.*, **60**, 2086–2088.
- [43] Li, B.B., Yu, D.P., and Zhang, S.L. (1999) *Phys. Rev. B*, **59**, 1645–1648.
- [44] Yoshikawa, M., Mori, Y., Obata, H. *et al.* (1995) *Appl. Phys. Lett.*, **67**, 694–696.
- [45] Hou, Y.T., Feng, Z.C., Li, M.F., and Chua, S.J. (1999) *Surf. Interface Anal.*, **28**, 163–168.
- [46] Lin, L.Y., Chang, C.W., Chen, W.H. *et al.* (2004) *Phys. Rev. B*, **69**, 075204.
- [47] Paillard, V., Puech, P., Laguna, M.A. *et al.* (1999) *J. Appl. Phys.*, **86**, 1921.
- [48] Novikov, S.V. and Malliaras, G.G. (2006) *Phys. Rev. B*, **73**, 033308.
- [49] Adu, K.W., Gutierrez, H.R., Kim, U.J. *et al.* (2005) *Nano Lett.*, **5**, 409–414.
- [50] Lin, K.F., Cheng, H.M., Hsu, H.C., and Hsieh, W.F. (2006) *Appl. Phys. Lett.*, **88**, 263117.
- [51] Zi, J., Zhang, K., and Xie, X. (1997) *Phys. Rev. B*, **55**, 9263–9266.
- [52] Paillard, V., Puech, P., Laguna, M.A. *et al.* (1999) *J. Appl. Phys.*, **86**, 1921–1924.
- [53] Zhang, S.L., Wu, S.N., Yan, Y. *et al.* (2008) *J. Raman Spec.*, **39**, 1578–1583.
- [54] Zhang, S.L., Hou, Y., Ho, K.S., Qian, B., and Cai, S. (1992) *J. Appl. Phys. Rev.*, **72**, 4469.
- [55] Rao, A.M., Richter, E., Bandow, S. *et al.* (1997) *Science*, **275**, 188.
- [56] Zhang, S.L., Ding, W., Yan, Y. *et al.* (2002) *Appl. Phys. Lett.*, **81**, 4446–4448.
- [57] Eklund, P.K. (2000) in *The XVIIIth International Conference on Raman Spectroscopy* (ed. J. Mink), John Wiley & Sons, Budapest.
- [58] Kanellis, G., Morhange, J.F., and Baslanski, M. (1980) *Phys. Rev. B*, **21**, 1543.
- [59] Li, B.B., Yu, D.P., and Zhang, S.L. (1999) *Phys Rev B*, **59**, 1645–1648.
- [60] Shen, M. and Zhang, S.L. (1993) *Phys. Lett. A*, **176**, 254–258.
- [61] Nemanich, R.J., Solin, S.A., and Martin, R.M. (1981) *Phys. Rev. B*, **23**, 6348–6356.

- [62] Yip, S.K. and Chang, Y.C. (1984) *Phys. Rev. B*, **30**, 7037–7059.
- [63] Zhang, S.L., Zhu, B.F., Huang, F. et al. (1999) *Solid State Commun.*, **111**, 647–651.
- [64] Yu, P.Y. and Cardona, M. (2004) in *Fundamentals of Semiconductors*, Springer Verlag, Berlin.
- [65] Kittel, C. (1986) *Introduction to Solid State Physics*, John Wiley & Co, New York.
- [66] Baroni, S., Gironcoli, S., Corso, A.D., and Giannozzi, P. (2001) *Rev. Mod. Phys.*, **73**, 515–562.
- [67] Qteishand, A. and Molinary, E. (1990) *Phys. Rev. B*, **42**, 7090–7096.
- [68] Thonhauser, T. and Mahan, G.D. (2004) *Phys. Rev. B*, **69**, 075213.
- [69] Liu, W., Liu, M.X., and Zhang, S.L. (2008) *Phys. Lett. A*, **372**, 2474–2479.
- [70] Özgür, Ü. and Ya. I. J. (2005). *Appl. Phys.* **98**, 041301.
- [71] Donald W Brenner, Olga A Shenderova. (2002) *J. Phys.: Condens. Matter*, **14**, 783–802.
- [72] Zhang, S. L., Zhang, Y., and Fu, Z. et al. (2006) *Appl Phys Lett.* **89**, 243108.
- [73] Yadav, H. K., Gupta, V., and Sreenivas K. et al. (2006) *Phys. Rev. Lett.* **97**, 085502.
- [74] Chassaing\_P\_M" P.-M. Chassaing, HYPERLINK F. Demangeot, and HYPERLINK Combe\_N" N. Combe (2009) *Phys. Rev. B* **79**, 155314.

# 9

## Routine Raman Spectra of Nanostructures

Routine Raman spectra are defined as those obtained by using pure samples under routine conditions, i.e., by routine laser excitation and in an atmospheric environment. The resulting single phonon Stokes spectra are named as characteristic or fingerprint spectra usually. The characteristic Raman spectrum of a specific object is the basis of the characterization and investigation of using Raman spectroscopy for this object.

In Chapter 8, based on physical analysis and theoretical deduction, we introduced common Raman spectral features of nanostructures. In this chapter we will show the Raman spectral features of nanostructures mainly based on experimental measurements of some typical samples. Concerning the experimental measurement of nanostructure Raman spectra, there are some “innate” difficulties, such as:

- (1) The Raman scattering signal from nanostructures is weak often.
- (2) It is difficult to obtain samples of high purity from many nanostructure materials.  
For example, nano-semiconductor samples often contain un-reacted raw materials, intermediate products, impurities, and defects arising from the reaction process, as well as becoming metamorphosed by oxidization and pollution due to their huge specific surface area.
- (3) The observed new or “abnormal” spectral features often encounter difficulty in finding a reasonable explanation based on traditional theory.

The difficulties mentioned above lead to characteristic Raman spectra being difficult to acquire and can result in wrong identification [1,2]. For example, a wrong characteristic Raman spectrum of a PSCVD growing nanocrystalline diamond [2] was used for more than ten years.

To overcome these “congenital” problems and avoid errors, experiments need to pay attention to appropriate technological procedures, as already described in Chapters 4 and 5. Also, the theoretical and experimental levels must be enhanced and enriched continuously.

Chapter 7 mentioned that the bulk materials with same crystal structures and symmetries have common Raman spectral features and their Raman spectra can be classified based on the symmetry of these structures. However, as mentioned in Chapter 8, there are obvious and important differences in the Raman spectral features between superlattices (SL)s and other nanostructure materials, as well as between polar and nonpolar semiconductors. Therefore, the Raman spectra of nanostructures will be classified and introduced according to the classification of nanomaterials mentioned above.

## 9.1 Characteristic Raman Spectra of Semiconductor Superlattices

After physical demonstration and theoretical calculations described in Chapter 8, we have learned that there are three categories and five kinds of phonon modes in semiconductor SLs: one of the categories contains optical phonon modes confined in the barrier layers and well layers, respectively; another is the folded acoustic phonon mode; while the third is the interface mode related to the interfaces of SLs. The latter is subdivided into two types: the macro type and the micro type. In addition, according to the vibration direction, they are further divided into the longitudinal and transverse modes. Figure 9.1 shows the spatial feature of vibration mode of SL phonons. The optical phonons confined in the barrier layers and well layers are labeled  $O_B$  and  $O_W$ , respectively. The folded acoustic phonon is labeled A, which is spread throughout the entire SL. The macro- and micro-interface phonons are labeled IF and MIF, respectively, of which the largest amplitudes are both localized at the interfaces but reduce with exponential and localized atomic layers, respectively. In this section, we introduce experimental identification and analysis of these modes.

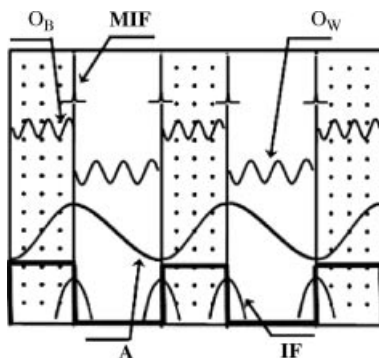


**Figure 9.1** Sketch of vibration modes of five kinds of SL phonons.  $O_W$  and  $O_B$  label the optical phonons confined in the barrier and well layers, respectively. A marks the folded acoustic phonons. IF and MIF are the labels of macro- and micro-interface phonons, respectively. Reprinted from S.-L. Zhang, *Raman Spectroscopy and Low-dimensional nanoscale Semiconductors*, Science Press, (2008)

In the phonon modes mentioned above, the folded acoustic phonon mode was observed in 1980 by Colvard. [3] The confined optical mode within the well layers and barrier layers were also observed by Jussrand *et al.* in 1984 [4] and Zhang *et al.* in 1986, [5] respectively. The macro-and micro-interface modes were identified by Sood *et al.* in 1985 [6] and Jin *et al.* in 1992 [7], respectively.

### 9.1.1 Folded Acoustic Phonon Mode

Section 8.1 pointed out that due to new longer periods in the growth direction of superlattices, bulk dispersion curves in the large Brillouin zone are folded into the small Brillouin zone. Because of this folding effect, acoustic phonon dispersion curves and light dispersion curves can intersect and, therefore, the Raman inactive acoustic phonon in a bulk material becomes Raman active in SLs. Therefore, the observation of acoustic phonon Raman spectra could become a test for the lattice dynamics of SLs. Thus, the observation of acoustic phonon SL in experiments became the first concern in the research of SL Raman spectroscopy.

In 1978, Barker *et al.* published the first observations of acoustic phonon Raman spectrum in SLs [8]. However, a real Raman spectrum from folded acoustic modes was observed in GaAs/AlAs SLs by Colvard *et al.* in 1980, which is shown in Figure 9.2 [3]. The figure clearly shows that there is a double mode structure at 63.1 and 66.9  $\text{cm}^{-1}$ . By considering the Fröhlich coupling correction and the electric-phonon coupling deformation potential, Colvard *et al.* used the elastic continuum model for phonons and the Kroig–Penney model for electrons, to calculate the folded acoustic modes. As shown in Figure 9.3, the calculated results not only fit the experimental data well but also explain the double mode spectral structure and other observed experimental phenomena, such as the Raman spectra selection rule and resonance enhancement effect. Since then, further observations of other folded acoustic phonon in different componential SL or multilayer structures have been made. Figure 9.4 shows that the Raman spectra of folded acoustic phonon modes were observed in the amorphous Si/Ge multi-layer structure of different periods constructed by different atomic monolayers of Si and Ge.

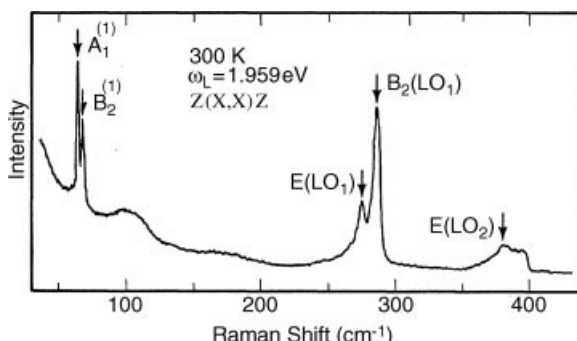


**Figure 9.2** Raman spectrum of SL GaAs/AlAs,  $A_1$  and  $B_2$ , are assigned to folded acoustic phonons [3]. Reprinted from C. Colvard, R. Merlin, M. V. Klein and A. C. Gossard, Observation of Folded Acoustic Phonons in a Semiconductor Superlattice, *Phys. Rev. Lett.*, 45, 298–301 (1980) with permission of the American Physical Society

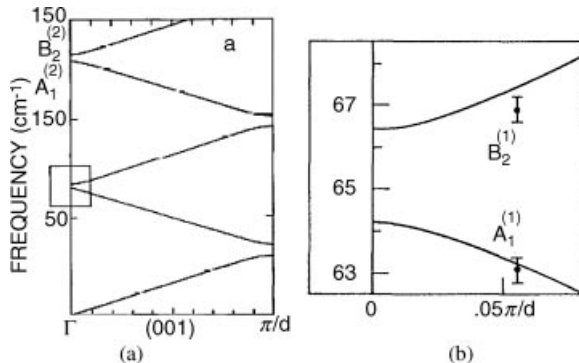


**Figure 9.3** Dispersion of longitudinal phonons in the SL. The region indicated by a square is shown in detail in (b), where the dots correspond to the experimental values for the phonon frequencies [3]. Reprinted from C. Colvard, R. Merlin, M. V. Klein and A. C. Gossard, Observation of Folded Acoustic Phonons in a Semiconductor Superlattice, *Phys. Rev. Lett.*, 45, 298–301 (1980) with permission of the American Physical Society

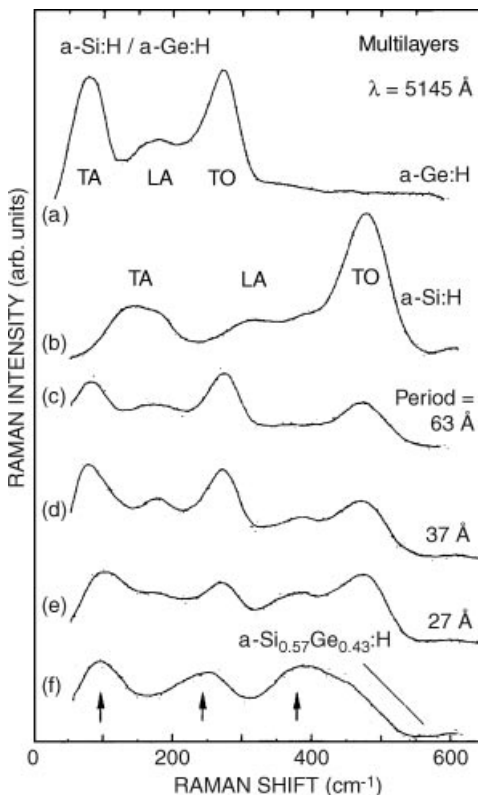


**Figure 9.4** Raman spectra of (a) a-Ge:H; (b) a-Si:H; (c)–(e) a-Si:H/a-Ge:H SLs with different period; and (f) a-Si<sub>0.57</sub>Ge<sub>0.43</sub>:H alloy. [9]. Reprinted from P. V. Somtos and L. Ley, Characterization of a-Si:H/a-Ge:H superlattices by Raman scattering, *Phys. Rev. B*, 36, 3325–3335 (1987) with permission of the American Physical Society

**Table 9.1** Parameters of sample used in Figure 9.5, where  $d$ ,  $\bar{x}$ ,  $n_1$ , and  $n_2$  represent period, average Al content, and layer thicknesses (in number of atomic monolayer) of  $(\text{GaAs})_{n1}/(\text{Ga}_{1-x}\text{Al}_x\text{As})_{n2}$ , respectively. Reprinted from B. Jusserand, D. Paquet and A. Regreny, "Folded" optical phonons in  $\text{GaAs}/\text{Ga}_{1-x}\text{Al}_x\text{As}$  superlattices, Phys. Rev. B, 30, 6245–6247 (1984) with permission of the American Physical Society

	$d(\text{\AA})$	$\bar{x}$	$n_1$	$n_2$
S2	29.2	0.123	6	4
S5	51	0.147	9	9
S7	54.4	0.141	12	7
S9	81.4	0.145	17	12

### 9.1.2 Confined Optical Mode

#### 9.1.2.1 Confined Longitudinal Optical (LO) Mode within the Well Layers of SLs

The confined optical phonons within the well layers of quantum well structures were first observed by Jusserand *et al.* in  $\text{GaAs}/\text{Ga}_{1-x}\text{Al}_x\text{As}$  SL [4]. Raman spectra in the  $z(x, y)\bar{z}$  configuration from four samples, with the parameters listed in Table 9.1 and shown in Figure 9.5, show that pitch arcs labeled 1, 2, 3, and 4 represent the change trend of Raman

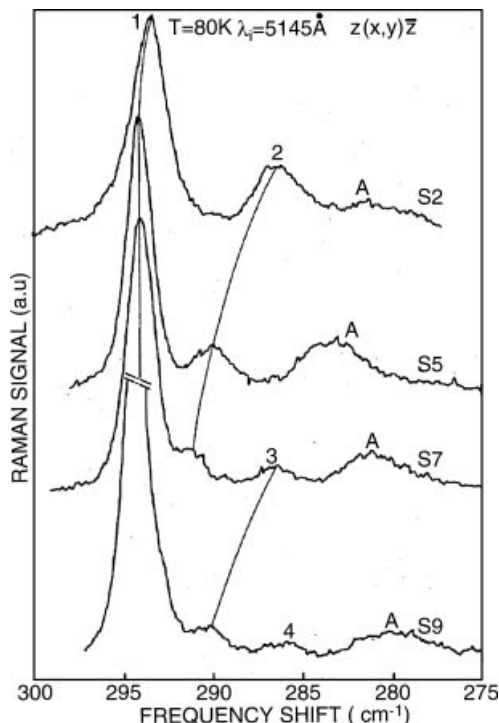


**Figure 9.5** Raman spectra of confined optical phonon of  $(\text{GaAs})_{n1}/(\text{Ga}_{1-x}\text{Al}_x\text{As})_{n2}$  SLs S2, S5, S7, and S9 [4]. Reprinted from B. Jusserand, D. Paquet and A. Regreny, "Folded" optical phonons in  $\text{GaAs}/\text{Ga}_{1-x}\text{Al}_x\text{As}$  superlattices, Phys. Rev. B, 30, 6245–6247 (1984) with permission of the American Physical Society

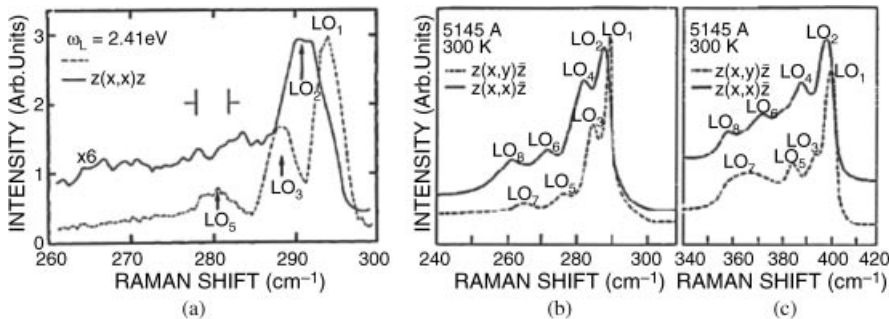


**Figure 9.6** Raman spectra of GaAs confined LO phonons (a) (b) and AlAs-confined LO phonons (c) in GaAs/AlAs SLs [10, 12]. Reprinted from S. L. Zhang, T. A. Gant, M. Delane, et al., Resonant Behaviour of GaAs LO Phonons in GaAs-AlAs Superlattice, Chin. Phys. Lett., 5, 113–116 (1988)

peak frequency of phonons with the same confined order. Figure 9.5 and Table 9.1 show that the change dependences of absolute frequency for the same confined ordered phonons and frequency difference between different confined ordered phonons with thickness of GaAs wells  $n_1$  and the size confinement effect on optical phonons of SLs is confirmed visually.

Since the work by Jussrand *et al.*, further research works on the optical phonons in quantum well structures were published, of which some samples are shown in Figure 9.6. Figures 9.6(a)–(c) show the Raman spectra of GaAs and AlAs confined LO phonons in GaAs/AlAs SLs, as observed by Sood *et al.* [10], Wang *et al.* [11], and Zhang *et al.* [12]. Figure 9.6 shows that the Raman scattering from not only odd but also even LO phonons appears and there is a selection rule: the phonons with odd (the number of confined order  $m = \text{odd}$ ) and even ( $m = \text{even}$ ) parities appear in the depolarized ( $x,y$ ) and polarized ( $x,x$ ) configurations, respectively.

Huang *et al.* interpreted the above experimental results based on their developed microscopic theory of Raman scattering [13]. In bulk semiconductors, in the dipole approximation, the Fröhlich interaction accompanied by polar semiconductors is not effective in Raman scattering, which means the dipole mode is impossible. However, the microscopic theory of Raman scattering deduced that even in the case of dipole approximation, the Fröhlich interaction does contribute to the Raman scattering due to the existence of barrier penetration and hole-mixing effects in MQWs and SLs, that is, the barrier to dipole mode is removed. However, the Fröhlich interaction of LO modes is not effective in any of the depolarization configurations.

#### 9.1.2.2 Confined Optical Mode Within the Barrier Layers of Supperlattices

The confined optical modes within the barrier layers of GaAs/AlAs SL were first observed in 1987 by Zhang *et al.*, as shown in Figure 9.7 [5]. The recorded spectral intensities of the modes were only 2–4 photons, which may be why the confined optical modes in the barrier layer were not observed together with the confined modes in the well layer.

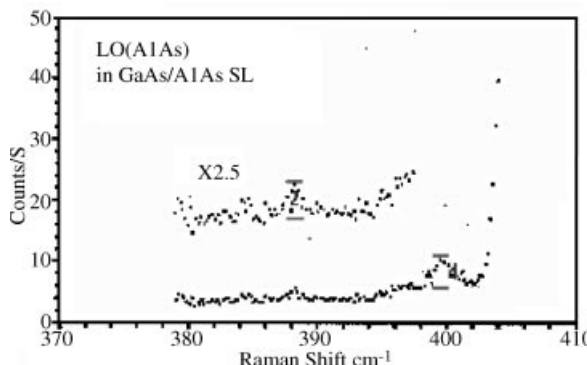


**Figure 9.7** Observed Raman spectra of the confined optical modes within the barrier layers of GaAs/AlAs SLs [5]. Reprinted from S.-L. Zhang, *Raman Spectroscopy and Low-dimensional nanoscale Semiconductors*, Science Press, (2008)

### 9.1.3 Interface Modes

#### 9.1.3.1 Macro Interface Modes

The interface mode in SLs is a unique vibration mode that does not exist in bulk materials. In 1984, Lassnig *et al.* published a theoretical work on the relations between phonon dispersion and the Fröhlich interaction in a polarized double heterojunction, in which macro-interface modes in SLs were expected [14]. Later, Sood *et al.* observed these interface phonons in GaAs/AlAs SLs by Raman scattering, which have frequencies close to the optical phonons of bulk GaAs and AlAs, and resonate stronger for laser energies near the exciton levels of the GaAs quantum wells [6].

Figure 9.8 shows typical Raman spectra of interface modes in samples A ( $d_1 = 2$  nm;  $d_2 = 2$  nm, where  $d_1$  and  $d_2$  are layer thicknesses of GaAs and AlAs, respectively) and B ( $d_1 = 2$  nm,  $d_2 = 6$  nm) in the frequency range of GaAs optical phonons, taken for the scattered light  $\omega_s$  in resonance with the first exciton in the GaAs quantum wells,  $\omega_1$ . In Figure 9.8, the peak marked  $LO_m$  ( $m$  is integral) corresponds to the LO phonon of point group  $D_{2d}$  symmetry  $A_1$  in SLs. Its energy is decided by  $\Omega_m = \Omega(m\pi/d_1)$ , where  $\Omega(q)$  is the LO mode dispersion relation along the [001] direction for bulk GaAs. Since  $d_1$  of Samples A and B are the same, their confined optical phonons have the same energy. However, for the IF peak in the high-energy side of  $LO_6$ , its frequencies in Samples A and B are different. Moreover, if the IF peak and  $LO_6$  are both taken as the confined LO mode, they do not fit well by using  $\Omega(q)$ , of which the vibration amplitude is different from zero in both materials and, therefore, they were assigned to the interface vibration. Figure 9.9 shows Raman spectra of Samples  $d_1 = d_2$ ,  $3d_1 = d_2$ , and  $d_1 = 3d_2$  in the AlAs phonon frequency range. In Figure 9.9, the Raman frequencies between LO and TO modes are consistent with the calculated results of interface modes shown in Figure 8.7, proving further that the observed new Raman peaks are from interface mode scattering.

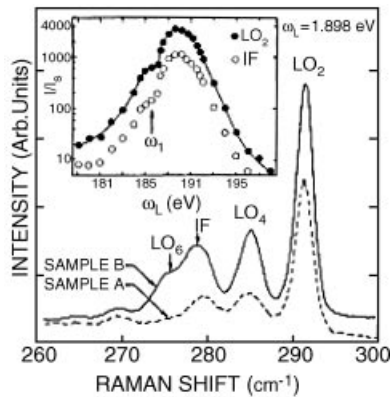


**Figure 9.8** Raman spectra for samples A and B in  $z(x,x)\bar{z}$  scattering configuration ( $x=[100]$ ,  $z=[001]$ ). The peaks labeled  $LO_m$  are the confined  $LO$  phonons and  $IF$  corresponds to the GaAs-like interface mode. The inset shows the resonant behavior of the  $LO_2$  and the  $IF$  mode, the intensities measured with respect to the Raman phonon of Si. Reprinted from A. K. Sood, J. Menéndez, M. Cardona, et al., Resonance Raman Scattering by Confined  $LO$  and  $TO$  Phonons in GaAs-AlAs Superlattices, *Phys. Rev. Lett.*, 54, 2115–2118 (1985) with permission of the American Physical Society

#### 9.1.3.2 Micro-interface Modes

In 1986, using the linear chain model with interplanar force constants, Fesolino *et al.* calculated the InAs/GaSb SL phonon spectrum [15]. The calculation shows that there exist new modes localized at the interface, which are highly dependent on the bond

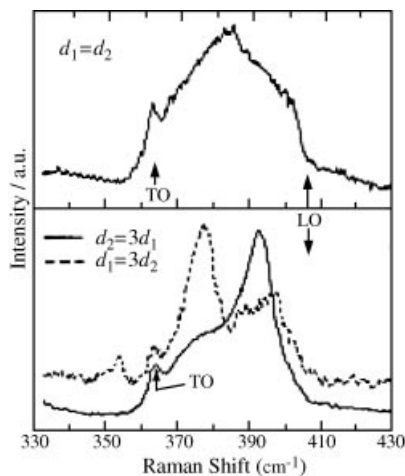


**Figure 9.9** AlAs-like interface modes for samples with different  $d_1$  and  $d_2$ , where  $d_1$  and  $d_2$  are the thicknesses of the GaAs and AlAs layers, respectively. All spectra correspond to the scattering  $z(x,x)\bar{z}$  configuration [6]. Reprinted from A. K. Sood, J. Menéndez, M. Cardona, et al., Resonance Raman Scattering by Confined  $LO$  and  $TO$  Phonons in GaAs-AlAs Superlattices, *Phys. Rev. Lett.*, 54, 2115–2118 (1985) with permission of the American Physical Society

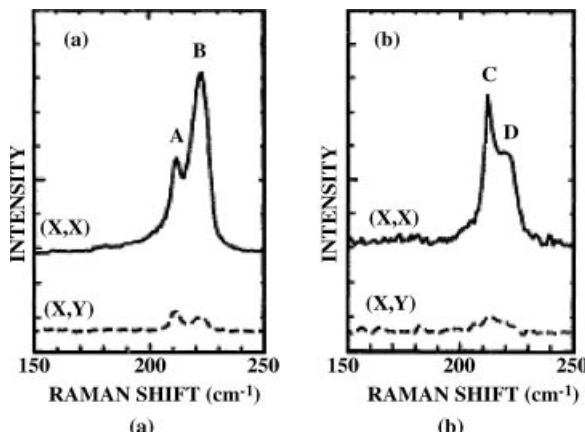


**Figure 9.10** Raman spectra of (a) sample S1 excited by the 502 nm line and (b) sample S2 excited by the 488 nm line in  $Z(X,X)\bar{Z}$  (solid line) and  $Z(X,Y)\bar{Z}$  (dashed line) configurations [7]. Reprinted from Y. Jin, Y. T. Hou, S. L. Zhang, et al., *InInterface Vibration Mode in CdSe/ZnTe Superlattices*, *Phys. Rev. B*, 45, 12141–12143 (1992)

composition (As-Ga bond or Sb-In bond) of the interface and the layer thicknesses of SLs, respectively. In addition, they also found that if the interface is between In and Sb atoms, the energies of the mode will be within the range of bulk InSb phonon spectra. Since the nature of localized modes is clear, these new modes should be easily observed. However, this mode has only been found in CdSe/ZnTe SLs by Jin *et al.* after eight years since the predication of existing a micro-interface mode by Fasolino *et al.* [7].

Jin *et al.* used two samples in their experiment: Sample S1 of 80-period  $(\text{CdSe})_4/(\text{ZnTe})_8$  and Sample S2 of 35-period  $(\text{CdSe})_8/(\text{ZnTe})_{12}$  SLs. Figure 9.10 shows the observed Raman spectra. In this figure, two peaks appear: that marked A is at  $209 \text{ cm}^{-1}$  and that marked B is at  $222 \text{ cm}^{-1}$ . From the polarization of the spectra, it can be seen that the two modes are in polarized mode with the  $A_1$  symmetry, where peaks A and C are ZnTe confined LO modes, while the peaks B and D are yet to be identified.

From Figure 9.10, it can be seen that although the thickness of GaAs and ZnTe for Samples S1 and S2 are different, the frequencies of peaks B and D are the same (at  $222 \text{ cm}^{-1}$ ), which give qualitative evidence for identifying the peaks B and D as the interface modes according to Fasolino. To confirm the identification, Jin *et al.* calculated the dispersion curves of the samples by using the linear chain model with the average force constant used by Fasolino and found that such a calculated frequency value is  $211 \text{ cm}^{-1}$ , which is inconsistent with observed data. When they assumed the force constants of all four kinds of bonds in the SLs to have the same values as in the corresponding bulk compounds, the calculated frequency was  $222 \text{ cm}^{-1}$  and consistent with the observed values, confirming the preliminary identification.

Figures 9.11(a) and (b) show the calculated phonon dispersion curves along [001] and the ion displacement patterns of the interface (IF) mode for Sample S1, respectively. From Figure 9.11(b), it can be seen that the ion displacement of the IF mode is strongly localized at the Zn-Se interface. This result not only confirms the identification for peaks B and D, but is

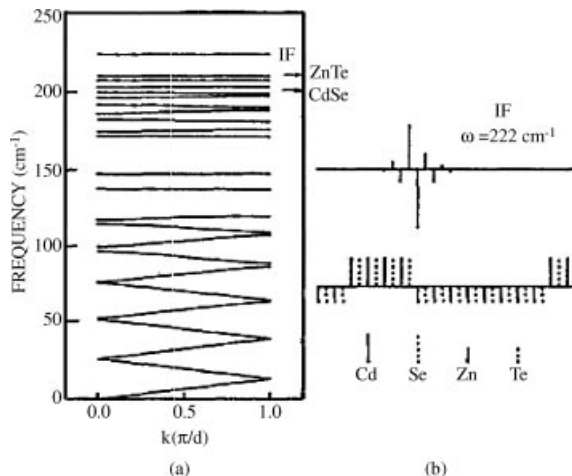


**Figure 9.11** (a) Calculated longitudinal-phonon dispersion of a (001) grown  $(\text{CdSe})_4/(\text{ZnTe})_8$  SL. The frequencies of LO ( $\Gamma$ ) phonons for bulk CdSe and ZnTe are marked by the arrows. (b) The upper part shows the displacement patterns for the topmost mode labeled IF. The positions of the ions are shown in the lower part [7]. Reprinted from Y. Jin, Y. T. Hou, S. L. Zhang, et al., InInterface Vibration Mode in CdSe/ZnTe Superlattices, *Phys. Rev. B*, 45, 12141–12143 (1992)

also is a tangible demonstration that this micro-interface mode is indeed highly localized at the interface of SLs.

## 9.2 Characteristic Raman Spectra of Nanosilicon

The Raman spectral investigation of nanomaterials not including SLs started from nonpolar semiconductors with the representative sample-porous silicon (PS) at the beginning of the 1990s. Therefore, the introduction of this topic will start with nanosilicon.

### 9.2.1 Characteristic Raman Spectrum of Porous Silicon (PS)

Due to the strong light emission in the range of visible light, PS exhibits the potential to be applied to optoelectronic devices and thus becomes the first nanomaterial that has caused great interest and extensive research of nanomaterials. Therefore, the correct identification of its intrinsic spectrum is significantly important in both application and science fields; however, its Raman spectral identification and applications were incorrect in early days.

#### 9.2.1.1 Earliest Raman Spectra of PS

The earliest PS Raman spectra were reported by Goodes *et al.* in 1988 and consists of two peaks, as shown in Figure 9.12(a). Goodes *et al.* believed that the two peaks were from the scattering of amorphous silicon and crystalline silicon, that is, PS is a two-phase mixed material of crystalline and amorphous silicon [16]. However, PS is composed of remaining nanometer-sized crystalline silicon after electrochemical corrosion of a crystalline silicon

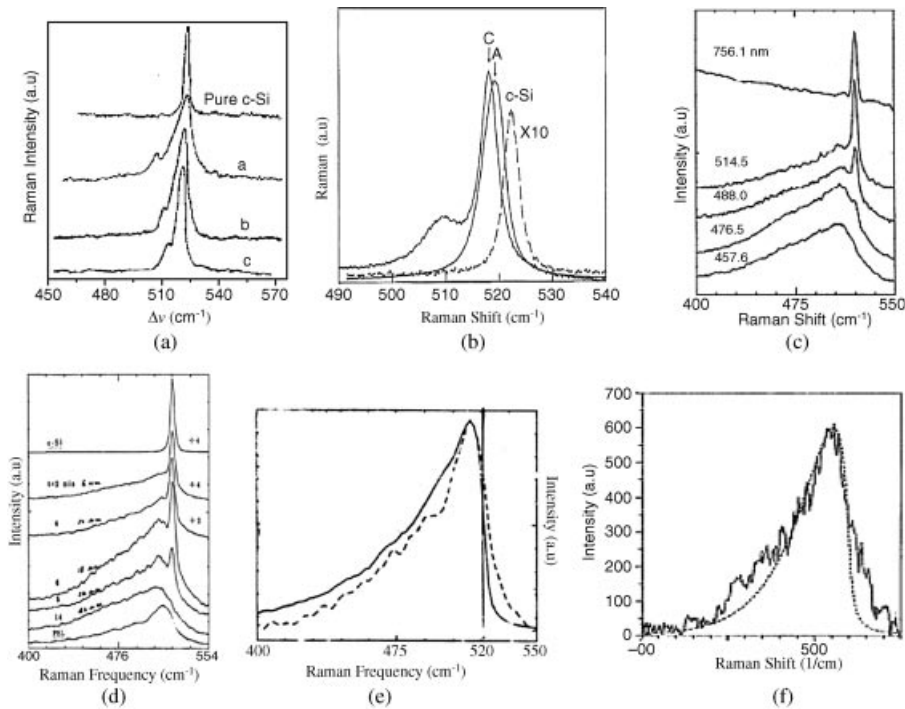


**Figure 9.12** Raman spectra of PS observed by Goodes et al. [16] (a) Reprinted from S. R. Goodes, et al., *The characterisation of porous silicon by Raman spectroscopy*, *Semicond. Sci. Tech.*, 3, 483–487 (1988) with permission of the Institute of Physics. Tsu et al. [17]. (b) Reprinted from R. Tsu, H. Shen and M. Dutta, *Correlation of Raman and photoluminescence spectra of porous silicon*, *Appl. Phys. Lett.*, 60, (1992) with permission of the American Institute of Physics. Zhang et al. [18]. (c–e) Reprinted from S. L. Zhang, Y. Hou, K. S. Ho, et al., *Raman investigation with excitation of various wavelength lasers on porous silicon*, *J. Appl. Phys.*, 72, 4469–4471 (1992), and Sui et al. [19] (f) Reprinted from Z. Sui, P. P. Leong, I. P. Herman, et al., *Raman analysis of light-emitting porous silicon*, *Appl. Phys. Lett.*, 60, 2086–2088 (1992) with permission of the American Institute of Physics. In (d), the Raman spectrum labeled PSL is from stripped PS film, which is repeated in (e). The solid and dotted lines in (e) and (f) respectively represent theoretical calculated spectra by micro-crystal model

wafer in HF. Therefore, this interpretation related to amorphous Si is inconsistent with the PS component mentioned above.

#### 9.2.1.2 Corrected Identification of Raman Spectrum of PS

In 1992, Tsu reported a PS Raman spectrum, which also consisted of two peaks, as shown in Figure 9.12(b), and was explained to be originated from longitudinal and transverse optical phonon scattering, respectively, due to the relief of degenerated optical phonons of silicon caused by the small size effect [17]. Therefore, the correct identification of PS Raman spectrum became a foremost work.

Zhang et al. took into account that PS samples consisted of an Si substrate and a PS thin-film and thus believed that the doublets shown in Figures 9.12(a) and (b) must be the

superposition of Raman peaks of Si substrate and PS thin film [18]. Based on this conjecture, Zhang *et al.* used the fact that the absorption coefficients are different for different light wavelengths, leading to different penetration depths in the sample for different wavelengths of laser. Thus, they detected Raman spectra from different layers of samples by using different wavelength laser excitations, of which the results are shown in Figure 9.12(c) [18].

Figure 9.12(c) cleverly exhibits that Raman spectral features from different-depth layers excited by different wavelengths are different. The spectrum excited by the long wavelength of 785 nm is similar to a silicon Raman peak, so is considered to be from a silicon substrate, mainly due to the laser having penetrated down to the silicon substrate. The spectrum excited by the short wavelength of 457 nm displays a broad and non-symmetrical peak and is possibly from the surface of the sample, as the thickness of the laser entering the sample is shallower. While for the excitation by middle wavelengths of 488 and 515 nm, which correspond to the middle penetration depth of the laser in the sample, the observed spectra consists of two peaks and is similar to those shown in Figures 9.12(a) and (b). From close observation, these two spectra are similar to the superposition of the two spectra excited by 785 and 465 nm. Therefore, it is reasonable to expect that the spectrum excited by 465 nm, that is, from the surface of sample, is the intrinsic spectrum of PS itself.

To confirm the above expectation, Zhang *et al.* measured Raman spectra of different PS samples with different thicknesses of PS films on an Si substrate from 6 to 42 nm and the results are shown in Figure 9.12(d), together with Raman spectra of bulk silicon and stripped PS film (labeled PSL) excited by the same wavelength. Figure 9.12(d) shows that the spectra of most thick and thin films are similar to those excited at longest and shortest wavelengths, as in Figure 9.12(c), confirming the above analysis of the feature of the PS intrinsic Raman spectrum. Sui *et al.* independently reported a Raman spectrum of stripped PS film, as shown in Figure 9.12(e) by a solid line. All the above results show that the intrinsic Raman spectrum of PS is a single peak and also confirm that the above identification for the PS Raman spectrum [16,17] is incorrect.

## 9.2.2 Characteristic Raman Spectra of Silicon Nanowires (Si NWs)

### 9.2.2.1 Characteristic Raman Spectrum of Optical Phonon in Si NWs [21]

Silicon nanowire was the earliest silicon nanomaterial synthesized by using laser ablation [20]. The characterization of samples showed that in addition to the formation of silicon nanowires,  $\text{SiO}_2$  nanomaterials and structural defects such as dislocations also appear. Figure 9.13(a) is an image of a high-resolution transmission electron microscope for a silicon nanowire sample. The measured Raman spectrum of the Si NW sample, together with crystalline silicon and nano- $\text{SiO}_2$ , are shown in Figure 9.13(b). From the comparison, the characteristic spectrum of Si NWs was extracted experimentally and is expressed by solid lines in Figure 9.13(c).

### 9.2.2.2 Characteristic Raman Spectrum of Acoustic Phonon in Si Nanocrystals

Section 8.2.1 mentioned that because of the changing or reducing of symmetry of nanostructures against bulks, Raman inactive modes in bulk crystals will develop into Raman active modes in nanocrystals. Acoustic phonons do not occur in bulk crystals due to the wave vector selection rule  $\mathbf{q} = 0$ . However, the wave vector selection rule is relaxed in nanocrystals and thus acoustic phonons are observed. Figure 9.14(a) shows such acoustic

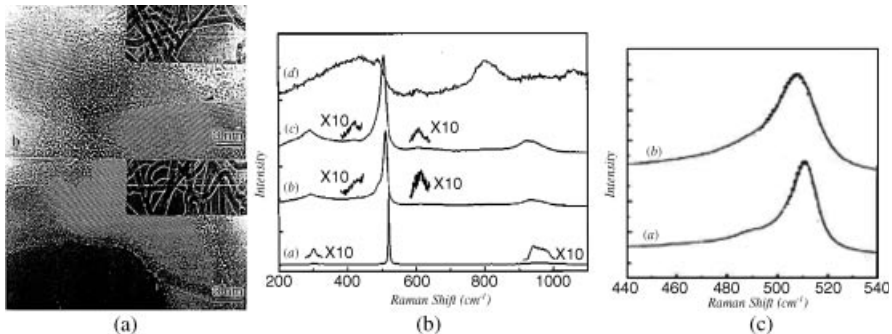


**Figure 9.13** (a) Image of high-resolution transmission electron microscope Raman spectra of Si NWs; (b) Raman spectra of a) c-Si, b) Si NW sample B; c) Si NW sample A, d) nano-SiO<sub>2</sub> wires [21] (c) Comparison of measured (solid line) and calculated (dotted line) first-order Raman spectra of a) Si NW sample B, b) Si NW sample A [21]. Reprinted from B. Li, D. Yu, and S. L. Zhang, Raman spectral study of silicon nanowires, Phys. Rev. B, 59, 1645–1648 (1999)

Raman spectra observed in Si nanocrystals [22]. The spectra exhibit an asymmetric broadened line shape with a “tail” in the high frequency region. This expanded direction of the “tail” is opposite to that of optical phonons shown in Figures 9.12 and 9.13; however, they match the slope rates of the bulk dispersion curves of optical and acoustic phonons of  $>0$  and  $<0$ , respectively. Figure 9.14(b) shows the calculated Raman spectra of the acoustic phonons confined in Si spheres, indicating that the agreement with the observations is good, such as in different frequency values of polarized and depolarized Raman spectra [23].

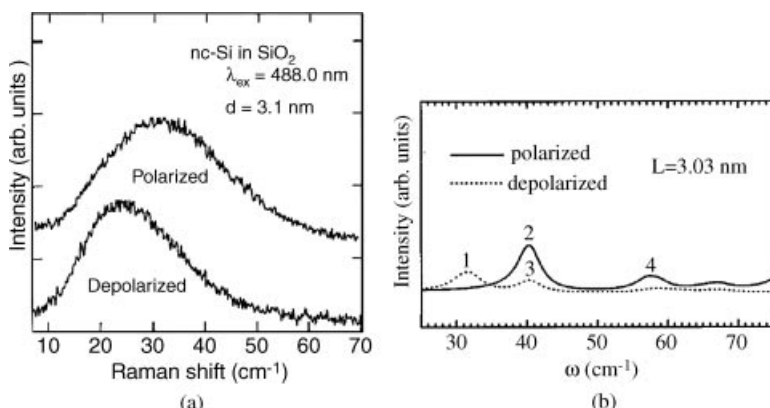


**Figure 9.14** (a) Observed polarized and depolarized Raman spectra of Si nanocrystals embedded in SiO<sub>2</sub> matrices [22]. Reprinted from M. Fujii, Y. Kanzawa, S. Hayashi et al., Raman scattering from acoustic phonons confined in Si nanocrystals, Phys Rev B, 54, R8373–R8376 (1996) with permission of the American Physical Society. (b) calculated Raman spectra from the acoustic phonons confined in Si spheres. The solid (dashed) lines stand for polarized (depolarized) Raman spectra [23]. Reprinted from J. Zi, K. Zhang and X. Xie, Microscopic calculations of Raman scattering from acoustic phonons confined in Si nanocrystals, Phys Rev B, 58, 6712–6715 (1998) with permission of the American Physical Society

**Table 9.2** Fitting sizes used in MC model, and actual sizes and shapes measured from TEM images for porous silicon and silicon nanowires. (a) Reprinted from Shu-Lin Zhang, et al., Raman investigation with excitation of various wavelength lasers on porous silicon, *J. Appl. Phys.* 72 4469 (1992). (b) Reprinted from B. Li, D. Yu, and S.-L. Zhang, Raman spectral study of silicon nanowires, *Phys. Rev. B*, 59, 1645–1648 (1999)

	Porous silicon [18]		Silicon nanowires [21]		
Size	$L_{\text{cal}}$	$d_{\text{pillae}}$	$L_{\text{cal}}$	$d_{\text{wire}}$	$d_{\text{grain}}$
Shape	2.0	1.8	9.5	13	10

### 9.2.2.3 Theoretical Calculation of Si NW Raman Spectrum

- Calculation by using micro-crystal (MC) model

By using the MC model described in Section 8.3, Raman spectroscopy of silicon nanowires with fitting  $L = 13$  nm was calculated and the results are shown in Figure 9.13(c) by a dotted line, from which it can be seen that the fitting results are good. The above results indicate that, on the one hand, experimental identification of NW Raman spectrum was proved and, on the other hand, the characteristic Raman spectrum of Si NWs correlated with the size confinement effect, as the MC model was only based on the size confinement effect.

Table 9.2 lists the theoretical fitting size  $L_{\text{cal}}$  used in the MC model, the actual sizes  $d$ , and shapes measured from TEM images of PS and silicon nanowires. The table shows that the above fitting sizes are consistent with the sizes of PS pillars  $d_{\text{pillar}}$  and the small grains  $d_{\text{grain}}$  with complete crystal lattices in silicon nanowires observed in their electron micrographs, respectively. Thus, for these kinds of silicon nanowires with no complete crystal lattice, only the crystal grains size in quantum wires, rather than the apparent diameter of the quantum wires, fit the calculated spectra well, that is, Raman scattering originated from the grains with a complete crystal lattice in such nanosamples. Note that the PS short pillars must be the complete crystal lattice itself, as they are the residual silicon due to HF corrosion for crystal silicon. The fitting size  $L$  used in MC model should be the size of integral crystal structures, which is correct as the MC model is based on crystal materials. However, the NW samples used in Ref [21] consist of many crystallites.

When comparing the Raman spectra of PS and Si NWs, respectively, as shown in Figures 9.12 and 9.13, it is found that the spectral characteristics of these two spectra are similar, that is, the frequency downshift and line shape broaden asymmetrically. This also reflects that both of them are constituted by silicon particles.

- Calculation by using micro-polarity model

To further understand Raman spectral features of nanosilicon from the micro-view, Shen *et al.* used the micro-polarity model to calculate the Raman spectroscopy of Si grains with sizes from 1 to 5 lattices with constant  $a$  (i.e., 0.54, 1.09, 1.63, 2.17, and 2.71 nm) and the results are shown in Figure 9.15(a).

In Figure 9.15(a), the LO and TO modes are obviously splitting in the case of smallest size and the splitting extent decreases with increase in size. This displays the size confinement effects and also the interpretation suggested by Tsu *et al.* [12]. But this is different from

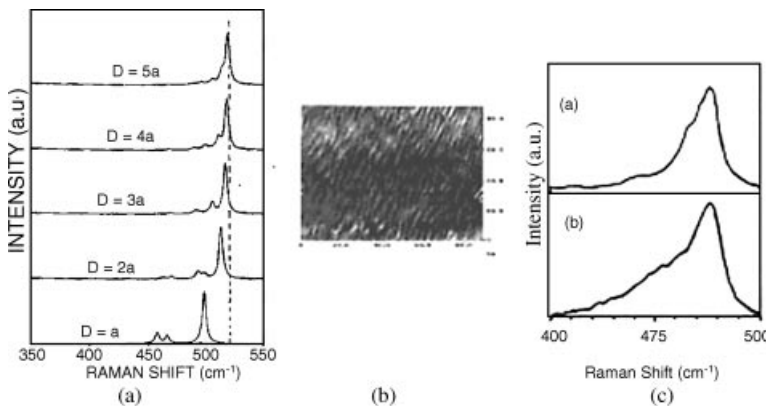


**Figure 9.15** (a) Raman spectra calculated for five different wires with side width  $D = 1, 2a, 3a, 4a$ , and  $5a$ , based on the micro-polarity model, where  $a$  is the lattice constant of silicon; (b) HRTEM of PS sample; (c) the measured (a) and calculated Raman spectra (b), the latter is the weighted superposition of calculated spectra with size distribution measured according to HRTEM shown in (b) [27]. Reprinted from S.-L. Zhang, *Raman Spectroscopy and Low-dimensional nanoscale Semiconductors*, Science Press, (2008)

measured spectral features. However, considering the sample sizes are distributed as shown in Figure 9.15(b), the Raman spectrum of the weighted superposition of calculated spectra with size distribution measured according to HRTEM is shown in Figures 9.15(c)-b, in which Figure 9.15(c)a is in good agreement with the experimental spectra shown in Figure 9.15(c)-b. This result predicts that the Raman spectra of the small-size silicon particles with uniform size should exhibit LO-TO split ones and the split will reduce with sample size increase. Obviously, confirmation of this argument by experiments is valuable.

### 9.2.3 Discussion on Origin of Nanosilicon Raman Spectra

The previous subsection mentioned the observed Raman features of nanosilicon: the frequency downshift and line shape broadened asymmetrically and considered these features to be originated from the size confinement effect. However, different interpretations for the origin of the above Raman features have been proposed, in which the laser heating (temperature) effect is the leading viewpoint.

#### 9.2.3.1 Interpretation of Laser Heating Effect [19,20]

In 2000, Gupta *et al.* measured the influence of excitation laser power density on Raman features of small diameter (5–15 nm) Si NWs, and the results of 8 nm diameter NWs are shown in Figure 9.16. In the figure, we see that at low power densities, a Lorentzian line is observed at  $520\text{ cm}^{-1}$ , the same value as that of the zone center LO (TO) phonon in bulk silicon. With increasing illuminated laser power, the Raman band downshifts and asymmetrically broadens at the low-frequency side. The solid curves overlaying the upper seven spectra in Figure 9.16 are from a Fano line-shape analysis, showing a good fit with experimental spectra. Based on the above results, they suggest that the downshifting is due to laser heating effect on the nanowire and the asymmetric line shape is due to Fano

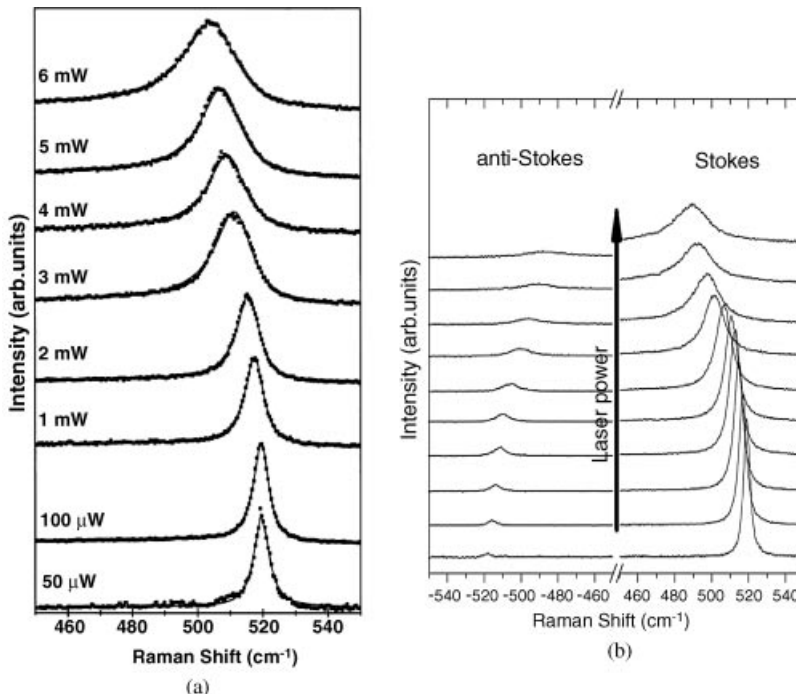


**Figure 9.16** (a) Stokes Raman spectra of  $d \approx 8$ -nm-diameter silicon nanowires on a quartz substrate measured with different laser power in air [24]. Reprinted from R. Gupta, Q. Xiong, C. K. Adu, et al., Laser-Induced Fano Resonance Scattering in Silicon Nanowires, *Nano Lett.*, 3, 627–631 (2003) with permission of the American Chemical Society. (b) Stokes and anti-Stokes Raman spectra of silicon nanowires measured with different laser power densities [25]. Reprinted from M.J. Konstantinović, Interplay between phonon confinement effect and anharmonicity in silicon nanowires *Physica E*, 38, 109–111 (2007) with permission of Elsevier

interference between scattering from the wave vector  $q = 0$  optic phonon and electronic continuum scattering from laser-induced electrons in the conduction band.

In 2007, Konstantinovic measured Raman spectra of Si NWs with a typical length of 10 μm and a diameter of about 50–500 nm and the results are shown in Figure 9.16(b) [25], displaying similar features to those in Figure 9.16(a). The author suggested an interpretation that the strong shift and broadening of the Raman peak was dominated by anharmonic effects originating from laser heating, while confinement played a secondary role.

For the interpretations mentioned above, we analyze it as follows:

- (1) Section 8.3.4 mentioned that the confinement effect of phonons is much stronger than that of electrons [26], while the confinement size of electrons in Si by theoretical calculation is about 5 nm [27]. Therefore, it should be expected that there is no size confinement effect on phonons in the Si NWs with a diameter larger than 5 nm, used in Ref. [24] and with 50–500 nm used in Ref. [25].
- (2) The Raman frequency of heated samples will shift compared with the sample at room temperature and the measured sample in Raman spectroscopy should keep the laser power

lower to avoid a rise in temperature. Therefore it is essential that the measurement to test the origin of intrinsic Raman feature change must be performed at room temperature.

- (3) The appearance of the Fano line shape originated from the continuous scattering of electrons due to coupling with phonons. Why nanocrystalline silicon and sample temperature increase stimulates Fano line shape scattering has not yet been interpreted [24,25].

The above analyzes indicate that as a testing experiment for the intrinsic Raman spectral features of nanosilicon, since the used samples and measured condition are incorrect, the experiments themselves in Refs. [19,20] have been ruled out. Therefore, the results do not negate the size confinement effect. In contrast, the experiments to test the size confinement effect on PS and Si NWs [18,21] both satisfy the above experimental requirements.

#### 9.2.3.2 Interpretation of Stress Effect

The interpretation of the stress effect mentioned that the change of space between atoms leads to occurring macro-stress and so affects the frequency and other spectral features of phonons.

The space between atoms in nanomaterials is usually different from that of corresponding bulk materials, which leads to the occurrence of stress and the shift of Raman frequency compared to those in bulk materials. However, for a practical nanosilicon sample with size 10 nm, the lattice constant is 0.5425 nm, 0.4% larger than the bulk silicon lattice constant of 0.541 nm. According to the frequency shift formula  $\Delta\omega = -nv\omega_0(a - a_0)/a_0$  (where  $n$  is the dimension of sample;  $v$  is the Gruneisen constant; and  $\omega_0$  is Raman frequency of bulk crystalline silicon), it can be deduced that the frequency shift caused by stress is about  $2 \text{ cm}^{-1}$ . In small-sized samples, since the Raman frequency shift caused by the size confinement effect in nanosilicon is often more than  $2 \text{ cm}^{-1}$  and larger than the shift induced by stress, this indicates that the Raman frequency shift induced by stress can be ignored.

### 9.3 Characteristic Raman Spectra of Nanocarbons

Section 8.2.4 mentioned that carbon has the allotropes of diamond, graphite, graphene, and fullerenes. Characteristic Raman spectra of carbon nanostructures are provided by various allotropes.

#### 9.3.1 Characteristic Raman Spectra of Nanodiamond

##### 9.3.1.1 Characteristic Raman Spectra of Cluster Diamond by Detonation

Characteristic Raman spectra of small-sized diamond, presented by synthetic diamond powder, have long been of interest [28–32]. The first characteristic Raman spectrum of nanoscale cluster diamond as a sample was published by Yoshikawa *et al.* in 1995 [29]. Figure 9.17 shows Raman spectra of a 4.3 nm cubic cluster diamond prepared by detonation of TNT explosives [29]. Figure 9.17(a) shows a difference in the frequency and line shape of characteristic peaks between bulk diamond and cluster diamond. Figure 9.17(b) shows the spectral fitting between experimental spectrum and calculated spectrum by applying the micro-crystal model, indicating that the size confinement effect is the origin of the nanodiamond spectral features shown in Figure 9.17(a).

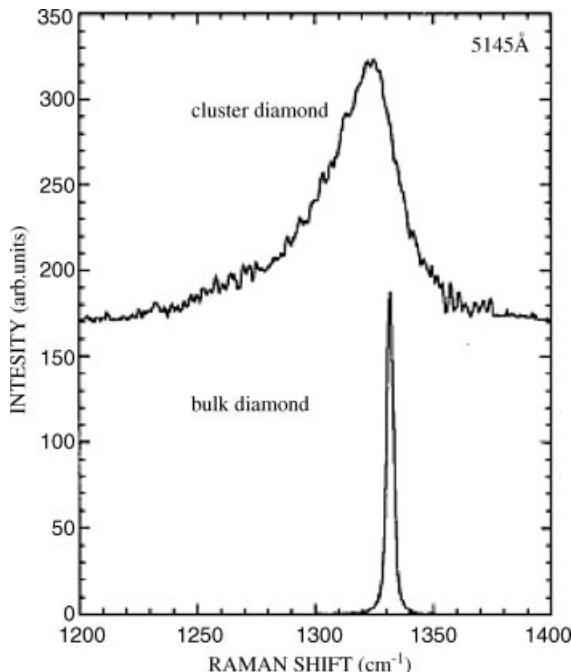


**Figure 9.17** Raman spectra of 5.4 nm cluster diamond and bulk diamond. [29]. Reprinted from M. Yoshikawa, Y. Mori, H. Obata, et al., Raman scattering from nanometer-sized diamond, *Appl. Phys. Lett.*, 67 (1995) with permission of the American Institute of Physics

### 9.3.1.2 Characteristic Raman Spectra of Nanocrystalline Diamond by CVD

The chemical vapor deposition (CVD) method can synthesize large numbers of nanocrystalline diamonds and thus is a method of important value in nanodiamond application. In 1988, Nemanich *et al.* [33] reported that the Raman peak at  $1145\text{ cm}^{-1}$  is the characteristic of the CVD synthesized nanodiamond. Since then, it has become a criterion for the identification of CVD synthesized nanodiamond, for example, according to the appearance of the Raman peak at  $1150\text{ cm}^{-1}$ , as shown in Figure 9.18, the author of Ref [30] believed that when the  $\text{Ar}^+$  ion atmosphere is more than 90% in CVD processing, nanocrystalline diamond is produced.

In Ref. [30], that Raman peak at  $1145\text{ cm}^{-1}$  was considered as the characteristic peak of the CVD synthesized nanodiamond, and the peak at  $1145\text{ cm}^{-1}$  originated from the downshift of the bulk diamond characteristic peak at  $1332\text{ cm}^{-1}$ , due to the size confinement effect. According to diamond dispersion curves, as shown in Figure 7.13(b), the frequency shift caused by the size confinement effect is upshifted for larger crystallites and cannot drop to  $1332 - 1145 = 187\text{ cm}^{-1}$ , even for smallest crystallites. Therefore, this criterion is questionable.

However, the Ferrari group in the Department of Engineering at the University of Cambridge argued that the peak located at  $1150\text{ cm}^{-1}$  should not be assigned to nanocrystalline diamond or other  $sp^3$ -bonded phases. In 2001, Roberts and Ferrari published a paper

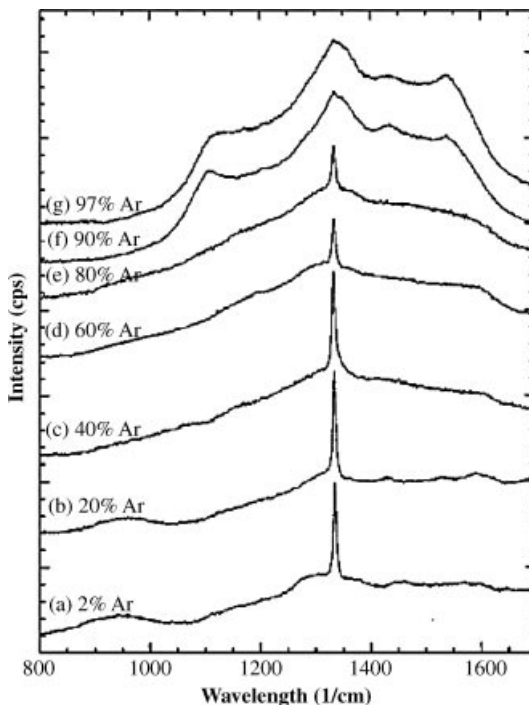
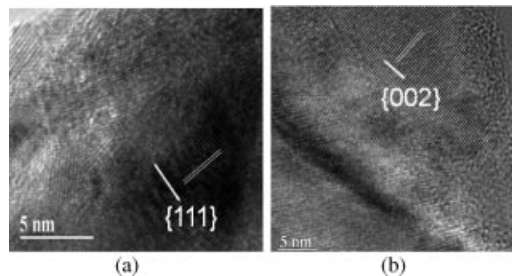


**Figure 9.18** Raman spectra of the As-grown diamond films with different volume percentages of Argas [30]. Reprinted from D.M. Gruen, Nanocrystalline Diamond Films, *Annual Rev. of Mat. Sci.*, 29, 211–259 (1999)

entitled “Origin of Nanocrystalline Diamond Raman Mode Located  $1150\text{ cm}^{-1}$ ,” in which they assigned the Raman mode located at  $1150\text{ cm}^{-1}$  to the intermediate produced in the CVD process, transpolyacetylene (TPA) segments at grain boundaries and surfaces. As a result, they negate the correlation of the Raman mode located at  $1150\text{ cm}^{-1}$  with any diamond structure based on chemical methods.

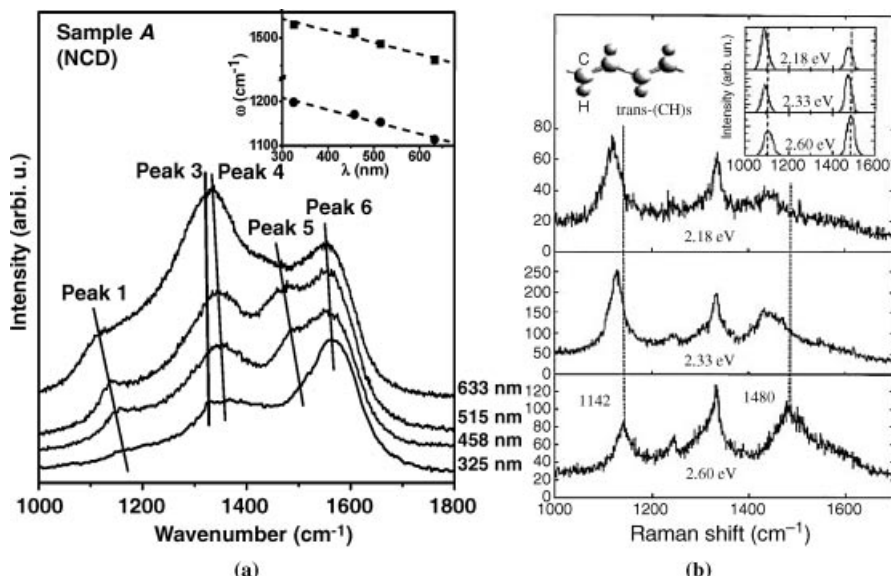
The same argument put forward by the Ferrari group was also put forward by the Zhang group in the department of Physics at Peking University. They came to the same conclusions as the Ferrari group, by using Raman spectra of CVD prepared nanocrystalline diamond (CVD-NCD) measured by changing excited wavelength and sample temperature. HRTEM images of two representative regions (a) and (b) on the CVD-NCD sample used are shown in Figure 9.19. In Figures 9.19(a) and (b), the crystalline grains with same average size of about 20 nm are found, while the spacing values between the striations are different in these two regions, and  $2.1\text{ \AA}$  and  $3.3\text{ \AA}$  in the regions (a) and (b), respectively, match the corresponding values of bulk diamond ( $2.1\text{ \AA}$ ) and graphite ( $3.4\text{ \AA}$ ), respectively, meaning the sample contains NCD and nanocrystalline graphite (NCG).

Figure 9.20(a) shows Raman spectra of a CVD-NCD sample excited by various wavelengths [34]. Each spectrum is fitted by seven peaks. The dependence of Raman frequencies on excitation wavelengths for peaks 1 and 5 are plotted in the inset of Figure 9.20(a). From the inset, it can be seen that the Raman frequencies of peaks 1 and 5



**Figure 9.19** HRTEM images of two regions *a* and *b* of the CVD prepared nano-crystalline diamond (CVD-NCD) sample [34]

exhibit downshifts of  $84\text{ cm}^{-1}$  and  $64\text{ cm}^{-1}$ , respectively. A downshift of the TPA peak frequencies with increasing laser wavelength is similar to the surface enhanced Raman scattering (SERS) of TPA in diamond films, as shown in Figure 9.20(b) [32]. The downshift of the Raman frequencies of peaks 1 and 5 versus the excitation wavelength is fitted by straight lines with corresponding slopes are  $-0.27$  and  $-0.21$ , respectively. The ratio of the slope,  $R$ , is  $1.29$ , closely matches the  $R$  value of single- and double- bond



**Figure 9.20** (a) Raman spectra of CVD diamond film Sample A excited by various wavelengths [34]. Reprinted from Y. Yan, et al., *Study of  $1145\text{cm}^{-1}$  Raman Peak of CVD Diamond Film*, Chinese Journal of Light Scattering, 16, 131–135 (2004). (b) SERS spectra of TPA in diamond film recorded for the different excitation energies; in the inset, computed Raman scattering of TPA chains with a conjugation length, which equals 20 double carbon-carbon bonds, is shown [32]. Reprinted from T. López-Ríos, É. Sandré, S. Leclercq and É. Sauvain, *Polyacetylene in Diamond Films Evidenced by Surface Enhanced Raman Scattering*, Phys. Rev. Lett., 76, 4935–4938 (1996) with permission of the American Physical Society.

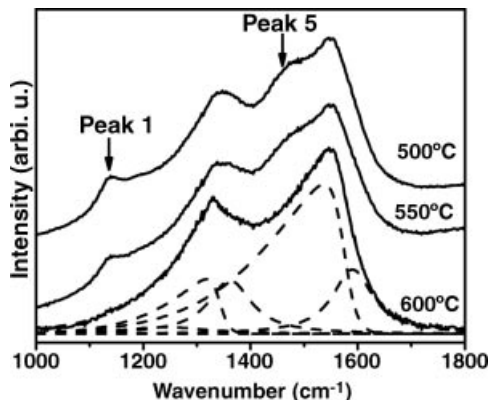
**Table 9.3** Raman frequency (in  $\text{cm}^{-1}$ ) and their assignments of Raman peaks of CVD-NCD sample

Peak	1	2	3	4	5	6
$\omega/\text{cm}^{-1}$	1125	1240	1328	1360	1474	1547
Assignment	SB-TPA	a-diamond	Nanodiamond	D-mode of graphite	DB-TPA	G-mode of graphite

TPA 1.20 [32]. Thus the above results identify peaks 1 and 5 to single-bond (SB) and double-bond (DB) TPA, respectively. The final assignments for all seven peaks are marked in Table 9.3. Peaks 2, 3, 4, and 6 in Figure 9.20(a) have been assigned to the Raman peaks of amorphous diamond (a-diamond), nanodiamond, D mode of graphite, and G mode of graphite [35].

Knowing the thermal properties of TPA, the sample was heated to remove TPA by evaporation. The spectra obtained from the heated sample are shown in Figure 9.21, which shows that when the heating temperature reaches 600 °C, both peaks 1 and 5 related to TPA disappearance, while the remaining peaks remain. The heating apparently has provided additional evidence that the peak at 1145  $\text{cm}^{-1}$  is from TPA related only.

**9.3.1.3 Common Features of Characteristic Raman Spectra of Nanocrystalline Diamonds**  
The premise of the characteristic Raman spectral identification is that the spectrum should be obtained from the pure material to be identified. However, the assignments listed in Table 9.3 imply that the sample consists of many components and structures. To satisfy the requirements of the characteristic Raman spectral identification mentioned above, the spectral fitting and deduction method was performed. Based on the Raman spectral line shape of nano- and bulk materials being asymmetric and Lorentzian, respectively [36], corresponding line shapes were chosen to fit the spectrum for different components and

**Figure 9.21** Raman spectra of CVD nanocrystalline diamond films at different heating temperatures [35]. Reprinted from S.-L. Zhang, *Raman Spectroscopy and Low-dimensional nanoscale Semiconductors*, Science Press, (2008)

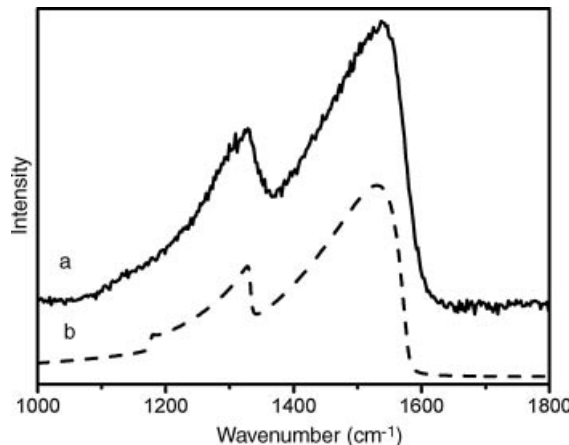


**Figure 9.22** Experimental (a) and calculated (b) spectra of nanocrystalline diamond and NCG in CVD-NCD sample [35]. Reprinted from S.-L. Zhang, *Raman Spectroscopy and Low-dimensional nanoscale Semiconductors*, Science Press, (2008)

structures in the heated sample at 600 °C, shown by dashed lines in Figure 9.22. Figure 9.22 shows the characteristic Raman spectra that consist of NCD and nano-crystalline graphite (NCG) only. To distinguish and also to confirm the above fitting results, a theoretical analysis was performed using the micro-crystal model. The calculated spectrum is shown in Figure 9.22 with a dashed line. Table 9.4 lists the Raman frequencies  $\omega_D/\omega_G$  and the line widths  $\Gamma_D/\Gamma_G$  for the observed and calculated NCD/NCG with those of bulk diamond and graphite together. Figure 9.22 and Table 9.4 show a good match, confirming the characteristic Raman spectra of NCD.

The features of identified characteristic Raman spectrum of NCD is an asymmetric and broadened peak with a  $4\text{ cm}^{-1}$  downshift compared to bulk diamond. The above identified features are strikingly similar to those shown in Figure 9.17, which is from a nanometer-sized cluster diamond prepared by detonation of TNT explosives [29]. This indicates that there is a common feature in characteristic Raman spectra of nanodiamond, no matter what the preparation method.

### 9.3.2 Characteristic Raman Spectra of Graphene

Graphene is an atomic mono-layer graphite sheet and is considered as typical nanostructured graphite. Figure 9.23(a) shows the Raman spectra of bulk graphite and graphene.

**Table 9.4** Raman frequencies  $\omega_D$  and  $\omega_G$ , and the line widths  $\Gamma_D$  and  $\Gamma_G$  for observed and calculated NCD and NCG (in  $\text{cm}^{-1}$ )

	$\omega_D$	$\Gamma_D$	$\omega_G$ ,	$\Gamma_D$
Observed	1328	106	1534	168
Calculated	1326	103	1536	168
Bulk	1332	~2	1580	~2

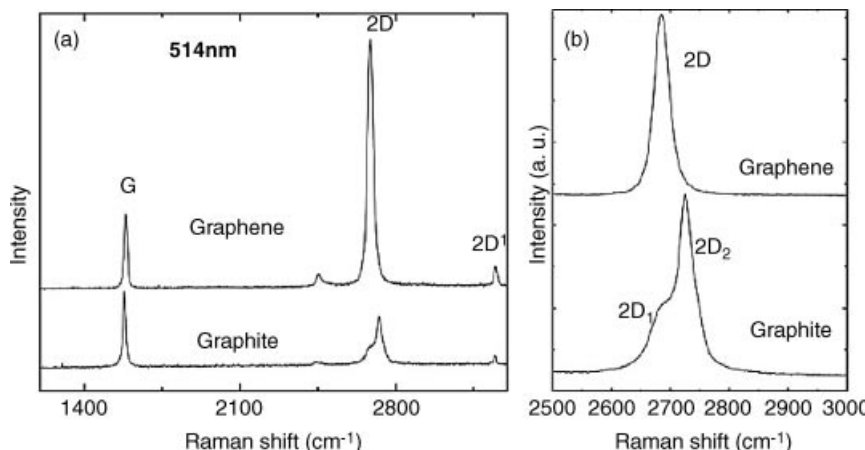


**Figure 9.23** (a) Raman spectra of graphene and graphite measured at 514.5 nm; (b) enlarged two-dimensional peaks in graphene and graphite [37,38]. Reprinted from A.C. Ferrari, Raman spectroscopy of graphene and graphite: Disorder, electron–phonon coupling, doping and nonadiabatic effects, *Solid State Communications* 143, 47 (2007) with permission of Elsevier

Figure 9.23 shows two intense spectral structures at  $\sim 1580\text{ cm}^{-1}$  and  $\sim 2720\text{ cm}^{-1}$ . The spectral structures at  $\sim 1580\text{ cm}^{-1}$  and  $\sim 2720\text{ cm}^{-1}$  are assigned as the *G* and *2D* modes, respectively.

The *G* mode is the  $E_{2g}$  mode with a tangential stretching vibration mode. The *G* mode involves an optical phonon mode between two dissimilar carbon atoms A and B in the unit cell, which exhibits a single Lorentzian peak at  $1582\text{ cm}^{-1}$ .

The *2D* spectral structure is a double phonon peak of *D* mode. While the *D* mode is the zone-boundary phonon and does not satisfy the Raman wave vector selection rule, it should not be seen in first-order Raman spectra of defect-free graphite and occurs only in sample with impurities and defects. Therefore, that no *2D* mode is observed in Figure 9.23 proves the absence of a significant number of defects in the graphene sample. Besides, the *2D* mode with double peaks in graphite becomes a single peak in graphene, as shown in Figure 9.23(b), which may also be interpreted by the difference in impurities and defects between graphite and graphene.

### 9.3.3 Characteristic Raman Spectra of Fullerene

It was seen in Figure 8.24 that a fullerene is any molecule composed entirely of carbon, in the form of a hollow sphere, ellipsoid, or tube. Buckyball- $C_{60}$  is the first prepared fullerene and so we will now discuss Raman spectrum of  $C_{60}$ .

#### 9.3.3.1 Characteristic Raman Spectrum of $C_{60}$ [39]

The discovery of  $C_{60}$ , the earliest of the fullerenes, greatly expanded the number of known carbon allotropes, which until recently were limited to graphite, diamond, and amorphous carbon such as soot and charcoal. Since non-traditional  $C_{60}$  is of great significance in science and technology, scientists quickly carried out extensive research, one of which is Raman spectroscopy.

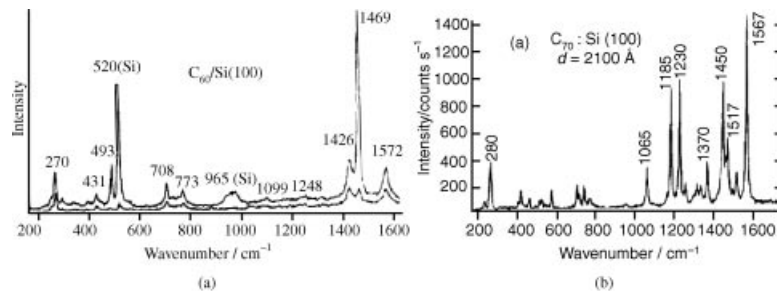


**Figure 9.24** (a) Polarized Raman spectra for  $C_{60}$  on a  $Si(100)$  substrate. The upper trace is for  $(\parallel, \parallel)$  polarization and shows both  $A_g$  and  $H_g$  modes. The lower trace is for the  $(\parallel, \perp)$  polarization and shows only  $H_g$  modes [41]. (b) Room temperature first-order Raman spectrum of a  $C_{70}$  film on an  $Si(100)$  substrate [39]. Reprinted from M. S. Dresselhaus, G. Dresselhaus and P. C. Eklund, Raman Scattering in Fullerenes, *J. Raman Spectroscopy*, 27, 351–371 (1996) with permission of John Wiley and Sons

Figure 9.24 shows the characteristic Raman spectrum of  $C_{60}$ . Tables 9.5 and 9.6 list the symmetry and frequencies of vibration modes in the  $C_{60}$  molecule. All of  $A_g$  and  $H_g$  Raman active modes expected by the theory mentioned in Section 8.2.4 have been observed and the observed frequencies are listed in Table 9.5.

### 9.3.3.2 Characteristic Raman Spectra of Carbon Nanotubes [46,47]

Carbon nanotubes were first found as a by-product in the growing progress of fullerene in 1991 by Iijima [46]. Carbon nanotubes have proven to be a unique system for the study of

**Table 9.5** Raman Frequency of intra-molecular vibration modes of the  $C_{60}$  molecule and their symmetries: experiment and models [39]. Reprinted from M. S. Dresselhaus, G. Dresselhaus and P. C. Eklund, Raman Scattering in Fullerenes, *J. Raman Spectroscopy*, 27, 351–371 (1996) with permission of John Wiley and Sons

$\omega_i (R)$	Expt		Theo	
	D <sup>a</sup>	J <sup>b</sup>	Q <sup>c</sup>	F <sup>d</sup>
	497.5	492	478	483
$\omega_1 (A_g)$				
$\omega_2 (A_g)$	1470.0	1468	1499	1470
$\omega_1 (A_g)$	273.0	269	258	268
$\omega_2 (A_g)$	432.5	439	439	438
$\omega_4 (A_g)$	711.0	708	727	692
$\omega_5 (A_g)$	775.0	788	767	782
$\omega_6 (A_g)$	1101.0	1102	1093	1094
$\omega_7 (A_g)$	1251.0	1217	1244	1226
$\omega_8 (A_g)$	1426.5	1401	1443	1431
$\omega_9 (A_g)$	1577.5	1575	1575	1568

<sup>a</sup> All experimental mode wave numbers in the table are derived from a fit to first-order and higher order Raman spectra [42].  
<sup>b</sup> Calculated mode wave numbers of Ref. [43].

<sup>c</sup> Calculated mode wave numbers of Ref. [44].

<sup>d</sup> Calculated mode wave numbers of Ref. [45].

**Table 9.6** Raman peak frequencies ( $\omega$ ), full widths at half maximum (FWHM  $\Delta\omega$ ), and integrated intensity ratio of D mode relative to G mode ( $I_D/I_G$ ) of HOPG carbon nanotubes prepared by the D-CNT and by the C-CNT

Material	Parameter	D mode	G mode
HOPG	$\omega/\text{cm}^{-1}$	1332	1583
	$\Delta\omega/\text{cm}^{-1}$	34	14
	$I_D/I_G$	0.051	
D-CNT	$\omega/\text{cm}^{-1}$	1336	1584
	$\Delta\omega/\text{cm}^{-1}$	42	22
	$I_D/I_G$	0.430	
C-CNT	$\omega/\text{cm}^{-1}$	1337	1604
	$\Delta\omega/\text{cm}^{-1}$	164	64
	$I_D/I_G$	3.564	

Raman spectra in one-dimensional systems, and at the same time Raman spectroscopy has provided an exceedingly powerful tool for the characterization of single-wall carbon nanotubes (SWCNT/SWNT).

Holden observed the first Raman spectra of SWCNTs, as shown in Figure 9.25 [48]. The completer Raman spectra of SWCNTs are shown in Figure 9.26, in which the spectra (a) and (b) are from a sample of SWCNT bundles and isolated SWCNT, respectively. In Figure 9.26(b), a metallic (top) and a semiconducting SWCNT (bottom) are shown, respectively [39]. The two dominant Raman features are the radial breathing mode (RBM) at low frequencies and the tangential (G band) multi-feature at higher frequencies. Other weak features, such as the disorder induced D band, the combination of in-plane optical and acoustic (iTOLA) band and the M band (an overtone of iTOLA mode) are also shown. When the background intensity is increased, a rich Raman spectrum is observed for the intermediate frequency phonon (IFM) mode, which lies between the RBM and G-band features [49,50].

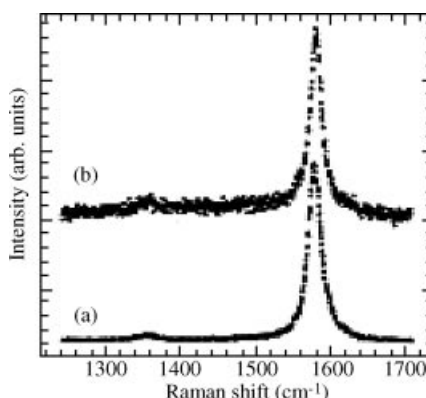


**Figure 9.25** Raman spectra of single wall carbon-tubes [48]. Reprinted from J. M. Holden, P. Zhou, X. X. Bi, et al., Raman scattering from nanoscale carbons generated in a cobalt-catalyzed carbon plasma Chem. Phys. Lett., 220, 186 (1994) with permission of Elsevier

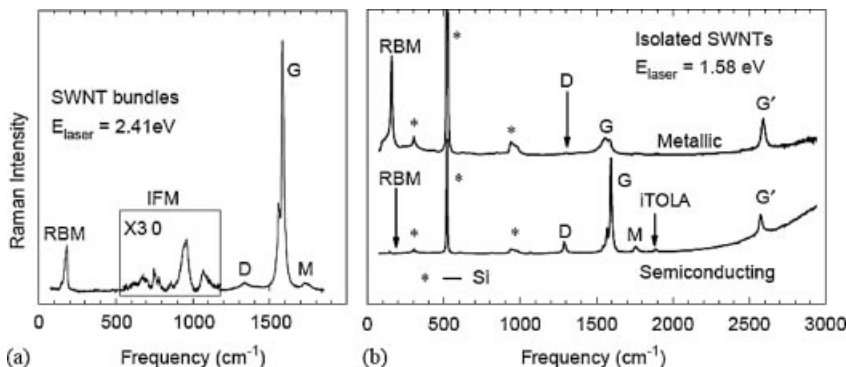


**Figure 9.26** (a) Raman spectra from SWNT bundles grown by high pressure gas phase decomposition of CO (HiPco) process [51]. Reprinted from M.S. Dresselhaus, G. Dresselhaus, R. Saito, et al., Raman spectroscopy of carbon nanotubes, *Physics Reports* 409, 47–99 (2005) with permission of Elsevier. (b) Raman spectra from a metallic (upper) and a semiconducting (lower) SWNT at the single nanotube level, where “\*” denotes the peaks of silicon substrate [52]

In the phonon modes shown in Figure 9.26, as some of them are important, they will be described in detail below:

#### (1) Radial breathing mode (RBM)

The RBM is a characteristic mode related to the diameter of carbon nanotubes, corresponding to the zero energy vibration mode perpendicular to the graphite plane. The RBM can be used to study the nanotube diameter ( $d_t$ ) through its frequency ( $\omega_{\text{RBM}}$ ), to probe the electronic structure through its intensity ( $I_{\text{RBM}}$ ) and to perform an ( $n, m$ ) assignment of a single isolated SWNT from analysis of both  $d_t$  and  $I_{\text{RBM}}$ .

The RBM Raman features correspond to the coherent vibration of the C atoms in the radial direction, as if the tube were “breathing,” as shown in Figure 9.27(a) (see color Plate 22 for

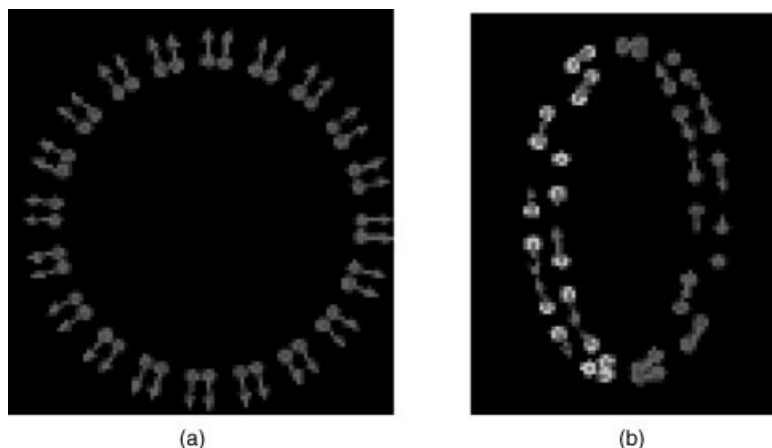


**Figure 9.27** Specific vibration manners of RBM (a) and G mode (b) [53]. Reprinted from S.-L. Zhang, *Raman Spectroscopy and Low-dimensional nanoscale Semiconductors*, Science Press, (2008)

the original Figure 9.27). These features are unique to carbon nanotubes and occur with frequencies of RBM between 120 and  $350\text{ cm}^{-1}$  for SWNTs with diameters in the range  $0.7\text{ nm} < d_t < 2\text{ nm}$ . These RBM frequencies are therefore useful in identifying whether a given carbon material contains SWNTs, through the presence of RBM modes, and for characterizing the nanotube diameter distribution in the sample through use of the relation  $\text{RBM} = A/d_t + B$ , where the A and B parameters are determined experimentally [54,55].

## (2) Graphite-like mode (G mode)

The G mode in SWNT is composed of several peaks and becomes a G band, as shown in Figure 9.28(a), which is due to the confinement effect along the SWNT circumferential

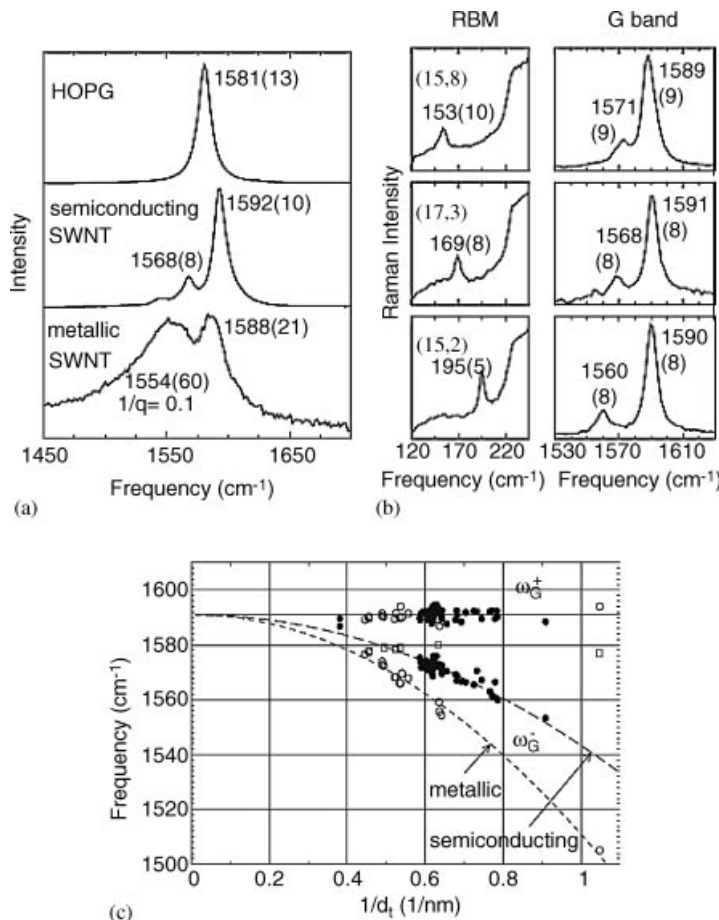


**Figure 9.28** (a) The G-band for HOPG, one semiconducting SWNT, and one metallic SWNT; (b) RBM and G-band Raman spectra for three semiconducting isolated SWNTs of the indicated ( $n, m$ ) values; (c) frequency versus  $1/d_t$  for the two most intense G-band features ( $\omega_G^-$  and  $\omega_G^+$ ) from isolated SWNTs [56]. Reprinted from A. Jorio, A. G. Souza Filho, G. Dresselhaus, et al. G-band resonant Raman study of 62 isolated single-wall carbon nanotubes, *Phys. Rev. B*, 65, 155412 (2002) with permission of the American Physical Society.

direction and the symmetry-breaking effects associated with SWNT curvature, as seen in Figure 9.28(b).

The line shape of the SWNT G-band can be seen in Figures 9.28(a) and (b). Figure 9.28(a) indicates that the G-band for SWNTs consists of two main components, one peak at  $1590\text{ cm}^{-1}$  ( $G^+$ ) and another at about  $1570\text{ cm}^{-1}$  ( $G^-$ ). The  $G^+$  feature is associated with carbon atom vibrations along the nanotube axis (LO phonon mode) and its frequency  $G^+$  is sensitive to charge transfer from additive dopants to SWNTs (upshifts in  $G^+$  for acceptors, and downshifts for donors, as in graphite intercalation compounds (GICs)) [57,58]. The  $G^-$  feature, in contrast, is associated with vibrations of carbon atoms along the circumferential direction of the SWNT (TO phonon), and its line shape is highly sensitive to whether the SWNT is metallic (Breit–Wigner–Fano (BWF) line shape) or semiconducting (Lorentzian lineshape), as shown in Figure 9.28(a) [59,60]. Charge transfer to SWNTs can lead to an intensity increase or decrease of the BWF feature [61,62].

Measurements on the G band at the single nanotube level show that the G-band is a first-order process [31], with the frequency  $G^+$  essentially independent of  $d_t$  or at the chiral angle, while  $G^-$  is dependent on  $d_t$  and whether the SWNT is metallic or semiconducting, but not at the chiral angle. Such diameter-dependent measurements can only be performed at the single nanotube level, and the results can be used along with measurements on other Raman features to corroborate  $(n, m)$  assignments carried out on the basis of the RBM feature. From the diameter dependence of the G band modes shown in Figure 9.28(c), it is clear that the G band for large diameter carbon nanotubes is similar to the one-peak G-band observed in graphite.

Therefore the G-band features can be used for: (1) diameter characterization; (2) to distinguish metallic and semiconducting SWNTs, through strong differences in their Raman line shapes [63,64]; (3) to probe the charge transfer arising from doping an SWCNT; and (4) to study the selection rules in the various Raman scattering processes and scattering geometries.

### (3) Disorder-induced mode (D mode)

The D mode occurring in disordered graphite is also observed in the range of  $1280\text{--}1350\text{ cm}^{-1}$  of CNT Raman spectra. Tan *et al.* investigated the Raman feature of highly oriented pyrolytic graphite (HOPG), carbon nanotubes prepared by the dc arc discharge method (D-CNT) and by the catalytic method (C-CNT) from the view of disorder [65]. Figure 9.29(a) shows the observed Raman spectra, from which the frequencies ( $\omega$ ), line widths (FWHM,  $\Delta\omega_G$  and  $\Delta\omega_D$ ), and the integrated intensity ratio of D mode relative to G mode ( $I_D/I_G$ ) of Raman spectral peaks are extracted and listed in Table 9.6 (a) and shown in Figure 9.29(b).

From Figure 9.29(b), it can be seen that the changes of  $I_D/I_G$  and line width  $\Delta\omega_G$  and  $\Delta\omega_D$  of D-CNT are very distinct, while the others have no obvious change. The  $I_D/I_G$  of C-CNT, D-CNT, and HOPG are both about eight times larger than the former. The studies with electron microscopy and X-ray diffraction by Saito *et al.* have suggested that the nanotubes prepared by the D-CNT are of better quality, meaning the disorder of D-CNT is less than C-CNT [66]. Therefore, the above Raman spectral results verify that parameter  $I_D/I_G$  can be used as a sensitive parameter to express disorder of CNTs, as has been used in graphite [67].

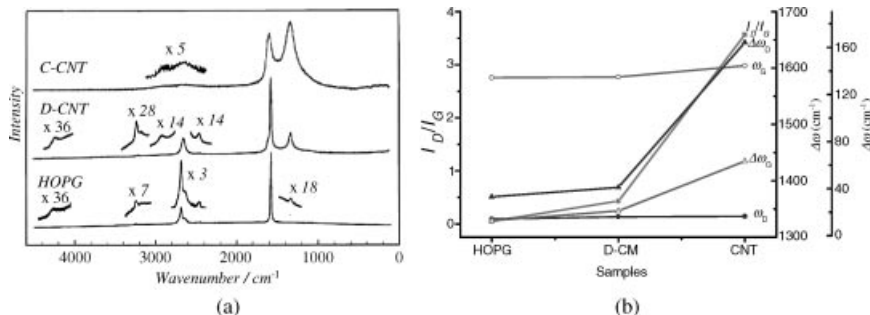


**Figure 9.29** (a) Raman spectra with excitation at 632.8 nm of HOPG, carbon nanotubes prepared by the dc arc discharge method (D-CNT) and by the catalytic method (C-CNT) and (b) the dependence of Raman spectral wavelengths ( $\omega_G$  and  $\omega_D$ ), full widths at half maximum (FWHM,  $\Delta\omega_G$  and  $\Delta\omega_D$ ) and integrated intensity ratio of D mode relative to G mode ( $I_D/I_G$ ) on HOPG and D-CNT [65]. Reprinted from P. Tan, et al., Comparative Study of Carbon Nanotubes Raman Prepared by D.C. Arc Discharge and Catalytic Methods, *J. Raman Spectroscopy*, 28, 369–372 (1997)

## 9.4 Characteristic Raman Spectra of Polar Nano-Semiconductors

The Raman spectra discussed in Section 9.2 for nanosilicon and in Section 9.3 for carbon nanostructures are both involved as non-polar materials. In this section we discuss characteristic Raman spectrum of polar nano-semiconductors. SiC was the first reported polar nano-semiconductor [68] and was investigated by Raman spectroscopy in detail [69]. Therefore the Raman spectrum of an SiC nano-semiconductor as a specimen of polar nano-semiconductors is to be discussed first and then the Raman spectrum of other polar nano-semiconductors will be described.

### 9.4.1 Characteristic Raman Spectra of SiC Nanorods [69]

#### 9.4.1.1 Crystallographic Property and Size

X-ray diffraction spectra of the SiC NR sample shown in Figure 9.30(a) indicates that the crystalline structure of SiC NRs is predominantly that of zincblende 3C-SiC [70]. The EM images of SiC NRs, as shown in Figure 9.30(b), exhibit that most NRs contain a high density of defects, which are thought to be a rotational twin, stacking fault, and so on. Therefore, although the diameters of NRs range from 3 to 30 nm and their lengths are more than 1 mm, the size of crystal grains in rods are less than the rod diameters. Section 9.2.2 verified, for the nano-semiconductors without integral crystal lattice, that Raman scattering of nano-semiconductors originated from grains with complete crystal lattice in such samples. Therefore, it is only the objects with complete crystal lattices in SiC NRs that produce nano-semiconductor Raman scattering.

#### 9.4.1.2 Raman Spectral Feature and Assignment

Raman spectra of SiC NRs are shown in Figure 9.31(a), in which there are two spectral features. The first is that the line shapes of spectral peaks are all broadened and similar to that of photoluminescence (PL). To identify whether these peaks are Raman, the anti-Stokes

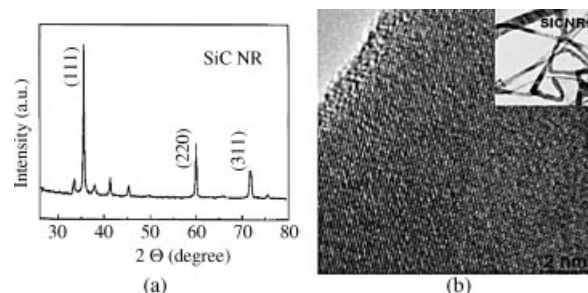


**Figure 9.30** (a) X-ray diffraction spectrum; (b) HRTEM images of SiC-NR sample. The insert in (b) show the TEM image of integral SiC NR samples [70]. Reprinted from W. Han, et al., Continuous synthesis and characterization of silicon carbide nanorods, *Chem. Phys. Lett.*, 265, 374–378 (1997) with permission of Elsevier

Raman spectra of SiC nanorods has been measured, as shown in Figure 9.31(b), together with the Stokes spectrum. According to the universal characteristics of Raman spectra, that the Stokes and anti-Stokes frequency must be equal, the results in Figure 9.31(b) prove that Raman spectrum shown in Figure 9.31(a) is not a PL spectrum but a Raman spectrum.

Another feature of the Raman spectrum shown in Figure 9.31(a) is that there are three Raman spectral structures at low, middle, and high frequencies of  $\sim 791$ ,  $\sim 864$ , and  $\sim 924\text{ cm}^{-1}$ , respectively. These features are different to that of the corresponding bulk 3C SiC film, which shows two optical phonon modes: a TO mode at  $796\text{ cm}^{-1}$  and a LO mode at  $972\text{ cm}^{-1}$  [71]. Sections 6.3.3 and 8.2.1 mentioned that for nanomaterials the crystal structures of nano- and bulk-materials are the same and thus the dispersion curve of bulk materials can be borrowed from NMs. Therefore, it is reasonable to identify the peak at ca.  $791\text{ cm}^{-1}$  in the SiC-NR sample to be TO-like, as its frequency approaches that of the

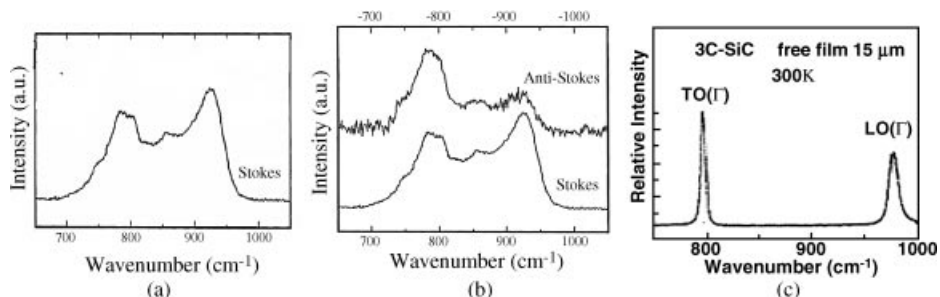


**Figure 9.31** Stokes (a) and anti-Stokes (b) Raman spectra of SiC-NR [69]. Reprinted from S. L. Zhang, et al., Effect of defects on optical phonon Raman spectra in SiC nanorods, *Solid State Commun.*, 111, 647–651 (1999) and Raman spectra of bulk 3C-SiC film [71]. Reprinted from Z. C. Feng, A. J. Mascarenhas, W. J. Choyke et al., Raman scattering studies of chemical vapor deposited cubic SiC films of (100) Si, *J. Appl. Phys.*, 64, 3176–3186 (1988) with permission of the American Institute of Physics.

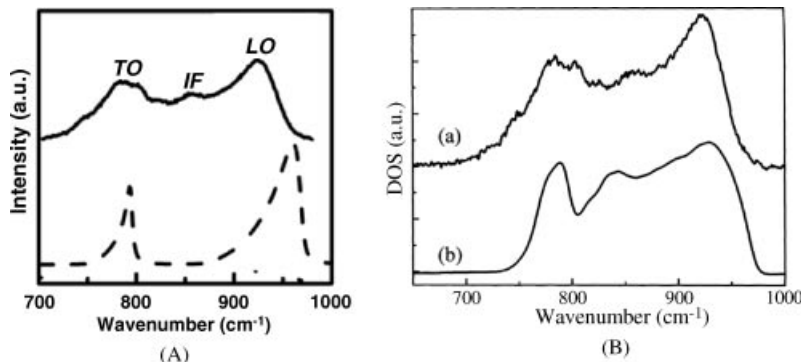


**Figure 9.32** (a) Observed Raman spectra (solid line) and calculated Raman spectra by micro-crystal model (dashed line) [73]. Reprinted from S.-L. Zhang, *Raman Spectroscopy and Low-dimensional nanoscale Semiconductors*, Science Press, (2008). (b) reduced Stokes Raman spectrum corresponding to the Raman spectrum of the SiC-NR sample (a) and calculated effective PDOS for a rectangular SiC-NR with a cross section of  $24 \times 24$  mono-layers. The Gaussian broadening factor is  $5 \text{ cm}^{-1}$  (b), where LO, TO, and IF represent the longitudinal, transverse optical phonon, and interface mode, respectively [69]. Reprinted from S. L. Zhang, et al., Effect of defects on optical phonon Raman spectra in SiC nanorods, *Solid State Commun.*, 111, 647–651 (1999)

bulk SiC TO mode at  $796 \text{ cm}^{-1}$ . However, the peaks at  $\sim 864$  and  $\sim 924 \text{ cm}^{-1}$  have no counterparts in bulk SiC and could not be identified.

To work out the assignment of the Raman peaks at  $\sim 864$  and  $\sim 924 \text{ cm}^{-1}$ , the theoretical Raman spectrum of SiC NRs was calculated by the micro-crystal model described in Section 8.3 and the results are shown in Figure 9.32(a) as a dashed line, together with experimental spectrum as a solid line. The results give a peak in the high region of  $\sim 967 \text{ cm}^{-1}$ , which is far higher than observed peak at  $924 \text{ cm}^{-1}$  and a red shift of a few  $\text{cm}^{-1}$  for the bulk peaks at  $\sim 924 \text{ cm}^{-1}$ , implying the peak could not be induced by the size confinement effect. The defects can introduce a new Raman mode, therefore it is assumed that these two peaks result from the Raman scattering of defects in the samples. However, we did not find any new Raman peaks related to traditional defects in observed spectra. Therefore, the conventional confinement and common defect effects cannot be applied. In addition, no peak in the middle frequency region appears in the calculated spectrum, which disagrees with the observed spectral features.

A salient point, usually ignored, is that the decreasing of nanocrystal size will break the translation symmetry and the Raman spectrum will manifest an amorphous feature. Hereby, by using the microscopic dipole quantum wires model [72], the Raman spectra of SiC NRs was calculated based on the formula of amorphous Raman spectra (7.141) and the calculated spectrum is shown in (b) of Figure 9.32(B). The LO peak in the calculated spectrum is at  $936 \text{ cm}^{-1}$  close to the experimental data. Interestingly, a peak appears at ca.  $840 \text{ cm}^{-1}$ , which coincides with the observed Raman peak in the middle region. Thus observed peaks at  $\sim 864$  and  $\sim 924 \text{ cm}^{-1}$  can be assigned to interface-like modes and LO-like modes, respectively, of which the assign of formal is due to the feature of interface modes, that is, its frequency localizes between frequencies of TO and LO modes.

#### 9.4.1.3 Origin of New Raman Features

The above assignment of Raman spectra of SiC NRs indicates that the corrected assignment is based on amorphous Raman spectral formula. However, it should be noted that the calculated LO and the interface-like mode peaks in SiC-NRs are not the peaks in the phonon density of states, as in amorphous materials. We note that if the Fröhlich electro-phonon interaction is not taken into account, there will be no such peaks. The weighted PDOS of SiC-NRs with different sizes have also been calculated, showing that these LO and interface-like peaks are insensitive to size. This is a strong indication that it is the Fröhlich interaction accompanied in the optical phonons of polar semiconductors, rather than the size confinement effect, that is responsible for the Raman features of SiC-NRs.

#### 9.4.2 Raman Spectra of Nano-ZnO

The characteristic Raman spectrum of ZnO nanomaterials will be discussed by using the nanoparticles (NPs) as the sample.

##### 9.4.2.1 Crystallographic Property and Sizes of ZnO NPs

Figure 9.33 shows that ZnO nanoparticle is the hexagonal wurtzite phase and their average diameter of crystal grains are  $\sim 8$  nm [74].

##### 9.4.2.2 Raman Spectral Feature of ZnO NPs

Raman spectra excited by 515 nm of bulk- and NP-ZnO are shown in Figure 9.34 and their frequencies and assignment of single phonon Raman peaks are listed in Table 9.7 [73]. From the table it can be seen that a novel feature is that the frequencies of NP-ZnO samples are equivalent to those of bulk-ZnO within experimental error.

#### 9.4.3 Raman Spectra of Other Polarized Nano-Semiconductors

The novel Raman features discussed in Sections 9.4.1 and 9.4.2 are all related to the polar nano-semiconductors. It is an interesting question whether discovered novel Raman spectral features in the above are universal for all of polar nano-semiconductors. To answer this, the

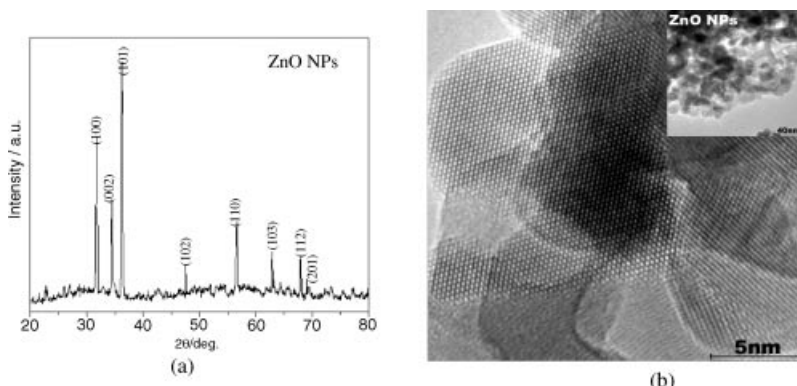


**Figure 9.33** X-ray diffraction spectra (a) and HRTEM images (b) of ZnO nanoparticles [74]. Reprinted from F. Yuan, et al., Preparation and properties of zinc oxide nanoparticles coated with zinc aluminate, *J. Mater. Chem.*, 13, 634–637 (2003)

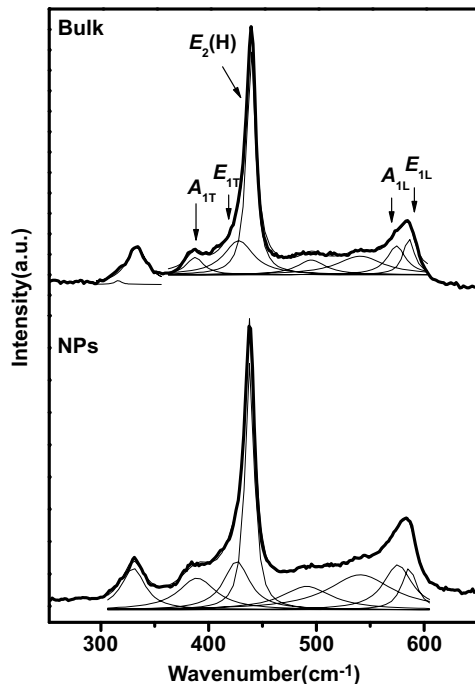


**Figure 9.34** Raman spectra excited by 515 nm of bulk and nanoparticles (NPs) ZnO

observation of Raman spectra of more polar nano-semiconductors is needed, and has been investigated for GaN nano-particles (NPs) and CdSe nano-rods (NRs).

#### 9.4.3.1 Crystallographic Property and Sizes

X-ray diffraction spectra and HRTEM images of GaN NPs [75] and CdSe NRs are shown in Figure 9.35 [76]. The X-ray diffraction spectra indicate that the samples are both crystalline. The HRTEM images show that the samples consist of a collection of grains with different distribution sizes. The average sizes of the crystalline grains in the samples are about 7 and 4 nm for GaN NPs and CdSe NRs, respectively.

#### 9.4.3.2 Observed Raman Spectra

Observed Raman spectra of GaN NPs and CdSe NRs are shown in Figures 9.36(a) [77] and (b) [72], respectively. The frequencies and assignment of Raman peaks are listed in Table 9.8 together with those of bulk- [78] and NP-GaN samples [77].

**Table 9.7** Observed and average frequencies  $\omega_{Ave}$  ( $\text{cm}^{-1}$ ) of phonon of bulk- and nanoparticle (NP)ZnO samples

Sample	$E_2(L)$	$A_{1T}$	$E_{1T}$	$E_2(H)$	$A_{1L}$	$E_{1L}$
Bulk	99	385	426	437	572	584
NPs	97	387	424	436	574	584
Difference	2	2	2	1	-2	0

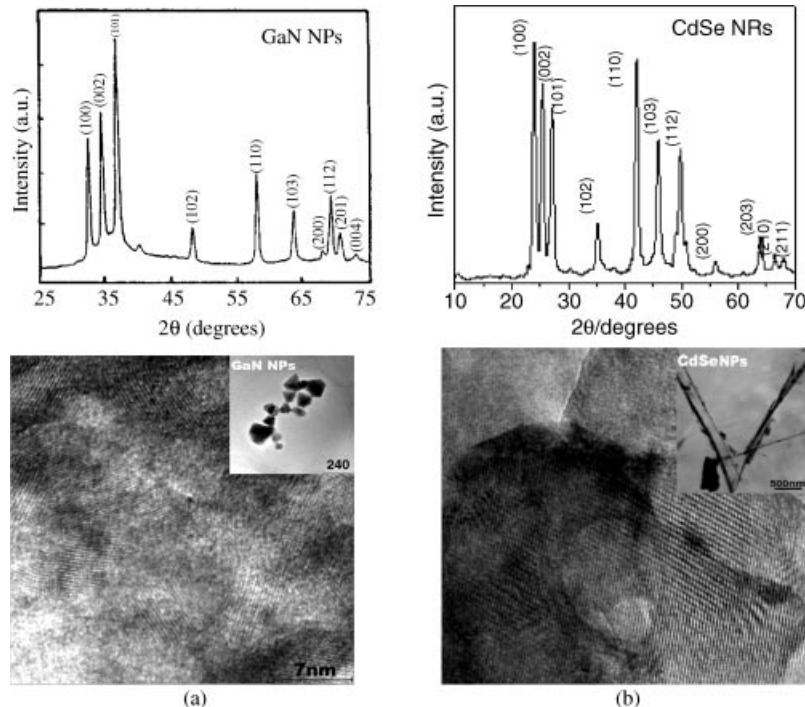


**Figure 9.35** X-ray diffraction spectra (upper) and high-resolution transmission electron microscope image (HRTEM) images (lower) of samples GaN NPs (a) [75] and CdSe NRs (b) [76]. The inserts show the images of whole samples taken by low-resolution electron microscopes. Reprinted from Z. X. Deng, L. B. Li and Y. D. Li, Novel inorganic-organic-layered structures: Crystallographic understanding of both phase and morphology formations of one-dimensional CdE ( $E = S, Se, Te$ ) nanorods in ethylenediamine, *Inorg. Chem.*, 42, 2331 (2003) with permission of the American Chemical Society

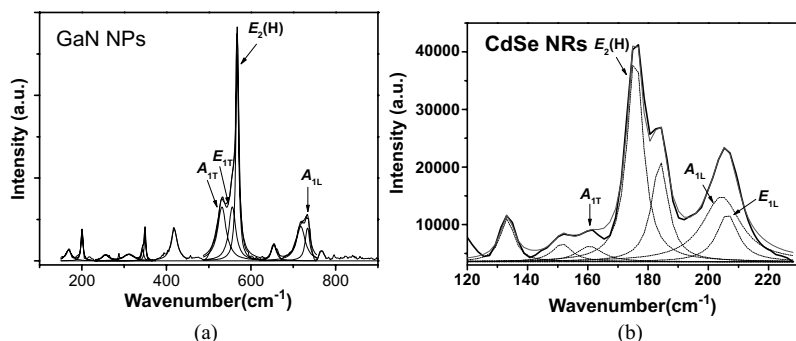


**Figure 9.36** Observed Raman spectra of GaN NPs (a) [77] and CdSe NRs (b) [72]

**Table 9.8** Observed frequencies  $\omega$  ( $\text{cm}^{-1}$ ) and assignment of Raman peaks for GaN nanoparticles (NPs)

Sample	$E_2(\text{L})$	$A_{1\text{T}}$	$E_{1\text{T}}$	$E_2(\text{H})$	$A_{1\text{L}}$	$E_{1\text{L}}$
GaN NPs		531	556	568	733	
Bulk-GaN [78]	144.0	531.8	558.8	567.6	734.0	741.0
Error		1	3	0	1	

**Table 9.9** Observed frequencies  $\omega$  ( $\text{cm}^{-1}$ ) and assignment of Raman peaks of CdSe nanoparticles (NPs) samples [72]

Peak	1	2	3	4	5	6	7	8
Assignment $\omega/\text{cm}^{-1}$	$A_{1\text{T}}/E_{1\text{T}}$ 17.5	$E_2$ 183.6	$A_{1\text{L}}/E_{1\text{L}}$ 205.3		298.7	2LO 408.5	464.0	583.6

From the figures and table, it can be seen that the spectral features are similar to those observed in ZnO samples above, in frequency features between bulk- and nanosamples.

In summary, the above experimental results show that Raman scattering frequencies of optical phonons in polar nano-semiconductors are equivalent to those in corresponding bulk semiconductors.

## 9.5 Multiple-Phonon Raman Spectra

In the previous section, we only discussed single-phonon Raman spectrum, or say first-order Raman spectrum. In this section we introduce multi-phonon (MP) Raman spectra of nanostructures. One of the important characteristics of MP Raman spectra is that the  $k$ -order of the MP Raman peak frequency  $\omega_k$  is related to the first-order single-phonon Raman frequency  $\omega_1$  as

$$\omega_k = k\omega_1 \quad (9.1)$$

Another important characteristic is that the intensity of MP Raman scattering decreases greatly with the increase of order  $k$  of the MP. This leads to the observation that the MP scattering spectrum is difficult and the MP Raman spectra has often to be measure under resonance scattering conditions usually. In the outgoing resonance, that is, the case that the incident light energy  $E_i$ , phonon energy  $E_{ph}$  and electron gap energy  $E_g$  fit the following the relation:

$$E_g = E_i - kE_{ph} \quad (9.2)$$

The hot luminescence process will also match. Moreover, the hot luminescence and MP scattering accompanied with outgoing resonance processes display similar spectral features, and it is of considerable importance to distinguish them.

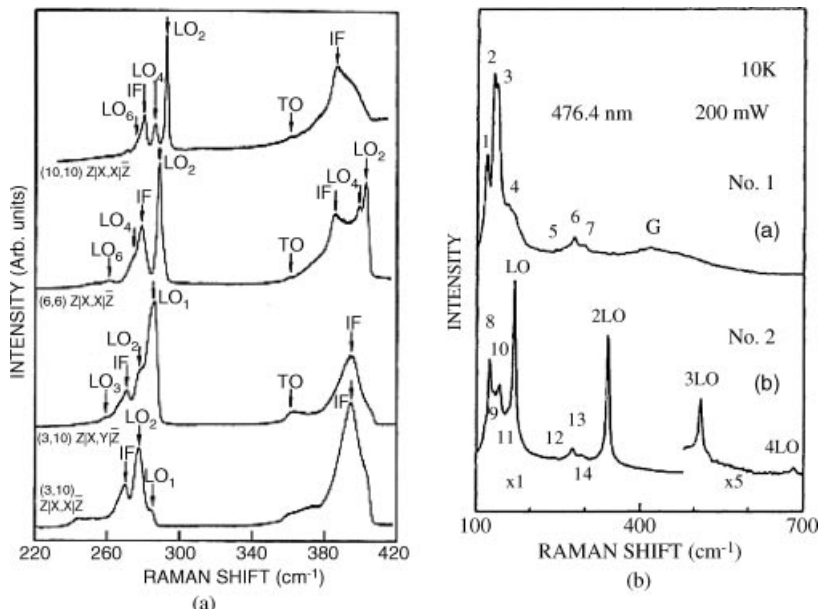


**Figure 9.37** Raman spectra of MP for  $(GaAs)_m/(AlAs)_n$  ( $m,n = 10,10; 6,6; 3,10$  atomic single layer) SLs [79]. Reprinted from D. J. Mowbray, M. Cardona, and K. Ploog, Multiphonon resonant Raman scattering in short-period GaAs/AlAs superlattices, *Phys. Rev. B*, 43, 11815–11824 (1991) with permission of the American Physical Society and  $(HgTe)/(CdTe)$  (Sample 1 = 6.4/6.0 nm and Sample 2 = 8.0/4.0) SLs [82]. Reprinted from Z. C. Feng, S. Perkowitz, and O. K. Wu, Raman and resonant Raman scattering from the HgTe/CdTe superlattice, *Phys. Rev. B*, 41, 6057–6060 (1990) with permission of the American Physical Society.

### 9.5.1 MP Raman Scattering of Superlattices (SLs)

Since the 1980s, MP Raman spectra of SLs, including confined optical modes and macro-interface modes, have been observed and investigated extensively [79–84].

#### 9.5.1.1 MP Raman Spectra of Confinement Optical and Macro-Interface Modes

Figures 9.37(a) and (b) show the MP Raman spectra of confinement optical and macro-interface modes of GaAs/AlAs and  $(HgTe)/(CdTe)$  SL with different thicknesses. The figures clearly show MP Raman spectra of confined longitudinal optical (LO) mode, confined transverse optical (TO) mode, and macroscopic interface (MIF). However, before 1993, there was no MP Raman spectrum of confined optical modes in barrier layers and microscopic interface modes were reported. We now highlight these two types of MP Raman spectra.

#### 9.5.1.2 MP Raman Spectra of Confinement Optical Mode Restricted Within Barrier Layers [85]

Figure 9.38(a) shows an MP spectra with 13th-order MP in a multi-quantum-well short-period SL  $(CdTe)_2(ZnTe)_4/ZnTe$ . Since the measurement was performed at outgoing resonance, it is the first work in analyses of experimental results to exclude the possibility

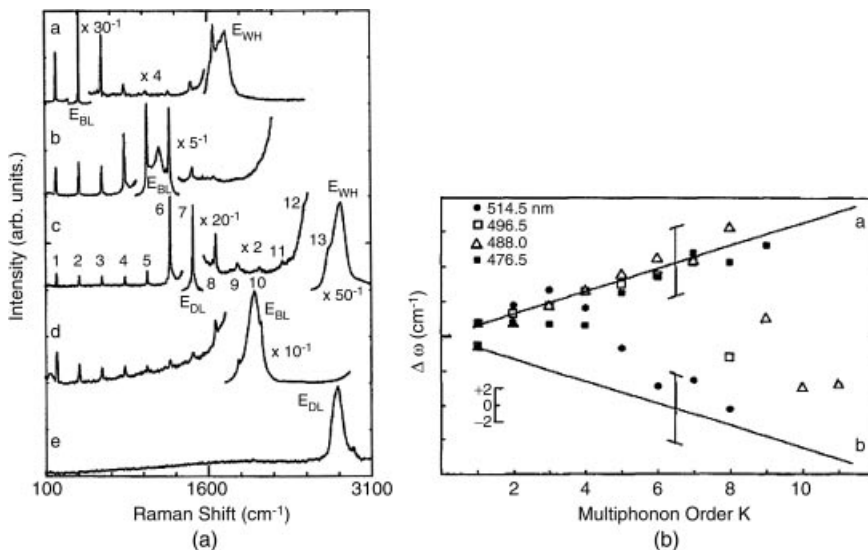


**Figure 9.38** (a) MP Raman spectra of a multi-quantum-well short-period SL ( $\text{CdTe}_2(\text{ZnTe})_4/\text{ZnTe}$ ) sample in a  $Z(XX)Z$  configuration with excitation laser lines of 514.5 nm (a), 496.5 nm (b), 488.0 nm (c), 476.5 nm (d), and 457.9 nm (e), of which the incident photon energies,  $E_{in}$ , are 2.41, 2.50, 2.60, and 2.71 eV, in order. (b) deviation  $\Delta\omega$  of the observed MP frequencies of ZnTe LO phonons  $LO_B$  and  $LO_W$  from the calculated MP frequencies by  $k\omega_{LO}$ .  $k$  is the MP order and  $\omega_{LO}$  equals the observed frequencies of first-order  $LO_B$  (represented by the solid line a) or  $LO_W$  (represented by the solid line b). The positions of the solid lines a and b at integer  $k$  values ( $k > 1$ ) represent the calculated MP frequency positions for ZnTe phonons  $LO_B$  and  $LO_W$ , and were drawn so that the intervals at the same  $k$  value between solid lines a and b are equal to the calculated MP frequency difference of  $LO_B$  and  $LO_W$ . The vertical bars represent experimental error [85]. Reprinted from S. L. Zhang, et al., Multiphonon Raman scattering resonant with two kinds of excitons in a  $(\text{CdTe})_2(\text{ZnTe})_4/\text{ZnTe}$  short-period-superlattice multiple quantum well, *Phys. Rev. B*, 47, 12937–12940 (1993).

that the spectra are from hot luminescence. Based on resonance Raman scattering, is a one-step coherent process and the scattering spectrum is precisely correlated with the energy and polarization of incident light, and excluding can be achieved by check the polarization spectra [86].

Table 9.10 lists the measured depolarization ratios of different order MP spectra and finds that the polarization memory is not lost. Therefore it can be determined that the spectra shown in Figure 9.38(a) are MP Raman spectra under outgoing resonance.

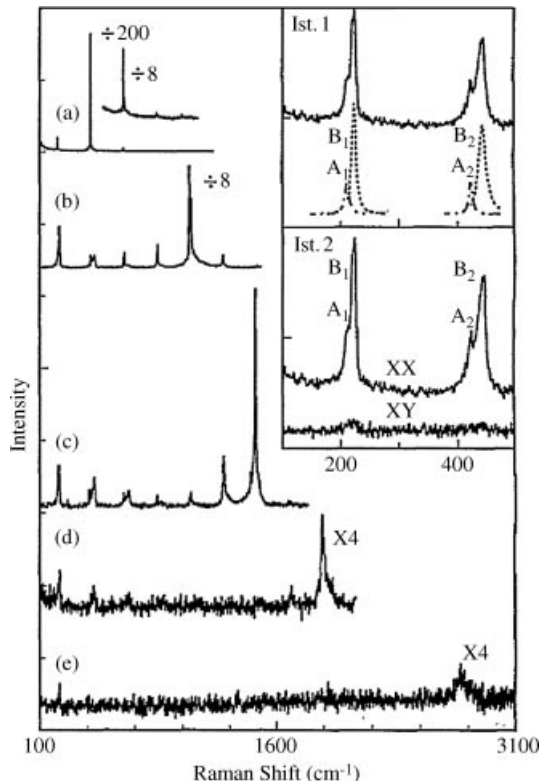
**Table 9.10** The depolarization ratios of the ZnTe longitudinal-optical (LO) multiphonon Raman lines

$E_{in}$ (eV)	1 LO	2 LO	3 LO	4 LO	5 LO	6 LO	7 LO	8 LO	9 LO
2.41	$\omega$ $I_{dp}$	209.5 2.5	420 1.7	630 1.6	836 2	(1040) 1.6	1244 2	1454 2	1658 1.5

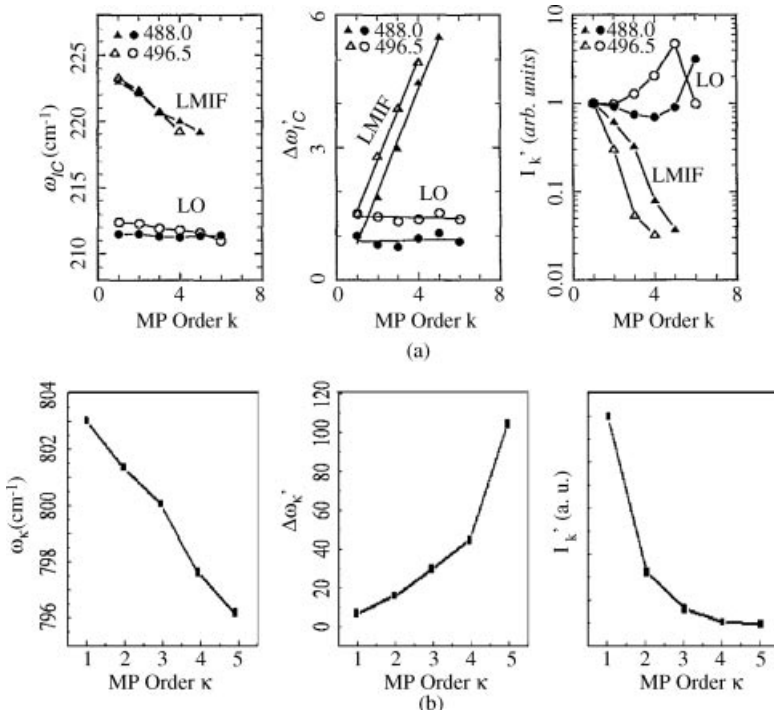
To identify the single phonon type corresponding to MP, the observed frequencies of MP were compared to the calculated MP frequencies by using Equation (9.1) for the frequencies of confined LO phonon within wells and barriers  $\text{LO}_W$  and  $\text{LO}_B$ . Figure 9.38 (b) drew this comparison, from which it can be seen that in an MP Raman spectrum excited 476.6 nm laser, the observed MP frequencies of phonon  $\text{LO}_b$  match the calculated ones, indicating that MP scattering from confined LO phonons within barriers are observed.

#### 9.5.1.3 MP Raman Spectra of Microscopic Interface Phonon [87]

Zhang *et al.* measured MP Raman spectra of 80-period  $(\text{CdTe})_2/(\text{ZnTe})_4$  SLs (AB/CD-type), using 488 and 497 nm wavelength lasers and the results are shown in Figure 9.39. From the figure, we see that there is another MP mode, and that the dependence of frequencies  $\omega_k$ , line width  $\Delta\omega_k$ , and intensity  $I_k$  with MP order  $k$  is different from that of the bulk-like LO mode shown in Figure 9.40(a), meaning it is different from the recognized law of bulk materials and from MP Raman scattering of the micro-interface-mode.



**Figure 9.39** MP Raman spectra excited by (a) 514.5 nm, (b) 496.5 nm, (c) 488.0 nm, (d) 476.5 nm, and (e) 457.9 nm laser lines at 80 K for the  $(\text{CdSe})_4/(\text{ZnTe})_4$  SL sample [87]. Reprinted from S. L. Zhang, *et al.*, Defect-like nature of the interface in AB/CD type superlattices, *Phys. Rev. B*, 52, 1477–1480 (1995)



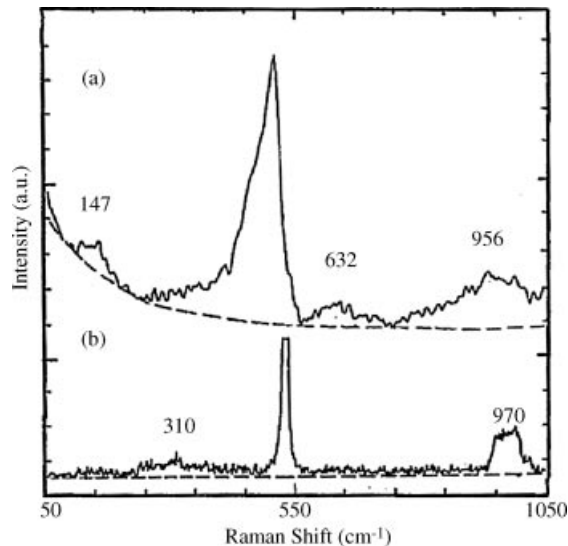
**Figure 9.40** Dependence of frequencies  $\omega_k$ , line width  $\Delta\omega_k$ , and intensity  $I_k$  with MP order  $k$  of MP Raman spectra for the ZnTe bulk-like LO and Zn-Se LMIF modes in the  $(\text{CdSe})_4/(\text{ZnTe})_4$  SL with excitation of 488.0 and 496.5 nm (a) [87]. Reprinted from S. L. Zhang, C. L. Yang, Y. T. Hou, et al., Defect-like nature of the interface in AB/CD type superlattices, *Phys. Rev. B*, 52, 1477–1480 (1995) and the localized mode in color centered SrI [88]. Reprinted from T. P. Martin, Multiple-order Raman scattering by a localized mode, *Phys. Rev. B*, 13, 3617–3622 (1976) with permission of the American Physical Society

Figure 9.40(b) shows the dependence of frequencies  $\omega_k$ , line width  $\Delta\omega_k$ , and intensity  $I_k$  with an MP order  $k$  of MP Raman spectra of color centered SrI localized mode change with MP order  $k$  [88]. Comparing Figure 9.40(b) with Figure 9.40(a), we can see that the similarity between them is good. This indicates that the MP Raman spectra of the micro-interface mode shows the characteristics of defect spectra, meaning the micro-interface mode in SL is the defect mode. Thus, MP Raman reveals that the SL interface is similar to the defects in bulk materials and thus the SL is a defect structure.

## 9.5.2 MP Raman Spectra of Other Nanomaterials

### 9.5.2.1 MP Raman Spectra of Porous Silicon

In bulk silicon, the second-order spectrum has already been observed and studied [89–91]. The second-order MP of the phonon mode at 960 cm $^{-1}$  can be easily observed and was identified as the scattering from the 2LO mode at the boundary of the Brillouin zone.



**Figure 9.41** MP spectrum of pure PS membrane without silicon substrate a) and bulk silicon b) [92]. Reprinted from S. L. Zhang, X. Wang, K. S. Ho, J. Li, P. Diao and S. Cai, Raman spectra in a broad frequency region of p-type porous silicon, *J. Appl. Phys.*, 76, 3016–3019 (1994)

Observed MP spectra of pure PS membrane without silicon substrate and bulk silicon are shown in Figures 9.41(a) and (b), respectively [92]. Figure 9.41(a) shows that there are two high-order peaks at 632 and 956 cm<sup>-1</sup>, which were identified as double phonon of (TA + TO) and 2TO modes, respectively. Comparing double phonon spectrum of PS with that of bulk silicon, some interesting phenomena are found. First, the double phonon (TA + TO) mode was not observed in bulk Si and PS, respectively, which can be attributed to the size confinement effect. Second, the single phonon TO mode corresponding to observed double phonon 2 TO is localized at the boundary rather than at center of the Brillouin zone, as is the case for bulk silicon. Third, the observed frequency of 2 TO in PS is less than that in bulk silicon. This may reflect that the analysis for nanoscale materials by using bulk dispersion relation is inappropriate, which has been confirmed by subsequent theoretical calculation of the silicon nanoparticles dispersion relation [93], as described in Section 8.3.

### 9.5.2.2 MP Raman Spectra of Carbon Nanotube

Since the discovery of carbon nanotubes, MP Raman scattering has been observed. Figure 9.42 shows the overall MP Raman spectra of MWCNT (a) and HOPG (b). The local enlargement MP Raman spectra of MWCNT (c, d) and HOPG (e) are also shown in this figure. From the figure, the fourth-order MP was observed. Based on Lorentz fitting, MP Raman mode frequencies, line widths, intensity ratios (relative to G peak), and the identification of modes are listed in Table 9.11. Figure 9.42 and Table 9.11 show that observed peaks in HOPG are much less than in MWCNT. In the Raman spectra of HOPG

**Table 9.11** MP Raman mode frequencies, linewidths, intensity ratios (relative to G peak) of MWCNT and HOPG

Sample	D	G	$E_{2g}'$	$G + A_{2a}$	$D^*$	D + G	2G	$2E_{2g}'$	3D	2D + G	4D	3D + G	2D = 2G
MWCNT	$\omega$ (cm <sup>-1</sup> )	1356	1582	1623	2456	2708	2949	3186	3245	4049	4289	4548	5343
	FWHM (cm <sup>-1</sup> )	32	16	10	82	50	116	14	14	76	76	5676	5878
		0.13	1.00	0.063	0.026	0.47	0.019	0.064	0.064	0.051	0.051		
HOPG	$\omega$ (cm <sup>-1</sup> )		1574		2445	2682	2720	3164	3240	4058	4294		5666
	FWHM (cm <sup>-1</sup> )		16		50	50	50	12	12	90	90		
		1.00		0.033	0.18	0.46	0.092	0.092	0.092	0.051	0.051		

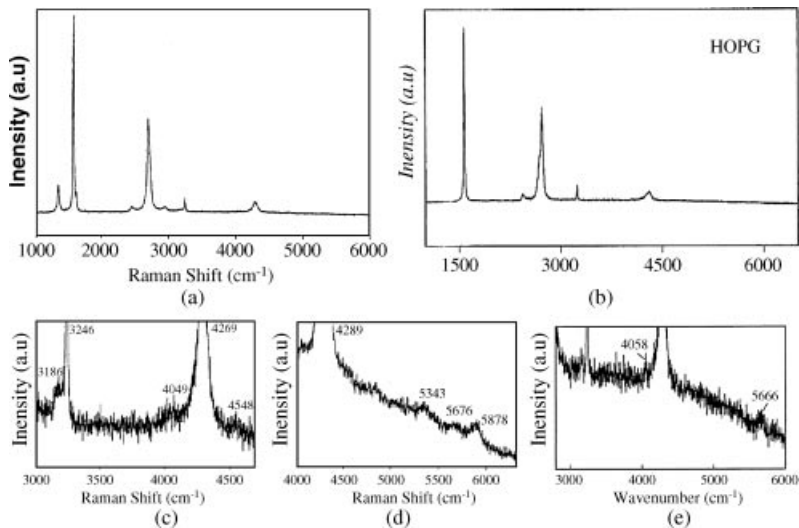


**Figure 9.42** Overall MP Raman spectra of MWCNT (a) and HOPG (b); local enlargement MP Raman spectra of MWCNT (c, d) and HOPG (e) [94]. Reprinted from H. Fumin, Y. K. To, T. Pingheng, et al., Raman Spectra of Carbon Nanotubes and Their Temperature Effect, Chn J. Light Scattering, 10, 10 (1998)

shown in Figure 9.42, the single phonon modes D and  $E_{2g}'$  and MP modes (D + G), (2G + D), 4D, and (2G + 2D) do not appear.

The above results may be interpreted as follows. Raman scattering of phonon modes are decided by phonon dispersion relations and phonon wave vector selection rules of  $\mathbf{q} = 0$ . Section 8.2.4 mentioned for carbon nanotubes that the forming of dispersion curves of carbon nanotubes can be considered as the folding of phonon dispersion curves of the graphite sheet and thus the number of phonon branches will greatly increase. Therefore, it is expected that the number of observed phonon modes in CNT Raman spectra is much larger than in HOPG. A similar phenomenon appears in SLs, as the forming of phonon dispersion curves also can be considered as the folding of phonon dispersion curves of corresponding bulk materials.

#### 9.5.2.3 MP Raman Spectra of Polarized Nano-Semiconductors

Studies on MP Raman spectra of polar nano-semiconductor are constantly published. For example, Demangeot *et al.* observed third-order MP Raman scattering of an LO phonon in a ZnO nanoparticle with 8 nm diameter, as shown in Figure 9.43 together with that in bulk ZnO [95]. From the figure, we see that the frequencies of MP match Equation (9.1), which is different from the MP case of porous silicon.

Recently, Xia *et al.* reported observed Raman spectra of MP including longitudinal acoustic (LA), polar and nonpolar modes of optical phonons ( $A_{1L}$  and  $E_2(H)$ ) in polar

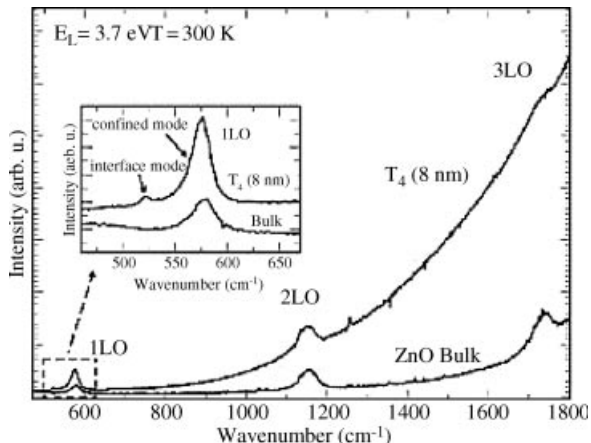


**Figure 9.43** MP Raman spectra of 8 nm-diameter particle and bulk ZnO samples. Inset gives details of the spectra in the first-order range [95]. Reprinted from F. Demangeot, V. Paillard, P. M. Chassaing, et al., Experimental study of LO phonons and excitons in ZnO nanoparticles produced by room-temperature organometallic synthesis, *Appl. Phys. Lett.*, 88, 071921 (2006) with permission of the American Institute of Physics

nano-semiconductor ZnO nanoparticles, as shown in Figure 9.44, of which the frequencies of MP Raman peaks are listed in Table 9.12 [96]. The results show that MP frequencies of optical phonon, including polar and non-polar modes, fit Equation (9.1) well.

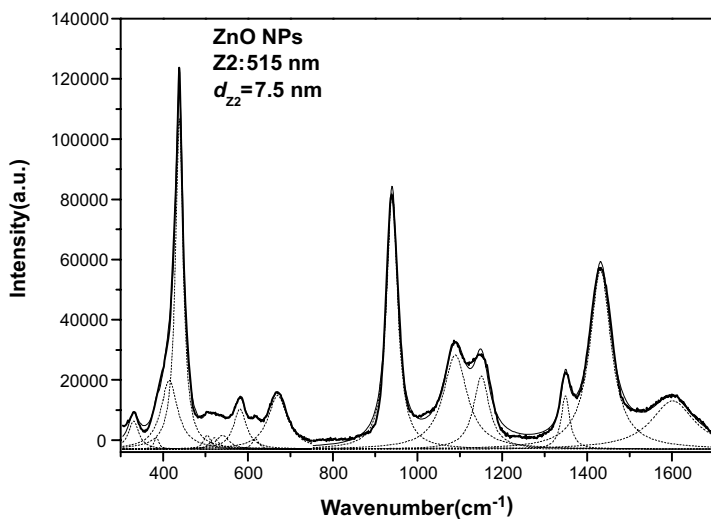


**Figure 9.44** Observed MP Raman spectra of polar nano-semiconductors ZnO nanoparticles [96]

**Table 9.12** Frequencies and assignment of MP Raman peaks for polar nano-semiconductors ZnO nanoparticles (NPs) [96]

	ZnO NPs	Bulk ZnO [76]
$2E_2(L)^M$	331	334
$A_{1T}$	385	380
$E_{1T}$	415	407
$E_2(H)$	438 540	437
$A_{1L}$		574
$A_{1L} + E_2(L)$	670	
$2E_2(H)$	940 1089 1151 1349	1084 1149
$3E_2(H)$	1431 1601	

## 9.6 Anti-Stokes Raman Spectra

In prior discussions in this chapter, we were only concerned about the Stokes spectrum. In this section, we will discuss the anti-Stokes spectrum.

### 9.6.1 Universal Characteristics of Raman Scattering Related to Anti-Stokes Raman Scattering

Chapter 1 pointed out that the absolute value of frequencies of the anti-Stokes and Stokes Raman spectra are equal, which is one of the two universal characteristics of Raman scattering. If  $\omega_S$  and  $\omega_{AS}$  represent Stokes and anti-Stokes Raman frequencies respectively, and we define  $\Delta$  as the difference of the absolute value between anti-Stokes and Stokes Raman frequencies, then this universal feature can be expressed as

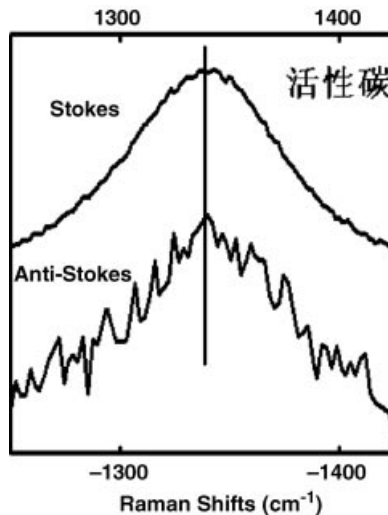
$$\Delta \equiv |\omega_{AS}| - |\omega_S| \equiv 0 \quad (9.3)$$

Figure 9.45 exhibits observed Stokes and anti-Stokes Raman spectra of activated carbon, which clearly displays the universal characteristics of  $\Delta = 0$ .

This universal feature was often used to distinguish Raman spectrum from other kinds of spectra, such as photoluminance. In Section 9.4.1, this universal feature of Raman spectra has been used successful in identifying Raman spectrum of SiC nanorods.

### 9.6.2 Abnormal anti-Stokes Raman Scattering (AARS) of Carbon Nanotubes [97]

Zhang *et al.* first observed abnormal anti-Stokes Raman scattering (AARS) in carbon nanotubes [98,99]. They found that  $\Delta \neq 0$  in the multi-walled carbon nanotube D mode, as shown in Figure 9.46. Then Kneipp *et al.* also observed AARS of  $\Delta \neq 0$  in the G-mode of



**Figure 9.45** Observed Stokes and anti-Stokes Raman spectra of activated carbon. Reprinted from S.-L. Zhang, *Raman Spectroscopy and Low-dimensional nanoscale Semiconductors*, Science Press, (2008)

single-walled carbon nanotubes [102]. Kneipp *et al.* interpreted this  $\Delta \neq 0$  phenomenon as peaks at the sides of Stokes and anti-Stokes not being in the same mode; one is metallic and another is semiconductive [100]. Some ones consider it to be induced by the carbon nanotube samples being the multi layers or temperature effects. Obviously, the authenticity examination for the above universal characteristics will contribute to an understanding of basic physical laws: whether the invariance of time reversal is still effective in the light-scattering process in nanostructures.

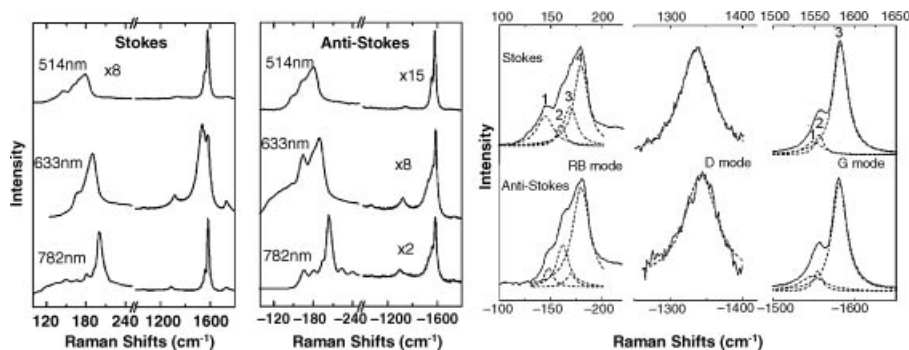


**Figure 9.46** Stokes and anti-Stokes Raman spectra of SWCNTs excited at 515, 633, and 782 nm (a) and Lorentzian fitting of the Stokes and anti-Stokes RB, D, and G bands of SWCNTs excited at 515 nm (b) [97]. Reprinted from S. L. Zhang, *et al.*, Abnormal anti-Stokes Raman scattering of carbon nanotubes, *Phys. Rev. B*, 66, 035413 (2002)

**Table 9.13** Difference of Stokes and anti-Stokes Raman frequencies  $\Delta$  ( $\text{cm}^{-1}$ ) of the RB, D, and G modes of SWCNTs and MWCNT.  $\lambda_L$  and P are the exciting wavelength in nm and the power of a 782 nm laser in %

$\lambda_L/P$	RB <sub>1</sub>	RB <sub>2</sub>	RB <sub>3</sub>	RB <sub>4</sub>	D	G <sub>1</sub>	G <sub>2</sub>	G <sub>3</sub>
<b>SWCNT</b>								
515	-2	0	+2	+1	+5	-1	-1	-1
633	0	-1	-2		+8	+5	0	-1
782	+1	-1			+11	0	+1	0
100%					+14	+1		
50%					+13	+1		
<b>MWCNT</b>								
633					+7	-1		

To confirm if AARS is due to the features mentioned above, Zhang *et al.* performed more investigations and published their results in Ref. [97]. Figure 9.46(a) shows the Stokes and anti-Stokes Raman spectra of SWCNT samples excited by different wavelengths at 515, 633, and 782 nm [99]. From Figure 9.46(a), we see that the shapes of the Stokes and anti-Stokes G peaks excited at 515 and 782 nm are characteristics of semiconducting CNTs [101]. In contrast, the spectra excited at 633 nm show asymmetric line shapes and are indicative of metallic and semiconducting CNTs in the Stokes and anti-Stokes regions, respectively. Typical Lorentzian spectral fits for RB, D, and G bands in spectra excited by 515 nm are performed and the fitting results are shown in Figure 9.46(b) and listed in Table 9.13. Figure 9.46(b) and Table 9.13 show that the RB and G modes consist of multiple peaks of RB<sub>1</sub>, RB<sub>2</sub>, RB<sub>3</sub>, RB<sub>4</sub>, and G<sub>1</sub>, G<sub>2</sub>, G<sub>3</sub>, while the D peak can be adequately fitted by only one peak, making it easier to compare the individual Stokes peak with its corresponding anti-Stokes peak.

Table 9.13 shows no AARS with different excitation wavelength for the G and RB modes to within the frequency accuracy of the Raman spectrometer, except for the G<sub>1</sub> peak in the spectrum excited at 633 nm. The latter is due to the asymmetry of the line shapes [102]. In contrast, all  $\Delta$  for D peak are significantly larger than zero. Thus, all AARS are due to a possible artifact from the asymmetric line shape of the Stokes and/or anti-Stokes peaks. Furthermore, AASR scattering exists for the D mode for all excitation wavelengths, ruling out the possibility that AARS results from strong excitation wavelength dependence of Raman peaks.

### 9.6.3 Origin and Nature of AARS of Carbon Nanotubes [97]

The above results indicate that AARS in CNT is present in the D mode unambiguously and independent of changes in excitation wavelength, sample temperature, or wall number of CNTs.

The universal characteristic that the absolute value of frequencies of the anti-Stokes and Stokes Raman spectra are equal is the embodiment of the invariance of time reversal, one of the basic laws of physics. Therefore, to make the origin and nature of AARS clear is related to the availability of basic physical laws in nanostructures.

Note that the changes of temperature and wall layer numbers of samples and excitation wavelengths do not change the global nanoscale tubular structure that is characteristic of

**Table 9.14** Measured  $\Delta$  values of single-walled carbon nanotubes (SWCNT), multi-walled carbon nanotubes (MWCNT), crystal graphite (HOPG) and the crystal graphite with gold ions doping (HOPGAu) [94]. Table 1 in S. L. Zhang, F. M. Huang, L. X. Zhou, Y. Zhan, K. T. Yue, Study on the Abnormal Anti2Stokes Raman Spectra of Carbon Nanotubes, Chin. J. Light Scattering, 11, 110 (1999)

Sample	MWCNT	SWCNT	HOPG	HOPGAu
$\Delta =$	+7( $\neq 0$ )	+7( $\neq 0$ )	/( $= 0$ )	-7.7( $\neq 0$ )

CNTs, and the changing of excitation wavelengths will selectively excite the tubes of different diameter [53], while changing sample temperature can alter the C–C bond length [103]. This suggests that AARS is likely to be a basic characteristic of the global nanoscale tubular structure. Since CNTs are essentially cylindrical tubes of nanoscale diameters formed by rolling a graphite sheet, the tubular structure can be considered as a defect-like structure compared with a flat graphite sheet. Therefore authors in Ref. [97] proposed that AARS in CNTs originates from the defect-like property of the nanoscale tubular structure itself. To check this proposition, Stokes and anti-Stokes spectra of SWCNT, MWCNT, pure crystal graphite (HOPG), and HOPG with gold ions doping (HOPGAu) have been measured and the obtained  $\Delta$  values are listed in Table 9.14. From the table it is found that  $\Delta = 0$  and  $\Delta \neq 0$  are for HOPG, and HOPGAu, respectively, confirming the above the proposition.

The amount of deviation of the tubular structure from the flat graphite sheet should represent the defect-like degree of nanoscale tubes. This means that the defect-like degree of nanoscale tubes can be characterized by tube diameter  $d$ . Thus, it can be deduced that the  $d \rightarrow \infty$  corresponds to the perfect HOPG and the  $d$  decreasing indicates the increasing of the defect-like degree of CNTs. Thus,  $\Delta$  should decrease with increasing  $d$  and approach to zero as  $d \rightarrow \infty$ . To probe this prediction, average size  $\langle d \rangle$  and corresponding  $\Delta$  of CNTs have been measured simultaneously. The results are shown in Figure 9.47, which shows that  $\Delta$  decreases with increasing  $d \rightarrow \infty$  and confirms that AARS originates from the global nanoscale tubular structure of CNTs and reflects the defect-like nature of the CNT structure.

To gave an interpretation of AARS based on theory, Zhang *et al.* [99] also provided the calculated electron energy band, electron density of states, and phonon dispersion curve of three carbon nanotube samples (14,0), (9,9), and (17,0), as shown in Figure 9.48. From the electron energy band structure shown in this figure, it can be see that there is a condition to produce double resonance Raman scattering in carbon nanotubes, and the double resonance of theoretical Equation [102] was used.

According to electron energy bands and phonon dispersion curves of the carbon nanotubes shown in Figure 9.48,  $\Delta$  of carbon nanotubes is calculated. Table 9.15 lists the calculated results of three carbon nanotube samples (14,0), (9,9), and (17,0). From the table, it can be seen that the calculated results are in close agreement with experimental values, confirming the Raman scattering of  $\Delta \neq 0$  can be explained by the double resonance mechanism.

Moreover, because the double resonance in bulk materials can only be caused by defects and stress [100], the successful demonstration of double resonance mechanism also

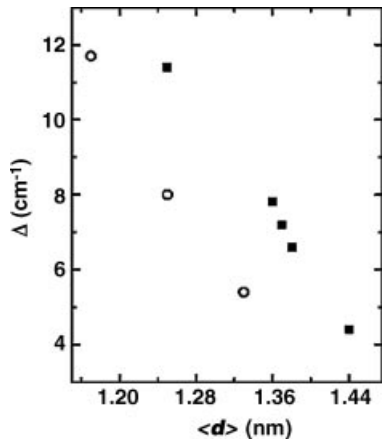


**Figure 9.47** Stokes and anti-Stokes Raman frequencies difference  $\Delta$  versus average diameter,  $\langle d \rangle$ , for D mode at different spots of sample excited at 515 nm (solid square) and at the same spot excited at 616, 633, and 782 nm (open circle) for SWCNT samples [99]. Reprinted from S. L. Zhang, X. Hu, H. Li, et al., Abnormal anti-Stokes Raman scattering of carbon nanotubes, *Phys. Rev. B*, 66, 035413 (2002)

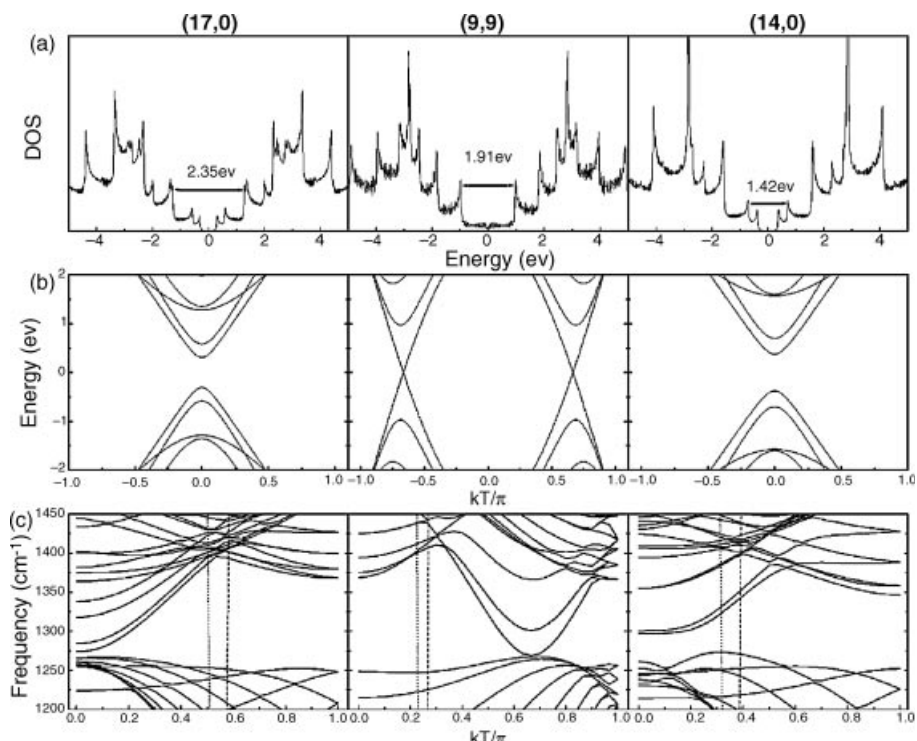


**Figure 9.48** Calculated electron density of states (DOS) (a) and dispersion curves of the electron (b) and phonon (c) of (17,0), (9,9), and (14,0) CNTs [99]. Reprinted from S. L. Zhang, X. Hu, H. Li, et al., Abnormal anti-Stokes Raman scattering of carbon nanotubes, *Phys. Rev. B*, 66, 035413 (2002)

**Table 9.15** Calculated and observed Stokes and anti-Stokes Raman frequencies  $\omega_S$  and  $\omega_{AS}$  and corresponding frequency difference  $\Delta$  of (17,0), (9,9), and (14,0) CNTs [99]

Tube	v(eV/q)	q	$\omega_S$ (cm <sup>-1</sup> )	$\omega_{AS}$ (cm <sup>-1</sup> )	$\Delta$ (cm <sup>-1</sup> )
(17,0)	Calc.	4.44	0.50	1388	
			0.58		-1349
	Obs.			1337	-1342
			0.22	1399	+5
(9,9)	Calc.	7.92			
			0.27		-1408
	Obs.			1314	-1322
(14,0)	Calc.	4.49			+9
			0.39		-1342
	Obs.			1287	+11
				-1298	

provides further proof that carbon nanotubes are defect structures. Because the  $\Delta \neq 0$  is derived from the special tube structure of nanocarbon, on the one hand, it should not be regarded that traditional principles of Raman scattering do not stand in carbon nanotubes; on the other hand, it can be inferred in other nanoscale systems of special-shaped structures, such as tubular structures, that anomalous phenomena of the universal Stokes characteristics are likely to occur.

The viewpoint on the defect nature of the CNT tube structure is similar to the conclusion in SLs that the interface structure in SL possesses the defect-like nature [103].

## References

- [1] (a) Zhang, S.L., Hou, Y.T., He, G.S., Qian, B.D., and Cai, S.M. (1992) *J. Appl. Phys.*, **72**, 4469–4471.(b)Zhang, S.L. (2008) *Raman Spectroscopy and Low-dimensionsal Nanoscale Semiconductors*(in Chinese), Science Press, Beijing.
- [2] Ferrari, A.C. and Robertson, J. (2001) *Phys. Rev.*, **64**, 075414.
- [3] Colvard, C., Merlin, R., Klein, M.V., and Gossard, A.C. (1980) *Phys. Rev. Lett.*, **45**, 298–301.
- [4] Jusserand, B., Paquet, D., and Regreny, A. (1984) *Phys. Rev. B*, **30**, 6245–6247.
- [5] Zhang, S.L., Levi, D.H., Gant, T.A., Klein, M.V., and Klem, J., and Morkoç, H. (31 Aug-3 Sep 1986) *Raman Investigation of Confined Optic Phonons and their Annealing Effects in GaAs/AlAs Superlattices*. Proc. 10th of ICORS, Eugene Oregon, USA pp. 9–4; (b).
- [6] Sood, A.K., Menéndez, J., Cardona, M., and Ploog, K. (1985) *Phys. Rev. Lett.*, **54**, 2115–2118.
- [7] Jin, Y., Hou, Y.T., Zhang, S.L., Li, J., Yuan, S.X., and Qin, G.G. (1992) *Phys. Rev. B*, **45**, 12141–12143.
- [8] Barker, A.S. Jr., Merz, J.L., and Gossard, A.C. (1978) *Phys. Rev. B*, **17**, 3181–3196.
- [9] Somtos, P.V. and Ley, L. (1987) *Phys. Rev. B*, **36**, 3325–3335.
- [10] Sood, A.K., Menéndez, J., Cardona, M., and Ploog, K. (1985) *Phys. Rev. Lett.*, **54**, 2111–2114.
- [11] Wang, R.P., Jiang, D., and Ploog, K. (1988) *Solid State Commun.*, **65**, 661–663.
- [12] Zhang, S.L., Gant, T.A., Delane, M., Klein, M.V., Klem, J., and Morkoc, H. (1988) *Chin. Phys. Lett.*, **5**, 113–116.
- [13] Huang, K., Zhu, B.F., and Tang, H. (1990) *Phys. Rev. B*, **41**, 5825–5842.
- [14] Lassnig, R. (1984) *Phys. Rev. B*, **30**, 7132–7137.

- [15] Fasolino, A., Molinari, E., and Maan, J.C. (1986) *Phys. Rev. B*, **33**, 8889–8891.
- [16] Goodes, S.R., Jenkins, T.E., Beale, M.I.J., Benjamin, J.D., and Pickering, C. (1988) *Semicod. Sci. Tech.*, **3**, 483–487.
- [17] Tsu, R., Shen, H., and Dutta, M. (1992) *Appl. Phys. Lett.*, **60**, 112–114.
- [18] Zhang, S.L., Hou, Y., Ho, K.S., Qian, B., and Cai, S. (1992) *J. Appl. Phys.*, **72**, 4469–4471.
- [19] Sui, Z., Leong, P.P., Herman, I.P., Higashi, G.S., and Temkin, H. (1992) *Appl. Phys. Lett.*, **60**, 2086–2088.
- [20] Yu, D.P., Lee, C.S., Bello, I., Zhou, G.W., and Bai, Z.G. (1998) *Solid State Commun.*, **105**, 403–407.
- [21] Li, B., Yu, D., and Zhang, S.L. (1999) *Phys. Rev. B*, **59**, 1645–1648.
- [22] Fujii, M., Kanzawa, Y., Hayashi, S., and Yamamoto, K. (1996) *Phys. Rev. B*, **54**, R8373–R8376.
- [23] Zi, J., Zhang, K., and Xie, X. (1998) *Phys. Rev. B*, **58**, 6712–6715.
- [24] Gupta, R., Xiong, Q., Adu, C.K., Kim, U.J., and Eklund, P.C. (2003) *Nano Lett.*, **3**, 627–631.
- [25] Chang, G. (2007) *Physica E*, **38**, 109–111.
- [26] Yip, S.K. and Chang, Y.C. (1984) *Phys. Rev. B*, **30**, 7037–7059.
- [27] Shen, M.Y. and Zhang, S.L. (1993) *Phys. Letts. A*, **176**, 254–258.
- [28] Yoshikawa, M., Mori, Y., Maegawa, M., Katagiri, G., Ishida, H., and Ishitani, A. (1993) *Appl. Phys. Lett.*, **62**, 3114–3116.
- [29] Yoshikawa, M., Mori, Y., Obata, H., et al. (1995) *Appl. Phys. Lett.*, **67**, 694–696.
- [30] Gruen, D.M. (1999) *Annu. Rev. of Mat. Sci.*, **29**, 211–259.
- [31] Ferrari, A.C. and Robertson, J. (2001) *Phys. Rev. B*, **64**, 075414.
- [32] López-Ríos, T., Sandré, É., Leclercq, S., and Sauvain, É. (1996) *Phys. Rev. Lett.*, **76**, 4935–4938.
- [33] Nemanich, R.J., Glass, J.T., Lucovsky, G., and Shroder, R.E. (1988) *J. Vac. Sci. Technol. A*, **6**, 1783–1787.
- [34] Yan, Y., Zhang, S.L., Hark, S.K., et al. (2004) *Chinese J. Light Scattering*, **16**, 131–135.
- [35] Yan, Y., Zhang, S.L., Zhao, X., Han, Y. and Hou, L. (Dec 07–12 2001) *Proc. Chinese Conf. Light Scattering*, Xiamen Fujian; (2003) *Chinese Sci. Bull.*, **48**, 2562–2563.
- [36] Zi, J., Zhang, K.M., and Xie, X.D. (1997) *Phys. Rev. B*, **55**, 9263–9266.
- [37] Ferrari, A.C., Meyer, J.C., Scardaci, C., et al. (2006) *Phys. Rev. Lett.*, **97**, 187410.
- [38] Calizo, I., Balandin, A.A., Bao, W., Miao, F., and Lau, C.N. (2007) *Nano Lett.*, **9**, 2645–2649.
- [39] Dresselhaus, M.S., Dresselhaus, G., and Eklund, P.C. (1996) *J. Raman Spectrosc.*, **27**, 351–371.
- [40] Wang, K.A., Wang, Y., Zhou, P., et al. (1992) *Phys. Rev. B*, **45**, 1955–1958.
- [41] Eklund, P.C., Zhou, P., Wang, K.A., Dresselhaus, G., and Dresselhaus, M.S. (1992) *J. Phys. Chem. Solids*, **53**, 1391–1413.
- [42] Dong, Z.H., Zhou, P., Holden, J.M., Eklund, P.C., Dresselaus, M.S., and Dresselhaus, G. (1993) *Phys. Rev. B*, **48**, 2862–2865.
- [43] Jishi, R.A., Mirie, R.M., and Dresselhaus, M.S. (1992) *Phys. Rev. B*, **45**, 13685–13689.
- [44] Quong, A.A., Rederson, M.R., and Feldman, J.L. (1993) *Solid State Commun.*, **87**, 535–539.
- [45] Feldman, J.L., Broughton, J.Q., Boyer, L.L., Reich, D.E., and Kluge, M.D. (1992) *Phys. Rev. B*, **46**, 12731–12736.
- [46] Iijima, S. (1991) *Nature*, **354**, 56–58.
- [47] Iijima, S. and Ichihashi, T. (1993) *Nature*, **363**, 603–605.
- [48] Holden, J.M., Zhou, P., Bi, X.X. et al. (1994) *Chem. Phys. Lett.*, **220**, 186.
- [49] Fantini, C., Jorio, A., Souza, M. et al. (2004) *Phys. Rev. Lett.*, **93**, 087401.
- [50] Brar, V.W., Samsonidze, G.G., Dresselhaus, M.S. et al. (2002) *Phys. Rev. B*, **66**, 155418.
- [51] Dresselhaus, M.S., Dresselhaus, G., Saito, R., and Jorio, A. (2005) *Phys. Rep.*, **409**, 47.
- [52] Eklund, P., Holden, J., and Jishi, R. (1995) *Carban*, **33**, 959.
- [53] Zhang, S.L. (2008), *Raman spectroscopy and Low-dimensional Nano-semiconductors*, Science Press, Beijing China.

- [54] Jorio, A., Saito, R., Hafner, J.H. *et al.* (2001) *Phys. Rev. Lett.*, **86**, 1118–1121.
- [55] Souza Filho, A.G., Chou, S.G., Samsonidze, G.G. *et al.* (2004) *Phys. Rev. B*, **69**, 115428.
- [56] Jorio, A., Souza Filho, A.G., Dresselhaus, G. *et al.* (2002) *Phys. Rev. B*, **65**, 155412.
- [57] Dresselhaus, M.S. and Dresselhaus, G. (1981) *Adv. Phys.*, **30**, 139–326.
- [58] Enoki, T., Endo, M., and Suzuki, M. (2003) *Graphite Intercalation Compounds and Applications*, Oxford University Press, New York.
- [59] Pimenta, M.A., Marucci, A., Empedocles, S.A. *et al.* (1998) *Phys. Rev. B*, **58**, R16016–R16019.
- [60] Brown, S.D.M., Jorio, A., Corio, P. *et al.* (2001) *Phys. Rev. B*, **63**, 155414.
- [61] Corio, P., Santos, P.S., Brar, V.W., Samsonidze, G.G., Chou, S.G., and Dresselhaus, M.S. (2003) *Chem. Phys. Lett.*, **370**, 675–682.
- [62] Corio, P., Jorio, A., Demir, N., and Dresselhaus, M.S. (2004) *Chem. Phys. Lett.*, **392**, 396–402.
- [63] Jorio, A., Pimenta, M.A., Filho, A.G.S., Saito, R., Dresselhaus, G., and Dresselhaus, M.S. (2003) *New J. Phys.*, **5**, 1–17.
- [64] Dresselhaus, M.S., Dresselhaus, G., Jorio, A., Souza Filho, A.G., Samsonidze, G.G., and Saito, R. (2003) *J. Nanosci. Nanotechnol.*, **3**, 19–37.
- [65] Tan, P., Zhang, S.L., Yue, K.T., Fumin, Z., Shi, X., and Zhou and, Z. (1997) *J. Raman Spectrosc.*, **28**, 369–372.
- [66] Saito, Y., Yoshikawa, T., Bandow, S., Tomita, M., and Hayashi, T. (1993) *Phys. Rev. B*, **48**, 1907–1909.
- [67] Nakamura, K., Fujitsuka, M., and Kitajima, M. (1990) *Phys. Rev. B*, **41**, 12260–12263.
- [68] Dai, H., Wong, E.W., Lu, Y.Z., Fan, S., and Lieber, C.M. (1995) *Nature*, **375**, 769–772.
- [69] Zhang, S.L., Zhu, B.F., Huang, F., *et al.* (1999) *Solid State Commun.*, **111**, 647–651.
- [70] Han, W., Fan, S., Li, Q., Liang, W., Gu, B., and Yu, D. (1997) *Chem. Phys. Lett.*, **265**, 374–378.
- [71] Feng, Z.C., Mascarenhas, A.J., Choyke, W.J., and Powell, J.A. (1988) *J. Appl. Phys.*, **64**, 3176–3186.
- [72] Huang, K. and Zhu, B.F. (1988) *Phys. Rev. B*, **38**, 13377–13386.
- [73] Zhang, S.L., Shao, J., Hoi, L.S., *et al.* (2005) *Phys. Stat. Sol. (c)*, **2**, 3090.
- [74] Yuan, F., Hu, P., Yin, C., Huang, S., and Li, J. (2003) *J. Mater. Chem.*, **13**, 634–637.
- [75] Li, H.D., Yang, H.B., Zou, G.T., *et al.* (1997) *J. Cryst. Growth*, **171**, 307–310.
- [76] Deng, Z.X., Li, L.B., and Li, Y.D. (2003) *Inorg. Chem.*, **42**, 2331.
- [77] Li, H.D., Zhang, S.L., Yang, H.B., *et al.* (2002) *J. Appl. Lett.*, **91**, 4562–4567.
- [78] Davydov, V.Y., Kitaev, Y.E., Goncharuk, I.N., *et al.* (1998) *Phys. Rev. B*, **58**, 12899–12907.
- [79] Mowbray, D.J., Cardona, M., and Ploog, K. (1991) *Phys. Rev. B*, **43**, 11815–11824.
- [80] Meynadier, M.H., Finkman, E., Sturge, M.D., Worlock, J.M., and Tamargo, M.C. (1987) *Phys. Rev. B*, **35**, 2517–2520.
- [81] Nakashima, S., Wada, A., Fujiyasu, H., Aoki, M., and Yang, H. (1987) *J. Appl. Phys.*, **62**, 2009.
- [82] Feng, Z.C., Perkowitz, S., and Wu, O.K. (1990) *Phys. Rev. B*, **41**, 6057–6060.
- [83] Shahzad, K., Olego, D.J., Van de Walle, C.G., and Cammack, D.A. (1990) *J. Lumin.*, **46**, 109–136.
- [84] Suh, E.K., Bartholomew, D.U., Ramdas, A.K. *et al* (1987) *Phys. Rev. B*, **36**, 4316–4331.
- [85] Zhang, S.L., Hou, Y.T., Shen, M.Y., Li, J., and Yuan, S.X. (1993) *Phys. Rev. B*, **47**, 12937–12940.
- [86] Takagahara, T. (1980) *Relaxation of Elementary Excitations*, Springer Series in Solid State Sciences, vol. 18 (eds R. Kubo and E. Hanamura), Springer-Verlag, New York, p. P45.
- [87] Zhang F S.L., Yang, C.L., Hou, Y.T. *et al* (1995) *Phys. Rev. B*, **52**, 1477–1480.
- [88] Martin, T.P. (1976) *Phys. Rev. B*, **13**, 3617–3622.
- [89] Rajalakshmi, M., Arora, A.K., Bendre, B.S., and Mahamuni, S. (2000) *J. Appl. Phys.*, **87**, 2445–2448.
- [90] Fonoberov, V.A. and Balandin, A.A. (2004) *Phys. Rev. B*, **70**, 233205.

- [91] Alim, K.A., Fonoberov, V.A., Shamsa, M., and Balandina, A.A. (2005) *J. Appl. Phys.*, **97**, 124313.
- [92] Zhang, S.L., Wang, X., Ho, K.S., Li, J., Diao, P., and Cai, S. (1994) *J. Appl. Phys.*, **76**, 3016–3019.
- [93] Hu, X. and Zi, J. (2002) *J. Phys.: Condens. Matter*, **14**, L671–L677.
- [94] Huang, F., Yue, K.T., Tan, P. *et al.* (1998) *Chn J. Light Scattering*, **10**, 10.
- [95] Demangeot, F., Paillard, V., Chassaing, P.M. *et al* (2006) *Appl. Phys. Lett.*, **88**, 071921.
- [96] Xia, L. (2011) Phd Thesis, Peking University.
- [97] Zhang, S.L., Hu, X., Li, H. *et al* (2002). *Phys. Rev. B*, **66**, 035413.
- [98] Zhang, S.L., Huang, F.M., Zhou, L.X., Zhan, Y., and Yue, K.T. (1999) *Chin. J. Light Scattering*, **11**, 110.
- [99] Li, H. *et al.* (August 20–25 2000) *Proceedings of the Seventeenth International Conference on Raman Spectroscopy* (eds S.L. Zhang and B.F. Zhu), Pub. by John Wiley & Sons, Ltd, Beijing China, Invited Talk, p. 532.
- [100] Kneipp F.K., Kneipp, H., Corio, P. *et al* (2000) *Phys. Rev. Lett.*, **84**, 3470–3473.
- [101] Pimenta, M.A., Marucci, A., Empedocles, S.A. *et al* (1998) *Phys. Rev. B*, **58**, R16016–R16019.
- [102] Kneipp, K., Kneipp, H., Corio, P. *et al* (2000) *Phys. Rev. Lett.*, **84**, 3470–3473.
- [103] Zhang, S.L., Yang, C.L., Hou, Y.T. *et al.* (1995) *Phys. Rev. B*, **52**, 1477–1480.

# 10

## Raman Spectroscopy of Nanostructures with Exciting Laser Features

Raman spectrum is the recording of Raman scattering generated by an object under light irradiation and, therefore, must be correlated with the features of the exciting light and objects, of which the influence will be discussed in this and next chapters, respectively. Light has mainly three features: wavelength, polarization, and intensity, which reflect the energy, vibration direction relative to the light propagation direction, and oscillation amplitude of the light wave, respectively. This chapter introduces the Raman spectra of nanostructures with change of light features, mainly, of nano-semiconductors.

### 10.1 Raman Spectra with Changing of Exciting Light Wavelengths – Resonant Raman Spectra

The change in the wavelength of light means a change in light (photon) energy. Sections 2.3 and 7.5 described that when the energy of the incident light  $E_i$  is adjusted such that it or the scattered light energy  $E_s$  coincide with an electronic transition of scattered objects,  $E_g$ , the Raman scattering intensity will be greatly enhanced, resulting in the occurrence of so-called resonant Raman scattering (RRS).

#### 10.1.1 Raman Scattering Intensity Enhancement Induced by Resonant Raman Scattering

The RRS leads to the enhancement of the Raman scattering intensity, so that Raman scattering spectra with very weak intensity is observed much easy. For example, in bulk objects, very weak high-order (multi-phonon) Raman spectra are mostly observed in RRS. Chapter 9 mentioned that the Raman scattering intensities from nanostructures are weak. To overcome this difficulty, RRS plays a key role. For example, the confined transverse optical (TO) Raman

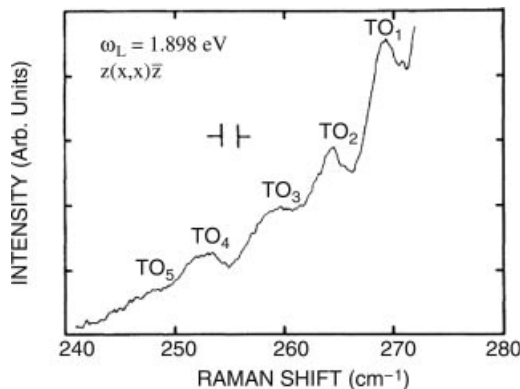


**Figure 10.1** Resonant Raman spectra of the confined TO phonon in GaAs/AlAs superlattices [1]. Reprinted from A. K. Sood, J. Menéndez, M. Cardona, and K. Ploog, Resonance Raman Scattering by Confined LO and TO Phonons in Ga As-AlAs Superlattices, Phys. Rev. Lett., 54, 2111–2114 (1985) with permission of the American Physical Society

scattering in superlattices (SL) is very weak. With the help of resonant spectral technology, Sood *et al.* observed five-order confined TO Raman spectra for the first time, as shown in Figure 10.1 [1]. For example, Figure 10.2 shows the atomic force microscopy image and MP Raman spectra of simple root ZnSe NW, which indicates clearly in RRS that the MP Raman scattering from a mono-root nanowire up to six-order was observed (see color Plate 23 for the original Figure 10.2).

#### 10.1.1.1 RRS in Multi-Quantum Wells (MQWs) and Superlattices (SLs)

Information on electron energy band structures in bulk objects can be provided experimentally by common spectra such as absorption, emission, and photoluminescence(PL) spectra but is impossible by Raman spectra. According to Section 6.4.1, the electron energy levels in SLs are split into many separated sub-bands with small energy gap. Resonant Raman

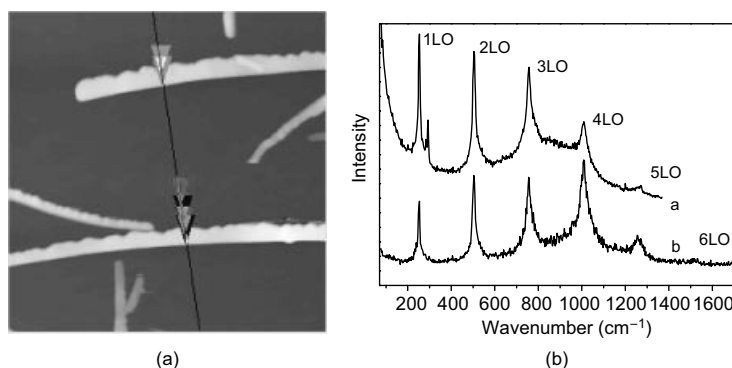


**Figure 10.2** Atomic force microscopy (range is  $2 \times 2 \mu\text{m}$ ) (a) and MP Raman spectra excited by the laser of 442 nm with 0.04 mW power (a) of mono- root ZnSe nanowire. In (a), the white horizontal sawtooth-like bar is the ZnSe sample, while the fine slash is the scanning path in the Raman measurement [19]

enhancement in MQWs and SLs happens when the incident laser energy matches the electron sub-band. Thus the profile of RRS intensity will directly reflect the electron sub-band structure of MQWs and SLs, meaning Raman spectrum can provide the information of electron sub-bands in MQWs and SLs.

The RRS in semiconductor SLs was first observed by Manuel *et al.* in 1978 [2], then by Colvard *et al.* [3], Zucker *et al.* [4], and Sood *et al.* [1]. All the above works show that the resonant intensity profile definitely corresponds to the electron sub-band structures. The RRS of MQW samples by Zucker *et al.* proved that the information of electron energy level obtained by resonant Raman spectra was credible in terms of anastomosis between the exciton emission spectra and the intensity profile of resonant Raman spectra, both in experimental observations and theoretical calculations [4]. Figures 10.3 and 10.4 show a

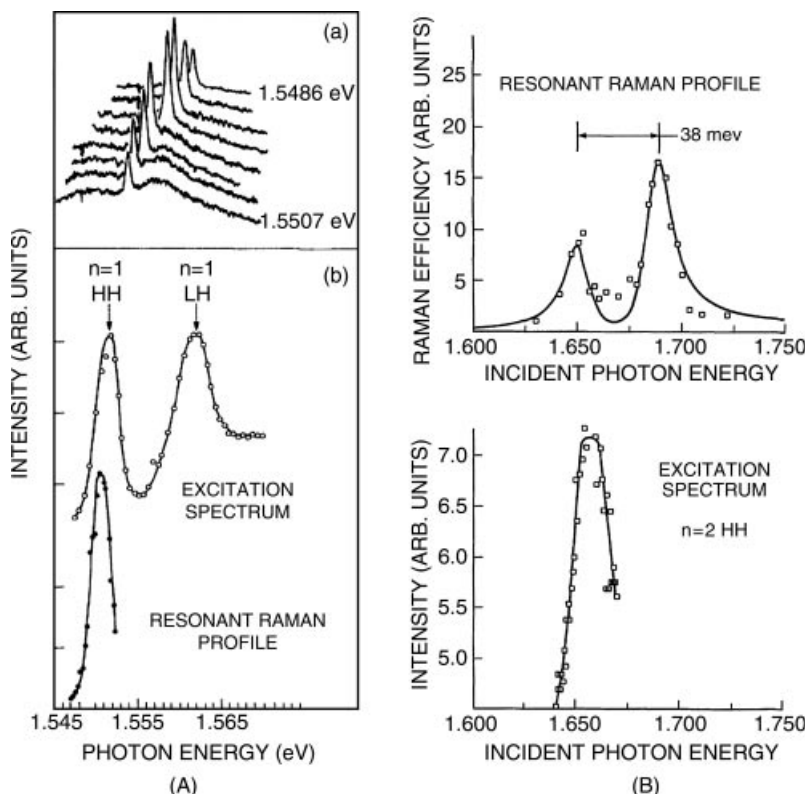


**Figure 10.3** (A) (a) Resonant enhancement of the Raman spectrum from a 96-Å MQW heterostructure, as the incident laser is tuned near the  $n=1$  heavy-hole exciton. (b) The comparison of the resonant profile with the excitation spectrum. (B) Comparison of the resonant Raman profile with the excitation spectrum obtained from a 102-Å quantum-well sample in the energy range of the  $n=2$  exciton. Data points are corrected for absorption. The solid line is a theoretical fit to the resonant profile [4]. Reprinted from J. E. Zucker, A. Pinczuk, D. S. Chemla, A. Gossard and W. Wiegmann, Phys. Rev. Lett., Raman scattering resonant with Quasi-Two-Dimensional Excitons in Semiconductor Quantum Wells, Phys. Rev. Lett., 51, 1293–1296 (1983) with permission of the American Physical Society

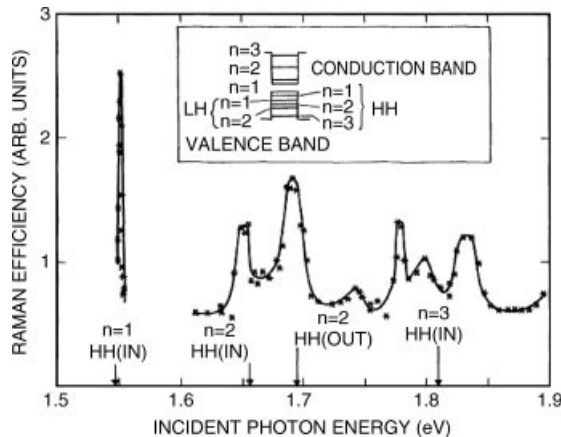


**Figure 10.4** Resonant Raman profile for a 102- $\text{\AA}$  MQW heterostructure. The arrows indicate exciton energies calculated with the single-quantum-well model [4]. Reprinted from J. E. Zucker, A. Pinczuk, D. S. Chemla, A. Gossard and W. Wiegmann, Phys. Rev. Lett., Raman scattering resonant with Quasi-Two-Dimensional Excitons in Semiconductor Quantum Wells, Phys. Rev. Lett., 51, 1293–1296 (1983) with permission of the American Physical Society

correspondence between resonant Raman intensity profile and transition energies of quantum well (QW) sub-bands, by comparing between experiment and theory.

The experimental results shown above were consistent only with the selection rule  $\Delta n = 0$  ( $\Delta n$  is the difference of the resonance sub-band index) and also not involved in the highly confined order  $m$  of longitudinal optical (LO) phonons. The authors of Ref. [5] observed resonant Raman spectra of multiple-order confined LO phonons of  $(\text{GaAs})_{6\text{nm}}/(\text{AlAs})_{2\text{nm}}$  SL, as shown in Figures 10.5(a) and (b), which show the comparison of the resonant Raman profiles of multiple confined  $\text{LO}_m$  modes with  $m = 2, 4, \text{ and } 6$ , with calculated transition

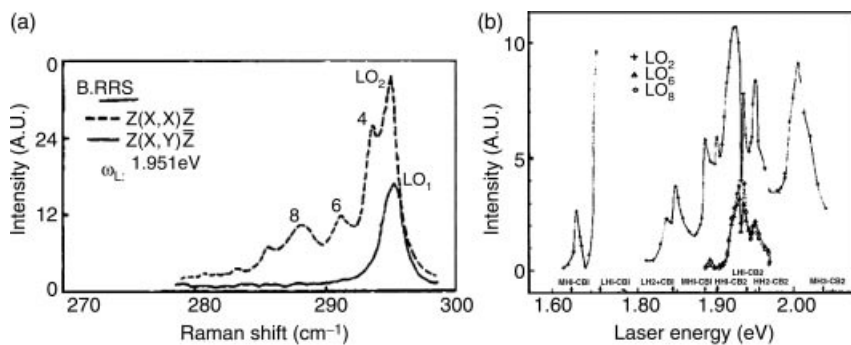


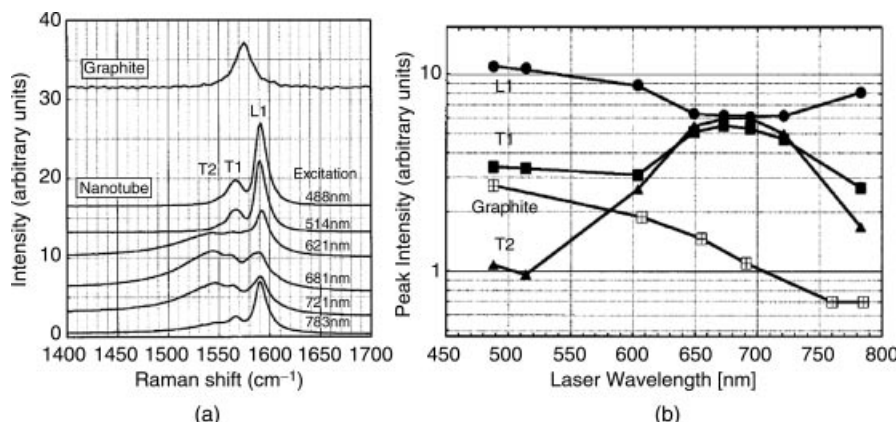
**Figure 10.5** (a) Resonance Raman spectra and (b) comparison of resonance profile with calculated value of the sub-band transition energy (indicated by the arrow) for  $\text{GaAs}_{6\text{nm}}/\text{AlAs}_{2\text{nm}}$  superlattice [5]. Reprinted from S. L. Zhang, T. A. Gant, M. Delane, M. V. Klein, J. Klem and H. Morkoc, Resonant Behavior of LO Phonons in a GaAs-AlAs Superlattices, Chin. Phys. Lett., 5, 113–116 (1988)

energies between light and heavy holes. The energies of profile peaks match the calculated transition energies well. The results shown in Figures 10.4 and 10.5 indicate collaboratively that we cannot only obtain the structure and energies of MQW and SL electron sub-bands from resonant Raman spectra but also prove directly the size confined effect on electrons by using Raman spectra.

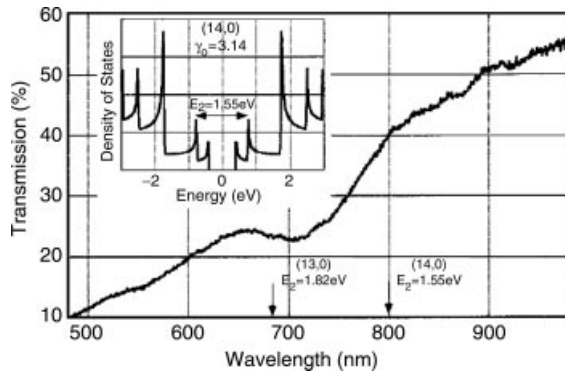
#### 10.1.1.2 In Carbon Nano-tubes (CNTs)

Figure 10.6(a) shows Raman spectra of optical phonons centered at  $1580\text{ cm}^{-1}$ , excited by lasers of wavelengths from 488 to 783 nm from single-wall carbon nanotubes(CNT)s with the average diameter 1.1 nm, of which the peak at  $1590.9\text{ cm}^{-1}$  is denoted as L1, and peaks at  $1567.5$  and  $1549.2\text{ cm}^{-1}$  are denoted as T1 and T2, respectively, and the numbers 1 and 2 refer to the subscript of wave vector  $k_n$  ( $n = 1, 2$ ) zone-folded onto the  $\Gamma$  point. Figure 10.6(b) shows the Raman peak intensity with different incident laser energies for L1, T1, and T2 peaks. Figure 10.6(b) shows that the scattering intensities display anomalies in the vicinity of 690 nm, where it appears as a minimum in the longitudinal components L1 and a maximum in the transverses T1 and T2.

Figure 10.7 shows the calculated density of electron states and an optical transmission spectrum of the CNT sample. The optical-transmission measurement also exhibits a dip in the same photon energy in the vicinity of 690 nm. The anomalies are caused by the incident laser beam resonant with the zone-folded electronic structures in nanotubes. These results provide direct experimental evidence of the critical point in the density of states(DOS) produced by the cylindrical symmetry of nanotubes.



**Figure 10.6** (a) Raman-scattering spectra between  $1400$  and  $1700\text{ cm}^{-1}$  from single-walled nanotubes of diameter 1.1 nm excited by the incident laser of wavelengths from  $488$  to  $783\text{ nm}$ , where L1, T1, and T2 denote the peaks at  $1590.9$ ,  $1567.5\text{ cm}^{-1}$ , and  $1549.2\text{ cm}^{-1}$ , respectively. The top spectrum is from graphite (HOPG) excited at  $488\text{ nm}$ ; (b) variations of Raman peak intensity for L1, T1, T2, and graphite peak at  $1580\text{ cm}^{-1}$  [6]. Reprinted from A. Kasuya, M. Sugano, T. Maeda, et al., Resonant Raman scattering and the zone-folded electronic structure in single-wall nanotubes, *Phys. Rev. B*, 57, 4999–5001 (1998) with permission of the American Physical Society



**Figure 10.7** Optical transmission spectrum measured in the wavelength region from 480 to 980 nm. The inset shows the DOS calculated for the tube with diameter 1.096 nm of type (14,0), with the zigzag tube with 14 hexagons around the circumference. The band parameter  $\gamma_0 = 3.14$  [6]. Reprinted from A. Kasuya, M. Sugano, T. Maeda, et al., Resonant Raman scattering and the zone-folded electronic structure in single-wall nanotubes, *Phys. Rev. B*, 57, 4999–5001 (1998) with permission of the American Physical Society

#### 10.1.1.3 In SiC Nanorods (NRs) [7,8]

Yan *et al.* measured Raman spectrum of SiC nanorods (NR) in the back scattering configuration at room temperature excited by three wavelength lasers of 488, 515, and 633 nm, as shown in Figure 10.8(a). The fitted peaks in the figure were assigned so that the peak around  $770\text{ cm}^{-1}$  is identified as the second-order peak of remnant  $\text{SiO}_2$  in the

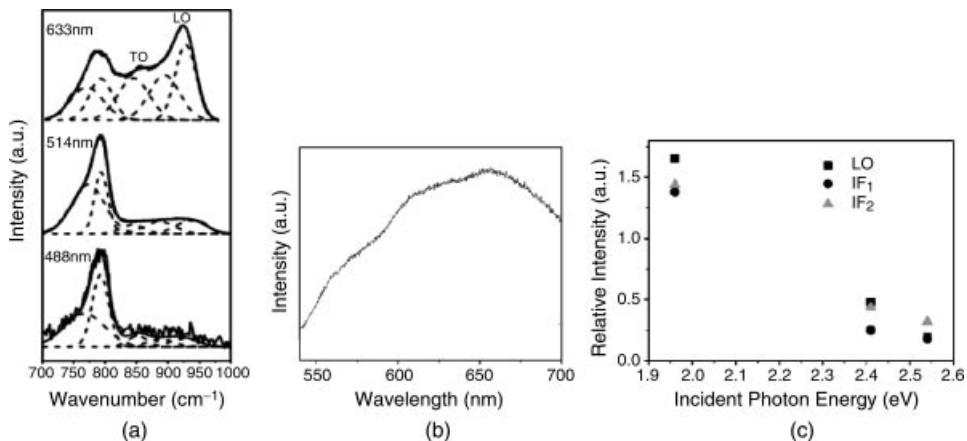


**Figure 10.8** Observed (solid lines) and fitted (dashed lines) Raman spectra (a), PL spectrum and (b) dependence of relative intensity of LO/IF modes to TO mode on excitation wavelengths (c) for SiC NRs excited at different wavelengths [8]. Reprinted from S. L. Zhang, et al., Solid State Commun., Effect of changing incident wavelength on Raman features of optical phonons in SiC nanorods and TaC nanowires, 126, 649–651 (2003)

**Table 10.1** The values of relative intensities of LO and IF modes to that of the TO mode at different excitation wavelengths  $\lambda$ . Reprinted from Y. Yan, et al., Effect of changing incident wavelength on Raman features of optical phonons in SiC nanorods and TaC nanowires, Solid State Commun., 126, 649–651 (2003)

$\lambda$	TO	IF <sub>1</sub>	IF <sub>2</sub>	LO
633 nm	1.00	1.38	1.44	1.65
514 nm	1.00	0.25	0.44	0.48
488 nm	1.00	0.18	0.16	0.19

sample [9], while the peaks at 793 and 928 cm<sup>-1</sup> are assigned to the transverse optical(TO) and LO modes, respectively. The other peaks at 838 and 882 cm<sup>-1</sup> are due to the interface (IF) mode scattering from different kinds of interfaces in the sample. The relative intensities of LO/IF modes to TO mode on excitation wavelengths for SiC NRs are listed in Table 10.1 and shown in Figure 10.8(b). From the figure it can be seen that there is a huge variation of relative intensity  $I$  of the LO and IF modes to the TO mode when changing the incident wavelength.

Section 9.4.1 mentioned that the first-order Raman spectrum of optical phonons in SiC NRs is mainly due to the Fröhlich interaction rather than the quantum size confinement. Moreover, the LO and TO modes have different scattering mechanisms: the former is induced by the Fröhlich interaction and the latter is due to the deformation potential. The dependences of scattering cross section  $\sigma$  on gap energy  $E_g$  and incident light energy  $\hbar\omega$  on deformation and Fröhlich interactions are expressed as [10,11]

$$\sigma \propto \begin{cases} (E_g - \hbar\omega)^{-1}, & \text{for deformation interaction} \\ (E_g - \hbar\omega)^{-1}, & \text{For fröhlich interaction} \end{cases} \quad (10.1)$$

The above equation shows that with the trend of incident light energy away from the electron transition energy  $E_g$ , the scattering intensity decrease of the LO mode induced by the Fröhlich interaction is much faster than that of TO modes induced by deformation potential. As a result, Raman scattering of the LO mode is most intense and can be seen clearly in resonance.

Figure 10.8(b) shows the PL spectrum of an SiC NR sample. The PL peaks are at about 650 nm, indicating the gap energy is about 1.91 eV. The assumption of energy region of resonance is  $E_g \pm 0.1$  eV, which means that the Raman spectra excited by 633 nm is at in-resonance, as its energy difference from the  $E_g$  is only (1.96–1.91) eV = 0.05 eV. The energies of incident lasers with 515 and 488 nm corresponding to 2.41 and 2.54 eV, respectively, are away from the electron transition energy in order. Figure 10.8(c) clearly shows that the observed Raman relative intensities agree well with the above deduction.

In addition, the similar Raman and PL spectra with SiC NRs also appear in the case of TaC NRs [8]. Therefore the above result further confirms the proposition in Section 9.4.1 that the Raman scattering mechanism of optical phonon in SiC NRs has general significance, in other words, the first-order Raman spectrum of optical phonons in polar nano-semiconductors originates from the Fröhlich interaction rather than the quantum size confinement.

### 10.1.2 Raman Frequency Variation with Excited Laser Wavelengths

Chapter 1 pointed out that the frequency of Raman scattering should not change with the excited laser wavelengths, which is one of the two universal features of Raman scattering. This feature has been proved in bulk objects. But the phenomenon to violate this feature was observed in RRS spectra of nanostructures. In this section, we discuss this abnormal phenomenon.

#### 10.1.2.1 In CNTs [12]

In 1997, Rao *et al.* reported that Raman frequency changes with excited laser wavelengths were observed in CNTs, as shown in Figure 10.9. The figure shows clearly that the frequencies of the D mode changes when the incident laser wavelength is changed from 514.5 to 1320 nm. They explained this abnormal phenomenon with the diameter selection effect under RRS.

Their interpretation was that at the resonant Raman scattering, the incident laser energy must equal or be close to certain electron energy levels of CNTs and a certain electron energy level must corresponds to a certain sample with certain nanosize due to the quantum confined effect (QCE). This implies that Raman spectrum of CNTs at RRS must come from Raman scattering of a definite sized sample corresponding to a certain laser energy. Thus when CNT samples are size distributed, the resonant scattering excited by different laser wavelengths must come from different diameters of CNTs in the samples, meaning that there is a size

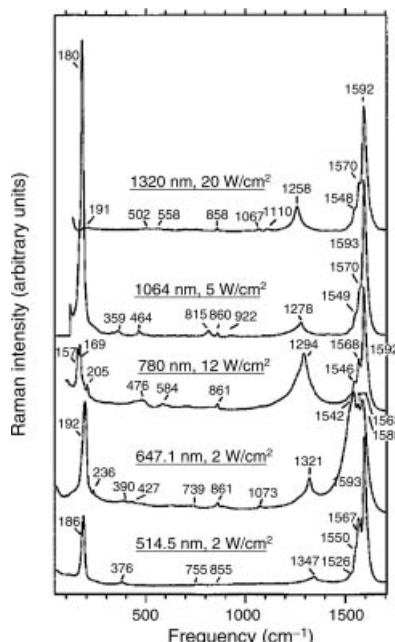


**Figure 10.9** Room temperature Raman spectra for SWCNTs, excited at five different laser frequencies. The vibration frequency for each peak is indicated [13]. Reprinted from G. Y. Zhang, G. X. Lan, and Y. F. Wang, *Vibration Spectroscopy in Lattices*, (2001)

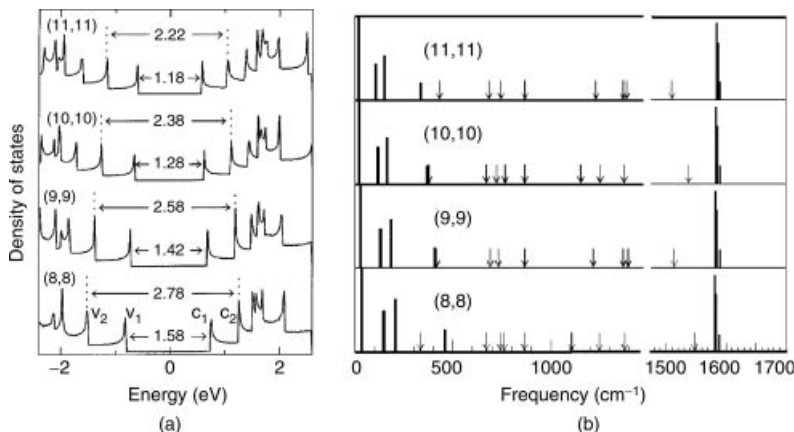


**Figure 10.10** (a) Electronic DOS calculated with a tight binding model for (8,8) (9,9), (10,10), and (11,11) armchair nanotubes. The Fermi energy is located at 0 eV. Wave vector conserving optical transitions can occur between mirror image spikes, that is,  $v_1 \rightarrow c_1$  and  $v_2 \rightarrow c_2$ . Reprinted from S.-L. Zhang, Y. Hou, K. S. Ho, et al., Raman investigation with excitation of various wavelength lasers on porous silicon, *J. Appl. Phys.*, 72, 4469–4471 (1992). (b) Calculated Raman spectra for armchair  $(n,n)$  nanotubes,  $n=8$  to 11. The downward pointing arrows indicate the positions of the remaining weak Raman-active modes [12]. Reprinted from S.-L. Zhang, W. Ding, Y. Yan, et al., Variation of Raman feature on excitation wavelength in silicon nanowires, *Appl. Phys. Lett.*, 81, 4446–4448 (2002).

selection for size-distributed nanosamples at RRS. Thus the Raman scattering phenomenon shown in Figure 10.9 is named as diameter-selective Raman scattering (DSRS).

In the same report [12], Rao *et al.* also provided theoretical calculated electronic DOS and Raman frequency of different diameter CNTs, as shown in Figures 10.10(a) and (b), respectively, and should be expected in small diameter single wall CNTs. The results in Figures 10.10(a) prove that the experimental laser at 1005 nm, 780 nm, and 488 nm energies 1.17 eV, 1.59 eV, and 2.14 eV, respectively, are in resonance with the electron energy levels of CNTs (11,11), (8,8,) and (10, 10), respectively, indicating that the RRS experiment selects the different sizes of CNTs. The results in Figure 10.10(b) indicate that different diameter CNTs have different Raman frequencies. Thus, Rao *et al.* proved DSRS by using theoretical calculations.

Later, it was verified by experimental result that DSSE is the reflection simultaneously of the QCE on electrons and the finite size effect (FSE) on phonons in size-distributed samples, rather than the invalidity of the Raman scattering principle in nanosystems.

#### 10.1.2.2 In Silicon Nanomaterials [13,14]

The Raman spectra of crystal silicon, porous silicon (PS) and silicon nanowires (NWs) excited with various wavelength lasers are shown in Figures 10.11(a)–(c), respectively. These figures clearly show that the optical phonon frequency of crystal silicon remains invariable with different excitation wavelengths, while it exhibits for PS and Si NWs changes of Raman frequency with excited laser wavelengths, which is named the resonance size selection effect(RSSE) in Ref. [14].

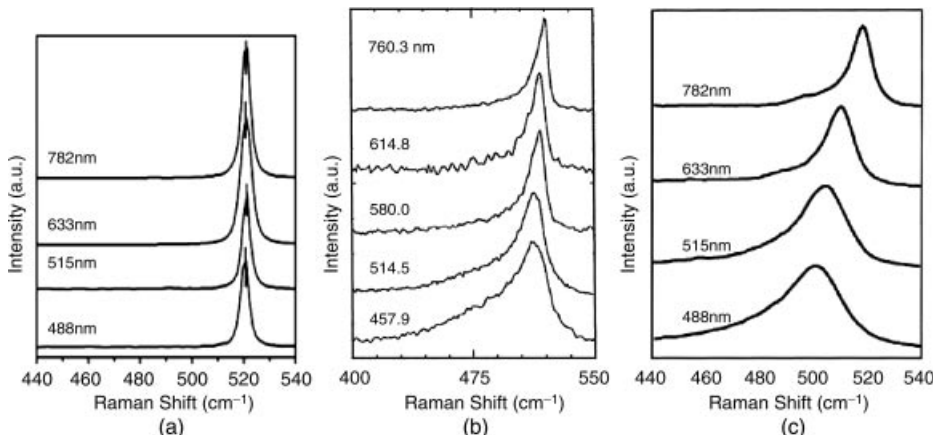


**Figure 10.11** Raman spectra excited with various wavelength lasers of crystal silicon (a). Reprinted from S.-L. Zhang, W. Ding, Y. Yan, et al., Variation of Raman feature on excitation wavelength in silicon nanowires, *Appl. Phys. Lett.*, 81, 4446–4448 (2002). PS [14a] (b), and silicon NWs (c) [14b]. Reprinted from S. L. Zhang, W. Ding, Y. Yan, et al., Variation of Raman feature on excitation wavelength in silicon nanowires, *Appl. Phys. Lett.*, 81, 4446–4448 (2002)

According to the description of DSRS by Rao *et al.*, the appearance of DSRS must satisfy three requirements:

- (1) Electrons and phonons must both possess the size confinement effect, i.e., the energies of electrons and phonons will change with sizes.
- (2) The sample is a size distributed one.
- (3) Raman scatterings are resonant with the electron energy level.

The above requirements mean that when the sample exists in the QCE on electrons and the FSE on phonons, the resonant scattering at certain excited wavelengths will select certain resonant-sized specimen in size-distributed nanosamples. Thus the Raman spectra with in-resonance, near-resonance, and non-resonance will be from the specimens with single-size, average-size of the resonant specimens in certain size region, and average-size of whole sample, respectively. Elaborating on the above, it should be expected that when two nanosamples have different size distributions but the same peak size, their Raman spectra should be the same and not the same in in-resonance and near-resonance, respectively.

Figure 10.12(a) shows PL spectra of silicon NWs Samples C and D. The two spectra profiles are different but have the same peak energies of  $\sim 2.54$  eV, which indicates that the size distributions of Samples C and D are different but a same peak size corresponds to selected sizes by  $\sim 2.54$  eV. Thus it should be expected that when the incident laser wavelength is 488 nm (2.52 eV) and 633 nm (1.96 eV), the Raman scatterings are at in-resonance and near-resonance and corresponding Raman spectra of Samples C and D must be the same and different, respectively. Raman spectra of Samples D and C excited by 488 nm and 633 nm wavelength lasers are shown in Figures 10.12(b) and (c), respectively. These figures prove the above expectation and thus the mechanism of DSRS/RSSE experimentally. This also explains that if the measured sample appears in

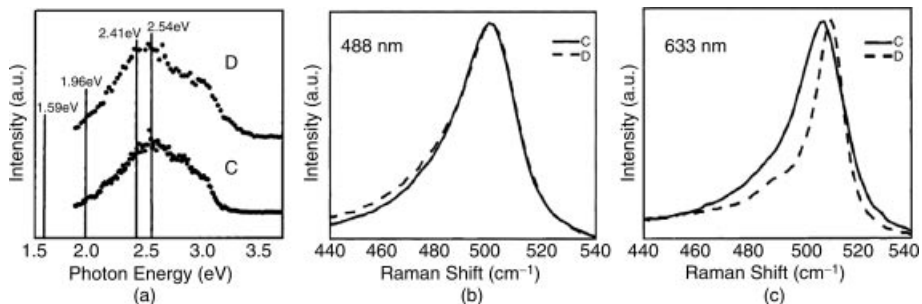


**Figure 10.12** PL and Raman spectra of Si NW Samples C and D. Four vertical lines in PL spectra correspond to four positions of excitation laser energies. Raman spectra shown in (b) and (c) with solid and dashed lines are excited at 488 and 633 nm, respectively [14]

DSRS/RSSE, the sample must exist with the size confinement effect on electrons and phonons simultaneously.

#### 10.1.2.3 In Polar Nanosemiconductors

The change of Raman frequency with excited laser wavelengths was observed in CNTs and nanosilicon and interpreted by RSSE originating from the size confinement effect on electrons and phonons simultaneously. Note that CNTs and nanosilicon are both polar non-semiconductors, so it is interesting to check if this novel phenomenon exists in polar nano-semiconductors, although it has been thought that RSSE should be present in all size-distributed nano-semiconductors [14]. In this section, we will show Raman scattering frequency variations with excited laser wavelengths, i.e., to check whether polar nano-semiconductors have RSSE.

The samples to check RSSE are the same group samples used in Chapter 9 for investigation of routine Raman spectra of nano-semiconductors: ZnO, GaN nanoparticles (NPs) and SiC, CdSe NWs. The high resolution electronic microscope images and X-ray diffraction spectra of these samples were shown in Figures 9.30, 9.33 and 9.35. These figures verify that these samples consist of complete crystal grains of different sizes and the average sizes of crystal grains ZnO, GaN NPs, SiC, and CdSe NRs are 8 nm, 7 nm, 10 nm, and 4 nm, respectively.

The PL spectra of ZnO, GaN NPs, SiC, and CdSe NRs are shown in Figure 10.13. It can be seen from the PL spectra that the Raman spectra excited by 325, 488, 515, 633, and 785 nm lasers meet the requirement of resonant Raman spectral excitation. The Raman spectra from those excitation wavelengths of the samples are shown in Figure 10.14(a). The fitted Raman frequencies are plotted versus excitation wavelengths in Figure 10.14(b), in which the lines are drawn as a guide by eyes. The largest variation of the fitted frequencies of all bands is less than  $2\text{--}3\text{ cm}^{-1}$ . Considering that the Raman measurements were performed with two different Raman instruments and with several different excitation wavelengths, these deviations are within measurement accuracy. Moreover, we note that the frequency shift of Si NWs in the excitation energy (wavelength) region of 0.96 eV (488–785 nm) is  $17\text{ cm}^{-1}$  [12]. The frequency shift in Figure 10.14 is negligible. Thus, we conclude that the Raman frequencies of optical vibration modes in so many polar nano-semiconductors do not shift with excitation

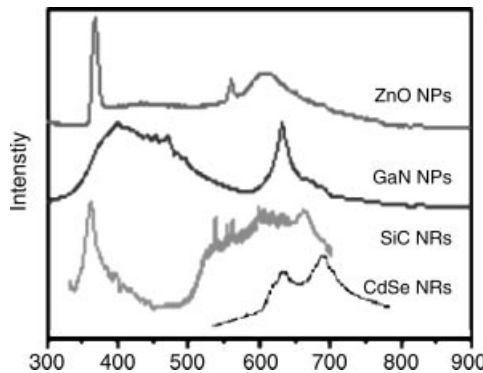


**Figure 10.13** PL spectra of ZnO, GaN NPs, SiC, and CdSe NRs, where PL of CdSe NRs and others are excited by 515 and 325 nm lasers, respectively. The vertical lines denote the energy positions of excitation lasers with 325, 488, 515, 633, and 785 nm [13]. Reprinted from S.-L. Zhang, et al., Lack of dependence of the Raman frequency of optical vibrational modes on excitation wavelength in polar nanosemiconductors, *Appl Phys Lett*, 89, 063112 (2006)

wavelength, indicating that, unlike non-polar nano-semiconductors, the optical modes of polar nano-semiconductors do not show the RSSE in the Raman spectra, which are opposite from RSSE phenomenon observed in non-polar CNT and nanosilicon and different from predictions [14]. Moreover, this result implies that the FSE, a basic effect in nanomaterials, does not exhibit in the optical phonons of polar

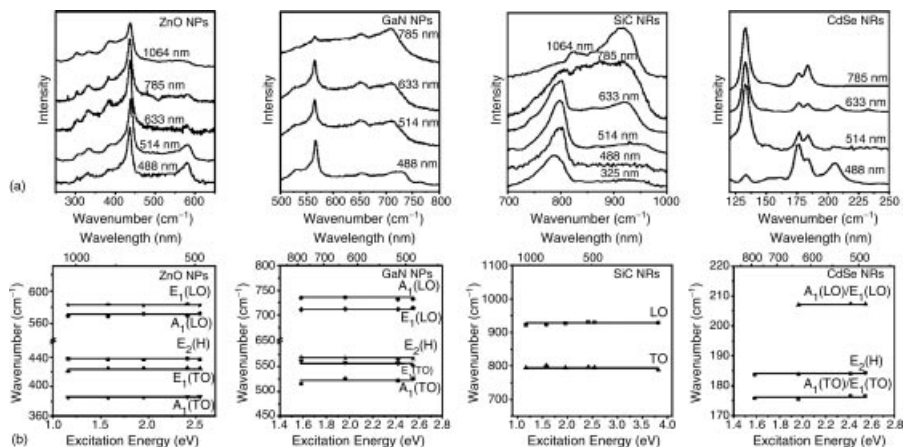


**Figure 10.14** (a) Raman spectra excited at various wavelengths. Reprinted from C. Colvard, T. A. Gant, M. V. Klein, et al., Folded acoustic and quantized optic phonons in (GaAl)As superlattices, *Phys. Rev. B*, 31, 2080–2091 (1985) with permission of the American Physical Society. (b) dependence of Raman frequency on excitation wavelength/energy for ZnO NPs, GaN NPs, SiC NRs, and CdSe NRs [15]. Reprinted from S. L. Zhang, T. A. Gant, M. Delane, et al., Resonant Behavior of GaAs LO phonons in a GaAs-Al<sub>x</sub>As superlattice, *Chin. Phys. Lett.*, 5, 113–116 (1987)

nano-semiconductors. Of course, this deduction needs more experimental and theoretical work to confirm it, such as to obtain Raman spectra from directly different sizes of nano-semiconductors, which will be introduced in Chapter 11.

## 10.2 Raman Spectra with Exciting Laser Polarization

In Sections 2.2.1 and 3.1.2, the basic knowledge of polarized Raman spectra excited by polarized light has been described. In this section we introduce the polarized Raman spectra of nanostructures.

Polarized spectrum measurement requires the crystallographic orientation of crystal samples to be fixed in space. Superlattices (SLs) and QWs have definite crystallographic orientations, so the polarized Raman spectra are important in the Raman spectra of these samples. However, at present most of nano-semiconductors do not have definite orientations in space, resulting in their polarization spectra being difficult to investigate.

### 10.2.1 Polarized Raman Spectra of SLs

Chapter 6 specified that SLs/QWs structures are layered structures of perpendicular grown direction z, therefore the polarized spectrum is usually measured under the backscattered configuration  $Z(i, j)\bar{Z}$  ( $\bar{Z} = -Z$ ,  $i, j = X, Y, Z$ ) and is seldom used to measure right-angle configuration,  $X(i, j)Y$ . The Raman scattering experiments of backscattering configuration can only detect phonons with wave vector  $q_z = 0$ , where the longitudinal and transverse vibration modes appear in configurations of  $i = j$  and  $i \neq j$ , respectively.

Figures 10.15(a) and (b) show Raman spectra in the  $Z(X, X)\bar{Z}$  and  $Z(X, Y)\bar{Z}$  configurations for folded acoustic and confined GaAs optical phonons of SL GaAs/AlAs, respectively [16]. As mentioned in Chapter 8, Figure 10.15 proves that longitudinal acoustic phonon modes can only be observed in parallel polarization ( $x, x$ ) and the

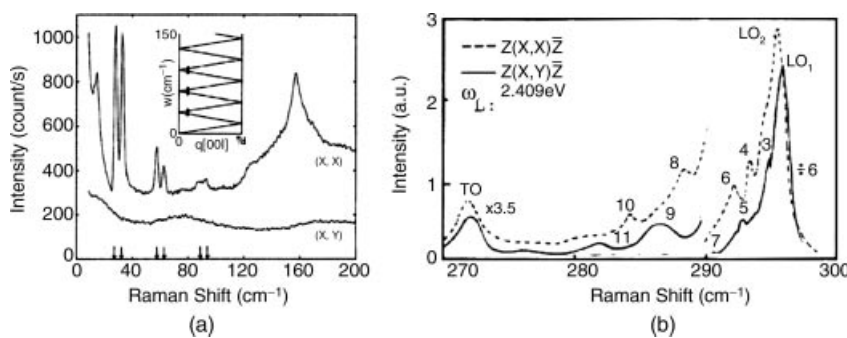


**Figure 10.15** Raman spectra of longitudinal acoustic phonons (a) and confined GaAs LO phonons (b) in GaAs/AlAs SLs [3,16]; in (a), the arrows indicate predicated peak frequencies determined by X-ray diffraction data. Reprinted from J. E. Zucker, A. Pinczuk, D. S. Chemla, et al., Optical Vibrational Modes and Electron-Phonon Interaction In GaAs Quantum Wells, Phys. Rev. Lett., **53**, 1280–1283 (1984) with permission of the American Physical Society

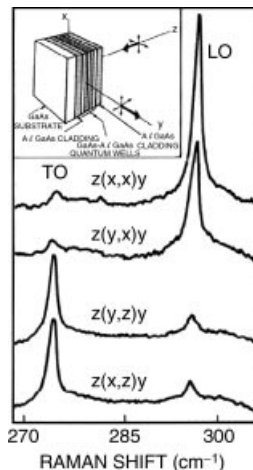


**Figure 10.16** Right-angle Raman spectra. Incident photon energy is 1.55 eV. Propagation directions for incident and scattered light are labeled by first and last letters, with the respective polarizations in parentheses. Inset shows the geometry for right-angle scattering (001) is along  $z$  direction [17]. Reprinted from G. S. Duesberg, I. Loa, M. Burghard, K. Syassen and S. Roth, Polarized Raman Spectroscopy on Isolated Single-Wall Carbon Nanotubes, *Phys. Rev. Lett.*, **85**, 5436–5439 (2000) with permission of the American Physical Society

confined LO modes with odd modes ( $n = 1, 3, 5, 7, 9, 11, \dots$ ) and the even-modes (confined order  $n = 2, 4, 6, 8, 10, \dots$ ) were observed in  $(x\ y)$  and  $(x,x)$  polarization configurations, respectively.

Figure 10.16 shows Raman spectra from a GaAs/GaAlAs multiple QW [17]. These Raman spectra were the first and rare measurements at right-angle configuration of the scattering light propagating in the layer plane and polarized along the SL axis, making the detection of phonons with wave vector  $q \neq 0$  possible in QWs and SLs. Chapter 9 mentioned that the TO mode is related to the short-range deformation potential electronic-phonon interaction, while the LO mode is related additionally to long-range Coulomb (Fröhlich) interactions. Raman spectra of the former and latter can only be obtained at cross and parallel polarization geometry configurations, respectively. This implies that at the right-angle configuration  $Z(i, j)Y$  ( $Z$  is along the SL axis), LO and TO Raman peaks can be observed when the polarizations of incident and scattered light are both at the layer plane and the scattering light polarization is parallel to the axis of SLs, respectively. This is proved by the experimental results shown in Figure 10.16.

### 10.2.2 Nanomaterials

As mentioned at the beginning of this section, the polarization spectrum of nanomaterials cannot be obtained; however, the polarized Raman spectra of mono-root or single-particle nanocrystalline samples can be measured. We will introduce two samples of such kinds of polarized Raman spectra below.

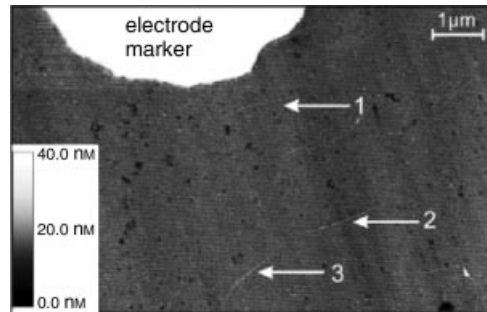


**Figure 10.17** SFM image of well-separated individual SWCNTs and small bundles of SWCNTs adsorbed on a glass substrate. The end of a gold electrode used as a marker can be seen at the upper left. The height of object No. 1 corresponds to that of an individual SWCNT, while Nos. 2 and 3 are small ropes of SWCNTs [18]. Reprinted from G. S. Duesberg, I. Loa, M. Burghard, K. Syassen and S. Roth, Polarized Raman Spectroscopy on Isolated Single-Wall Carbon Nanotubes, *Phys. Rev. Lett.*, 85, 5436–5439 (2000) with permission of the American Physical Society

#### 10.2.2.1 Polarization Raman Spectra of Mono-Root Carbon Nanotube

A polarized Raman spectrum of CNTs was obtained for discrete CNTs or a bunch of a few-root CNTs in the field ion microscope image, as shown in Figure 10.17 [18]. Due to the limitation of microscope resolution, from the image we cannot distinguish the mono-root tube from a few discrete bundle tubes. However, as the tubes are parallel with each other, it does not affect the credibility of measured polarized spectra.

Figure 10.18(A) shows Raman spectra of Sample 1 (a thin single-walled carbon nanotube (SWCNT) rope), shown in Figure 10.17 in the VV configuration for various angles  $\alpha_i$  between the rope axis and the polarization of the incident laser beam; the inset depicts the experimental geometry. From the spectra we see that the spectral intensity of  $G_1$ ,  $G_2$ , D, and RB-mode reach the maximum when the incident and scattering light polarization are parallel to each other (denoted as VV) and parallel with the axis of CNTs ( $\alpha_j = 0$  or  $\alpha_j = 180^\circ$ ). However, when  $\alpha_j = 90^\circ$ , no signal is detected, which is consistent with expectations. The relationship between the spectral intensity of  $G_1$ ,  $G_2$ , and D-modes in the parallel polarization configuration and RB mode in the parallel and vertical (denoted with VH) configuration and angle  $\alpha_j$ , are shown in Figure 10.18(B). It is strange that the spectral intensity of the RB mode in VV and VH polarization configurations has the same angle relationship expressed as by the solid line

$$I(\alpha_i) \propto \cos^2(\alpha_i) \quad (10.2)$$

The above dependence of Raman spectra intensity on angle deviates from the selection rules expected from traditional theory. The authors attributed this to the strong anisotropy of the nanotube geometry, while the traditional theory is built on the basis of isotropic materials.

#### 10.2.2.2 Polarization Raman Spectra of Mono-Root ZnSe Nanocrystalline Belt

A ZnSe nanocrystalline belt was grown by MOCVD and then formed dispersed samples by gluing to a GaAs substrate. Figure 10.19 is the morphological image of a single dispersed

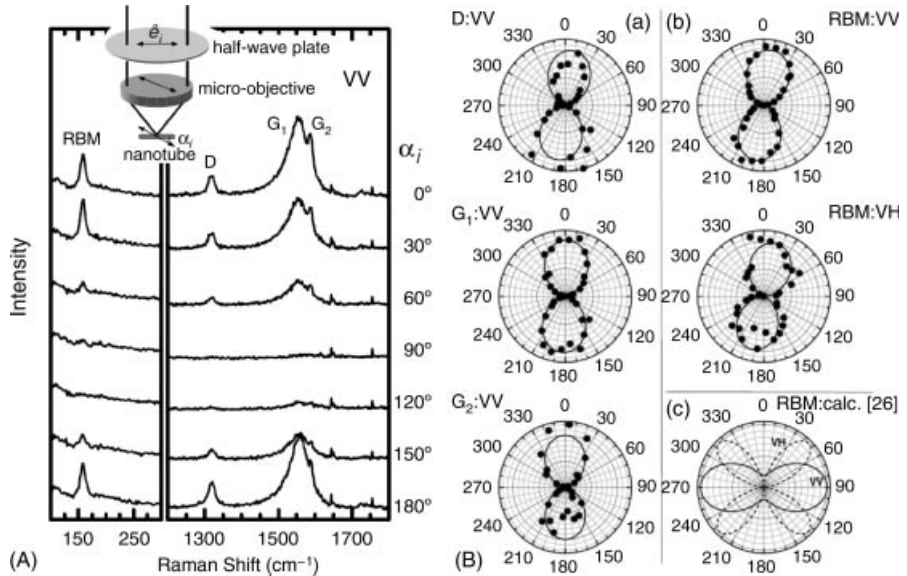


**Figure 10.18** (A) Raman spectra of a thin SWCNT rope in the W configuration for various angles  $\alpha_i$  between the rope axis and the polarization of the incident laser beam, as depicted in the inset. For  $\alpha_i = 0^\circ$  and  $180^\circ$ , the polarization of the incident radiation is parallel to the axis of the SWCNTs as determined from SFM images with an accuracy of  $\pm 10^\circ$ . (B) Polar diagrams show the Raman mode intensities  $I$  of SWCNTs as a function of the angle  $\alpha_i$  between the polarization of the incident light and the nanotube axis.  $I(\alpha_i)$  for (a) the components  $G_1$  and  $G_2$  of the  $G$  line and for the  $D$  line in the  $VV$  scattering configuration and (b) the  $RBM$  in the  $VV$  and  $VH$  configurations. The two fold symmetry of these modes, which can be modeled by  $I(\alpha_i) \propto \cos^2(\alpha_i)$ , has been observed in all investigated objects. (c) calculated  $I(\alpha_i)$  for the  $RBM$  of a  $(10,10)$  tube under non-resonant conditions after data of [18]

ZnSe nanobelt on the GaAs substrate [19]. The ZnSe nanobelt belongs to a cubic crystal structure, of which bulk ZnSe has a band gap of 2.68 eV [20] and LO and TO modes located at 252 and 208 cm<sup>-1</sup> [21], respectively.

From Figure 10.20, we see that, except for the expected LO, TO modes of GaAs substrate and LO, TO modes of ZnSe nanobelts, there are a few weak peaks located at 227 cm<sup>-1</sup> and 240 cm<sup>-1</sup>. As there is only an amono-root ZnSe nanobelt in the laser spot, Raman peak intensity is only 1/20 of Raman peaks of GaAs substrate, the spectral spectrum is enlarged and fitted, as shown in the inset of Figure 10.20. The phonon energy with peak frequency of 227 cm<sup>-1</sup> is 28 meV, which is very close to the calculated energy of the surface mode of the ZnSe (110) face at 27.2 meV [22] and so can be attributed to the scattering from surface mode.

With choosing a mono-root and straighter ZnSe nanowire, and keeping laser illumination on the same spot of the sample, polarized Raman spectra of two different included angles between wire and polarization direction of incident laser,  $\theta = 45^\circ$  and  $90^\circ$ , are measured and shown in Figure 10.21. Due to the result that  $\theta = 0^\circ$  is the same as that of  $\theta = 90^\circ$ , its Raman spectra cannot be seen in Figure 10.21. The figure shows that at  $\theta = 90^\circ$ , the intensity of the

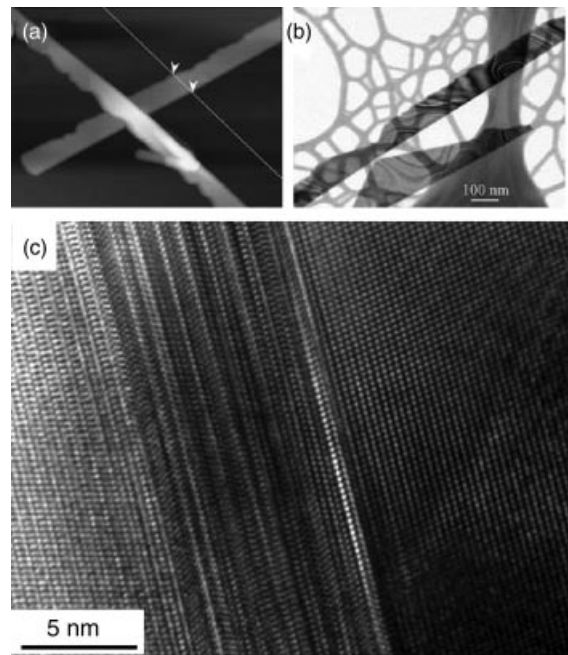


**Figure 10.19** Atomic force microscope (AFM) image (a); TEM bright field image (b) and high resolution TEM image (c) for ZnSe nanocrystalline belt. (c) shows the emergence of twin defects [19]

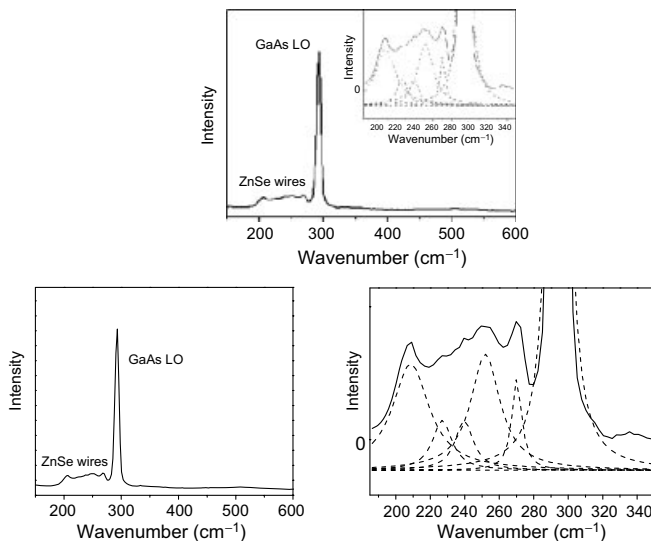


**Figure 10.20** Observed Raman spectra of single-root ZnSe nanocrystalline belt glued onto GaAs substrate. The inset is fitted Raman spectra of ZnSe sample [19]

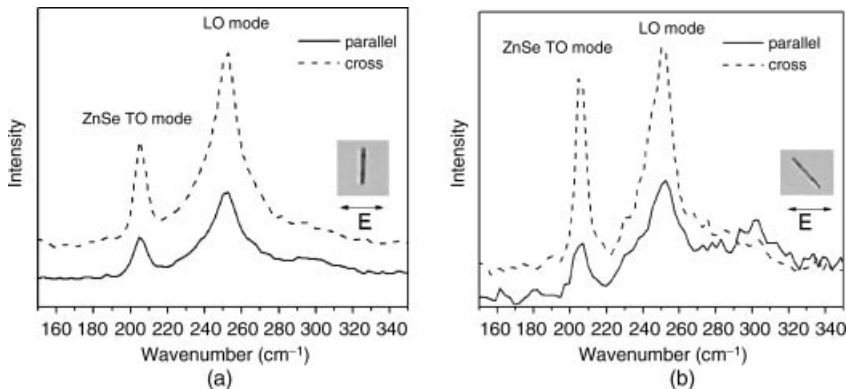


**Figure 10.21** Polarized Raman spectra of single-root ZnSe nanowire for excitation light polarized direction at  $90^\circ$  (a) and  $45^\circ$  (b). The solid and dashed lines indicate the parallel and vertical polarization configuration, respectively [19]. Reprinted from K. A. Alim, V. A. Fonoberov and A. A. Balandin, Origin of the optical phonon frequency shifts in ZnO quantum dots, *Appl. Phys. Lett.*, 86, 053103 (2005) with permission of the American Institute of Physics

LO mode is relative to that of the TO mode, being nearly two times and nearly equal, respectively. While at  $\theta = 45^\circ$ , the intensity of LO modes is relative to that of TO modes, there is no significant difference in both parallel and vertical polarized configuration.

When the direction of crystal axis and experimental configuration are fixed, we speculate the relative intensity changes of LO and TO modes according to the polarization selection rule. The above experimental results are totally different from the polarization law deduced by theoretical calculations for the (100), (110), (111), (112), and (113) five common crystal faces of cubic crystal in back-scattering geometry. For example, the simplest criterion is that observed LO and TO modes do not vanish when  $\theta$  is set as any value.

This result is similar to that of the above SWCNTs. Considering that the measured CNTs and ZnSe nanoribbons are also similar in geometry, the results here provide independent proof of the interpretation of the results of SWCNTs.

### 10.3 Raman Spectra with Exciting Laser Intensity

The micro- and macro-theory of light scattering discussed in Chapter 2 explained that the differential scattering cross section  $\frac{d^2\sigma}{d\Omega dE_0}$  of representing scattered light intensity is proportional to the square of incident light electric field strength  $|E_0|^2$ . If other experimental conditions do not change, Raman spectral features will be induced to change. For example, first, the spectral intensity will increase naturally. Second, other Raman spectral features other than intensity, such as the frequency, line width, line shape and so on, will change with incident light intensity. Third, when the pulsed laser is used as the power supply and the incident light intensity is very large, the linear Raman scattering will become non-linear Raman scattering. The first and third phenomena are reflections of the conventional property and natural change of light scattering itself, respectively. In this section, the second phenomenon occurring in nanostructures will be introduced.

At present, the experimental Raman spectra are often carried out on a micro-Raman spectrometer and the size of the laser illuminated spot on samples is only about  $1 \mu\text{m}^2$ . Therefore, when the same power of laser is used, the illuminated light power density, which corresponds to the electric field strength  $|E_0|^2$  in a micro-Raman spectrometer, is thousands of times larger than in non-micro spectrometers. In addition, nanostructure samples take the form of dispersed powder and the thermal conductivity is poor compared with that of bulk samples. Thus, the effects of illuminated laser intensity on the Raman spectrum, especially heating effects, have become an extraordinary subject in Raman spectroscopic study of nanostructures.

In nanostructures, the systematic study of the change of Raman spectral features with incident laser intensity started from CNTs [23], which has attracted much attention [24–26]. Recently, the study on laser irradiation effects on nanostructures has become an important field in material science and Raman spectroscopy, resulting in a number of significant results, which were published recently [27–35].

We will conduct a brief discussion limited to the above-mentioned second phenomenon, only involving the change of routine Raman spectral features and the significances reflected by these changes in material properties.

### 10.3.1 Laser Intensity and Temperature

#### 10.3.1.1 Power and Power Density of Lasers

The so-called laser intensity means the laser output power  $p$ . In practice, the laser intensity concerned in Raman scattering experiments means the power density  $\rho$  of incident laser at the measured point on samples rather than the output power  $p$  of the laser, as  $\rho$  is the expression of  $|E_0|^2$ . Therefore, the parameter of so-called incident light intensity is the power density  $\rho$  rather than the power  $p$ . The power density is defined as the power per unit area, i.e.,  $\rho \equiv p/\text{cm}^2$ . Figure 10.22 shows that for the same sample, the same laser power, but not the

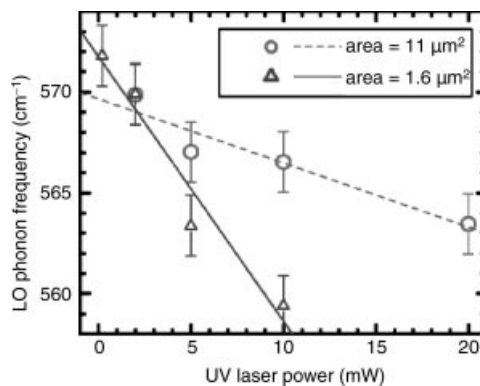


**Figure 10.22** LO phonon frequency shift in ZnO quantum dots as a function of excitation laser power. Laser wavelength is 325 nm. Circles and triangles correspond to the illuminated sample areas of  $11 \mu\text{m}^2$  and  $1.6 \mu\text{m}^2$  [29]. Reprinted from H. D. Li, K. T. Yue, Z. L. Lian, et al., Temperature dependence of the Raman spectra of single-wall carbon Nanotubes, *Appl. Phys. Lett.*, 76, 2053–2055 (2000)

same illuminated area, the shifts of LO phonon frequencies in these two cases are very different. This indicates that there is no direct correlation of phonon frequency shift between Raman spectral features and incident laser power.

#### 10.3.1.2 Laser Heating Effects and Temperature Determination

Section 1.2.2 mentioned that the temperature can be obtained by using the intensity ratio of Stokes to anti-Stokes Raman peak, as

$$I_s/I_{as} = D_{s-as}[(\omega_L - \omega)/(\omega_L + \omega)]^4 e^{\hbar\omega/kT} \quad (10.3)$$

where,  $D_{s-as}$  is the response coefficient ratio of the Stokes to anti-Stokes peaks for the spectrometer;  $\omega_L$  and  $\omega$  are the frequencies of incident laser and the Raman frequency shift, respectively;  $k$  is Boltzmann constant; and  $T$  is absolute temperature. This measured temperature is that of the laser illuminated point on samples and obtained spectra with the real temperature at the same measured point at the same time. Obviously, this is the best way to obtain the spectra with sample temperature.

#### 10.3.1.3 Temperature Determination in Raman Spectral Experiments

Under normal Raman spectral experiments,  $\omega_L \gg \omega$ ,  $[(\omega_L - \omega)/(\omega_L + \omega)]^4 \approx 1$ , thus when Equation (10.3) is used to deduce temperature, it can be simplified as

$$T = (\hbar\omega/k)/\ln(I_s/I_{as}) \quad (10.4)$$

However, when the Raman peak frequency used to deduce temperature is larger, for example, about  $2000\text{ cm}^{-1}$  at  $515\text{ nm}$  excitation,  $[(\omega_L - \omega)/(\omega_L + \omega)]^4$  is 0.44, i.e., not equal to 1. Therefore, in order to obtain the accurate temperature, it is necessary to consider various factors. Under normal circumstances, temperature  $T$  can be obtained using the following equation:

$$T = (\hbar\omega/k)/[\ln(I_s/I_{as}) - \ln(D_{s-as}\omega_{s-as})] \quad (10.5)$$

where  $\omega_{s-as} = [(\omega_L - \omega)/(\omega_L + \omega)]^4$ .

Equation (10.5) is correct only under non-resonant conditions when using Raman spectra to measure temperature. Therefore, the measured temperature is reliable only at non-resonance scattering. For example, it is impossible to gain the temperature when it is near UV excitation for diamond, as the Raman spectrum is in resonance at this case.

Moreover, in order to improve the accuracy of measured temperatures, we can measure the temperatures from various phonon modes and then take their average as the formal temperature data.

- Reliability of temperature determination by Raman spectra

Figure 10.23(a) shows the temperature dependence of the frequencies of different phonon modes, the  $E_{2g}$  mode (GM) and radial breathing mode (RBM), for the same SWCNT sample heated by a laser and a heating stage, of which the temperature data of the former and latter were obtained by the above calculation and the reading of the heating stage, respectively. Table 10.2 listed the temperature efficiency measured by GM and RBM. The good consistency between the data in Table 10.2 indicates the reliability of temperature

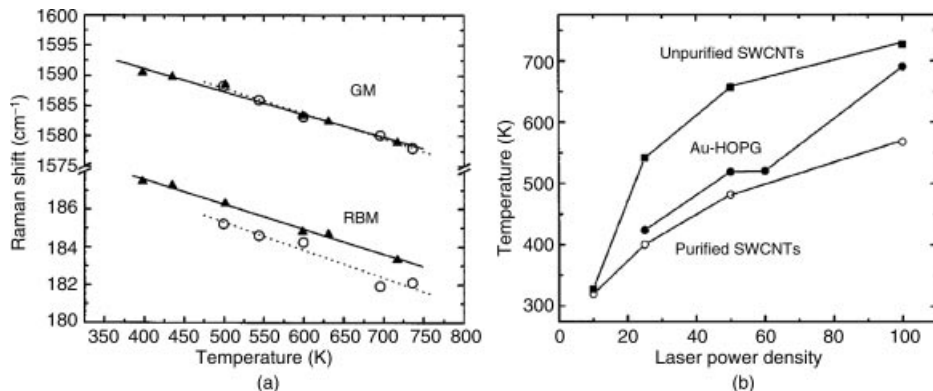


**Figure 10.23** (a) Temperature dependence of the frequencies of the GM and RBM for SWCNTs heated by laser (marked by the symbol solid triangle and solid fitted lines) and by a Linkam TH600 stage (marked by the symbol hollow circle and the dashed fitted line); (b) temperatures calculated from Raman peaks of the unpurified SWCNT, purified SWCNT, and Au-HOPG as a function of incident laser power [24]. Reprinted from S. Kouteva-Argirova, Tz. Argirov, D. Wolfgramm, et al., Influence of local heating on micro-Raman spectroscopy of silicon, *J. Appl Phys*, 94, (2003) with permission of the American Institute of Physics

measurement by Raman spectra with above method and also that the frequency change of GM and RBM under laser illumination originates from the heating effect of lasers.

- Relation between laser power density(LPD) and temperature

The temperature variation induced by laser illumination with different nanosamples has been measured, as shown in Figure 10.23(b). The measured samples are unpurified SWCNT, purified SWCNT, and Au-ion implanted HOPG (Au-HOPG). As seen in Figure 10.23(b), the temperatures induced by the same LPD differ, indicating the ability to induce temperature effects is relation with the features of nanosamples. Therefore, in the inspection of the temperature effect on nanostructures, laser power or LPD should not be used as the scale of temperature directly.

### 10.3.2 Low-Intensity (Power Density) Laser Irradiation

- Laser electric field strength and Raman spectral features

The laser intensity effects on Raman spectral features are reflected in various aspects, such as the intensity, frequency, line shape, and line width. Figure 10.24 shows the first-order

**Table 10.2** Frequency Shift Temperature coefficients ( $10^{-2} \text{ cm}^{-1}/\text{K}$ ). Reprinted from D. Li, et al., Temperature dependence of the Raman spectra of single-wall carbon Nanotubes, *Appl. Phys. Lett.*, 76, 2053–2055 (2000)

	GM	RBM
Laser	−3.8	−1.3
Heating stage	−4.2	−1.5

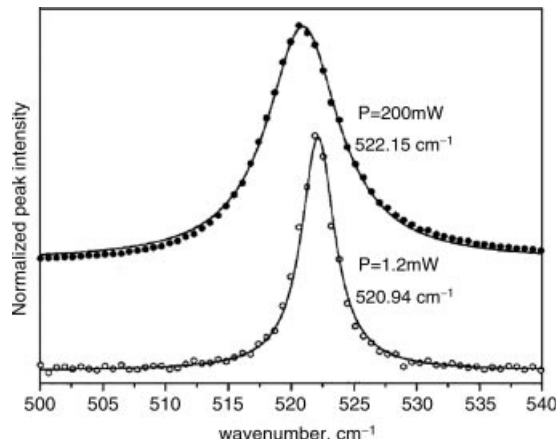


**Figure 10.24** First-order silicon-Raman peaks normalizing to their maximal intensity. The spectra at 1.2 mW laser power (open circles) and 200 mW (full circles) exhibit symmetric and slight asymmetry, respectively [35]. Reprinted from K. W. Adu, H. R. Gutiérrez, U. J. Kim, et al., Inhomogeneous laser heating and phonon confinement in silicon nanowires: A micro-Raman scattering study, *Phys. Rev. B*, 73, 155333 (2006) with permission of the American Physical Society

optical phonon Raman spectra of Si samples at two different laser powers of irradiation. From Figure 10.24, it can be seen that when the laser irradiation power increases to 200 mW, the number of Raman vibration modes does not change but the frequency, line shape, and line width of Raman spectra induce significant changes. This reflects that the composition and structure of samples do not change with laser irradiation, meaning the component and crystal structure of samples do not vary and only the structure parameters of the sample, such as atomic (ionic) distance and bond angle and so on, are changed.

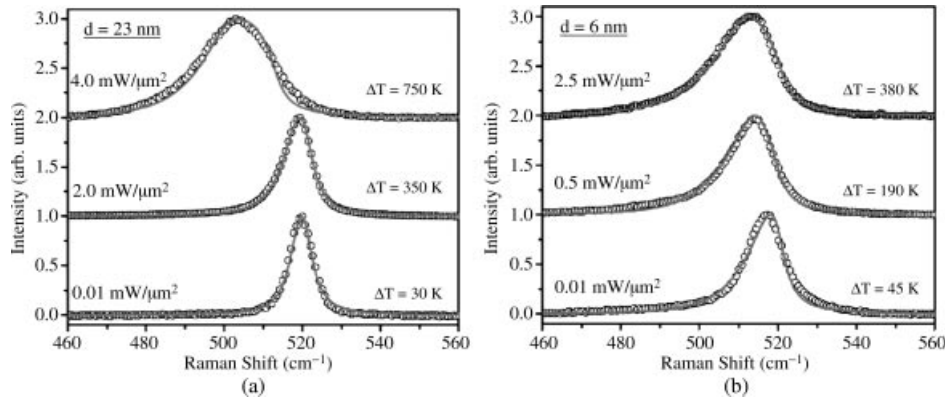
- Power density of excited laser and size of nanostructures

It was found that the power density of excited laser has different effects on Raman spectral features for different sizes of nanostructures. For example, Figure 10.25 shows the Raman spectra of Si NWs with average diameters  $d = 6 \text{ nm}$  and  $23 \text{ nm}$  for different power density excitation. It is clearly shown that the spectral features are different, as if they are excited by similar excitation power density (such as  $2.5 \text{ mW}/\mu\text{m}^2$  and  $2.0 \text{ mW}/\mu\text{m}^2$ ) for these two samples with  $d = 6 \text{ nm}$  and  $d = 23 \text{ nm}$ , respectively.

#### 10.3.2.1 Sample Configuration and Temperature Effects on Spectra

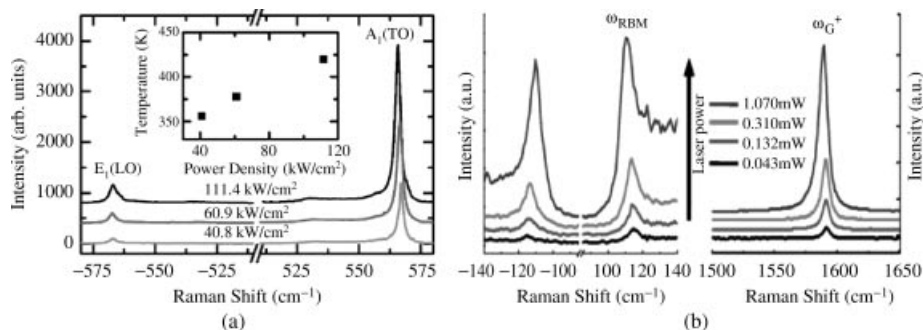
- Isolated or suspending nanomaterials

Figure 10.26 shows Raman spectra of a freestanding single GaN nanorod (a), and suspending isolated single-layer CNTs (b) with lasers of different powers or power density. Raman spectra of Stokes and anti-Stokes lines were both measured to estimate the temperature with various laser power or LPDs (see color Plate 24 for the original Figure 10.26). The estimated temperatures from  $I_{AS}/I_S$  calculations are plotted in the inset of Figure 10.26(a) and listed in Table 10.3, respectively.



**Figure 10.25** Raman spectra with LPD of  $514.5 \text{ nm}$  excitation for the average diameter  $d = 6 \text{ nm}$  (a) and  $d = 23 \text{ nm}$ . Reprinted from C. L. Hsiao, L. W. Tu, T. W. Chi, et al., Micro-Raman spectroscopy of a single freestanding GaN nanorod grown by molecular beam epitaxy, *Appl. Phys. Lett.*, 90, (2007) with permission from the American Institute of Physics. (b) Si NWs. The open circles and solid lines are observed and calculated spectra, respectively.  $\Delta T$  is the maximum increase in the sample temperature [30]

For RBM and the  $G^+$  modes of isolated mono-layer CNTs, the frequency down shifts the FWHM is broadened, and the  $I_{AS}/I_S$  increases with increased laser power, of which the relative data in Figure 10.26 are listed in Table 10.3. In Raman spectra of suspending GaN nanorods, it is shown that with increasing LPD the frequency is red-shift and integrated intensity depends linearly on the power density, with the  $A_1(\text{TO})$  mode having a much higher rate of change than other modes. The results shown in Figure 10.26 indicate that the laser heating effect is more significant for suspended and freestanding samples than those sitting on a substrate. Moreover, both spectra show trends that the frequencies decrease and



**Figure 10.26** Stokes and anti-Stokes Raman spectra of freestanding single GaN nanorod GaN (a) and suspending isolated single-layer CNTs. Reprinted from F. Huang, et al., Temperature dependence of the Raman spectra of carbon nanotubes, *J. Appl. Phys.*, 84, 4022–4024 (1998). (b) with lasers with different power densities [33,34]. Reprinted from H. D. Li, et al., Temperature dependence of the Raman spectra of single-wall carbon Nanotubes, *Appl. Phys. Lett.*, 76, 2053–2055 (2000)

**Table 10.3** The frequency, FWHM,  $I_{AS}/I_S$  of RBM and the frequency of G-mode from fitting by Lorentzian line shape for Figure 10.26(b). Each row corresponds to results obtained by a fixed laser power [34]. Reprinted from Y. Zhang, et al., Laser-Heating Effect on Raman Spectra of Individual Suspended Single-Walled Carbon Nanotubes, *J. Phys. Chem. C*, 111, 1988–1992 (2007) with permission of the American Chemical Society

Power (mW)	$\omega_{RBM}(\text{cm}^{-1})$	FWHM( $\text{cm}^{-1}$ )	$I_{AS}/I_S$	$\omega_G^+(\text{cm}^{-1})$
0.043	115.2	6.8	0.46	1592.2/*
0.132	115.0	6.8	0.58	1591.7/1587.9
0.310	114.3	7.6	0.68	1591.0/1585.1
1.070	111.6	9.1	0.96	1589.6/1586.7

line widths broaden with laser power increase, which further quantitatively shows the change trend mentioned previously.

- Bunched CNTs

Figures 10.27(a) and (b) show Raman spectra of multi-walled carbon nanotubes (MWCNT) and single-walled carbon nanotubes (SWCNT), respectively, with different temperatures induced by illuminated 515 nm lasers of different powers. It can be seen from Figure 10.27 that the Raman peak frequencies of RM, G, and D\* modes shift down with temperature increase induced by incident laser intensity increase. In addition, the same phenomenon is also observed in activated carbon (A-C) samples [36] but not in highly oriented pyrolytic graphite (HOPG) samples with increase of excited laser intensity [37].

Figures 10.28(a) and (b) show the frequency change of D and G modes for samples D-CNT, C-CNT, and A-C, while Figure 10.28(c) shows the frequency of  $E'_{2g}$  and D\* modes versus the average temperature of Samples D-CNT, in which a straight line can be fitted to each peak for each sample, meaning Raman frequency changes of all modes are linear with temperatures for all samples.

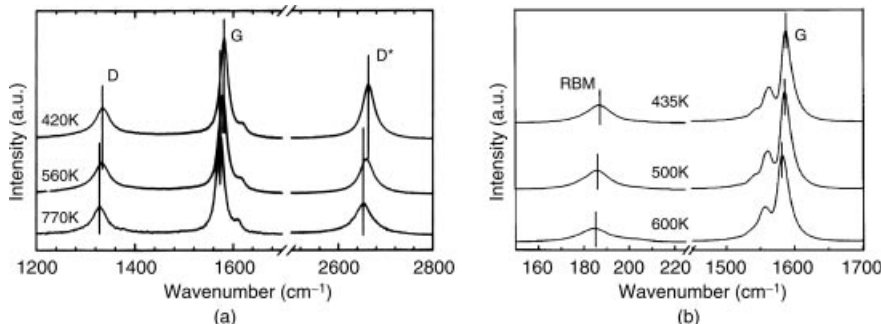


**Figure 10.27** Raman spectra of bunched multi-wall (a) and single wall. Reprinted from F. Huang, et al., Temperature dependence of the Raman spectra of carbon nanotubes, *J. Appl. Phys.*, 84, 4022–4024 (1998). (b) CNTs with different temperatures induced by illuminated lasers of different powers [23,24]

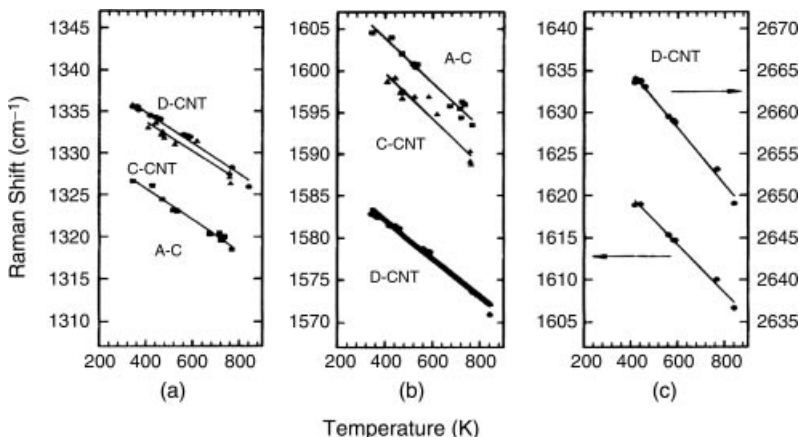


**Figure 10.28** The dependence of phonon frequencies on sample temperatures for D mode at  $\sim 1320 \text{ cm}^{-1}$  (a),  $E_{2g}$  mode at  $\sim 1620 \text{ cm}^{-1}$  (b), and the  $E'_{2g}$  mode at  $\sim 1620 \text{ cm}^{-1}$  and  $D^*$  mode at  $\sim 2640 \text{ cm}^{-1}$  (c) of C-CNT, D-CNT, and A-C samples [23]

According to the fit in Figure 10.27 by the least square method and relative references [36–38], the slope and intercept values of the fitting straight lines to the mode frequency change with sample temperature are listed in Table 10.4. From the table, it can be seen for the G-mode that the absolute slope value of SWCNT is larger than those of MWCNT, polycrystalline graphite GL and HOPG, while the slopes of MWCNT, GL, and HOPG are almost the same.

Table 10.5 lists the slope and intercept values from Figure 10.28 which show that the slope values are dependent on the type of Raman modes and have little correlation with sample types. In addition, the slopes are nearly the same for the same Raman mode, such as the D mode, even if they belong to different types of samples. However, the slopes are different for the different Raman modes, even if they are from the same sample. The absolute value of the G-mode slope is larger than the D-mode. The value of slopes G- and  $E'_{2g}$ - modes are almost the same for the D-CNT sample. In addition, the slope of the  $D^*$  mode is nearly double of that of the D mode, which means that the  $D^*$  mode the second-order of D-mode.

**Table 10.4** Slopes and intercepts of the fitted straight line for the GM and RBM of the SWCNT in Figure 10.27(b) and the reported results of the MWCNT, graphite (GL) and HOPG. Reprinted from H. D. Li, et al., Temperature dependence of the Raman spectra of single-wall carbon Nanotubes, *Appl. Phys. Lett.*, 76, 2053–2055 (2000)

Sample	SWCNT [24]	MWCNT [38]	GL [36]	HOPG [37]
Slope( $10^{-2} \text{ cm}^{-1}/\text{K}$ )	GM RBM	-3.8 -1.3	-2.8	-3.0 -2.8
Intercept ( $\text{cm}^{-1}$ )	GM RBM	1606 193	1611	

**Table 10.5** The slopes and intercepts of the straight line fit in Figure 10.27 [23]. Reprinted from F. Huang, et al., Temperature dependence of the Raman spectra of carbon nanotubes, *J. Appl. Phys.*, 84, 4022 (1998)

Sample	Parameter	D	G	$E'_{2g}$	$D^*$
D-CNT	Slope ( $\text{cm}^{-1}/\text{K}$ )	-0.019	-0.023	-0.029	-0.034
	Intercept ( $\text{cm}^{-1}$ )	1342	1591	1631	2697
C-CNT	Slope ( $\text{cm}^{-1}/\text{K}$ )	-0.018	-0.028	...	...
	Intercept ( $\text{cm}^{-1}$ )	1341	1661	...	...
A-C	Slope ( $\text{cm}^{-1}/\text{K}$ )	-0.019	-0.027	...	...
	Intercept ( $\text{cm}^{-1}$ )	1333	1615	...	...

The above-mentioned changes of Raman frequency with sample temperature exhibit an interesting regularity. These regular changes are thought to be ascribed to the unique structural features of CNTs.

First, like any material, the lattice expansion of CNT must occur and its C–C bond becomes longer due to temperature rise. As a result, the interaction force constants between neighboring carbon atoms become smaller and the phenomenon of Raman frequencies of all vibration modes moving down with increasing temperature as expected, are shown in Figures 10.27 and 10.28.

Second, the tube-like structure makes the restoring force of C–C bonds in the graphite plane to decompose two components along the radial and tangential directions of the tube, both of which are smaller than the original. The tangential component is inversely proportional to the diameter of CNTs, that is, the smaller the diameter, the larger the tangential component, which leads to an expanse of the C–C band on the tubes with smaller diameter. Based on the above, the phenomenon that the slope of SWCNTs is smaller than that of other carbon materials, as listed in Table 10.5 can be interpreted as the special structural feature of a single-walled tube. The SWCNT is made of curling of a single graphite sheet, so the smaller the tube diameter, the greater the curvature of the tube. The theory and experiment both indicate that when the graphite sheet forms a tube, its C–C bond length will be longer [39], leading to C–C bond force constants become smaller and making the CNT structure relatively easy to expand when compared to the planar structure of graphite. However, for MWCNTs, the diameters of inner and outer tubes are between 10 and 50 nm [40,41] and are larger than 1.1–1.4 nm diameters of a single-walled tube with 1 order of magnitude [40,41], therefore the effect induced by the small diameter of tubes is very small and can be ignored. In addition, the space of graphite sheets of MWCNT is very small and similar to that of graphite [42]. Therefore, it should be expected for the slope of Raman frequency to change with temperature of GM modes, as listed in Table 10.5.

Third, Figure 10.23(b) shows that the temperature effects by laser heating are different for different samples; in addition, it is found that no temperature shift is observed for the HOPG within the same range of variation in laser power used in the experiments of Figure 10.23(b) [24]. On the one hand, the sample Au-HOPG is  $\text{Au}^+$  ions injected and thus must generate artificial impurities (i.e., Au ions) and defects; on the other hand, impurities in purified SWCNT must be less than unpurified SWCNT, so the phenomenon shown in Figure 10.23(b) can be expected.

The above phenomena were also observed by Watanabe *et al.* [42]. They reported that when the sample temperature increased from 25 to 400 °C, the G-mode frequency of HOPG changed very little, but the frequency of the disorder-induced D mode changed. However, after HOPG was implanted by ions, the change of Raman spectral features with temperature was observed for all phonon modes.

It is revealed that the above phenomena are similar to the results expressed in Table 9.15 of Section 9.6.3, which mentioned the CNT is a defect-like structure. Therefore, it is reasonable to believe that the strength or weakness of the temperature effect is related to the features of impurities and defects of subjects, that is, the stronger temperature effect must occur in CNT rolled-up by HOPG and not HOPG, as well as in the implanted Au-HOPG and not HOPG.

The relationship between the D-CNT Raman peak width (FWHM) and the sample temperature induced by laser irradiation, obtained from the spectra in Figure 10.27, are shown in Figure 10.29. It can be seen from the figure that the line widths of D mode and D\* mode increase with temperature increment and the line width of the D\* mode is double the first-order D mode. However, Raman peak widths of G mode and E'2g mode cannot show obvious change.

The above results show that the thermal effects of laser radiation is obvious in CNTs and has larger temperature coefficient of Raman frequency shift with sample temperature. The temperature coefficient of the Raman frequency shift with sample temperature plays a key role in the determination of CNT temperature and has been widely applied in the temperature measurement of CNTs [26].

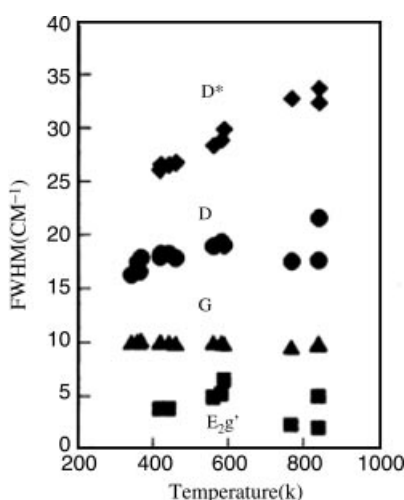


**Figure 10.29** Raman peak width (FWHM) of D-CNT with the incident laser intensity (temperature) of D, G, E'₂g, and D\* modes of CNT, where the line width values of E'₂g and D\* modes move down 5 cm⁻¹ and up 10 cm⁻¹, respectively. Reprinted from S.-L. Zhang, H. Li, K. T. Yue, et al., Effects of intense laser irradiation on Raman intensity features of carbon nanotubes, Phys. Rev. B, 65, 073401 (2002)

### 10.3.3 Irradiation with High Laser Power Density

When a  $25 \sim 30$  mW Ar<sup>+</sup> laser is focused on samples passing through the illuminated optics of a micro-Raman spectrometer, the power on the sample will be  $3 \sim 5$  mW. Moreover, if a  $50 \times$  microscope objective is used to focus light onto the sample, the spot diameter on the sample is  $1 \sim 2 \mu\text{m}$  and the power density will reach  $10^5 \text{ W/cm}^2$ . Therefore, high power density irradiation of samples is easy to realize and so the effects induced by high power density irradiation is a problem requiring attention.

#### 10.3.3.1 Damage of Samples with High Power Density Irradiation

It is commonly understood that high power density irradiating will damage samples. For example, Figure 10.30 shows a microscope image of unpurified SWCNT illuminated at 514.5 nm with a power density of  $25 \times 10^3 \text{ W/cm}^2$ . The dark strip and speck seen in the figure were induced by intense laser irradiation, which is usually associated with damage. However, the Raman spectra of SWCNT before illumination still records at the dark spot, verifying that the CNTs were not damaged by laser irradiation. This result proves that to judge if the sample is damaged should be based on scientific methods, such as Raman spectra, rather than on appearance alone.

#### 10.3.3.2 Disappearance of Vibration Modes with High Power Density Irradiation

Irradiation on mono-root nanosamples can rule out the effects from other objects and reflects the irradiation effect only. Figure 10.31 shows the Raman spectra of a single-root

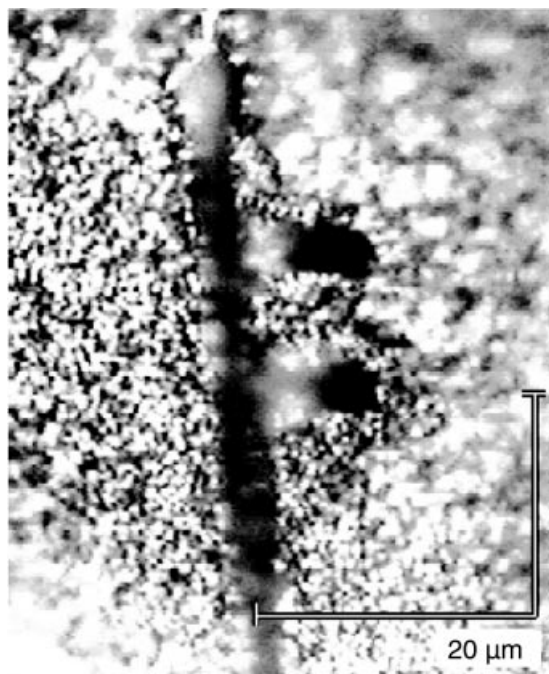


**Figure 10.30** Microscope image of unpurified SWCNT illuminated at 514.5 nm with a power density of  $25 \times 10^3 \text{ W/cm}^2$  [25].

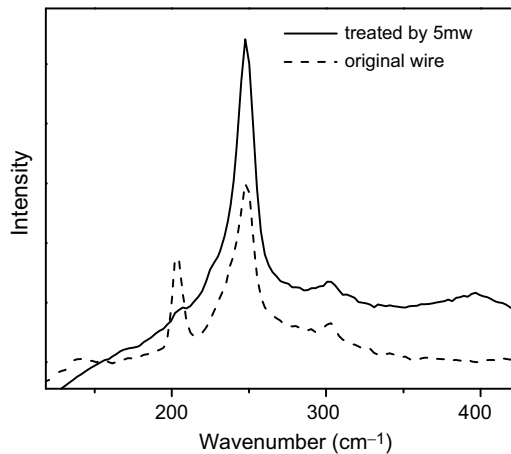


**Figure 10.31** Raman spectra of mono-root ZnSe NW before (dotted line) and after (solid line) irradiation by high power density laser [19]. Reprinted from S.-L. Zhang, H. Li, K. T. Yue, et al., Effects of intense laser irradiation on Raman intensity features of carbon nanotubes, *Phys. Rev. B*, 65, 073401 (2002)

ZnSe NW before and after irradiation by a high power density laser. The figure shows that the LO and TO modes can be observed in Raman spectrum before high power density irradiation, but the TO mode disappears and the absolute intensity of the LO mode increases after irradiation.

Due to the restrictions of selection rules, the TO mode is absent from an ideal ZnSe crystal. Therefore, the appearance or not of the TO mode indicates the sample quality as being poor or good, respectively, while the above result also proves that laser irradiation can improve crystal quality.

#### 10.3.3.3 Purification of Samples with High Power Density Irradiation

The results shown in Figures 10.30 and 10.31 indicate that high power density irradiation can improve the quality of samples, such as reducing defects and getting rid of impurities, of which further work is reported in Ref. [25].

Figure 10.32 is the Raman spectra of SWCNTs measured at the same sampling point with varied LPD at non-resonant excitation of 515 nm (a) and resonant excitation of 633 lasers (b). Theoretical calculations show that Figure 10.32(b) are Raman spectra of (9,9) armchair tubes by RSSE. These spectra were taken at low LPD (1%) first and shown as the top spectrum. LPD was gradually increased from the top spectrum at 1% of  $10^5 \text{ W/cm}^2$  downwards to 100% in the middle spectrum and then decreased gradually to 1%, in the lowest spectrum.

The band at around  $1590 \text{ cm}^{-1}$  corresponds to the  $E_{2g}$  mode in graphite materials and is referred to as the G band [43]. This band splits into several peaks in SWCNTs. The split peaks of the G band are at around 1573, 1590, and  $1599 \text{ cm}^{-1}$  with 514.5 nm excitation (see Figure 10.32(a)) and at 1506, 1540, 1563, and  $1590 \text{ cm}^{-1}$  with 632.8 nm excitation (see Figure 10.32(b)). The peak at  $1337 \text{ cm}^{-1}$  in Figure 10.32 relates to structural disorders, such as impurities and/or defects and size limitation, and is absent in pure crystalline graphite

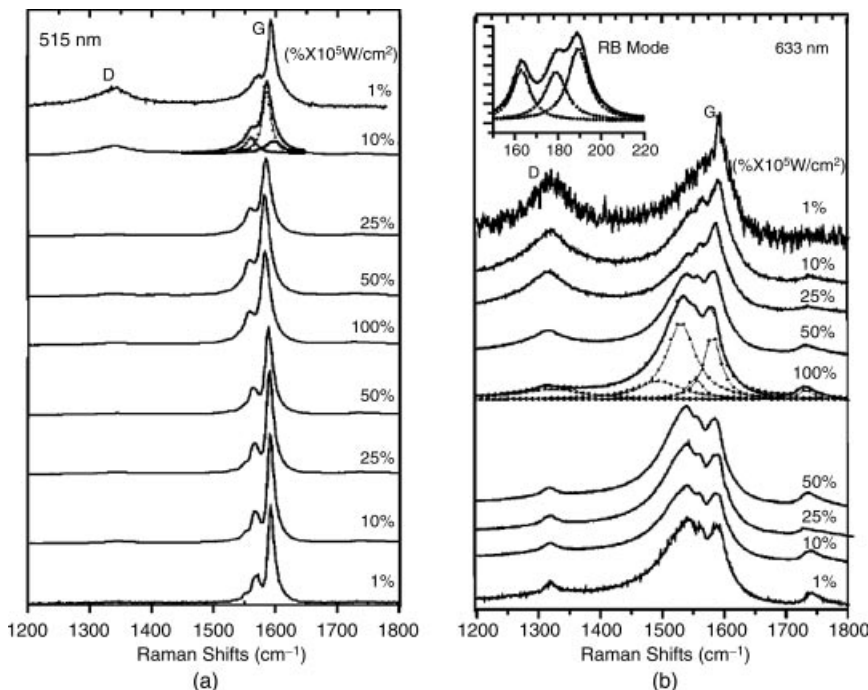


**Figure 10.32** Raman spectra of unpurified SWCNT samples irradiated at 514.5 (a) and 632.8 (b) nm in sequence from top to bottom with power density at the sample of 1, 10, 25, 50, 100, 50, 25, 10, and 1%  $\times 10^5$  W/cm<sup>2</sup>, respectively. The dashed lines show typical fitted spectra [25]. Reprinted from S.-L. Zhang, H. Li, K. T. Yue, et al., Effects of intense laser irradiation on Raman intensity features of carbon nanotubes, Phys. Rev. B, 65, 073401 (2002)

material such as HOPG. Thus, the intensity of the D peak is usually seen as a measure of the degree of disorder in graphite material.

Figure 10.32 shows that the frequencies of the G peak increase with increasing LPD and the change is reversible. The dependence of the frequencies of the strongest G peak at 1590 cm<sup>-1</sup> in Figure 10.32(a) and at 1540 cm<sup>-1</sup> in Figure 10.32(b) on LPDs are plotted in the top panel of Figure 10.33 with solid and empty squares, respectively. The reversible dependency on LPD can be seen in Figure 10.33. This confirms that the measured sample was not damaged in the irradiation process. In contrast, the Raman intensities of the G peaks and the D peak also change with LPD, but the process is not reversible.

We introduce a disorder parameter  $a \equiv I_D/I_G$ , where  $I_D$  and  $I_G$  are the integrated intensity of the D peak and the G peaks, respectively. A small  $a$  represents a low degree of disorder. The spectra of an SWCNT sample, purified by traditional methods [44], was measured with the same irradiation process, as shown in Figure 10.32. The G peak at 1591 cm<sup>-1</sup> in Figure 10.32(a) and at 1590 cm<sup>-1</sup> of the purified CNT sample have been used to calculate the disorder parameters  $\alpha_{\text{unpuri}}$  and  $\alpha_{\text{puri}}$ , respectively. The dependence of  $\alpha_{\text{unpuri}}$  and  $\alpha_{\text{puri}}$  on LPD is shown in the middle panel of Figure 10.33 with triangles. Note that  $\alpha_{\text{unpuri}}$  decreases rapidly in the initial increase in LPD, but remains basically unchanged in the subsequent decrease of LPD. This indicates that as LPD increases, the sample becomes better ordered

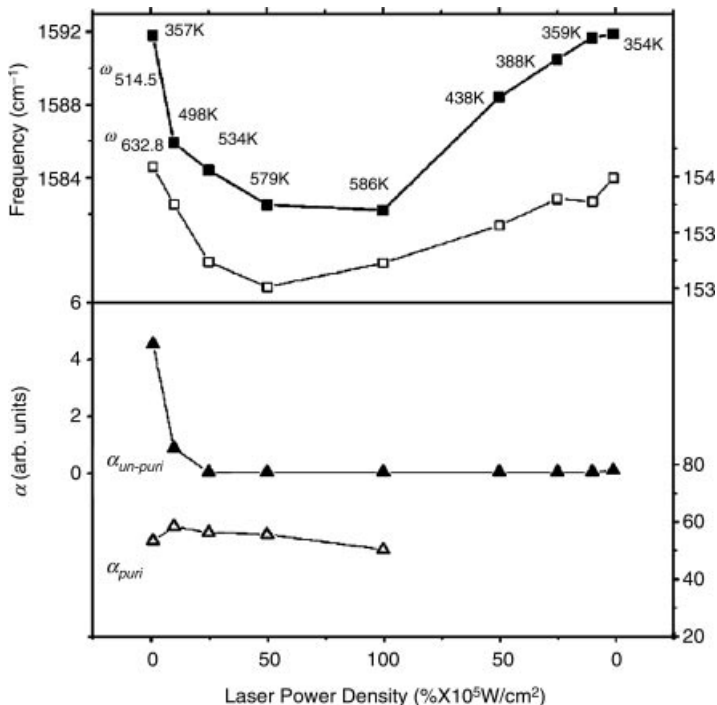


**Figure 10.33** Raman frequencies  $\omega_{514.5}$  and  $\omega_{632.8}$ , as well as Raman intensity ratios  $\alpha_{unpuri}$  and  $\alpha_{puri}$  versus LPD [25]

and the degree of disorder remains low, even when LPD decreases. In contrast,  $\alpha_{puri}$  is constant throughout the entire process of increase and subsequent decrease of LPD. Comparing the behavior of an LPD, we can conclude that heating with intense laser irradiation can lead to the loss of impurities and so results in a purified CNT sample. This result suggests a simple and fast CNT purification method using intense laser irradiation.

Unpurified samples contain a large number of impurities, such as amorphous carbon, nanoparticles of carbon, C<sub>60</sub>, and so on. With sample temperature rise, on the one hand, some of impurities are oxidized into CO<sub>2</sub> and leave the samples; on the other hand, the crystallization degree increases due to the annealing effect. As a result, the samples are purified and the  $\alpha$  value significantly decreases. In the temperature reduction process, the frequencies of G modes reverse and D modes no longer appear, indicating that the crystallization fixes and the impurities do not exist. From the behavior of  $\alpha_{unpuri}$  versus LPD shown in Figure 10.33, it can be worked out that the temperature at which impurities will be removed completely is about 534 K, which is similar to the impurities oxidation temperature (473 ~ 623 K) in SWCNT samples reported by Ref. [46] and further proves that intense laser irradiation can be a fast purification method of CNTs.

Moreover, the new methods to purify and optimize CNTs by strong power density laser irradiation have more advantages compared to other chemical and physical methods. For it is the laser interaction directly with samples, and there are no chemicals involved, which

avoids introducing other impurities; In addition, because it is non-contact, it can be operated from a distance, and the purification can be dealt with in special experiment conditions. In the devices treatment process, the laser purification method shows its irreplaceable role, for it is undesirable to deal with samples using chemical methods.

In recent years, laser intensity effects on the Raman spectra of has become a controversial topic [45–48]. The studies on silicon NWs have shown that the thermal conductivity of nano-semiconductors is poor [48], which induces the local temperature of the sample to rise very high after irradiated by the laser, resulting in the features of Raman spectrum changing significantly [47]. From the above studies of the relationship between laser irradiation and Raman spectra, low thermal conductivity may be the general properties of nanostructures.

## References

- [1] Sood, A.K., Menéndez, J., Cardona, M., and Ploog, K. (1985) *Phys. Rev. Lett.*, **54**, 2111–2114.
- [2] Manuel, P., Sai-Halasz, G.A., Chang, L.L., Chang, C.A., and Esaki, L. (1976) *Phys. Rev. Lett.*, **37**, 1701–1704.
- [3] Colvard, C., Gant, T.A., Klein, M.V., et al. (1985) *Phys. Rev. B*, **31**, 2080–2091.
- [4] Zucker, J.E., Pinczuk, A., Chemla, D.S., Gossard, A., and Wiegmann, W. (1983) *Phys. Rev. Lett.*, **51**, 1293–1296.
- [5] Zhang, S.L., Gant, T.A., Delane, M., Klein, M.V., Klem, J., and Morkoc, H. (1988) *Chin. Phys. Lett.*, **5**, 113–116.
- [6] Kasuya, A., Sugano, M., Maeda, T., et al. (1998) *Phys. Rev. B*, **57**, 4999–5001.
- [7] Yan, Y., Huang, F.M., Zhang, S.L., Zhu, B.F., Zhi, S.E., and Fan, S.S. (2001) *Chin. Sci. Bull.*, **15**, 1256–1257.
- [8] Yan, Y., Zhang, S.L., Fan, S., Han, W., Meng, G., and Zhang, L. (2003) *Solid State Commun.*, **126**, 649–651.
- [9] Gogolin, A.A. and Rashba, E.F. (1976) *Solid State Commun.*, **19**, 1177–1179.
- [10] Martin, R.M. (1971) *Phys. Rev. B*, **4**, 3676–3685.
- [11] Ts'en, K.T. (1993) *J. Mod. Phys. B*, **7**, 4165–4185.
- [12] Rao, A.M., Richter, E., Bandow, S., et al. (1997) *Science*, **275**, 187–191.
- [13] Zhang, G.Y., Lan, G.X., and Wang Y.F., *Vibration Spectroscopy in Lattices*, Hight Education Press, 2001.
- [14] (a) Zhang, S.L., Hou, Y., Ho, K.S., Qian, B., and Cai, S. (1992) *J. Appl. Phys.*, **72**, 4469–4471.  
(b) Zhang, S.L., Ding, W., Yan, Y., et al. (2002) *Appl. Phys. Lett.*, **81**, 4446–4448.
- [15] Zhang, S.L., Zhang, Y., Liu, W., et al. (2006) *App. Phys. Lett.*, **89**, 063112.
- [16] Zhang, S.L., Gant, T.A., Delane, M., Klein, M.V., Klem, J., and Morkoc, H. (1987) *Chin. Phys. Lett.*, **5**, 113–116.
- [17] Zucker, J.E., Pinczuk, A., Chemla, D.S., Gossard, A., and Wiegmann, W. (1984) *Phys. Rev. Lett.*, **53**, 1280–1283.
- [18] Duesberg, G.S., Loa, I., Burghard, M., Syassen, K., and Roth, S. (2000) *Phys. Rev. Lett.*, **85**, 5436–5439.
- [19] Yan, Y. (2004) Phd Thesis, Peking University.
- [20] Smith, C.A., Lee, H. W. H., Leppert, V. J., and Risbud, S.H. (1999) *Appl. Phys. Lett.*, **75**, 1688.
- [21] Mehendale, M., Sivananthan, S., Pötz, W., and Schroeder, W.A. (1998) *J. Electronic Materials*, **27**, 752.
- [22] Tutuncu, H.M. and Srivastava, G.P. (1998) *Phys. Rev. B*, **57**, 3791–3794.

- [23] Huang, F., Yue, K.T., Tan, P., *et al.* (1998) *J. Appl. Phys.*, **84**, 4022–4024.
- [24] Li, H.D., Yue, K.T., Lian, Z.L., *et al.* (2000) *Appl. Phys. Lett.*, **76**, 2053–2055.
- [25] Zhang, L., Li, H., Yue, K.T., *et al.* (2002) *Phys. Rev. B*, **65**, 073401.
- [26] Kneipp, K., Kneipp, H., Corio, P., *et al.* (2000) *Phys. Rev. Lett.*, **84**, 3470–3473.
- [27] Jalilian, R., Sumanasekera, G.U., Chandrasekharan, H., and Sunkara, M.K. (2003) *Phys. Rev. B*, **74**, 155421.
- [28] Mavi, H.S., Prusty, S., Shukla, A.K., and Abbi, S.C. (2003) *Thin Solid Films*, **425**, 90–96.
- [29] Alim, K.A., Fonoberov, V.A., and Balandin, A.A. (2005) *Appl. Phys. Lett.*, **86**, 53103.
- [30] Adu, K.W., Gutiérrez, H.R., Kim, U.J., and Eklund, P.C. (2006) *Phys. Rev. B*, **73**, 155333.
- [31] Ravindran, T.R. and Badding, J.V. (2006) *J. Mater. Sci.*, **41**, 7145.
- [32] Xu, X.X., Yu, K.H., Wei, W., *et al.* (2006) *Appl. Phys. Lett.*, **89**, 253117.
- [33] Hsiao, C.L., Tu, L.W., Chi, T.W., *et al.* (2007) *Appl. Phys. Lett.*, **90**, 043102.
- [34] Zhang, Y., Son, H., Zhang, J., Kong, J., and Liu, Z. (2007) *J. Phys. Chem. C*, **111**, 1988–1992.
- [35] Kouteva-Argirova, S., Argirov, T., Wolfframm, D., and Reif, J. (2003) *J. Appl. Phys.*, **94**, 4946–4949.
- [36] Everall, N.J., Lumsdon, J., and Christopher, D.J. (1991) *Carbon*, **29**, 133.
- [37] Erbil, A., Postman, M., Dresselhaus, G., and Dresselhaus, M.S. (1982) *Phys. Rev. B*, **25**, 5451–60.
- [38] Huang, F.M., Yue, K.T., Tan, P.H., *et al.* (1998) *J. Appl. Phys.*, **84**, 4022.
- [39] Saito, R., Dresselhaus, G., and Dresselhaus, M.S. (1998) *Physical Properties of CNTs*, Imperial college Press, London.
- [40] Shi, Z., Zhou, X., Jin, Z., *et al.* (1996) *Solid. State. Commun.*, **97**, 371–375.
- [41] Kiang, C.H., Endo, M., Ajayan, P.M., Dresselhaus, G., and Dresselhaus, M.S. (1998) *Phys. Rev. Lett.*, **81**, 1869–1872.
- [42] Tuinstra, F. and Koenig, J.L. (1970) *J. Chem. Phys.*, **53**, 1126.
- [43] Pimenta, M.A., Marucci, A., Empedocles, S.A., Bawendi, M.G., and Dresselhaus, E.B. (1998) *Phys. Rev. B*, **58**, 16016–16020.
- [44] Shi, Z.J., Lian, Y.F., Zhou, X.H., *et al* (1999) *J. Phys. Chem. B*, **103**, 8698.
- [45] Watanable, H., Takahashi, K., and Iwaki, M. (1993) *Nucl. Instru. Meth. Phys. Res. B*, **80**, 1489.
- [46] Gupta, R. *et al.* (2003) *Nano. Lett.*, **3**, 627.
- [47] Piscane, S. *et al.* (2003) *Phys. Rev. B*, **68**, 241312–R.
- [48] Scheel, H. *et al.* (2006) *Appl. Phys. Lett.*, **88**, 233114.

# 11

## Raman Spectra with Samples of Nanostructures

The feature of measured samples may not affect the Raman spectral feature in bulk matter, but it is not the case in nanostructures. For example, geometrical factors, such as the size and shape of samples, have no effects on Raman spectral features of bulk matter of macroscopic size, however, in nanostructures, the size and shape of samples have an essential effect on Raman spectral features. This chapter introduces the effects induced by these two factors, together with the compositions and micro-structure of samples.

### 11.1 Effects of Sample Sizes on Raman Spectra of Nanostructures

The size parameters to describe nanostructures have some differences. For example, the thickness of wells  $d_1$ , thickness of barriers  $d_2$ , and period of superlattice  $d \equiv d_1 + d_2$  are for quantum wells/superlattices, while the diameters are mainly for other nanostructures, such as the nanowires, nanoparticles, nanorods and nanotubes. We will study how these parameters affect Raman spectral features of nanostructures.

Based on the introduction in Chapter 8, we have learned theoretically that the dispersion curve of folded acoustic phonon, confined optical phonon, and macroscopic interface phonon in superlattices are described by Equations (8.10)–(8.15) and (8.20)–(8.22) and the Raman spectrum of nanocrystals is expressed by Equation (8.68) of the microcrystal model. All of the above theoretical equations are related to the size of sample. The experimental results of the resonant size selection effect (RSSE), mentioned in Section 9.1 show entirely different behaviors for non-polar and polar semiconductors. As mentioned above, there is an obvious difference of Raman spectral features for different forms of nanostructures, therefore this chapter will be based on different forms of nanostructures.

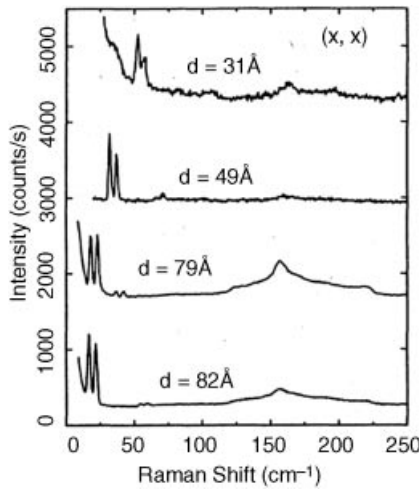


**Figure 11.1** Raman spectra of superlattice GaAs/AlAs with different superlattice periods. Reprinted from C. Colvard, T. A. Gant, M. V. Klein, R. Merlin, R. Fischer, H. Morkoc and A. C. Gossard, Folded acoustic and quantized optic phonons in (GaAl)As superlattices, Phys. Rev. B, 31, 2080–2091 (1985) with permission of the American Physical Society

### 11.1.1 Effects of Sample Sizes on Raman Spectral Features of Superlattices (SLs)

#### 11.1.1.1 Folded Acoustic Phonons

Colvard *et al.* measured the Raman spectra of four GaAs/AlAs superlattices with different period  $d$  [1]. The results are shown in Figure 11.1 which show that folded acoustic phonons and the frequency difference between acoustic doublet phonons are influenced by the size parameter-period  $d$  of samples.

#### 11.1.1.2 Confined Optical Phonons

Merlin *et al.* measured the Raman spectra of two GaAs/AlAs SLs with different structural parameters [2], as shown in Figure 11.2. Table 11.1 lists the observed frequencies and theoretical calculated Raman shifts of measured optical modes for the samples. The table shows that the Raman shifts of optical modes differ also with size parameters.

Regarding the quantum confinement effect (QCE) on macroscopic interface modes and microscopic interface modes, this has been described in the comparison between experiment and theory in Section 9.1.3 where characteristic Raman spectrum was discussed.

The good agreement between experimental and theoretical results mentioned above indicates also that the theoretical expectation in Chapter 8 is correct and believable.

### 11.1.2 Effects of Sample Sizes on Raman Spectral Features of Non-polar Semiconductors

The RSSE occurring in non-polar semiconductors Si, diamond, and carbon nanotube has indirectly shown that the Raman frequencies change with sample size [3–5]. Here, this phenomenon will be confirmed directly by using samples of various sizes.

**Table 11.1** Observed Raman shift of confined optical phonons for two GaAs/AlAs superlattices with different structural parameters. The data in brackets are theoretical calculated Raman shift of  $E(LO_1)$  and  $E(LO_2)$  [2]. Reprinted from R. Merlin, C. Colvard, M. V. Klein, et al., Raman scattering in superlattices: Anisotropy of polar phonons, *Appl. Phys. Lett.*, 36, (1980) with permission of the American Institute of Physics

$d_{\text{GaAs}}-d_{\text{AlAs}}$	$B_2(LO_1)$	$E(LO_1)$	$B_2(LO_2)$	$E(LO_2)$	$E(LO_1)$	$E(LO_2)$
5–5 nm	290	271	401	360	280 (2711.9)	378 (380.6)
1.4–1.1 nm	288	266	399	358	277 (276.1)	382 (377.2)

Figure 11.3 shows the observed Raman results with sample sizes for typical non-polar nano-semiconductors Ge and Si. Figure 11.4 shows the Raman spectra with sample sizes of typical nanocarbons, nanodiamonds, and SWCNT [8–10]. All the spectra above show similar relations between sample size and Raman spectral features in experimental results: the Raman spectral frequency downshift, line width broadening, and line shape display more asymmetry with decreasing sample size [11–15]. In addition, all the observed Raman spectra can be fitted to the microcrystal model well, in which the observed Raman frequency change within these nanosample sizes matches the regularity worked out in RSSE, as described in Section 10.1.2. This confirms that the speculation based on the

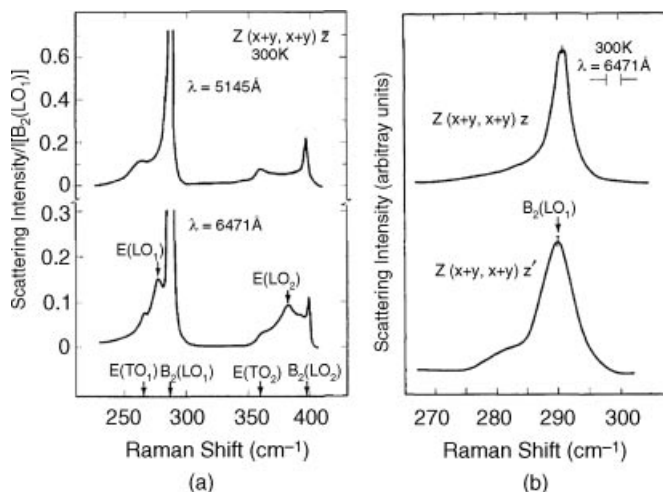


**Figure 11.2** (a) Raman spectra of the 1.4 nm GaAs-1.1 nm AlAs superlattice. The scattering intensity has been normalized to the  $B_2(LO_1)$  mode intensity for comparison. Arrows give frequencies listed in Table 11.1. (b) Raman spectra of the 5.0 nm GaAs-5.0 nm AlAs superlattice in the backscattering (upper) and near forward scattering configuration (lower). In the latter, the scattering angle outside the sample is  $14.5^\circ$  [2]. Reprinted from R. Merlin, C. Colvard, M. V. Klein, et al., Raman scattering in superlattices: Anisotropy of polar phonons, *Appl. Phys. Lett.*, 36, (1980) with permission of the American Institute of Physics

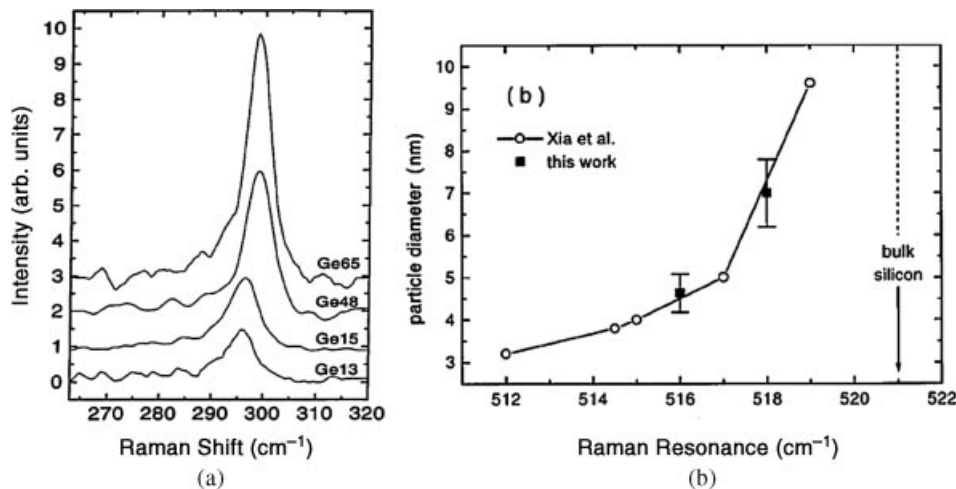


**Figure 11.3** (a) Raman spectra of some typical non-polar nanostructures with sample sizes for (a) Ge nanocrystals corresponding to different mean radii of 6.5 nm (Ge65), 4.8 nm (Ge48), 1.5 nm (Ge15), and 1.3 nm (Ge13) [8]. Reprinted from C. E. Bottani, C. Mantini, P. Milani, et al., Raman, optical-absorption, and transmission electron microscopy study of size effects in germanium quantum dots, *Appl. Phys. Lett.*, 69, (1996) with permission of the American Institute of Physics. (b) the relation between Raman frequencies and sizes of nano-Si [6,7]. Reprinted from M. Ehbrecht, B. Kohn, F. Huisken, M. A. Laguna and V. Paillard, Photoluminescence and resonant Raman spectra of silicon films produced by size-selected cluster beam deposition, *Phys. Rev. B*, 56, 6958–6964 (1997) with permission of the American Physical Society.

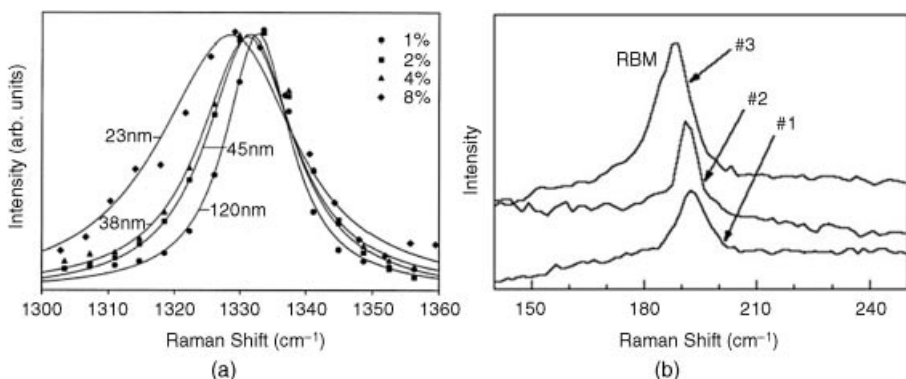


**Figure 11.4** Raman spectra of (a) nanodiamond with grain sizes 23, 38, 45, and 120 nm (data of the solid line from the microcrystal model) [9]. Reprinted from Z. Sun, J. R. Shi, B. K. Tay and S. P. Lau, UV Raman characteristics of nanocrystalline diamond films with different grain size *Diamond and Related Materials*, 9, 1979–1983 (2000) with permission of Elsevier. (b) radial breathing mode (RBM) of SWNTs with diameter 1.5 nm (#1), 5 nm (#2), and 5 nm (#3) [10]. Reprinted from G. S. Duesberg, I. Loa, M. Burghard, K. Syassen and S. Roth, Polarized Raman Spectroscopy on Isolated Single-Wall Carbon Nanotubes, *Phys. Rev. Lett.*, 85, 5436–5439 (2000) with permission of the American Physical Society.

RSSE of nanowire Si in Section 10.1.2, that is, the Raman frequency of phonons in nano-semiconductors must change with size of samples, is correct for non-polar semiconductors [3–5].

### 11.1.3 Effects of Sample Sizes on Raman Spectral Features of Polar Semiconductors

Section 10.1.2 mentioned that there is no RSSE in polar nano-semiconductors with size distribution, that is, Raman spectral frequencies of optical phonons in polar nano-semiconductors do not change with excited wavelengths, which implies that their phonon frequencies are independent of sample size and differ from the RSSE observed in non-polar semiconductors, such as carbon nanotubes and Si nanowires with size distribution [3,4]. This indicates that there is no FSE on optical phonons in polar nano-semiconductors, which is the opposite of the general concept of the FSE and should be tested by using different sizes of nanosamples directly, which is introduced below.

To make the test results reliable and believable, first, the size distribution of all the samples should be as small as possible, since larger size distribution will widen the line width of spectra and lower the resolution of frequency. Second, the impurity and defect content should be as small as possible to avoid disturbing the spectra. In addition, the shape of samples should be spherical so that theoretical simulation is convenient to perform. After the observation of electron microscope, we found the following ZnO nanoparticles are good in fitting the above requirements.

Electron microscope images of the eight ZnO nanoparticle (NP) samples used are shown in Figure 11.5. From the figure we see that all nanoparticles are basically spherical. The average diameter  $\bar{R}$  and the deviation  $\Delta R$  from  $\bar{R}$  are listed in Table 11.2, showing that the size uniformity of all samples is good, with a size deviation of less than about 10%.

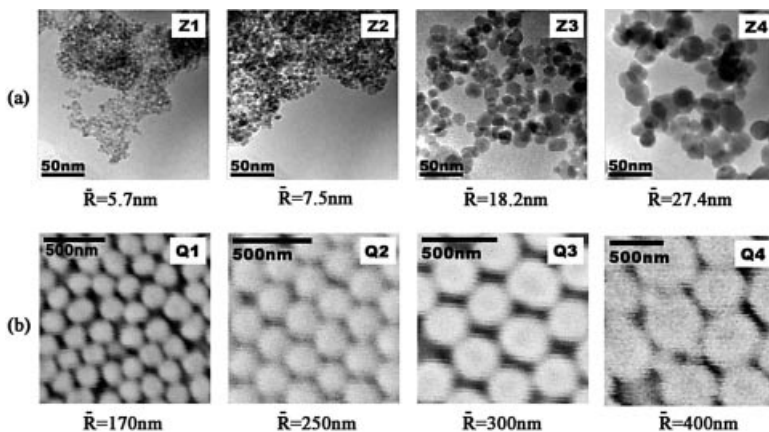


**Figure 11.5** HRTEM (a) and SEM (b) images of ZnO nanoparticles, with average size  $\bar{R}$  shown below each image [16]. Reprinted from S. L. Zhang, et al., Study of the size effect on the optical mode frequencies of ZnO nanoparticles with nearly uniform size, *Appl. Phys. Lett.*, 89, 243108 (2006)

**Table 11.2** Average diameter  $\bar{R}$  (nm) and diameter deviation  $\Delta R$  (nm) of nanoparticle ZnO samples [16]. Reprinted from S. L. Zhang, et al., Study of the size effect on the optical mode frequencies of ZnO nanoparticles with nearly uniform size, *Appl. Phys. Lett.*, 89, 243108 (2006)

Sample	Z1	Z2	Z3	Z4	Q1	Q2	Q3	Q4
$\bar{R}$ (nm)	5.7	7.5	111.2	27.4	170	250	300	400
$\Delta R$ (nm)	0.6	0.9	1.7	1.8	10	10	9	12

Through research, we found that the impurity and defect content of the samples also fit the requirements [17].

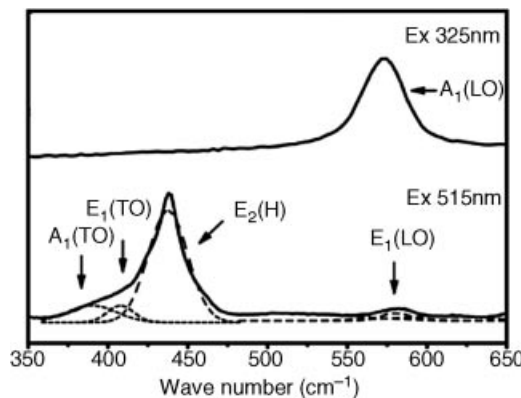
#### 11.1.3.1 Single Phonon (SP) Raman Spectra

Figure 11.6 shows Raman spectra of a typical ZnO NP sample (Z2) excited by 325 nm and 515 nm lasers. To make the measured frequency more precise, the two strongest Raman peak assigned to  $E_2(H)$  and  $A_1(LO)$  optical phonons were used for comparison.

Figures 11.7(a) and (b) show the Raman spectra of  $E_2(H)$  and  $A_1(LO)$  optical modes with sample sizes, respectively. The spectra in Figure 11.7 were fitted by using Lorentzian line shape, and the fitted values of Raman frequency with sample sizes are listed in Table 11.3. Figure 11.7(c) depicts the dependences of Raman frequency on sample sizes for  $E_2(H)$  and  $A_1(LO)$  modes and shows that their frequency does not change with size. Thus, no RSSE on optical phonons  $E_2(H)$  and  $A_1(LO)$  is confirmed.

#### 11.1.3.2 Multi-Phonon (MP) Raman spectra

The above subsection proves that there is no FSE on single phonon (SP) optical modes of ZnO NPs. In this subsection we will check that is there no FSE on the optical multi-phonon (MP) by the same group of ZnO NP samples used in the above subsection.



**Figure 11.6** First-order Raman spectra of 7.5 nm ZnO nanoparticles excited at 325 nm (upper) and 515 nm (lower) [16]. Reprinted from S. L. Zhang, et al., Study of the size effect on the optical mode frequencies of ZnO nanoparticles with nearly uniform size, *Appl. Phys. Lett.*, 89, 243108 (2006)

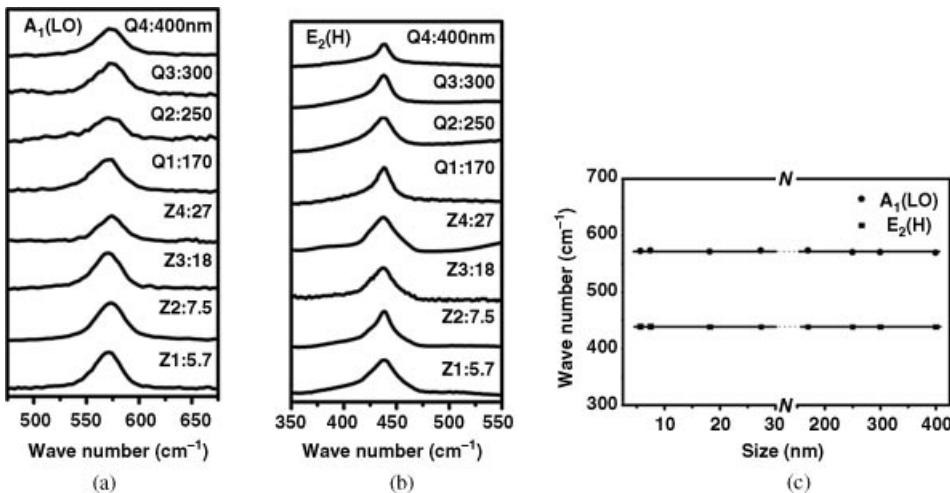


**Figure 11.7** Raman spectra of (a)  $E_2(H)$  and (b)  $A_1(\text{LO})$  modes labeled with the sample size, excited at 515 and 325 nm, respectively. (c) Raman frequency variation of the  $E_2(H)$  and  $A_1(\text{LO})$  modes with the sizes of ZnO nanoparticles [16]. Reprinted from S. L. Zhang, et al., Study of the size effect on the optical mode frequencies of ZnO nanoparticles with nearly uniform size, *Appl. Phys. Lett.*, 89, 243108 (2006)

The Raman spectra of  $A_{1\text{L}}$  and  $E_{1\text{L}}$  optical modes of samples Z1–Z4 and Q1–Q3 are shown in Figure 11.8(a), where the spectra with dashed lines are fitted by Lorentzian. Table 11.4 lists the observed frequencies  $\omega$ , observed average frequencies  $\omega_{\text{Ave}}$ , expected frequencies of  $k$  order MP  $\omega_{\text{Ept}} = k \times \omega_{\text{Ave}}$ , relative error of frequencies of SP,  $\omega_{\text{rr}} = (\omega - \omega_{\text{Ave}})/\omega_{\text{Ave}}$ , MP frequencies  $\omega_{\text{Err}} = (\omega - \omega_{\text{Ept}})/\omega_{\text{Ept}}$ , integral intensity  $I_k$ , and relative integral intensity  $I_{R,k}$  ( $= I_k/I_1$ ) of  $k$  order phonons. The dependence of observed MP frequency  $\omega$  on sample size  $d$  is shown in Figure 11.8(b). The horizontal lines

**Table 11.3** Raman frequencies  $\omega_{E2(H)}$  and  $\omega_{A1(LO)}$  of  $E_2(H)$  and  $A_1(\text{LO})$  modes of nanoparticle ZnO with particle sizes (average size  $\bar{R} \pm \text{deviation } \Delta R$ ). Reprinted from S. L. Zhang, et al., Study of the size effect on the optical mode frequencies of ZnO nanoparticles with nearly uniform size, *Appl. Phys. Lett.*, 89, 243108 (2006)

Sample	Size(nm)	$\omega_{E2(H)}$ ( $\text{cm}^{-1}$ )	$\omega_{A1(LO)}$ ( $\text{cm}^{-1}$ )
Z1	$5.7 \pm 0.6$	439	572
Z2	$7.5 \pm 0.9$	439	573
Z3	$111.2 \pm 1.7$	438	571
Z4	$27.4 \pm 1.8$	438	573
Q1	$170 \pm 10$	438	573
Q2	$250 \pm 10$	438	570
Q3	$300 \pm 9$	438	570
Q4	$400 \pm 12$	438	569

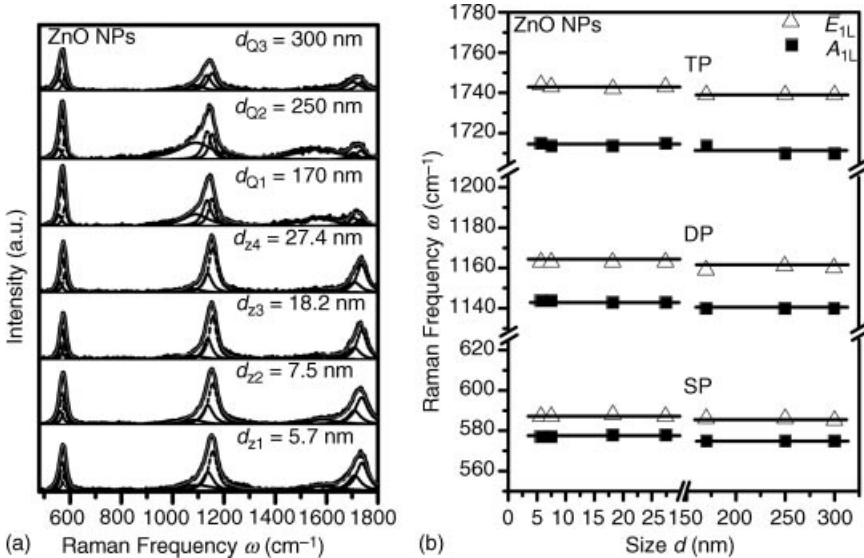


**Figure 11.8** (a) Observed (solid lines) and fitted (dashed lines) optical MP Raman spectra of ZnO NPs of nearly uniform size; (b) dependence of observed MP Raman frequency  $\omega$  on sample sizes  $d$  for  $A_{1L}$  and  $E_{1L}$  modes of ZnO NP samples; where SP, DP, and TP represent the single, double, and three phonons, respectively

in Figure 11.8(b) are drawn using  $\omega_{\text{Ave}}$ . In Table 11.4 we see that the relative error  $\omega_{\text{Err}}$  of  $A_{1L}$  and  $E_{1L}$  of SP and MP are all less than 1.1%, indicating the error is within the appropriate experimental accuracy. From Table 11.4 and Figure 11.8(b), we find that  $\omega_{\text{Ept}}$  and  $\omega_{\text{Ave}}$  of SP for  $A_{1L}$  and  $E_{1L}$  modes of sample groups Z and Q are different, which may be caused by different preparation methods of the two sample groups and thus we can neglect this difference in our discussion [16]. Table 11.4 and Figure 11.8(b) indicate that there is also no FSE on  $A_{1L}$  and  $E_{1L}$  modes in MP Raman scattering, as in the case of SP Raman scattering described in the above subsection.

#### 11.1.4 Reliability of No FSE on Phonons

The SP and MP Raman spectra of ZnO NPs with various sizes indicate that there is no FSE on the optical phonon modes in ZnO NP samples. This result is totally the opposite of the conventional conception that FSE has a basic effect on nanostructures; it is a very interesting academically and before starting further investigation, the phenomenon of no FSE on phonons should be questioned.

It is reasonable to question that no FSE on phonons may be due to there being no QCE on used samples. One of the solutions to the above question is to check that there is a QCE on the electronic structures of samples, that is, whether the QCE is absent totally. PL spectra of semiconductors can originate from free exciton (FX) or bound exciton. FX is the eigen excitation state of electron hole pairs with the lowest energy in low excitation density of intrinsic semiconductors, which is directly related to QCE. The binding energy of FX is

**Table 11.4** Observed frequencies  $\omega$  ( $\text{cm}^{-1}$ ), observed average frequencies  $\omega_{\text{Ave}}$  ( $\text{cm}^{-1}$ ), expected frequencies  $\omega_{\text{Ept}}$  ( $\text{cm}^{-1}$ ), and the relative error  $\omega_{\text{rr}} = (\omega - \omega_{\text{Ept}})/\omega_{\text{Ept}}$  (%) in  $k = 1, 2$ , and 3 order MP Raman spectra of  $A_{1L}$  and  $E_{1L}$  modes for samples Z1–Z4 and Q1–Q3

Mode		Z1	Z2	Z3	Z4	Q1	Q2	Q3
$A_{1L}$	$\omega$	577	577	578	578	575	575	575
	$\omega_{\text{Ave}}$			577.3			574.9	
	$\omega_{\text{rr}}$	0.0	-0.1	0.1	0.1	0.1	0.0	-0.1
$E_{1L}$	$\omega$	587	587	588	587	586	586	585
	$\omega_{\text{Ave}}$			587.1			585.9	
	$\omega_{\text{rr}}$	-0.1	0.0	0.1	0.0	0.0	0.1	-0.1
$2A_{1L}$	$\omega$	1144	1144	1143	1143	1140	1140	1140
	$\omega_{\text{Ave}}$			1143.5			1140.0	
	$\omega_{\text{Ept}}$			1154.7			1149.8	
	$\omega_{\text{Err}}$	-0.9	-0.9	-1.0	-1.0	-0.8	-0.8	-0.9
$2E_{1L}$	$\omega$	1163	1163	1163	1163	1159	1161	1160
	$\omega_{\text{Ave}}$			1162.8			1159.8	
	$\omega_{\text{Ept}}$			1174.2			1171.7	
	$\omega_{\text{Err}}$	-1.0	-1.0	-1.0	-1.0	-1.1	-1.0	-1.0
$3A_{1L}$	$\omega$	1715	1714	1714	1715	1714	1710	1710
	$\omega_{\text{Ave}}$			1714.5			1711.2	
	$\omega_{\text{Ept}}$			1732.0			1724.7	
	$\omega_{\text{Err}}$	-1.0	-1.0	-1.0	-1.0	-0.6	-0.8	-0.9
$3E_{1L}$	$\omega$	1744	1743	1742	1743	1739	1739	1739
	$\omega_{\text{Ave}}$			1742.9			1739.1	
	$\omega_{\text{Ept}}$			1761.3			1757.6	
	$\omega_{\text{Err}}$	-1.0	-1.1	-1.1	-1.1	-1.1	-1.0	-1.0

about 60 meV and larger than the thermodynamic energy at room temperature. Thus, optical transition of free electron can be used to test QCE, even at room temperature.

To guarantee the reliability of PL spectral measurements, first, the size of samples must be small enough, that is, close to the Bohr radius 0.9 nm of ZnO electrons. If the size of samples is much larger than the Bohr radius, the influence of QCE on band-gap cannot be reflected. Thus, three ZnO NP samples with smaller sizes used in previous Raman spectral measurement Z1, Z2, and Z4 were used in PL spectra measurements. Figure 11.9 shows the high resolution electron microscope of samples Z1, Z2, and Z4, where the insets are the selected-area electron diffraction patterns and indicate that all samples consist of structurally clean ZnO nanocrystals with wurtzite structure.

Second, PL and Raman experiments must be performed under the same conditions. For example, the samples used should be from the same group. The PL and Raman spectral measurements need to be performed simultaneously on the same Raman spectrometer excited by the same laser with the same geometry.

According to the above requirements, the PL spectra of sample Z1, as a representative sample, were obtained at temperatures from 10 to 300 K and are shown in Figure 11.10(a), where the inset is a typical fitting spectrum at 250 K. In the figure, the two PL bands, A and B, are present in the entire temperature range and show an obvious red-shift as the temperature

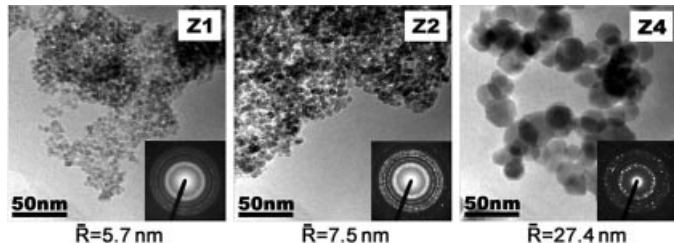


**Figure 11.9** HRTEM images of the ZnO NP samples of Z1, Z2, and Z4 [17]. Reprinted from Z. D. Fu, et al., Study on the quantum confinement effect on ultraviolet photoluminescence of crystalline ZnO nanoparticles with nearly uniform size, *Appl. Phys. Lett.*, 90, 263113 (2007)

increases. According to the expressed equation of exciton recombination energy at temperature  $T$ ,

$$E_X(T) = E(T) - 0.06 = E(0) - \frac{\alpha T^2}{T + \beta} - 0.06, \quad (11.1)$$

where  $E(T)$  is inter-band emission energy and follows the Varshni equation [18], and the calculated  $E_X(T)$  of bands A and B versus temperature are plotted by solid and dashed lines together with observed ones as squares and circles in Figure 11.10(c). The fitting of calculated results with experimental results is good, suggesting that the red-shift of band A with increasing temperature can be contributed to temperature-induced band-gap shrinkage [19]. Thus, it is probable that PL band A originate from the inter-band exciton transition.

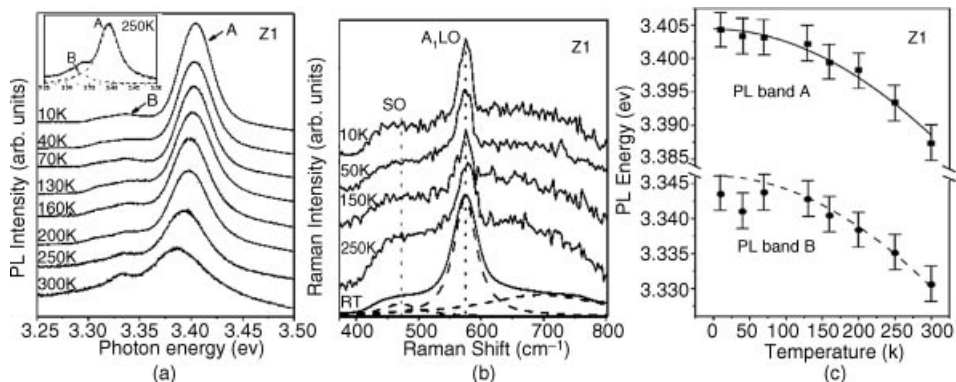


**Figure 11.10** PL (a) Raman and (b) spectra and observed and calculated energies of FX and FX-1SO bands; (c) for sample Z1 (5.7 nm) from 10 to 300 K (room temperature, RT) [17]. Reprinted from Z. D. Fu, et al., Study on the quantum confinement effect on ultraviolet photoluminescence of crystalline ZnO nanoparticles with nearly uniform size, *Appl. Phys. Lett.*, 90, 263113(2007)

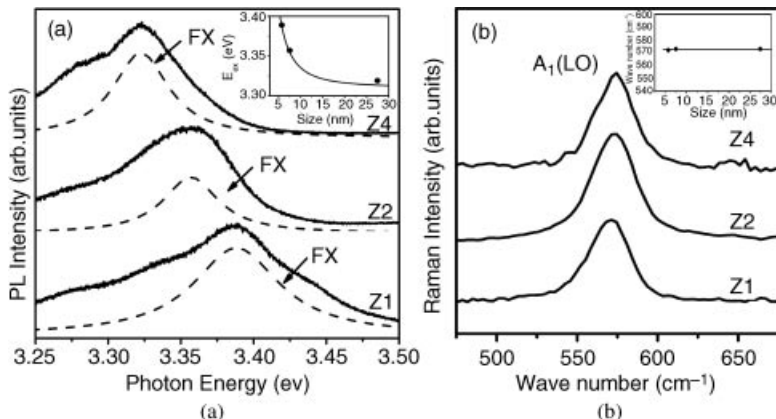


**Figure 11.11** PL (a) and Raman (b) spectra of ZnO NP samples (Z1, Z2, and Z4) at room temperature [17]. Reprinted from Z. D. Fu, et al., Study on the quantum confinement effect on ultraviolet photoluminescence of crystalline ZnO nanoparticles with nearly uniform size, *Appl. Phys. Lett.*, 90, 263113(2007)

Figure 11.10(b) shows observed Raman spectra, where the dashed line is the fitted spectrum. According to fitting results and Ref. [20], the intense peak at  $575\text{ cm}^{-1}$  and the shoulder peak at  $470\text{ cm}^{-1}$  are assigned to  $A_1(\text{LO})$  and the surface optical (SO) mode, respectively. As seen in Figure 11.10, neither the SO mode nor the  $A_1(\text{LO})$  mode changes with temperature. The obtained energy of the SO phonon is 58.3 meV, close to the energy difference between bands A and B in Figure 11.10. Thus, we attribute band B to FX recombination accompanied by the first-order SO phonon, denoted as FX-1SO.

Thus, we have enough reasons to use observed PL spectra of the FX shown in Figure 11.10 to test QCE on electrons in ZnO NPs. Figures 11.11(a) and (b) show observed room temperature PL and Raman spectra measured under the same conditions for different sizes of ZnO NP samples Z1, Z2, and Z4.

Based on the theory of QCE, the confined ground-state exciton energy ( $E_{\text{ex}}$ ) versus the average particle size  $\bar{R}$  can be expressed approximately by the following formula: [21]:

$$E_{\text{ex}} = E_g - \frac{13.6\mu}{m_e \varepsilon_r^2} + \frac{2\pi^2 \hbar^2}{(m_e^* + m_h^*) \bar{R}^2}$$

where  $E_g$  is the band-gap energy (3.37 eV) of bulk ZnO; the second term is the binding energy (60 meV); and  $\varepsilon_r$  is electricity constant and is 5.8. The third term describes the confinement of spherical quantum dots,  $m_e^*$  and  $m_h^*$ , which are the reduced masses of electrons and holes and are 0.32 and 0.34 times the mass of the electron,  $m_e$ , respectively. The calculated  $E_{\text{ex}}$  is listed in Table 11.5 and also curved in the inset of Figure 11.11(a) as the solid line. From the table and figure inset, we see that the theoretical calculation is in agreement with the experimental data. This confirms that the observed blue shift of FX emission energy with decreasing sample size originates from the QCE.

However, Raman spectra in Figure 11.11(b) show that there is definitely no finite size effect (FSE) on the optical phonon  $A_1(\text{LO})$  mode, although QCE on electronic structures

**Table 11.5** PL energy  $E_{\text{ex}}$  of free exciton emission peak obtained from experiments and theoretical calculations for ZnO NP samples Z1, Z2, and Z4 [17]. Reprinted from Z. D. Fu, et al., Study on the quantum confinement effect on ultraviolet photoluminescence of crystalline ZnO nanoparticles with nearly uniform size, *Appl. Phys. Lett.*, 90, 263113 (2007)

Sample		Z1	Z2	Z4
$E_{\text{ex}}$ (eV)	Experiment	3.388	3.355	3.313
	Theory	3.389	3.357	3.319

exists in the same series of samples. Based on the above results, it is confirmed that the electron and optical phonon structures do and do not possess QCE in polar nano-semiconductor ZnO, respectively. Thus, no FSE on optical phonons in polar nano-semiconductors is reliable and rather than that it dose not have any QCE in the measured samples.

### 11.1.5 Effect of Sample Sizes on Polarization Selection Rule

Section 10.2 mentioned that to date, the polarization Raman spectra in nanostructures can be investigated easily by experimental methods using only for a few samples, such as superlattices and carbon nanotubes. Especially, on the ultra-thin superlattices or multi-quantum wells (MQWs) with the well and barrier layers only containing a few atoms monolayer, the effect of sample sizes on the polarization selection rule should be displayed easily.

The effect of sample sizes on the polarization selection rule has been observed in the ZnSe-based short-period-superlattice multiple-quantum wells (SPSL-MQWs) [19]. The sample of SPSL-MQWs is an SPSL-MQW  $[(\text{CdSe})_1(\text{ZnSe})_3]_{15}/(\text{ZnSe})_{130}$ , in which the wells consist of a short-period superlattice  $(\text{CdSe})_1(\text{ZnSe})_3$  (where the subscripts are the number of atom monolayers). Ref. [19] reported that the selection rules of the ZnSe LO<sub>1</sub> modes in quantum wells and ZnSe LO modes in barrier layers of superlattices are only observed in the polarization configuration, which is contrary to the conventional polarization selection rule [20]. This has been attributed to the special electron behavior in such short-period superlattice [19].

In addition, a violation of the normal Raman selection rule in polarized Raman spectra of interface (IF) phonon modes of the ultra-thin  $(\text{GaAs})_4/(\text{AlAs})_2$  superlattice (the subscripts are the number of atomic monolayers) was observed, as shown in Figure 11.12. Based on theoretical calculation, the four observed peaks at 279, 287, 378, and  $391 \text{ cm}^{-1}$  were identified to the low-frequency GaAs-like, the high frequency GaAs-like, the low-frequency AlAs-like, and the high-frequency AlAs-like IF modes, respectively, as listed in Table 11.6. In Figure 11.12, a striking polarization selection rule of interface modes was observed that all four IF modes can be observed in both  $(x,x)$  and  $(x,y)$  geometries, which is contrary to conventional theory. The conventional theory [20] predicts that in the case of a GaAs (AlAs) layer thicker than an AlAs (GaAs) layer, the parity of the high-frequency GaAs (AlAs)-like and low-frequency AlAs (GaAs)-like IF modes are odd (even). Furthermore, only Raman scattering due to the IF mode with even (odd) parity should be observed in the parallel (perpendicular) polarization configuration. All four IF modes together in either polarization in the backscattering geometry should not be observed. Yet, all four modes have been observed in both geometries, as listed in Table 11.6.

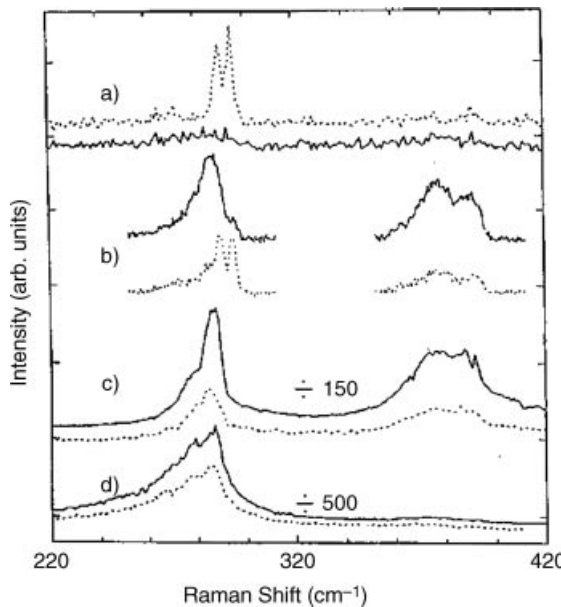


**Figure 11.12** Raman spectra of  $(\text{GaAs})_4/(\text{AlAs})_2$  excited by lasers with different energies: (a) 2.136 eV, (b) 2.036 eV, (c) 2.011 eV, (d) 1.937 eV; where subscripts are the number of atom monolayers [21]. Reprinted from S. L. Zhang, et al., Abnormal selection rules of interface modes in ultrathin GaAs/AlAs superlattice, *J. Appl. Phys.* 88, 6403(2000)

This abnormal phenomenon may be attributed to the special electronic structure of the ultra-thin  $(\text{GaAs})_4/(\text{AlAs})_2$  superlattice. In deriving the Raman selection rules of LO and IF modes of SLs, an assumption is made that the electron wave function is essentially confined and has a definite parity [20]. This assumption cannot be satisfied for ultra-thin SLs, as in the sample used here. Thus, the derived selection rules do not apply to this sample. To confirm this analysis, the ground state wave function of the conduction electron of the  $(\text{GaAs})_4/(\text{AlAs})_2$  superlattice samples was calculated [21] by

**Table 11.6** The calculated and observed frequencies and the selection rules of IF modes using the dielectric continuous model for  $(\text{GaAs})_4/(\text{AlAs})_2$ . Reprinted from S. L. Zhang, et al., Abnormal selection rules of interface modes in ultrathin GaAs/AlAs superlattice, *J. Appl. Phys.* 88, 6403 (2000)

Phonon Modes	GaAs-like mode		AlAs-like mode		
	Low frequency	High frequency	Low frequency	High frequency	
Frequency ( $\text{cm}^{-1}$ )	Theo. Obs.	277 279	285 287	375 378	389 391
Selection rule	Theo. [20] Obs.	XY XY, XX	XX XY, XX	XX XY, XX	XY XY, XX

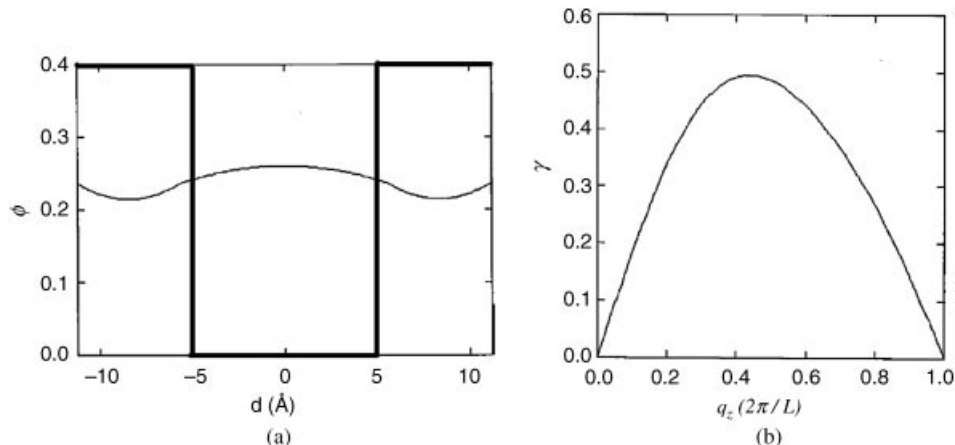


**Figure 11.13** The calculated ground state electron wave function of the conduction band (a) and the mixing ratio,  $\gamma$ , of the odd parity component to the even parity component of the ground electron wave function, due to sub-band dispersion (b) for the SL sample  $(\text{GaAs})_4/(\text{AsAl})_2$  [21]. Reprinted from S. L. Zhang, et al., Abnormal selection rules of interface modes in ultrathin GaAs/AlAs superlattice, *J. Appl. Phys.* 88, 6403(2000)

using the following dispersion equation of the conduction band electrons of SLs [22]:

$$\cos(k_z d) = \cos(\alpha d_1) \cos(\delta d_2) + \frac{1}{2} \left( \frac{\alpha m_1}{\delta m_2} - \frac{\delta m_2}{\alpha m_1} \right) \sinh(\alpha d_1) \sinh(\delta d_2) \quad (11.2)$$

The result is shown in Figure 11.13(a). The average probability of the electron in the barriers is about 0.7862 times that in the wells. Thus, the electron wave function of the sample is an extended one and is not clearly confined. Furthermore, the extended electron wave functions will lead to the dispersion of the electron. As a result, except when the electrons are at the edge of the sub-bands, the electrons will lose their definite parity [20]. To describe the extent of parity mixing in electrons, a parameter  $\gamma$  was defined as the ratio of the odd component to the even component for the ground state electron wave function. The calculated results are shown in Figure 11.13(b). We can see that the curve becomes very steep away from the edges. Thus, parity mixing is considerable as long as the electrons deviate slightly from the sub-band edge. Since both the original odd modes and the original even modes can couple with the electrons through Fröhlich interaction, and also through the deformation potential interaction, both even and odd modes should be observed in both  $(x,x)$  and  $(x,y)$  polarized configurations.

The above calculated results indicate that the electron wave function extends deeply into the AlAs barriers, instead of being confined in the GaAs wells. This also results in a relaxation of the restriction in the parity of the electron wave function. Both these factors contradict the basic assumptions of conventional theories of a confined electron wave function with a definite parity. As a result, the confined object returns to an expanded one, as in bulk materials and the superlattices, selection rules derived from conventional theories do not apply to ultra-thin SLs. Therefore, all four IF modes of the ultra-thin  $(\text{GaAs})_4/(\text{AsAl})_2$

superlattice in both polarization configurations should be expected. Furthermore, the result also indicates that conventional theory for bulk (thicker) systems needs to be modified in ultra-thin systems of practical scale and that the practical size scale in nanostructures must consider that the difference in nanoscale will change the properties of nanostructures essentially.

## 11.2 Effects of Sample Shapes on Raman Spectra in Nanostructures

The so-called shape discussed in the sample shape effects is that its geometry pattern is asymmetrical, of which the simplest samples are transverse and vertical asymmetrical objects. In this section, we will mainly take the superlattices with transverse and vertical asymmetry as an example, to discuss the effect of sample shape on Raman spectra in nanostructures.

### 11.2.1 Geometrical Parameters and Potential Shapes of Superlattices (SLs)

The effect of shape expressed by geometrical parameters on Raman spectra in nanostructures is achieved practically through the physical factors induced by geometrical parameters of samples, in which the potential is one of the key factors.

As shown in the upper part of Figure 11.14(a), an ideal SL is a periodic structure of two different material plates of several nanometers, of which the interface between the plates is

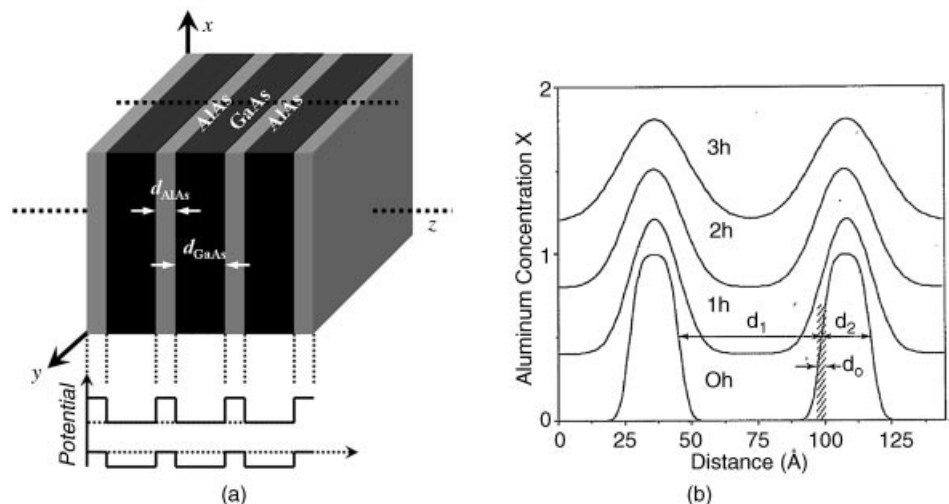


**Figure 11.14** (a) Structure pattern and corresponding potential shape of superlattices; (b) compositions profile of superlattice from fit of X-ray data for four annealing times. A value of 1.0 corresponds to 100% AlAs. Successive curves are shifted upwards by 0.40 for clarity. The parameters  $d_1$ ,  $d_2$ , and  $d_0$  are indicated for the unannealed profile [23]. Reprinted from D. Levi, et al., Raman study of the effects of annealing on folded LA and confined LO phonons in GaAs-AlAs superlattices, Phys. Rev., B, 36, 8032 (1987).

**Table 11.7** Superlattice structural parameters versus annealing time.  $D$  is the superlattice period;  $d_1$  is the GaAs layer thickness;  $d_2$  is the AlAs layer thickness; and  $d_0$  is the interface width.  $D$  is derived directly from X-ray data, while  $d_1$ ,  $d_2$ , and  $d_0$  are from a fit of an error-function profile to the profile generated by X-ray Fourier coefficients. Variation of the period  $D$  is due to inhomogeneities across the superlattice layers. Reprinted from D. Levi, et al., Raman study of the effects of annealing on folded LA and confined LO phonons in GaAs-AlAs superlattices, *Phys. Rev. B*, 36, 8032 (1987)

	d	$d_1$	$d_{2r}$	$d_0$
0	72.0	54.4	17.7	4.0
30	70.9	54.5	16.3	7.6
60	70.9	54.2	16.7	9.2
90	72.0	53.0	111.9	11.0
120	71.8	54.8	17.0	11.7
150	73.5	55.0	111.5	14.0
180	72.3	55.0	17.3	14.9

sharply defined. The key geometrical parameters describing SLs are the thickness of plates  $d_1$ ,  $d_2$ , and period  $d = d_1 + d_2$ . Correspondingly, the ideal shapes of potential wells and potential barriers are both square, as shown in the lower part of Figure 11.14(a).

The effect of geometrical parameters  $d_1$  and  $d_2$  on Raman spectral features was described in Section 9.1. This subsection introduces the effect of potential well/barrier shape change on Raman spectral features, which is related and equivalent to the change of sample shape.

The change of potential shape can be achieved by using annealing of samples. The annealing will result in the interchange of different atoms (ions) on two plates passing the interface between plates, which induce the deviation of the annealing SL structure from ideal structure and shape. Figure 11.14(b) shows the effect of annealing on potential shape induced by deviation in shape from ideal plate for a GaAs/AlAs SL [23].

In an ideal GaAs/AlAs superlattice, atoms Ga and Al only exist in the GaAs and AlAs layers, respectively. The annealing changes the Al concentration distribution with annealing time. From X-ray diffraction experiments and analytical calculations, as shown in Figure 11.13(b), it is seen that the potential structural shapes change from a near square shape to a conical shape. The structure parameters with annealing time are listed in Table 11.7, which expresses the change of SL geometrical parameter.

### 11.2.2 Effect of Sample Shape on Folded Longitudinal Acoustic (LA) Phonon in SLs

The Raman spectra of folded longitudinal acoustic (LA) phonons with annealing time are shown in Figure 11.15. The figure clearly shows that as the annealing time increases, that is, the deviation of quantum well shape from a nearly square potential well, the frequency of folded acoustic phonon and the frequency difference of doublet do not change, which agrees with the expectation of Equation (8.25). The equation indicates that the frequency of folded acoustic phonon and the frequency difference of doublets are related with only the period of superlattice  $d = d_1 + d_2$ . Therefore, when annealing does not change the

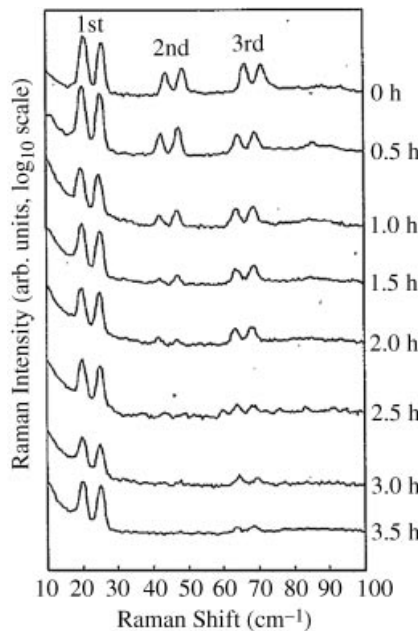


**Figure 11.15** Raman scattering spectra of folded acoustic phonons plotted on logarithmic scale for each annealing increment. Spectra were collected in pseudo-backscattering geometry at  $z(x,x)z$  using 500 mW from the 5145-Å line of an argon-ion laser. Samples were at room temperature [23]. Reprinted from D. Levi, et al., Raman study of the effects of annealing on folded LA and confined LO phonons in GaAs-AlAs superlattices, Phys. Rev., B, 36, 8032 (1987)

period of superlattice  $d = d_1 + d_2$ , the above experimental results should be expected, which also produces the reliable Equation (8.25) and experimental results at the same time.

However, Figure 11.15 also shows that the intensity and number of Raman peaks decrease with the deviation of quantum well shape from a near square potential well. This confirms that the intensity and number of folded acoustic phonon peaks can be used to monitor growth quality of superlattices. For example, the work in Ref. [24] has used this to verify that annealing can improve the interface quality of lattice mismatch superlattices.

### 11.2.3 Effect of Sample Shape on Optical Phonons in SLs

Figure 11.16(a) shows Raman spectra of optical phonon in a GaAs/AlAs superlattice with annealing time.

From the figure, first it can be seen that Raman frequencies of longitudinal optical (LO) modes of all confined orders  $m$  decrease with increasing annealing time, that is, with the deviation of quantum well shape away from an ideal one. It has been predicted theoretically that the dependents of optical phonon dispersion relations on its confined order  $m$  are parabolic and straight for the quantum wells with square and parabolic shapes, respectively.

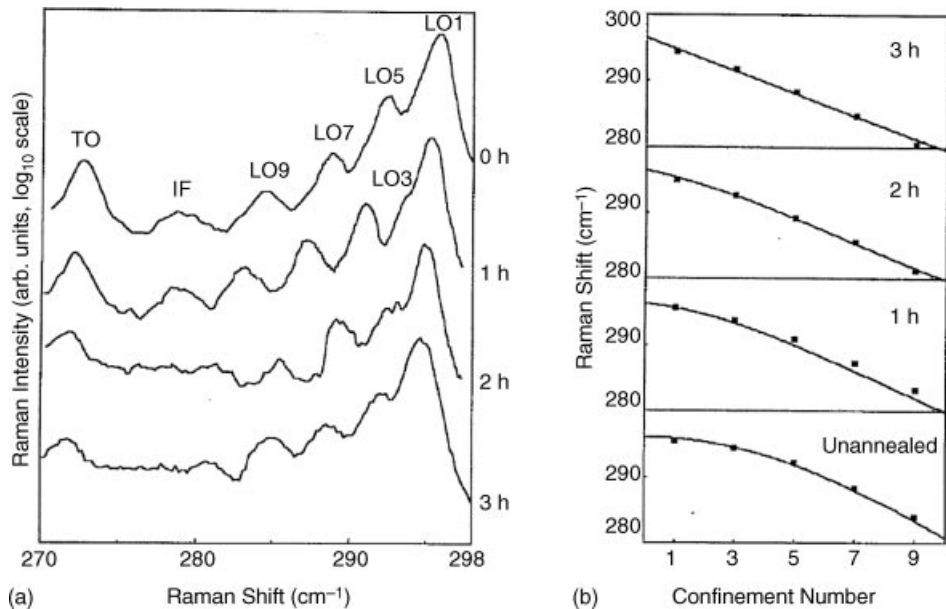


**Figure 11.16** (a) Logarithmic plot of Raman spectra of optical phonons showing for four annealing times. Confinement order is indicated on plot. IF and TO indicate interface and transverse optical phonons, respectively. Data were collected in pseudo-backscattering geometry at  $z(x,y)z$  using the 5145 Å line of an argon-ion laser. The sample temperature was 27 K, as measured by the ratio of Stokes to anti-Stokes intensities. (b) Experiment versus theory for confined LO phonon dispersion. Points are experimental values from Raman scattering, while lines are an interpolation between corresponding points from the effective-mass calculation. Dispersion changes from the parabolic curve of the square well for the unannealed sample to the linear curve characteristic of a parabolic well for the 3-h annealed sample [23]. Reprinted from D. Levi, et al., Raman study of the effects of annealing on folded LA and confined LO phonons in GaAs-AlAs superlattices, *Phys. Rev. B*, 36, 8032 (1987).

Figure 11.16(b) shows the observed dependents of Raman frequencies with different confined orders  $m$  on annealing times. Figure 11.15(b) shows that the dependency of Raman frequencies on confined orders  $m$  changing at different annealing times are from parabolic to straight with the increasing annealing times, indicating the shape of potential wells is from square-like to parabolic-like and reach to the parabolic potential well totally at annealing for 3 hours.

Second, in Figure 11.16(a), the transverse optical (TA) phonon can be clearly seen. Its peak positions shift downward with increasing annealing time. This behavior is similar to that of LO phonon and indicates the TA phonon is a confined mode.

#### 11.2.4 Effect of Sample Shape on Interface Phonon in SLs

The interface mode shown in Figure 11.16(a) exhibits the same frequency feature to that of an LA mode: the frequencies do not change with annealing time. The annealing

does not induce the change of layer thickness and the period of SLs and thus the geometrical positions of interfaces do not change. Based on the above geometrical features similar to the case of LA modes, no frequency change with annealing time should be expected.

### 11.3 Effects of Sample Component and Micro-structure on Raman Spectra in Nanostructures

Unlike the discussions on sample size and shape in Sections 11.1 and 11.2, the effects of compositions (including impurities) and microstructures (including defects) on Raman spectra are not unique in nanostructures and have been broadly investigated in macro-objects. In addition, the composition and microstructure of samples can be changed by external factors, besides the preparation of samples. Therefore the discussion in this section will cover the effects of external condition change on Raman spectra.

#### 11.3.1 Effect of Compositions on Raman Spectra in Nanostructures

The sample composition discussed here mainly relates to that of alloy nanostructures.

Tu and Persans studied how the change of alloy components in II-VI semiconductor nanocrystal would affect Raman spectra [25]. Figure 11.17(A) shows Raman spectra of  $\text{CdS}_x\text{Se}_{1-x}$  of size 10 nm enclosed in glass for three different components  $x$ . In the spectra,

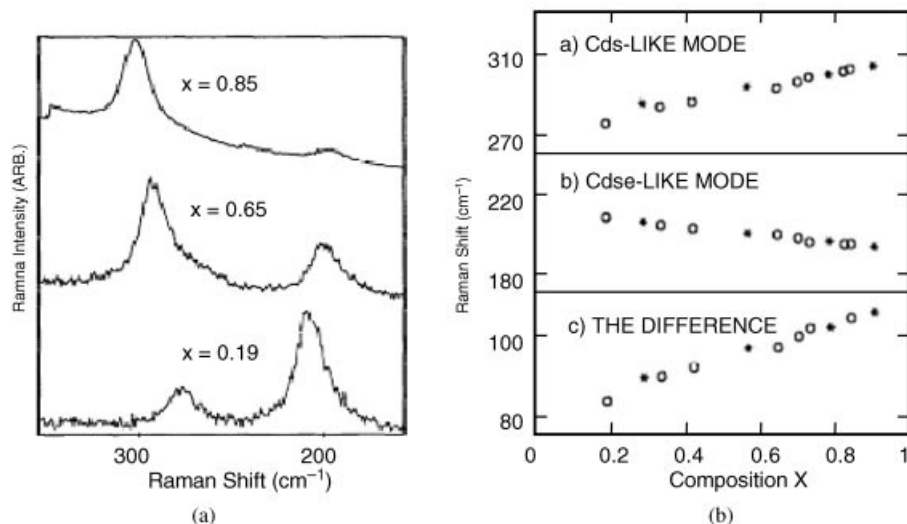


**Figure 11.17** Raman spectra with component  $x$  (a) and dependence of  $\text{CdS}$ -like and  $\text{CdSe}$ -like mode frequencies on component  $x$  (b) for  $\text{CdS}_x\text{Se}_{1-x}$  nanocrystals [25]. Reprinted from A. Tu and P. D. Persans, Raman scattering as a compositional probe of II-VI ternary semiconductor nanocrystals, *Appl. Phys. Lett.*, 58, 1506 (1991) with permission of the American Institute of Physics

the peaks at 200 and 300  $\text{cm}^{-1}$  are identified as the vibration modes of CdSe and CdS, respectively. Figure 11.17(a) shows that Raman frequencies of the double modes change with  $x$ . The panels (a), (b,) and (c) in Figure 11.17(B) show the dependences of Raman frequencies and their frequency difference on component  $x$  for CdS-like and CdSe-like modes, in which data with label “o” represent the data of corresponding bulk materials. The results shown in Figure 11.17(B) indicate that the influence regularity of component  $x$  on Raman frequency of nanocrystals are similar to that of bulk materials.

### 11.3.2 Effect of Impurities on Raman Spectra in Nanostructures

Nanomaterials usually contain various impurities and structural defects produced in the manufacturing process. In addition, the same type of material will include different impurities and structural defects, due to different preparation methods. For instance, the types and contents of impurities in carbon nanotubes produced by the catalytic and electric arc methods are different [26]. The line width and line shape of Raman peaks display the sample qualities. Wide and asymmetric Raman peaks generally reflect the contents of impurities, defects, and disorder degrees in samples. In this subsection, we will take carbon nanotube (CNT) as an example, to discuss the influence of impurities and defects on Raman spectra.

Raman spectra of carbon materials containing disorder factors of impurities and structural defects and so on must appear as a Raman peak near 1360  $\text{cm}^{-1}$ , which is called the D peak. In Raman scattering, the disorder makes the selection rule of phonon wave vector,  $\mathbf{q} = 0$ , fail and so the scattering of phonons with  $\mathbf{q} \neq 0$  becomes possible, which is the origin of the D peak. The D peak is thought to be the scattering from the phonons at M and K points of the Brillouin zone boundary. In addition, it has already been pointed out in Section 9.3.3 that in carbon materials with graphite and CNT structures, the G mode at 1550  $\text{cm}^{-1}$  is a characteristic peak that represents the order degree of crystals. Therefore, the intensity ratio of G mode to D mode can be used to judge the order degree of carbon samples. This subject was introduced in Section 9.3.3.

### 11.3.3 Effect of Micro-structure on Raman Spectra in Nanostructures

A material micro-structure (including defects) is usually formed in the preparation process; however, the change of material structures and structural defects also can be implemented in terms of the changes in the external environment or artificial method after preparation. There are many methods to change the external environment. To exert high pressure on samples is a widely used method to change the micro-structure of the material. The change of sample temperature can alter the properties and micro-structures of materials and affect Raman spectral features. The annealing technology is one method to reduce structural defects, which was introduced in Section 10.3.1.

#### 11.3.3.1 High Pressure Raman Spectroscopy [27]

The exerting of low pressure on samples will usually change the values of material parameters such as lattice constant, bond angle, and so on, but cannot change the structure of crystals, while the action of high pressure on samples will make the material structure

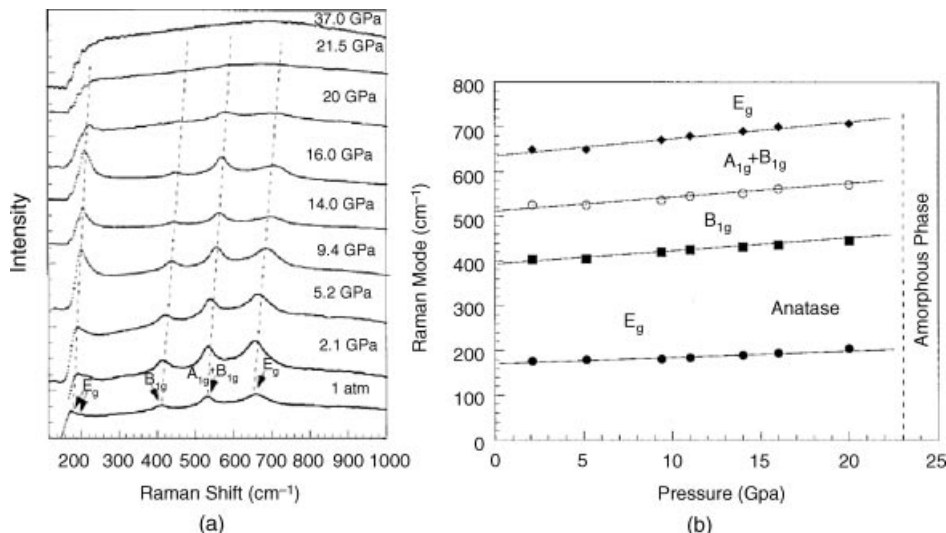


**Figure 11.18** High pressure Raman spectra (a) and pressure dependence of the Raman peak frequencies up to 24 GPa (b) for  $\text{TiO}_2$  nano-anatase crystal at room temperature [28]. Reprinted from Z. Wang and S. K. Saxena, Raman spectroscopic study on pressure-induced amorphization in nanocrystalline anatase ( $\text{TiO}_2$ ), *Solid State Commun.*, 118, 75–78 (2001) with permission of Elsevier

change from one crystal phase to another crystal phase. Of course, in the case of the above two external factors, the corresponding change of Raman spectra features will be different.

- High pressure Raman spectra of nanocrystalline anatase ( $\text{TiO}_2$ ) [28]

The high pressure Raman spectra of nanocrystalline anatase up to 37 GPa are shown in Figure 11.18(a). A significant spectral change occurs at the pressure of 24 GPa. As shown in Figure 11.18(b), the four strong Raman peaks, assigned to two  $E_g$  modes, one  $B_{1g}$  mode, and one  $A_{1g} + B_{1g}$  duplicated mode, shift to higher frequencies under compression. The three high wave-number modes have a similar Raman shift slope of  $2.7 \text{ cm}^{-1}/\text{GPa}$ , similar to those observed in bulk materials [29]. One low wave number mode ( $E_g$ ) shows a lower slope of  $1.5 \text{ cm}^{-1}/\text{GPa}$ , much lower than that in bulk materials [30]. With increasing pressure to about 24 GPa, all Raman modes disappear. Instead, a halo starts to form and remains up to the investigated pressure of 37 GPa (Figure 11.18(a)). The above results mean that the nano-anatase phase remains stable up to pressures as high as  $\sim 24$  GPa and a pressure induced amorphization occurs at pressures of about 24 GPa, while a macrocrystalline solid transforms to the  $\alpha\text{-PbO}_2$  structure at 2.6–4.5 GPa. This shows that an increased surface energy may stabilize the nano-anatase, suppressing the appearance of the anatase-to- $\alpha\text{-PbO}_2$  phase transformation and then lead to the amorphization of nano-anatase under strong compression.

- High pressure Raman spectra of InP/CdS nuclear/shell structure nanoparticle [30]

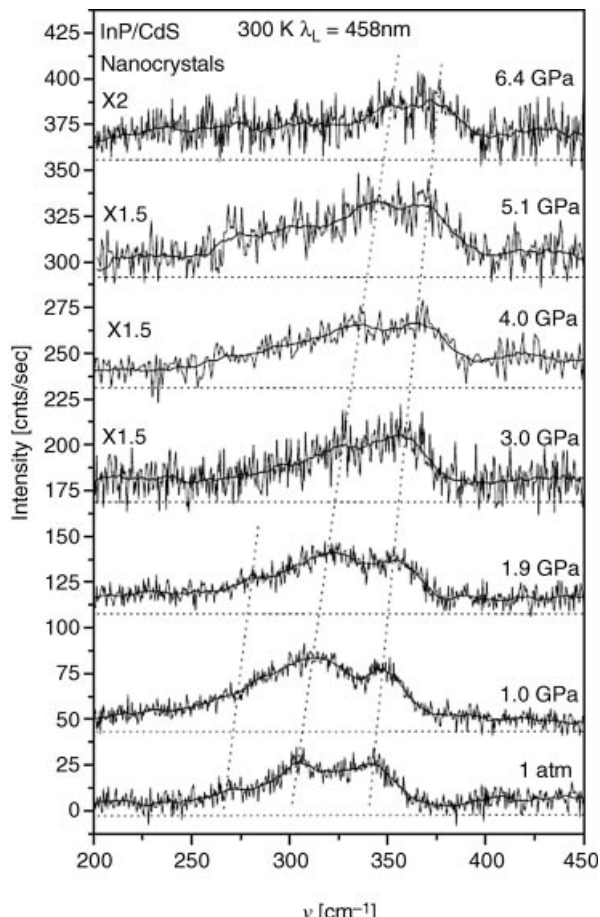


**Figure 11.19** Pressure-Raman spectra of InP/CdS nanoparticles at 300 K. Dashed lines show approximate shift of three main spectral features. Solid curves computed by numerical smoothing [30]. Reprinted from B. A. Weinstein, Raman spectroscopy under pressure in semiconductor nanoparticle, *Phys. Stat. Sol. (b)*, 244, 368–379 (2007) with permission of John Wiley and Sons

Similar to a superlattice consisting of a bedded structure of two different materials, nanoparticles could consist of a nuclear and shell structure in the two different materials. For example, an InP/CdS nanoparticle is made of InP, as nuclear, and CdS, as shell. Figure 11.19 is the pressure Raman spectra of an InP/CdS shell nanoparticle, which clearly shows the change situation of Raman peaks with pressure, yet without change of spectra structure. This indicates that there is no phase change before the pressure exceeds 6.4 GPa.

- High pressure Raman spectra of single-walled carbon nanotubes(SWNT) [31]

Figure 11.20(a) shows a high pressure Raman spectra of SWNTs. Figure 11.20(b) shows the pressure dependence of the three deconvolved Lorentzian peaks of RB modes. The above results show interesting behaviors in both the low frequency RBM and high frequency

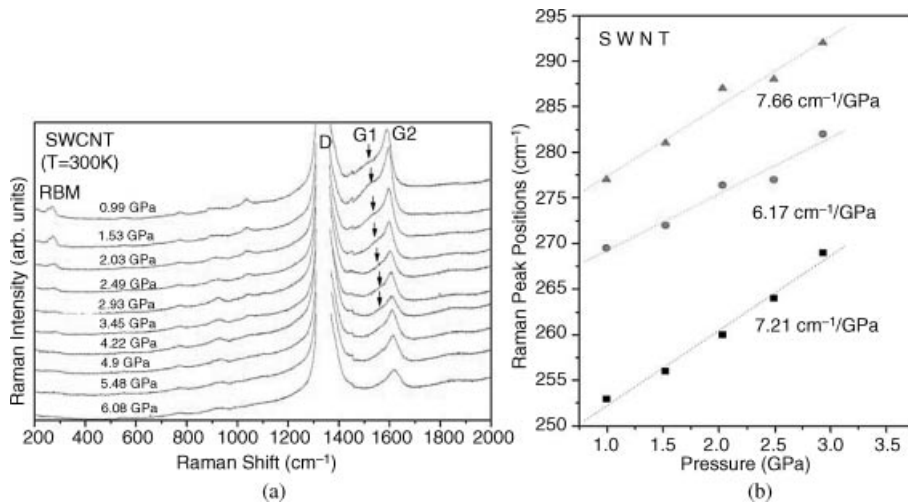


**Figure 11.20** High pressure Raman spectra at room temperature of SWNT bundles excited by the 514.5 nm of an Ar ion laser. SWNT Raman spectra (a) and graph of mode frequency's variation with pressure (b). The pressure dependence of the three deconvolved Lorentzian peaks [31]. Reprinted from H. Choi, P. Y. Yu, P. Tangney and S. G. Louie, Vibrational properties of single walled carbon nanotubes under pressure from Raman scattering experiments and molecular dynamics simulations, *Phys. Stat. Sol. (b)*, 244, 121–126 (2007) with permission of John Wiley and Sons

stretching modes G1 and G2. In particular, a stretching mode is found to have unusual pressure dependence, in that its frequency and width both change suddenly at  $\sim 3 \text{ GPa}$ . This result is understood in terms of the theoretically predicted softening of a low frequency “squashing mode” under pressure.

The above indicates that high-pressure Raman experiments and associated studies of semiconductor nanoparticles have advanced the understanding of ways in which the stability, localization, and vibration properties of these systems differ from bulk crystals.

### 11.3.3.2 High Temperature Raman Spectroscopy

There are several ways to raise sample temperature, such as traditional heating and laser irradiation. Raman spectroscopy related to the change of sample temperature by these two methods has been discussed in Section 10.3.

## References

- [1] Colvard, C., Gant, T.A., Klein, M.V. *et al.* (1985) *Phys. Rev. B*, **31**, 2080–2091.
- [2] Merlin, R., Colvard, C., Klein, M.V. *et al.* (1980) *Appl. Phys. Lett.*, **36**, 43–45.
- [3] Rao, A.M., Richter, E., Bandow, S. *et al.* (1997) *Science*, **275**, 187–191.
- [4] Zhang, S.L., Ding, W., Yan, Y. *et al.* (2002) *Appl. Phys. Lett.*, **81**, 4446–4448.
- [5] Yan, Y., Qu, T., Wang, J.C. *et al.* (2004) *Chin. J. Light Scattering*, **16**, 131–135.
- [6] Ehbrecht, M., Kohn, B., Huisken, F. *et al.* (1997) *Phys. Rev. B*, **56**, 6958–6964.

- [7] Xia, H., He, Y.L., Wang, L.C. *et al.* (1995) *J. Appl. Phys.*, **78**, 6705–6708.
- [8] Bottani, C.E., Mantini, C., Milani, P. *et al.* (1996) *Appl. Phys. Lett.*, **69**, 2409–2411.
- [9] Sun, Z., Shi, J.R., Tay, B.K., and Lau, S.P. (2000) *Diam. Relat. Mater.*, **9**, 1979–1983.
- [10] Duesberg, G.S., Loa, I., Burghard, M. *et al.* (2000) *Phys. Rev. Lett.*, **85**, 5436–5439.
- [11] Faraci, G., Gibilisco, S., Russo, P. *et al.* (2006) *Phys. Rev. B*, **73**, 033307.
- [12] Richter, H., Wang, Z.P., and Ley, L. (1981) *Solid State Commun.*, **39**, 625.
- [13] Faraci, G., Gibilisco, S., Pennisi, A.R., and Faraci, C. (2011) *J. Appl. Phys.*, **109**, 074311.
- [14] La Rosa, S. (2005) *Eur. Phys. J. B*, **46**, 457–461.
- [15] Sirenko, A.A., Fox, J.R., Akimov, I.A. *et al.* (2000) *Solid State Commun.*, **113**, 553–558.
- [16] Zhang, S.L., Zhang, Y., Fu, Z. *et al.* (2006) *Appl. Phys. Lett.*, **89**, 243108.
- [17] Fu, Z.D., Cui, Y.S., Zhang, S.Y. *et al.* (2007) *Appl. Phys. Lett.*, **90**, 263113.
- [18] Varshni, Y.P. (1967) *Physica (Amsterdam)*, **34**, 149.
- [19] Zhang, S.L., Hou, Y.T., Ho, K.S. *et al.* (1994) *Phys. Lett. A*, **186**, 433–437.
- [20] Huang, K., Zhu, B.F., and Tang, H. (1990) *Phys. Rev. B*, **41**, 5825–5842.
- [21] Zhang, S.L., Zhang, J., Yang, C.L. *et al.* (2000) *J. Appl. Phys.*, **88**, 6403.
- [22] Pan, S.H., Feng, S.M., and Yang, G.Z. (1990) *Acta Phys. Sin.*, **39**, 1446.
- [23] Levi, D., Zhang, S.L., Klein, M.V. *et al.* (1987) *Phys. Rev. B*, **36**, 8032.
- [24] Choi, C., Otsuka, N., Munns, G. *et al.* (1987) *Appl. Phys. Lett.*, **50**, 992.
- [25] Tu, A. and Persans, P.D. (1991) *Appl. Phys. Lett.*, **58**, 1506.
- [26] Tan, P., Zhang, S.L., Yue, K.T. *et al.* (1997) *J. Raman Spectroscopy*, **28**, 369–372.
- [27] Weinstein, B.A. (2007) *Phys. Stat. Sol. (b)*, **244**, 368–379.
- [28] Wang, Z. and Saxena, S.K. (2001) *Solid State Commun.*, **118**, 75–78.
- [29] Ohsaka, T., Yamaoka, S., and Shimomura, O. (1979) *Solid State Commun.*, **30**, 345.
- [30] Weinstein, B.A. (2007) *Phys. Stat. Sol. (b)*, **244**, 368–379.
- [31] Choi, I.H., Yu, P.Y., Tangney, P., and Louie, S.G. (2007) *Phys. Stat. Sol. (b)*, **244**, 121–126.

# 12

## Electron-Phonon Interactions in Raman Spectroscopy of Nanostructures

Section 7.5 described the basic requirements to induce Raman scattering. One requirement is that the energies, wave vectors, and polarizations between phonons and photons (light) must match each other. The frequencies of phonons and visible photons are  $\sim 10^{13}$  and  $\sim 10^{15}$  Hz, respectively, which results in the phonon and photon not being able to couple directly due to the energy difference of  $\sim 10^2$  Hz. Thus phonon Raman scattering has to have the help with an “intermediary,” which is usually the electrons in scattered objects. As a result, the interactions in phonon Raman scattering processes have to involve two types: photon-electron interaction and electro-phonon interaction. The electron-phonon interaction in solids has been described in Section 7.1.5. In this chapter, we discuss the electron-phonon interactions in nanostructures especially and their role in Raman spectroscopy of nanostructures.

### 12.1 Abnormal Raman Spectral Features in Nanostructures

In previous chapters, it was observed that there is no frequency shift with sample sizes in single phonon (SP) and multi phonon (MP) optical modes of the polar nano-semiconductors with quantum confinement effect (QCE) on electrons, although Raman frequency shift with sample sizes occurs in Raman spectra of optical phonons of non-polar nano-semiconductors and in acoustic phonons of both polar and non-polar nano-semiconductors.

Except for the manifestation in frequency shift with sample sizes mentioned above, other Raman spectral features also display different behavior with sample sizes, if we pay close attention to the Raman spectra mentioned in previous chapters. Figure 12.1 compares two Raman spectra from Chapter 11 and it shows clearly that the line shape

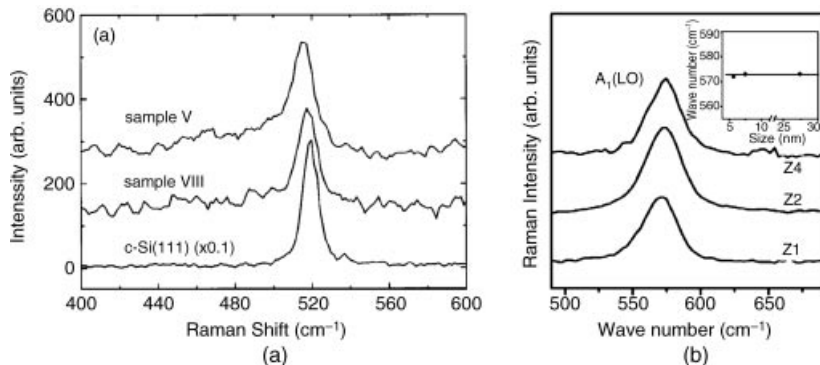


**Figure 12.1** Raman spectra of Si cluster samples V (4.63 nm) and VIII (7.03 nm) deposited on LiF and c-Si (111) sample [1] (a) Reprinted from M. Ehbrecht, et al Photoluminescence and resonant Raman spectra of silicon films produced by size-selected cluster beam deposition, *Phys Rev B*, 56, 6958 (1997) with permission of the American Physical Society, and ZnO NP samples Z1, Z2, and Z4 with average sizes of 5.7, 7.5, and 27.4 nm, respectively [2]. (b) Reprinted from Z. D. Fu, et al, Study on the quantum confinement effect on ultraviolet photoluminescence of crystalline ZnO nanoparticles with nearly uniform size, *Ap. Phys. Lett.*, 90, 263113 (2007)

does change and does not change with sample sizes for non-polar Si and polar ZnO nano-semiconductors, respectively. Similar behavior of lines shape changes can also be seen in MP Raman spectra.

The lack of changes of Raman spectral frequency and line shape with sample sizes indicate that there are no QCE on phonon energy and no finite size effect (FSE) on phonon momentum (wave vectors), respectively. These results are totally the opposite of the conventional conception that QCE and FSE are the basic effects on nanostructures. Therefore they are an “abnormal” phenomena and an interesting academic exercise to find its origin and nature.

## 12.2 Origin of No FSE on Phonons

### 12.2.1 Planar Phonon Dispersion Curves near the Center of Brillouin Zone

In 1997, the phenomenon of no FSE on phonon described in the above subsection had appeared in InSb quantum dots, as shown in Figure 12.2 [3]. Later, Demangeot *et al.* reported a similar phenomenon, as shown as in Figure 9.44, and pointed out that the LO phonon frequency depends very weakly on the nanoparticle size [4]. For this phenomenon the authors of Ref. [4] proposed that it could be understandable by observing the optical phonon dispersion curves, which are flat near the center of the Brillouin zone.

The proposition by Demangeot *et al.* [4] can be understood as follows. The FSE leads to the phonon wave vector selection rule  $\mathbf{q} = 0$  being relaxed and the phonons of  $\mathbf{q} \neq 0$  can join the scattering process, resulting in Raman frequencies changing with sample sizes. However, if the phonon dispersion curves near the center of the Brillouin zone ( $\mathbf{q} \approx 0$ ) are flat, then Raman frequencies should be not change with sample sizes.

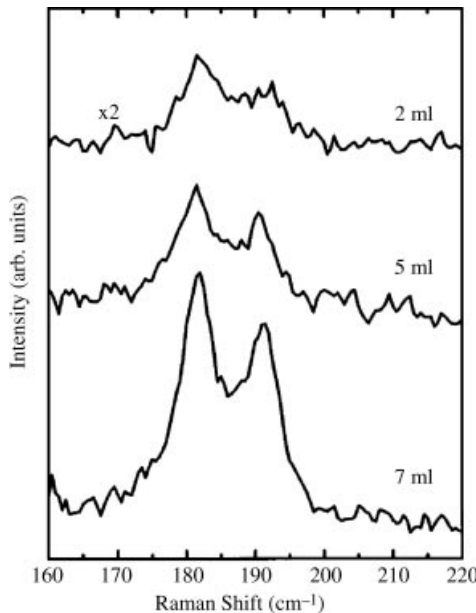


**Figure 12.2** Raman spectra of InSb quantum dot samples with 2, 5, and 7 MLs (i.e., 7.2, 18, and 25.2 nm); the peaks at 193 and 181 cm<sup>-1</sup> are attributed to the LO-like and the TO-like phonon modes, respectively [3]. Reprinted from G. Armelles, T. Utzmeier, P. A. Postigo et al, Raman scattering of InSb quantum dots grown on InP substrates, *J. Appl. Phys.* 81 (1997) with permission of the American Institute of Physics

For above proposal, we also notice that no FSE appears in MP Raman spectra shown in Figure 11.11(b). MP Raman spectrum represents the phonon density of states (PDOS) rather than the phonon dispersion curve, which cannot be interpreted by the proposition by Demangeot *et al.* Second, the proposition is based on the assumption that bulk dispersion curves are still effective in nano-semiconductors, that is, a so-called bulk-like approximation. However, it has been verified that the bulk-like approximation on phonon dispersion relation is not effective in nano-semiconductors with smaller sizes [5], therefore, the proposal will be of no avail for many nano-structures. Nevertheless, we will inspect the suggestion by Demangeot *et al.* [4] in terms of bulk dispersion curves.

According to bulk dispersion curves, Table 12.1 lists the estimated deviated values at 1/4 position away from the center of the Brillouin zone. We consider that if the deviated value is larger than the largest measured error of  $\sim 2\text{ cm}^{-1}$ , the corresponding dispersion curve cannot be considered as flat. From Table 12.1, we see that all the CdSe phonon modes satisfy this only, while at least one phonon mode does not satisfy the criteria of suggested for ZnO, GaN, and SiC nanosamples. Therefore the interpretation suggested by Demangeot *et al.* is not reasonable, even for bulk-like approximations.

Overall, the above interpretations for lack of FSE on phonons are unable to give a reasonable opinion. Note that all of the above interpretations are, in fact, based on conventional theory,

**Table 12.1** Estimated deviation wavenumber value at 1/4 away from the center of the Brillouin zone by using bulk dispersion curves; the bold numbers represent values that deviate more than the experimental error

Phonon Mode	Sample			
	ZnO		GaN	CdSe
$E_{1L}$	<b>8.7</b>	/	0	1.3
$A_{1T}$	1.3	/		
$A_{1L}$	/	1.3	<b>2.4</b>	1.3
$E_2(H)$	/	0	1.2	0.3
$E_{1T}$	/	0		
$E_2(L)$	/	<b>2.5</b>	<b>2.4</b>	0.3
	$\Gamma - \Sigma$	$\Gamma - A$		
				<b>3C-SiC</b>

which may be the reason why they are so unsuccessful. To seek a plausible interpretation, it seems that we have to get rid of the traditional concepts and start by analyzing all experimental facts comprehensively to discover possible experimental regularity.

### 12.2.2 Regularity of Observed Raman Spectral Feature and Origin of no FSE on Phonons

From the experimental results mentioned above and Refs. [6–9], a regular pattern can be found. The regular pattern is that the QCE and FSE on phonons appear in all of the acoustic phonons of either polar and non-polar nano-semiconductors, while no QCE and no FSE on phonons occur in the optical phonons of polar nano-semiconductors but not in the optical phonons of non-polar semiconductors.

Optical and acoustic phonons correspond to the out-of-phase and in-phase vibrations of two atoms in one unit [10]. Non-polar semiconductors consist of the same kind of atoms with no charge, thus any type of vibration of the atoms is impossible to cause any net movement of charge between the atoms, meaning the vibration only induces a deformation potential. However, polar semiconductors usually consist of two different types of atoms carrying opposite charges and the out-of-phase vibration of two such atoms in one unit will induce charge redistribution. As a result, the longitudinal optical (LO) phonons in polar bulk- and nano-semiconductors will occur a long-range electrostatic Coulomb potential. This potential will result in producing the so-called Fröhlich electron-phonon interaction. Note that in nano-semiconductors, such as spherical quantum dots, the transverse TO vibration mode possesses mixed LO–TO characters [11], meaning that the TO modes in polar nano-semiconductors also have an electrostatic potential, that is, the Fröhlich interaction. Thus, Raman scattering of optical phonons in polar nano-semiconductors is uniquely related to an extra Fröhlich electron-phonon interaction in all phonon modes, in addition to the deformation potential that all phonons possess. Therefore, the Fröhlich interaction seems to respond to the observed lack of FCE and suggests that the long-range Fröhlich interaction can be considered as the origin of abnormal lack of QCE and FSE phenomena described above.

## 12.3 Fröhlich Interaction in Nanostructures

### 12.3.1 Expression and Playing Role in Small Size Systems of Fröhlich Interaction

The Fröhlich interaction  $H_{\text{Fr}}$  has been described in Section 7.1.5 and can be expressed approximately as [12]

$$H_{\text{Fr}} \sim q^{-1} V^{-1/2} \quad (12.1)$$

where  $q$  is the phonon wave vector and  $V$  is the volume of samples. Equation (12.1) must lead to following results:

First, the inverse proportion relation of the Fröhlich interaction  $H_{\text{Fr}}$ , with wave vector  $q$  makes the phonon Raman scattering induced by the Fröhlich interaction occur mainly at the center of the Brillouin zone.

Second, the inverse square relation of the Fröhlich interaction  $H_{\text{Fr}}$  with volume  $V$  means that the Fröhlich interaction will be greatly enhanced in small-sized systems. Thus the Fröhlich interaction plays a distinct role that is different from that in bulk nanostructures, which has been pointed out in Raman scattering of superlattices earlier [12].

This gives more reasons for the above suggestion that the phenomenon of no FSE on the Raman scattering of optical phonons in polar nano-semiconductors originated from the Fröhlich electron-phonon interaction.

### 12.3.2 Fröhlich Interaction and Raman Spectral Features in Nano-Semiconductors

#### 12.3.2.1 Raman Frequency Feature Induced by Fröhlich Interaction

In the conventional Raman scattering theory of nano-semiconductors, the frequencies of bulk- and nano-semiconductors,  $\omega_{\text{Bulk}}$  and  $\omega_{\text{Nano}}$ , are predicated to be different and the frequencies of MP Raman spectra are the counterpart of whole PDOS [13], that is, in Raman frequencies of MP,  $\omega_k$  (the subscript  $k$  is the order number of MP) is usually not the integral times of SP Raman frequency  $\omega_1$ , that is,  $\omega_k \neq k\omega_1$ .

However, as mentioned above, the Fröhlich interaction in nano-semiconductors must result in the wave vector selection rule  $q = 0$  as still valid in optical phonons, which implies that the scattering from the phonons induced by the Fröhlich interaction still occur at the center of the Brillouin zone, either for SP and MP Raman scattering, meaning there exists the relations  $\omega_{\text{Bulk}} = \omega_{\text{Nano}}$  and  $\omega_k = k\omega_1$ . Thus, the so-called “abnormal” phenomena observed in Sections 9.42–9.43 and 11.1.3 should be predicted. This gives the above suggestion a solid confirmation that the Fröhlich interaction is the origin of the “abnormal” phenomena appearing in Raman scattering of optical phonons in polar nano-semiconductors.

#### 12.3.2.2 Raman Intensity Feature Induced by Fröhlich Interaction

The study in Ref. [14] points out that the Fröhlich coupling constant of the Raman scattering of double phonon is less than one. This favors the second-order in comparison with the third-order process, implying it should have  $I_1 < I_2 > I_3$  (where, the subscript number represents the order of MP). The observed Raman intensity change of ZnO NPs with the MP order is shown in Figure 12.3, in which both A<sub>1L</sub> and E<sub>1L</sub> optical modes show the same relation with the predication of  $I_1 < I_2 > I_3$ .

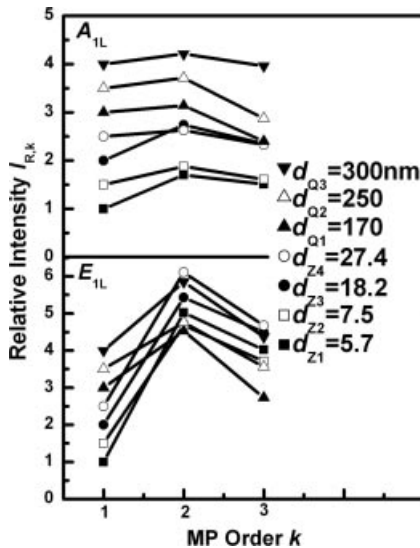


**Figure 12.3** Dependence of relative integral intensity on MP order of  $A_{1L}$  and  $E_{1L}$  modes MP scattering

Thus, the above suggestion on the origin of “abnormal” no FSE on phonons is obtained independent confirmation.

## 12.4 Theoretical Raman Spectra of Non-polar and Polar Nano-Semiconductors

To confirm suggestions on the origin of no FSE completely, it is needed to observe theoretical Raman spectral features and its regularity and origin.

### 12.4.1 Calculated Theoretical Raman Spectra

Based on the molecular dynamic calculation methods described in Sections 8.4 and (8.5), the theoretical spectra have been calculated for some non-polar and polar nano-semiconductors [15, 16]. Figure 12.4(a) shows the calculated Raman spectra of non-polar Si and diamond NPs and polar ZnO and InSb NPs. From Figure 12.4(a), it can be seen that the Raman peak frequencies of acoustic phonons in both polar and non-polar samples change with sample size, while the Raman peak frequencies with sample size do not change for optical phonons in polar ZnO and InSb NPs.

### 12.4.2 Comparing Between Theoretical and Experimental Raman Spectra

To perform the comparison between theoretical and experimental Raman spectra of nano-semiconductors, the dependences of frequency on sample sizes shown in Figure 12.4(a) are drawn in Figure 12.4(a). Correspondingly, the observed dependences of optical and acoustic phonon frequency on sample sizes are shown in Figure 12.4(c) [17–20]. The agreement

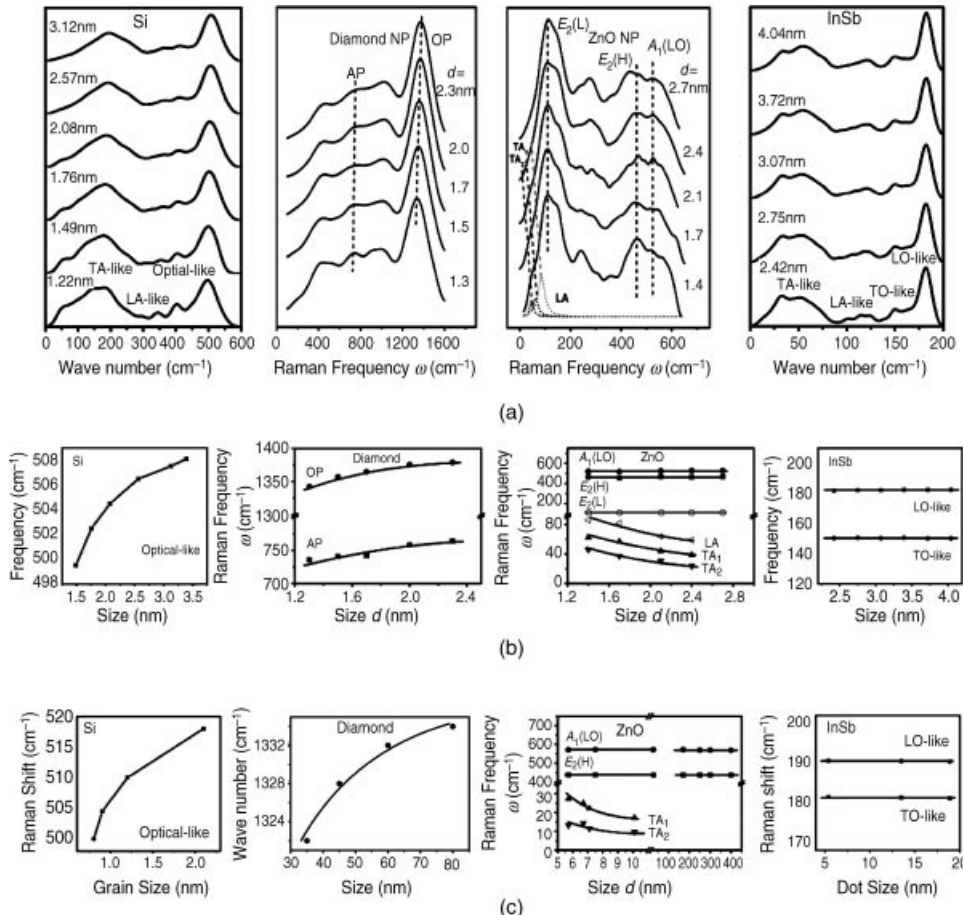


**Figure 12.4** Theoretical Raman spectra (a), as well as, theoretical (b) and experimental (c) dependences of phonon frequency on sample sizes for Si, diamond, ZnO, and InSb nanoparticles; in (c) the experimental date of Si [1], diamond [21], ZnO [17–19], and InSb [3] NPs. Where AP and OP are labeled for acoustic and optical phonons, respectively; A<sub>1</sub>(LO), E<sub>2</sub>(L), and E<sub>2</sub>(H) are labeled for longitudinal A<sub>1</sub>, low frequency, and high frequency E<sub>2</sub> phonons, in order; LA, TA<sub>1</sub>, and TA<sub>2</sub> are label for longitudinal and two transverse acoustic phonons, in order

between theoretical and experimental results is good. Especially, from Figures 12.4(b) and (c), we see that the trend and values of calculated frequency change of acoustic phonon in polar ZnO NPs on the sample size match the observed results well [17, 19], giving confirmation that the acoustic phonons in polar nano-semiconductors have FSE.

#### 12.4.3 Origin of no FSE Revealed by Theoretical Raman Spectral Calculation

Note that the largest distinction between the above calculations for polar and non-polar NPs is whether the charge is and is not taken into account, respectively, implying that the calculated spectra of polar and non-polar NPs are and are not associated to Fröhlich

interaction, respectively. This gives theoretically confirmation for the deduction that the observed no FSE phenomena originate from the Fröhlich interaction.

## 12.5 Amorphous Feature of Nanocrystal Raman Spectra of No FSE on Phonons and the Breaking of Translation Symmetry in Nano-Semiconductors

### 12.5.1 Simulation of Nano-Semiconductor Raman Spectra

#### 12.5.1.1 Simulation with Fitting to the Observed Raman spectra

The simulation of Raman spectra observed in nano-semiconductors was proposed by using the so-called microcrystal model (MCM), which was introduced in Section 8.3 and was exhibited that the MCM is a good model for non-polar nano-semiconductors.

However, the fitting by MCM for nano-semiconductors ZnO, GaN, CdSe, and SiC is unsuccessful. Figure 12.5 shows the calculated Raman spectra (dashed line) by MCM for these samples, together with observed Raman spectra (solid line). The comparison between calculated and observed spectra in Figure 12.5 indicates that the calculated spectra by MCM does not fit the observed spectra in three respects. First, the interface modes between LO- and TO-like modes in the experimental spectra cannot be reproduced. Second, the Raman frequency shifts relative to the bulk ones are too small for bulk-like LO mode. Third, the direction of the shoulder of some calculated Raman peaks are opposite to those of the observed peaks [20].

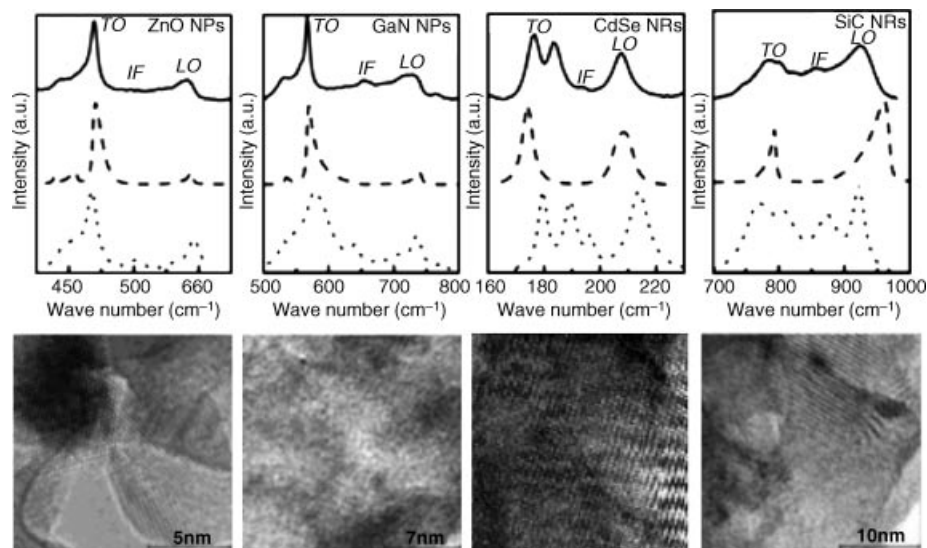


**Figure 12.5** Observed Raman spectra (solid line) and calculated Raman spectra by the MCM (dashed line) and ACM (dot line) for nano-semiconductors ZnO, GaN, CdSe, and SiC; where LO, TO, and IF represent the longitudinal, transverse, and optical phonon modes and interface mode, respectively. HRTEM image of each sample is shown underneath the Raman spectra.

As a comparison, the theoretical spectra calculated by ACM described in Section 8.4 for above samples, ZnO, GaN, CdSe, and SiC nano-semiconductors, has been done and are shown in Figure 12.5 by the dotted line. In contrast with that calculated by ACM, the fitting of calculated spectra by ACM to the observed ones is unexpectedly good and all of the three shortcomings in the MCM simulation mentioned above disappear.

#### *12.5.1.2 Amorphous Feature Appeared Raman Spectra of Nanocrystalline Semiconductors*

The proposition of QCE related to system energy and FSE related to system momentum are based on the systems still retaining their crystal features. The MCM is established based on the above conceptions and with the practical assumption that phonon dispersion curves of crystals still hold and the momentum is still conserved. Therefore, if the system fits MCM, it must be crystalline. Contrarily, if the observed Raman spectra cannot be fitted by MCM, this system must be amorphous.

Note that the HRTEM images shown in Figure 12.5 exhibit that all samples possess crystalline structure. This result indicates that Raman spectra of crystalline semiconductors possess amorphous features rather than crystalline features. This result shows clearly that the Raman spectra with no FSE on phonons relate to amorphous features.

#### **12.5.2 Amorphous Feature and Translation Symmetry**

Crystals are long-range order and must possess translation symmetry. In contrast, the appearance of amorphous features indicate that this system has long-range disorder and no translation symmetry. Moreover, the translation symmetry only exists as an infinite-size system [25] and where no translation symmetry implies that the corresponding system is a non-infinite-size system. This appears as a contradiction that in the nano-semiconductor with same size, different phonon systems display different symmetries.

However, no physical system is ever infinite in spatial extent practically, so the infinite-size system is defined as such a system that the boundary influence can be ignored. In fact, if the size of the material is 10 times larger than that of the concerned object, it can be considered as finite-size system and the translation symmetry can be considered as maintained [25]. Therefore, the practical size of an infinite-sized system is related to the active region size of objects.

The active region of deformation potential from short-range van der Waals force is mainly localized in the region covered by two atoms, which is of the order of 0.1 nm. On the other hand, long range Coulomb potential for a couple of anions and cations separated by  $r_{a-c}$ , is proportional to  $\sim 1/(r_{a-c})^2$ . Thus, the active region of the Fröhlich interaction can be estimated as  $\sim 10^2$  of the separated distance of two atoms in the lattice, that is, in the order of about 10 nm. This difference in the sizes of active regions between the Fröhlich and deformation potential interactions is insignificant for bulk materials, but is not so for nano-sized materials. For example, in the case of nano-semiconductors, the infinite system and then translation symmetry is not valid for the Fröhlich interaction. For deformation potentials, it will still be effective but will be relaxed, except for objects with very small size, for example, less than 2–3 nm [26].

The above discussion illustrates, on the one hand, that the nature of observed phenomena from no FSE on optical phonons in polar nano-semiconductors is the breaking of translation

symmetry. On the other hand, the discussion also explores an essential fact that the practical scale of the existing translation symmetry will be different for different objects in nanomaterials and is dependent on the active region of concerned objects. This implies that there is no unified scale criterion of the breaking of translation symmetry in Raman scattering of nanomaterials, although they possess unified size criterion in the case of bulk materials.

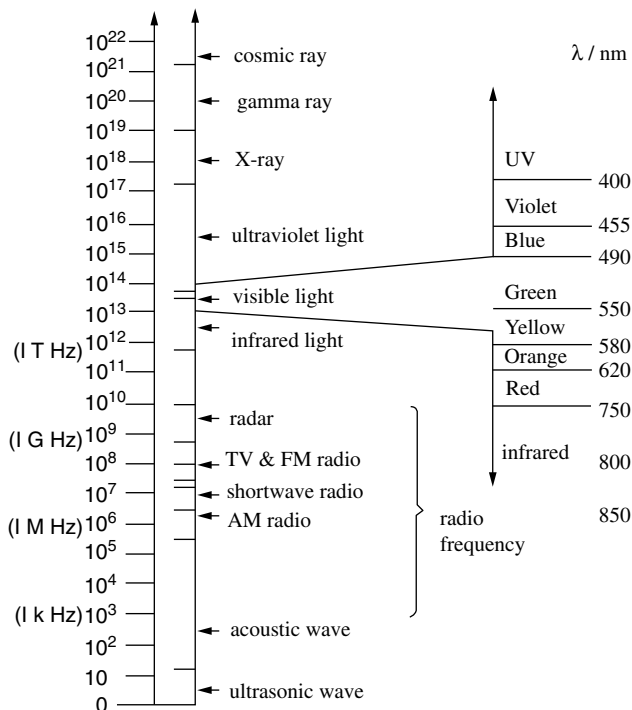
## References

- [1] Ehbrecht, M. *et al.* (1997) *Phys. Rev. B*, **56**, 6958.
- [2] Fu, Z.D. *et al.* (2007) *Appl. Phys. Lett.*, **90**, 263113.
- [3] Armelles, G., Utzmeier, T., Postigo, P.A. *et al.* (1997) *J. Appl. Phys.*, **81**, 6339.
- [4] Demangeot, F. *et al.* (2006) *Appl. Phys. Lett.*, **88**, 071921.
- [5] Hu, X. and Zi, J. (2002) *J. Phys.: Condens. Matter*, **14**, L671.
- [6] Chassaing, P.-M., Demangeot, F., Combe, N. *et al.* (2009) *Phys. Rev. B*, **79**, 155314.
- [7] Yadav, H.K., Gupta, V., Sreenivas, K., Singh, S.P., Sundarakannan, B., and Katiyar, R.S. (2006) *Phys. Rev. Lett.*, **97**, 085502.
- [8] Bottani, C.E., Mantini, C., Milania, P. *et al.* (1996) *APL*, **69**, 2409.
- [9] Ehbrecht, M., Kohn, B., Huisken, F. *et al.* (1997) *PRB*, **56**, 6958.
- [10] Born, M. and Huang, K. (1968) *Dynamical Theory of Crystal Lattice*, Oxford University Press, London.
- [11] Rajalakshmi, M., Sakuntalay, T., and Arora, A.K. (1997) *J. Phys.: Condens. Matter*, **9**, 9745.
- [12] Yu, P.Y. and Cardona, M., Fundamentals of semiconductors.
- [13] Leite, C.C. (1969) *et al. Phys. Rev. Lett.*, **22**, 780.
- [14] Rodríguez-Súaéz, R., Menéndez-Proupin, E., Trallero-Giner, C., and Cardona, M. (2000) *Phys. Rev. B*, **62**, 11006.
- [15] Liu, W., Liu, M., and Zhang, S.-L. (2008) *Phys. Lett. A*, **372**, 2474.
- [16] Li, D.Y. (2011) Bachelor thesis, School of Physics, Peking University.
- [17] Chassaing, P.-M. and Demangeot, F. (2009) *Phys. Rev. B*, **79**, 155314.
- [18] Yadav, H.K. and Gupta, V. (2006) *Phys. Rev. Lett.*, **97**, 085502.
- [19] Zhang, S.L., Zhang, Y., Fu, Z. *et al.* (2006) Study of the size effect on the optical mode frequencies of ZnO nanoparticles with nearly uniform size. *Appl. Phys. Lett.*, **89**, 063112.
- [20] Zhang, S.-L., Shao, J., Hoi, L.-S. *et al.* (2005) *Phys. Stat. Sol. (c)*, **2**, 3090–3095.
- [21] Yan, Y., Zhan, G.S.-L., Hark, S.K. *et al.* (2004) Study of  $1145\text{cm}^{-1}$  Raman Peak of CVD Diamond Film, Study of  $1145\text{cm}^{-1}$  Raman Peak of CVD Diamond Film, **16**, 131.
- [22] Zhang, S.-L., Hou, Y., Ho, K.-S. *et al.* (1992) *J. Appl. Phys.*, **72**, 4469.
- [23] Bottani, C.E., Mantini, C., Milania, P. *et al.* (1996) *Appl. Phys. Lett.*, **69**, 2409.
- [24] Yoshikawa, M., Mori, Y., Obata, H. *et al.* (1995) *Appl. Phys. Lett.*, **67**, 694.
- [25] Shuker, R. and Gammom, R.W. (1970) *Phys. Rev. Lett.*, **25**, 222.
- [26] Zi, J., Zhang, K.M., and Xie, X.D. (1997) *Phys. Rev. B*, **55**, 9263.

# Appendix I

## Electromagnetic Waves and Lasers

### I.1 Electromagnetic Wavelength [1]



## I.2 Laser Types

### I.2.1 Gas Lasers [1]

Gain Medium		Wavelength ( $\mu\text{m}$ )/ Wave Number ( $\text{cm}^{-1}$ )	Output Power	Pump Source	
Atomic	He-Ne	3.3913/2950	0.1–100 mW	Electrical discharge	
		1.52/6579			
		1.15/8696			
		0.6118/16345			
		0.63282/15798			
	He-Xe	0.5939/16838			
		3.508/2850	Several mW 5.2 W		
	He-Cu	0.5106/19585	0.5 W		
	CO <sub>2</sub>	10.6/943; 9.4/1064	Several W–100 kW		
		2.6~4/2500~3846	<30 W		
		4.8~8.3/1205~2083			
		F <sub>2</sub>	0.157/63694		
Molecular	N <sub>2</sub>	0.3371/29664	<10 mJ/pulse		
	Ionic	Ar <sup>+</sup>	0.5287/18914		
		0.51453/19430			
		0.50172/19926			
		0.49651/20135			
		0.48799/20487			
		0.47649/20981			
		0.47269/21150			
		0.46579/21463			
		0.45794/21831			
Excimer	Kr <sup>+</sup>	0.45451/21996			
		0.36379/27481			
		0.35111/28473			
		0.7993/12510	~3 W		
		0.75255/13285	~50–500 mW		
		0.6764/14784			
		0.64709/15450			
		0.56819/17595			
		0.5309/18835			
		0.416/24038			
Excimer	He-Cd <sup>+</sup>	0.44200/22645	<1 W		
		0.32500/30769			
	Ne-Cu <sup>+</sup>	0.260/38462;	<1 W		
		0.7808/12807			
	Ne-Ag <sup>+</sup>	0.8404/11899.1	<1 W		
		0.3181/31436.66			
	XeCl	0.308/32467.53	1–100 W		
	KrF	0.248/40322.58	1–100 W		
	ArF	0.193/51813	~100 mJ/pulse		
	XeF	0.353/28329	45 mW		
Excimer	XeCl	0.308/32468	50 mW		
	KrCl	0.222/45045	25 mW		
	N <sub>2</sub>	0.337/29674	5 mW		

### I.2.2 Solid/Semiconductor Lasers

Gain Medium		Wavelength ( $\mu\text{m}$ )/ Wave Number ( $\text{cm}^{-1}$ )	Pump Source
Solid	Nd: YAG	1.064/9398 0.532/18797 0.355/28169 0.226/44248	Flashlamp Laser diode
	Ho: YAG	1.9–2.2/5263–4545	
	Er: YAG	2.940/3401	
	Cr <sup>3+</sup> : Ruby	0.6943/14403 0.6929/14432.1	Flashlamp
	GaN AlGaNp, AlGaAs InGaAsP	0.4/25000 0.63–0.9/11111–15873 1.0–2.1/4762–10000	Electrical current

### I.2.3 Tunable Lasers

Gain Medium		Wavelength ( $\mu\text{m}$ )/ Wave Number ( $\text{cm}^{-1}$ )	Pump Source
Dye	Nile blue perchlorate	0.710–0.800/14100–12500	Electrical current
	Cresyl Violet Blue Perchlorate	0.670–0.710/14900–14100	
	Rhodamine B	0.590–0.690/16900–14500	
	Rhodamine 6G	0.560–0.660/17900–15200	
	Rhodamine 110	0.530–0.620/18900–16100	
	Fluorescein Sodium	0.530–0.580/18900–17200	
	Coumarin 6	0.520–0.560/19200–17900	
	Coumarin 102	0.460–0.520/21700–19200	
Solid	Coumarin 2	0.430–0.480/23300–20800	
	Ti: sapphire	0.700–1.064/14300–9400	Other laser

### I.3 Laser Lines and Ionic/Atomic Lines of Gas Lasers used Commonly in Raman Spectroscopy

#### I.3.1 Laser Lines and Ion Lines of Ar<sup>+</sup> Lasers [2]

Number	Wave Number (cm <sup>-1</sup> )	Wavelength (Å)	Peak height	Wave Number Values Relative to Laser Line (cm <sup>-1</sup> )				
				4,579	4,658	4,727	4,765	4,880
1	21,995	4,545.2	350					
2	21,903	4,564.3	23					
3	21,831	4,579.4	380	0				
4	21,783	4,589.4	530	48				
5	21,739	4,598.7	15	92				
6	21,688	4,609.6	819	143				
7	21,557	4,637.6	74	274				
8	21,463	4,657.9	366	368	0			
9	21,150	4,726.8	500	681	313	0		
10	21,126	4,732.2	23	705	337	24		
11	21,108	4,736.2	800	723	355	42		
12	20,981	4,764.9	470	850	482	169	0	
13	20,803	4,805.7	1150	1,028	660	347	178	
14	20,623	4,847.6	840	1,208	840	527	358	
15	20,547	4,865.5	40	1,284	916	603	434	
16	20,487	4,879.8	1600	1,344	976	663	494	0
17	20,450	4,888.6	90	1,381	1,013	700	531	37
18	20,384	4,904.4	60	1,447	1,079	766	597	103
19	20,267	4,932.8	460	1,564	11,96	883	714	220
20	20,266	4,942.8	10	1,605	1,237	924	755	261
21	20,135	4,965.1	530	1,696	1,328	1,015	846	352
22	20,107	4,972.0	270	1,724	1,356	1,043	874	380
23	19,959	5,008.9	830	1,872	1,504	1,191	1,022	528
24	19,926	5,017.2	330	1,905	1,537	1,224	1,055	561
25	19,750	5,061.9	790	2,081	1,713	1,400	1,231	737
26	19,639	5,090.5	5	2,192	1,824	1,511	1,342	848

19,444	5,141.5	27	2,387	2,019	1,706	1,537	1,043	691
19,430	5,145.2	95	2,401	2,033	1,720	1,551	1,057	705
19,364	5,162.8	7	2,467	2,099	1,786	1,617	1,123	771
30	19,353	5,165.7	21	2,478	21,10	1,797	1,628	1,134
31	19,313	5,176.4	26	2,518	2,150	1,837	1,668	1,174
32	19,269	5,188.2	3	2,562	2,194	1,881	1,712	1,218
33	19,163	5,216.9	8	2,668	2,300	1,987	1,818	1,324
34	18,909	5,287.0	75	2,922	2,554	2,241	2,072	1,578
35	18,842	5,305.8	4	2,989	2,621	2,308	2,139	1,645
36	18,521	5,397.8	4	3,310	2,942	2,629	2,460	1,966
37	18,503	5,403.0	3	3,328	2,960	2,647	2,478	1,984
38	18,487	5,407.7	4	3,344	2,976	2,663	2,494	2,000
39	18,336	5,452.2	3	3,495	3,127	2,814	2,645	2,151
40	18,329	5,454.3	6	3,502	3,134	2,821	2,652	2,158
41	18,190	5,496.0	7	3,641	3,273	2,960	2,791	2,297
42	18,183	5,498.1	3	3,648	3,280	2,967	2,798	2,304
43	18,175	5,500.5	3	3,656	3,288	2,975	2,806	2,312
44	17,984	5,559.0	10	3,847	3,479	3,166	2,997	2,505
45	17,940	5,572.6	4	3,891	3,523	3,210	3,041	2,547
46	17,830	5,607.0	12	4,001	3,633	3,320	3,151	2,657
47	17,692	5,650.7	8	4,139	3,771	3,458	3,289	2,795
48	17,680	5,564.5	3	4,151	3,783	3,470	3,301	2,807
49	17,462	5,725.1	3	4,369	4,001	3,688	3,519	3,025
50	17,417	5,739.9	3	4,414	4,046	3,733	3,564	3,070
51	17,318	5,772.7	7	4,513	4,145	3,832	3,663	3,169
52	17,275	5,787.1	3	4,556	4,188	3,875	3,706	3,212
53	17,197	5,813.4	5	4,634	4,266	3,953	3,784	3,290
54	17,106	5,844.3	4	4,725	4,357	4,044	3,875	3,381
55	17,058	5,860.7	3	4,773	4,405	4,092	3,923	3,429
56	16,993	5,883.1	5	4,838	4,470	4,157	3,988	3,494
57	16,977	5,888.7	11	4,854	4,486	4,173	4,004	3,510
58	16,909	5,912.4	19	4,922	4,554	4,241	4,072	3,578
59	16,861	5,929.2	6	4,970	4,602	4,289	4,120	3,626
60	16,701	5,986.0	6	5,130	4,762	4,449	4,280	3,786
61	16,691	5,989.6	6	5,140	4,772	4,459	4,290	3,796

(continued)

(Continued)

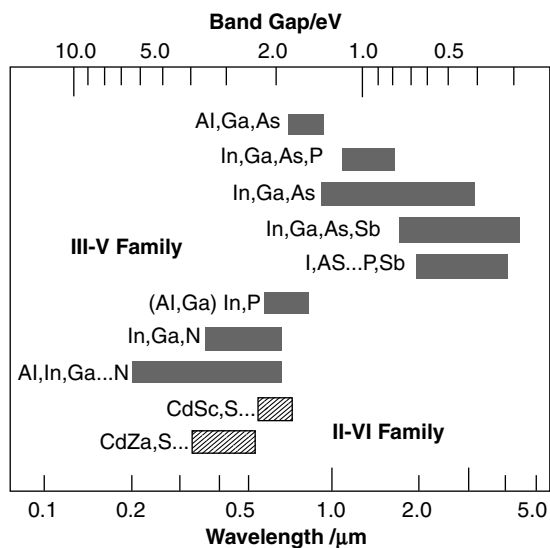
Number	Wave Number (cm <sup>-1</sup> )	Wavelength (Å)	Peak height	Wave Number Values Relative to Laser Line (cm <sup>-1</sup> )				
				4,579	4,658	4,727	4,765	4,880
62	16,572	6,032.6	48	5,259	4,891	4,578	4,409	3,915
63	16,541	6,043.9	16	5,290	4,922	4,609	4,440	3,946
64	16,515	6,053.4	8	5,316	4,948	4,635	4,466	3,972
65	16,498	6,059.7	15	5,333	4,965	4,652	4,483	3,989
66	16,449	6,077.7	6	5,382	5,014	4,701	4,532	4,038
67	16,391	6,099.2	5	5,440	5,072	4,759	4,590	4,096
68	16,378	6,104.1	44	5,453	5,085	4,772	4,603	4,109
69	16,348	6,115.3	1020	5,483	5,115	4,802	4,633	4,139
70	16,324	6,124.3	47	5,507	5,139	4,826	4,657	4,163
71	16,284	6,139.3	51	5,547	5,179	4,866	4,697	4,203
72	16,266	6,146.1	8	5,565	5,197	4,884	4,715	4,221
73	16,240	6,155.9	4	5,591	5,223	4,910	4,741	4,247
74	16,196	6,172.7	950	5,635	5,267	4,954	4,785	4,291
75	16,157	6,187.6	12	5,674	5,306	4,993	4,824	4,330
76	161,19	6,202.1	5	5,712	5,344	5,031	4,862	4,368
77	16,091	6,212.9	9	5,740	5,372	5,059	4,890	4,396
78	16,082	6,216.4	6	5,749	5,381	5,068	4,899	4,405
79	16,020	6,240.5	17	5,811	5,443	5,130	4,961	4,467
80	16,013	6,243.2	470	5,818	5,450	5,137	4,968	4,474
81	15,876	6,297.1	9	5,955	5,587	5,274	5,105	4,611
82	15,848	6,308.2	14	5,983	5,615	5,302	5,133	4,639
83	15,806	6,325.0	13	6,025	5,657	5,344	5,175	4,681
84	15,785	6,333.4	10	6,046	5,678	5,365	5,196	4,702
85	15,747	6,348.7	9	6,084	5,716	5,403	5,234	4,740
86	15,724	6,357.9	7	6,107	5,739	5,426	5,257	4,763
87	15,705	6,365.6	4	6,126	5,758	5,445	5,276	4,782
88	15,694	6,370.1	9	6,137	5,769	5,456	5,287	4,793
89	15,657	6,385.2	19	6,174	5,806	5,493	5,324	4,830
90	15,634	6,394.5	7	6,197	5,829	5,516	5,347	4,853
91	15,628	6,397.0	8	6,203	5,835	5,522	5,353	4,859

92	15,621	6,399.9	104	6,210	5,842	5,529	5,360	4,866	4,514	4,305	3,809
93	15,611	6,404.0	7	6,220	5,852	5,539	5,370	4,876	4,524	4,315	3,819
94	15,598	6,409.3	5	6,233	5,865	5,552	5,383	4,889	4,537	4,328	3,832
95	15,579	6,417.1	79	6,252	5,884	5,571	5,402	4,908	4,556	4,347	3,851
96	15,563	6,423.7	5	6,268	5,900	5,587	5,418	4,924	4,572	4,363	3,867
97	15,543	6,432.0	3	6,288	5,920	5,607	5,438	4,944	4,592	4,383	3,887
98	15,528	6,438.2	19	6,303	5,935	5,622	5,453	4,959	4,607	4,398	3,902
99	15,517	6,442.8	14	6,314	5,946	5,633	5,464	4,970	4,618	4,409	3,913
100	15,513	6,444.4	11	6,318	5,950	5,637	5,468	4,974	4,622	4,413	3,917
101	15,453	6,469.4	8	6,378	6,010	5,697	5,528	5,034	4,682	4,473	3,997
102	15,444	6,473.2	6	6,387	6,019	5,706	5,537	5,043	4,691	4,482	3,986
103	15,437	6,476.2	5	6,394	6,026	5,713	5,544	5,050	4,698	4,489	3,993
104	15,419	6,483.7	480	6,412	6,044	5,731	5,562	5,068	4,716	4,507	4,011
105	15,378	6,501.0	56	6,453	6,085	5,772	5,603	5,109	4,757	4,548	4,052
106	15,358	6,509.5	10	6,473	6,105	5,792	5,623	5,129	4,777	4,568	4,072
107	15,289	6,538.8	65	6,542	6,174	5,861	5,692	5,198	4,846	4,637	4,141
108	15,231	6,563.7	15	6,600	6,232	5,919	5,750	5,256	4,904	4,695	4,199
109	15,153	6,597.5	3	6,678	6,310	5,997	5,828	5,334	4,982	4,773	4,277
110	15,135	6,605.4	28	6,696	6,328	6,015	5,846	5,352	5,000	4,791	4,295
111	15,113	6,615.0	19	6,718	6,350	6,037	5,868	5,374	5,022	4,813	4,317
112	15,098	6,621.6	24	6,733	6,365	6,052	5,883	5,389	5,037	4,828	4,332
113	15,059	6,638.7	2800	6,772	6,404	6,091	5,922	5,428	5,076	4,867	4,371
114	15,047	6,644.0	5700	6,784	6,416	6,103	5,934	5,440	5,088	4,879	4,383
115	14,996	6,666.6	37	6,835	6,467	6,154	5,985	5,491	5,139	4,930	4,434

### I.3.2 Laser Lines and Atomic Emission Lines of He-Ne Laser [2]

Number	Wavelength (Å)	Wave Number (cm <sup>-1</sup> )	Wave Number Shift Relative to Laser Line (cm <sup>-1</sup> )
1	6,328.1646	15,798.002	0.000
2	6,334.4279	15,782.381	15.621
3	6,351.8618	15,739.064	58.938
4	6,382.9914	15,662.306	135.696
5	6,402.2460	15,615.202	182.800
6	6,421.7108	15,678.871	230.131
7	6,444.7118	15,512.310	285.692
8	6,506.5279	15,364.935	433.067
9	6,532.8824	15,302.951	495.051
10	6,598.9529	15,149.735	648.267
11	6,652.0925	15,028.714	769.288
12	6,666.8967	14,995.342	802.660
13	6,678.2764	14,969.790	828.212
14	6,717.0428	14,883.395	914.607
15	6,929.4672	14,427.144	1,370.858
16	7,024.0500	14,232.876	1,565.126
17	7,032.4128	14,215.950	1,582.052
18	7,051.2937	14,177.885	1,620.117
19	7,059.1079	14,162.191	1,635.811
20	7,173.9380	13,935.504	1,862.498
21	7,245.1665	13,798.503	1,999.499
22	7,438.8981	13,439.150	2,358.852
23	7,472.4383	13,378.828	2,419.174
24	7,448.8712	13,349.471	2,448.531
25	7,535.7739	13,266.384	2,531.618
26	7,544.0439	13,251.841	2,546.161
27	7,724.6281	12,942.045	2,855.957
28	7,839.0500	12,753.131	3,044.871
29	7,927.1172	12,611.457	3,186.545
30	7,936.9946	12,595.763	3,202.239
31	7,943.1805	12,585.954	3,212.048
32	8,082.4576	12,369.073	3,428.929
33	8,118.5495	12,314.085	3,483.917
34	8,128.9077	12,298.394	3,499.608
35	8,136.4061	12,287.060	3,510.942
36	8,248.6812	12,119.819	3,678.183
37	8,259.3795	12,104.120	3,693.882
38	8,266.0788	12,094.310	3,703.692
39	8,267.1166	12,092.792	3,705.210

### I.3.3 Stimulated Emission Wavelength Range of Semiconductor Lasers [1]



# Appendix II

## Standard Spectral Lines

### II.1 Spectral Lines of Mercury Lamp in Visible Range [3]

Color	Wavelength/nm	Strength
Violet	404.66*	Strong
	407.78	Medium
	410.81	Weak
	433.92	Weak
	434.75	Medium
	435.84*	Strong
Bluish green	491.60*	Strong
	496.03	Medium
	496.03	Medium
Green	535.41	Weak
	536.51	Weak
	546.07*	Strong
	567.59	Weak
Yellow	576.96*	Strong
	579.07*	Strong
	585.92	Weak
	589.02	Weak
Orange	607.26	Weak
	612.33	Weak
Red	623.44*	Medium
Deep Red	671.62	Medium
	690.72*	Medium
	708.19	Weak

\*The spectral lines comparatively stronger and often in calibration.

## II.2 Standard Lines of Neon Spectral Lamp [2]

Wave length (nm)	Wave number (cm <sup>-1</sup> )	Peak Height	Wave Number Shift Relative to the Laser Lines (cm <sup>-1</sup> )					
			488.0 nm	514.5 nm	632.8 nm	670.75 nm	784 nm	
1	533.08	18758.9	25	1732.89	677.44	-2956.13	-3850.23	-6003.81
	534.11	18722.7	20	1769.07	713.61	-2919.95	-3814.05	-5967.63
2	540.06	18516.5	60	1975.34	919.88	-2713.68	-3607.78	-5761.36
3	576.44	17347.9	80	3143.94	2088.49	-1545.08	-2439.17	-4592.76
4	582.02	17181.5	40	3310.26	2254.81	-1378.76	-2272.86	-4426.44
5	585.25	17086.7	500	3405.09	2349.63	-1283.93	-2178.03	-4331.61
	587.28	17027.7	100	3464.15	2408.69	-1224.87	-2118.97	-4272.55
7	588.19	17001.3	100	3490.49	2435.04	-1198.53	-2092.62	-4246.21
8	590.25	16942.0	60	3549.83	2494.37	-1139.19	-2033.29	-4186.87
	590.64	16930.8	60	3561.02	2505.56	-1128.01	-2022.10	-4175.68
9	594.48	16821.4	100	3670.38	2614.92	-1018.64	-1912.74	-4066.32
10	596.55	16763.1	100	3728.75	2673.29	-960.27	-1854.37	-4007.95
11	597.46	16737.5	100	3754.28	2698.82	-934.74	-1828.84	-3982.42
	597.55	16735.0	120	3756.80	2701.34	-932.22	-1826.32	-3979.90
12	598.79	16700.3	80	3791.46	2736.00	-897.56	-1791.66	-3945.24
13	602.99	16584.0	100	3907.78	2852.32	-781.24	-1675.34	-3828.92
14	607.43	16462.8	100	4029.00	2973.54	-660.02	-1554.12	-3707.70
15	614.31	16278.4	100	4213.38	3157.92	-475.64	-1369.74	-3523.32
16	616.36	16224.3	120	4267.56	3212.06	-421.50	-1315.60	-3469.18
17	618.21	16175.7	250	4316.07	3260.61	-372.95	-1267.05	-3420.63
18	621.73	16084.2	150	4407.65	3352.19	-281.37	-1175.47	-3329.05
19	626.65	15957.9	150	4533.93	3478.47	-155.09	-1049.19	-3202.77
20	630.48	15860.9	60	4630.87	3515.41	-58.15	-952.25	-3105.83
21	632.82	15802.3	7	4689.52	3634.06	0.50	-893.60	-3047.18
22	633.44	15786.8	100	4704.99	3649.53	15.97	-878.13	-3031.71
23	638.3	15666.6	120	4825.19	3769.73	136.17	-757.93	-2911.51
24	640.22	15619.6	200	4872.17	3816.72	183.15	-710.95	-2864.53
25	650.65	15369.2	150	5122.56	4067.10	433.54	-460.56	-2614.14
26	653.29	15307.1	60	5184.67	4129.21	495.64	-398.45	-2552.04
27	659.89	15154.0	150	5337.76	4282.31	648.74	-245.36	-2398.94
28	667.83	14973.9	90	5517.93	4462.48	828.91	-65.19	-2218.77
29	671.7	14887.6	20	5604.20	4548.75	915.18	21.09	-2132.50
30	692.95	14431.1	100	6060.75	5005.29	1371.73	477.63	-1675.95
31	702.41	14236.7	90	6255.10	5199.65	1566.08	671.98	-1481.60
	703.24	14219.9	100	6271.91	5216.45	1582.88	688.79	-1464.79
32	717.39	13939.4	100	6552.38	5496.93	1863.36	969.27	-1184.32
33	724.52	13802.2	100	6689.56	5634.10	2000.64	1106.44	-1047.14
34	747.24	13382.6	40	7109.22	6053.76	2420.20	1526.10	-627.48
35	748.89	13353.1	90	7138.71	6083.25	2449.69	1555.59	-597.99
36	753.58	13270.0	80	7221.81	6166.35	???	1638.69	-514.89
	754.4	13255.6	80	7236.24	6180.78	2547.21	1653.12	-500.47
37	772.46	12845.7	100	7546.15	6490.69	2857.13	1963.03	-190.55

(continued)

(Continued)

Wave length (nm)	Wave number (cm <sup>-1</sup> )	Peak Height	Wave Number Shift Relative to the Laser Lines (cm <sup>-1</sup> )					
			488.0 nm	514.5 nm	632.8 nm	670.75 nm	784 nm	
38	783.91	12756.6	300	7735.24	6679.78	3046.21	2152.12	-1.46
39	792.71	12615.0	400	7676.85	6821.39	3187.83	2293.73	140.15
40	793.7	12599.2	700	7892.58	6837.13	3203.56	2309.47	155.88
	794.32	12589.4	2000	7902.42	6846.96	3213.40	2319.30	165.72
41	808.25	12372.4	2000	8119.39	7063.94	3430.37	2536.27	382.69
42	811.85	12317.5	1000	8174.26	7118.80	3485.23	2591.14	437.56
43	812.89	12301.8	600	8190.02	7134.56	3500.99	2606.90	453.31
44	813.64	12290.4	3000	8201.36	7145.90	3512.33	2618.24	464.65
45	825.94	12107.4	2500	8384.39	7328.93	3695.36	2801.27	647.69
46	826.61	12097.6	2500	8394.20	7338.74	3705.18	2811.08	657.50
	826.71	12096.1	800	8395.66	7340.21	3706.64	2812.54	658.96
47	830.03	12047.8	6000	8444.05	7388.59	3755.02	2860.93	707.34
48	836.57	11953.6	1500	8538.23	7482.77	3849.21	2955.11	801.53
49	837.76	11936.6	8000	8555.21	7499.75	3866.19	2972.09	818.51
50	841.72	11880.4	1000	8611.37	7555.91	3922.35	3028.25	874.67
	841.84	11878.7	4000	8613.06	7557.60	3924.04	3029.94	876.36
51	846.34	11815.6	1500	8676.22	7620.76	3987.20	3093.10	939.52
52	848.44	11786.3	800	8705.47	7650.01	4016.44	3122.35	968.76
53	849.54	11771.1	5000	8720.73	7665.27	4031.71	3137.61	984.03
54	854.47	11703.2	600	8788.64	7733.18	4099.62	3205.52	1051.94
55	857.14	11666.7	1000	8825.10	7769.64	4136.08	3241.98	1088.40
56	859.13	11639.7	4000	8852.12	7796.66	4163.10	3269.00	1115.42
57	863.46	11581.3	6000	8910.49	7855.03	4221.47	3327.37	1173.79
58	864.71	11564.6	3000	8927.23	7871.78	4238.21	3344.11	1190.53
59	865.44	11554.8	15000	8936.99	7881.53	4247.97	3353.87	1200.29
	865.55	11553.3	4000	8938.46	7883.00	4249.43	3355.34	1201.75
60	867.95	11521.4	5000	8970.40	7914.94	4281.38	3387.28	1233.70
	868.19	11518.2	5000	8973.59	7918.13	4284.57	3390.47	1236.89
61	870.41	11488.8	2000	9002.96	7947.51	4313.94	3419.85	1266.26
62	877.17	11400.3	4000	9091.50	8036.05	4402.48	3508.39	1354.80
63	878.06	11388.7	12000	9103.06	8047.60	4414.04	3519.94	1366.36
	878.38	11384.6	10000	9107.21	8051.75	4418.19	3524.09	1370.51
64	885.39	11294.5	7000	9197.35	8141.89	4508.32	3614.23	1460.64
65	886.53	11279.9	1000	9211.87	8156.41	4522.85	3628.75	1475.17
	886.57	11279.4	1000	9212.36	8156.92	4523.36	3629.26	1475.68
66	891.95	11211.4	3000	9280.41	8224.96	4591.39	3697.29	1543.71
67	898.86	11125.2	2000	9366.60	9311.14	4677.58	3783.48	1629.90
68	914.87	10930.5	6000	9561.29	8505.83	4872.27	3978.17	1824.59
69	920.18	10867.4	6000	9624.36	8568.91	4935.34	4041.25	1887.66
70	922.01	10845.9	4000	9645.93	8590.48	4956.91	4062.81	1909.23
	922.16	10844.1	2000	9647.70	8592.24	4958.68	4064.58	1911.00
	922.67	10838.1	2000	9653.69	8598.23	4964.67	4070.57	1916.99
71	927.55	10781.1	1000	9710.71	8655.26	5021.69	4127.59	1974.01
72	930.09	10751.6	6000	9740.16	8684.70	5051.13	4157.04	2003.45

(Continued)

Wave length (nm)	Wave number (cm <sup>-1</sup> )	Peak Height	Wave Number Shift Relative to the Laser Lines (cm <sup>-1</sup> )					
			488.0 nm	514.5 nm	632.8 nm	670.75 nm	784 nm	
73	931.06	10740.4	1500	9751.36	8695.90	5062.33	4168.24	2014.66
74	931.39	10736.6	3000	9755.16	8699.71	5066.14	4172.04	2018.46
75	932.65	10722.1	6000	9769.67	8714.21	5080.65	4186.55	2032.97
76	937.33	10668.6	2000	9823.20	8767.74	5134.18	4240.08	2086.50
77	942.54	10609.6	5000	9882.17	8826.72	5193.15	4299.06	2145.47
78	945.92	10571.7	3000	9920.08	8864.63	5231.06	4336.97	2183.38
79	948.67	10541.1	5000	9950.73	8895.27	5261.71	4367.61	2214.03
80	953.42	10488.6	5000	10003.25	8947.79	5314.22	4420.13	2266.55
81	954.74	10474.1	5000	10017.75	8962.29	5328.73	4434.63	2281.05
82	966.54	10346.2	1000	10145.62	9090.16	5456.60	4562.50	2408.92
83	1029.54	9713.1	800	10778.73	9723.27	6089.71	5195.61	3042.03
84	1056.24	9467.5	2000	11024.26	9968.80	6335.24	5441.14	3287.56
85	1079.81	9260.9	1500	11230.91	10175.46	6541.89	5647.80	3494.21
86	1084.45	9221.3	2000	11270.54	10215.08	6581.52	5687.42	3533.84
87	1114.3	8974.2	3000	11517.56	10462.10	6828.54	5934.44	3780.86
88	1117.75	8946.5	3500	11545.26	10489.80	6856.24	5962.14	3808.56
89	1139.04	8779.3	1600	11712.48	10657.02	7023.46	6129.36	3975.78
90	1140.91	8764.9	1100	11726.87	10671.41	7037.85	6143.75	3990.17
	1152.27	8678.5	3000	11813.28	10757.82	7124.26	6230.16	4076.58
	1152.5	8676.8	1500	11815.01	10759.56	7125.99	6231.89	4078.31
91	1153.63	8668.3	950	11823.51	10768.06	7134.49	6240.39	4086.81
92	1160.15	8619.6	500	11872.23	10816.77	7183.21	6289.11	4135.53
	1161.41	8610.2	1200	11881.58	10826.12	7192.56	6298.46	4144.88
93	1168.8	8555.8	300	11936.02	10880.56	7247.00	6352.90	4199.32
94	1176.68	8498.5	2000	11993.32	10937.86	7304.29	6410.20	4253.61
95	1178.9	8482.5	1500	12009.32	10953.86	7320.30	6426.20	4272.63

# Appendix III

## Raman Tensors

### III.1 Raman Tensors and Symmetric Attributes [1]

Crystal system	Direction of principal axis	Point Groups		Raman Tensors
		International notation	Schoenflies notation	
<i>Uniaxial Crystal</i>				
Triclinic system	1 — C <sub>1</sub>			$\begin{pmatrix} a & d & e \\ d & b & f \\ e & f & c \end{pmatrix}$
Monoclinic system	2 m 2/m	C <sub>2</sub> C <sub>1h</sub> C <sub>2h</sub>		$\begin{pmatrix} a & d & 0 \\ d & b & 0 \\ 0 & 0 & c \end{pmatrix} \begin{pmatrix} 0 & 0 & e \\ 0 & 0 & f \\ e & f & 0 \end{pmatrix}$
Rhombic system	x  C <sub>2y</sub> z  C <sub>2z</sub>	222 mm2 mmm	D <sub>2</sub> C <sub>2v</sub> D <sub>2h</sub>	$\begin{pmatrix} a & 0 & 0 \\ 0 & b & 0 \\ 0 & 0 & c \end{pmatrix} \begin{pmatrix} 0 & 0 & d \\ d & 0 & 0 \\ 0 & 0 & 0 \end{pmatrix} \begin{pmatrix} 0 & 0 & e \\ 0 & 0 & 0 \\ e & 0 & 0 \end{pmatrix} \begin{pmatrix} 0 & 0 & 0 \\ 0 & 0 & f \\ 0 & f & 0 \end{pmatrix}$
	z  C <sub>2y</sub> z  C <sub>2z</sub>			$\begin{pmatrix} a & \Gamma_1 & B & \Gamma_2 \\ \Gamma_1 & \Gamma_2 & A'' & \Gamma_2 \\ B_g & A'' & \Gamma_2 & \Gamma_2^+ \\ A_g & \Gamma_1^+ & \Gamma_1^+ & \Gamma_2^+ \end{pmatrix}$

(continued)

(Continued)

Crystal system	Direction of principal axis	Point Groups		Raman Tensors
		International notation	Schoenflies notation	
Biaxial Crystal				
Trigonal system	$\begin{array}{ c} z \\ \hline z \\ z \end{array} \begin{array}{ c} C_3 \\ \hline C_3 \\ C_3 \end{array}$	3 $\bar{3}$ $\bar{3}$	$C_3$ $\bar{C}_3$ $\bar{C}_3$	$\begin{pmatrix} a & c & 0 \\ -c & a & 0 \\ 0 & 0 & b \end{pmatrix} \begin{pmatrix} d & e & f \\ e & -d & h \\ g & i & 0 \end{pmatrix} \begin{pmatrix} e & -d & -h \\ -d & -e & f \\ -i & g & 0 \end{pmatrix}$
Tetragonal system	$\begin{array}{ c} z \\ \hline z \\ z \end{array} \begin{array}{ c} C_3 \\ \hline C_3 \\ C_3 \\ x \perp \sigma_v \end{array}$	32 $\bar{3}m$ $\bar{3}m$ $3m$	$D_3$ $D_{2d}$ $C_{3v}$	$\begin{pmatrix} a & 0 & 0 \\ 0 & a & 0 \\ 0 & 0 & b \end{pmatrix} \begin{pmatrix} 0 & c & 0 \\ -c & 0 & 0 \\ 0 & 0 & 0 \end{pmatrix} \begin{pmatrix} 0 & d & 0 \\ d & 0 & e \\ 0 & f & 0 \end{pmatrix} \begin{pmatrix} d & 0 & -e \\ 0 & -d & 0 \\ -f & 0 & 0 \end{pmatrix}$
				$A_g \quad \Gamma_1^+ \quad E \quad \Gamma_2^++\Gamma_3^+$ $A_{1g} \quad \Gamma_1^+ \quad E_g \quad \Gamma_2^++\Gamma_3^+$ $A_1 \quad \Gamma_1 \quad A_2 \quad \Gamma_2 \quad E \quad \Gamma_3$ $A_{1g} \quad \Gamma_1^+ \quad A_{2g} \quad \Gamma_2^+ \quad E_g \quad \Gamma_3^+$
				$\begin{pmatrix} a & c & 0 \\ -c & a & 0 \\ 0 & 0 & b \end{pmatrix} \begin{pmatrix} d & e & 0 \\ e & -d & 0 \\ 0 & 0 & 0 \end{pmatrix} \begin{pmatrix} 0 & 0 & f \\ 0 & 0 & h \\ g & i & 0 \end{pmatrix} \begin{pmatrix} 0 & 0 & -h \\ 0 & 0 & f \\ -i & g & 0 \end{pmatrix}$
				$A_g \quad \Gamma_1^+ \quad B \quad \Gamma_2 \quad E \quad \Gamma_3+\Gamma_4$ $A_g \quad \Gamma_1^+ \quad B_g \quad \Gamma_2^+ \quad E_g \quad \Gamma_3^++\Gamma_4^+$

$z  C_4$	$x  \sigma_v$	$4mm$	$C_{4h}$	$\begin{pmatrix} a & 0 & 0 \\ 0 & a & 0 \\ 0 & 0 & b \end{pmatrix} \begin{pmatrix} 0 & c & 0 \\ -c & 0 & 0 \\ 0 & 0 & 0 \end{pmatrix} \begin{pmatrix} d & 0 & 0 \\ 0 & -d & 0 \\ 0 & 0 & 0 \end{pmatrix} \begin{pmatrix} 0 & e & 0 \\ e & 0 & 0 \\ 0 & 0 & 0 \end{pmatrix}$
$z  C_3$	$x  C_2'$	$422$	$D_4$	$\begin{pmatrix} 0 & 0 & f \\ g & 0 & 0 \\ 0 & g & 0 \end{pmatrix}$
$z  S_4$	$x  C_2'$	$\bar{4}2m$	$D_{2d}$	$\begin{pmatrix} 0 & 0 & f \\ 0 & 0 & 0 \\ 0 & 0 & f \end{pmatrix}$
$z  C_4$	$x  C_2'$	$4/mmm$	$D_{4h}$	$\begin{pmatrix} 0 & 0 & 0 \\ 0 & 0 & 0 \\ 0 & 0 & f \end{pmatrix}$
Hexagonal system		$A_1$	$\Gamma_1$	$\begin{pmatrix} A_1 & \Gamma_1 & \Gamma_2 & B_1 & \Gamma_3 & B_2 & \Gamma_4 & E & \Gamma_5 \\ A_{1g} & \Gamma_1^+ & A_{2g} & \Gamma_2^+ & B_{1g} & \Gamma_3^+ & B_{2g} & \Gamma_4^+ & E_g & \Gamma_5^+ \end{pmatrix}$
Hexagonal system		$A_1$	$\Gamma_1$	$\begin{pmatrix} a & c & 0 \\ -c & a & 0 \\ 0 & 0 & b \end{pmatrix} \begin{pmatrix} 0 & 0 & d \\ 0 & 0 & f \\ e & g & 0 \end{pmatrix} \begin{pmatrix} 0 & 0 & -f \\ 0 & 0 & d \\ -g & e & 0 \end{pmatrix} \begin{pmatrix} i & h & 0 \\ h & -i & 0 \\ 0 & 0 & 0 \end{pmatrix}$
Hexagonal system		$A'$	$\Gamma_1$	$\begin{pmatrix} h & -i & 0 \\ -i & -h & 0 \\ 0 & 0 & 0 \end{pmatrix}$
Hexagonal system		$A'$	$\Gamma_1$	$\begin{pmatrix} \Gamma_1 & \Gamma_2 & \Gamma_1 & \Gamma_5 + \Gamma_6 & E_1 & \Gamma_2 + \Gamma_3 \\ \Gamma_1' & \Gamma_2'' & \Gamma_1'' & \Gamma_5 + \Gamma_6 & E_2 & \Gamma_2 + \Gamma_3 \\ A_g & \Gamma_1^+ & E_{1g} & \Gamma_5^+ + \Gamma_6^+ & E_{2g} & \Gamma_2^+ + \Gamma_3^+ \end{pmatrix}$
Hexagonal system		$A'$	$\Gamma_1$	$\begin{pmatrix} a & 0 & 0 \\ 0 & a & 0 \\ 0 & 0 & b \end{pmatrix} \begin{pmatrix} 0 & 0 & 0 \\ 0 & 0 & c \\ 0 & c & 0 \end{pmatrix} \begin{pmatrix} 0 & 0 & -c \\ 0 & 0 & 0 \\ -c & 0 & 0 \end{pmatrix} \begin{pmatrix} 0 & 0 & -d \\ -d & 0 & 0 \\ 0 & 0 & 0 \end{pmatrix}$
Hexagonal system		$A_1$	$\Gamma_1$	$\begin{pmatrix} d & 0 & 0 \\ 0 & -d & 0 \\ 0 & 0 & 0 \end{pmatrix}$
Hexagonal system		$A_1$	$\Gamma_1$	$\begin{pmatrix} A_2 & \Gamma_2 & E_1 & \Gamma_5 & E_1 & \Gamma_6 \\ A_2' & \Gamma_2' & E'' & \Gamma_5' & E' & \Gamma_6' \\ A_{1g} & \Gamma_1^+ & A_{2g} & \Gamma_2^+ & E_{1g} & \Gamma_5^+ \\ A_{2g} & \Gamma_2^+ & A_{2g} & \Gamma_5^+ & E_{2g} & \Gamma_6^+ \end{pmatrix}$

(continued)

(Continued)

Crystal system	Direction of principal axis	Point Groups		Raman Tensors
		International notation	Schoenflies notation	
<i>Isotropic Crystal</i>				
Cubic system	$x \parallel C_2^x y \parallel C_2^y z \parallel C_2^z$	$23$ $m3$	$T$ $T_h$	$\begin{pmatrix} a & 0 & 0 \\ 0 & a & 0 \\ 0 & 0 & a \end{pmatrix} \begin{pmatrix} b & 0 & 0 \\ 0 & b & 0 \\ 0 & 0 & -2b \end{pmatrix} \begin{pmatrix} -\sqrt{3}b & 0 & 0 \\ 0 & \sqrt{3}b & 0 \\ 0 & 0 & 0 \end{pmatrix} \begin{pmatrix} 0 & 0 & 0 \\ 0 & 0 & c \\ 0 & d & 0 \end{pmatrix}$
	$x \parallel C_4^x y \parallel C_4^y z \parallel C_4^z$			$\begin{pmatrix} 0 & 0 & c \\ 0 & 0 & 0 \\ d & 0 & 0 \end{pmatrix} \begin{pmatrix} 0 & c & 0 \\ d & 0 & 0 \\ 0 & 0 & 0 \end{pmatrix}$
	$x \parallel C_4^x y \parallel C_4^y z \parallel C_4^z$			$\begin{pmatrix} A & \Gamma_1 & E \\ A_g & \Gamma_1^+ & E_g \end{pmatrix} \begin{pmatrix} b & 0 & 0 \\ 0 & b & 0 \\ 0 & 0 & a \end{pmatrix} \begin{pmatrix} -\sqrt{3}b & 0 & 0 \\ 0 & \sqrt{3}b & 0 \\ 0 & 0 & 0 \end{pmatrix} \begin{pmatrix} 0 & 0 & 0 \\ 0 & 0 & c \\ 0 & -c & 0 \end{pmatrix}$
	$x \parallel C_4^x y \parallel C_4^y z \parallel C_4^z$			$\begin{pmatrix} 0 & 0 & c \\ 0 & 0 & 0 \\ -c & 0 & 0 \end{pmatrix} \begin{pmatrix} 0 & c & 0 \\ -c & 0 & 0 \\ 0 & 0 & 0 \end{pmatrix} \begin{pmatrix} 0 & 0 & 0 \\ d & 0 & 0 \\ 0 & d & 0 \end{pmatrix}$
	$A_l$ $A_{1g}$	$432$ $\bar{4}3m$ $m3m$	$O$ $T_d$ $O_h$	$\begin{pmatrix} 0 & 0 & d \\ 0 & 0 & 0 \\ d & 0 & 0 \end{pmatrix} \begin{pmatrix} 0 & d & 0 \\ d & 0 & 0 \\ 0 & 0 & 0 \end{pmatrix}$
				$\begin{pmatrix} A_l & \Gamma_1 & E \\ A_{1g} & \Gamma_1^+ & E_g \end{pmatrix} \begin{pmatrix} T_l & \Gamma_4 \\ T_{1g} & \Gamma_4^+ \\ T_{2g} & \Gamma_5^+ \end{pmatrix}$

## III.2 Applications of Raman Tensors

### III.2.1 For Differential Scattering Cross Section (DSCS)

DSCS is described by the equation  $d\sigma/d\Omega \approx |e_i^s x_{ij} e_j^i|^2$ , in which  $e_i^s$  and  $e_j^i$  label the polarizing directions of the scattered and incident light field along with  $i$  and  $j$ , respectively, and  $x_{ij}$  expresses the  $i$  and  $j$  components of Raman tensors, where  $i$  and  $j$  are components of Cartesian coordinates  $x$ ,  $y$ , and  $z$ .

Under the right-angle scattering configuration, as shown in Figure III.1, the DSCS,  $d\sigma/d\Omega$ , expressed by Raman tensors are illustrated as

#### 1. For Representative Point Groups

##### (1) Orthorhombic Point Groups $D_2$

$$A(\Gamma_1) : \begin{pmatrix} 0 \\ 0 \\ 1 \end{pmatrix} \begin{pmatrix} a & 0 & 0 \\ 0 & b & 0 \\ 0 & 0 & c \end{pmatrix} \begin{pmatrix} 0 \\ 0 \\ 1 \end{pmatrix} = (0, 0, c) \cdot (0, 0, 1) = c \rightarrow \frac{d\sigma}{d\Omega} \sim C^2$$

$$B_2(\Gamma_2) : \begin{pmatrix} 0 \\ 0 \\ 1 \end{pmatrix} \begin{pmatrix} f \\ g \end{pmatrix} \begin{pmatrix} 0 \\ 0 \\ 1 \end{pmatrix} = (f, 0, 0) \cdot (0, 0, 1) = 0$$

$$B_1(\Gamma_3) : \begin{pmatrix} 0 \\ 0 \\ 1 \end{pmatrix} \begin{pmatrix} d \\ e \end{pmatrix} \begin{pmatrix} 0 \\ 0 \\ 1 \end{pmatrix} = 0$$

$$B_1(\Gamma_3) : \begin{pmatrix} 0 \\ 1 \\ 0 \end{pmatrix} \begin{pmatrix} d \\ e \end{pmatrix} \begin{pmatrix} 1 \\ 0 \\ 0 \end{pmatrix} = (0, e, 0) \cdot (0, 1, 0) = e \rightarrow \frac{d\sigma}{d\Omega} \sim e^2$$

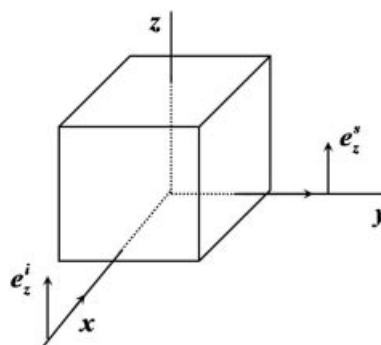


**Figure III.1** Right-angle scattering geometric configuration

(2) The Triangle Lattice  $D_{4h}$ : Rutile Titania  $\text{TiO}_2$ 

$$A_{01}(\Gamma_{1g}^+) : \begin{pmatrix} 0 \\ 0 \\ 1 \end{pmatrix} \begin{pmatrix} a & & \\ & a & \\ & & b \end{pmatrix} \begin{pmatrix} 0 \\ 0 \\ 1 \end{pmatrix} = (0, 0, 1) \cdot (0, 0, b) = b \rightarrow \frac{d\sigma}{d\Omega} \sim b^2$$

$$E_g(\Gamma_5^+) : \begin{pmatrix} 0 \\ 0 \\ 1 \end{pmatrix} \begin{pmatrix} & f \\ g & \end{pmatrix} \begin{pmatrix} 1 \\ 0 \\ 0 \end{pmatrix} = (1, 0, 0) \cdot (f, 0, 0) = f \rightarrow \frac{d\sigma}{d\Omega} \sim f^2$$

$$A_{1g}(\Gamma_1^+) : \begin{pmatrix} 1 \\ 0 \\ 0 \end{pmatrix} \begin{pmatrix} a & & \\ & a & \\ & & b \end{pmatrix} \begin{pmatrix} 0 \\ 0 \\ 1 \end{pmatrix} = (0, 0, 1) \cdot (a, 0, 0) = a \rightarrow \frac{d\sigma}{d\Omega} \sim a^2$$

$$B_{1g}(\Gamma_3^+) : \begin{pmatrix} 1 \\ 0 \\ 0 \end{pmatrix} \begin{pmatrix} d & & \\ & -d & \\ & & 0 \end{pmatrix} \begin{pmatrix} 1 \\ 0 \\ 0 \end{pmatrix} = (1, 0, 0) \cdot (d, 0, 0) = d \rightarrow \frac{d\sigma}{d\Omega} \sim d^2$$

$$B_{2g}(\Gamma_4^+) : \begin{pmatrix} 0 \\ 1 \\ 0 \end{pmatrix} \begin{pmatrix} & e \\ e & \end{pmatrix} \begin{pmatrix} 1 \\ 0 \\ 0 \end{pmatrix} = (0, 1, 0) \cdot (0, e, 0) = e \rightarrow \frac{d\sigma}{d\Omega} \sim e^2$$

 (3) The Cubic Lattice  $O_h$ :

## (1) Diamond-Structure Si (inversion symmetry)

$$A_1(\Gamma_1^+) : \begin{pmatrix} 1 \\ -1 \\ 0 \end{pmatrix} \begin{pmatrix} a & & \\ & a & \\ & & a \end{pmatrix} \begin{pmatrix} 1 \\ 1 \\ 0 \end{pmatrix} = 0$$

$$3E(\Gamma_3^+) : \begin{pmatrix} 1 \\ -1 \\ 0 \end{pmatrix} \begin{pmatrix} -\sqrt{3}b & & \\ & \sqrt{3}b & \\ & & 0 \end{pmatrix} \begin{pmatrix} 1 \\ 1 \\ 0 \end{pmatrix} = -\sqrt{3}b \rightarrow \frac{d\sigma}{d\Omega} \sim 3b^2$$

## (2) Marmatite-Structure ZnS, GaP, GaAs (anti-inversion symmetry)

$$A_1(\Gamma_1) : \begin{pmatrix} 1 \\ 1 \\ 1 \end{pmatrix} \begin{pmatrix} a & & \\ & a & \\ & & a \end{pmatrix} \begin{pmatrix} 1 \\ 1 \\ 1 \end{pmatrix} = a \rightarrow \frac{d\sigma}{d\Omega} \sim a^2$$

$$\begin{pmatrix} 1 \\ 1 \\ 1 \end{pmatrix} \begin{pmatrix} & d \\ d & \end{pmatrix} \begin{pmatrix} 1 \\ 1 \\ 1 \end{pmatrix} = \frac{1}{3}(d+d) \rightarrow \frac{4}{3}d^2$$

$$T_2(\Gamma_5) : \begin{pmatrix} 1 \\ 1 \\ 1 \end{pmatrix} \begin{pmatrix} d \\ d \\ d \end{pmatrix} \begin{pmatrix} 1 \\ 1 \\ 1 \end{pmatrix} \rightarrow \frac{4}{3}d^2 \quad \left\} \frac{d\sigma}{d\Omega}|_{total} = \frac{4}{3}d^2 \right.$$

$$\begin{pmatrix} 1 \\ 1 \\ 1 \end{pmatrix} \begin{pmatrix} d & d \\ d & d \end{pmatrix} \begin{pmatrix} 1 \\ 1 \\ 1 \end{pmatrix} \rightarrow \frac{4}{3}d^2$$

## 2. For Some Representative Semiconductor [5]

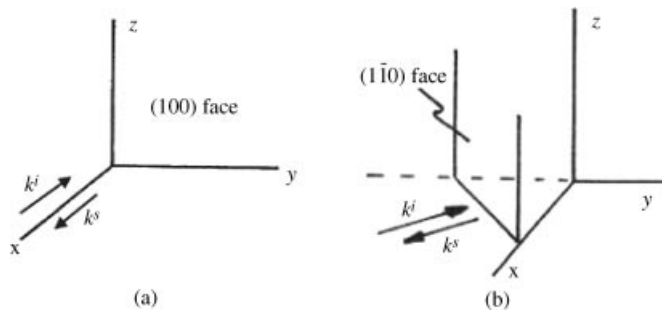
	Scattering Cross Section	Polarizing Direction of Incident Light	Polarizing Direction of Scattered Light	DSCS
Si	[001]	(100)	(100)	$a^2 + 4b^2s$
	[001]	(100)	(010)	$d^2$
	[001]	(110)	(110)	$3b^2$
	[001]	(110)	(110)	$a^2 + b^2 + d^2$
GaP	[100]	(100)	(100)	$a^2 + 4b^2$
	[100]	(100)	(011)	$d^2$
	[111]	(111)	(111)	$a^2 + \frac{4}{3}d^2$
	[111]	(111)	( $\bar{2}$ 11)	$2b^2 + \frac{1}{3}d^2$
	[110]	(110)	(1 $\bar{1}$ 0)	$a^2 + b^2 + d^2$
	[110]	(110)	(1 $\bar{1}$ 0)	$b^2 + \frac{2}{3}d^2$

### III.2.2 For Polarization Selection Rules

#### 1. Zinc blende Structure

Only  $\Gamma_5$  optical phonon is Raman active in the zinc blende structure. Since different phonon displacements  $\mathbf{u}$  correspond to different components of Raman Tensors, we have

$$\begin{aligned} \mathbf{u}/x &\rightarrow \Gamma_{5,x} \begin{pmatrix} \cdot & \cdot & \cdot \\ \cdot & \cdot & d \\ \cdot & d & \cdot \end{pmatrix} \\ \mathbf{u}/y &\rightarrow \Gamma_{5,y} \begin{pmatrix} \cdot & \cdot & \cdot \\ \cdot & \cdot & d \\ d & \cdot & \cdot \end{pmatrix} \\ \mathbf{u}/z &\rightarrow \Gamma_{5,z} \begin{pmatrix} \cdot & d & \cdot \\ d & \cdot & \cdot \\ \cdot & \cdot & \cdot \end{pmatrix} \\ \mathbf{u}/(x, y, 0) &\rightarrow \frac{1}{\sqrt{2}}(\Gamma_{5,x} + \Gamma_{5,y}) \end{aligned}$$

**Figure III.2** Back Scattering Geometric Geometry

Under the back scattering configuration shown in Figure III.2a, when we select

$$\begin{aligned} \mathbf{e}^i &= (0, 1, 0) \\ \mathbf{e}^s &= (0, 0, 1) \end{aligned}$$

only  $\Gamma_{5,x}$  of the displacement  $\mathbf{u}/(x, y, 0)$  has a contribution to scattering and LO phonon is one with its displacement  $\mathbf{u}$  parallel to wave vector  $\mathbf{k}$ , i.e.,  $\mathbf{u}/\parallel \mathbf{k}$ , therefore under the above configuration, only LO phonon can be observed.

With the back scattering geometric disposal shown in Figure III.2 (a), only  $\Gamma_{5,x}$ , a component of the displacement  $\mathbf{u}/(x, y, 0)$  contributes to scattering. The LO phonon is a component of displacement  $\mathbf{u}$ , which is parallel to wave vector  $\mathbf{k}$ , in other words, the phonon of  $\mathbf{u}/\parallel \mathbf{k}$ . So we can only observe the LO phonon with such a disposal.

With the back scattering configuration, as shown in Figure III.2b, if we choose

$$\begin{aligned} \mathbf{e}^i &= (0, 0, 1) \\ \mathbf{e}^s &= (1, 1, 0) \end{aligned}$$

only  $\Gamma_{5,x}$  and  $\Gamma_{5,y}$  of the displacement  $\mathbf{u}/(x, y, 0)$  contributes to the scattering. Since the TO phonon is one with the component of displacement  $\mathbf{u}$  perpendicular to wave vector  $\mathbf{k}$ , i.e., the phonon of  $\mathbf{u} \perp \mathbf{k}$ . Therefore, we can observe only the TO phonon scattering at the above configuration.

At the back scattering configuration, as shown in Figure III.2b, the polarization selection rules for zinc blende crystal are listed below:

Crystal Faces	Polarizing Direction of Incident Light	Polarizing Direction of Scattered Light	Component of Raman Tensors
(100)	(0-1-1)	(0-1-1)	$a^2 + b^2 + d^2 (LO)$
(100)	(011)	(01-1)	$3b^2$ (Forbidden)
(100)	(010)	(001)	$d^2 (LO)$
(100)	(010)	(010)	$a^2 + 4b^2$ (Forbidden)
(1-10)	(110)	(110)	$a^2 + b^2 + d^2 (TO)$
(1-10)	(001)	(001)	$a^2 + 4b^2$ (Forbidden)
(1-10)	(001)	(110)	$d^2 (TO)$
(1-10)	(111)	(111)	$a^2 + \frac{4}{3}d^2$ (TO)

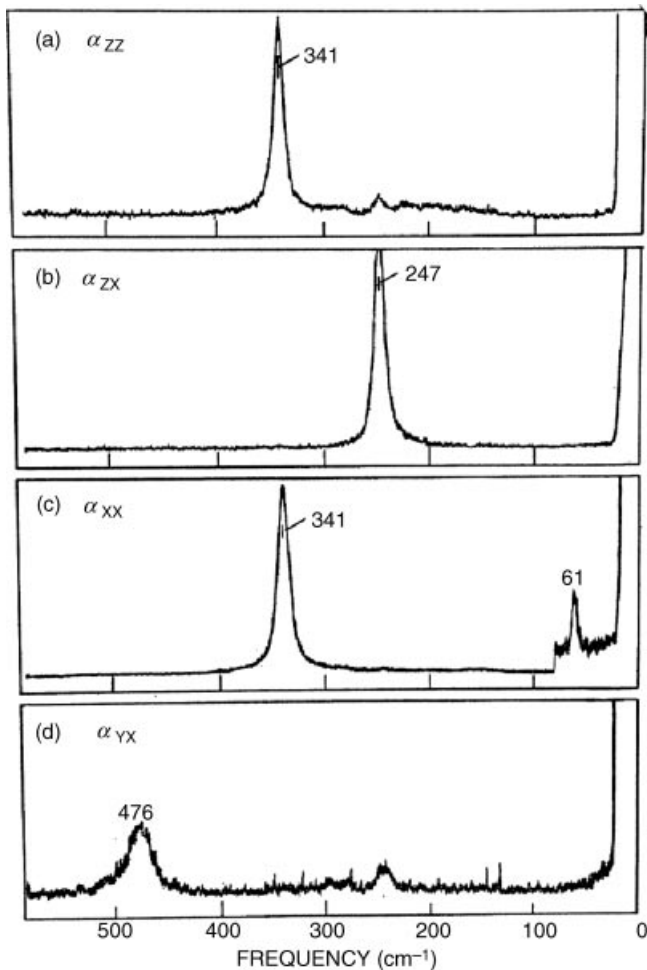


**Figure III.3** Raman spectra of  $\text{MnF}_2$  crystal: (a)  $\alpha_{zz}$  component showing the  $A_{1g}$  phonon at  $341 \text{ cm}^{-1}$  and a very weak two-phonon band; (b)  $\alpha_{zx}$  component showing the  $E_g$  phonon at  $247 \text{ cm}^{-1}$ ; (c)  $\alpha_{xx}$  component showing the  $A_{1g}$  and  $B_{1g}$  phonons at  $341$  and  $61 \text{ cm}^{-1}$ , respectively. The gain is increased by a factor of 10 to show the  $B_{1g}$  phonon clearly; and (d)  $\alpha_{yx}$  component showing the  $B_{2g}$  phonon at  $476 \text{ cm}^{-1}$  and a leakage of the much stronger  $E_g$  phonon [6]

## 2. Rutile Structure

As an example to show the manifesting of polarization selection rules on Raman spectra, the first-order Raman spectra  $\text{MnF}_2$  are shown in Figure III.3. The figures indicate that four Raman-active phonon frequencies of  $A_{1g}$ ,  $B_{1g}$ ,  $B_{2g}$ , and  $E_g$  symmetries modes predicted by group theory have been measured in the corresponding geometric configurations.

# Appendix IV

## Constitution, Polarity, and Symmetry Structure of Crystals

### IV.1 Constitution, Polarity, and Crystal Structure of Crystals

Condensed matter is constituted by atoms and molecules through the interactions between them. Condensed matter constituted through different types of interactions process different physical properties. Due to the different arrangement in the geometric space of constituted atoms, ions, and molecules, condensed matter is classified into solid, liquid, and liquid crystal. A solid is classified further into crystal and amorphous, based on whether there is along-range order.

The constitution of condensed matter is by means of the bonding mode of atoms or molecules due to the “electrical” interaction of electrons outside the atomic nucleus. The bonds can be classified into five kinds: ionic, covalent, metallic, hydrogen, and van der Waals bonds. Correspondingly, they induce the ion crystals, covalent crystals, metallic crystals, molecular crystal, and hydrogen-bond crystals with different crystal structures and symmetries. The crystals related to semiconductors are mainly in the following two categories.

#### IV.1.1 Polar Crystals/Ionic Crystals

The basic particles in ionic crystals are positive and negative ions. The Coulomb interaction between ions makes these particles constituting ionic crystals with the form of ionic bond, which are also known as the polar crystals. NaCl, MgO, CoCl, LiF, FeO, and so on, are all ionic crystals.

The crystal structures of ionic crystals have: the sodium chloride (face-centered cubic); cesium chloride (cubic); sphalerite (cubic, i.e., ZnS, SiC); wurtzite (hexagonal, i.e., ZnS, ZnO); fluorite (cubic, LiO<sub>2</sub>); and rutile (body-centered cubic, CdSe, GeO<sub>2</sub>) structures.

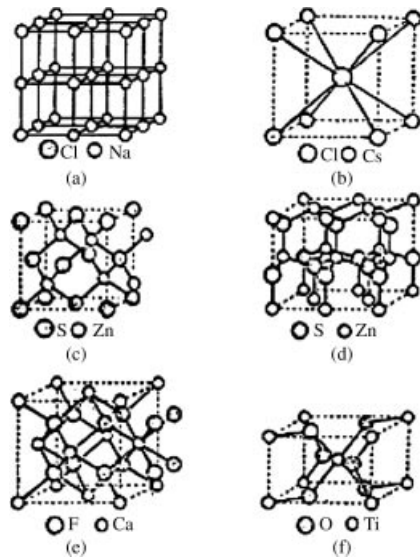


**Figure IV.1** Some typical crystal structures: (a) Sodium chloride; (b) Cesium chloride; (c) Sphalerite ( $ZnS$ ); (d) Wurtzite ( $ZnS$ ); (e) Fluorite ( $CaF_2$ ); and (f) Rutile ( $TiO_2$ ) [4]

#### IV.1.2 Covalent Crystals/Homopolar Crystals

The crystal constituted by covalent bonds is known as covalent crystal or homopolar crystal. However, when atoms A and B are the heterogeneous atoms, the forming covalent bonds often contain the ionic bond component and the crystal is the transition form of the covalent and ionic combination. Therefore, the pure covalent bond crystals have only diamond, Si, Ge, and gray Sn.

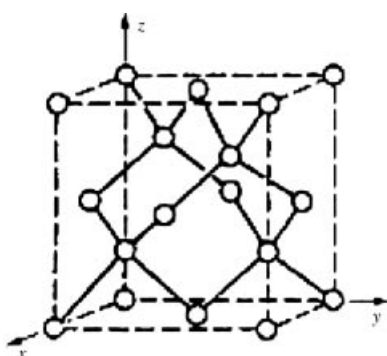


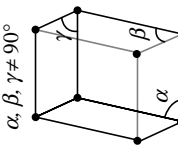
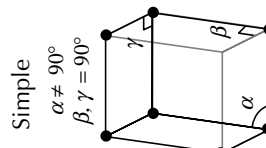
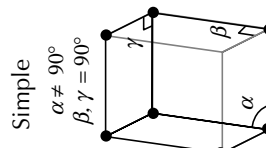
**Figure IV.2** Diamond crystal structure [7]

Usually, we introduce the term “ionicity,”  $f_i$ , to describe the ionic composition in the covalent bond constitution. Moreover, the effective ionic charge is used to represent the total effective ion charge  $q^*$  in components. The crystal structures of covalent crystals have: diamond (tetrahedron, i.e., diamond, Si) zinc blende; wurtzite (i.e., ZnS, ZnO, HgS, and CuCl); and silicate (i.e., quartz crystal) structures.

#### IV.1.3 Crystal Structure of Typical Semiconductors

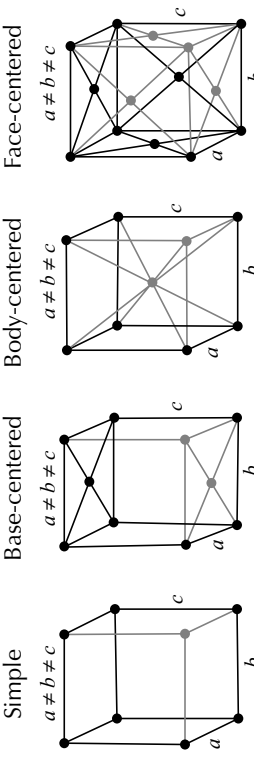
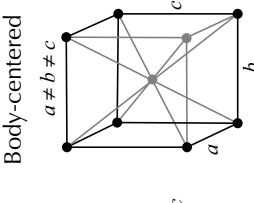
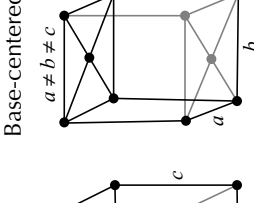
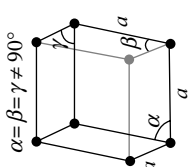
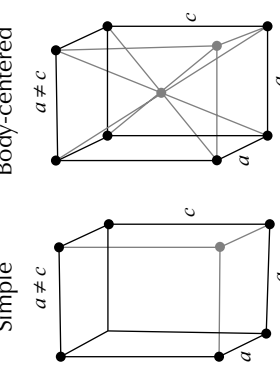
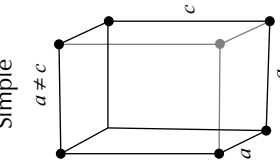
Crystal	Crystal Structure	Crystal	Crystal Structure
Diamond	Diamond	PbSe	Zinc blende (ZnS)
Si	Diamond	PbTe	Zinc blende (ZnS)
Ge	Diamond	AlN	Zinc blende (ZnS)
InAs	Zinc blende (ZnS)	GaN	Zinc blende (ZnS)
InSb	Zinc blende (ZnS)	InN	Zinc blende (ZnS)
SiC	Zinc blende (ZnS)	ZnO	Zinc blende (ZnS)
InP	Zinc blende (ZnS)	PbS	Zinc blende (ZnS)
AlAs	Zinc blende (ZnS)	MgO <sub>2</sub>	Rutile
AlP	Zinc blende (ZnS)	MnF <sub>2</sub>	Rutile
AlSb	Zinc blende (ZnS)	MnO <sub>2</sub>	Rutile
GaP	Zinc blende (ZnS)	SnO <sub>2</sub>	Rutile
GaAs	Zinc blende (ZnS)	GeO <sub>2</sub>	Rutile
GaSb	Zinc blende (ZnS)	ZnO <sub>2</sub>	Rutile
CdTe	Zinc blende (ZnS)	MnO <sub>2</sub>	Rutile
CdS	Zinc blende (ZnS)		

## IV.2 Syngony and its Basic Vector, Bravais Lattice, and Point Group Symmetry [7]

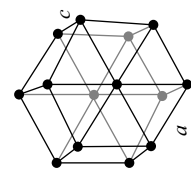
Syngony	Characteristics of Unit Cell Basic Vectors of $a_1, a_2, a_3$	Bravais Lattice	Point Group
Triclinic	$a_1 \neq a_2 \neq a_3$ <i>Inequality</i> of included angles $\alpha$ ( $a_1 \wedge a_2$ ), $\beta$ ( $a_2 \wedge a_3$ ) and $\gamma$ ( $a_3 \wedge a_1$ )		$C_1, C_{\bar{1}}$
Monoclinic	$a_1 \neq a_2 \neq a_3$ $a_2 \perp a_1, a_3$	 	$C_2, C_{1h}, C_{2h}$ $\alpha \neq 90^\circ$ $\beta, \gamma = 90^\circ$

(continued)

(Continued)

Syngony	Characteristics of Unit Cell Basic Vectors of $a_1, a_2, a_3$	Bravais Lattice	Point Group
Orthorhombic	$a_1 \neq a_2 \neq a_3$ $a_1, a_2, a_3$ are perpendicular to each other	 <p>Simple  <math>a \neq b \neq c</math></p>  <p>Face-centered  <math>a \neq b \neq c</math></p>  <p>Body-centered  <math>a \neq b \neq c</math></p>	$D_2, C_{2v}, C_{2h}$
Rhombohedral	$a_1 = a_2 = a_3$ $\alpha = \beta = \gamma \neq 90^\circ$	 <p><math>\alpha = \beta = \gamma \neq 90^\circ</math></p>	$C_3, C_{3i}, D_3, D_{3v}, D_{3d}$
Tetragonal	$a_1 = a_2 \neq a_3$ $\alpha = \beta = \gamma = 90^\circ$	 <p>Simple  <math>a \neq c</math></p>  <p>Body-centered  <math>a \neq c</math></p>	$C_4, C_{4h}, D_4, C_{4h},$ $D_{4h}, S_4, D_{2d}$

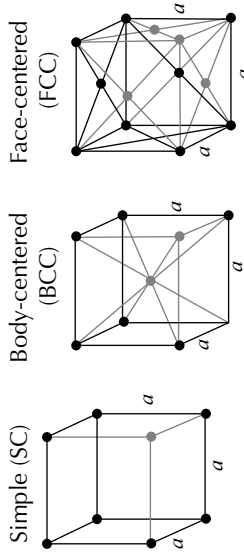
$C_6, C_{6h}, D_6, C_{3h},$   
 $C_{6v}, D_{3h}, D_{6h}$



Hexagonal  
 $a_1 = a_2 \neq a_3$   
 $a_3 \perp a_1, a_2$   
Included angle  $\alpha = 120^\circ$

Cubic  
 $a_1 = a_2 = a_3$   
 $\alpha = \beta = \gamma = 90^\circ$

$T, T_h, T_d, O, O_h$



# Appendix V

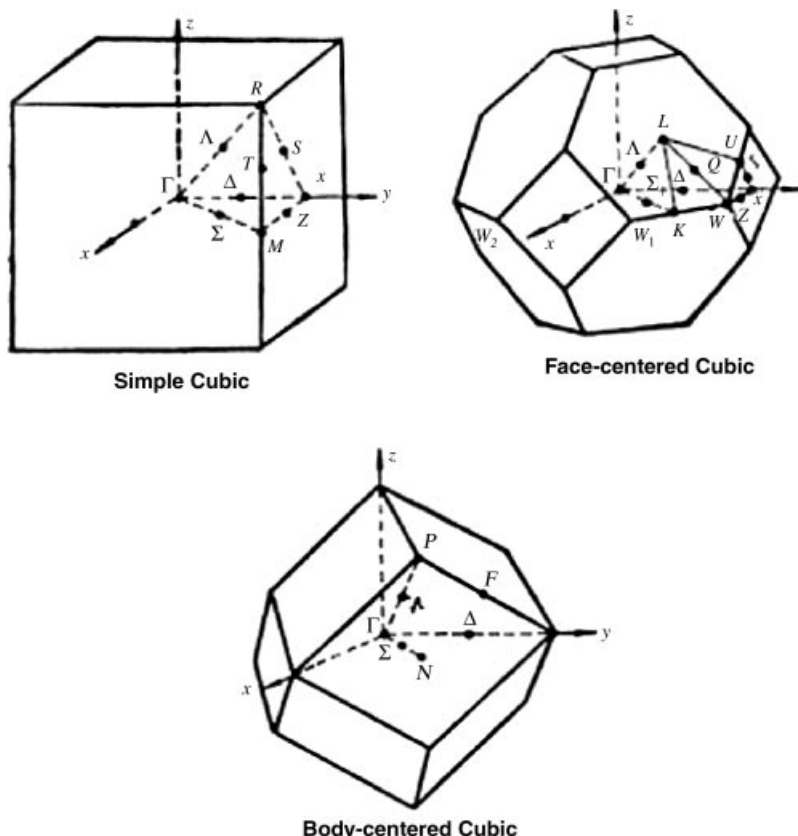
## Brillouin Zones, Vibration Modes, and Raman Spectra of Typical Ordinary and Semiconducting Crystals

### V.1 Brillouin Zones and Symmetrical Points of Cubic System [4]

Simple Cubic		Face-centered Cubic		Body-centered Cubic	
Symbol	Coordinate	Symbol	Coordinate	Symbol	Coordinate
$\Gamma$	(0, 0, 0)	$\Gamma$	(0, 0, 0)	$\Gamma$	(0, 0, 0)
$X$	$\frac{\pi}{a}(0, 1, 0)$	$X$	$\frac{2\pi}{a}(0, 1, 0)$	$H$	$\frac{2\pi}{a}(0, 1, 0)$
$R$	$\frac{\pi}{a}(1, 1, 1)$	$L$	$\frac{2\pi}{a}\left(\frac{1}{2}, \frac{1}{2}, \frac{1}{2}\right)$	$P$	$\frac{2\pi}{a}\left(\frac{1}{2}, \frac{1}{2}, \frac{1}{2}\right)$
$M$	$\frac{\pi}{a}(1, 1, 0)$	$K$	$\frac{2\pi}{a}\left(\frac{3}{4}, \frac{3}{4}, 0\right)$	$N$	$\frac{2\pi}{a}\left(\frac{1}{2}, \frac{1}{2}, 0\right)$
$\Delta$	$\frac{\pi}{a}(0, a, 0)$	$W$	$\frac{2\pi}{a}\left(\frac{1}{2}, 1, 0\right)$	$\Delta$	$\frac{2\pi}{a}(0, a, 0)$
$\Lambda$	$\frac{\pi}{a}(a, a, a)$	$U$	$\frac{2\pi}{a}\left(\frac{1}{4}, 1, \frac{1}{4}\right)$	$\Lambda$	$\frac{2\pi}{a}\left(\frac{a}{2}, \frac{a}{2}, \frac{a}{2}\right)$
$\Sigma$	$\frac{\pi}{a}(a, a, 0)$	$\Delta$	$\frac{2\pi}{a}(0, a, 0)$	$\Sigma$	$\frac{2\pi}{a}\left(\frac{a}{2}, \frac{a}{2}, 0\right)$

(Continued)

Simple Cubic		Face-centered Cubic		Body-centered Cubic	
Symbol	Coordinate	Symbol	Coordinate	Symbol	Coordinate
$T$	$\frac{\pi}{a}(1, 1, a)$	$\Lambda$	$\frac{2\pi}{a}\left(\frac{a}{2}, \frac{a}{2}, \frac{a}{2}\right)$		
$E$	$\frac{\pi}{a}(a, 1, 0)$	$\Sigma$	$\frac{2\pi}{a}\left(\frac{3}{4}a, \frac{3}{4}a, 0\right)$		
$S$	$\frac{\pi}{a}(a, 1, a)$	$Z$	$\frac{2\pi}{a}\left(\frac{a}{2}, 1, 0\right)$		
		$S$	$\frac{2\pi}{a}\left(\frac{a}{4}, 1, \frac{a}{4}\right)$		

Note:  $0 < a < 1$ **Figure V.1** Brillouin Zones in Cubic Syngony [4]

## V.2 Vibrational Modes and their Symmetries of Several Crystals [8]

Typical Crystals	Classification of Symmetry	Symmetry of Vibrational Modes			
		Acoustic	Optical (Raman-active)	Optical (Non Raman-active)	Other Crystals
NaNO <sub>2</sub>	<i>mm2</i>	C <sub>2v</sub>	$\Gamma_1 + \Gamma_2 + \Gamma_4$	$3\Gamma_1 + 3\Gamma_2 + \Gamma_3 + 2\Gamma_4$	CaMoO <sub>4</sub> , SrMoO <sub>4</sub>
CaWO <sub>4</sub>	4/ <i>m</i>	C <sub>4h</sub>	$\Gamma_1^- + (\Gamma_3^- + \Gamma_4)^*$	$2\Gamma_1^+ + 5\Gamma_2^+$ $+ 5(\Gamma_3^+ + \Gamma_4^+)$	
BaTiO <sub>3</sub>	<i>4mm</i>	C <sub>4v</sub>	$\Gamma_1 + \Gamma_5$	$3\Gamma_1 + \Gamma_3 + 4\Gamma_5$	
SrTiO <sub>3</sub>	4/ <i>mmm</i>	D <sub>4h</sub>	$\Gamma_2^- + \Gamma_5^-$	$\Gamma_1^+ + 2\Gamma_3^+ + \Gamma_4^+ + 3\Gamma_5^+$	
TiO <sub>2</sub>	4/ <i>mmm</i>	D <sub>4h</sub>	$\Gamma_2^- + \Gamma_5^-$	$2\Gamma_2^+ + \Gamma_1^- + 3\Gamma_2^-$ $+ \Gamma_4^- + 5\Gamma_5^-$	MnF <sub>2</sub> , FeF <sub>2</sub> , CoF <sub>2</sub>
SiO <sub>2</sub>	32	D <sub>3</sub>	$\Gamma_2^- + \Gamma_3^-$	$\Gamma_2^+ + \Gamma_3^+ + \Gamma_4^+ + \Gamma_5^+$ $4\Gamma_1 + 8\Gamma_3$	
$\alpha$ -quartz					
Bi	$\bar{3}m$	D <sub>3d</sub>	$\Gamma_2^- + \Gamma_3^-$	$\Gamma_1^+ + \Gamma_3^+$	As, Sb
LiI <sub>O<sub>3</sub></sub>	6	C <sub>6</sub>	$\Gamma_1 + (\Gamma_5 + \Gamma_6)$	$4\Gamma_1 + 5(\Gamma_2 + \Gamma_3)$ $+ 4(\Gamma_5 + \Gamma_6)$	
ZnS	<i>6mm</i>	C <sub>6v</sub>	$\Gamma_1 + \Gamma_5$	$\Gamma_1 + \Gamma_5 + 2\Gamma_6$	ZnO, CdS, BeO
Zn	6/ <i>mmm</i>	D <sub>6h</sub>	$\Gamma_2^- + \Gamma_5^-$	$\Gamma_3^+$	Be, Mg, Cd
ZnS	$\bar{4}3m$	T <sub>d</sub>	$\Gamma_5^-$	$\Gamma_6^+$	GaAs, GaP
CaTiO <sub>3</sub>	<i>m3m</i>	O <sub>h</sub>	$\Gamma_4^-$	$\Gamma_5^-$	BaTiO <sub>3</sub> , SrTiO <sub>3</sub>
CaF <sub>2</sub>	<i>m3m</i>	O <sub>h</sub>	$\Gamma_4^-$	$\Gamma_4^+$	SrF <sub>2</sub> , BaF <sub>2</sub> , AuAl <sub>2</sub>
Diamond	<i>m3m</i>	O <sub>h</sub>	$\Gamma_4^-$	$\Gamma_5^+$	Si, Ge
NaCl	<i>m3m</i>	O <sub>h</sub>	$\Gamma_4^-$	$\Gamma_4^-$	KBr, NaI
CsCl	<i>m3m</i>	O <sub>h</sub>	$\Gamma_4^-$	$\Gamma_4^-$	

\*Two modes in the brackets are degenerate ones.

### V.3 Structures, Symmetries, and Raman Spectra of Several Semiconducting Crystals

Semiconductor	Cubic				Hexagonal			Tetragonal
Point Group	Si	Diamond	SiC	GaAs	GaN	ZnO	CdSe	TiO <sub>2</sub>
Crystal Structure	<i>O<sub>h</sub></i>				<i>T<sub>d</sub></i>			
Lattice Constant <i>a</i>	Diamond 5.431 Å				Zinc Blend 4.36 Å			
Bravais Lattice	Face-centered Cubic		Wurtzite 5.65 Å		a = 3.186 Å	a = 3.249 Å	a = 4.30 Å	a = 3.785 Å
Atomic Number in Cell	2		c = 5.178 Å		c = 5.207 Å	c = 7.02 Å	c = 9.514 Å	
Symmetry of Raman Modes	<i>T<sub>2g</sub></i>		<i>T<sub>2</sub></i>		2 <i>A<sub>1</sub></i> + 2 <i>E<sub>1g</sub></i> + 2 <i>A<sub>2g</sub></i> + <i>B<sub>2g</sub></i>			6
Raman Frequencies (cm <sup>-1</sup> ) of vibrational modes	LO + TO: 520*	LO + TO: 1331	TO: 796 LO: 972	TO: 269 LO: 292	E <sub>2</sub> (L): 144.0* A <sub>1</sub> r: 531.8 E <sub>1</sub> r: 559.9 E <sub>2</sub> (H): 567.6 A <sub>1</sub> l: 734.0 E <sub>1</sub> l: 741.0	E <sub>2</sub> (L): 101 A <sub>1</sub> r: 380 E <sub>1</sub> r: 413 E <sub>2</sub> (H): 444 A <sub>1</sub> l: 579 E <sub>1</sub> l: 591	E <sub>2</sub> (L): 34.0 A <sub>1</sub> r: 169.1 E <sub>1</sub> r: 174.0 E <sub>2</sub> (H): 177.6 A <sub>1</sub> l: 213.0 E <sub>1</sub> l: 213.9	B <sub>1g</sub> : 143 E <sub>g</sub> : 450 A <sub>1g</sub> : 612 B <sub>2g</sub> : 826
Raman spectrogram	Figure V.2 (a) and (b)	Figure V.3 (a and (b))	Figure V.4	Figure V.5	Figure V.6	Figure V.7 (a) and (b)	Figure V.8 (a) and (b)	Figure V.9 (a) and (b)

\*Summation of two modes shows that these two modes are degenerate.

\*\*A<sub>1</sub>, E<sub>1</sub> are the polar optical vibration modes, E<sub>2</sub> is non-polar optical vibration mode.

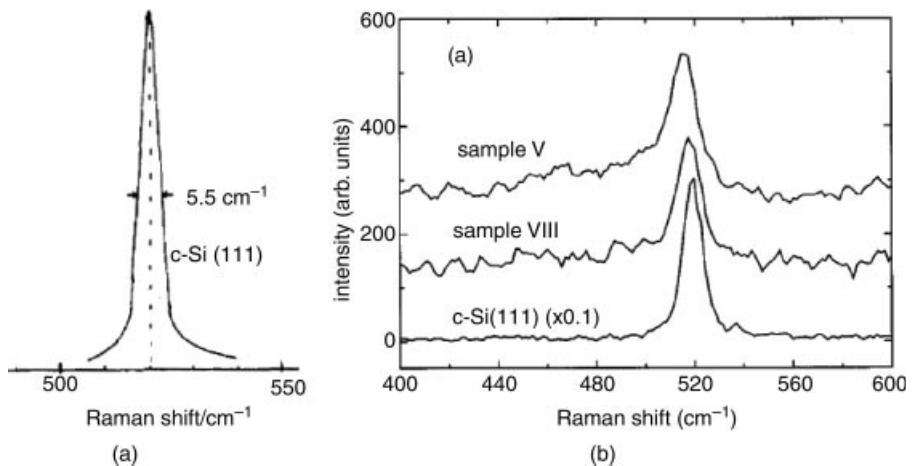


**Figure V.2** Raman spectra of (a) bulk-silicon [9] and (b) nano-silicon [10]. The nano-silicon samples are deposited on LiF and the sizes of samples V and VIII are 4.95 and 7.03 nm, respectively

The subscript “1” indicates that this vibration mode corresponds to the irreducible representation being symmetrical with the C<sub>3</sub>-axis of the vertical main axis. The polarized directions of A<sub>1</sub>-mode and E<sub>1</sub>-mode are parallel to the crystal axis and perpendicular to the plane including the crystal axis, respectively.

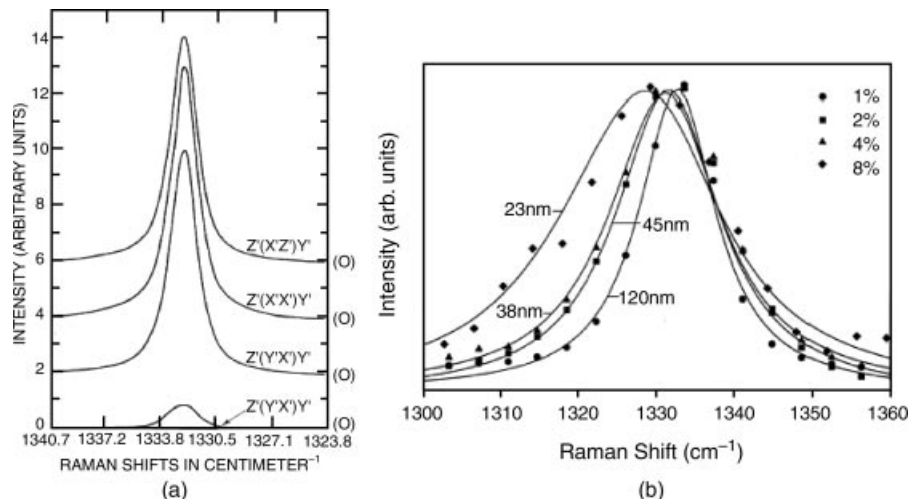


**Figure V.3** Raman spectra of (a) bulk-diamond [11] and (b) nano-diamond with grain size 23, 38, 45, and 120 nm (data of the solid line from the microcrystal model) [12]

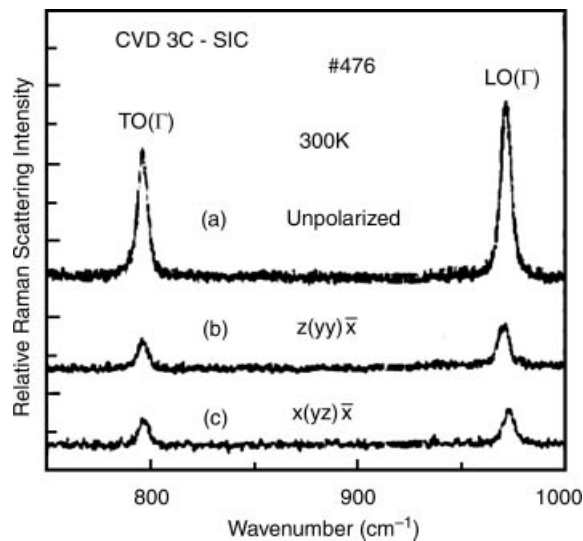


**Figure V.4** Raman spectra of SiC [13]

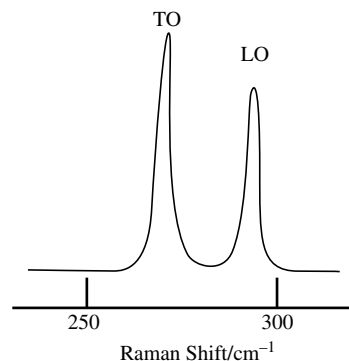


**Figure V.5** Raman spectra of GaAs [14]

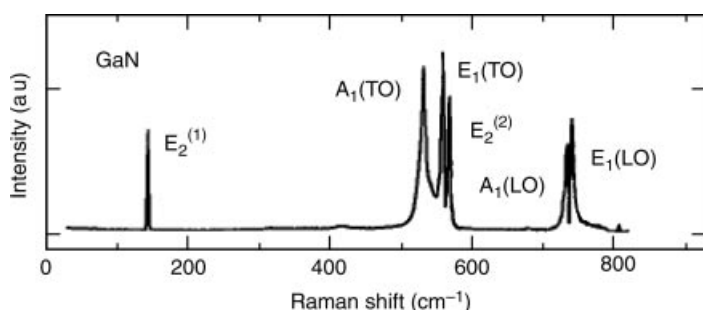


**Figure V.6** Raman spectra of GaN [15]

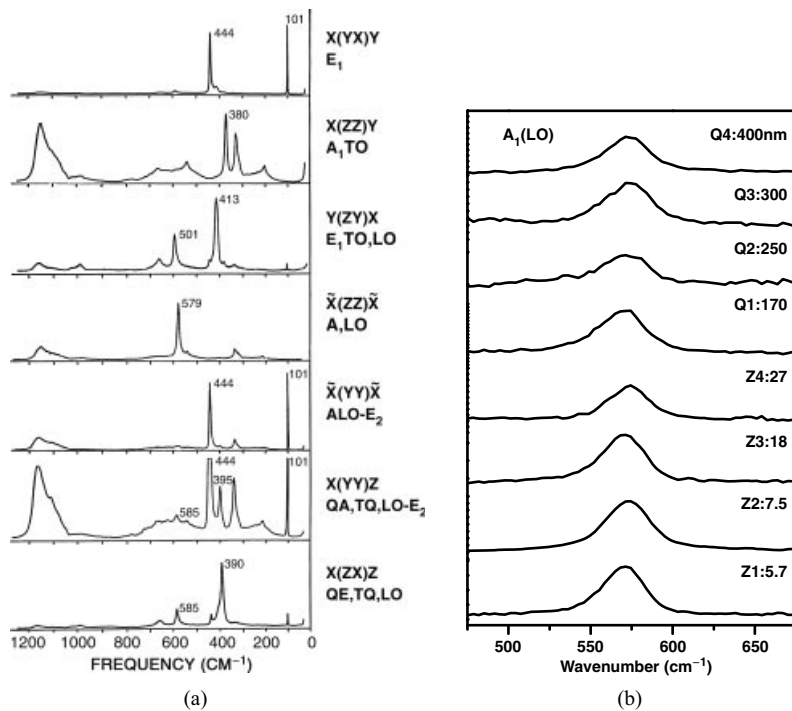


Figure V.7 Raman spectra of (a) bulk-ZnO [16] and (b) nano- ZnO [17]

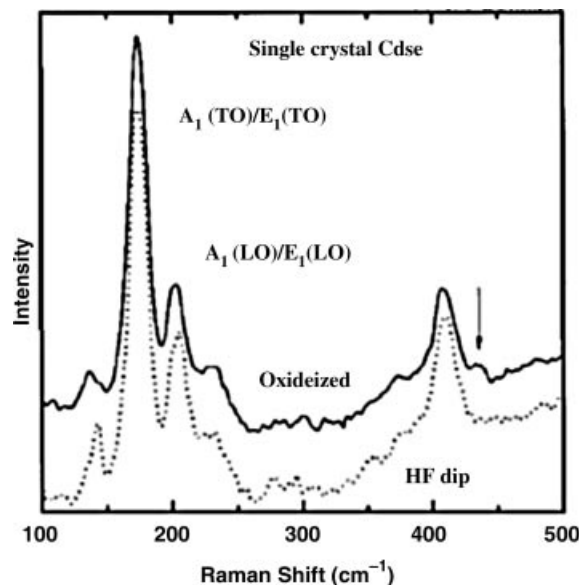
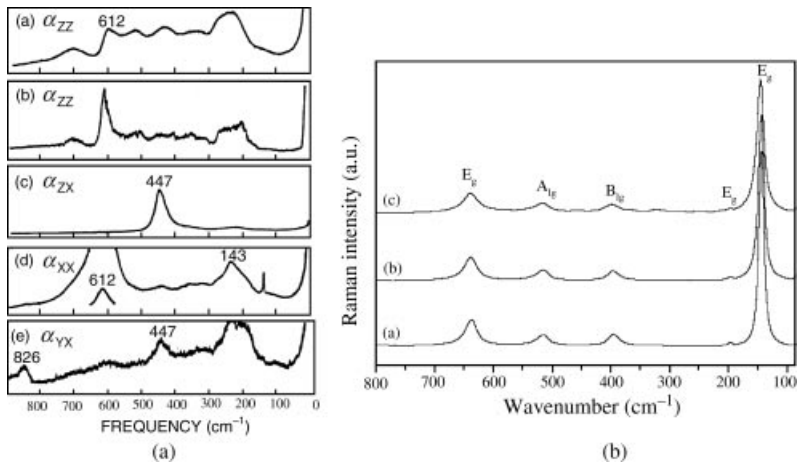


Figure V.8 Raman spectra of oxidized and HF cleaned single crystal CdSe (0001) [18].



**Figure V.9** Raman spectra of (a) bulk-TiO<sub>2</sub> with Rutile phase [19] and (b) nano-TiO<sub>2</sub> with Anatase phase [20]. In (b), the sample (a) is bulk and the sizes of sample (b) and (c) are 30 and 12 nm, respectively

The subscripts “T” and “L” behind the subscript “1” express vertical and longitudinal modes, respectively. The symbols “L” and “H” in the bracket of E<sub>2</sub> modes are used to distinguish the low- and high-frequency modes, respectively.

# Appendix VI

## Physical Parameters, Constants, and Units

### VI.1 Periodic Table of the Elements

Group #	1	2	3	4	5	6	7	8	9	10	11	12	13	14	15	16	17	18
Period																		
1	1 H																	2 He
2	3 Li	4 Be																5 B
3	11 Na	12 Mg																6 C
4	19 K	20 Ca	21 Sc	22 Ti	23 V	24 Cr	25 Mn	26 Fe	27 Co	28 Ni	29 Cu	30 Zn	31 Ga	32 Ge	33 As	34 Se	35 Br	36 Kr
5	37 Rb	38 Sr	39 Y	40 Zr	41 Nb	42 Mo	43 Tc	44 Ru	45 Rh	46 Pd	47 Ag	48 Cd	49 In	50 Sn	51 Sb	52 Te	53 I	54 Xe
6	55 Cs	56 Ba	*	72 Hf	73 Ta	74 W	75 Re	76 Os	77 Ir	78 Pt	79 Au	80 Hg	81 Tl	82 Pb	83 Bi	84 Po	85 At	86 Rn
7	87 Fr	88 Ra	**	104 Rf	105 Db	106 Sg	107 Bh	108 Hs	109 Mt	110 Ds	111 Rg	112 Cn	113 Uut	114 Uuo	115 Uup	116 Uuh	117 Uus	118 Uuo
* <u>Lanthanides</u> (Lanthanoids)	57 La	58 Ce	59 Pr	60 Nd	61 Pm	62 Sm	63 Eu	64 Gd	65 Tb	66 Dy	67 Ho	68 Er	69 Tm	70 Yb	71 Lu			
** <u>Actinides</u> (Actinooids)	89 Ac	90 Th	91 Pa	92 U	93 Np	94 Pu	95 Am	96 Cm	97 Bk	98 Cf	99 Es	100 Fm	101 Md	102 No	103 Lr			

**VI.2 Electronic Structure of Atoms [20]**

Element	K		L		M			N		Ground Term	Ionization Voltage(eV)
	1.0 1s	2.0 2s	2.1 2p	3.0 3s	3.1 3p	3.2 3d	4.0 4s	4.1 4p			
H	1	1	—	—	—	—	—	—	—	$^2S_{1/2}$	13.599
He	2	2	—	—	—	—	—	—	—	$^1S_0$	24.581
Li	3	2	1	—	—	—	—	—	—	$^2S_{1/2}$	5.390
Be	4	2	2	—	—	—	—	—	—	$^1S_0$	9.320
B	5	2	3	1	—	—	—	—	—	$^2P_{1/2}$	8.296
C	6	2	4	2	—	—	—	—	—	$^3P_0$	11.256
N	7	2	5	3	—	—	—	—	—	$^4S_{3/2}$	14.545
O	8	2	6	4	—	—	—	—	—	$^3P_2$	13.614
F	9	2	7	5	—	—	—	—	—	$^3P_{3/2}$	17.418
Ne	10	2	8	6	—	—	—	—	—	$^1S_0$	21.559
Na	11	Configuration of Ne	1	—	—	—	—	—	—	$^2S_{1/2}$	5.138
Mg	12		2	—	—	—	—	—	—	$^1S_0$	7.644
Al	13		2	1	—	—	—	—	—	$^2P_{1/2}$	5.984
Si	14		2	2	—	—	—	—	—	$^3P_0$	8.149
P	15		2	3	—	—	—	—	—	$^4S_{3/2}$	10.484
S	16		2	4	—	—	—	—	—	$^3P_2$	10.357
Cl	17		2	5	—	—	—	—	—	$^3P_{3/2}$	13.01
Ar	18		2	6	—	—	—	—	—	$^1S_0$	15.755
K	19	Configuration of Ar	—	1	—	—	—	—	—	$^2S_{1/2}$	4.339
C	20		—	2	—	—	—	—	—	$^1S_0$	6.111
Sc	21		1	2	—	—	—	—	—	$^2D_{3/2}$	6.538
Ti	22		2	2	—	—	—	—	—	$^3F_2$	6.818
V	23		3	2	—	—	—	—	—	$^4F_{3/2}$	6.743
Cr	24		5	1	—	—	—	—	—	$^7S_3$	6.764
Mn	25		5	2	—	—	—	—	—	$^6S_{5/2}$	7.432
Fe	26		6	2	—	—	—	—	—	$^5D_4$	7.868
Co	27		7	2	—	—	—	—	—	$^4F_{9/2}$	7.862
Ni	28		8	2	—	—	—	—	—	$^3F_4$	7.633
Cu	29		10	1	—	—	—	—	—	$^2S_{1/2}$	7.724
Zn	30		10	2	—	—	—	—	—	$^1S_0$	9.391
Ga	31		10	2	1	—	—	—	—	$^2P_{1/2}$	6.00
Ge	32		10	2	2	—	—	—	—	$^3P_0$	7.88
As	33		10	2	3	—	—	—	—	$^4S_{3/2}$	9.81
Se	34		10	2	4	—	—	—	—	$^3P_2$	9.75
Br	35		10	2	5	—	—	—	—	$^2P_{3/2}$	11.84
Kr	36		10	2	6	—	—	—	—	$^1S_0$	13.996

Element	Inner Layer Configuration	N		O			P	Ground Term	Ionization Voltage (eV)
		4.2 4d	4.3 4f	5.0 5s	5.1 5p	5.2 5d	6.0 6s		
Rb 37	Configuration of Kr	—	—	1	—	—	—	<sup>2</sup> S <sub>1/2</sub>	4.176
Sr 38		—	—	2	—	—	—	<sup>1</sup> S <sub>0</sub>	5.692
Y 39		1	—	2	—	—	—	<sup>2</sup> D <sub>3/2</sub>	6.377
Zr 40		2	—	2	—	—	—	<sup>3</sup> F <sub>2</sub>	6.835
Nb 41		4	—	1	—	—	—	<sup>6</sup> D <sub>1/2</sub>	6.881
Mo 42		5	—	1	—	—	—	<sup>7</sup> S <sub>3</sub>	7.10
Tc 43		6	—	1	—	—	—	<sup>6</sup> S <sub>5/2</sub>	7.228
Rn 44		7	—	1	—	—	—	<sup>5</sup> F <sub>5</sub>	7.365
Rh 45		8	—	1	—	—	—	<sup>4</sup> F <sub>9/2</sub>	7.461
Pd 46		10	—	—	—	—	—	<sup>1</sup> S <sub>0</sub>	8.334
Ag 47	Configuration of Pd	—	1	—	—	—	—	<sup>2</sup> S <sub>1/2</sub>	7.574
Cd 48		—	2	—	—	—	—	<sup>1</sup> S <sub>0</sub>	8.991
In 49		—	2	1	—	—	—	<sup>2</sup> P <sub>1/2</sub>	5.785
Sn 50		—	2	2	—	—	—	<sup>3</sup> P <sub>0</sub>	7.342
Sb 51		—	2	3	—	—	—	<sup>4</sup> S <sub>3/2</sub>	8.637
Te 52		—	2	4	—	—	—	<sup>3</sup> P <sub>2</sub>	9.01
I 53		—	2	5	—	—	—	<sup>2</sup> P <sub>3/2</sub>	10.454
Xe 54		—	2	6	—	—	—	<sup>1</sup> S <sub>0</sub>	12.127
Cs 55	From 1s to 4d layer containing a total of 46 electronics	—	The 5s and 5p layers containing 8 electronics	—	1	—	—	<sup>2</sup> S <sub>1/2</sub>	3.893
Ba 56		—		—	2	—	—	<sup>1</sup> S <sub>0</sub>	5.210
La 57		—		1	2	—	—	<sup>2</sup> D <sub>3/2</sub>	5.61
Ce 58		2		—	2	—	—	<sup>3</sup> H <sub>4</sub>	6.54
Pr 59		3		—	2	—	—	<sup>4</sup> I <sub>9/2</sub>	5.48
Nd 60		4		—	2	—	—	<sup>5</sup> I <sub>4</sub>	5.51
Pm 61		5		—	2	—	—	<sup>6</sup> H <sub>5/2</sub>	5.55
Sm 62		6		—	2	—	—	<sup>7</sup> F <sub>0</sub>	5.63
Eu 63		7		—	2	—	—	<sup>8</sup> S <sub>7/2</sub>	5.67
Gd 64		7		—	2	—	—	<sup>9</sup> D <sub>2</sub>	6.16
Tb 65		9		—	2	—	—	<sup>6</sup> H <sub>15/2</sub>	6.74
Dy 66		10		—	2	—	—	<sup>5</sup> I <sub>3</sub>	6.82
Ho 67		11		—	2	—	—	<sup>4</sup> I <sub>15/2</sub>	6.02
Er 68		12		—	2	—	—	<sup>3</sup> H <sub>6</sub>	6.10
Tm 69		13		—	2	—	—	<sup>2</sup> F <sub>7/2</sub>	6.18
Yb 70		14		—	2	—	—	<sup>1</sup> S <sub>0</sub>	6.22
Lu 71		14		1	2	—	—	<sup>2</sup> D <sub>3/2</sub>	6.15

Element		Inner Layer Configuration	O		P			Q	Ground Term	Ionization Voltage (eV)
			5.2 5d	5.3 5f	6.0 6s	6.1 6p	6.2 6d			
Hf	72	From 1s to 5p layer containing a total of 68 electronics	2	—	2	—	—	—	$^3F_2$	7.0
Ta	73		3	—	2	—	—	—	$^4F_{3/2}$	7.88
W	74		4	—	2	—	—	—	$^5D_0$	7.98
Re	75		5	—	2	—	—	—	$^6S_{5/2}$	7.87
O	76		6	—	2	—	—	—	$^5D_4$	8.7
Ir	77		7	—	2	—	—	—	$^4F_{9/2}$	9.2
Pt	78		8	—	2	—	—	—	$^3D_3$	8.88
Au	79		—	1	—	—	—	—	$^2S_{1/2}$	9.223
Hg	80		—	2	—	—	—	—	$^1S_0$	10.434
Tl	81		—	2	1	—	—	—	$^2P_{1/2}$	6.106
Pb	82		—	2	2	—	—	—	$^3P_0$	7.415
B	83		—	2	3	—	—	—	$^4S_{3/2}$	7.287
Po	84		—	2	4	—	—	—	$^3P_2$	8.43
At	85		—	2	5	—	—	—	$^2P_{3/2}$	9.5
Rn	86		—	2	6	—	—	—	$^1S_0$	10. 74 5
Fr	87	From 1s to 5d layer containing a total of 78 electronics	—	2	6	—	1	$^2S_{1/2}$	4.0	
Ra	88		—	2	6	—	2	$^1S_0$	5.2 77	
Ac	89		—	2	6	1	2	$^2D_{3/2}$	6.9	
Th	90		—	—	—	2	2	$^3F_2$	6.1	
Pa	91		2	2	6	1	2	$^4K_{11/2}$	5.7	
U	92		3	2	6	1	2	$^5L_6$	6.0 8	
Np	93		4	2	6	1	2	$^6L_{11/2}$	5.8	
Pu	94		5	2	6	1	2	$^7F_0$	5.8	
A	95		6	2	6	1	2	$^8S_{7/2}$	6.0 5	
m	96		7	2	6	1	2	$^9D_2$		

Note:

1. The table is taken from Blokhintsev, D.I. (1959) *Principles of Quantum Mechanics*, Higher Education Press. The ionization voltage of the table is taken from Yang, F. (2000) *Atomic Physics*, Version 3, Higher Education Press.

2. In the table, K, L, M, N, O, P, and Q represent the electronic shell of different principal quantum numbers. The ground term in the table is marked S, P, D, and F, equivalent to the total electronic orbital angular momentum  $L = 0, 1, 2, 3$  and so on. The number in the bottom right-hand corner of the letters is the total angular momentum J (orbital + spin). The number in the higher upper corner is the multiplicity of the item,  $2s + 1$ , where s is the total spin (for 1/2 integer times), so the ground item is represented by  $^{2s+1}L_J$ . For example, the electron occupation case of Li is (1s)<sup>2</sup>2s, so the total orbital angular momentum is L = 0, total angular momentum 1/2 (outer layer – electron spin), and the total spin s = 1/2. Then, the ground item of Li is  $^2S_{1/2}$ .

### VI.3 Common Physical Constant and the Performance Parameters of Optical Glass

#### VI.3.1 Physical Constant

Electron Charge ( $e$ )	$1.60217733 \times 10^{-19} \text{ C}$
Rest Mass of Free Electron ( $m_e$ )	$9.1093897 \times 10^{-31} \text{ kg}$
Speed of Light in Free Space ( $c$ )	$2.99792458 \times 10^8 \text{ m s}^{-1}$
Planck Constant ( $h$ )	$6.6260755 \times 10^{-34} \text{ J s}^{-1}$
Normalized Planck Constant ( $\hbar$ )	$1.05457266 \times 10^{-34} \text{ J s}^{-1}$
Boltzmann Constant ( $k$ )	$1.380658 \times 10^{-23} \text{ J/K} = 8.617385 \times 10^{-5} \text{ eV/K}$
Proton Mass/Electron Mass Ratio	1836.1
Reciprocal of Fine Structure Constant ( $1/\alpha$ )	137.0359895
Boer Radius ( $a_0$ )	$0.529177249 \times 10^{-10} \text{ m}^{-1}$
Rydberg Constant ( $R$ )	$1.0973731534 \times 10^7 \text{ m}^{-1}$
Magnetic Constant in Free Space ( $\mu_0$ )	$12.566370614 \times 10^{-7} \text{ N/A}^2$ [or H/m] $(4\pi \times 10^{-7})$
Electric Constant in Free Space ( $\epsilon_0$ )	$8.854187817 \times 10^{-12} \text{ A/s(V/m)} [\text{or F/m}]$
Avogadro Constant ( $N_A$ )	$6.0221367 \times 10^{23}/\text{mol}$
Freezing Point of Water	273.16 K
Liquid Nitrogen Temperature (1 atm)	77.348 K
Liquid Helium Temperature (1 atm)	4.216 K
$k_B T$ at Room Temperature (300 K)	25.85 meV
The Wavelength Range of Visible Light	Purple/ $\sim$ 400 nm (3 eV) $\leftrightarrow$ Red/ $\sim$ 800 nm (1.55 eV)

#### VI.3.2 Common Unit Conversion

$$\text{Wavelength } \lambda(\mu\text{m}) = 1.2398/\text{Energy } E(\text{eV})$$

$$\text{Wave Number } v \text{ (Periodic Number in 1 cm)} = 1/\lambda \text{ (cm)}$$

$$1 \text{ J} = 1 \text{ kg m}^2 \text{ s}^{-2} = 1 \text{ N/m} = 10^7 \text{ erg} = 6.25 \times 10^{18} \text{ eV}$$

$$1 \text{ F} = 1 \text{ s}/\Omega = 1(\text{A/s})/\text{V} = 1 \text{ C}^2/\text{J} = 1(\text{A}^2 \text{ s}^{-1})/\text{W} = 1 \text{ C/V}$$

$$1 \text{ H} = 1(\Omega \text{ s}^{-1})$$

$$1 \text{ C} = 1(\text{A s}^{-1}) = 6.2414 \times 10^{18} \text{ e}$$

$$1 \text{ \AA} = 10^{-4} \mu\text{m} = 10^{-8} \text{ cm} = 10^{-10} \text{ m}$$

$$1 \text{ dyn} = 1/980.665 \text{ gf} = 10^{-5} \text{ N}$$

$$1 \text{ dyn/mm}^2 = 10^{-4} \text{ bar}$$

$$1 \text{ kbar} = 0.1 \text{ GPa} = 10^8 \text{ Pa} = 10^8 \text{ N m}^{-2} = 10.1972 \text{ kgf mm}^{-2}$$

$$1 \text{ PSI} = 0.07031 \text{ kgf cm}^{-2} = 6894.76 \text{ N m}^{-2} = 6.89476 \times 10^{-2} \text{ bar}$$

$$1 \text{ kgf} = 9.80665 \text{ N} = 9.80665 \times 10^5 \text{ dyn}$$

Conversion of units of energy:

Corresponding Physical Quantity	Conversion Formula	0.1 eV	1.0 eV
The Wavelength of Free Electron Wave $\lambda_e$	$h^2/2m\lambda_e^2 = E$	3.88 nm	1.23 nm
The Speed of Electron $v$	$mv^2/2 = E$	$1.88 \times 10^7 \text{ cm s}^{-1}$	$5.93 \times 10^7 \text{ cm s}^{-1}$
Temperature $T$	$kT = E$	$1.16 \times 10^3 \text{ K}$	$1.16 \times 10^4 \text{ K}$
The Wavelength of Electromagnetic Wave $\lambda$	$hc/\lambda = E$	12.4 $\mu\text{m}$	1.24 $\mu\text{m}$
The Frequency of Electromagnetic Wave $v$	$hv = E$	$2.42 \times 10^{13} \text{ Hz}$	$2.42 \times 10^{14} \text{ Hz}$
Magnetic Field $H$	$ehH/2\pi mc = E$	$8.64 \times 10^7 \text{ G s}^{-1}$	$8.64 \times 10^8 \text{ G s}^{-1}$

### VI.3.3 Performance Parameters of Optical Glass

**Table VI.1** Prism of Fused Silica, Quartz Crystal, Crown Glass, and Flint Glass. The Dispersion of 60° [21]

$\lambda$ (nm)	Materials	$n$	$dn/d\lambda$ ( $\text{nm}^{-1}$ )	$d\theta/d\lambda$ (rad/nm)	Liner Dispersion ( $F=50 \text{ cm}$ )	
			( $\times 10^{-4}$ )	( $\times 10^{-4}$ )	$dI/d\lambda$ (mm/nm)	$d\lambda/dI$ (nm/mm)
200	Fused Silica	1.55	13	21	1.0	1.0
	Quartz Crystal	1.65	16	28	1.4	0.7
300	Fused Silica	1.49	2.8	4.3	0.21	4.6
	Quartz Crystal	1.58	3.2	5.3	0.26	3.8
400	Fused Silica	1.47	1.1	1.6	0.08	12.5
	Crown Glass	1.53	1.3	2.03	0.10	10.0
600	Flint Glass	1.76	5.1	10.6	0.53	1.9
	Crown Glass	1.52	0.36	0.54	0.03	37
	Flint Glass	1.72	1.0	2.0	0.10	10

Note: The data of Quartz Crystal is in terms of normal light. The data of Crown Glass and Flint Glass is in terms of UBK7 glass and SF1 glass.

**Table VI.2** Common Materials of Prism [21]

Material	Transmission Area ( $\mu\text{m}$ )	Suitable Wavelength Range ( $\mu\text{m}$ )
Glass	0.4–3	0.4–0.8
Special Glass	0.3–3	0.3–0.8
Quartz	0.2–3.5	0.2–2.7
LiF	0.12–6	0.7–5.5
CaF <sub>2</sub>	0.12–9	5–9
NaCl Crystal	0.2–17 (absorbed at 3.2 and 7.1)	3–16
KCl Crystal	0.2–21	8–16
KBr Crystal	0.21–28	15–28
TlBr <sub>i</sub>	0.5–40	24–40

## References

- [1] Liu, S. and Li, F. (2006) *Technology and Application of Photonics*, Guangdong Science and Technology Press, Anhui Science and Technology Press.
- [2] Technical literature of Spex 1403 (1982) Spex Industries, Inc, Metuchen, NJ.
- [3] Jia, Y.R., Wang, G.Z., and Ling, P.L., eds. (1987) *Physical Experiments in Universities*, Fudan University Press, Shanghai.
- [4] Zhang, G.Y., Lan, G.X., and Wang, Y.F. (2001) *Lattice Vibration Spectroscopy*, Second edition, Higher Education Press, Beijing.
- [5] Weinstein, B.A. and Cardona, M. (1972) *Solid State Commun.* **10**, 961.
- [6] Porto, S.P.S., Fleury, P.A., and Damen, T.C. (1967) *Phys Rev*, **154**, 522.
- [7] Zong, X.F. and Wen, Y.M. (2001) *Fundamentals of Material Physics*, Fudan University Press, Shanghai.
- [8] Hayes, W. and London, R. (1978) *Scattering of Light in Crystals*, J. Wiley and Sons, New York.
- [9] Vepiek, S. *et al.* (1981) *J. Phys. C: Solid State Phys.*, **14**, 295–308.
- [10] Ehbrecht, M., Kohn, B., Huisken, F., Laguna, M.A., and Paillard, V. (1997) *Phys. Rev. B*, **56**, 6958–6964.
- [11] Solin, S.A. and Ramdas, A.K. (1970) *Phys. Rev. B*, **1**, 1687.
- [12] Sun, Z., Shi, J.R., Tay, B.K., and Lau, S.P. (2000) *Diam. and Rel. Mat.*, **9**, 1979–1983.
- [13] Feng, Z.C., Mascarenhas, A.J., Choyke, W.J., and Powell, J.A. (1988) *JAP*, **64**, 3176.
- [14] Mooradian, A. and Wright, G.B. (1966) *Solid State Commun.*, **4**, 431.
- [15] Davydov, V.Y., *et al.* (1998) *Phys. Rev B*, **58**, 12899.
- [16] Arguello, C.A., Rousseau, D.L., and Porto, S.P.S. (1969) *Phys. Rev*, **181**, 1351.
- [17] Zhang, S.L., Zhang, Y., Fu, Z., *et al.* (2006) *Appl. Phys. Lett.*, **89**, 243108.
- [18] Masson, D.P., Lockwood, D.J., and Graham, M.J. (1997) *J. Appl. Phys.* **82**, 1632.
- [19] Choi, H.C., Jung, Y.M., and Kim, S.B. (2005) *Vib. Spect.* **37**, 33.
- [20] Broxhon, L.H. (1959) *Principle of Quantum Mechanism*, Chinese translation version, People Education Press, Beijing.
- [21] Lv, S.H. and Zhu, Y.K., eds. (1991) *Experimental Technology of Modern Physics I*, Higher Education Press, Beijing.

# Index

- 3T3-L1 cells, 173
- AARS, *see* abnormal anti-Stokes Raman scattering
- AB/BC type superlattices, 258–60
- AB/CD type superlattices, 260–61
- ABCM, *see* adiabatic bond charge model
- Abert mode, 69
- ab initio* calculations, 298–306
- dispersion relations of phonons, 299–300
  - molecular dynamic calculations, 302–6
  - Si nanowires, 301Si/Ge superlattices, 300
- abnormal anti-Stokes Raman scattering (AARS), 352–4
- acoustic lattice wave, 207
- adiabatic approximation, 201, 235, 298
- adiabatic bond charge model (ABCM), 219–20
- see also* bond charge model
- adiabatic status, 201
- alginate films, 168
- amorphous crystal model (ACM), 427
- amorphous crystals
- Boson peak, 244–246
  - lattice dynamics, 229–30
  - phonon density of state (PDOS), 229–30
  - Raman spectra of, 241–2
  - vibration density of state (VDOS), 242–44
- amorphous features, 246, 427
- and translation symmetry, 339, 427–8
- amorphous silicon, 160, 230, 245–6
- amorphous solids, 199
- annealing, 252, 410–411, 413
- and change of potential shape in superlattices, 409
- anti-Stokes frequency, 9–10
- anti-Stokes Raman spectra, 352–7
- and universal characteristics of Raman scattering, 352
- anti-Stokes scattering, 43–4
- apertureless Raman spectrometers, 128–9
- aperture probes, 60
- archaeology applications, 177
- art applications, 177
- atomic light scattering, 8
- classical theory of, 28, 31
  - quantum mechanical theory of, 42–43
- backward detected CARS (Epi-CARS), 139
- BCB, *see* brilliant cresyl blue
- benzene, 142, 154
- biological cells, 144, 170
- biomedical applications, 146–50, 166–75
- organic molecules and tissues, 168–71
  - pharmacology, 174–175
  - sample preparation, 166–7
  - studies of dynamic processes, 171–4
- biomolecules, 54
- containing chromophores, 108
- blazing grating, 68, 69
- Bohr radius, 187, 188, 193
- bond charge linear chain model, 262–64
- bond charge model, 218–20
- bond model, 217–18
- bond polarizability model, 289, 290
- Born, Max, 15
- Born–Karman model, 208–9, 213, 214
- Born–Oppenheimer approximation, 201, 298
- Born–Oppenheimer energy surface, 299
- Bose–Einstein distribution, 210, 240
- Bose peak, *see* Boson peak
- Boson peak, 244–6

- brain metastases, 174  
 breast calcifications, 118  
 Breit–Wigner–Fano line shape, 336  
 Brewster angle, 86–7  
 brilliant cresyl blue (BCB), 132, 133  
 Brillouin, L., 19  
 Brillouin scattering, 8–9, 19  
 Brillouin scattering spectrometer,  
*see* Fabry–Perot coherent spectrometer  
 broadband CARS, 139, 141–2  
 Broglie wavelength, 187, 188  
 buckminsterfullerene, *see* C<sub>60</sub>  
 buckyballs, 271
- C<sub>60</sub>, 272  
 characteristic Raman spectrum of, 330–331  
 cancer, 118, 149–50, 166, 170–1  
 carbon nanostructures, 271–9  
*see also* carbon nanotubes (CNTs); graphene;  
 fullerenes; nanocarbons  
 carbon nanotubes (CNTs), 271, 272  
 abnormal anti-Stokes Raman scattering  
 in, 352–4  
 as defect structures, 357, 386  
 characteristic Raman spectra of, 332–5  
 disorder-induced mode (D mode), 336–7,  
 389–92, 414  
 enhancement of Raman scattering  
 intensity, 365–6  
 graphite-like mode (G mode), 335–6, 389–92,  
 413  
 laser intensity effects, 382–92  
 mono-root, 375  
 multiple-phonon Raman spectra of, 343  
 polarized Raman spectra of, 375  
 purification by laser irradiation, 389–92  
 radial breathing mode, 334–5  
 Raman frequency variations, 368–73  
 resonant Raman spectra, 365–6, 368–9  
*see also* multi-walled carbon nanotubes  
 (MWCNTs); single-walled carbon  
 nanotubes (SWCNTs)  
 CARS, *see* coherent anti-Stokes Raman  
 scattering  
 CCD, *see* charge-coupled device  
 CCl<sub>4</sub>, 94–7  
 first Raman spectrum, 13  
 polarized Raman spectra of, 96–7  
 structure and symmetry of, 95  
 vibration modes, 96–7
- CdS  
 multiple phonon Raman spectra of, 110  
 phonon dispersion curves, 218  
 phonon frequencies, 270  
 CdSe  
 characteristic Raman spectra of, 340–3  
 crystallographic property and sizes, 341  
 Raman frequency variations, 371–2  
 simulation of Raman spectra, 426–27  
 CdSe/ZnTe superlattices, 317–18  
 CdS<sub>x</sub>Se<sub>1-x</sub>, 413  
 CE mechanism, *see* chemical enhancement  
 (CE) mechanism  
 characteristic length, 187–8  
 charge-coupled device (CCD), 72–74, 85  
 chemical enhancement (CE) mechanism, 135–6  
 chemical samples, 86  
 chemical transfer (CT), 121  
 chemical vapor deposition (CVD), 326–9  
 chemistry applications, 158–9, 179  
 chocolate, 106  
 chromatic resolution rate, 81  
 Clark, Robin, 177  
 ClC<sub>4</sub>, 9  
 clusters, 190, 192  
 gold, 190  
 CNTs, *see* carbon nanotubes  
 coaxial cables, 190  
 coherent anti-Stokes Raman scattering  
 (CARS), 138–44  
 backward detected (Epi-CARS), 139  
 broadband, 139, 141–2  
 dual-pump technique, 142  
 experimental techniques, 138–9  
 forward detected (F-CARS), 139  
 interferometric (iCARS), 140  
 lipid-containing specimens, 173  
 microscopy, 144–5  
 polarized (P-CARS), 140, 173  
 principle of, 137  
 spectra, 140–4  
 spectroscopic features and  
 application, 138–40  
 time-resolved, 140  
 coherent Stokes Raman scattering (CSRS),  
 137, 144  
 collimator, 65  
 collision process, 21  
 colloids, 7, 135, 188  
 combination scattering, 12

- Compton, A.H., 6  
 Compton scattering, 8, 12, 32  
 condensed matter, 158–65  
     defined, 158–65  
     low-dimensional structures, 164–5  
     microstructure and symmetry, 160  
     nanoscale structures, 164–5  
     phase transition, 160–62  
     physical parameters, 162–4  
     *see also* solids  
 confocal optical path, 63  
 converging lens, 65  
 CoSi electrode, 180  
 cosmic rays, 90, 91  
 crystal lattice, 199  
     *see also* lattice dynamics;  
     superlattices (SLs)  
 crystals  
     Raman scattering and symmetry, 232–4  
     Raman spectra of, 241–2  
     *see also* amorphous crystals; ionic crystals;  
     small crystals  
 CSRS, *see* coherent Stokes Raman scattering  
 CT, *see* chemical transfer  
 CVD, *see* chemical vapor deposition  
 Czerny–Turner mode, 69  
  
 dark current, 74  
 DCP, *see* dual circular polarization  
 Debye theory, 244, 246  
 deduction methods, 91–93  
 defects, 413  
 density functional theory, 298  
 dephasing length, 187  
 depolarization degree, 52–54, 97  
 diameter-selective Raman scattering  
     (DSRS), 369, 370  
 diamond, 93, 218, 219  
     microstructure and symmetry, 160  
     PDOS of, 297  
     phonon dispersion curves, 220–2  
     simulation of Raman spectra, 426  
     theoretical Raman spectra, 424, 425  
     *see also* nanodiamond  
 dielectric continuous model, 224–  
     for superlattices, 256–8  
 dielectric fluctuation correlation  
     function, 239–40  
 dielectric fluctuation correlation  
     model, 236  
  
 dielectric tensor, 236–9, 240, 241  
 differential scattering cross section, 23–4, 27,  
     28, 32  
     classical expression of, 24  
     and dielectric fluctuation correlation  
         function, 239–41  
     of light scattering of isolated atom, 29  
     quantum mechanics expression of, 24–6  
     and quantum transition probability,  
         39–40  
     and Raman frequency spectrum, 48  
 differential scattering probability, 21–22  
 diffraction limit rule, 123–4  
 dipole lattice model, 262  
 dispersion addition mode, 69–71  
 dispersion relation  
     *ab initio* calculation of, 298–9  
     defined, 155  
     in ionic crystals, 226–7  
     in micro-crystals, 292  
     of optical phonon in superlattices, 257  
     in single-walled carbon nanotubes,  
         277–9  
 dispersion subtraction mode, 69–71  
 dispersive effect, 75, 88  
 D mode, 336–7, 414  
 DNA, 167–9  
     SERS measurement, 166  
 double-quadrature spectral interferometry  
     (DQSI), 141  
 double resonant Raman scattering  
     (DRRS), 109–10  
 DQSI, *see* double-quadrature spectral  
     interferometry  
 DRRS, *see* double resonant Raman scattering  
 drugs, 174, 175, 179  
 DSRS, *see* diameter-selective Raman scattering  
 dual circular polarization (DCP), 54  
*Dynamical Theory of Crystal Lattices*, 15  
  
 elastic collision, 21  
 elastic continuum model, –, 254–6, 311  
 elastic scattering, 8, 21  
 electrical dipole moment, 26–8, 31  
 electrical dipole radiation, 26–7  
 electromagnetic (EM) mechanism, 134  
 electromagnetic wave scattering, *see* photon  
     scattering  
 electronic industry, 179–80  
 electron light scattering, 8

- electron–phonon interactions  
     in nanostructures, 419–29  
     in solids, 210–13  
     *see also* Fröhlich interactions
- electron scattering, 6
- elementary excitations, 8, 199  
     Raman spectral features of, 155
- EM mechanism, *see* electromagnetic (EM) mechanism
- energy conservation law, 10
- EPA, 149
- Epi-CARS, *see* backward detected CARS
- excited state, 209
- experimental apparatus, *see* Raman spectrometer
- extra-condition Raman spectroscopy,  
     114–15  
     *see also* high pressure Raman spectroscopy;  
     high temperature Raman spectroscopy
- extreme conditions, *see* extra-condition Raman spectroscopy
- Fabry-Perot coherent spectrometer, 101–102
- Fano line-shape, 323
- far-field spectrum, 5
- F-CARS, *see* forward detected CARS
- finite size effect, 192–6, 249, 296
- first principles calculations, *see ab initio* calculations
- fluid inclusions, 175
- folded acoustic phonon modes, 310–13, 396,  
     410–11
- food industry, 180–1
- force constant model, 214–16, 215
- forward detected CARS (F-CARS), 139
- Fourier transform (FT) spectrometers,  
     97–101, 104  
     application for Raman spectroscopy, 101  
     characteristics of, 101  
     components of, 99–100  
     free spectral region, 69  
     frequency-mixing processes, 137  
     frequency spectrum, 5  
     Fröhlich interactions, 212, 314, 315, 422–3, 427  
         in SiC nanorods, 338, 366–7  
     Fröhlich model, 249
- FT spectrometers, *see* Fourier transform (FT) spectrometers
- fullerenes, 271–2  
     characteristic Raman spectra of, 331–7  
     *see also* carbon nanotubes (CNTs)
- $\text{Ga}_{1-x}\text{Al}_x\text{As}$ , 283
- GaAs  
     phonon dispersion curves of, 221  
     quantum wire, 279
- GaAs/GaAlAs superlattices  
     confined optical phonon mode, 313–15  
     crystallography of, 191  
     effect of annealing on potential shape, 410  
     effect of sample shape on optical phonons, 411–2  
     effect of sample size on polarization selection rule, 406–9  
     effect of sample size on Raman spectra, 396  
     folded acoustic phonon modes, 311  
     macroscopic interface modes, 258, 315–6  
     photon dispersion curves of, 250, 256, 260,  
         262–4  
     polarized Raman spectra of, 373  
     resonant Raman spectra of, 364  
     structure of, 251,
- GaAs/GaAlAs superlattices, 313–14, 368–9
- gamma ray scattering, 7
- GaN  
     phonon dispersion curves, 221  
     calculated spectra of, 425–26
- GaN nanoparticles  
     characteristic Raman spectra of, 337–43  
     cosmic ray disturbance spectra, 91  
     crystallographic properties and sizes, 341  
     Raman frequency variations, 369–72
- GaN nanorods, 383
- Gaussian beam, 57–759
- Ge  
     effect of sample size on Raman spectra, 397  
     phonon density of state (PDOS), 114,  
     phonon dispersion curves, 220  
     simulation of Raman spectra, 426  
     two-phonon Raman spectrum, 114, 115
- geology applications, 175–6
- geometric optic matching, 74–5
- GICs, *see* graphite intercalation compounds
- G mode, 333–4, 414
- gold clusters, 190
- graphene, 271–2  
     characteristic Raman spectra of, 330
- graphite, 160–1, 271  
     laser intensity effects, 381  
     nanocrystalline, 327, 329  
     *see also* graphene; highly oriented pyrolytical graphite (HOPG)

- graphite intercalation compounds (GICs), 336  
 grating equation, 66, 68, 69  
 gratings, 63–7  
   blazing, 68, 69  
   defined, 69  
   dispersion rate of, 69  
   free spectral region of, 69  
   holographic, 68  
   number in spectrometers, 69–71  
   plane/curved surface, 68  
   reflecting, 68  
   types of, 68  
   working wavelength of, 69  
 grating satellites, 66  
 grating spectrometers, 101  
   *see also* Raman spectrometer  
 ground state, 209
- H520 cells, 170, 171  
 handwriting identification, 181  
 harmonic approximation, 202  
 Hartree–Fock approximation, *see* mean field approximation  
 Helmholtz function, 243  
 highly oriented pyrolytical graphite (HOPG), 271  
   abnormal anti-Stokes Raman scattering in, 353  
   Au-doped, 355, 381, 386  
   D mode in, 336–7  
   laser intensity effects in, 381, 392, ,  
   multiple-phonon Raman spectra of, 343  
 high order Raman spectroscopy, *see* multiple-phonon Raman spectroscopy (MPRS)  
 high pressure Raman spectroscopy, 117, 414–7  
 high temperature Raman spectroscopy, 417  
   *see also* temperature  
 HL, *see* hot luminescence  
 holographic grating, 68  
 HOPG, *see* highly oriented pyrolytical graphite  
 hot luminescence (HL), 111–12  
 hot spots, 120  
 Huang, Kun, 15  
 Huang equation, 224–9, 257  
 Huang–Zhu model, 262
- iCARS, *see* interferometric CARS  
 image spectrum, 5  
 impulsive stimulated Raman scattering (ISRS), 148
- impurities, 413  
   disturbance spectra from, 89, 92  
 InAs/GaSb superlattices, 261,  
 incident particles, 5–8  
 industrial applications, 178–81  
   chemical and pharmaceutical industry, 179  
   electronic and semiconductor industry, 179–80  
   food industry, 180–81  
 inelastic collision, 21  
 inelastic scattering, 8–9, 21  
 infinite-size system, 427  
 InP/CdS nanoparticles, 416  
 InSb  
   clusters, 302  
   nanoparticles, 425, 428  
   quantum dots, 420  
 intensity dispersion, 78, 90  
 interface phonon modes, 315–18  
   effect of sample shape on, 411  
   macro modes, 315–6  
   micro modes, 283, 316–18, 344  
   multiple-phonon Raman spectra of, 343  
   of quantum well wires, 281–3  
 interference spectrometers, 97–104  
 interferometric CARS (iCARS), 140  
 ion crystal slab model, 253–4  
 ionic crystals, 224–7  
   dispersion relation of longitudinal wave, 227–8  
   dispersion relation of long optical wave, 226–7  
   dispersion relation of transverse wave, 228–9  
   electrostatic field, 224–5  
   high frequency electric field, 225  
   ionic polarization model, 225–7  
 isotropization, 78  
 ISRS, *see* impulsive stimulated Raman scattering
- judicature, 181–2
- KBr<sub>1-x</sub>I<sub>x</sub>, 249  
 KD<sub>2</sub>PO<sub>4</sub>, 162  
 KDP, 161  
 Keating model, 218,  
 Kerr effect, 137  
 KH<sub>2</sub>PO<sub>4</sub> (KDP), 161  
 Krishnan, K.S., 16  
 Kroig–Penney model, 311  
 Kubo theory, 196

- Landsberg, G. 12  
 Langrangian equation of motion, 300  
 lasers, 16  
   basic features of, 56–9  
   coherency, 57  
   directionality, 57  
   and disappearance of vibration modes, 388  
   Gaussian features of beam, 57–9  
   heating effect, 323–5, 380, 382–7  
   high-brightness, 57  
   high power density irradiation, 388–92  
   intensity effects, 378–92  
   low-intensity irradiation, 381–7  
   monochromaticity, 56–57  
   polarization, 57  
   power of/power density of, 379–80  
   purification of samples by, 389–92  
   sample damage by, 388  
   types of, 59  
 lattice dynamics, 200–213  
   of amorphous matter, 229–30  
   bond charge model, 218–20  
   bond model, 217–18  
   classical mechanics theory, 202–4  
   dielectric continuous model, 224–9  
   elastic continuous model, 222–4  
   electron–phonon interactions, 210–3  
   force constant model, 214–16, 277  
   macroscopic model of, 213, 222–9  
   microscopic model of, 213–22  
   of one-dimensional double atom chain, 204–9  
   quantum mechanics theory, 209–10  
   of semiconductor superlattices, 254–64  
   shell model, 216–17  
   simplification of motion equation, 200–202  
   of three-dimensional crystals, 213–14  
   *see also* superlattices (SLs)  
 lattice relaxation model, 111  
 lattice waves, 202–4  
   acoustic, 207  
   optical, 207  
 light scattering, 19–44  
   of atoms, 28–9, 31, 41–2  
   basic features of, 34–9  
   classical theory of, 19, 31–9  
   classification based on change in energy, 8–9  
   frequency characteristics, 35–7  
   intensity characteristics, 37  
   macroscopic theory of, 19, 26–39  
   microscopic theory of, 19, 39–44  
   of molecules, 29–31, 42–43  
   phase characteristics, 38  
   polarization characteristics, 38  
   quantum mechanical theory of, 19, 43  
   scattering experiments, 6, 20–21  
   types of, 7–8  
 lightning rod effect, 134–6  
 line dispersive rate, 80–1  
 linear chain model, 258–61  
 linear spectrum, 5  
 lipids, 144, 149–50, 173  
 liquid samples, 85–6  
 lithium ion batteries, 191  
 Littrow mode, 69  
 Lorentzian line shape, 336  
 low-dimensional structures, 164–5, 188  
   *see also* nanostructures  
 LTS relation, *see* Lyddano–Sachs–Teller (LTS) relation  
 Lyddano–Sachs–Teller (LTS) relation, 227  
 Mach-Zehnder interferometer, 140  
 macro-polarization, 29–30, 236  
 magic numbers, 190  
 Mandelstam, L., 12  
 Maxwell equations, 237–8  
 MC model, *see* micro-crystal (MC) model  
 mean field approximation, 202  
 meat, 180  
 mesoscopic structures, 187  
   *see also* nanostructures  
 Michelson interferometer, 97–9, 100, 101  
 microbes, 119  
 micro-crystal (MC) model, 283–96  
   archetypes of, 283–85  
   basic assumptions of, 285–6  
   calculation of Raman spectra of Si NWs, 322–23  
   dispersion relation, 291  
   line width, 291  
   presentation and applied extent of, 289–92  
   simulation of Raman spectra by, 426–27  
   successful application of, 285–6  
   testing of applied conditions, 292–6  
   weighting function, 291  
 micro-optical fluidic system, 167  
 micro-polarity model, 322  
 micro-polarization, 29  
 microscopic interface mode, 261, 344, 396  
 Mie, C. 7

- Mie scattering, 8  
 mineralogy applications, 175–6  
 molecular bonds, 154–5  
 molecular dynamic calculations, 302–6  
   of phonon density of state, 302–6  
 molecular scattering, 7, 8  
 molecules  
   classical theory of light scattering, 29–31  
   quantum mechanical theory of light scattering, 42–43  
   three atom, 33  
 momentum conservation law, 49  
   and size-scale, 195  
 monochromators  
   adjustment of, 84–5  
   number of gratings in, 69–71  
 motion equation, 28–9, 200–2, 205, 208  
 Lagrangian, 302  
   *see also* Huang equation  
 mouse lens proteins, 171  
 mouse tissue, 171, 172  
 MP Raman spectra, *see* multiple-phonon (MP) Raman spectra  
 MPRS, *see* multiple-phonon Raman spectroscopy  
 multi-order spectrum, 5  
 multiple-phonon (MP) Raman spectra, 343–52  
   of carbon nanotubes, 348  
   of highly oriented pyrolytical graphite (HOPG), 350  
   of polar nanosemiconductors, 350–52  
   of porous silicon, 347–8  
   of superlattices, 344–7  
 multiple-phonon Raman spectroscopy (MPRS), 110–14  
   and hot luminescence, 111–12  
   and lattice relaxation model, 111  
   and polarizability model, 110–11  
   two-phonon Raman scattering, 114  
   *see also* multiple-phonon (MP) Raman spectra  
 multi-quantum wells (MQWs)  
   enhancement of Raman scattering intensity, 361–7  
   resonant Raman spectra, 361–7  
 multiple slits interference factor, 66  
 multi-walled carbon nanotubes (MWCNTs), 272, 350  
   abnormal anti-Stokes Raman scattering, 352  
   laser intensity effects in, 381–6  
   multiple-phonon Raman spectra of, 348  
 MWCNTs, *see* multi-walled carbon nanotubes  
 nanocarbons, 325–37  
   *see also* carbon nanostructures; carbon nanotubes (CNTs); graphene; fullerenes  
 nanodiamond  
   characteristic Raman spectra of, 325–30  
   common features of characteristic Raman spectra, 329–30  
   prepared by CVD, 326–29  
   prepared by detonation, 325  
 nanomaterials (NMs), 264–83  
   artificial, 188–90  
   common Raman spectral features of, 264–6  
   natural, 188  
   nonpolar semiconductor small crystals, 267–8  
   polar semiconductor small crystals, 268–71  
   *see also* nanostructures  
 nanoparticles, 190  
 nanorods, 190  
 nanosemiconductors, 424–5  
   *see also* nonpolar nanosemiconductors; polar nanosemiconductors  
 nanosilicon  
   application of bulk phonon dispersion, 266  
   characteristic Raman spectra, 318–25  
   laser heating effect in, 323–5  
   origin of Raman spectra, 323–5  
   Raman frequency variations, 368–73, 397  
   slab model, 252  
   stress effect, 325  
   *see also* porous silicon (PS); silicon; silicon nanoparticles; silicon nanorods; silicon nanowires  
 nanostructures  
   abnormal Raman spectral features of, 309, 368–73, 419–20, 424  
   anti-Stokes Raman spectra, 352–7  
   characteristic length, 187–8  
   chemical properties of, 191  
   crystallography of, 191–2  
   defined, 187  
   dimension, 188  
   effects of changes in exciting laser intensity, 378–92  
   effects of changes in exciting laser polarization, 373–8  
   effects of changes in wavelength of light, 361–73

- nanostructures (*Continued*)  
 effects of impurities on Raman spectra, 414  
 effects of sample composition on Raman spectra, 413–14  
 effects of sample micro-structure on Raman spectra, 413–7  
 effects of sample shape on Raman spectra, 279–83, 409–13  
 effects of sample size on Raman spectra, 382, 395–409  
 electron–phonon interactions in, 419–28  
 finite size effect, 192–95, 249, 296  
 history of study, 196  
 multiple-phonon Raman spectra of, 343–52  
 physical properties of, 190–91  
 polarized Raman spectra of, 373–4  
 specific surface effect, 192, 195  
 ways of studying, 196–7  
*see also* nanomaterials (NMs)
- nanotubes, 190
- nanowires, 190  
 shape effect of samples, 279–83  
 national security, 181–2  
 NC-Si, 293–95
- near-field (NF) optical microscope, 121, 126–30
- near-field (NF) optics, 121–124  
 techniques of, 124–6
- near-field (NF) Raman microscope, 126–30
- near-field (NF) Raman spectrometer, 126–30
- near-field (NF) scanning optical microscope (NSOM, SNOM), 122, 125–6
- near-field Raman spectroscopy (NFRS), 121–30, 164
- near-field spectrum, 5
- neutron scattering, 6
- Newton equation, 200, 204–8  
 of three-dimensional crystals, 213–14
- NF optics, *see* near-field (NF) optics
- NFRS, *see* near-field Raman spectroscopy
- NiSi, 162
- nitrogen, 141
- NLO, *see* nonlinear optics
- NLRS, *see* nonlinear Raman spectroscopy
- noise spectra, 88, 89  
 reducing, 90–93
- nonlinear optics (NLO), 136–7
- nonlinear Raman spectroscopy (NLRS), 137–8  
*see also* coherent anti-Stokes Raman scattering (CARS); stimulated Raman scattering (SRS)
- nonlinear spectrum, 5
- nonpolarized spectrum, 5
- nonpolar nanosemiconductors  
 effects of sample sizes on Raman spectra, 397  
 theoretical Raman spectra of, 424–6
- nonpolar semiconductor slab model, 251–3
- nonpolar semiconductor small crystals, 267–8
- nonvisible excited Raman spectroscopy, 106
- nonvisible spectrum, 5
- NSOM, *see* near-field (NF) scanning optical microscope
- nuclear/shell structures nanoparticles, 415
- nucleotides, 167
- Nyquist-theorem approach, 268
- olivine, 175
- omega-3 fatty acids, 149–50
- one-dimensional double atom chain, 204–9
- optical effects, 3–4
- optical filters, 62
- optical lattice wave, 209
- optical path, 63  
 design of, 77–8  
 improvement of, 86–7
- optical phonon modes, 279–81, 310, 313–5, 343, 396, 411–12
- optical spectrum, *see* spectrum
- organic molecules, 167–71
- oxygen, 142
- particle collision model, 21, 245
- P-CARS, *see* polarized CARS
- PDOS, *see* phonon density of state
- pesticides, 179
- pharmaceutical industry, 179
- pharmacology, 174
- phase transition, 161–2
- phonon density of state (PDOS)  
 amorphous crystals, 229–30, 241–2, 297–8  
 molecular dynamic calculations of, 302–6  
 single walled carbon nanotubes, 278  
 and two-phonon Raman spectrum, 114
- phonons, 8, 155, 199, 209–10  
*ab initio* calculation of dispersion relation, 298–302  
*see also* folded acoustic phonon modes; interface phonon modes, optical phonon modes; electron–phonon interactions
- photolithography, 189–90
- photomultiplier tube (PMT), 72–74, 85

- photon scattering, 7  
 piezoelectric effect, 211  
 plasma lines, 60  
*PMT, see* photomultiplier tube  
 Pockels effect, 137  
 polariton, 229  
 polarizability tensor, 27–8, 30, 38, 51, 111  
 polarization, 10, 29–30, 38  
     macroscopic, 29–30, 236  
     microscopic, 29  
 polarization effects, 75–7, 78  
 polarization selection rule, 10, 51–52, 232, 378, 449–51  
     effect of sample size on, 406–9  
 polarized CARS (P-CARS), 140, 173  
 polarized Raman spectra, 49–52, 115–16  
     intensity expression of, 50  
     of carbon nanotubes, 375–8  
     of superlattices/quantum wells, 373–4  
     of ZnSe nanobelts, 375–8  
 polarized spectrum, 5  
     *see also* polarized Raman spectra  
 polar nanosemiconductors  
     characteristic Raman spectra of, 337–43  
     effects of sample sizes on Raman spectra, 396–401  
     multiple-phonon Raman spectra of, 343–52  
     quantum confinement effect in, 370, 396  
     Raman frequency variations, 371–373  
     theoretical Raman spectra of, 424–26  
 poly-2,5-bis(p-methoxybenzoyloxy)  
     styrene, 158–8  
 polychromators, 71  
 polydiacetylene nanocrystal, 130  
 porous silicon (PS)  
     characteristic Raman spectra of, 318–20  
     corrected identification of Raman spectrum, 319–20  
     earliest Raman spectra of, 318  
     multiple-phonon Raman spectra of, 347–8  
     Raman frequency variations, 368  
     residual crystalline silicon in, 318, 320  
 potential well, 192–94  
 powder samples, 86  
 probes, 60, 132–133  
 PS, *see* porous silicon  
 pump-probe techniques, 117  
 pyridine, 119, 120  
 QCE, *see* quantum confinement effect  
 quantized field theory, 39  
 quantum confinement effect (QCE), 192–94, 196, 370, 396, 419–20  
 quantum confinement theory, 196  
 quantum dots, 189–90, 420, 422  
 quantum transition probability, 39–9  
 quantum wells (QWs), 189, 190–91  
     confined optical phonon mode, 313–15  
     polarized Raman spectra of, 373–4  
     *see also* multi-quantum wells (MQWs)  
 quantum well wires, 279–83  
 quantum wires, 189–90, 279–83  
 quartz, 175  
 quasi-particles, 8  
 QWs, *see* quantum wells  
 radial breathing mode (RBM), 279, 334  
 rainbow, 3  
 Raman, C.V., 10–13  
 Raman activity, 32–34, 232  
 Ramanathan, K.R., 12  
 Raman frequency, 9–10  
 Raman optical activity (ROA), 54, 116  
 Raman optical microscope, 62–63  
 Raman scattering, 8–9  
     discovery of, 10–13  
 Raman selection rule, 33, 232  
 Raman shift, *see* Raman frequency  
 Raman spectra  
     basic features of, 9–10  
     characteristic, 309  
     and energy of excitation sources, 48–9  
     first, 13  
     and momentum of incident and scattered light, 49  
     and polarization of incident and scattered light, 49–50  
     routine, 309  
     *see also* polarized Raman spectra  
 Raman spectral measurements, 47–55  
     technological problems, 54, 128  
     *see also* Raman spectrometer; spectral data processing  
 Raman spectrometer, 56–79  
     adjustment of, 83–5  
     amendment of spectral intensity, 78–9  
     angular dispersion, 69, 70, 80  
     apertureless, 128–9  
     apparatus control, 74

- Raman spectrometer (*Continued*)  
 chromatic resolution rate, 81  
 collection of scattered light, 62  
 collimator, 65  
 confocal optical path, 63  
 converging lens, 65  
 design of, 77–9  
 environments of measured samples, 63  
 factors related to geometric optics, 74–5  
 factors related to physical optics, 75–7  
 gratings, 65–9, 87  
 illumination of excitation light, 60–2  
 improvement of optical path, 86–7  
 intensity dispersion of, 78, 90  
 layout of, 55–6  
 light source part, 56–9  
 line dispersive rate, 80–1  
 near-field, 126–30  
 performance parameters, 79–83  
 reading, 82  
 sample optics part, 59–63, 83–4, 86  
 sample preparation, 85–6  
 scanning parameters, 87–8  
 slits, 64–5, 82, 88  
 spectral acquisition part, 71–74  
 spectral dispersion part, 63–71, 84–5  
 spectral resolution rate, 80–82  
 use of optical microscope with, 62–3  
*see also* spectral data processing
- Raman spectroscope, 119
- Raman spectroscopy, historical  
 development, 13–16
- Raman tensors, 116, 232
- Rayleigh criterion, 80
- Rayleigh scattering, 8–9, 31, 38, 44, 92
- Rayleigh’s Law, 7
- RBM, *see* radial breathing mode
- real spectra, 88
- reflecting grating, 68
- resonant Raman scattering (RRS), 106–110, 361–73  
 application, 107–8  
 in carbon nanotubes, 365–6  
 enhancement of Raman scattering  
 intensity, 361–7  
 incoming and outgoing resonances, 108  
 in multi-quantum wells, 362–5  
 and Raman frequency variations, 368–73  
 in SiC nanorods, 366–7  
 in superlattices, 362–5
- resonant size selection effect (RSSE), 369, 370–72, 395, 400
- resonant size-selection Raman scattering, 108
- RNA, 168
- ROA, *see* Raman optical activity
- RRS, *see* resonant Raman spectroscopy
- RSSE, *see* resonance size selection effect
- ruby crystal, 160
- Rutherford, E., 6
- RWL model, 283–6
- scanning near-field optical microscope (SNOM),  
*see* near-field (NF) scanning optical microscope (NSOM, SNOM)
- scanning tunnel microscope (STM), 125
- scattered circular polarization (SCP), 54
- scattering, 5–7  
 anti-Stokes, 43–4  
 atomic light, 8  
 Brillouin, 8–9, 19  
 combination, 12  
 Compton, 8, 12, 32  
 elastic, 9, 21  
 electron, 6, 8  
 gamma ray, 7  
 inelastic, 8–9, 21  
 Mie, 8  
 molecular, 7, 8  
 neutron, 6  
 photon, 6  
 Raman, 8–9  
 Rayleigh, 8–9, 31, 38, 43–4  
 solid light, 8  
 spin, 8  
 Stokes, 43–4  
 Thomson, 8, 32  
 Tyndall, 7–8  
 X-ray, 7  
*see also* light scattering; scattering experiments
- scattering cross section, 22–24  
 classical expression of, 24  
 quantum physical expression of, 24–6
- scattering experiments, 6, 20–21
- scattering probability, 21–22
- Schrödinger equation, 200, 201–2  
 and *ab initio* calculations, 298, 299  
 time-dependent, 40–41
- SC model, *see* spatial correlation (SC) model
- SCP, *see* scattered circular polarization

- semiconductor industry, 179–180  
 SERS, *see* surface-enhanced Raman spectroscopy  
 shell model, 216–17  
 short-period-superlattice multiple-quantum wells (SPSL-MQWs), 406  
**SiC**  
 PDOS of, 296  
 simulation of Raman spectra, 426–7  
*see also* SiC nanorods; SiC nanowires  
**SiC nanorods**, 92  
 characteristic Raman spectra of, 337–43  
 crystallographic property and sizes, 336  
 enhancement of Raman scattering intensity, 366–7  
 resonant Raman spectra, 366  
**SiC nanowires**, 369–71  
**Si/Ge**, 300, 311  
**silicon**  
 amorphous, 160, 229, 241–2  
 crystalline, 160, 242, 243, 369  
 dispersion curves of, 155  
 NF Raman spectroscopy of, 130  
 PDOS of, 296  
 phonon dispersion curves, 220–22  
 simulation of Raman spectra, 417  
 stress measurement, 162–163  
*see also* nanosilicon; porous silicon (PS); silicon nanocrystals; silicon nanoparticles; silicon nanowires  
 silicon nanocrystals, 320–22  
 silicon nanoparticles,  
   PDOS calculation, 302–3  
   in solar cells, 191  
   theoretical Raman spectra, 424, 425  
 silicon nanowires, 292  
   *ab initio* calculations, 299  
   characteristic Raman spectra of, 320–22  
   laser heating effect, 323–25  
   optical phonons in, 320  
   Raman frequency variations, 368  
   size and laser intensity effect, 381  
   theoretical calculation of Raman spectrum, 322–23  
**Si<sub>3</sub>N<sub>4</sub>**, 162–4  
 single electron approximation, *see* mean field approximation  
 single electron theory, 202, 210  
 single-phonon Raman scattering, 111  
 single slit diffraction factor, 66, 68  
 single spectrum, 5  
 single-walled carbon nanotubes (SWCNTs), 190, 272–79  
 abnormal anti-Stokes Raman scattering in, 352–4  
 characteristic Raman spectra of, 333–6  
 high-pressure Raman spectra of, 414–7  
 laser intensity effects, 378, 379–81  
 NF Raman spectroscopy, 165  
 phonon dispersion relations, 276–9  
 purification by laser irradiation, 389–92  
 structure of, 273–75  
 TERS spectra, 165  
 types of, 276  
 size confinement effect, 279  
*see also* finite size effect  
 slab model, 251–53  
 slits, 64–5, 82, 88  
 SLs, *see* superlattices  
 small crystals  
   nonpolar semiconductor, 267–8  
   polar semiconductor, 268–71  
**Smekal, A.**, 19  
**z-Sn**, 220  
**SNOM**, *see* near-field (NF) scanning optical microscope  
 solar cells, 191  
 solid light scattering, 8  
 solids, 199–246  
   amorphous, 199  
   conditions of occurrence of Raman scattering, 230–2  
   crystal symmetry, 232  
   crystalline, 199  
   dielectric fluctuation correlation model, 236–41  
   electron–phonon interactions, 210–13  
   lattice dynamics, 200–230  
   macroscopic model of lattice dynamics, 213, 222–29  
   microscopic model of lattice dynamics, 213–22  
   microstructure and symmetry, 160, 200  
   quantum mechanics theory of Raman scattering, 234–6  
   Raman scattering theories, 230–46  
*see also* condensed matter  
 space-resolved Raman spectroscopy, 118–19  
 spatial correlation (SC) model, 285  
 specific surface effect, 192, 195

- spectral data processing, 88–93  
 acquisition of spectral parameters, 93  
 correction of intensity dispersion, 90  
 deduction methods, 91–93  
 fitting, 90–1, 93  
 reduction of noise spectra, 90–93  
 smoothing, 90–1  
 spectra from environment, 89–90  
 spectra from sample, 89  
 spectra from spectrometer, 88–9
- spectrum  
 classification based on optical effects, 3–4  
 classification based on spectral parameters, 4–5  
 defined, 3  
 far-field, 5  
 frequency, 5  
 image, 6  
 linear, 5  
 multi-order, 5  
 near-field, 6  
 nonlinear, 5  
 nonpolarized, 5  
 nonvisible, 5  
 polarized, 5  
 single, 5  
 spontaneous, 5  
 steady state, 5  
 stimulated, 5  
 transient (time resolved), 5  
 visible, 5  
*see also* Raman spectra  
 spin scattering, 8  
 spontaneous spectrum, 5  
 SPSL-MQWs, *see* short-period-superlattice  
 multiple-quantum wells  
 SRL microscope, *see* stimulated Raman Lose (SRL) microscope  
 SRS, *see* stimulated Raman scattering  
 standard spectral lines, 84–5  
 static electricity equation, 226, 257  
 steady state spectrum, 5  
 stimulated Raman Lose (SRL)  
 microscope, 149–50  
 stimulated Raman scattering (SRS), 145–50  
 microscopy, 148–50  
 principle and features, 145–6  
 spectroscopy, 146–8  
 stimulated spectrum, 5
- STM, *see* scanning tunnel microscope  
 Stokes frequency, 9–10  
 Stokes scattering, 43–4  
 stray light, 62, 83  
 stress  
 in nanosilicon, 325  
 measurement of, 162–163  
 substrate effect, 135  
 sunflower oil margarine, 180  
 superlattices (SLs), 189, 191–2, 250–64  
 AB/BC type, 258–9  
 AB/CD type, 260–1  
 bond charge linear chain model, 262–4  
 characteristic Raman spectra of, 310–18  
 dielectric continuous model, 256–8  
 effects of sample shapes on Raman spectra, 396, 409–13  
 effects of sample sizes on Raman spectra, 396  
 elastic continuum model, 254–256  
 enhancement of Raman scattering  
 intensity, 361–7  
 folded acoustic phonon modes, 311–13, 396, 410–11  
 geometrical parameters of, 409–10  
 Huang–Zhu model, 262  
 interface phonon modes, 310, 315–18  
 ion crystal slab model, 253–4  
 lattice dynamic models, 254–64  
 linear chain model, 258–61  
 multiple-phonon Raman spectra of, 344–7  
 nonpolar semiconductor slab model, 251–3  
 optical phonon modes, 310, 313–15, 344–5, 396, 411–12  
 polarized Raman spectra of, 373–4  
 potential shapes of, 409  
 resonant Raman spectra, 362–5  
 surface-enhanced Raman spectroscopy (SERS), 86, 119–21  
 biological sample measurements, 166–8  
 DNA measurement, 166  
 enhancement mechanism of, 120–21, 134, 135  
 micro-optical fluidic system, 167  
 sample substrates in, 120  
 single nucleotide measurement, 167  
 surface vibration mode, 254  
 SWCNTs, *see* single-walled carbon nanotubes  
 symmetric operations, 95  
 symmetry, 33–4, 232  
 Synge, E.H. 125

- TaC nanorods, 367  
 Taylor expansion, 30, 111, 202  
 temperature, 115, 379–81, 414  
*see also* high temperature Raman spectroscopy; lasers, heating effect  
 TERS, *see* tip-enhanced Raman spectroscopy  
 Thomson scattering, 8, 32  
 three-dimensional crystals, 213–14  
 time-dependent perturbation theory, 41  
 time-dependent Schrodinger equation, 40–1  
 time-resolved CARS, 140  
 time resolved Raman spectroscopy (TRRS), 116–18  
     development and application of, 118  
     technology of, 116–18  
 $\text{TiO}_2$ , 415  
 tip-enhanced Raman spectroscopy (TERS), 130–36  
     enhancement mechanism of, 134–6  
     instrument development, 132–134  
     studies of biological samples, 168  
     studies of DNA, 168  
     studies of single wall carbon nanotubes, 165  
     theoretical basis, 132–34  
 tobacco mosaic virus, 168, 170  
 transient spectrum, 6  
 translation symmetry, 194–195, 427–28  
 TRRS, *see* time resolved Raman spectroscopy  
 Tu686 cells, 170, 171  
 two-phonon continuous spectrum, 114  
 two-phonon line spectrum, 113–14  
 two-phonon Raman scattering, 112–13  
     and phonon density of state (PDOS), 114  
 Tyndall scattering, 7–8  
 uncertainty principle, 48, 285  
     and momentum diffusion, 195  
 valence force field model, 218  
 VDOS, *see* vibration density of state  
*Vibrational Spectra and Structure of Polyatomic Molecules*, 14  
 vibration density of state (VDOS), 242–46  
 visible spectrum, 5  
 wave selection rule, 320  
 Wu, Ta-You, 14  
 X-ray scattering, 7, 48  
 $\text{YBaCu}_x\text{O}_{7-x}$ , 215–16  
 ZnO  
     effect of different geometric configurations, 232, 233  
     effect of different pressure, 114, 115  
     simulation of Raman spectra, 426–27  
*see also* ZnO crystals; ZnO nanoparticles  
 ZnO crystals, 51  
 ZnO nanoparticles, 92, 93, 190, 340  
     characteristic Raman spectra of, 340  
     crystallographic property and sizes, 340  
     multiple-phonon Raman spectra of, 348–50  
     PDOS calculation, 302  
     quantum confinement effect, 399–402  
     Raman frequency variations, 371–2  
     theoretical Raman spectra, 424–6  
 ZnSe nanobelts, 376  
 ZnSe nanowires, 362, 376, 378  
 zone folding method, 277  
 $\text{ZrO}_2$ , 106, 115, 116